Searching for traces of life in a Mars analogue rock : The Kitty's Gap Chert

Laura Clodoré

UNIVERSITÉ D'ORLÉANS

ÉCOLE DOCTORALE SANTÉ, SCIENCES BIOLOGIQUES ET CHIMIE DU VIVANT

CENTRE DE BIOPHYSIQUE MOLÉCULAIRE

THÈSE présentée par :

Laura CLODORÉ

soutenue le : **12 décembre 2023**

pour obtenir le grade de : **Docteur de l'Université d'Orléans**
Discipline/ Spécialité : Géologie/ Exobiologie

À la recherche de traces de vie dans une roche analogue de Mars : le chert de Kitty's Gap

THÈSE dirigée par :

Mme WESTALL Frances	Directrice de recherche émérite, CNRS-CBM, Orléans
M. FOUCHER Frédéric	Ingénieur de recherche, CNRS-CEMHTI, Orléans

RAPPORTEURS :

M. van Zuilen Mark	Chargé de recherche, CNRS-Laboratoire Geo-Ocean, Plouzané
Mme STUEEKEN Eva Elisabeth	Maître de conférence, School of Earth & Environmental Sciences, St Andrews, United Kingdom

---

JURY :

M. MOREIRA Manuel	Professeur, Université d'Orléans, CNRS-ISTO, Orléans, Président du jury
M. van Zuilen Mark	Directeur de recherche, CNRS-Laboratoire Geo-Ocean, Plouzané
Mme STUEEKEN Eva Elisabeth	Maître de conférence, School of Earth & Environmental Sciences, St Andrews, United Kingdom
M. BONTOGNALI Tomaso	Chargé de recherche, Space Exploration Institute, Neuchâtel, Suisse
M. MUSTIN Christian	Directeur de recherche, CNES, Paris
M. BRÉHÉRET Jean-Gabriel	Professeur émérite, Université de Tours, Laboratoire GéoHydrosystèmes Continentaux (GeHCO), Tours
Mme WESTALL Frances	Directrice de recherche émérite, CNRS-CBM Orléans
M. FOUCHER Frédéric	Ingénieur de recherche, CNRS-CEMHTI, Orléans

À mon père

Remerciements

Je tiens d'abord à remercier le Centre National d'Études Spatiales (CNES) et l'Université d'Orléans pour le financement de cette thèse, ainsi que le Synchrotron SOLEIL et Europlanet Society pour leurs subventions m'ayant permis d'accéder à différents équipements de laboratoire.

Je souhaite remercier Eva Jakab-Toth, ancienne directrice du Centre de Biophysique Moléculaire et Matthieu Réfrégiers, l'actuel directeur, pour m'avoir permis d'effectuer ma thèse de doctorat dans les meilleures conditions au sein de leur laboratoire. Je remercie en particulier Matthieu pour sa bienveillance et l'aide qu'il m'a apportée tout au long de cette thèse, notamment en m'orientant vers l'utilisation de différentes lignes de lumière au Synchrotron et les possibilités de carrière après la thèse.

Je remercie chaleureusement ma directrice de thèse, Frances Westall, et mon co-directeur de thèse, Frédéric Foucher, sans qui cette thèse n'aurait jamais vu le jour. Tous deux m'ont transmis leur passion pour la recherche, ainsi que l'envie d'en apprendre toujours plus. Leur complémentarité a contribué au déroulement de cette thèse dans des conditions optimales. Frances m'a aidé à alimenter mon intérêt et mes connaissances pour la géologie martienne et l'exploration spatiale et m'a toujours encouragé à chaque étape de mon projet. Frédéric m'a appris à avoir un esprit critique, à rédiger des résultats scientifiques de façon claire et rigoureuse et m'a aussi formé à la spectroscopie Raman. Enfin, je les remercie également pour m'avoir poussé à participer de nombreuses conférences internationales où j'ai pu m'exprimer en anglais devant une audience nombreuse et où j'ai pu rencontrer des personnes venant de différents horizons et travaillant dans diverses disciplines liées à l'exobiologie.

Je remercie les membres du jury, Mark van Zuilen et Eva Elisabeth Stueeken pour avoir accepté d'être les rapporteurs de mon travail de thèse, ainsi que Manuel Moreira, Tomaso Bontognali, Christian Mustin et Jean-Gabriel Bréhéret pour avoir accepté d'examiner ce travail.

Je souhaite remercier particulièrement Keyron Hickman-Lewis, ancien doctorant de Frances Westall et « consultant scientifique » de ma thèse, qui m'a donné de précieux conseils tout au long de ces trois dernières années, qui m'a permis d'utiliser certains instruments du muséum d'histoires naturelles de Londres et qui a contribué significativement à mes travaux de thèse. Je le remercie également pour m'avoir accompagné à mon tout premier congrès aux États-Unis.

Je souhaite évidemment remercier les membres de l'équipe d'Exobiologie du CBM : Pamela Guerillot, Tetyana Milojevic, Denise Koelbl et Sebastian Gfellner pour les discussions intéressantes et les bons moments que nous avons passés ensemble lors de nos excursions à Orléans, à Châteauneuf-sur-Loire et au château d'Artigny. Je remercie spécialement Pamela, doctorante, qui est devenue une véritable amie et confidente au cours de ma deuxième moitié de thèse, qui m'a apporté ses lumières sur le monde fascinant de la microbiologie et avec qui j'ai apprécié faire des pauses pour jouer à la crapette.

Je souhaite remercier les autres doctorants et stagiaires de passage dans l'équipe d'Exobiologie : Bérénice, Romain, Sofia, Julian qui a eu la lourde tâche de m'aider dans les analyses des échantillons au cours de son stage, Michaela et Rebecca pour avoir été pour la plupart mes

compagnons de bureau et dont les discussions enrichissantes ont contribué à améliorer mon expérience du doctorat.

Je souhaite aussi remercie les personnes qui ont contribué directement et indirectement à mes travaux de thèse : Sylvain Janiec et Cédric Demeurie pour la préparation des lames minces, David Troadec pour la préparation des coupes FIB, ainsi que les personnes en charge des instruments que j'ai utilisés, Stéphanie Sorieul, Jean Jouve, Ida di Carlo, Bernard Gratuze, Virginie Bazin, Hélène Lecoq, Guillaume Collet, Stéphane Petoud, Frédéric Jamme, Wren Montgomery, Solenn Réguer, Audrey Saulduboiset Fabienne Warmont. Je remercie également Thierry Sauvage pour m'avoir gentiment prêté de précieux standards et pour les discussions pertinentes sur le PIXE.

Je remercie également l'ensemble des accompagnants administratifs et notamment Christine Gabant pour m'avoir aidé pour mes nombreux ordres de mission. Je remercie aussi l'informaticien du labo, Alain Boyer, qui a installé tous les logiciels dont j'avais besoin pour traiter mes données.

Enfin, je remercie les doctorants qui ont participé à la formation et au concours Ma thèse en 180 secondes à Orléans avec moi pour la session 2022 : Samuel, Timothée, Manon, Julien, Nafissa, Vanessa et Malek, et avec qui j'ai vécu une aventure hors du commun au cours de laquelle j'ai appris à vulgariser mon sujet de thèse et à être plus à l'aise pour m'exprimer en public. Je remercie tout particulièrement nos formidables formateurs : Quentin et Gaëlle, pour nous avoir transmis leur savoir avec patience et efficacité et nous avoir appris à prendre confiance en nous.

Je souhaite remercier Florent, mon compagnon, pour avoir supporté mes longs monologues sur mon sujet de thèse et l'exobiologie en générale, et dont le soutien infaillible m'aura permis de mener à terme ce projet.

Pour terminer, je remercie ma famille et en particulier ma maman qui m'a toujours soutenu tout au long de mes années d'étude et qui m'a transmis son courage et sa persévérance pour atteindre tous les objectifs que je me suis fixés. Merci pour avoir cru en moi !

Foreword

The list of abbreviations used in this thesis manuscript for English words and French research organizations/laboratories/platforms is reported below:

a	anatase
Abs	absorbance
ADF	annular dark field
AIFIRA	Applications Interdisciplinaires de Faisceaux d'Ions en Région Aquitaine
ALD	analytical laboratory drawer
APXS	Alpha-Particle X-ray Spectrometer
BIF	banded iron formations
BSE	backscattered electrons
c	crust
C	cells
CBM	Centre de Biophysique Moléculaire
CCD	charge coupled device
CENBG	Centre d'Etudes Nucléaires de Bordeaux-Gradignan
ChemCam	Chemistry & Camera
CheMin	Chemistry & Mineralogy
CLUPI	Close-UP Imager
C_M	mass concentration
CM	carbonaceous matter
CNRS	Centre National de la Recherche Scientifique
COSPAR	Committee on Space Research
CRISM	Compact Reconnaissance Imaging Spectrometer for Mars
CRPG	Centre de Recherches Pétrographiques et Géochimiques
cs	coarse silt
cts	counts
D1	disordered (Raman band)
D2	disordered (Raman band)
DISCO	Dichroism, Imaging and mass Spectrometry for Chemical and biOlogical systems
DUV	deep-ultraviolet
EDX	energy-dispersive X-ray
EF	enrichment factor
EPS	extracellular polymeric substances
ERO	Earth Return Orbiter
f	feldspar
FIB	focused ion beam
FTIR	Fourier-transform infrared
FWHM	full width at half maximum
G	graphite (Raman band)
Ga	billion years (a point in time)
GC-MS	gas chromatograph-mass spectrometry
H	hydromuscovite
HIM	helium ion microscopy
HiRISE	High Resolution Imaging Science Experiment
HREE	heavy rare-earth element
HR-TEM	high-resolution transmission electron microscopy
HWM	high water mark
I	intensity

ICMN	Interface, Confinement, Matériaux et Nanostructures
ICP-AES	inductively coupled plasma atomic emission spectrometry
ICP-MS	inductively coupled plasma mass spectrometry
ICP-OES	inductively coupled plasma optical emission spectrometry
IDPs	interplanetary dust particles
IEMN	Institut d'Electronique, de Microélectronique et de Nanotechnologie
IF	iron formations
IR	infrared
IRAMAT	Institut de Recherche sur les ArchéoMATériaux
ISAR	International Space Analogue Rockstore
ISEM	Infrared Spectrometer for ExoMars
ISM	interstellar medium
ISSOL	International Society for the Study of the Origin of Life
ISTO	Institut des Sciences de la Terre d'Orléans
KB	Kirkpatrick-Baez
KG-vsc.	Kitty's Gap volcano-sedimentary complex
LA-ICP-MS	laser ablation inductively coupled plasma mass spectrometry
LD	laser desorption
LIBS	laser induced breakdown spectroscopy
LOD	limit of detection
LREE	light rare-earth element
LWM	low water mark
M	molar mass
m	number of atoms of oxygen
Ma	million years (a point in time)
Ma_MISS	Mars Multispectral Imager for Subsurface Studies
MACLE	Microscopie, imAgeries et ressourCes anaLytiquEs
MAHLI	Mars Hand Lens Imager
MAV	Mars Ascent Vehicle
MER	Mars Exploration Rover
MicrOmega	Micro Observatoire pour la minéralogie, l'eau, les glaces et l'activité
MISS	Microbially Induced Sedimentary Structures
MOMA	Mars Organic Molecule Analyzer
MREE	middle rare-earth element
MRO	Mars Reconnaissance Orbiter
MSL	Mars Science Laboratory
MSR	Mars Sample Return
MuQ	Mud from Queensland
MVRF	multiphase volcanic rock fragment
Myr	million years (duration)
n	number of atoms of a chemical element
N/A	non-applicable
NIST	National Institute of Standards & Technology
nM	nanomoles per liter
OMEGA	Observatoire pour la Minéralogie, l'Eau, les Glaces et l'Activité
OS	Orbiting Sample
PAH	polycyclic aromatic hydrocarbon
pH	potential of hydrogen
PIXE	proton-induced X-ray emission
PIXL	Planetary Instrument for X-ray Lithochemistry
Q	quartz
R^2	coefficient of determination

RBS	Rutherford Backscattering Spectrometry
REE	rare-earth element
RGB	red, green, blue
RLS	Raman Laser Spectrometer
ROI	region of interest
SAM	Sample Analysis at Mars
SCS	sampling and caching subsystem
SDD	silicon drift detector
SE	secondary electrons
SEM	scanning electron microscopy
SHERLOC	Scanning Habitable Environments with Raman and Luminescence for Organics and Chemicals
SRF	Sample Receiving Facility
SRL	Sample Retrieval Lander
SRP	Sample Receiving Project
STEM	scanning transmission electron microscopy
TEM	transmission electron microscopy
TLS	tunable laser spectroscopy
TTG	Tonalites, Trondhjemites, Granodiorites
TV	thermal volatilization
vc	very coarse sand
VISIR	visible and infrared spectroscopy
VNIR	visible and near-infrared
X	chemical element
X_nO_m	oxide
XRF	X-ray fluorescence

Table of contents

Summary of Figures

Chapter I:

Chapter II:

Chapter III:

Chapter IV:

Summary of Tables

Chapter II:

Chapter III:

Chapter IV:

Chapter V:

Chapter I: State of the art

I. Introduction

This manuscript described my thesis work carried at the CNRS in Orléans, in the exobiology team at the Centre de Biophysique Moléculaire (CBM) between November 2020 and September 2023. This opening chapter therefore begins with the definition of "exobiology". I then pass onto the geological context in which the first life forms could emerge on the primitive Earth, from the Hadean eon (4.54–4.0 Ga) to the Paleoarchean era (3.6–3.2 Ga), before looking at the conditions that allowed the emergence of life and the possible locations where it took place.

It continues with a discussion on the formation and preservation of microbial fossils through the geological record, as well as the description of the oldest traces of terrestrial fossil life found to date. On Earth, the earliest fossil records have been destroyed due to plate recycling and erosional mechanisms. The oldest rocks still present on Earth have also been subjected to metamorphism that has degraded the possible traces of life they may have contained. In addition, most of the fossils found in rocks dating from the Precambrian (<2.5 Ga) are microscopic. The detection and identification of the most ancient traces of life are thus particularly delicate. The successful interpretation of putative traces of life is based on multiple physico-chemical characteristics that increase the probability of a biological origin (i.e., biosignatures) and require the use of numerous analytical methods.

The question of the possible appearance of life on Mars and of its possible detection is then raised. If Earth and Mars had very different fates, they were relatively similar more than ca. 3.8 Ga, with the presence of liquid water at the surface in particular. After 4.0–3.5 Ga, Mars lost most of its atmosphere and consequently liquid water at its surface.

Similar local conditions on early Earth and Mars indicate that early Martian traces of life may have been similar to their terrestrial counterparts. However, due to the degradation of the surface conditions after the Hesperian, the supposed traces of life expected on Mars are either in the form of fossils preserved in the rocks, or in dormant or active forms still living in the subsurface. The possibility of biomolecule preservation in the subsurface is also discussed.

Current and future missions to Mars aim to explore the habitability of paleoenvironments to establish whether the conditions could have supported the appearance and development of life, as well as looking for evidence of traces of current or past life preserved in the rocks. A sample return mission will also allow analysis of Martian rocks with the latest advanced technologies in terrestrial laboratories in the 2030s.

The objective of my thesis was to use a combination of different complementary techniques in order to maximize the detection of fossil traces of life and their associated biosignatures in early terrestrial rocks, then to use these results to optimize the protocols that will be used to search for life in situ on Mars and in returned samples.

II. Exobiology

A. Origin, definition

The term “exobiology” was introduced in the 1960s by an American geneticist and microbiologist, Joshua Lederberg, in his article entitled “Approaches to Life beyond the Earth” (Lederberg, 1960). He worked in particular with the COSPAR (Committee on Space Research) to establish protocols for the sterilization of spacecraft in the context of the preparation of lunar and planetary missions. Initially, exobiology designated the field devoted to the study of life in extraterrestrial conditions and then became a more extensive science that included the study of the origin, distribution and evolution of life in the Universe, as well as the processes and structures related to living (Raulin, 2008). The first missions dedicated to the search for traces of life were the Viking 1 and Viking 2 missions which sent two probes to Mars in 1975 in order to conduct experiments to detect signs of a biological activity in Martian regolith (Klein et al., 1976; Klein, 1979). At the same time, the astronomer Carl Sagan, who worked with Joshua Lederberg, was the first exobiologist to adopt a multi- and inter-disciplinary approach while making this new field known to the public through an excellent popularization activity, including many documentaries and books.

Exobiology (or Astrobiology, a term developed more recently, in the 1990s by NASA) brings together many disciplines such as physics, chemistry, biochemistry, biology, geology, geochemistry, planetology, humanities and social sciences, etc. However, the exobiological community has existed with prebiotic chemists such as Stanley Miller who showed that it is possible to obtain amino acids (i.e., molecules of interest for life) from simple compounds under conditions simulating the early Earth environment (Miller, 1955). In the 1970s, an international learned society which covered all areas related to the origin of life was created: ISSOL (International Society for the Study of the Origin of Life). ISSOL had an important French contribution, including the chemist André Brack who became its President in the 1990s and who created the Exobiology team at CBM in 1982.

B. The exobiology team activities (CBM)

The exobiology team is particularly interested in the origin of life and its evolution on Earth and elsewhere in the Universe. It addresses the theme of exobiology as a whole, from prebiotic chemistry to space exploration, including micro-paleontology. In particular, there are four types of activities focused on the search for traces of life on Mars, directly related to my thesis subject: analogues, methodology, micropaleontology and geo-microbiology. Analogue rock samples are terrestrial materials used to validate and optimize analysis protocols, test new instruments or even prepare for the future return of Martian samples planned for the 2030s (Bost, 2012; Bost et al., 2013, 2015; Foucher et al., 2021a). In particular, the team created the ISAR (International Space Analogue Rockstore) which brings together a collection of well-characterized rocks and minerals, including igneous rocks (basalt, komatiite, trachyte, rhyolite...), sediments (carbonates, hydrothermal chert...) and various minerals (apatite, calcite, gypsum, opal, rutile...), whose geochemical and mineralogical composition is representative of extraterrestrial bodies like Mars or the Moon. The development of methods and instrumentation for space exploration is also at the heart of the team's activities (Foucher et al., 2019, 2021b), in particular the development of methodologies to detect and identify fossil traces of life in situ and in the laboratory. Micropaleontology consists of studying the oldest fossil traces of life preserved in rocks dating back from the Archean (>3.3 Ga) (Westall et al., 2001, 2006a, 2006b, 2011a). Finally, geo-microbiology is concerned with the preservation of microbial biosignatures (Orange et al., 2009; Gaboyer et al., 2017), as well as the interactions between chemolithotrophic

microorganisms and minerals in order to study specific alteration textures and formation of minerals useful for the search for traces of life in ancient rocks or on Mars (Milojevic et al., 2019, 2021).

III. Study of fossil traces of life from early Earth

Before talking about the emergence of life on Earth and the formation and preservation of fossil traces of life, I will briefly review the geological history of the primitive Earth (4.54–3.2 billion years, Ga) which allows to contextualize the recording of the oldest traces of life.

A. Brief summary of the geological history of early Earth (4.54–3.2 Ga)

1. The Hadean eon (4.54–4.0 Ga):

The history of the primitive Earth during the first eon, the Hadean, is very little known due to the lack of preservation of the oldest crust owing to the destructive processes of plate tectonics, impacts and weathering and erosion mechanisms that continually reshape the surface of the planet. After planetary accretion (ca. 4.54 Ga), the Earth was constantly bombarded by asteroids and meteorites resulting from the formation of the solar system and was continuously heated by internal radioactivity coming both from the residual heat during the accretion and heat produced by radioactive elements (^{40}K, ^{235}U, ^{238}U, ^{232}Th), giving rise to a magmatic ocean where the outer part of the planet was completely melted (Arndt and Nisbet, 2012). During differentiation of the magmatic ocean, the heavy elements flowed towards the center of the planet while the light elements rose towards the surface, forming a metallic core and a silicate mantle, respectively. The Hf-W data suggest that differentiation took place very early, about 30 million years (Myr) after the end of the Earth accretion (Kleine et al., 2002). The crystallization of the core released even more heat and the liquid iron contained in the core created a magnetic field around the planet by dynamo effect, protecting the atmosphere of the planet from solar winds.

Several million years after its formation (ca. 4.51 Ga), it is thought that the Earth collided with a Mars-size protoplanet named Theia (Barboni et al., 2017), which caused the mixing of the outer layers of the two planets. The heaviest elements contributed to feed the core of the Earth, while the vaporized ejecta from the mantle of the projectile condensed to form the Moon (Sleep, 2010). The energy of the impact was so great that upper mantle rocks were completely vaporized, forming a photosphere that radiated its heat to space at a temperature of 2300 K (about 2000°C). The heat was evacuated from the mantle by convection movement in the photosphere, and after a thousand years, when the mantle was sufficiently cooled, the atmosphere was composed of a few hundred bars of H_2O, 100–200 bars of CO_2 and ca. 1 bar of other gas such as N_2 (Sleep, 2010).

Less than 150 Myr after the end of the Earth accretion (**Fig. I.1**), a first stable continental crust existed as evidenced by the presence of detrital zircons ($ZrSiO_4$) from the Jack Hills, Western Australia. The oldest zircon is dated around 4404 ± 8 million years (Ma), and shows a similar mineral composition (quartz, feldspars and micas) to those of modern granitoids that are the main components of the continents (Wilde et al., 2001). In addition, analyses of the oxygen isotopic signature, $\delta^{18}O$ (normalized $^{18}O/^{16}O$ ratio of sample to standard, the seawater), of zircons revealed the interaction of magma parent of zircon crystals with liquid water, suggesting the existence of liquid water oceans as early as 4.40–4.35 Ga (Wilde et al., 2001; Mojzsis et al., 2001; Cavosie et al., 2005). Indeed, the surface of the Earth reached a temperature of approximately 1300 K (about 1000°C) after a few million years, which

allowed the formation of a solid rim of basaltic composition separating the atmosphere from the hot interior (Pinti, 2005). When the Earth's surface was sufficiently cooled (about <600 K), atmospheric water vapor condensed to form oceans of liquid water (Pinti, 2005). Water was probably brought soon after the end of the Earth accretion by hydrated carbonaceous chondrites (carbon-rich meteorites) coming from the outer asteroid belt, as demonstrated by the isotopic ratio of hydrogen (deuterium/hydrogen) measured in modern seawater that is similar to the D/H ratio of water inclusions in carbonaceous chondrites (Morbidelli et al., 2000).

Figure I.1: *Artist's impression of the Hadean Eon (sourced from https://commons.wikimedia.org/wiki/File:Hadean.png).*

At that time, the Sun was about 30% less bright than today (Bahcall et al., 2001), which could have resulted in the planetary surface being covered with a thick layer of ice. However, it has been proposed that high concentrations of atmospheric greenhouse gases like CO_2 could have prevented the oceans from freezing, thereby maintaining a surface temperature of 500 K (about 230°C; Sleep, 2010). For the temperature to drop below 100°C and allow the appearance of life (the maximum temperature for survival of hyperthermophiles is from 80 to 110°C according to Rothschild and Mancinelli, 2001; or 120°C according to Clarke, 2014), a large part of the dissolved atmospheric CO_2 removed through crustal recycling after being adsorbed by the precipitation of calcium and magnesium carbonates (Shaw, 2008; Sleep, 2010).

The end of the Hadean eon occurred at 4.031 Ga, the age of the oldest rocks identified, the Acasta gneisses (Canada; Bowring and Williams, 1999; Iizuka et al., 2009). The Acasta gneisses, whose original rocks, the protoliths, are plutonic rocks resulting from the slow cooling of a magma (and have crystals visible to the naked eye, like granite), have been subject to many episodes of metamorphism after its formation.

To summarize, the conditions (in particular, liquid water and continental crust) necessary for the implementation of a prebiotic chemistry as well as for the appearance of life were potentially met less

than 150 Myr after the accretion of the planet, although habitability may have appeared somewhat later (Westall et al., 2023b).

2. The early Archean eon (4.0–3.2 Ga):

The Archean is the second geological eon which extends from 4.0 to 2.5 Ga and which is divided into four eras, which each lasts 300 to 400 million years. The period where the oldest traces of fossil life on Earth have been found, and which are presented in this section, extends from the Eoarchean (4.0–3.6 Ga) to the Paleoarchean (3.6–3.2 Ga).

The Archean terrains still cover a significant part of the planet today and form cratons, i.e., vast volumes of continental crust that have been stable for several billion years. Among these cratons, the oldest crop out in Canada, Greenland, South Africa and Australia. The oldest rocks from these cratons are dated to around 3.8 Ga. They are mostly old plutonic rocks, such as the Amîtsoq (West Greenland; Moorbath et al., 1977) and the Uivak (Canada; Hurst et al., 1975) gneisses dating respectively from ca. 3.7 and 3.6 Ga. There are also rocks of sedimentary and volcano-sedimentary origins such as the 3.8–3.7 Ga association of Isua supracrustal terranes (Polat and Hofmann, 2003) and Akilia Banded Iron Formations (or BIF; Nutman et al., 1997) in West Greenland, and the 4.3–3.7 Ga Nuvvuagtittuq supracrustal terranes in Canada (Cates and Mojzsis, 2007). The oldest terrains of continental dimension are the Kaapvaal (South Africa) and Pilbara (Australia) cratons which formed between ca. 3.6 and 3.1 Ga (Nelson et al., 1999). They are composed of three lithological units: 1) a granito-gneissic base of TTG (for Tonalites, Trondhjemites and Granodiorites) composition which represents about 80% of the volume of the cratons, 2) volcanic rocks and sediments known as greenstone belts, and 3) late granitoids which crosscut the first two formations (this last unit will not be described here; Laurent et al., 2014).

The TTG of these cratons are rocks similar to those of Acasta and Amîtsoq, having crystallized between 15 and 25 km deep, thus providing valuable information on the composition and internal structure of the Archean continental crust (Moyen and Martin, 2012). Indeed, these rocks are granitoids along with granites, a set of acidic igneous rocks (rich in silica), which constitute the Archean continental crust. The TTG were formed by the partial melting of a mafic oceanic crust (rich in iron, magnesium and calcium; Martin and Moyen, 2002), suggesting that plate tectonics may have been active as early as 3.8 Ga because the modern continental crust is formed following the subduction of an oceanic crust in the mantle. Nevertheless, recent studies (Moyen and Laurent, 2018) pointed out that the production of TTG did not necessarily require plate tectonics (the timing and origin of plate tectonics do not reach consensus today); and that they could have been produced by mantle plumes.

During the Archean, protocontinental crust was present, as attested by the presence of TTG. However, most of the continental rocks formed plateau-like structures that remained submerged, with little emergent landmass (Lowe and Byerly, 1999). Nevertheless, there are some indications of emerged lands, such as the presence of poorly sorted conglomerates indicative of flash floods in the Barberton Greenstone Belt (Lowe and Byerly, 2020).

Information about the conditions that prevailed on the surface of the planet in the Archean are provided by greenstone belts composed of volcano-sedimentary rocks that were deposited about 3.5 to 3.2 Ga (Hickman and Van Kranendonk, 2012), at relatively shallow water depths in depositional basins on top of protocontinents (i.e., above the TTG; Lowe and Byerly, 1999), the sedimentary successions forming thin layers between thick deposits of lavas. The volcanic rocks are mainly

komatiites, i.e., ultramafic lavas formed at high melting temperatures of the order of 1600–1650°C, indicating greater terrestrial heat production in the Archean mantle than today (Nisbet et al., 1987). Other rocks include mafic to acidic lavas (such as MgO-rich basalts and SiO_2-rich rhyolites, respectively) and sedimentary rocks (e.g., clays, sandstones, cherts, BIFs).

In addition to indications of a warmer mantle, protocontinents with emerged landmasses, the information delivered by the rocks gives us additional information on the conditions that reigned in the Archean. In particular, the sedimentary rocks reveal significant hydrothermal activity and a reducing atmosphere during this geological eon. The sedimentary rocks, as well as the underlying volcanics, have all been thoroughly silicified (from 86% up to 99%) and are therefore termed “cherts”. The Hadean-Paleoarchean oceans were supersatured in silica originating from hydrothermal fluids, surface weathering and devitrification of volcanic sediments in water (Westall et al., 2023a). The Paleoarchean sediments comprise volcaniclastics and volcanic ashfall, as well as biogenic and chemical precipitates, including BIFs, which consist of alternating centimetric bands rich in iron oxides and siliceous cherts resulting from the precipitation of iron and silica dissolved in water, testifying to the reducing nature of the atmosphere (iron is mobile only in its reduced form, Fe^{2+}; Pickard, 2003).

By 3.5 Ga, the temperature of the oceans was estimated from a cool 26°C (Hren et al., 2009; Blake et al., 2010) to ca. 50°C and up to ca. 70°C (Robert and Chaussidon, 2006; van den Boorn et al., 2010; Marin-Carbonne et al., 2012; Tartèse et al., 2016), based on oxygen, silicon and hydrogen isotopic signatures preserved in cherts, which fractionation depend on the temperature (for example, O_2 content decreases with increasing temperature; Robert and Chaussidon, 2006). The primitive atmosphere was composed of CO_2, H_2O and N_2, with small amount of CO and H_2, providing by the degassing of the magmatic ocean during Hadean and/or the contributions of extraterrestrial volatile elements by meteorites (Catling and Kasting, 2007; Stüeken et al., 2020). The pH of Archean oceans was probably variable, with alkaline conditions arising from weathering of mafic to ultramafic crust (Kempe and Degens, 1985; García-Ruiz et al., 2020) and acidic conditions from hydrogen-rich hydrothermal fluids and CO_2-rich atmosphere (Morse and Mackenzie, 1998; Catling and Zahnle, 2020). Recent studies suggest the pH of the early oceans was slightly acidic compared to today (Halevy and Bachan, 2017; Krissansen-Totton et al., 2018). The salinity of the Archean oceans was estimated to be similar to twice times the modern values (Knauth, 1998; Marty et al., 2018), and their composition in transition metals and metalloids essential for life (such as Fe, V, Ni, As and Co) was richer than today due to leaching of the mafic to ultramafic composition of the Archean continental crust (Hickman-Lewis et al., 2020c). However, certain transition metals would have been less soluble under anoxic conditions, such as Cu, Zn and Mo (Zerkle, 2005; Dupont et al., 2010; Rickaby, 2015; Robbins et al., 2016; Moore et al., 2017).

To summarize, the Archean landscape is composed of mostly submerged continents forming oceanic plateaus in the middle of potentially warm, anoxic (acidic) and metal-rich liquid water oceans (**Fig. I.2**). The reducing atmosphere and oceans could constitute environments that may be conducive to prebiotic organic synthesis and/or development of life before <4 Ga. However, at a global scale, the environment of early Earth is considered extreme and its microbial inhabitants were therefore necessarily extremophiles, i.e., organisms that can live in extreme conditions of temperature (thermophiles), pressure (piezophiles), salinity (halophiles), acidity (acidophiles), etc.

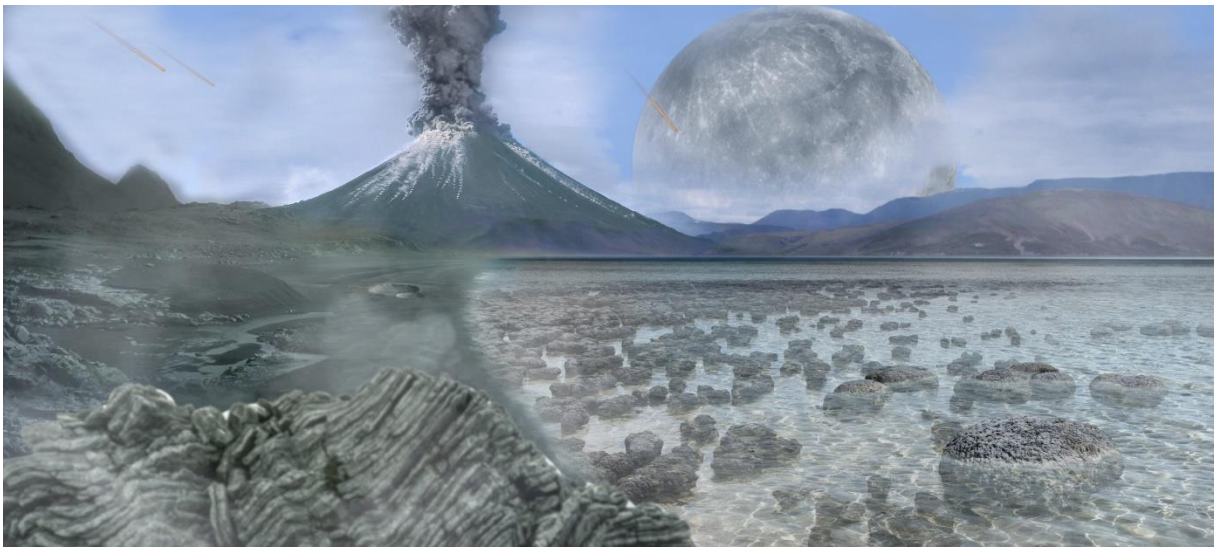

Figure I.2: *Artist's impression of the Archean Eon (sourced from https://commons.wikimedia.org/wiki/File:Archean.png).*

B. The appearance of life (4.3–4.0 Ga)

As described above, the conditions (liquid water, emerged continents, surface temperature) were met during the Hadean (between 4.4 and 4.2 Ga) for life to appear. However, it is difficult to establish today when the emergence of life took place or, in other words, how we passed from the non-living to the living matter. What we do know is that the physico-chemical and geological conditions are compatible with life from perhaps as early as 4.4 Ga but possibly later. In addition, the fossil record tells us that life was already established with certainty 3.5 Ga ago (oldest evidence of traces of life), and, by that date, had already differentiated. Moreover, there are indications of life in the 3.8–3.7 Ga Greenland rocks (Rosing, 1999; Hassenkam et al., 2017), and possibly in a 4.15 Ga zircon crystal as indicated by carbon isotope signatures (Bell et al., 2015). We are thus certain that life had to have emerged before 3.8 Ga and possibly before 4.15 Ga.

The first living organisms would have used the organic molecules formed on the primitive Earth in an abiotic way as a source of carbon and energy. But how were these organic molecules synthesized on the primitive Earth? What are the other conditions necessary for the emergence of life? What are the best places to the appearance of life?

1. Prebiotic chemistry

Prebiotic chemistry can be defined as a set of abiotic processes leading to the formation of biomolecules or, in other words, as the study of chemical evolution leading to the transition from “non-living” to “living” systems (Bruylants et al., 2011).

Organic matter, together with water, energy and essential elements and transition metals, is a prime ingredient for prebiotic chemistry and the origin of life. A large proportion of organic molecules at the surface of the Hadean Earth came from exogenous sources (Maurette, 2006), i.e., meteorites. Carbonaceous chondrites contain up to 4% of organic matter (e.g., Stoks and Schwartz, 1982; Pizzarello et al., 2012; Furukawa et al., 2019), while micrometeorites may be highly enriched in organic matter, some up to 80% (e.g., Matrajt et al., 2004; Maurette, 2006; Dobrică et al., 2009). Extraterrestrial

organic matter from meteorites have been incorporated into early terrestrial sediments (Gourier et al., 2019), making it available for prebiotic reactions. Another source of organic matter is from terrestrial processes: from hydrothermal systems, atmospheric gases and impact processing. In particular, the reducing conditions in hydrothermal systems could have been an important source of biomolecules on the primitive Earth (Holm and Andersson, 2005). Modern analyses (Parker et al., 2014) of a Miller's experiment conducted in 1958 have demonstrated that Earth's early atmosphere may have formed bioessential molecules such as amino acids (molecules that make up proteins) and peptides (chains of more or less long amino acids). In addition, bombardment of the Earth's surface by meteor and comets can cause the formation of a mixture of organic molecules, including complex organic molecules such as fatty acids (molecules formed of a chain of carbons linked to hydrogens terminated by an acid group –COOH) or amines (organic compounds derived from ammonia NH_3 in which at least one of the hydrogen atoms has been replaced by a carbon group) (Furukawa et al., 2019; Ferus et al., 2020).

Liquid water is an ideal solvent that allows chemical reactions (Brack, 1993; Westall and Brack, 2018). Different energy sources include photonic (i.e., light), chemical (from organic or inorganic sources), or heat (from thunderstorms, meteor impacts, hydrothermal sources…) sources. Essential elements are also required, such as H, N, O, P and S, as well as transition metals (especially Fe). Minerals are also important ingredients for prebiotic chemistry as they promote the catalysis of reactions, such as clays, basaltic glasses, pyrite or other reactive materials (Westall et al., 2023a). Indeed, mineral surfaces promote: 1) the concentration of molecules in order to favor reactions between molecules; 2) the stabilization of the molecules formed (by preventing their rapid degradation) and their structural conformation (i.e., the spatial arrangement of atoms in a molecule) allowing the reactivity and selectivity of organic reactions; and 3) the chemical evolution by which molecular complexity increases (Westall et al., 2018).

In addition to these requirements, the presence of natural gradients of temperature, pH, ionic concentration and/or energy is crucial for the diffusion of essential components for prebiotic chemistry and primitive metabolisms that can be transported by seawater, hydrothermal fluids or rivers, for example (Westall et al., 2018, 2023b).

2. Locations for prebiotic chemistry

Many types of locations have been proposed for the emergence of life: hydrothermal environments (Westall et al., 2018), impact craters (impact events can brought the necessary chemical ingredients for life and catalytic substrates; Osinski et al., 2020), pumice rafts (catalysts and molecules needed for the earliest stages of life were found in pumice rafts; Brasier et al., 2013), deep seated fault zones (Schreiber et al., 2012), and radioactive minerals (Adam et al., 2018).

The most commonly considered locations for the emergence of life are hydrothermal environments, where the contact of hot water with reactive mineral surfaces could have provided chemical energy for prebiotic reactions (Westall et al., 2018). Among the different types of hydrothermal environments, there are subaerial springs and submarine environments (including shallow water and deep ocean environments associated with plume-related hot spot). These environments are characterized by many gradients that can fuel prebiotic reactions, including temperature, solute concentrations, pH, and redox gradients (Villafañe-Barajas and Colín-García, 2021).

Subaerial springs (**Fig. I.3**) are commonly associated with volcanism, where they can form clusters of several hundreds or thousands of vents whose physico-chemical parameters differ in terms of temperature, fluid chemistry (pH, elemental composition), content in gas, etc. (Van Kranendonk et al., 2018; Damer and Deamer, 2020; Van Kranendonk et al., 2021). This diversity offers a high number of possibilities to start prebiotic reactions over a period of a few million years, and exposed surfaces provide access to UV radiation that may have supplied the energy to initiate prebiotic processes (Westall et al., 2023a).

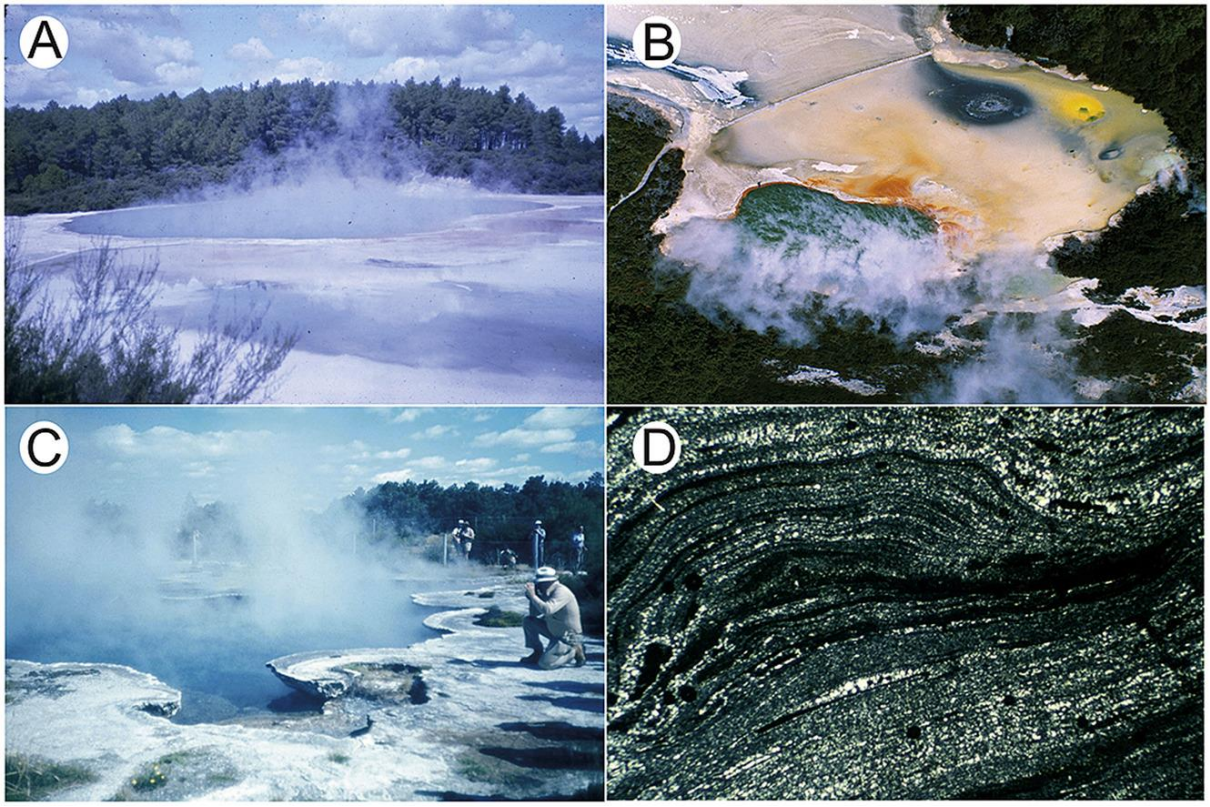

Figure I.3: *Subaerial hot springs. (**A**, **B**) Photographs of the Champagne Pool hot springs in Rotorua (Taupo Volcanic Zone) where colors in (**B**) are due to pigmented bacteria. Hot springs, also called thermal springs, are here produced by geothermally heated groundwater by shallow magmatic intrusions in a volcanic area. (**C**) Chemically-precipitated sediments mostly composed of silica and clays. (**D**) Thin section of a sinter deposit (hot spring mineral precipitates) where the dark material represents microbial remnant intercalated with silica grains (after Pirajno, 2020).*

Shallow water environments are generally located above wave base and are characterized by river effluent entering shallow basins that formed on protocontinents around volcanic edifices (Hickman-Lewis et al., 2020a). In these basins, seawater is mixed with fresh water from rivers, seeping into fractures in the basaltic crust before to be mixed with subsurface hydrothermal fluids, resulting in a hydrothermal effluent of relatively low temperatures. These shallow water environments could be suitable for prebiotic chemistry (Westall et al., 2018), where the porous silica gel resulting from the ubiquitous silica-saturated seawater may have played a role in the concentration and dehydration of prebiotic molecules (Westall et al., 2023a).

Deep ocean environments (**Fig. I.4**) are characterized by hydrothermal systems producing focused vent edifices, such as black smokers (high temperature, acidic, Fe-rich type events) or white smokers

(cooler, acidic, Zn-rich type vents), as well as more diffuse vents (lower temperature, lower metal contents, and less acidic pH fluids type vents). These kinds of environments favored the formation of metal-rich fluids and small organic molecules via serpentinising reactions, i.e., reactions between seawater and minerals (olivine, pyroxenes) contained in the rocks forming the oceanic crust, and the porous reactive minerals may have facilitated the prebiotic chemical reactions by concentrating molecules (Westall et al., 2018; 2023b).

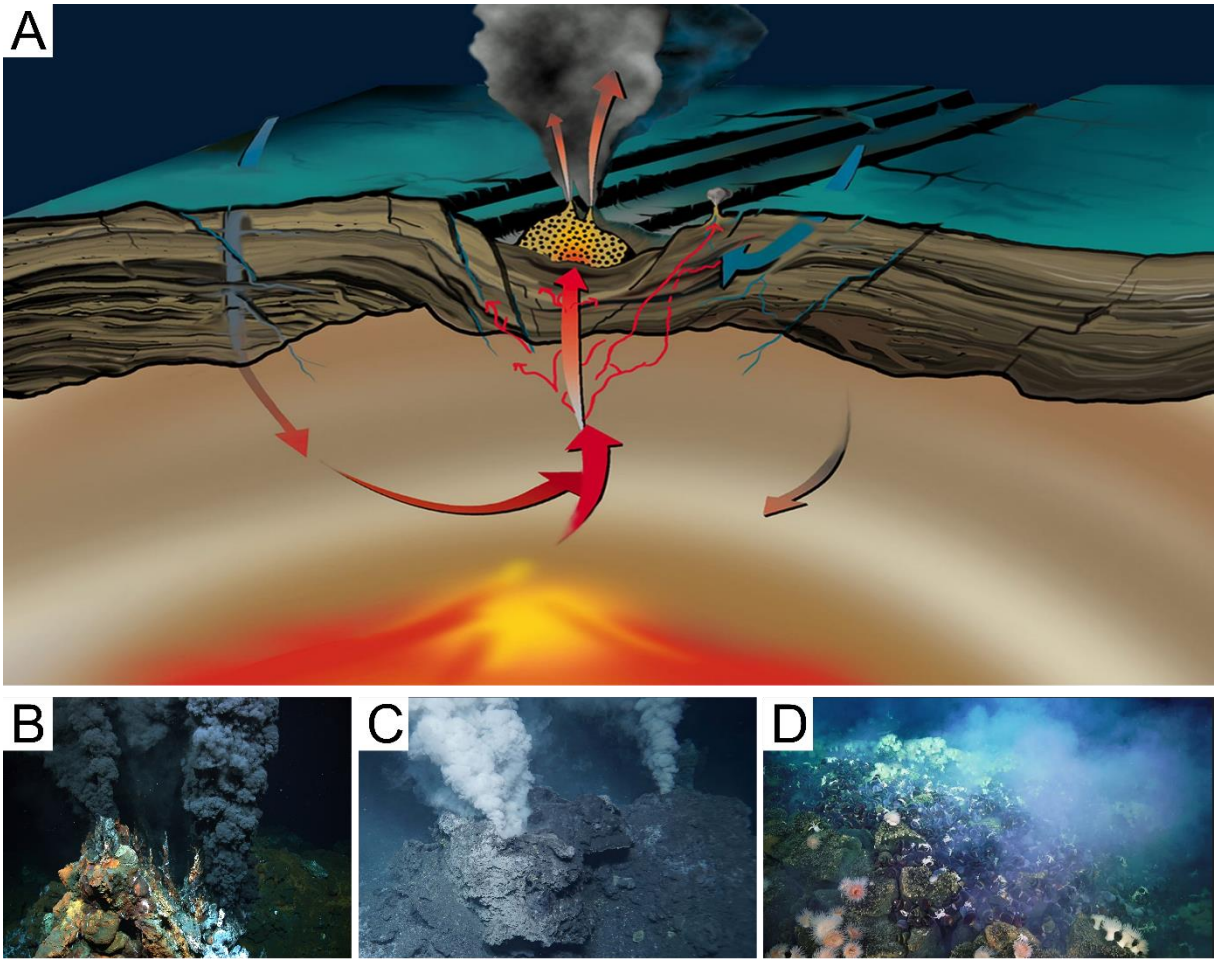

Figure I.4: *Deep sea hydrothermal vents. (**A**) Sketch showing hydrothermal vents formed in volcanic active areas on mid-ocean ridges where the rise of magma forms a magma chamber at a depth of a few kilometers and its cooling creates cracks in the seafloor in which cold sea water (about 2°C) infiltrates and heats up (nearly 2000°C). Then, the hot and acidic water rises towards the ocean floor by leaching metals (e.g., iron, zinc, copper and cobalt) from the surrounding rocks through openings in the ocean floor, known as hydrothermal vents. The temperatures emitted by these vents can reach 350–400°C (sourced from the Woods Hole Oceanographic Institution). (**B**, **C**) Black and white smoker vents, respectively (sourced from MARUM – Center for Marine Environmental Sciences, University of Bremen). (**D**) Diffuse venting (sourced from https://sevenseasmedia.org/underwater-fire-exploring-submarine-volcanoes/).*

In these submarine environments, the ocean played a key role in protecting organic molecules from UV radiation (Cleaves and Miller, 1998), and from heavy cometary and meteoritic bombardment (Nisbet and Sleep, 2001).

To summarize, conditions for prebiotic reactions leading to the formation of macromolecules probably took place in a liquid water medium and were likely associated with hydrothermalism on land or in submarine environments. These reactions were facilitated by the concentration of prebiotic molecules on the reactive mineral surfaces which aggregated to form more complex molecules until the formation of evolved cells.

C. Biosignatures

When searching for traces of life in the early terrestrial rocks, a question arises: what are the biosignatures associated with past traces of primitive life? To answer this question, we first need to understand how life forms may be preserved in general, before looking at the record of the oldest traces of life found in geological archives (i.e., the rocks) up to now, and the preservation of the first life forms appeared on Earth, i.e., microorganisms and their associated biosignatures.

1. Fossilization of biological remains

Ancient living organisms can be preserved over geological time as fossils. Fossils are debris (e.g., bones, plants, shells) or traces (e.g., footprints, tracks, excrements) of a living organism preserved in sedimentary deposits (definition of the Larousse encyclopedia). In order to be preserved over long periods of geological time, any signature of life must be cemented in its mineralogical context, i.e., be mineralized, and survive to potential physical (e.g., erosion and impacts) or chemical (e.g., hydrothermal fluids and percolating groundwaters) destruction (Westall et al., 2021). The preservation of biogenic remains is favored in environments with a high conservation potential where sediments accumulate more quickly, such as in lakes or marine basins, leading to the burial of organisms (Schopf, 1975). During what is called mineralization, physico-chemical processes lead to the replacement of organic matter by mineral matter, while the form and often the fine structure of the organism is well preserved (**Fig. I.5**).

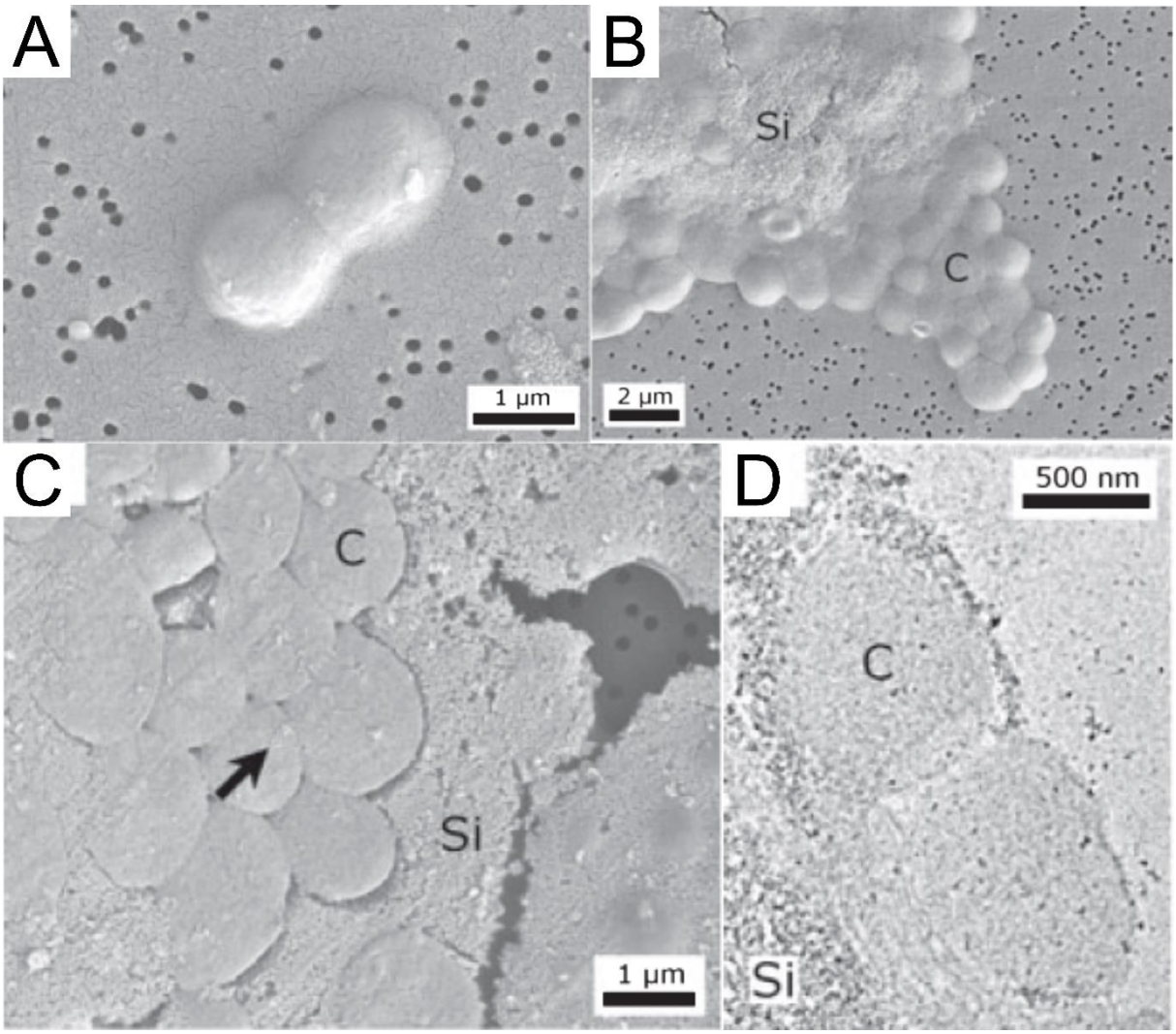

Figure I.5: *Experimental fossilization of cells. Scanning electron microscopy (SEM) micrographs of (**A**) fresh, dividing Pyrococcus abyssi cells (C), (**B**) aggregates of cells (C) and light silica precipitates (Si) after 24h of silicification, (**C**) cells (C) trapped in the amorphous silica precipitate (Si) after 24h; silica particles precipitated on the cells are visible (black arrow). Transmission electron microscopy (TEM) micrograph of (**D**) cells (C) with silica (Si) deposited around the cell envelope after 1 month (after Orange et al., 2009).*

2. The oldest fossil record

Although a large part of the fossil record has disappeared due to surface reshaping by plate tectonics and weathering and erosion processes, it has been claimed that the oldest fossil record document traces of life that may date back to the Late Hadean/Early Archean (Eoarchean). Indeed, Eoarchean (4.0–3.6 Ga) rocks may have recorded early life activity but they experienced intense metamorphism (temperature >500°C, pressure >4 kbar; e.g., Boak and Dymek, 1982; O'Neil et al., 2012) having degraded the organic matter potentially of biological origin present in the rocks, and making them difficult to interpret (Alleon and Summons, 2019). The oldest purported morphological traces of life are hosted at the 4.3–3.7 Ga Nuvvuaqittuq terrane as hematite filaments and tubes that resemble modern iron oxidizing filamentous microorganisms (Dodd et al., 2017; Papineau et al., 2022). However, this data is highly controversial and not considered reliable (McMahon, 2019; Greer et al., 2020; Lan

et al., 2022). In addition, the oldest purported chemical traces of life are coming from a 4.1 Ga zircon crystal with a carbon isotope signature of graphite of –24‰ (Bell et al., 2015), as well as sediments in the 3.8–3.7 Ga Isua terrane whose carbon isotope signature (Rosing, 1999) and remnant organic molecules (Hassenkam et al., 2017) are compatible with a biological origin. However, the putative stromatolites from the same Isua Greenstone Belt (Nutman et al., 2016, 2019) are believed to be metamorphic artefacts (Allwood et al., 2018; Zawaski et al., 2020).

Potential traces of life occur in younger Paleoarchean (3.6–3.2 Ga) rocks that are less metamorphosed, some of which are also controversial (Alleon and Summons, 2019). Rocks from the 3.48 Ga Dresser Formation (Pilbara, Australia) have preserved putative stromatolites, microfossils and sulfur and carbon isotopic compositions (e.g., Walter et al., 1980; Buick et al., 1981; Buick, 1990; Ueno et al., 2001, 2006, 2008), but most of these have been questioned regarding their biogenicity (e.g., Lowe, 1994; Lollar and McCollom, 2006; Wacey et al., 2018; Alleon and Summons, 2019). In addition, carbonaceous matter occurs in these rocks as disseminated clots or in fine laminae (Morag et al., 2016), but is not directly associated with stromatolites or microfossils. Rocks from the 3.46 Ga Apex Chert Formation (Pilbara, Australia) contain carbonaceous filaments enriched in light carbon isotopes initially interpreted as degraded remains of cyanobacteria (Schopf and Packer, 1987), but these microfossils have been reinterpreted as filaments of inorganic carbon formed during the circulation of hydrothermal fluids (Brasier et al., 2002, 2005; Pinti et al., 2009; Wacey et al., 2016), probably through Fischer-Tropsch reactions (i.e., reactions of carbon monoxide and hydrogen produced by hydrothermal alteration of basaltic rocks during serpentinization, producing alkanes and other organic molecules). Well-preserved stromatolites occur in the 3.4 Ga Strelley Pool Formation (Pilbara, Australia; Allwood et al., 2006, 2007), as well as other examples of controversial traces of life, including film-like, spheroidal and lenticular forms interpreted as putative microfossils (e.g., Sugitani et al., 2010, 2013; Lepot et al., 2013; Sugitani et al., 2015a).

Rocks from the Onverwacht and Fig Tree Groups of the Barberton Greenstone Belt (South Africa, ca. 3.5–3.2 Ga) host a variety of microbial biofilms and mats, stromatolites, as well as diverse carbonaceous structures interpreted as potential microfossils (e.g., Knoll and Barghoorn, 1977; Walsh and Lowe, 1985; Walsh, 1992; Westall et al., 2001; Tice and Lowe, 2004; Westall et al., 2006b; van Zuilen et al., 2007; Glikson et al., 2008; Westall et al., 2011b; Homann et al., 2015; Westall et al., 2015a; Homann et al., 2016; Hickman-Lewis et al., 2018, 2020b, 2020c) although some that could be abiotic artefacts. Filamentous microfossils are very rare in the carbonaceous cherts of the Onverwacht Group and their biogenicity remains equivocal, although filamentous microstructures of carbonaceous composition have been documented in the 3.45 Ga Hooggenoeg cherts (Walsh, 1992) and the 3.42 Ga Buck Reef Chert (Walsh and Lowe, 1985; Walsh, 1992). Spheroidal microfossils with carbonaceous walls belong to the most common group of putative microfossils in these cherts and were identified in the Hooggenoeg cherts as clusters of spheroidal, cell-like objects of 2–10 µm in diameter (Glikson et al., 2008) and in the Buck Reef Chert as large spheroids and ellipsoids (>10 µm in length) of 4.5–12.8 µm in diameter (Walsh, 1992), but their simple morphology could be formed abiotically. Lenticular microfossils preserved in the Buck Reef Chert (Walsh, 1992; Oehler et al., 2017) and other cherts from the Upper Onverwacht Group (Pflug, 1966, 1967; Pflug et al., 1969) are the earliest reported and currently best studied microfossils in the Barberton Greenstone Belt and are similar to those reported from the 3.4 Ga Strelley Pool Formation (Sugitani et al., 2015b; Oehler et al., 2017) and the 3 Ga Farrel Quartzite (Sugitani et al., 2007) in the Pilbara Craton where their biogenicity is well established.

Definitive evidence of traces of life are found in the ca. 3.5 Ga Pilbara (Australia) and Barberton (South Africa) Greenstone Belts where both chemotrophic, i.e., organisms using the oxidation of reduced

organic molecules (chemoorganotrophs) or minerals (chemolithotrophs) as an energy source for their metabolism (Rasmussen, 2000; Westall et al., 2006a, 2011a; Ueno, 2007), and phototrophic, i.e., organisms using sunlight as an energy source (Hofmann et al., 1999; Allwood et al., 2006; Noffke et al., 2013), life forms have been interpreted as fossil remains. These early life forms were probably anaerobic and (hyper)thermophilic (and maybe halophilic) since they inhabited anaerobic (giving the predominantly anaerobic conditions in early Earth), hydrothermal, shallow water environments dominated by a warm (salty) seawater (Westall et al., 2015a, 2023b; Hickman-Lewis and Westall, 2021).

The sedimentary rocks found in the Pilbara and Barberton Greenstone Belts preserved fossils ranging from macroscopic to microscopic scales (**Fig. I.6**), including macroscopic stromatolites in the 3.43 Ga Strelley Pool Chert (Australia; **Fig. I.6A**; Hofmann et al., 1999; Allwood et al., 2006; Brown et al., 2020), several hundred micrometers thick phototrophic biofilms in the 3.47 Ga Middle Marker horizon (South Africa; **Fig. I.6B**; Hickman-Lewis et al., 2018, 2019, 2020a, 2020b), a few hundred micrometers spherical fossils in the 3.22 Ga Moodies Group Chert (South Africa**; Fig. I.6C**; Javaux et al., 2010), microscopic lenticular fossils in a black chert from the 3.4 Strelley Pool Formation (Australia; **Fig. I.6D**; Sugitani et al., 2013), and submicroscopic coccoidal fossils in the 3.45 Ga Kitty's Gap Chert (Australia; **Fig. I.6E**; Westall et al., 2006a, 2011a, 2015b).

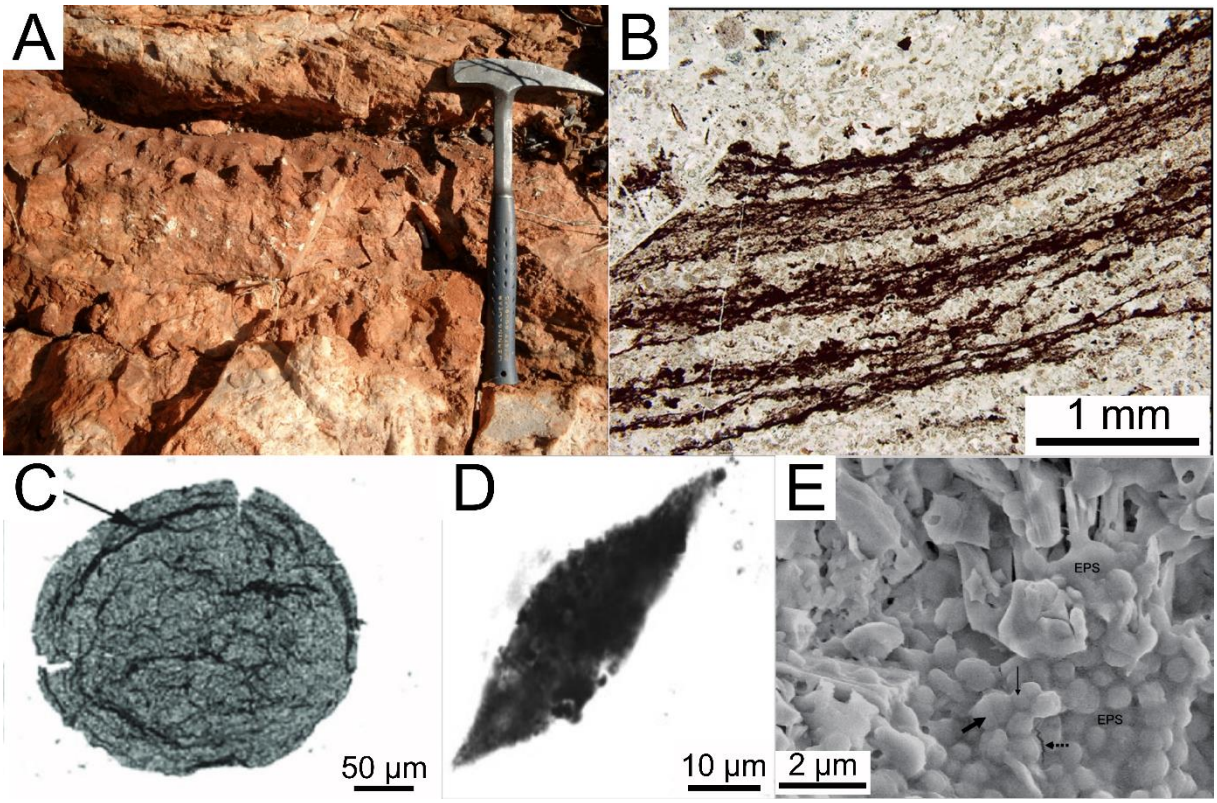

Figure I.6: *Diverse macroscopic to microscopic fossils in Pilbara and Barberton Greenstone Belts. (**A**) Conical stromatolites from the 3.43 Ga Strelley Pool Chert in Western Australia (modified after Brown et al., 2020). (**B**) Crinkly, filament-like lamination interpreted as microbial mats from the Middle Marker horizon in South Africa (modified after Hickman-Lewis et al., 2018). (**C**) Irregular, spherical carbonaceous structure interpreted as an organic-walled microfossil from the 3.22 Ga Moodies Group in South Africa (modified after Javaux et al., 2010). (**D**) Lenticular structure interpreted as a microfossil with internal opaque particles (sulfides and/or carbonaceous particles) in a carbonaceous laminated*

*black chert containing abundant and diverse microfossils from the 3.4 Ga Strelley Pool Formation in Western Australia (modified after Sugitani et al., 2013). (**E**) Colony of coccoids at the edge of a silicified large volcanic particle altered in hydromuscovite, visible as foliated mineral at the top of the micrograph, in the Kitty's Gap Chert in Western Australia (modified after Westall et al., 2006a). Note the EPS (extracellular polymeric substances) coats both the minerals and the coccoids.*

3. Preservation of traces of microbial life

The most ancient traces of life correspond to those of unicellular organisms, i.e., prokaryotic organisms such as bacteria or archaea, but due to their small size (<10 µm) and absence of hard parts, the fossilization of these unicellular organisms requires exceptional preservation conditions. To preserve their physical structure, the microorganisms need to be 1) rapidly encapsulated or replaced by a mineral which reproduces the shape of the cell (permineralization), 2) rapidly entombed by anoxic sediments, permafrost or ice, which "mummifies" the cell, or 3) embedded in a mineral cement during their lifetime (Westall and Hickman-Lewis, 2018; Westall et al., 2021).

Mineral encapsulation is a process defined as biologically influenced by fossilization (Li et al., 2013). During this process, ions from the immediate environment of the cells or other microbial products, such as extracellular polymeric substances (EPS), are passively fixed (chelated) to the functional groups (i.e., groups of atoms attached to the carbon chains of organic molecules) of the organic matter. Fixation can also occur where a metal such as iron creates a bond between functional groups and the fossilized mineral (Ferris et al., 1988). Then, the organic substrate, the cells or other microbial products are completely encapsulated during the polymerization of the fossilizing mineral (**Fig. I.7**; Westall and Hickman-Lewis, 2018). Nevertheless, not all microbial cells are preserved in the same way during the process of mineral encapsulation, depending on the cell-wall structure of the different type of prokaryotes (i.e., Gram-positive and Gram-negative bacteria, or archaea; Westall, 1997), and/or the robustness and tolerance of microbial species to environmental changes (Orange et al., 2009). These fossilization differences between microorganisms are particularly important because they tell us that what we find in the rock record is a small portion of microbial communities.

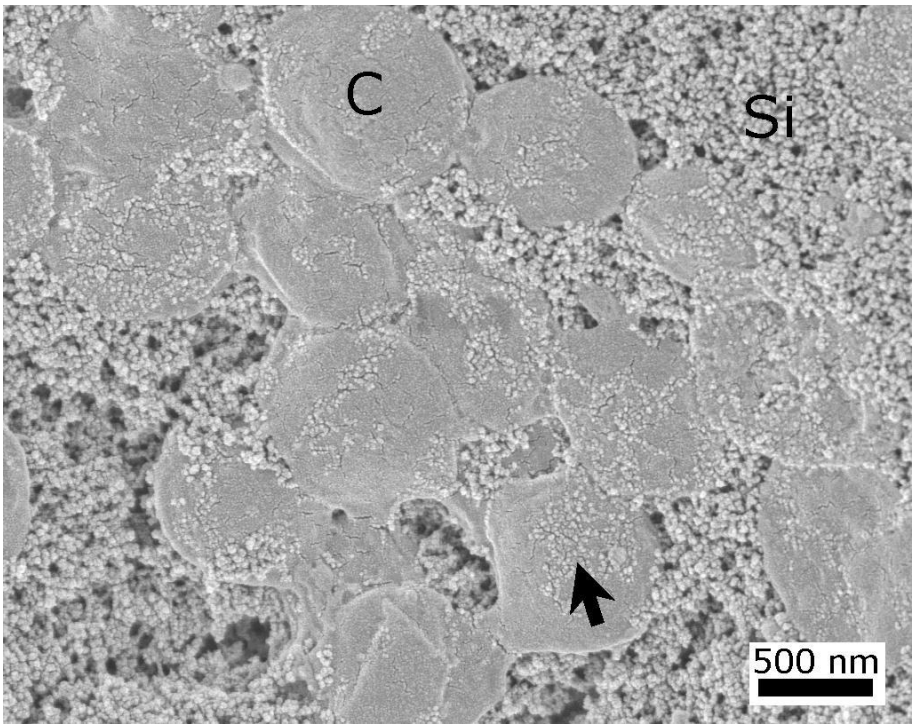

Figure I.7: *Mineral encapsulation of cells. SEM micrograph of Pyrococcus abyssi cells (C) after 9 months of experimental fossilization, trapped in a silica precipitates (Si); silica particles precipitated on the cell wall are visible (black arrow; after Orange et al., 2009).*

Finally, to pass into the rock record and be preserved over long geological time scales, microbial remains or their degraded components must be lithified into sediments (Westall and Hickman-Lewis, 2018). However, after the initial process of fossilization, various factors, such as diagenesis, weathering, metamorphism and impact shock can lead to the alteration or even to the destruction of microfossils preserved in the sedimentary successions (Orange et al., 2009). In general, the physical remains of cells, colonies and mats are rarely preserved; only 10% of cellular organic matter is estimated to be preserved in the rock record, and only poorly preserved remains or generic organic matter (i.e., EPS) from cell degradation trapped in a mineral cement are usually found (Walsh and Lowe, 1999; van Zuilen et al., 2007). Nevertheless, the record of early life is surprisingly rich despite the degradation of rocks during geological processes, the main reason for which being that most the well-preserved Archean sediments were rapidly silicified and silica is one of the more stable minerals at the surface of the Earth. Once silicified, the rocks are difficult to chemically alter after their lithification, and the cherts are therefore very faithful archives of geochemistry over billions of years (e.g., van Zuilen et al., 2007; Gourcerol et al., 2016).

Note that, even if a cell is rapidly fossilized, the entrapped organic matter will continue to degrade. In aerobic environments, the organic compounds are oxidized, leaving a mineral mould, whereas in anaerobic environments, they are better preserved although they undergo gradual degradation over time (Westall and Hickman-Lewis, 2018). Indeed, during metamorphism, the buried organic matter undergoes the effects of pressure and temperature which break it down, becoming increasingly mature. Consequently, the structure and the composition of the organic molecules evolve with the loss of the elements H, O, N and S and of the functional groups, thus leading to their transformation in aromatic, refractory molecules, called kerogen (e.g., Durand, 1980). Although these molecules appear

as highly degraded fragments of ancient biological macromolecules, it is still possible to identify biological characteristics, called biosignatures.

4. *Definition of biosignatures*

Biosignatures can be defined as features characteristic of life, including morphological, organic and metabolic signatures that are preserved in minerals, sediments and rocks (**Fig. I.8**; Westall and Cavalazzi, 2011; Mustard et al., 2013; Neveu et al., 2018).

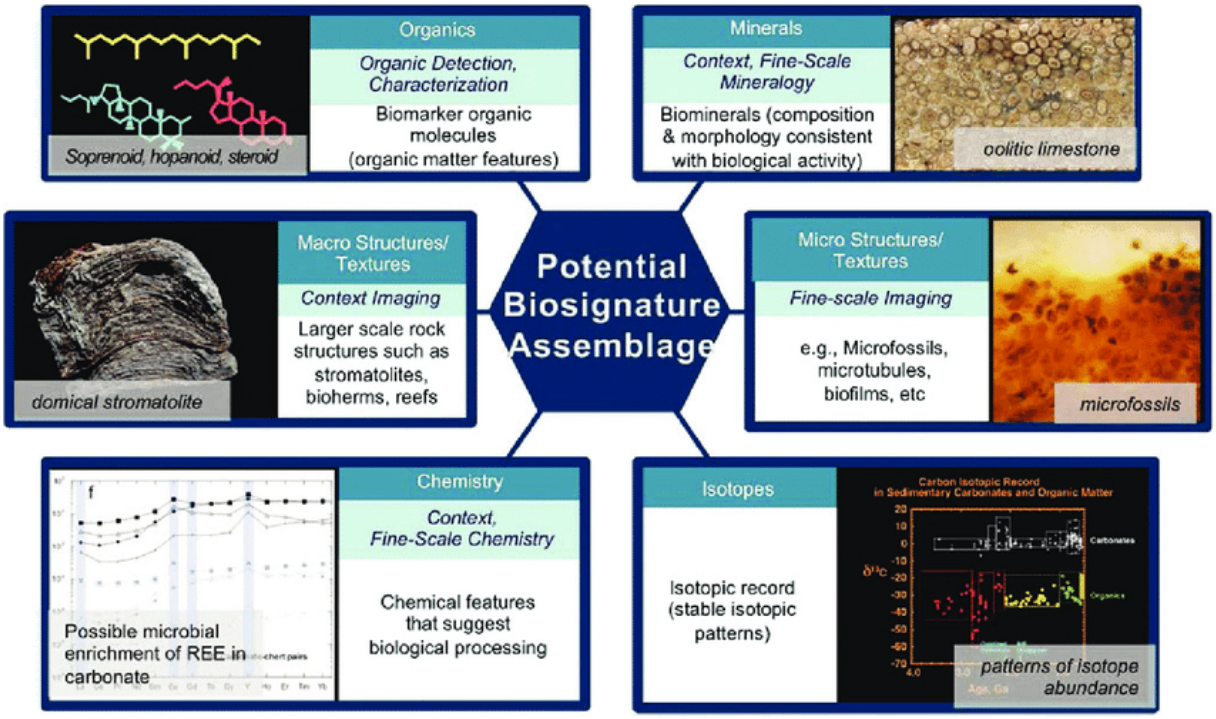

Figure I.8: *Different types of biosignatures identified by the Mars 2020 Science Definition Team (after Mustard et al., 2013).*

5. *Morphological biosignatures*

Morphological biosignatures comprise a wide range of macroscopic to microscopic structures formed by microorganisms, such as microbially induced sedimentary structures (MISS), microbialites, microbial mats, biofilms and microfossils, as well as alteration textures on the surface of rocks and minerals (in particular microborings).

- *Microbially Induced Sedimentary Structures (MISS):*

MISS are primary sedimentary structures formed by the interaction of microorganisms with sediment resulting in macroscopic, anastomosing laminated structures composed of an accumulation of sediments preserving microbial mats (Noffke, 2009). The microorganisms responsible of the formation of these structures are benthic photosynthetic microorganisms (i.e., using sunlight as a source of energy) living in aqueous environments that form highly organized communities called biofilms composed of the individual cells and EPS (Noffke and Awramik, 2013).

- *Microbialites:*

Microbialites are organosedimentary deposits made up of benthic microbial communities that can influence/induce the precipitation of minerals (Burne and Moore, 1987). Microbialites include stromatolites, thrombolites, oncolites, biolaminites and crusts. In particular, the stromatolites are vertical sedimentary structures similar to MISS but which have precipitated calcium carbonate within the EPS in addition to trapping and binding of sediment particles (Noffke and Awramik, 2013), contributing to the lithification of the structures. The repeating of these processes form multiple layers characteristic of stromatolites (**Fig. I.6A**; Allwood et al., 2006; Noffke and Awramik, 2013).

- *Microbial mats:*

Microbial mats are composed of finely laminated structures, each representing colonies of microorganisms (mainly, bacteria and archaea), intercalated between sediment particles in a wet environment (Westall and Rincé, 1994). Microbial mats are usually held together and bound to their substrates by slimy EPS secrete by the microorganism. They are typically formed by photosynthetic microorganisms, which dominate the upper layers, while the lower layers, comprising the degraded remains of the phototrophic primary producers, are dominated by heterotrophic microorganisms. Typically, microbial mats are formed during periods of quiet hydraulic conditions during which microbial cells assemble on a planar sedimentary surface to form the organic mesh of a carpet-like microbial mat that are the basis of MISS (**Fig. I.6B**; Noffke, 2009).

- *Biofilms:*

Biofilms are defined as laterally extensive developments of microbial colonies encased in a polymer matrix of EPS that occur on a sediment surface during a short period of non-deposition (Westall et al., 2006a). Biofilms can form in a wide range of environments and adapt to various physical and chemical conditions, such as temperature, pH, and nutrient availability. In particular, biofilms provide protection for microorganisms, allowing them to survive in harsh environmental conditions by creating a microenvironment with controlled redox and pH conditions, and providing concentrations of nutrients. Biofilms may be formed by phototrophic microorganisms as well as non-phototrophic ones.

- *Microfossils:*

Microfossils are the fossilized remains of individual cells. They occur where they are replaced or impregnated (permineralized) by minerals and then preserved by a cementing mineral (**Fig. I.7**). Individual microbial cells are rare, most organisms occurring in colonies. They include the carbonaceous remains of filamentous microorganisms forming thread-like structures up to several micrometers in diameter and tens or hundreds of micrometers in length (e.g., Walsh, 1992; Westall et al., 2006a; Cavalazzi et al., 2021); spheroidal or coccoidal cells occurring both solitary and grouped with variable size, showing evidence for cell division, cell wall breakdown, or deflated coccoid surface textures consistent with cell lysis (**Fig. I.6C, E**; e.g., Westall et al., 2006a, 2011a; Wacey et al., 2011; Sugitani et al., 2013); as well as lenticular cells that are large, thick-walled structures with single or double internal cavities and diaphanous carbonaceous coatings (**Fig. I.6D**; e.g., Walsh, 1992; Wacey et al., 2011; Sugitani et al., 2013).

- *Microborings:*

Microborings are created on a fine-scale by the activities of rock boring microorganisms and include, for example, microtubules that are tubular cavities with circular cross-section and variable diameters occurring by the dissolution of volcanic glass by microorganisms (crypto- and chasmo-endolithic, i.e., microbes living inside rock pores and cracks, respectively) for nutrients and essential elements (Furnes et al., 2004, 2007; McLoughlin et al., 2010; Foucher et al., 2010).

6. Organic biosignatures

Organic biosignatures designate fossil organic molecules, called biomarkers, resulting from the decomposition of microorganisms. Organic molecules are difficult to preserve over billions of years due to a variety of factors. They are inherently unstable and tend to break down over time, and this process is accelerated by exposure to heat, light, and radiation, which can cause chemical reactions that break down the molecules (LaRowe and Van Cappellen, 2011; Arndt and LaRowe, 2018). Additionally, organic molecules can be broken down by microorganisms, which can consume them as a source of energy (LaRowe and Van Cappellen, 2011; Arndt and LaRowe, 2018). Finally, geological processes such as erosion and tectonic activity can also contribute to the degradation of organic molecules over time (Ghassal and El Atfy, 2022).

However, several key aspects can contribute to the preservation of organic molecules over geological time scales, such as redox state (i.e., reducing conditions often associated with limited oxygen availability promote the preservation of organic carbon), diagenetic alteration (i.e., the changes that occur to organic matter during diagenesis, the process that converts sediments to rock, can affect its preservation by encapsulating it), or sulfur content (i.e., the presence of sulfur can lead to the formation of organosulfur compounds, which are more resistant to degradation) (Broz, 2020). The organic molecules can also be preserved during cell mineralization or by close association with phyllosilicates (i.e., clay minerals, such as iron/magnesium smectites) sheets of which the finely layered structure, high surface area, and the negatively charged surfaces can fixed the organic molecules (Kleber et al., 2005; Hazen and Sverjensky, 2010; Summons et al., 2011). In addition, they can be found in inclusions of minerals, such as halite (Winters et al., 2013).

Generally, complex organic molecules such as membrane lipids are more resistant to degradation and can persist longer. In particular, the insoluble part of organic matter, often found in sedimentary rocks, is mainly composed of aromatic (two to four aromatic rings) and aliphatic (short and branched aliphatic chains) hydrocarbons with functional groups like nitrile, carboxyl and ether (Naraoka, 2014). The refractory, insoluble fraction of organic matter is called kerogen, in contrast to the soluble fraction called bitumen, which is made up of smaller macromolecules and simpler species such as amino acids, alcohols and sugars, and dissolves more easily in organic solvents (Alleon and Summons, 2019; Chan et al., 2020).

The biomarkers molecules that can sometimes be identified are organic compounds, such as polyaromatic hydrocarbons, amines, fatty acids/lipids, carboxylic acids (molecules comprising a carboxyl group -COOH), amino acids, etc. Other characteristics of fossil organic molecules can also suggest a biological origin (Summons et al., 2008, 2011):

- enantiomeric excess (the excess of one enantiomer, i.e., of the left or right shape that a molecule takes, compared to another is typical of life forms while the use of opposite enantiomers is generally widespread in non-biological processes);

- diastereoisomeric preference (diastereomers are defined as compounds –isomers– which have the same molecular formula and sequence of bonded elements but which are non-superimposable and non-mirror images);
- structural isomer preference (life prefers to use a limited subset of all the isomers that would be chemically feasible);
- repeating constitutional sub-units or atomic ratios (life uses a limited number of simpler subunits, therefore we can expect to find repeating units, for example, the predominance of even-carbon numbered in fatty acids);
- systematic isotopic ordering at molecular and group level (the repeating subunit conformation of biomolecules can result in an observable isotopic ordering in the molecular fingerprint);
- uneven distribution patterns of clusters, such as C-number, concentration, or $\delta^{13}C$, of structurally related compounds (life employs a restrictive range of biochemicals, for examples, C_{14}–C_{20} in fatty acids, while the range is more extensive in the organic matter found in meteorites).

7. Metabolic biosignatures

Metabolic biosignatures refer to biosignatures that result from the metabolic activities of microorganisms on their immediate surroundings, such as gas production (e.g., CO_2, CH_4, H_2), isotopic fractionation (e.g., carbon, sulfur), elemental concentration (preferential accumulation of trace metals associated with organic matter) and formation of biominerals (e.g., pyrite, calcite, apatite).

- *Gases:*

The production of gases, such as carbon dioxide (CO_2), methane (CH_4), hydrogen (H_2), nitrous oxide (N_2O) and sulfur dioxide (SO_2), may be mediated by microbial metabolic activity. Carbon dioxide can be produced by sulfate reducers that use sulfate as an electron acceptor for the degradation of organic compounds (Widdel and Hansen, 1992; Muyzer and Stams, 2008). Methane is produced during methanogenesis where methanogenic archaea use carbon dioxide as an electron acceptor (Liu and Whitman, 2008). Hydrogen is produced during fermentation where microbes break down organic matter through many different pathways, the byproducts of which can be combined by enzymes (i.e., proteins that catalyze chemical reactions in cells) to produce hydrogen (Muyzer and Stams, 2008; Valdez-Vazquez and Poggi-Varaldo, 2009).

- *Isotopes:*

Stable isotopes such as C, H, O, N, S and Fe can be used as biosignatures. Indeed the cell material is often enriched in lighter isotopes and this enrichment may be preserved in the dead cell material or organic compounds derived from living systems (Summons et al., 2008). Carbonaceous microfossils are most often analyzed for their isotopic signature in $\delta^{13}C$ (normalized $^{13}C/^{12}C$ ratio of sample to standard, Pee Dee Belemnite), since metabolic processes result in negative $\delta^{13}C$ values (Schidlowski, 2001). In particular, the fixation of inorganic carbon by autotrophs produces light carbon isotopes, i.e., the organic carbon is enriched ^{12}C relative to the inorganic carbon compounds from which it originated (Nier and Gulbransen, 1939). However, negative carbon isotope fractionation (between -40‰ and 0‰) is consistent with many biological pathways, making it difficult to detect specific metabolisms. A restricted range of $\delta^{13}C$ values can enhance the biogenicity of the carbonaceous materials. In addition, carbon isotopic analyses must be combined with other analytical techniques to confirm their biogenic origin (e.g., Hickman-Lewis et al., 2020c).

Other isotopes can also be used by combining $\delta^{13}C$ measurements with $\delta^{34}S$ (normalized $^{34}S/^{32}S$ ratio of sample to standard, Vienna-Canyon Diablo Troilite) to better constrain the dominant biogeochemical processes (Wacey et al., 2011; Bontognali et al., 2012). In particular, sulfur-based metabolisms produce fractionation of sulfur isotopes, such as sulfate reduction by bacteria in hydrogen sulfide, which yields light sulfur isotopes with negative $\delta^{34}S$ values (Harrison and Thode, 1958; Sim et al., 2011), or microbial disproportionation of the elemental sulfur reservoir (S^0, S_2O_3, or SO_3^{2-}), where sulfide is depleted in ^{34}S and sulfate is enriched in ^{34}S (Bak and Pfennig, 1987; Canfield, 2001). Iron isotopes can also be combined with carbon isotopes measurements to study the distribution of microorganisms on the primitive Earth, as Fe(II) was the most important electron donor available in the Archean oceans, implying that anaerobic Fe(II) oxidation may have been an important metabolic pathway (Widdel et al., 1993; Beard et al., 1999). Indeed, the oxidation of Fe(II) into Fe(III) produces enrichment in heavy iron isotopes (Welch et al., 2003; Balci et al., 2006). Other metabolic pathways also produce fractionation of iron isotopes, such as dissimilatory iron reduction, where the reduction of Fe(III) coupled to the oxidation of organic matter yields light iron isotopes (Beard et al., 1999; Crosby et al., 2007), or bacterial Fe assimilation (assimilatory metabolism), which favors uptake of heavy isotopes into the cell (Brantley et al., 2001, 2004).

- *Trace metals:*

Unusual concentrations of trace metals can be associated with microorganisms and their metabolic products for different purposes such as the stability of the cell wall, requirement of metals by microorganisms for their enzymatic activities, or concentration of toxic elements by microorganism (active adsorption), as well as chelation of trace metals after the death of microorganisms (passive adsorption) (Westall and Cavalazzi, 2011; Hickman-Lewis et al., 2020c).

- *Biominerals:*

Biominerals can be formed actively and passively by microorganisms in biologically controlled and biologically induced processes, respectively (Westall and Cavalazzi, 2011). Perry et al., (2007) distinguished between biominerals as direct indicators of life and organominerals as indirect indicators of life. Biominerals are inorganic-based structures either directly or indirectly precipitated by microbial metabolisms; elements in the local environment may be taken up and incorporated into functional groups directly by microorganisms (Mann, 2001), which are then precipitated to produce minerals such as calcite ($CaCO_3$), magnetite (Fe_3O_4), gypsum ($CaSO_4.2H_2O$), and silica ($SiO_2.nH_2O$). In addition, the presence of organic molecules can promote the formation of metastable polymorphs (i.e., minerals with the same chemical formula but a different crystalline structure, such as calcite, aragonite and vaterite with the formula $CaCO_3$, but formed under different conditions) in biominerals under abiotic (i.e., with the presence of non-biological organic molecules; Cosmidis et al., 2019), or biotic conditions. Indeed, the organic molecules act as templates for nucleation (Falini et al., 1996) and stabilize unstable mineral intermediates (Addadi et al., 2003). Alternatively, metastable polymorphs can be formed by changes in the local chemical environment within internal vesicles (Uebe and Schüler, 2016) or in the extracellular medium (Rodriguez-Navarro et al., 2007) as a result of metabolic activity.

On the other hand, organominerals are not directly produced by living cells, although they are generally associated with life. Most organominerals are formed by the interaction of by-products of biological organic molecules with inorganic compounds (Perry et al., 2007), and include desert varnish (i.e., silica-layered rock coatings; e.g., Engel and Sharp, 1958), bacterial encrustations (i.e., Fe-Mn

oxyhydroxides formed outside of bacteria; e.g., Ferris et al., 1987), stromatolitic carbonate deposits (e.g., Riding, 1991), and endolithic microborings filled with minerals (e.g., McLoughlin et al., 2007).

D. Abiotic processes mimicking biosignatures

Abiotic processes can mimic any type of biosignature (morphological, textural, organic, isotopic, chemical/elemental or mineralogical), generating false biosignatures (McMahon and Cosmidis, 2022). In particular, life-like abiotic materials are produced by non-equilibrium processes, often in the presence of water and organic matter, conditions similar to those that can actually give rise to and sustain life (McMahon and Cosmidis, 2022).

1. False morphological biosignatures

- *Pseudomicrobialites:*

Pseudolaminations mimicking the different layers of microbialites can be formed under abiotic conditions such as variable energy/sediment input during deposition and self-organization during recrystallisation, diagenesis, metamorphism and chemical alteration (**Fig. I.9A**; Brasier et al., 2017; Allwood et al., 2018; Brasier et al., 2019; Zawaski et al., 2020). For example, stromatolite-like forms characterized by convex laminations can be mimicked by various abiotic growth processes, including diffusion-limited aggregation and oscillating chemical reactions (**Fig. I.9B**; McLoughlin et al., 2008; Chan et al., 2019; Johannessen et al., 2020; Papineau, 2020).

- *Inorganic biomorphs:*

Biomorphs are any abiotic structure that shows a morphological resemblance to living or fossil microbes. In particular, inorganic biomorphs are formed by reactions between fluids and minerals, such as in chemical gardens (plant-like structures formed by reactions between transition metal salts and aqueous anionic solutions of, for example, carbonate or silicate; **Fig. I.9C**; Barge et al., 2015; McMahon, 2019; Kotopoulou et al., 2021), carbonate-silica biomorphs (inorganic objects composed of amorphous silica and crystalline carbonates which can adopt various morphologies such as helicoidal filaments, worm-shaped braids and flat leaf-shaped sheets; **Fig. I.9D**; García-Ruiz et al., 2003, 2009; Kellermeier et al., 2012; Opel et al., 2018; Rouillard et al., 2018), and fibrous crystals, trichites and other crystallites (strong or irregular curvature induced during the growth or deformation of fibrous or acicular crystals can generate shapes reminiscent of those of filamentous microorganisms; **Fig. I.9E**; Cloud, 1976; Muscente et al., 2018).

- *Organic biomorphs:*

Organic biomorphs are produced from aqueous solutions when minerals are formed in the presence of organic molecules, such as carbon-sulfur biomorphs (spherical and tubular microscopic objects composed of elemental sulfur and encapsulated in an organic envelope; **Fig. I.9F**; Cosmidis and Templeton, 2016; Cosmidis et al., 2019), and other organic biomorphs (aggregation of organic compounds into spheres in the presence of water such as membranes vesicles formed from the assembly of fatty acids produced by abiotic Fischer-Tropsch reactions under hydrothermal conditions, coacervates or proteinoid microspheres; **Fig. I.9G**; Fox and Yuyama, 1963; Brooke and Fox, 1977; Koga et al., 2011; Deamer, 2017).

- *Pseudobioalteration textures:*

Some features resembling microborings are actually ambient inclusion trails, such as snaking and tunnel-like cavities, formed by the propulsion of mineral crystals through lithified substrates, which typically contain organic matter (**Fig. I.9H**; Wacey et al., 2008; Lepot et al., 2009, 2011; McLoughlin and Grosch, 2015).

These morphological examples illustrate the difficulty of distinguishing actual microbial remnants from their abiotic counterparts based on morphological criteria alone (Buick, 1990; Brasier et al., 2002; Schopf et al., 2002; García-Ruiz et al., 2003), and the necessity to perform organic, isotopic, elemental or mineralogical mapping to strengthen the interpretation of these structures (McKay et al., 1996; Cady et al., 2003; Rasmussen et al., 2008; Cavalazzi et al., 2011; Oehler and Cady, 2014).

2. *False organic biosignatures*

Moreover, abiotic organic molecules can be preserved in rock formations, sometimes co-occurring with biological organic molecules. Abiotic organic molecules can be derived from exogenic sources, such as meteorite infall and interplanetary dust particles (e.g., Sephton, 2002; Botta and Bada, 2002; Sephton et al., 2004; Steele et al., 2016), or from endogenic sources, such as water-rock interactions through serpentinization of mafic/ultramafic rocks and Fischer-Tropsch reactions (e.g., Lindsay et al., 2005; van Zuilen et al., 2007; Etiope et al., 2011; Schrenk et al., 2013), thermal maturation of organic-rich mudrocks (e.g., Parkes et al., 2007; McCarthy et al., 2011), as well as hydrothermal activity, magmatic degassing and thermal metamorphism of carbonates (e.g., Giggenbach, 1997; Sephton and Hazen, 2013).

3. *False metabolic biosignatures*

- *Isotopic pseudosignatures:*

Several abiotic processes can produce false isotopic biosignatures in the carbon, sulfur, nitrogen and iron systems. In particular, abiotic processes can generate isotope fractionation in carbon (e.g., Fischer-Tropsch reactions can produce CH_4 and other organic compounds with very negative $\delta^{13}C$ values, similar to biologically fixed carbon; Horita, 2005), sulfur (e.g., hydrothermal and photochemical processes can lead to sulfide with negative $\delta^{34}S$ values, similar to microbially reduced sulfide; Farquhar et al., 2001; Thomazo et al., 2009), nitrogen (e.g., fixation of nitrate by lightning or Fischer-Tropsch reactions can produce $\delta^{15}N$ values, similar to biological values; Kung et al., 1979; Thomazo et al., 2009; Stüeken, 2016), and iron (e.g., preferential binding of heavy Fe isotopes by organic ligands in solution or isotopic exchange between Fe minerals during diagenesis or metamorphism; Whitehouse and Fedo, 2007; Hyslop et al., 2008; Lotfi-Kalahroodi et al., 2021).

- *Pseudobiominerals:*

Inorganically precipitated minerals generally possess crystalline prismatic forms, with straight faces and sharp angles, unlike biominerals, which often have rounded or curved surfaces and overall morphologies that can be extremely complex (McMahon and Cosmidis, 2022). Organic-mineral associations can be found under abiotic conditions in which organic molecules can be passively adsorbed on the surface of minerals (e.g., Lagaly, 1984), and minerals can also participate in the polymerization of adsorbed molecules into larger, life-like molecules (e.g., Lambert, 2008). The texture

of minerals (i.e., the size of the crystallites and their organization) is different between abiotic minerals and biominerals, the latter being formed by the addition of preformed mineral nanoparticles to form polycrystalline materials (De Yoreo et al., 2015). However, it has been demonstrated that polycrystalline textures can also be reproduced abiotically in the laboratory by the addition of organic additives (e.g., Oaki et al., 2006).

- *Chemical signatures in biominerals:*

Organisms can preferentially accumulate or exclude certain elements from their intracellular medium or internal compartments (McMahon and Cosmidis, 2022). As a result, intracellular biominerals may display enrichments of specific elements compared with the chemistry of the extracellular environment, i.e., enrichments and co-location of trace metals associated with organic matter, that is not the case for abiotic organic matter (Hickman-Lewis et al., 2020c).

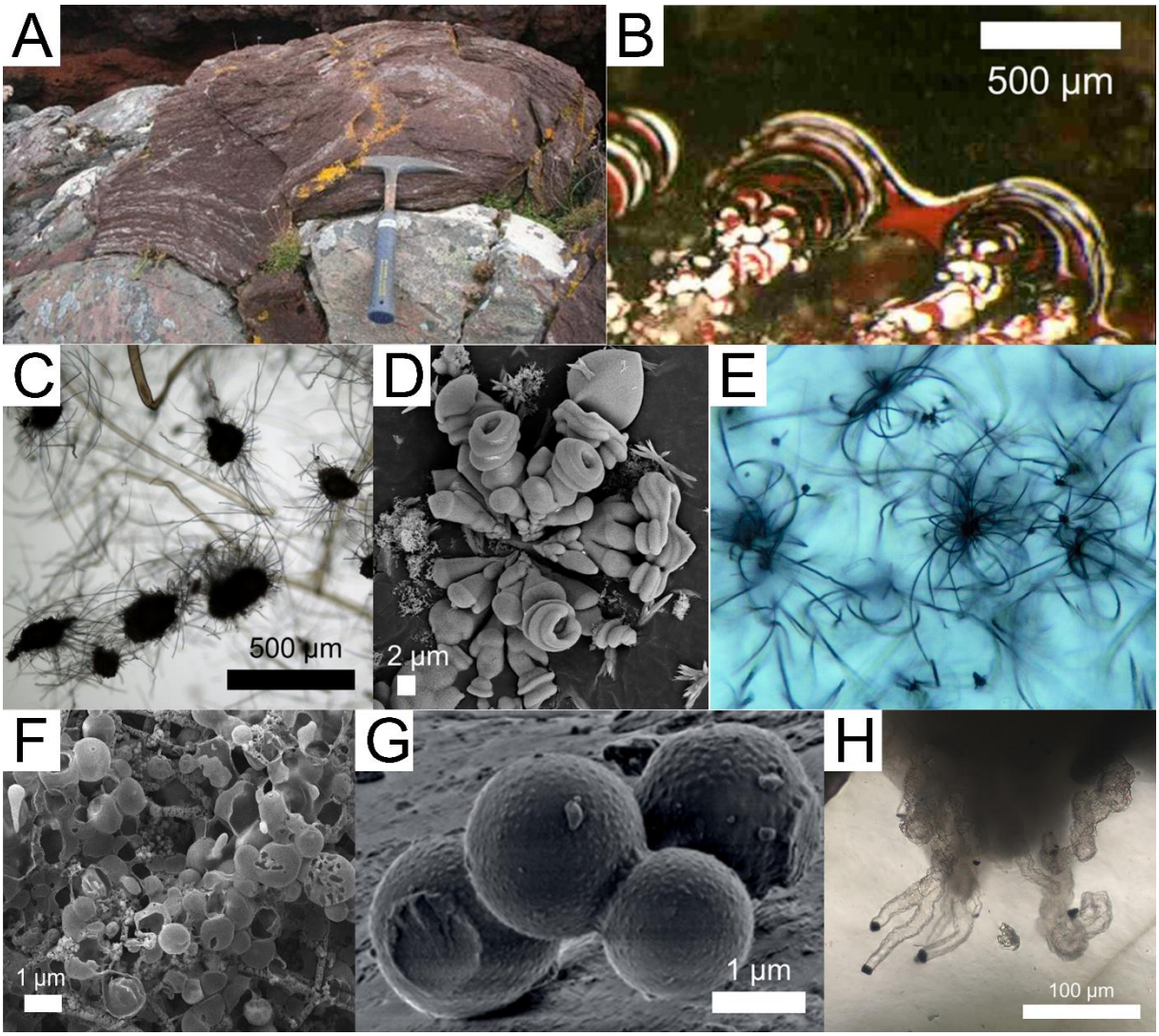

Figure I.9: *Examples of false biosignatures. (**A**) Pseudomicrobialites: laminated siltstones draping the surface of gneiss boulders (modified after Brasier et al., 2017). (**B**) Stromatolite-like laminated domes formed by aerosolized colloidal paint sprayed onto flat surfaces (modified after McLoughlin et al., 2008). (**C**) Chemical gardens: rosettes of tubes emerging from seed crystals (modified after McMahon, 2019). (**D**) Carbonate-silica biomorphs: mushroom-like biomorphs (sourced from J. Rouillard and S.*

*Borenstazjn, Institut de Physique du Globe de Paris). (**E**) Asteroidal trichites radiating from a central grain of magnetite (Cougar Mountain, Oregon; sourced from https://www.sourcecatalog.com/terminology/terminology.html). (**F**) Carbon-sulfur biomorphs: spheres with visible organic envelopes (sourced from C. Nims, University of Michigan). (**G**) Other types of organic biomorphs: organic microspheres obtained from RNA and quartz mixtures under diagenetic conditions (Criouet et al., 2021). (**H**) Pseudobioalteration textures: ambient inclusion trails resembling microborings in agate from the Pentland Hills Volcanic Formation, Edinburgh, Lower Devonian (McMahon and Cosmidis, 2022).*

E. Criteria for a claim of life detection

The measurements of features of life must meet certain criteria for a claim of life detection which convinces a majority of the scientific community (Neveu et al., 2018). Neveu et al. defined two sets of criteria, namely instrumental criteria and contextual criteria.

The instrumental criteria include:

- The sensitivity, i.e., The concentration measured must be greater than the limit of quantification to be detected.
- The absence of contamination, i.e., Any contamination signal has to be sufficiently well characterized in order to be distinguished from the signal specific to the sample (avoid false positives).
- The repeatability, i.e., The ability to repeat measurements under similar conditions (avoid fluke).

The contextual criteria encompass:

- The detectability, i.e., No physical, chemical or geological conditions encountered by the sample prevent its detection at the time of analysis (avoid false negatives).
- The preservation, i.e., The conditions must not have deteriorated the sample too much in any environment at any time, including during sampling (avoid false negatives).
- The reliability, i.e., A feature of life has to be distinguished from abiotic backgrounds (avoid false positives).
- The compatibility, i.e., The feature must be consistent with what we know of life on Earth.
- The last-resort hypothesis, i.e., The biological hypothesis is the only plausible hypothesis that can explain the origin of the observed structures.

However, caution is advised when attempting to interpret putative traces of life because certain abiotic processes may lead to observable biosignatures mimicking those associated with biological processes (see the section *III.D. Abiotic processes mimicking biosignatures*). In particular, false-positive signals, i.e., signals due to contamination (signals intrinsic to the instrument hardware or method, and abiotic environmental signals) have to be distinguished from the signal indigenous to the sample analyzed by using negative controls and blanks (evaluation of the level of contamination) and by properly characterizing all abiotic processes that could interfere with the signal and modify or even erase original traces of life (Neveu et al., 2018). In addition, false-negative signals, i.e., signals indicating that a particular feature is determined as non-biological in origin but it is in fact a true trace of life or an absence of signal, can be prevented by using positive controls to determine the detectability of the

feature at the conditions of the life-detection measurement and by comparing the rates of biological (abiotic) synthesis and abiotic (biological) consumption (Hoehler, 2017; Neveu et al., 2018).

Multiple measurements are therefore necessary to satisfy all of these criteria and increase the probability of confirming the biological origin of putative traces of life.

F. Importance of the geological context in the preservation of biosignatures

The study of the geological and mineralogical context of the traces of life provides information on the depositional environment in which the potential biosignatures were preserved, in particular, on the processes of fossilization and long-term preservation of these biosignatures (Westall et al., 2021).

The presence of biosignatures in the geological record depends on several factors (Summons et al., 2011). In particular, the rate of production of traces of life in habitable environments must exceed its rate of destruction due to abiotic processes such as erosion, diagenesis, high pressures and temperatures, radiation, impact or biological recycling (using of reduced organic matter by organotrophs). Also, some types of biosignatures are less degradable and some environments are more conducive to their preservation.

Some examples of habitable environments with potential to preserve biosignatures include hydrothermal spring systems, subaqueous environments, subaerial environments, subsurface environments and iron-rich environments (Hays et al., 2017).

1. Hydrothermal spring systems

Hydrothermal spring systems are described in the section *III.B.2. Locations for prebiotic chemistry*. To summarize, hydrothermal spring systems provide liquid water, basic elements necessary for life, such as C, H, O, N, S, P, Mg, Fe, Zn, and other trace elements, as well as energy sources, such as sunlight and energy from oxidation-reduction (redox) chemical reactions. They also provide a diversity of pressure, temperature, redox state and fluid composition conditions that support diverse microorganisms that can adapt to changing environmental conditions and thus survive longer (Nakamura and Takai, 2014). Hydrothermal spring systems can preserve evidence of the microorganisms that lived there, particularly through mineral deposits (Walter and Des Marais, 1993; Cady and Farmer, 2007; Westall et al., 2015b; McCollom et al., 2016). Mineral precipitates (e.g., silica) encrust and permineralize microbes, thus preserving various biosignatures such as microfossils, textures, biofabrics and organic compounds (biomarkers; **Fig. I.10A**).

2. Subaqueous environments

Subaqueous environments include lakes, deltas and playa lakes. The sedimentary deposits associated with these aqueous environments can concentrate and preserve the organic matter. In particular, deltas are important sedimentary environments for biosignature preservation because they contain diverse sub-environments to support and preserve abundant microorganisms. Deltas correspond to the mouth of rivers that flow into a body of water (lake, sea, ocean) and are formed by the faster supply of sediments than their erosion (Colella and Prior, 1990; Olariu and Bhattacharya, 2006).

Subaqueous deposits (e.g., river, delta and lake deposits) can preserve biosignatures associated with upstream subaerial life and in situ aquatic life. The potential biosignatures include organic structures

(e.g., cells), preserved organic molecules, biominerals and isotopic markers. The preservation of organic matter is facilitated by the rapid sedimentation of deltas, by the anoxic conditions that prevail at the bottom of the deltas, as well as the size of sedimentary grains, including finer particles, which have larger surface areas to support reactions with organics and facilitate their deposition, burial and long-term preservation (Müller and Suess, 1979; Berner, 1989; Mayer, 1994). Anoxic conditions in the water column and sediments can also enhance the potential preservation of organic matter through sulfurization of molecules by sulfur mineral encapsulation or direct sulfurization (Raven et al., 2016).

3. Subaerial environments

Subaerial environments include all environments at the surface or in the near surface not covered by a body of water, such as cold springs and soils, and they exist over a range of climatic conditions. Cold springs are characterized by the emergence of water at ambient temperature from the subsurface to the surface where water generally flows along fractures. Changes in chemical conditions occur when water emerges to the surface, leading to the precipitation of mineral deposits. Soils form when rain or snowmelt percolates down through surface rocks or sediments to cause top-down chemical weathering. Soils are typically composed of smectites, kaolinites and other phyllosilicates. They are preserved in the geological record as paleosols, i.e., fossil soils preserved after their formation by burial under sediments and generally lithified, whose observation allows to study the past climate and aqueous conditions as well as to identify macro- and microbiota (Sheldon and Tabor, 2009). The subaerial environments provide various habitats at the surface and in the near-surface to support diverse microbial communities (chemotrophic and phototropic microbial communities).

Subaerial environments can preserve a variety of biosignatures, such as textural, organic, chemical, mineralogical and isotopic biosignatures. Cold springs produce a diversity of mineral deposits such as clays, carbonates, sulfates/salts and amorphous minerals that multiply the mechanisms of preservation of biosignatures. In addition, the available energy produces abundant biomass in cold sources, which concentrates more biosignatures. Paleosols formed under reducing conditions generally concentrate well-preserved organic molecules at the top and in their subsurface horizons, whereas paleosols formed under oxidizing conditions have poor preservation potential. The preservation of biosignatures in paleosols therefore requires that the paleosurface of paleosols has been buried quickly to avoid their oxidation. The concentrations of organic carbon preserved in Archean and Proterozoic paleosols in terrestrial cratons range from 0.01 to 0.36 wt.% (**Fig. I.10B**; Rye and Holland, 2000; Watanabe et al., 2004).

4. Subsurface environments

Subsurface environments include shallow aquifers, deeper igneous crust, deep sediment deposits and caves. Surface habitable environments provide liquid water, nutrient and energy sources, as well as physical porous spaces and temperatures low enough to support life (Michalski et al., 2013; Parnell and McMahon, 2016). With increasing depth, pore size decreases and temperatures increase, which imposes a limit on habitability at the deep surface, which is estimated to be around 10–15 km on Earth (Michalski et al., 2013). The subsurface provides stable conditions over long periods of time (millions of years or more) that allows life to adapt to the environment and energy sources to accumulate. Caves also provide a protection from inclement surface conditions, and a variety of localized chemical gradients, and constitute an intermediate environment between the surface and the subsurface (Boston and Alexander, 2016).

Many types of biosignatures can potentially be produced by subsurface communities, including macroscopic patterns, microbial fossils, textures, organic and inorganic compounds, biominerals and isotopes (**Fig. I.10C**). In particular, interactions between fluids and rocks in the subsurface lead to the precipitation of secondary minerals that create favorable environments for the preservation of biosignatures.

5. Iron-rich environments

Iron-rich environments form when anoxic groundwater (or hydrothermal fluids) rich in reduced iron flows through permeable rocks. Iron-rich habitats are primarily subsurface and subaqueous habitats, such as groundwater circulating in permeable rocks, ferruginous marine and lacustrine settings, as well as deep-sea hydrothermal vents. Groundwater can also be expressed at the surface to form subaerial habitats, such as iron seeps and springs. Iron-rich environments are preserved in the geological record as iron formations (IFs) that are finely laminated aqueous deposits that may contain more than 15% iron (see the section *III.A.2. The early Archean eon (4.0–3.2 Ga)* for more information). These sedimentary deposits are often Precambrian in age and accumulated in deep ocean basins or shallow platform areas with reduced inputs of iron and silica from deep ocean hydrothermal activity (Klein and Beukes, 1989; Morris, 1993). Several iron-rich environments can be habitable in the long term, including the large volume of certain iron deposits can provide energy and reduced iron inputs on geologic time scales. Iron is notably known as one of the most abundant redox active metals in Earth's crust, and oxidation of dissolved reduced iron can power microbial metabolisms under acidic and circumneutral conditions, as well as under aerobic and anaerobic conditions (Straub et al., 1996; Widdel et al., 1993). In addition, iron can also protect against UV radiation, delaying or preventing the breakdown of organic matter due to radiolysis (Parenteau and Cady, 2010).

Preservation of microorganisms occurs when cells are rapidly buried in fine-grained iron sediments, or rapidly encrusted or permineralized in fine-grained primary iron precipitates (Farmer, 1999). The biosignatures formed by the rapid encrustation of microbial cells in iron-rich minerals are morphological or textural biosignatures, as well as lipid biomarkers derived from the cellular remains of microorganisms, which can be preserved for a long time in iron-rich deposits (**Fig. I.10D**).

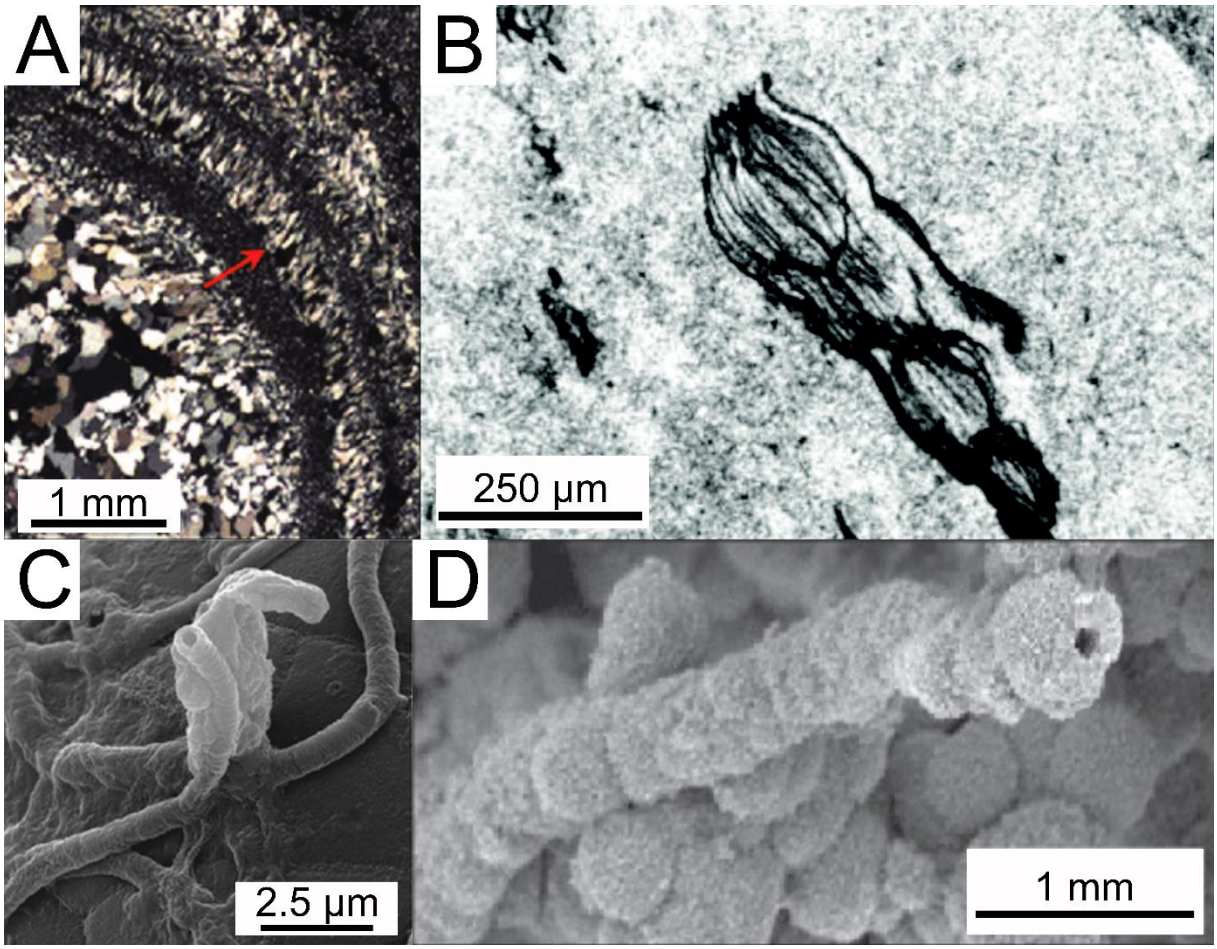

Figure I.10: *Examples of potential biosignatures in habitable environments. (**A**) Microbial palisade fabric (red arrow) oriented vertical to bedding in the 3.48 Ga Dresser Formation in Western Australia (modified after Djokic et al., 2017). (**B**) Opaque filamentous structures associated with 0.05–0.1 wt.% organic carbon in a 2.76 Ga basaltic paleosol in the Pilbara Craton (modified after Rye and Holland, 2000). (**C**) Tubular mineralized sheaths embedded in EPS found on black deposits from Cueva del Llano de los Caños cave in La Palma Island, Spain (modified after Riquelme et al., 2015). (**D**) Filamentous microbe encrusted by iron oxides from acid mine drainage at Iron Mountain in California (modified after Williams et al., 2017).*

IV. Search for habitability and traces of life on Mars

A. Definition of habitability

The term habitability has different meanings depending upon whether we are considering environments in which life could emerge, or environments that could host flourishing or even dormant life. Habitability for the emergence of life, as we know it, is quite different from habitability on Mars or the Earth today. Indeed, with respect to extant life, habitable environments may be large scale in time and space (the Earth's oceans, for instance), or highly ephemeral and rather limited in time and space (playa lakes in sabkha environments, outflow channels from hot springs, etc.). The brevity of existence of certain potentially habitable environments led to much debate regarding the episodic appearance of water at the surface of Mars even today and its potential for hosting viable life forms

(Rettberg et al., 2016). Environment that host dormant life forms are not really habitable because the organisms are in dormancy due to either a lack of carbon, water or energy.

Habitability can be defined as "the ability of an environment to support the activity of at least one known organism" (Cockell et al., 2016). However, as noted by Cockell et al. (2012), a habitable environment does not imply that it is necessarily inhabited. An environment is considered as habitable if it contains some essential ingredients, such as liquid water, nutrients (C, H, N, O, P, S and transition metals), an energy source (photonic or chemical) and appropriate physicochemical conditions (Cockell et al., 2012).

B. The past habitability of Mars

Extensive mineralogical and geomorphological evidence indicates that persistent liquid water was present during the Noachian/early Hesperian eras in many locations at the surface of Mars such as valley networks (Hynek et al., 2010), alluvial fans in craters (Moore and Howard, 2005), phyllosilicate minerals indicating aqueous alteration of the basaltic crust (Poulet et al., 2005), and sulfate minerals formed in acidic environment by water evaporation (Gendrin et al., 2005). Phyllosilicates are found in the oldest terrains dating from the Noachian (first geological period of Mars extending up to 3.7 Ga, according to the Hartman & Neukum scale), while sulfates appear in relatively young terrains, dated from the end of the Noachian to the Hesperian (second geological period lasting from 3.7 to 3.2 Ga, according to the same scale; Bibring et al., 2006). After the formation of phyllosilicates and sulfates, iron oxides are formed but do not require the presence of water unlike the other two minerals. Iron oxides are mostly formed during the last geological period of Mars, the Amazonian (3.2 Ga–today; Bibring et al., 2006).

Iron oxides are ubiquitous on Mars in the bulk crust, lava outflows and dust, and are formed by the oxidation of reducing iron supplied through mineral dissolution from basalt weathering. Iron oxides are correlated with the abundance of sulfur in Columbia Hills materials in Gusev crater (Ming et al., 2006; Morris et al., 2006), and occur as hematite (Fe_2O_3) mineral deposits in Meridiani Planum (Klingelhofer et al., 2004), suggesting the weathering of basalts by sulfuric acid formed by the oxidation of reduced sulfur compounds, elemental sulfur or SO_2 (McLennan et al., 2005; Tosca et al., 2005; Des Marais, 2010).

Many networks of dendritic valleys have been reported in the terrains dating from the Noachian and the beginning of the Hesperian, whose water could have come mainly from the frequent impacts of meteorites and volcanism during this period, giving rise to warm local conditions (Wordsworth et al., 2013). If life therefore appeared on Mars when liquid water was still present on its surface (<3.5 Ga), it could have colonized short-lived habitable habitats such as lakes, impact craters associated with hydrothermalism, impact lakes or rivers (Westall et al., 2013, 2015b), especially if the habitats were interconnected (Cockell et al., 2012).

The environmental conditions on the surface of Mars began to deteriorate during the Late Noachian/Early Hesperian (Carr and Head III, 2010) due to the disappearance of the primitive atmosphere which has been eroded by solar winds (Jakosky and Phillips, 2001; Jakosky, 2021) and/or impacts (Brain and Jakosky, 1998), resulting in a slow drop in ground pressure and temperature. A part of the water escaped to space, whereas another part was transported either to the poles, or in the subsurface (Clifford, 1993; Clifford and Parker, 2001; Lammer et al., 2013), as a deep cryosphere (i.e.,

water ice; Clifford et al., 2010; Weiss and Head, 2017) or as briny groundwater (Burt and Knauth, 2003; Stillman et al., 2016), and in hydrated minerals (Ehlmann et al., 2011; Mustard, 2019).

C. Early Earth and early Mars

Despite very different global conditions, the environments of early Earth and early Mars were locally similar. Indeed, both planets were characterized by a CO_2-rich, anoxygenic atmosphere, bodies of liquid water on their surface, and the availability of organic molecules and bioessential elements (e.g., C, H, N, O, P, S, Mg, Cl, K, Ca) brought by rocks and meteorites (Des Marais, 2010). Moreover, their environments were affected by similar geological and aerial processes, such as volcanism whose magma produces basaltic rocks of similar compositions, hydrothermalism associated with processes of volcanic activity (although the presence of vents has not yet been demonstrated on Mars), and impacts of meteorites and asteroids (**Fig. I.11**; Westall et al., 2015b).

However, the environments of the two planets vary greatly on a planetary scale. Unlike the abundance and frequency of water on early Earth (ocean planet), water on the surface of early Mars was likely present in a few locations geographically separated and episodically (regular cycle of wet and dry conditions) (Cockell et al., 2012; Westall et al., 2013, 2015b). As a consequence, habitability would have been punctuated in space and time on the surface of Mars (Westall et al., 2013, 2015b).

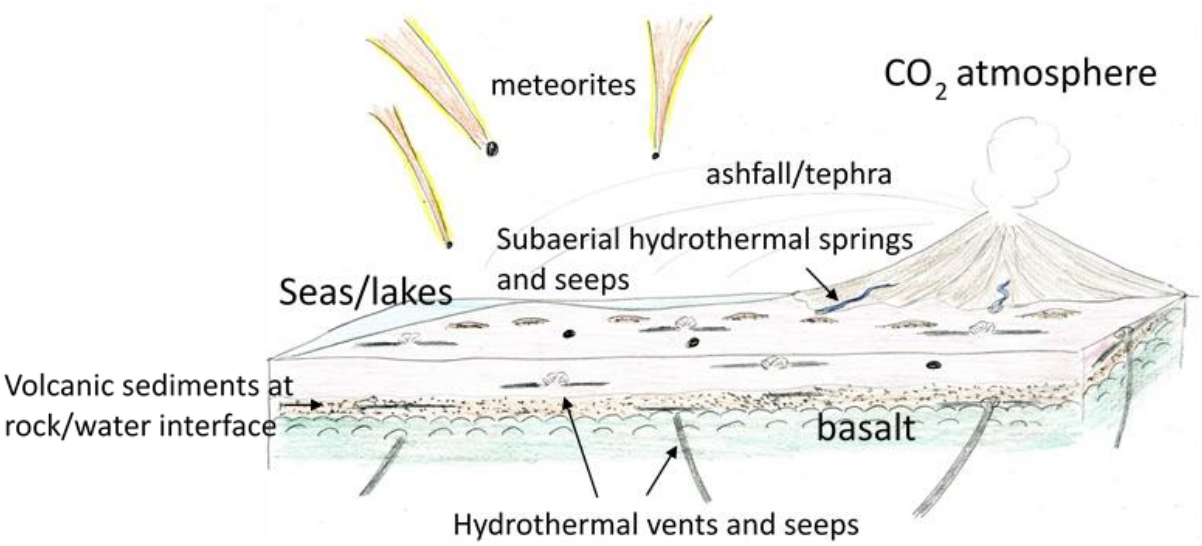

Figure I.11: *Sketch showing a geological environment on early Earth. This habitable environment is characterized by liquid water, a CO_2-rich atmosphere, a source of energy (sunlight, rocks and minerals), the availability of carbon and other chemical elements from meteorites, volcanic ash, volcanic sediments, basaltic rocks, hydrothermal fluids and seawater (adapted from Westall et al., 2015b).*

D. The possible appearance of life on Mars

As described above, the early environments of Earth and Mars had similarities in the local scale; habitable conditions for the emergence of life are believed to have existed on early Mars. From what we understand about the origin of life and the early cells, if life appeared on Mars, it is likely to have been similar to early life on Earth (but not identical). On early Earth, the first living cells were probably very small, comparable in size to micelles (spheroidal aggregates of amphiphilic molecules

characterized by a hydrophilic chain directed to the solvent and a hydrophobic chain directed to the interior) (Luisi et al., 2006) or viruses due to their minimal number of metabolic and reproductive components. Cells dating from 3.45 Ga whose morphology has been well preserved are still just as small, with a size of less than 1 µm (Westall et al., 2006a, 2011a). If primitive Martian microorganisms appeared, they probably possessed similar characteristics.

As on early Earth, the volcanic and hydrothermal environment on early Mars would have supported chemoautotrophic life-forms (organisms that use chemical reactions as energy sources and CO_2 as a carbon source) whose energy sources include oxidation of hydrogen sulfide, elemental sulfur, ferrous iron, molecular hydrogen, and ammonia (chemolithotrophs) or oxidation of organic sources, such as the degraded remains of microorganisms (chemoorganotrophs; Gargaud and Amils, 2011). Other forms of life based on anoxygenic photosynthesis, whose energy source is sunlight (phototrophic organisms) and carbon source is dioxide carbon, could have developed on Mars, although the lack of continuous habitability on the planet makes this evolutionary phase less likely. On Earth, photosynthesis developed at least at 3.5 Ga ago in shallow coastal areas where microorganisms had direct access to sunlight (Tice and Lowe, 2004; Allwood et al., 2006; Westall et al., 2006b). On Mars, shallow water environments may also have been prevalent.

After the deterioration of surface conditions on Mars, potential microbial life could have found refuge in the subsurface (Michalski et al., 2013). In fact, the subsurface present favorable conditions for current habitability. Hydrated phases and hydrothermal alteration products (e.g. iron/magnesium smectites and serpentine) were detected in central peaks of craters (Rogers, 2011; Ehlmann et al., 2011; Quantin et al., 2012; Osinski et al., 2013), which are natural probes of the Martian subsurface. Impact central uplifts also show that the greatest alteration occurred at depths greater than 5 km (Ehlmann et al., 2011). In addition, a cryosphere is estimated to occur at a depth of ca. 2.5 km at the equator to ca. 6.5 km at the poles (Fanale, 1976; Clifford, 1993), and a briny groundwater could be located deeper in the crust where radiogenic heating and lithostatic pressure (i.e., vertical pressure due to the weight of a column of rock above a given depth) would allow liquid water to exist above the freezing point (Clifford et al., 2010). The habitability of the subsurface is estimated to occur at a depth of ca. 6–15 km according a geothermal gradient temperature of ca. 10–20°C/km (Solomon and Head, 1990; Michalski et al., 2013).

Microorganisms in this deep biosphere would thus use different possible metabolic mechanisms based on hydrogen, carbon dioxide or abiotic hydrocarbons, and the carbon for the biomass would come from the magmatic carbon naturally present in the basalts (Steele et al., 2012). The oldest forms of life on Earth were probably chemoautotrophs and thermophiles, which were able to inhabit the subsurface by taking advantage of chemical gradients linked to serpentinization reactions (Martin, 2011). It is therefore possible that ancient and simple forms of life could have found refuge in the subsurface of Mars.

E. What traces of life can we expect to find on Mars today?

Due to the current conditions on the surface of Mars, we would rather expect to find fossil traces of life preserved in rocks and resembling those occurring in the early terrestrial record (chemotrophs or phototrophs). If microbial life appeared on Mars and found refuge in the subsurface when surface conditions deteriorated, we may also find a dormant microbial life form, waiting for better conditions to colonize the surface again, or even an extant life form living in subsurface habitats, such as

hydrothermal systems, deep groundwater systems, serpentinizing systems and diagenetic environments (Onstott et al., 2019).

A third possibility, which will be the object of the ExoMars mission (see the section *IV.G.4. ExoMars*), is the presence of biomolecules preserved in the subsurface of Mars (Westall et al., 2015b). These include possible prebiotic molecules that were able to form on the surface of Mars when the conditions necessary for their production were met. But their detection on the surface is difficult because of the destruction of the most volatile compounds by radiation and photochemical processes (Summons et al., 2011). However, the most refractory compounds are able to survive these processes and could be potentially detected using instruments on board the rovers.

An alternative hypothesis promoted by space agencies like NASA and ESA is that the Martian life we are looking for could be different from life as we know it on Earth (based on water and carbon), requiring a broader definition of life. An agnostic approach thus targets life based on different chemical processes, searching for more universal biosignatures such as organic signatures (complex molecules that are not associated with life on Earth; e.g., Marshall et al., 2021), and chemical and isotopic signatures (specific accumulations of elements or isotopes that are not typical of abiotic geological and mineralogical processes, or disequilibrium redox chemistries not consistent with abiotic redox reactions; e.g., Frank et al., 2013; Kempes and Krakauer, 2021). Agnostic tools and techniques could enable the search for life within a broader framework, especially as we go far from life on Earth (Johnson et al., 2018).

F. Where are the best places to search for past life on Mars?

According to Vago et al. (2017), several parameters must be considered in the search for traces of life in particular places on Mars: 1) the age; 2) the nature, duration, and connectivity of aqueous environments; and 3) the sediment deposition, burial, diagenesis, and exhumation history. Thus, to maximize our chance to find signs of past life on Mars, we must aim for the geologic period of Mars where water-rich interconnected locations predominate, namely during the pre- to late-Noachian periods (older than 3.6 Ga), and look for environments having preserved evidence of prolonged, low-energy, aqueous activity that may have favored the development of microorganisms. The locations of interest for the investigation of fossil traces of life are water-lain sedimentary deposits, in particular in fine-grained sediments containing phyllosilicates phases where organic molecules are better preserved. Other considerations should be taken into account such as the burial and diagenetic conditions of the sediments that would allow the preservation of fossil traces of life from the harsh surface conditions, as well as relatively recent exhumation of the overlying sediments allowing them to be re-exposed on the surface.

Ancient locations that have been able to preserve fossil traces of life include lacustrine and deltaic sedimentary deposits as well as hydrothermal deposits (Hays et al., 2017). In addition, impact craters should be considered as prime sites in the search for evidence of past life on Mars (Osinski et al., 2020).

G. Search for traces of life on Mars

Several present and future missions on Mars explore the geological environment of the planet to establish if the conditions could have support life. Another goal of these missions, in particular for Mars 2020 and ExoMars missions, is to search for evidence of past or present life preserving in the Martian rocks (**Fig. I.12A, C**). In addition, the Mars 2020 Perseverance rover is collecting Martian samples that

will be brought to the Earth as part of the Mars Sample Return mission for further laboratory analyses (**Fig. I.12B**).

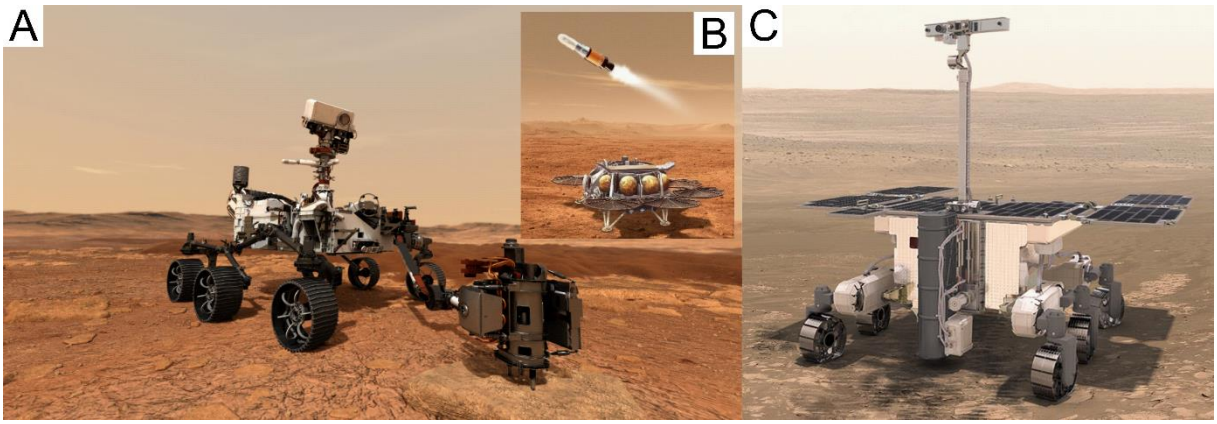

Figure I.12: *Artist's view of Mars 2020, Mars Sample Return and ExoMars missions. (**A**) The Mars 2020 rover Perseverance drilling a Martian rock to collect samples that will be analyzed by the rover's instruments and eventually returned to Earth (NASA image). (**B**) Rocket containing Martian rock samples launched from a lander on Mars to be sent to Earth (NASA image). (**C**) The ExoMars rover, Rosalind Franklin exploring the surface of Mars to search for traces of life (ESA image).*

1. Mars Science Laboratory (MSL)

Since August 2012, the NASA MSL Curiosity rover is exploring the 155-km-wide Gale impact crater located in Aeolis Mensae region, with its 5-km-high mountain, Aeolis Mons (or Mount Sharp), occupying the central part of the crater. Gale crater was chosen as a landing site of Curiosity because of the previous detection by high-resolution images of HiRISE camera onboard Mars Reconnaissance Orbiter (MRO) of the former presence of water, evidenced by morphological and mineralogical features, and the presence of stratigraphic sequences of sedimentary rocks of several meters that were deposited between 3.6 to 3.2 Ga ago (Grotzinger et al., 2012). This mission is not intended to search for extant life because the rover has not the capability of detect extant life processes. Nevertheless, the habitability and preservation conditions for possible ancient Martian life can be evaluated thanks to a suite of instruments that measure isotopic composition of inorganic and organic carbon in rocks and soils, molecular, elemental and mineralogical concentrations and abundances, specific rock textures, as well as concentration and isotopic composition of atmospheric gases such as methane (Grotzinger et al., 2012).

The rover found mineralogical and chemical evidence of past habitable environments on Mars. In particular, the exploration of Mount Sharp and surrounding plain revealed the presence of former bodies of water, in particular ancient streams, lakes and deltas which may have remained stable for up to 10,000 years in the crater (Grotzinger et al., 2015). Moreover, the lower strata of the mound are composed of sedimentary rocks made up of hydrated minerals (phyllosilicates) that are indicative of water-rock interactions and the higher strata contain sulfate-bearing minerals. This mineralogical transition suggests the deposition of sediments from a warmer and wet climate to a cold and dry climate (Bibring et al., 2006; Rampe et al., 2020). The rover also detected a diversity of organic molecules derived from possible Martian sources (e.g., hydrothermal, atmospheric, biological) and/or exogenous (e.g., interplanetary dust particles, meteorites; Freissinet et al., 2015; Eigenbrode et al., 2018). They include aromatic and aliphatic compounds, such as benzoic acid, S-containing molecules,

such as thiophene, and possibly amides (organic compound composed of a nitrogen atom bonded to a carbonyl group, C=O), carboxyl or carbonyl groups (Eigenbrode et al., 2018), all molecules occurring in meteorites.

2. Mars 2020

Since February 2021, the NASA Mars 2020 Perseverance rover (**Fig. I.12A**) is exploring the 45-km-wide Jezero crater located west of a flat plain called Isidis Planitia to determine the habitability of the paleoenvironments and characterize materials with high potentiality of traces of life preservation. In addition, another objective of this mission is to search for potential evidence of past life using the multiple instruments on board the rover and to collect samples for future analyses in terrestrial laboratories in the 2030s (see the section *IV.G.3. Mars Sample Return* for more information) thanks to a sampling and caching subsystem (SCS) that permits to collect rock cores (dimension of 13 mm diameter by >60 mm depth corresponding to ca. 15 g of sample mass) and regolith samples in clean and sterile individual tubes hermetically sealed (Farley et al., 2020). Jezero crater was chosen as a landing site for Perseverance for its astrobiological potential and the possibility to understand the planetary evolution in the region surrounding Jezero. Indeed, orbital observations showed that the crater contains a sequence of fluvio-lacustrine rocks deposited in an open-system lake (Farley et al., 2020). This ancient lake dates from 3.6 Ga old and was fed by a river via a delta. In addition, the MRO's CRISM (Compact Reconnaissance Imaging Spectrometer for Mars) instrument has revealed that the crater contains clays (Fe/Mg-smectite) and carbonates associated with the sedimentary deposits, indicating chemical alteration of rocks by water, and that could have preserved ancient life (Goudge et al., 2015, 2017; Bosak et al., 2021). The instruments of Perseverance have the ability to provide information regarding the texture, mineralogy, elemental and molecular composition of targeted rocks.

The first samples analyzed and collected by Perseverance are rocks of igneous origin, including olivine cumulated rich in olivine and pyroxene minerals and basaltic to basaltic andesite lava flows dominated by pyroxene and plagioclase minerals from the Séítah and Máaz formations, respectively, and an atmospheric sample (Farley et al., 2022; Simon et al., 2023). Fluorescence spectroscopy data identified the presence of potential aromatic organic materials in association with the altered minerals of the igneous units of the crater floor (Scheller et al., 2022; Sharma et al., 2023). Other additional rocks were identified and collected by the rover, namely sedimentary rock samples, including sulfate minerals that could have entrapped ancient microorganisms and/or organic compounds (Benison et al., 2023), and regolith samples composed of a mixture of sedimentary and igneous grains, from the delta front and the upper fan that the rover is currently climbing (https://www.nasa.gov/feature/jpl/nasa-s-perseverance-collects-first-mars-sample-of-new-science-campaign, Apr. 5, 2023). Pairs of samples are collected for each targeted rock, one sample of which is deposited in a cache and the other is kept in the belly of the rover (Simon et al., 2023). At the time these lines are written, 20 sample cores (https://mars.nasa.gov/mars-rock-samples/#20, Jun. 23, 2023) have been collected and 3 witness tubes pre-filled with diverse materials to test the possibility of terrestrial contamination, of which 9 samples plus the atmospheric sample have already been deposited to the Three Forks Sample Depot in January 2023, a backup cache on the surface of Mars. The cache serves as a backup in case the rover is unable to deliver the samples.

3. Mars Sample Return (MSR)

The MSR mission (**Fig. I.12B**) is a joint NASA-ESA mission to collect samples from the surface of Mars and return them to Earth for further scientific investigation. The mission is divided into four key elements: 1) the Mars 2020 mission (Perseverance rover) which is responsible for the selection, acquisition and caching of the samples; 2) the Sample Retrieval Lander (SRL) that will recover the samples which will be delivered by the rover or two Ingenuity-like helicopters (in case of technical problems with Perseverance) and store them thanks to a robotic arm in the Orbiting Sample (OS) container placed in the Mars Ascent Vehicle (MAV) that will launch the OS into Mars orbit; 3) the Earth Return Orbiter (ERO) that will capture and load the container for the return to Earth; and 4) the Sample Receiving Project (SRP) that will receive the samples on Earth and making them available for the science community (Muirhead et al., 2020). Return samples will serve several purposes, including reconstructing the formation and weathering of samples to understand the geology of Mars, assessing the potential biological history of Mars, providing new information on planetary-scale formation and evolution in the inner solar system, and identifying and characterizing potential risks and resources to the human exploration of Mars (Farley et al., 2020). The samples collected by Perseverance are organized in two groups (only one of which will be technically recovered): 1) a group of 10 samples deposited in the Three Forks Sample Depot, and 2) a group of 33 samples that will be carried by the rover, including duplicates of the samples in the Three Forks Depot (see the document *Terms of reference for the Measurement Definition Team* available on NASA and ESA websites).

MSR samples are scheduled to arrive on Earth in October 2033 to be transported to a dedicated location, the Sample Receiving Facility (SRF) where they will undergo a series of analyses to perform through three main elements carried out simultaneously: 1) Initial Sample Characterization, 2) Sample Safety Assessment, and 3) Science Investigations.

- *The Initial Sample Characterization:*

The Initial Sample Characterization gathers the minimum of observations and analyses describing the returned samples and consists of three phases, each successively more invasive: 1) non-destructive or minimally destructive pre-basic characterization of all the samples where the dust is removed and measurements taken before opening the tubes containing the samples to avoid losing information; 2) non-destructive or minimally destructive basic characterization of the collection of samples whose tubes are opened to carry out measurements which include weighing, photographic documentation and optical observations; and 3) preliminary examination of samples which may require their division into subsamples and their preparation for destructive analyses which will be essential for the allocation of material by the scientific community for investigation (Tait et al., 2022).

- *The Sample Safety Assessment:*

The Sample Safety Assessment main objective is to determine if the returned samples are not harmful for the Earth (e.g., environment, biosphere, geochemical cycles) on the basis of the hypothesis that the samples could contain Martian life (positive hypothesis). Four elements composed this assessment, namely the probability of a past life in the samples, a targeted subsampling strategy, decision criteria and the test sequence. In particular, the test sequence encompasses the investigations and associated analytical measurements necessary to assess the security of the samples which can be grouped into three main categories: 1) documentation of the 3-D structure and the associated chemical and mineralogical information, some of which may require the sample preparation; 2) determination of the presence or absence of organic matter and its origin (terrestrial or martian) in the samples by studying the characteristics (molecular patterns and isomeric variations) associated with individual

species (e.g., amino acids, lipids) and the presence of macromolecules; and 3) determination of the presence and origin of biomarkers for life as we know it (chemical processes similar to terrestrial organisms) and for life as we do not know it (unanticipated detection of complexity that is not associated with life as we know it on Earth, nor with abiotic chemical processes), i.e., an agnostic approach (Kminek et al., 2022).

- *The Science Investigations:*

The Science Investigations will permit to analyze returned samples using advanced laboratory instruments and sample preparation methods that are impossible to carry out through in situ space exploration missions. Nevertheless, due to the limited amount of material (<ca. 1 kg) and unique scientific value of these samples, it will be necessary to conduct the minimum number of measurements within the SRF and make samples available for more sophisticated laboratory analyses. But before to release samples to other laboratories, they will have to be analyzed and possibly sterilized to prove that they are safe, which can alter the samples and cause the loss of scientific information forever. In particular, the time-sensitive samples are exposed to the degradation of organic matter of potential biological origin, the modification of the composition of the atmospheric gas located in the upper part of the tubes, exchanges between minerals and volatiles, and the oxidation/reduction of redox-sensitive materials (Tosca et al., 2022). In addition, the time-sensitive samples can also be sterilization-sensitive. Indeed, sterilization processes such as dry heat and gamma-irradiation can affect organic molecules of biological or abiotic origins, as well as hydrous minerals and hydrous amorphous solids by breaking chemical bonds (Velbel et al., 2022). The investigations of time-sensitive and sterilization-sensitive samples have thus to be completed on unsterilized samples inside biocontainment and on short timescale to maximize the amount of scientific information (Tosca et al., 2022; Velbel et al., 2022).

4. ExoMars

The ESA ExoMars Rosalind Franklin rover (**Fig. I.12C**), whose launch was initially scheduled for 2018 but has been postponed to 2028, will seek clues of past or present life on Mars in the 200-km-wide Oxia Planum basin located at the eastern margin of Chryse Planitia, near the equator, and at the outlet of the Coogoon Valles system. The region is particularly flat and contains ca. 4 Ga old clay-rich deposits detected by the OMEGA (Mars Express probe) and CRISM (Mars Reconnaissance Orbiter probe) spectrometers that correspond to vermiculite-smectite type of clays (Carter et al., 2016; Quantin-Nataf et al., 2021). A younger fluvio-deltaic sedimentary system of ca. 3.9 Ga old overlying the clay-bearing unit also occurred as indicated by the observations of a fan-shaped depositional sedimentary feature at the outlet of Coogoon Valles showing a hydrated silica nature and associated with many inverted channels (Quantin-Nataf et al., 2021; Davis et al., 2023). Inverted channels indicate important environmental changes, from a fluvial erosion to a heavy erosion phase where the latest surficial layers being more resistant are the latest sediments remaining in the landscape. These orbital observations suggest that this landing site has recorded two aqueous environments occurring during the Noachian: 1) the deposition of ca. 100 m widespread clay-rich deposits, and 2) the development of a fluvio-deltaic system that post-dates the clay-rich deposits, indicating a later period of surface water and probably even a standing body of water (Quantin-Nataf et al., 2021). Recent evaluation of the orbital data suggests that at least a part of the Oxia Planum sediments is of alluvial origin, with fluvial activity being of an episodic nature (Davis et al., 2023). These features make this site particularly interesting for its potential past habitability and the preservation of physical and chemical signatures characteristic of past life.

The particularity of the Rosalind Franklin rover is to possess a drill that allows to penetrate and obtain samples from the subsurface, up to 2 meters deep where organic molecules could have been preserved (Vago et al., 2017). Because of the thin atmosphere of Mars, its surface is constantly bombarded by solar and space radiation which may have cause the alteration of potential organisms or biomolecules exposed on the surface (UV radiation) up to a few meters deep (ionizing radiation). In addition, the exposure of mineral phases containing chlorides to UV radiation leads to the formation of reactive oxidative species (perchlorates) which can destroy the chemical biosignatures. During the nominal mission, the rover will perform a set of measurements to characterize the geological environment and assess the presence of biosignatures by carrying out investigations from the panoramic to the molecular scale. The rover's Pasteur payload instruments comprises panoramic instruments (cameras, an IR spectrometer, and a ground-penetrating radar), contact instruments to study rocks and collected samples (a close-up imager and an IR spectrometer in the drill head), and the analytical laboratory, including a visual + IR imaging spectrometer, a Raman spectrometer and a laser desorption (LD), thermal volatilization (TV) gas chromatograph-mass spectrometer (GC-MS; Vago et al., 2017). Once arrived at a scientific place of interest, the rover will locate targets of interest thanks to its panoramic camera and the infrared spectrometer located on the mast. Then it will approach 3 meters away from an outcrop to obtain visual and spectral information while analyzing the subsurface with the penetrating radar to characterize the geological context. Then the outcrop will be imaged at high resolution by the close-up imager to better understand the deposit environment and look for morphological biosignatures, before collecting drill cores (3 cm long, 1 cm diameter). These samples will then be introduced into the analytical laboratory drawer (ALD) where they will be crushed then analyzed with infrared and Raman spectrometers, and the Mars Organic Molecule Analyzer (LD, TV GC-MS) to identify mineralogy and presence of organic molecules (Vago et al., 2017). Then the rover will move to another location to repeat the same sequence of operations with a speed of a few meters per sol (i.e., one Martian day that is 24 hours plus 40 minutes).

The Rosalind Franklin rover is thus well appropriate for the search for signs of life in situ and will be complementary with the analyses carried out on samples returned from Mars in laboratory.

V. Research questions of this thesis

This thesis project is centered around two central questions:

1) **How can we maximize the detection of microfossils and their associated biosignatures in early terrestrial rocks?**

The fossil record provides information about the life forms that existed in the past and the environmental conditions that allowed their preservation. However, the oldest fossil records have been erased from the Earth's geological history and it is more difficult to find fossil traces of life when going back in time, especially since most fossil traces of life dating from the Precambrian (<2.5 Ga) are microfossils whose detection and identification as well as the characterization of associated biosignatures is made particularly difficult.

2) **What are the most relevant techniques to use in order to optimize the detection of traces of life in Martian rocks?**

Due to the limited possibility of evolution of life on Mars, we hypothesize that putative ancient Martian life, dating from the late Noachian to early Hesperian, would be relatively similar to chemotrophs detected in Paleoarchean (ca. 3.2–3.5 Ga) terrestrial rocks, i.e., a form of microbial life leaving very subtle fossilized traces (Westall et al., 2006a, 2015b). However, such traces of life are particularly delicate to analyze on Earth even with sophisticated laboratory instrumentation. Thus, their documentation will be more difficult on Mars using in situ instrumentation (Azua-Bustos, 2023), which underlines the importance of a return mission of samples.

VI. An analogue of fossil traces of Martian life: the microfossils from the 3.45 Ga Kitty's Gap Chert

In order to help the detection of traces of life in Martian rocks in situ and/or in samples returned to Earth, I studied the microfossils associated with ancient volcano-sedimentary materials from the 3.45 Ga Kitty's Gap Chert, East Pilbara, Australia, considered to be good analogues of ancient sedimentary martian rocks (Westall et al., 2011a, 2015b). In particular, the depositional environment of the sediments of the Kitty's Gap Chert is relatively similar to that of the Martian sediments of Gale crater or Jezero crater of Noachian age, i.e., a shallow-water volcanic sedimentary environment (e.g., de Vries, 2004; Westall et al., 2006a). The Australian sediments were also influenced by tides and hydrothermalism. While hydrothermal activity occurred on Mars, there were no tides. In addition, the sediments of Kitty's Gap were lithified by a fine-grained silica cement (chert), but it is not generally the case for the Martian sediments.

Previous studies documented the presence of some of the oldest known traces of life on Earth in the form of silicified microorganisms interpreted as anaerobic, autotrophic chemolithotrophs that coat the surfaces of volcanic grains and occur in the volcanic dust-rich matrix of the rock (Westall et al., 2006a, 2011a, 2015b). Most of the interpreted microfossils are coccoidal structures of less than 1 µm in size forming monolayer colonies from several micrometers to several tens of micrometers in size on the surface of volcanic grains (**Fig. I.6E**). They are always associated with a film-like phase interpreted as EPS produced by microbes to attach themselves to the surface of minerals from which they can absorb chemical elements more efficiently. The purported microfossils are carbonaceous; carbon isotopic compositions of individual, millimeter thick, microfossil-containing sediment layers range from –25.9‰ to –27.8‰ (Westall et al., 2006a) and are compatible with microbial fractionation (Schidlowski, 2001). However, the low biomass production rate and metabolic productivity of the interpreted chemolithotrophs resulted in low concentrations of only 0.01–0.05 wt.% of total organic carbon in the sediments (Westall et al., 2006a). In addition to the colonies of coccoids, detrital fragments of microbial filaments and phototrophic mats also occur, together with rare rod-shaped microorganisms (Westall et al., 2006a).

Because of their simple morphology, these purported fossilized microorganisms are still considered to be controversial despite numerous indicators of their syngenicity and biogenicity (e.g., Wacey, 2009). Studies of abiotic biomorphs have also highlighted the difficulties in interpreting biogenicity (e.g., García-Ruiz et al., 2003, 2009; Cosmidis and Templeton, 2016; Criouet et al., 2021). If potential traces of primitive life exist in returned samples from Mars, and if they resemble interpreted primitive microfossils in the Kitty's Gap Chert and other early Earth horizons, definitive interpretations of their biogenicity will be hotly debated. For this reason, the Kitty's Gap microfossils provide an ideal subject for testing advanced techniques to document complementary types of biosignatures. Such sequences of analyses can be considered trial runs of the approaches needed if similar potential microfossils occurred in samples returned from Mars. Moreover, the original interpretation of the microfossils in

the Kitty's Gap Chert was made using technologies that have since been improved. New understanding of what constitutes reliable biosignatures (e.g., Meadows et al., 2022) and new state of the art technologies are now available that can shed light on the biogenicity of the structures and their microenvironment (Brasier et al., 2015).

VII. Notions of biogenicity and syngenicity

A. Biogenicity

"Biogenicity refers to any chemical and/or morphological signature preserved in rocks, minerals, ice, or dust particles that are uniquely produced by past or present organisms" (McLoughlin, 2014). To assess the biological origin of potential microfossils, biogenicity criteria are used, which can be divided into four different categories (Westall, 2008; McLoughlin, 2014):

- The geological context: conditions compatible with microbial life (temperature, pressure, pH, salinity, energy sources, basic and other trace elements…);
- The structural characteristics: morphological appearance of the microorganisms (size and shape, cell division, evidence of living and dead cells...), and colonial and biofilm characteristics (association of individuals of the same species, association of different species in a same colony, association with EPS…);
- The biogeochemical characteristics: biomarkers, isotopes (C, N, S, Fe...), and biofunctional major (P, S, N...) and trace (V, Fe, Co, Ni, Zn...) elements;
- Evidence of interaction between individual microorganisms and their biofilms with their microenvironment: microbial mats, biolaminations, alteration textures, biominerals…

The degree of reliability of biogenicity is thus enhanced by the complementary evidence provided by various types of biosignatures (e.g., Cady et al., 2003; Cavalazzi et al., 2011), and the detailed study of any geological context, as well as the consideration of potential abiotic explanations.

B. Syngenicity

"Syngenicity refers to the age of an organic residue compared to the age of the rock in which it occurs" (Oehler and Cady, 2014). In other words, an organic residue is said to be syngenetic if it was formed at the same time as the host rock which contains it. In the context of searching for traces of life, it is important to assess syngenicity to understand the origin of any organic material found in ancient rocks. This criterion is thus complementary to the biogenicity criteria presented previously.

Some examples of evidence for syngenicity of organic remains include a Raman signature consistent with the age and thermal maturity of the enclosing rock, their permineralization in a mineral matrix, their distribution with respect to mineral grains, and no evidence for further migration of organic materials through fractures in the rock.

VIII. Thesis objectives

The first objective of my thesis was to combine multiple complementary analyses techniques in order to fully characterize the purported fossilized traces of life of the Kitty's Gap Chert, and, thus, evaluate their biogenicity and syngenicity. My approach, based on a maximum of physico-chemical data to

confirm the biogenicity of the investigated structures, provides an example of the degree of analytical rigor that will be needed to search for potential traces of life in Martian rocks. This includes:

- Documentation of the paleoenvironment through study of sedimentary facies (e.g., laminations, micro-ripples, lenticular bedding, orientation of volcanic clasts), petrology (e.g., nature, composition, size and shape of clasts), mineralogy (including biominerals) and geochemistry (e.g., major, trace and rare-earth elements);
- Physical characterization of carbonaceous phases: micro- and nanostructure (e.g., diffuse carbon, films, particles), and crystallography (amorphous or graphitized);
- Chemical characterization of the carbonaceous matter: analysis of elemental and molecular composition of carbonaceous materials in the sediments;
- Distribution of carbonaceous materials in the rock: detection and localization of carbonaceous deposits, in particular with respect to volcanic particle surfaces and the volcanic dust-filled sedimentary matrix.

The second objective was to propose a protocol for the analysis of returned Martian samples, which includes the selection of the most relevant analysis techniques to detect fossil traces of life.

Chapter II describes the geological context of the Kitty's Gap Chert, as well as the samples studied and their preparation. Then, the different analytical methods used are presented.

Chapter III is divided into two distinct parts, the first of which traces the paleodepositional environment of the silicified volcanic sediments of the Kitty's Gap Chert through sedimentological, petrological, mineralogical and geochemical analyses of the samples. The second part is about the study of carbonaceous matter in the silicified volcanic sediments of the Kitty's Gap Chert, whose characterization through physical and geochemical analyses, as well as its distribution at several scales, is essential to identify biosignatures within and assess its biogenicity.

Chapter IV discusses the main results allowing to reconstruct the paleoenvironment of the Kitty's Gap Chert and to demonstrate the syngenicity and biogenicity of the carbonaceous matter. These are also compared with data from the literature.

Chapter V discusses how the study of Kitty's Gap Chert microfossils can help to select analytical techniques to be used to analyze samples returned from Mars.

Finally, chapter VI gives the main conclusions of this study and the proposal for an analysis protocol for Martian samples.

IX. Résumé en français

Ce manuscrit décrit mes travaux de thèse menés au CNRS d'Orléans, dans l'équipe d'exobiologie du Centre de Biophysique Moléculaire (CBM) entre novembre 2020 et septembre 2023. Ce projet s'inscrit largement dans le thème de l'exobiologie, terme qui a été introduit pour la première fois par le généticien et microbiologiste américain Joshua Lederberg dans un article paru en août 1960, intitulé « *Approaches to Life beyond the Earth* ». Au départ, l'exobiologie désignait spécifiquement le domaine consacré à l'étude de la vie dans le milieu extraterrestre, avant de s'élargir à l'étude de l'origine, de la distribution et de l'évolution de la vie dans l'Univers, ainsi que les processus et les structures liés au vivant. L'équipe d'exobiologie du CBM aborde le thème de l'exobiologie dans son ensemble, depuis la chimie prébiotique jusqu'à l'exploration spatiale, incluant l'étude d'échantillons analogues, le développement de méthodes et d'instruments pour l'exploration spatiale, la micropaléontologie pour étudier les plus anciennes traces de vie sur Terre et la géo-microbiologie qui concerne la préservation de biosignatures microbiennes et les interactions entre des microorganismes et des minéraux.

L'étude de l'histoire géologique de la Terre primitive (4,54–3,2 milliards d'années) permet de retracer les conditions d'habitabilité favorables à l'apparition de la vie sur Terre et de contextualiser l'enregistrement des plus anciennes traces de vie fossiles. L'histoire du début de la Terre primitive, l'Hadéen (4,54–4,0 milliards d'années), est très peu connue en raison de la destruction des terrains les plus anciens par le recyclage de la croûte, les impacts et les mécanismes d'altération et d'érosion qui remodèlent sans cesse la surface de notre planète. Cependant, on sait que les conditions nécessaires à une chimie prébiotique étaient réunies près de 150 millions d'années après l'accrétion de notre planète, comme le démontre la présence de zircons détritiques qui attestent d'une croûte continentale stable et d'océans d'eau liquide entre 4,40 et 4,35 milliards d'années (**Figure I.1**).

Les terrains les plus anciens datent du début de l'Archéen (4,0–3,2 milliards d'années). Il s'agit de vastes volumes de croûte continentale préservée (des cratons) qui contiennent parmi les plus vieilles roches connues sur Terre, dont la plupart affleurent au Canada, au Groenland, en Afrique du sud et en Australie. La roche la plus ancienne est le gneiss d'Acasta daté à 4,031 milliards d'années dont la roche mère est une roche plutonique qui provient du refroidissement lent d'un magma et qui a subi plusieurs épisodes de métamorphisme. Les plus vieux terrains de dimension continentale sont les cratons de Kaapvaal (Afrique du sud) et de Pilbara (Australie) formés entre 3,6 et 3,1 milliards d'années et dont l'étude nous permet de reconstruire les conditions environnementales qui régnaient à l'Archéen. Les cratons sont majoritairement composés de TTG (Tonalites, Trondhjemites et Granodiorites) et de ceintures de roches vertes. Les TTG forment une croûte protocontinentale dont la plupart des roches constituent des plateaux en grande partie submergés. Les ceintures de roches vertes surmontant ces protocontinents sont constituées de roches sédimentaires intercalées entre des dépôts de lave, dont les roches volcaniques sont principalement des komatiites formées à des températures de fusion élevées (1600–1650°C), indiquant un manteau plus chaud à l'Archéen par rapport à aujourd'hui. De plus, les roches sédimentaires révèlent une importante activité hydrothermale (cherts formés par la sursaturation de silice dans l'eau de mer issue principalement de fluides hydrothermaux) et des conditions réductrices (formations de fer rubanées formées par la précipitation de fer ferreux).

À 3,5 milliards d'années, la température des océans est estimée entre 26°C et 60–70°C selon les différents modèles, avec un pH variable et une salinité une à deux fois plus élevée que celle des océans actuels. La composition des océans en métaux essentiels pour le vivant (Fe, V, Ni, As, Co…) est également plus riche qu'aujourd'hui en raison du lessivage de la croûte continentale Archéenne de composition mafique à ultramafique (très riche en Fe, Mg et Ca), bien que certains métaux de

transition soient moins disponibles en conditions anoxiques. L'atmosphère était composée principalement de CO_2, H_2O et N_2 et de gaz en traces (CO, H_2) provenant du dégazage de l'océan magmatique et/ou d'éléments volatils apportés par les météorites. Les particularités des océans et de l'atmosphère sont ainsi favorables à la synthèse de matière organique prébiotique et/ou au développement de la vie avant 4 milliards d'années (**Figure I.2**). Cependant, les premières formes de vie microbiennes sont nécessairement extrêmophiles en raison des conditions extrêmes de l'environnement global de la Terre primitive (températures élevées, acidité, salinité…).

Dès 4,4–4,2 milliards d'années, les conditions (eau liquide, continents émergés, température de surface…) sont donc réunies pour permettre l'émergence de la vie. La chimie prébiotique est un ensemble de réactions ayant pu conduire à la transition du non-vivant vers le vivant. Pour ce faire, on sait que plusieurs ingrédients clés sont nécessaires tels que de la matière organique (terrestre et/ou extraterrestre), de l'eau (solvant), des sources d'énergie (photoniques, chimiques ou thermiques), des éléments essentiels (H, N, O, P, S et métaux de transition), ainsi que des surface minérales (verres volcaniques, pyrite…) pour catalyser les réactions. La présence de gradients de température, pH, concentration ionique et/ou d'énergie sont également importants pour permettre la diffusion des composants essentiels pour la chimie prébiotique et le fonctionnement des métabolismes primitifs dans l'eau de mer, les fluides hydrothermaux ou les rivières. Ainsi, plusieurs types d'environnements ont été proposés pour l'émergence de vie, en particulier, les systèmes hydrothermaux de surface (**Figure I.3**) et/ou subaquatiques (**Figure I.4**) dont les surfaces minérales réactives fournissent de l'énergie chimique pour les réactions prébiotiques au contact de l'eau chaude et facilitent également la concentration de molécules prébiotiques qui s'assemblent pour former des molécules plus complexes jusqu'à l'apparition de cellules « vivantes ».

La fossilisation des organismes vivants permet de les préserver au fil des temps géologiques (**Figure I.5**), bien qu'une grande partie des organismes fossilisés aient disparu de l'enregistrement fossile en raison de la tectonique des plaques et des processus d'altération et d'érosion en surface. L'enregistrement fossile le plus ancien documente des traces de vie datant de la fin de l'Hadéen/du début de l'Archéen (4,0–3,6 milliards d'années), dont la plupart sont souvent très controversées en raison de la subtilité des preuves obtenues et de l'intense métamorphisme subi par les roches. Les traces de vie fossiles les plus convaincantes sont des restes microbiens datant de 3,5 milliards d'années (**Figure I.6**). Les plus anciennes traces de vie sur Terre sont des organismes unicellulaires, c'est-à-dire des organismes procaryotes tels que les archées et les bactéries, dont la petite taille (<10 µm) et l'absence de parties dures ont nécessité des conditions de préservation exceptionnelles. L'encapsulation minérale est un processus de fossilisation qui permet de préserver la structure physique des microorganismes grâce à l'interaction des ions de l'environnement de la cellule avec les groupes fonctionnels de la matière organique (**Figure I.7**). Pour passer dans l'enregistrement géologique et être préservés à travers les temps géologiques, les restes cellulaires doivent être lithifiés dans les sédiments. Malgré une fossilisation rapide, la matière organique lithifiée se dégrade avec le métamorphisme pour se transformer en kérogène à partir duquel il est possible d'identifier des biosignatures (**Figure I.8**). Cependant, de nombreux processus abiotiques peuvent donner lieu à des signatures similaires à ce que produit le vivant sur Terre (**Figure I.9**). L'interprétation de traces de vie supposées doit ainsi être basée sur des mesures multiples qui satisfont un certain nombre de critères permettant d'augmenter la probabilité de confirmer une origine biologique. Une analyse détaillée du contexte géologique et minéralogique des traces de vie fournit également des informations sur l'environnement de dépôt dans lequel les biosignatures potentielles ont pu être préservées (**Figure I.10**).

L'étude de l'habitabilité et la recherche de traces de vie sur Mars est abordée grâce à la comparaison de la Terre et de Mars primitives dont les environnements à l'échelle microbienne partagent de nombreuses similarités (atmosphère riche en CO_2, eau liquide, disponibilité de molécules organiques et d'éléments bioessentiels… ; **Figure I.11**). Cependant, les conditions à la surface de Mars se sont dégradées après 4,0–3,5 milliards d'années avec la disparition de l'atmosphère primitive et de l'eau liquide en raison d'un refroidissement plus rapide. Par opposition, la Terre a continué d'être habitable durant la même période avec la diversification de ses environnements et de sa biodiversité. En raison des conditions locales similaires entre la Terre primitive et Mars primitive, les traces de vie martiennes sont probablement similaires à celles retrouvées dans les roches terrestres anciennes. Cependant, avec la dégradation des conditions de surface après l'Hespérien, les traces de vie supposées sur Mars sont soit préservées sous forme de fossiles dans les roches, soit en dormance ou toujours actives, vivant en subsurface. Une autre possibilité est la préservation de biomolécules dans le sous-sol de Mars. Une hypothèse alternative suggère une vie martienne basée sur des caractéristiques différentes par rapport à la vie telle que nous la connaissons sur Terre (basée sur l'eau et le carbone), nécessitant une définition plus large de la vie avec la recherche de biosignatures universelles. Les missions actuelles et futures sur Mars ont pour objectifs de caractériser l'habitabilité des paléoenvironnements martiens afin d'établir si les conditions ont pu favoriser l'apparition et le développement de la vie, ainsi que de chercher des indices de traces de vie actuelles ou passées préservées dans les roches (**Figure I.12A, C**). Un autre objectif est de rapporter des échantillons de roches sur Terre grâce à une mission de retour d'échantillons qui permettra des analyses avec les dernières technologies de pointe disponibles dans les laboratoires (**Figure I.12B**).

Le sujet principal de cette thèse concerne l'étude de traces de vie fossiles dans des sédiments volcaniques du chert de Kitty's Gap (Australie) datant de 3,45 milliards d'années et dont l'environnement de dépôt est relativement similaire à certains environnements martiens au Noachien (3,7–4,1 milliards d'années), malgré certaines différences concernant le dépôt (hydrothermalisme et marées) et la lithification des sédiments (chert). L'objectif principal de cette thèse est de combiner plusieurs méthodes d'analyse complémentaires afin de maximiser la détection de traces de vie fossiles et leurs biosignatures associées dans les roches terrestres primitives. Le second objectif concerne l'application de ces résultats à la recherche de traces de vie dans les échantillons de retour de Mars et la proposition d'un protocole d'analyse pour optimiser la détection de traces de vie martiennes.

Le chapitre 2 décrit le contexte géologique du chert de Kitty's Gap, ainsi que les échantillons étudiés et leur préparation, puis les différentes méthodes d'analyses utilisées. Le chapitre 3 décrit l'environnement de dépôt des sédiments volcaniques du chert de Kitty's Gap et la caractérisation de la matière carbonée qu'ils contiennent afin d'identifier des biosignatures et d'évaluer sa biogénicité. Le chapitre 4 discute des principaux résultats obtenus qui permettent de reconstruire le paléoenvironnement du chert de Kitty's Gap et de démontrer la syngénicité et la biogénicité de la matière carbonée. Ces résultats sont également confrontés avec les données de la littérature. Le chapitre 5 est dédié à l'application de cette étude aux échantillons de retour de Mars. Enfin, le dernier chapitre donne les principales conclusions de cette étude et propose un protocole d'analyse des échantillons martiens.

Chapter II: Materials & Methods

I. Introduction

This second chapter first describes the geological context of the Kitty's Gap Chert from which the samples were taken. The chert is composed of silicified volcanic sediments that were deposited by rivers on a beach around 3.45 Ga ago and crossed by contemporary hydrothermal silica veins.

The samples taken in the field in 2000 are three pieces of rock from the outcrop of the Kitty's Gap Chert, one of which comes directly from a hydrothermal vein (00AU37b) and the other two come, respectively, from a few centimeters from the hydrothermal vein (00AU39) and from 15 meters east of the hydrothermal vein (00AU40).

The sample 00AU37b was analyzed to obtain geochemical information about the hydrothermal source, whereas the other two rock samples located around the source (00AU39 and 00AU40) were analyzed in different formats using multi-scales and complementary methods: from the description of hand samples to nanoscale analysis of FIB sections, through bulk analysis of powders, local analysis of rock slabs and microscale analysis of thin sections.

A table summarizing the different methods used to analyze the samples from the Kitty's Gap Chert during this thesis project is provided at the end of the chapter.

II. Materials

A. Geological setting

The Kitty's Gap Chert is a well-preserved sedimentary stratigraphic unit within the Pilbara craton, Australia, forming part of the Panorama Formation, in the Coppin Gap Greenstone Belt (**Fig. II.1**). The sedimentary horizon in question is part of the Kitty's Gap volcano-sedimentary complex (KG-vsc.) comprising felsic volcanics, minor basalts, and volcaniclastic sedimentary rocks (i.e., made up of debris of volcanic rocks and minor terrigenous sand and mud; Zou et al., 2013) that were deposited in a subaqueous environment influenced by normal fault activity (**Fig. II.1C**; Nijman et al., 1998; de Vries, 2004). In fact, the Coppin Gap Greenstone Belt underwent a phase of extension (i.e., tectonic regime resulting from the stretching of the earth's crust or the lithosphere) towards the west for a period of at least 20 million years (de Vries, 2004). The KG-vsc. is exposed over a total length of about 5 kilometers and is sandwiched between pillow basalts of the Apex Basalt (below) and Euro Basalt (above). The silicified sediments of the Kitty's Gap Chert form the top the KG-vsc., and are underlain by felsic volcanics and overlain by volcanics of basaltic composition, of which felsic rocks have been dated at 3446 ± 5 Ma by U-Pb SHRIMP dating (de Vries, 2004; de Vries et al., 2006). The silicified sedimentary succession is more than 40 meters thick (de Vries et al., 2010).

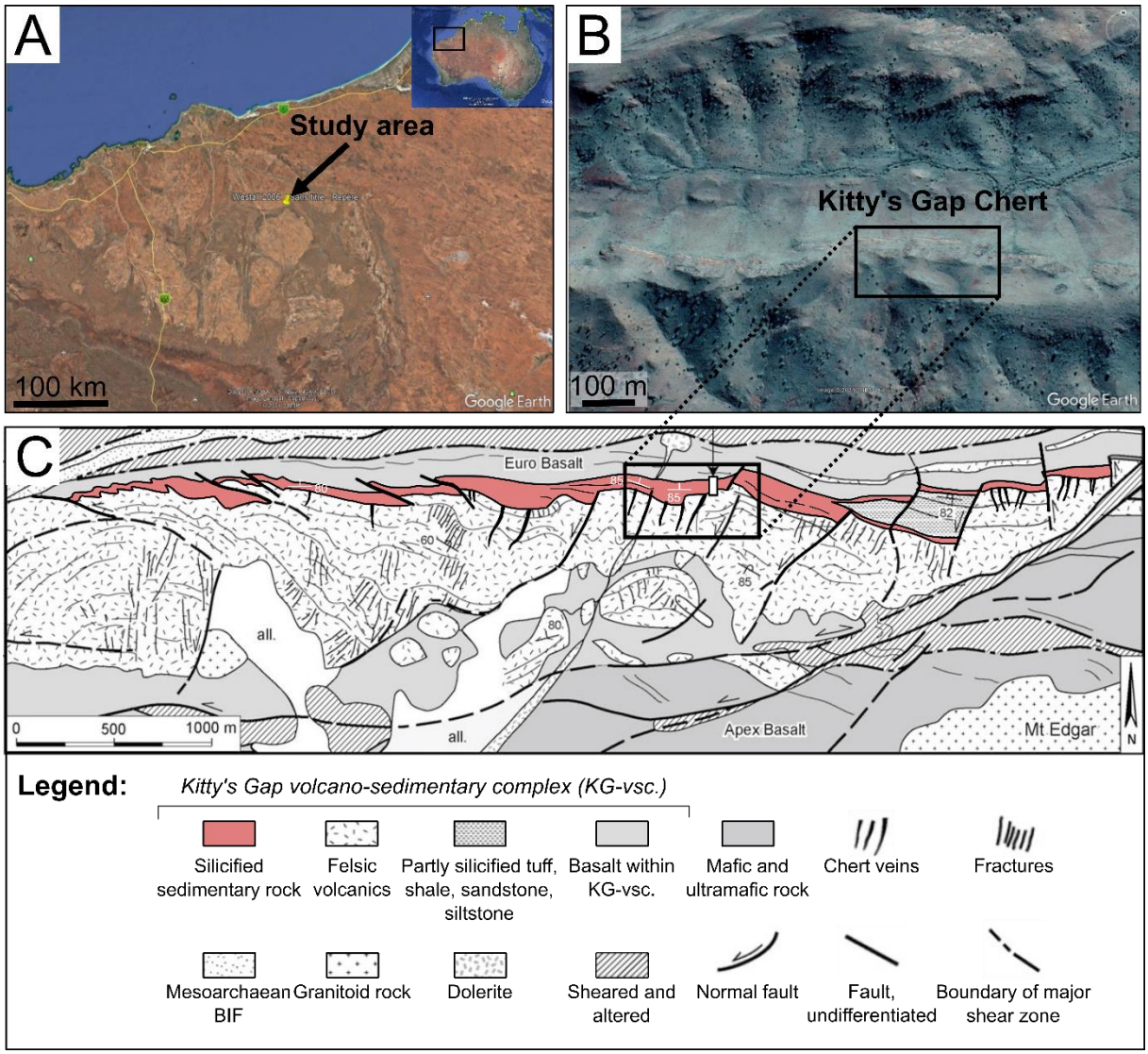

Figure II.1: *Location of the Kitty's Gap Chert. (**A**) Satellite image (Google Earth) of the Pilbara Craton within Australia; black arrow indicates the location of the Kitty's Gap Chert. (**B**) Satellite image (Google Earth) of the Kitty's Gap Chert with black box indicating the location of the main study area from which the studied samples were obtained. (**C**) Detailed geological cross-section of the Kitty's Gap volcano-sedimentary sequence (KG-vsc.; modified after de Vries, 2004).*

The Kitty's Gap Chert is a typical example of silicified volcaniclastic sediments (80–99 % of silica) deposited in a shallow-water littoral environment in the vicinity of hydrothermal vents linked to a volcanic system (**Fig. II.2**; de Vries, 2004; de Vries et al., 2006; Westall et al., 2006a, 2011a). The sediments originate locally from the weathering of emerged landmasses composed of felsic volcanic rocks and basaltic lava flows, as well as by the ejection of volcanic ash stemming from volcanic eruptions (de Vries, 2004). The sediments were silicified during and immediately after their deposition by Si-enriched Archean seawater (de Vries, 2004; van den Boorn et al., 2010). Silica was also sourced from abundant hydrothermal veins reaching into the lowermost layer of the sediments (de Vries, 2004; de Vries et al., 2010) as well as via silica-saturation of pore waters owing to devitrification of volcanic clasts during diagenesis (Westall et al., 2023a). After diagenesis, the rocks underwent regional metamorphism (greenschist facies according to the Raman geothermometer measurement made in this study and described in the section *III.D. Raman spectroscopy*; Wijbrans and McDougall, 1987).

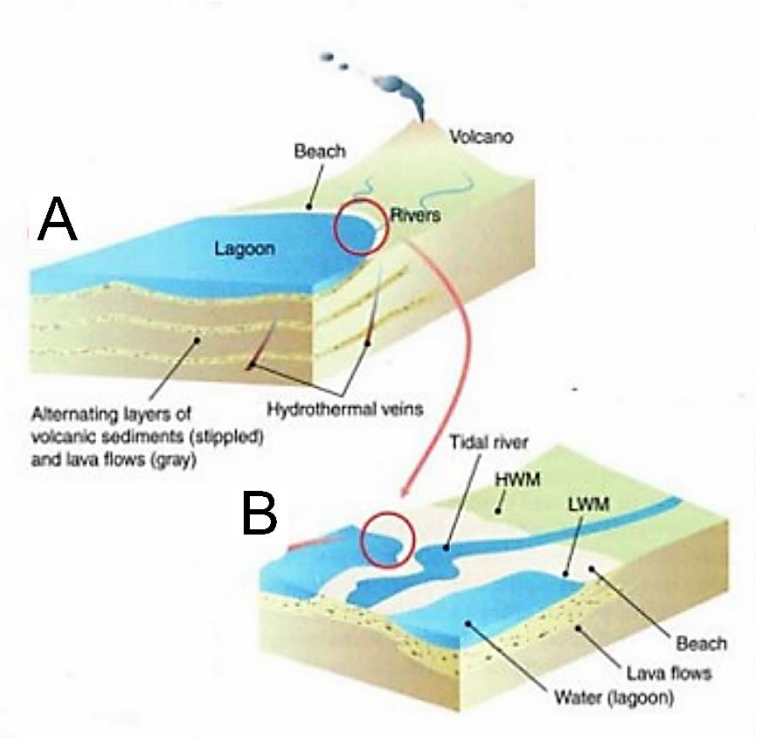

Figure II.2: *A hypothetical coastal landscape on early Earth similar to the landscape in which the volcaniclastic sediments of the Kitty's Gap Chert were deposited 3.5 Ga ago. (**A**) An erupting volcano spreads volcanic ash over the surrounding plain and into the lagoon; rivers transport eroded sediments into the lagoon and a band of beach sediments is deposited around the lagoon; alternating layers of lava flows and fine layers of sediments lie beneath the lagoon and coastal plain; hydrothermal veins cut through layers of lava and sediment to reach the surface. (**B**) Enlargement of the beach showing a tidal channel cutting through the beach sediments. HWM, high water mark; LWM, low water mark (modified after Westall, 2005).*

The silicified sediments now crop out in the form of an east-west oriented ridge, clearly visible in the landscape, in which the volcano-sedimentary layers dip vertically or are slightly overturned due to tectonic activity (**Fig II.3**). Mafic lavas are intercalated between the sedimentary layers (**Fig. II.3D**; de Vries, 2004).

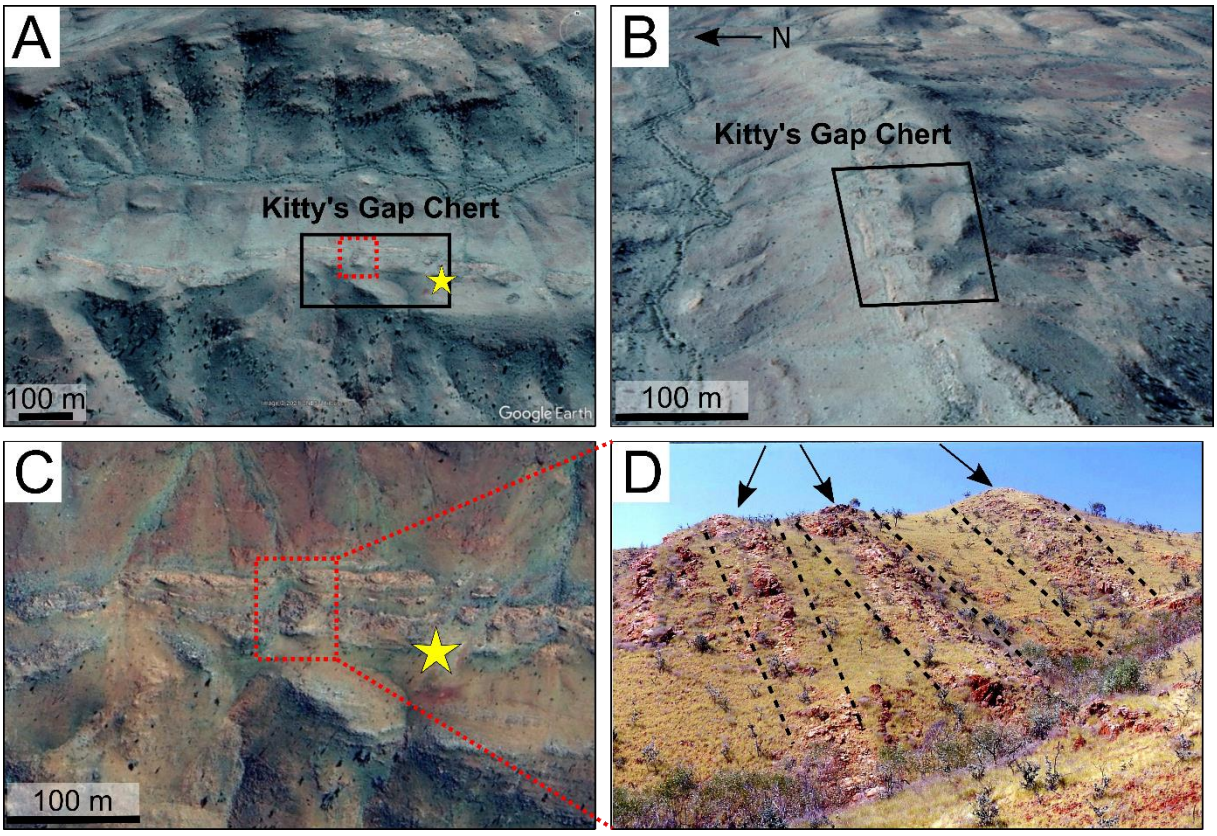

Figure II.3: *Aerial and field images of the Kitty's Gap Chert.* ***(A)*** *Satellite image (Google Earth) of the Kitty's Gap Chert with black box indicating the location of the main study area from which the studied samples were obtained and red dotted box indicating the area corresponding to the image displayed in* ***(C)****.* ***(B)*** *Satellite image (Google Earth) of the same area seen in profile; black arrow indicates the direction of north.* ***(C)*** *Close-up view (Google Earth) of the outcrop of the Kitty's Gap Chert with red dotted box showing the location of the outcrop on the field in* ***(D)****.* ***(D)*** *Field photograph of the outcrop of the Kitty's Gap Chert showing vertical bars of silicified sediments (black arrows and black dashed lines) separated by mafic lavas. Photograph taken by Frances Westall in August 2000. The yellow star in* ***(A)*** *and* ***(C)*** *corresponds to the location where the samples were collected.*

B. Sample collection and preparation

The Kitty's Gap Chert is characterized by three distinct units: units A and B, composed of silicified volcaniclastic materials (forming the main part of Kitty's Gap), and unit C, which is thicker, less silicified and mainly composed of shale containing illite and kaolinite (the latter being post-metamorphic due to surface weathering) with fine-grained sandstone and minor chert (**Fig. II.4A**; de Vries et al., 2010). The samples analyzed in this study were extracted from the unit A, composed of *en echelon* stacking of cherts lenses, tens of meters wide, surrounded by even-bedded chert. The lenses each represent a channel deposit and are separated by poorly exposed, probably intrusive intervals of igneous (mafic or felsic) origin (de Vries, 2004; de Vries et al., 2010). The chert lenses 1 and 2 comprise dark and light grey sedimentary deposits with a well-preserved granular texture, and are characterized by a generally fining upward trend in grain size (de Vries, 2004). Primary sedimentary structures can also be observed throughout the lenses, from low-angle oblique bedding at the bottom, through extensive cross-bedding at the meter-scale, to small-scale ripples to parallel bedding at the top (de Vries et al., 2010).

The samples were collected from the lower 4 meters of the chert lens 1, in the lower part of the sedimentary succession (**Fig. II.4B**; 120°04.53'E; 20°53.62'S) by Frances Westall in 2000. Sample 00AU37b was taken from sediments brecciated by an intruding hydrothermal vein, at the base of chert lens 1. Sample 00AU39 was taken from a few centimeters away from the hydrothermal vein, at the base of chert lens 1, and sample 00AU40 from approximatively 15 meters east of the hydrothermal vein, at the top of chert lens 1.

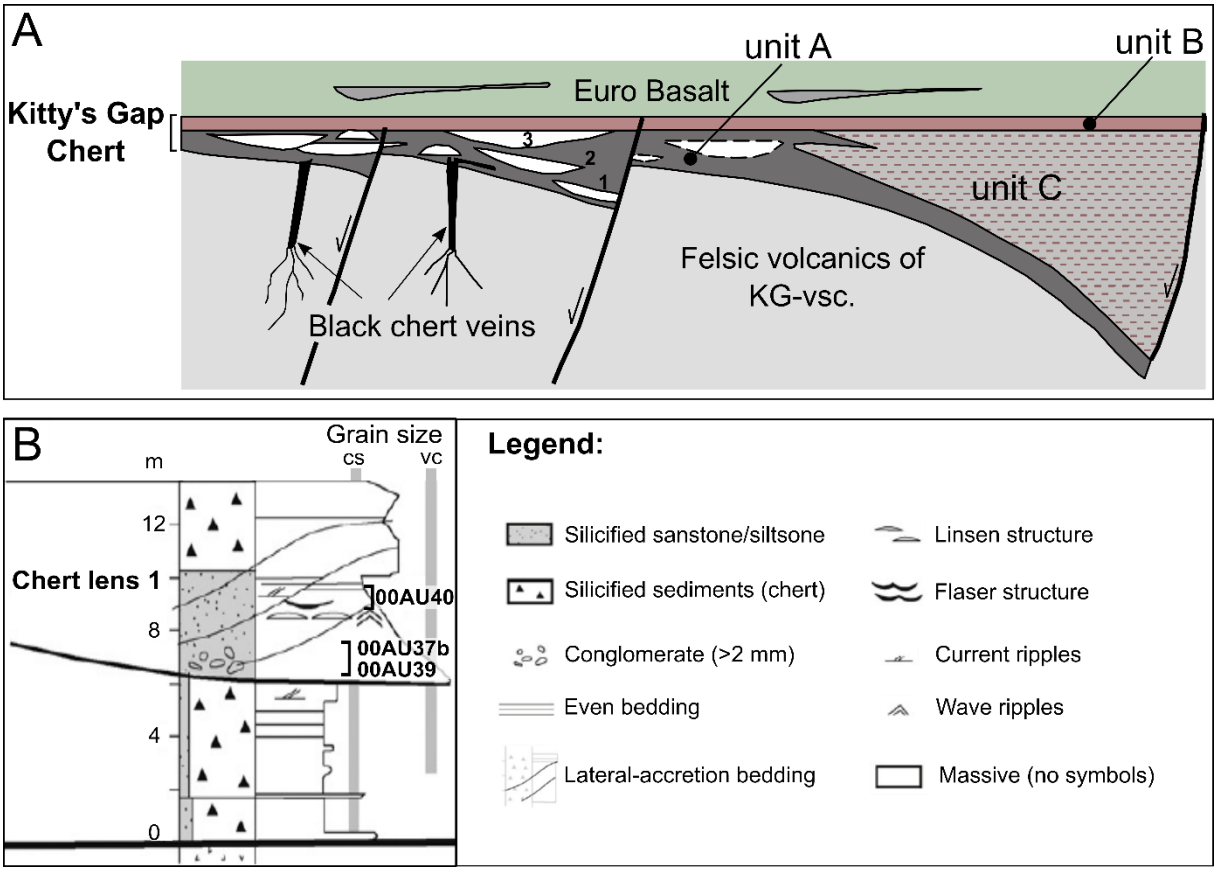

Figure II.4: *Cross-section and sedimentary log of the Kitty's Gap Chert. (**A**) Schematic drawing (not to scale, width of geological cross-section approximately 1.5 km) of silicified sediments of the Kitty's Gap Chert and chert lenses, including chert lenses numbered 1–3 from unit A (modified after de Vries et al., 2010). (**B**) Sedimentary log of chert lens 1 in the Kitty's Gap Chert of which samples from this study are part, with grain size: coarse silt (cs) and very coarse sand (vc) (modified after de Vries et al., 2010).*

The samples were observed and analyzed in a number of formats. At the outcrop and hand sample scale, raw samples (unprepared) and sawn and polished rock samples (slabs) were used for hand sample description, as well as LA-ICP-MS analysis and X-ray fluorescence spectroscopy, respectively. Powdered rock samples (<80 µm grain size) were prepared at CRPG laboratory (Nancy, France) for ICP-MS/OES analysis. Polished thin sections (30 µm and 70 µm thick) were prepared at ISTO-CNRS laboratory (Orléans, France) and by the company Thin Section Lab (Toul, France) for optical microscopy, SEM, energy-dispersive X-ray (EDX) spectroscopy coupled to SEM, Raman spectroscopy, DUV fluorescence spectroscopy, X-ray fluorescence spectroscopy, FTIR spectroscopy and PIXE. Focused ion beam (FIB) sections (100 nm thick) were prepared at IEMN-CNRS laboratory (Lille, France) using a ZEISS Crossbeam microscope for TEM/STEM and EDX spectroscopy coupled to STEM. A flow diagram of the preparation procedure is displayed in **Figure II.5**.

For sample 00AU37b, a powder and one thin section 30 µm thick were prepared to obtain geochemical information about the hydrothermal source. For samples 00AU39 and 00AU40, slabs a few centimeters thick, powders, 70 µm thick thin sections, and FIB sections were prepared for multiscale and multi-technique analysis. In addition, detached thin sections, 30 µm and 70 µm thick, were also prepared from 00AU39 and 00AU40. All samples are part of the International Space Analogue Rock Store (ISAR) collection from CBM-CNRS laboratory (Orléans, France, http://isar.cnrs-orleans.fr/isar/; Bost et al., 2013).

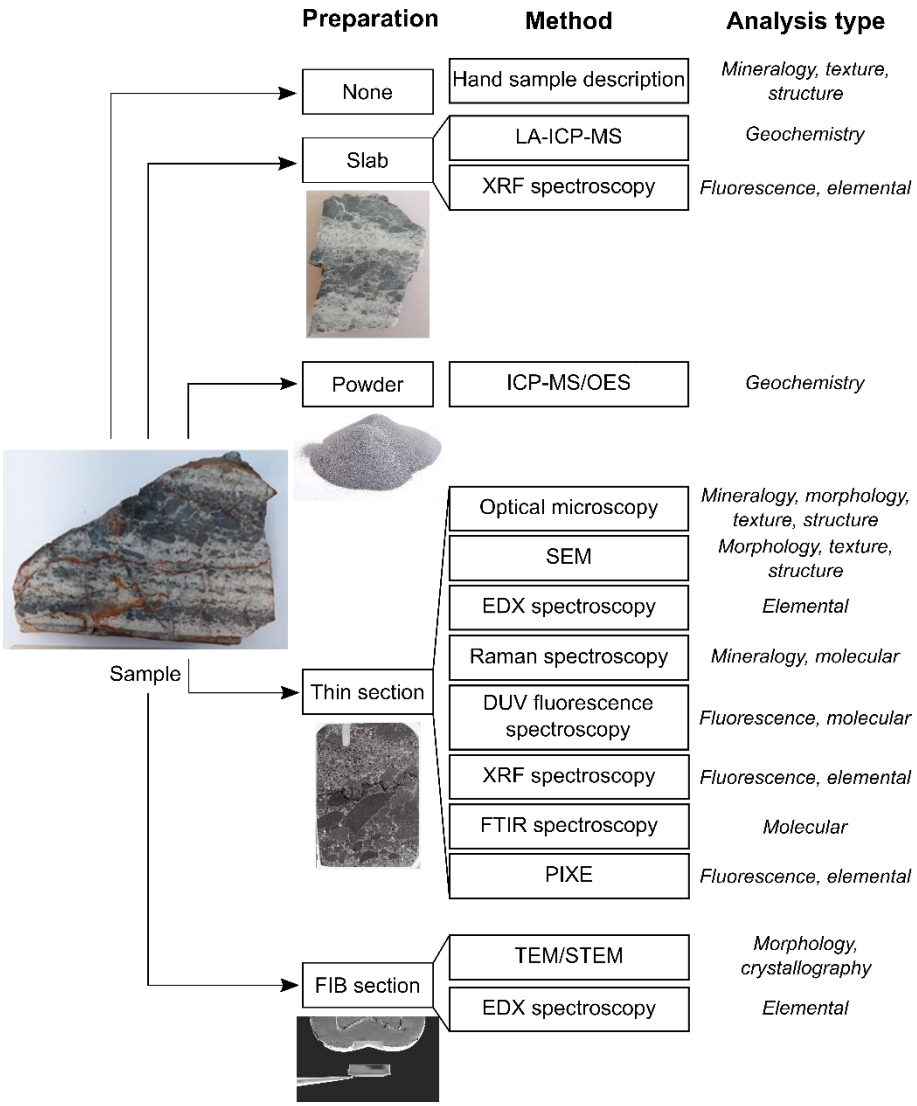

Figure II.5: *Flow diagram summarizing the different types of preparation for the different laboratory methods used for the characterization of samples from the Kitty's Gap Chert. For the analysis type, morphology is distinguished from structure where the former refers to the physical characteristics of carbonaceous matter, while the latter relates to rock structure, i.e., the arrangement of minerals and rocks in their geological context. The texture of the rock characterizes the arrangement of the crystals at different scales (sample, thin section...), including their physical appearance, size and shape, as well as their alteration by physio-chemical processes and/or by biological processes.*

III. Methods

A. Optical microscopy

Two microscopes, a Nikon Eclipse Ti equipped with a Nikon DS-Fi3 camera and an Olympus BX51 equipped with a Pixelink M20-CYL camera, were used at CBM, CNRS, Orléans, France. The first microscope was used to produce high-resolution image mosaics (<1 µm/pixel) of the full thin sections to document the larger scale structures and textures of the rocks and to locate regions of interest (ROIs). I used the second microscope to analyze the petrological context, as well as to observe the alteration of volcanic clasts and the distribution of the carbonaceous deposits. I chose and took photographs of specific ROIs using transmitted and reflected polarized light, at different magnifications (×50, ×200, ×500 and ×1 000).

B. Scanning Electron Microscopy (SEM)

1. Principle

The principle of scanning electron microscopy (SEM) is based on the interaction of electrons with a sample surface to study the morphology of the structures observed. An electron microscope uses a beam of electrons, which are accelerated and then focused on the sample using magnetic lenses (**Fig. II.6A**). The superficial layers of the sample then emit low energy secondary electrons (about 50 eV; **Fig. II.6B**) collected by a detector, which amplifies the signal to form a black and white image representative of the topography of the sample surface (Goldstein et al., 2017).

Higher energy electrons can also be collected by the detector, namely backscattered electrons (**Fig. II.6C**), whose energy reach up to 30 keV. These electrons are sensitive to the atomic number of the atoms constituting the sample. Thus, the heaviest atoms will give off more electrons and will therefore appear brighter, allowing to study the surficial composition of the sample (Goldstein et al., 2017). Finally, the electron beam can also ionize the atoms so that they emit X-rays (**Fig. II.6D**), whose energy depends on the elemental composition of the sample, thus making it possible to obtain a map of the chemical composition (Goldstein et al., 2017).

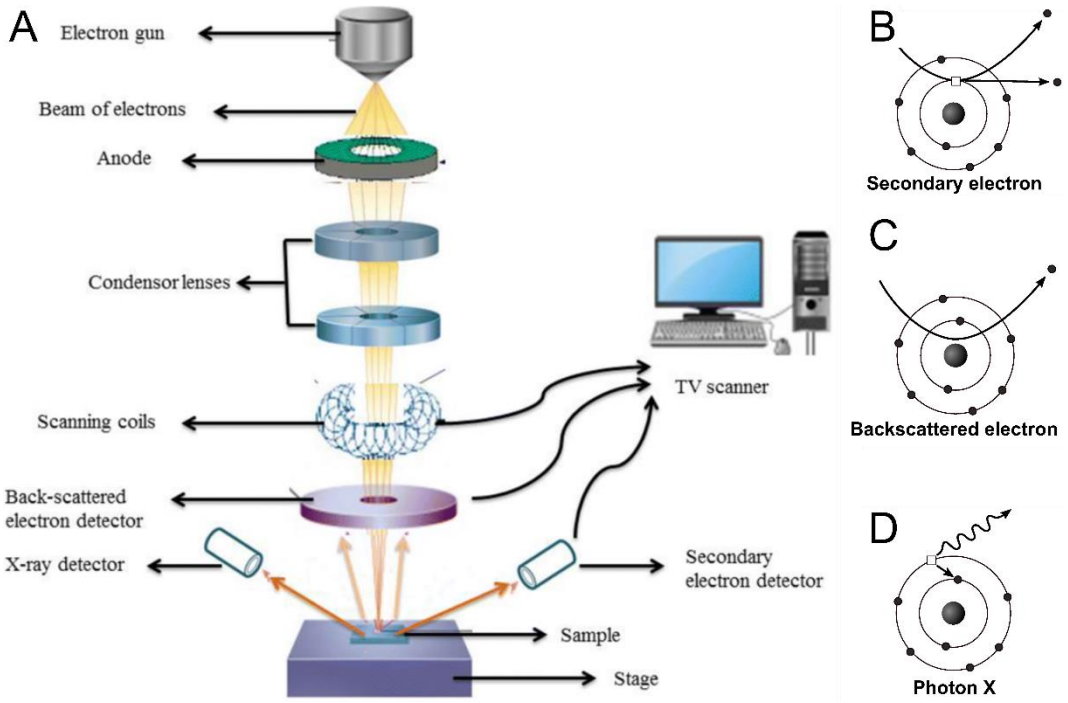

Figure II.6: *SEM principle. (**A**) Schematic of a scanning electron microscope with its different components (modified after Munir et al., 2021). Interaction between matter and electrons can generate either ejection of (**B**) secondary electrons and (**C**) backscattered electrons, or (**D**) emission of X-ray photons.*

2. *Instrumentation*

Three scanning electron microscopes, a Merlin Compact Zeiss (ISTO-CNRS, Orléans, France), a JEOL JSM-IT800 (MACLE facility, CNRS, Orléans, France) and a JEOL JSM-IT500 (Imaging and Analysis Centre, Natural History Museum of London, United Kingdom), were used to acquire high-resolution images of the carbonaceous structures (cells, filaments…) on thin sections coated with a platinum-palladium mixture. A thin section (00AU40c) was first metallized with gold in 2000 (gold particles can sometimes be observed in the SEM images). The ROIs were observed in two modes of imaging: secondary electrons (SE) and backscattered electrons (BSE) modes. SE were used to obtain high-resolution images up to a few nanometers of spatial resolution. BSE were used to distinguish the different component phases at submicrometric scale. Other parameters include: a 5–20 keV energy beam, a magnification from ×25 to ×60 000, and a 10–14 mm working distance. SEM were equipped with an energy-dispersive X-ray (EDX) spectrometer used to map major elements, from carbon to iron.

3. *Data treatment*

I processed the elemental maps and the spectra obtained during the EDX (coupled to SEM) analyses of samples using the *AZtec* software. Several maps were acquired during the analyses of samples, allowing to visualize the distribution of elements through the observed structures. For each area analyzed with EDX, I created color-coded compositions by superimposing the elemental maps obtained for different elements (e.g., Si, O, Al, K, Ti, C, Fe). For each area analyzed with EDX, a spectrum is also associated to the global area for which I confirmed the elements identified for each peak. Spot analyses were also carried out in some areas to acquire several spectra from different structures of interest for which I confirmed the elements identified for each peak.

C. (Scanning) Transmission Electron Microscopy (S-TEM)

1. Principle

As for SEM, transmission electron microscopy (TEM) uses a beam of electrons, which is concentrated on the sample. However, unlike the SEM where they are collected on the surface in reflection, the electrons are collected below the sample, in transmission. This technique is therefore only suitable for samples thin enough to permit the transmission of the electrons. The beam is magnified by other lenses and then detected so that an high resolution image down to atomic resolutions can be obtained (Amelinckx et al., 2008). The diffraction of electrons can also be exploited by placing the detector in the focal plane and no longer in the image plane of the beam in order to visualize the diffraction figure and to characterize the crystallography (e.g., organization of matter – i.e., amorphous, semi-crystalline or crystallized, crystallographic orientation, crystal domain size; Amelinckx et al., 2008).

A variation is the scanning transmission electron microscopy (STEM) where the beam is focused at a particular point on the sample (not across the entire surface). The transmitted beam is detected and scanning allows the sample to be visualized at very high resolution (until ca. 0.1 nm). This technique also makes it possible to produce chemical maps of the sample by analyzing the X-rays emitted by the atoms (Amelinckx et al., 2008).

2. Instrumentation

Two TEM/STEM instruments, a JEOL ARM200 CFEG (MACLE facility, CNRS, Orléans, France) and a PHILIPS CM20 (ICMN, CNRS, Orléans, France), were used to obtain nanoscale resolution images of the morphology (e.g., particle size and shape) and the crystallography of minerals and carbonaceous matter in FIB sections. TEM imaging and STEM observations were carried out using a 200 keV energy beam, with a current of 15 µA, and a spatial resolution of ca. 0.1 nm. Major element analyses were performed by EDX, from carbon to iron.

3. Data treatment

I used *the JED-2200 Analysis Station* software to process the data obtained with EDX (coupled to TEM). Elemental maps and spectra were acquired during the analyses. I created color-coded compositions by superimposing up to three elemental maps of different elements (e.g., Si, Al, C) with the STEM image obtained for a specific area. For each area, a spectrum is associated for which I identified the elements for each peak by selecting elements from a periodic table. Spot analyses were also performed in some areas of interest to obtain several spectra from specific structures for which I identified the elements. I also quantified the spectra to get the mass percentage of each compound (e.g., Al_2O_3, SiO_2, K_2O, TiO_2) in order to compare the relative concentrations between the different compounds.

Furthermore, I studied the crystallography of minerals and carbonaceous matter by using the *ImageJ* software in order to determine their structure and identify the mineral phases and carbonaceous matter. From the high-resolution TEM images, I used the Fourier Transform to determine the position of the planes of atoms and reconstruct the entire crystal structure. Then I plotted a profile passing through at least 2 planes of atoms in the image to calculate the interplanar distance. Another

possibility is to use the diffraction images obtained directly during the analyses and plot the profile to calculate the interplanar distance.

D. Raman spectroscopy

1. Principle

Raman spectroscopy, named after its Indian discoverer Chandrashekhara Venkata Râman, is mostly a non-destructive, vibrational spectroscopy technique based on the Raman effect. The Raman effect is the physical phenomenon by which a medium can slightly modify the energy of the light circulating in it, that is called inelastic scattering of photons. This energy shift is due to an energy exchange between the incident photons (light) and the scattered medium (molecules), corresponding to an energy exchange into molecular vibrations in the sample (e.g., stretching, bending and rotating; Lewis and Edwards, 2001).

Depending on the energy involved between the incident light and the vibrating molecules, two types of inelastic scattering can be produced: 1) the Stokes effect, which occurs when the scattered photons have a greater wavelength (thus a smaller energy) than that of the incident photons, and 2) the anti-Stokes effect, which occurs when the scattered photons have a smaller wavelength (thus a greater energy) than that of the incident photons. However, a large part of the scattered light is elastic, called Rayleigh scattering, for which the incident photons and the scattered photos have the same wavelength (conservative of the same energy). The measurement of this shift in energy makes it possible to determine certain properties of the material, especially the characterization of its molecular composition. At room conditions, the Stokes part of the Raman signal is more intense than the anti-Stokes part, explaining its preferential use in Raman analyses (Foucher et al., 2017).

During Raman analysis, a beam of monochromatic light (here, a green laser at 532 nm) is directed onto the sample and the scattered light is sent to a monochromator allowing its intensity to be measured using a CCD (for charge coupled device*)* detector. The signal collected is represented in a graph showing the number of photons (intensity) as a function of the wavenumber expressed in cm^{-1}. Indeed, Raman spectra show the energy shift of the scattered photons with respect to the excitation source, of which the laser wavelength corresponds to 0 cm^{-1}. A Raman spectrum displays several bands corresponding to the different vibration modes of a molecule or of a crystal. Identification is generally made by comparing the collected spectrum with reference spectra found in databases or the literature.

2. Instrumentation

I recorded Raman spectra and images on thin sections of the rock samples using a WITec Alpha 500RA (**Fig. II.7**) at CBM, CNRS, Orléans, France, in order to detect, identify and map the mineral phases and carbonaceous matter. For the data acquisition, I used a green Nd:YAG frequency doubled laser with an excitation wavelength of 532 nm, and ×20 or ×50 objectives with numerical apertures of 0.40 and 0.75 and measured spot sizes of ca. 1.6 µm and ca. 0.8 µm diameter, respectively. I set the laser power between 5 and 14 mW at the sample surface. The spatial resolution of the maps depends on the ratio of the scan size over the number of spectra per line but was approximatively about 1 µm/spectrum. The average spectral resolution was approximatively 3 cm^{-1} using a 600 g/mm grating. Acquisition time was 0.1 to 0.4 seconds per spectrum/pixel. For more details about Raman spectroscopy imaging protocols, the reader is directed to Foucher et al. (2017).

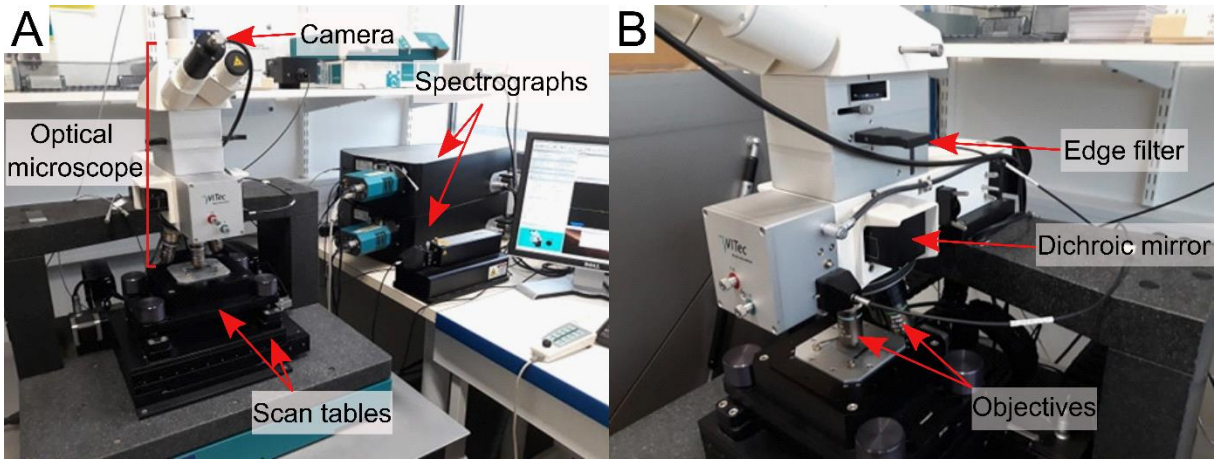

Figure II.7: *Raman spectrometer setup. (**A**) Photograph of the WITec Alpha 500 RA Raman spectrometer used for samples analyses. The optical microscope allows identification of the areas of the samples to be analyzed and to focus the laser on the samples thanks to its objectives. The samples are placed on a sample holder located above two scan tables; a piezoelectric scan table that can analyze an area of 200 µm × 200 µm in the horizontal plane and 20 µm in the vertical direction, placed itself above a motorized scan table allowing wider movements (15 cm × 10 cm horizontally and 2 cm vertically). The spectrographs (one for the green laser below and one for the red laser above) contain the monochromator equipped with diffraction gratings, which makes it possible to diffract the light by selecting the narrowest possible range of wavelengths, and the CCD detector, which counts the number of photons. (**B**) Close-up view of the system showing the edge filter which allows to cut out the Rayleigh band to allow only the Stokes and anti-Stokes bands to pass, the dichroic mirror which allows to reflect part of the photon wavelengths and to transmit another part, and microscope objectives which are fixed on an objective turret and allow observations at different magnifications.*

3. *Data treatment*

The software I used to process the Raman data is called *WITec Project Four*, which allows processing of images and spectra acquired during sample analyses. I first proceeded to create filters to select peaks of interest on the spectra obtained. For example, the main quartz peak is located at 465 cm^{-1}, thus I selected an area of the spectrum between 430 and 550 cm^{-1}. I also created a filter for the baseline level representative of the fluorescence by selecting an area where there is a priori no mineral or organic phase of interest in order to be able to remove the baseline level later.

Once the filters were created for different peaks, I produced maps corresponding to the concentrations of the compounds constituting my sample, where each pixel on a map corresponds to a spectrum. From the baseline filter, I created a mask indicating the value from which the baseline is indeed present by referring to the map (e.g., "x1>3500" where x1= baseline level), then I calculated the average spectrum of each phase by averaging the spectra associated to a map and removing the baseline level (e.g., "(x1>500)*(x2<3500)" where x1= mineral phase and x2= baseline level). Another possibility to remove the fluorescence is to apply the fluorescence mask to all the spectral data in order to keep only the phases without fluorescence and then produce new maps for each phase on which the fluorescence will no longer appear (black areas, i.e., without pixels).

Once the average spectra are generated, I then processed the spectra for each phase by subtracting the baseline, which allows selection of the areas of the spectrum that I want to keep and to remove

the areas that do not interest me (Rayleigh band and cosmic rays in particular), and remove the baseline, so that the base of each peak in the spectrum is at the same level. Other treatments can be applied to the spectra (smoothing of the spectrum, fit of the spectrum using a mathematical approximation such as Gaussians, operation on the intensity to increase it...), but they will not be detailed here because the baseline subtraction is sufficient to obtain a correct spectrum for the identification of the phases. The identification of the mineral phases was carried out using the *CrystalSleuth* software, which contains a library of reference minerals that can be compared with the spectra obtained during a Raman analysis.

I finally created color-coded compositions from the maps obtained by stacking them in layers, placing the dominant phase (quartz) below and the other phases (e.g., anatase, hydromuscovite, carbonaceous matter) above by adjusting the transparency of the layers. The color-coded compositions thus make it possible to observe the spatial distribution of the different phases and their association.

From the spectrum of the carbonaceous matter, it is possible to calculate the maximum temperature recorded by the carbonaceous matter. Kouketsu et al. (2014) developed a Raman geothermometer applicable for low-grade to medium-grade carbonaceous matter (ca. 150–400°C) by determining the full width at half maximum (FWHM) of the D1 and D2 (disordered carbon) bands (**Fig. II.8**).

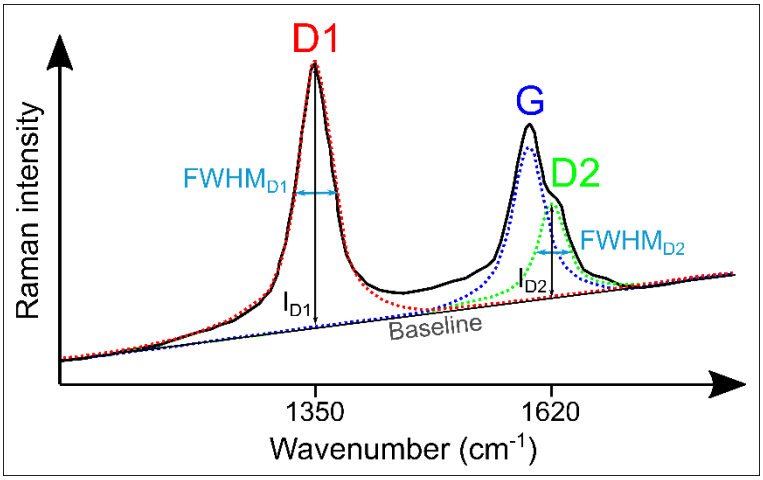

Figure II.8: *Deconvolution of the Raman spectrum of carbonaceous matter (in black) in three bands. The D1 (in red) and D2 bands (in green) are representative of disordered carbon while the G band (in blue) is associated with graphite (modified after Foucher et al., 2015). Only the full width at half maximum (FWHM) of the D1 and D2 bands are shown here, according to the method used by Kouketsu et al. (2014) to estimate the metamorphic temperature for the carbonaceous matter. I_{D1} and I_{D2} = intensity of the D1 and D2 bands, respectively.*

Then, the FWHM values of the D1 and D2 bands can be used to estimate the metamorphic temperature (T°C) for the carbonaceous matter using the following equations (Kouketsu et al., 2014):

$$T°C = -2.15(FWHM_{D1}) + 478 \quad (1)$$

(coefficient of determination, R^2 = 0.970)

$$T°C = -6.78(FWHM_{D2}) + 535 \quad (2)$$

(R^2 = 0.968)

E. Synchrotron radiation Deep-UltraViolet (DUV) fluorescence (micro)spectroscopy

1. *Principle*

The principle of deep-ultraviolet (DUV) fluorescence spectroscopy is based on the interaction of electrons and matter to determine the molecular composition of a sample (**Fig. II.9**). The sample is exposed to UV radiation (here, 275 nm) whose constituent molecules will undergo one or more electronic transitions, i.e., the passage of an electron from one energy level to another. The excited electrons of the molecules thus move from a ground state to vibrational levels of higher electronic levels by absorption of a photon. Collisions with other molecules induce a loss of energy, which implies a displacement towards the lowest vibrational level of the excited electronic state. The molecule then relaxes into one of the ground vibrational states by emitting a photon. During this process, the photons acquire different energies, therefore different wavelengths, which are recovered by a detector. The excitation spectrum of a sample is recorded as the intensity luminescence as a function of excitation wavelength expressed in nanometers (Gaft et al., 2015).

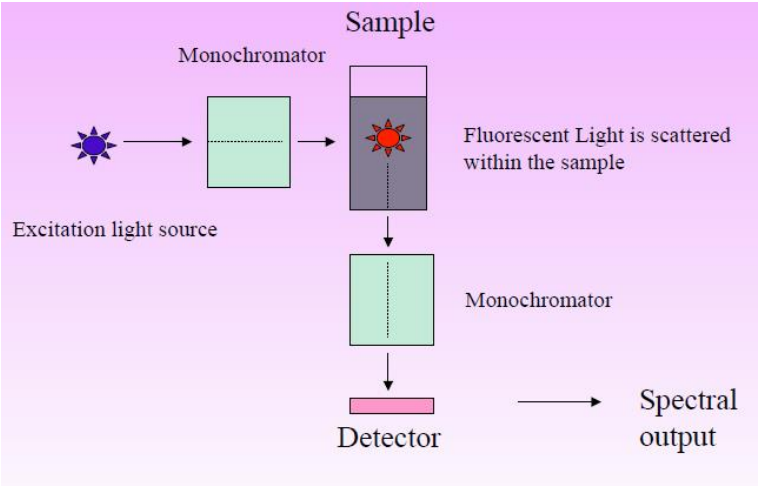

Figure II.9: *Principle of fluorescence spectroscopy. A spectrofluorometer contains a light source, two monochromators (one for the selection of the excitation wavelength and another for analysis of the emitted light), a sample holder and a detector measuring the intensity of the light (sourced from https://chemistry-dictionary.yallascience.com).*

2. *Instrumentation*

DUV fluorescence spectroscopy (excitation wavelength 275 nm) was performed on detached thin sections using Telemos, a DUV microscope, and Polypheme, a DUV inverted microspectrofluorometer, at the DISCO beamline, Synchrotron SOLEIL, Saint-Aubin, France. This method was used to identify and map aromatic compounds, minerals and metallic oxides in the samples. Microscopy observations were made using a ×100 objective with a spatial resolution of 7.2 µm/pixel (glycerin immersion). Different filters were used to detect the aromatic molecules (329–351 nm and 352–388 nm; Ménez et al., 2018), minerals and metallic oxides (412–438 nm, 420–480 nm, and 499–529 nm; MacRae and Wilson, 2008; Gaft et al., 2015; Zhyrovetsky et al., 2017). The spectrometer acquires spectra between 285 and 550 nm using a ×100 objective and an acquisition time of 10 seconds per spectrum/pixel.

3. *Data treatment*

For data acquired with the Telemos microscope, I used the *ImageJ* software to produce color-coded compositions showing the distribution of aromatic molecules and minerals as well as their association. For this, I chose 3 filters among the filters used during the acquisition (filters of aromatic molecules, minerals and metal oxides) to assign them to the R, G and B channels.

For data acquired with the Polypheme microspectrofluorometer, I used the *LabSpec 6* software to process spectra and images acquired during sample analyses. For each spectrum, I applied the same series of treatment. I first removed cosmic rays from the spectrum. Then I modeled the measured spectrum using a mathematical approximation, such as Gaussian and Lorentzian peaks, allowing the peaks to be fitted and to obtain information, such as their position, amplitude, full width at half maximum height (FWHM) and area. I then corrected the baseline to produce a spectrum with a zero, flat baseline. Finally, I selected the peaks of interest to be mapped. The map generated for each peak appears in grayscale where the brighter areas correspond to higher intensity of the peak. The detected molecule is therefore more concentrated relative to the other areas, which appear darker.

F. Fourier-Transform InfraRed (FTIR) spectroscopy

1. *Principle*

Fourier-transform infrared (FTIR) spectroscopy is a non-destructive analytical technique that allows identification of chemical species, such as molecules, functional groups and cation-anion pairs by the detection of molecular vibrations (e.g., stretching, bending and rotation) characteristic of specific chemical bonds (Benning et al., 2004). Like any absorption spectroscopy, FTIR spectroscopy is used to measure the amount of light absorbed by a sample at different wavelengths. To do this, an infrared beam is directed towards a Michelson interferometer, which modulates each wavelength at a different speed (**Fig. II.10**). The interferometer contains mirrors, including a mobile mirror, making it possible to vary the path traveled by the light, which will give rise to interferences during the recombination of the two beams. The modulated beam is then reflected towards the sample which will absorb the light before reaching the detector which transforms it into an electrical signal. The signal appears as an interferogram, i.e., the light absorbed as a function of the position of the mirror (sum of all beam velocities), which is converted into an infrared spectrum by a mathematical tool called Fourier Transform (FT), where the absorbance is plotted as a function of wavenumber (in cm^{-1}).

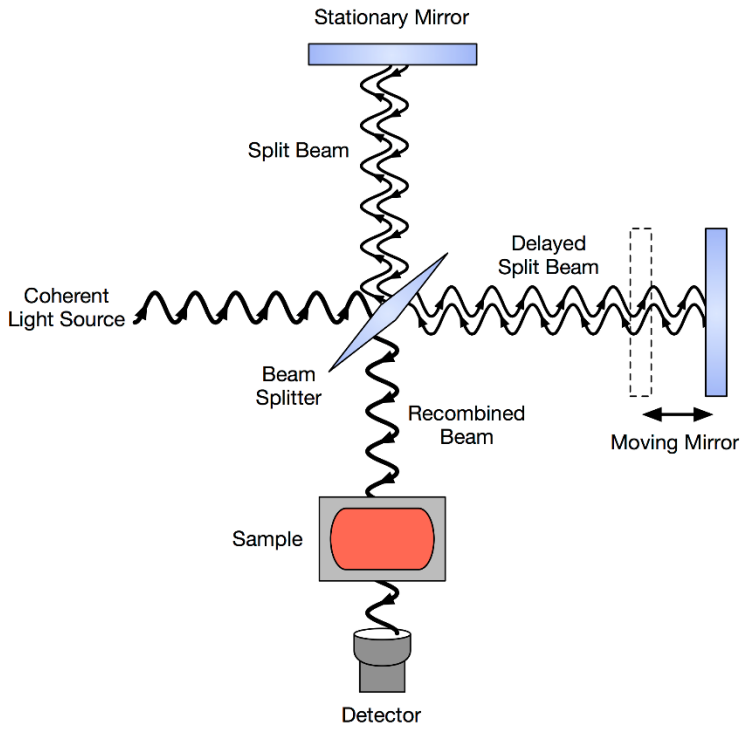

Figure II.10: *Theoretical diagram of the operation of infrared spectroscopy (sourced from https://commons.wikimedia.org/wiki/File:FTIR_Interferometer.png).*

2. *Instrumentation*

Transmission FTIR mapping and spectra were acquired on detached thin sections using a Thermo Nicolet iN40 Infrared Imaging Microscope at the Imaging and Analysis Centre, Natural History Museum, London, United Kingdom, in order to determine the molecular composition of the carbonaceous matter, focusing on aliphatic compounds within the wavenumber range 2800–3040 cm^{-1}, and aromatic/alkenic compounds within the wavenumber range 1300–1800 cm^{-1}. Multiple analyses were made with a 30 µm spatial resolution and a 4 cm^{-1} spectral resolution. A reference background spectrum in air was taken before each analysis and subtracted from the sample spectrum.

DUV fluorescence spectroscopy analyses are complementary to FTIR spectroscopy analyses to study the molecular composition of the carbonaceous matter, particularly because the aromatic region is overlaid with mineral phases in FTIR.

3. *Data treatment*

The software I used to process the FTIR data is called *OMNIC Picta*. It allows processing of images and spectra acquired during sample analyses. With the software, it is possible to display the maps and spectra collected in two separate windows where each point on the map corresponds to a specific spectrum. I selected several peaks of interest on the spectra in the aliphatic (between 2800 and 3040 cm^{-1}) and the aromatic (between 1300 and 1800 cm^{-1}) regions in order to extract maps for each peak showing the distribution and relative concentration (in absorbance) of different chemical species. At the same time, I extracted spectra in areas from the maps where the absorbance is high and which coincide with the location of the carbonaceous matter detected with the Raman spectrometer. Then,

I identified several peaks of interest with to the *OMNIC Spectra* software, corresponding to specific chemical species that I compared with data from the literature and reference databases (see the *Infrared Spectral Interpretation* knowledge base of Thermo Fisher Scientific, 2008–2009). I also compared the spectra obtained for different structures of interest from a same sample in order to study the intensity and diversity of the peaks in the aliphatic and the aromatic regions.

IR signatures of aliphatic CH_2 and CH_3 ratios were used to estimate the length of the aliphatic chain and the degree of branching in the carbonaceous matter. These, in turn, were used to interpret the likely nature of precursor organic molecules (i.e., pre-degradation), such as membrane lipids, using the following equations, where $Abs(CH_3)$ and $Abs(CH_2)$ refer to the absorbance peaks of the asymmetric stretching bands of the aliphatic CH_3 (end-methyl, 2960 cm^{-1}) and CH_2 (methylene, 2925 cm^{-1}) after linear baseline correction (Lin and Ritz, 1993; Igisu et al., 2009):

$$\frac{CH_2}{CH_3} = \frac{Abs(CH_2)}{Abs(CH_3)} = \frac{Abs(\sim 2925\ cm^{-1})}{Abs(\sim 2960\ cm^{-1})} \quad (3)$$

$$\frac{CH_3}{CH_2} = R_{3/2} = \frac{Abs(CH_3)}{Abs(CH_2)} = \frac{Abs(\sim 2960\ cm^{-1})}{Abs(\sim 2925\ cm^{-1})} \quad (4)$$

G. Synchrotron radiation X-Ray Fluorescence (XRF) spectroscopy

1. *Principle*

X-ray fluorescence (XRF) spectroscopy is a micro-destructive technique that uses a physical property of matter, X-ray fluorescence, to determine the elemental composition of a sample. When a material is exposed to X-rays, the atoms constituting it undergo ionization whereby the electrons are ejected from the atomic orbitals (phenomenon comparable to EDX). The atoms are then in an excited state and the de-excitation takes place by the transition of an electron from a higher level to a lower level of energy (**Fig. II.11**), the transition of which releases energy in the form of an X-ray photon. The energy of the X-ray photon corresponds to the difference in energy between the levels involved. It is therefore characteristic of the atom where the emission was generated. The distribution of the energies of all the photons emitted is presented in an energy spectrum in which the intensity (number of photons detected) is represented as a function of energy (in keV). The energy spectrum makes it possible to characterize the elemental composition of a sample where each peak corresponds to the electronic transition of a specific chemical element (Jenkins, 1999).

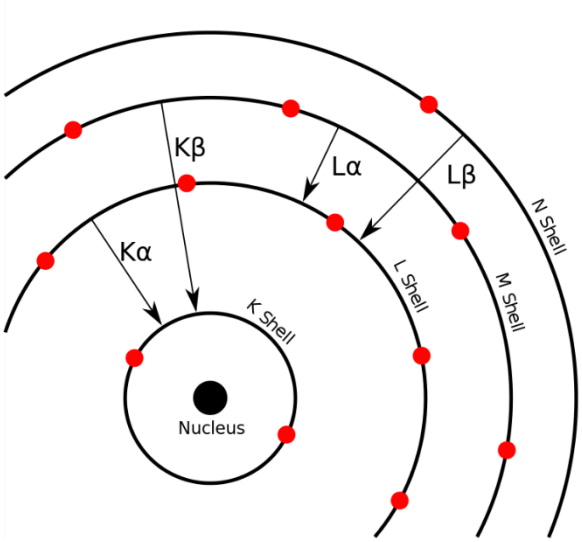

Figure II.11: *Denomination of atomic shells and of characteristic emission lines in an atom. The fallout of an electron from an upper layer to a lower layer (electronic transition) implies that the latter has previously lost one of its electrons. The transition from an L shell to a K shell is called Kα, the transition from an M shell to a K shell, Kβ, etc., where each of these transitions generates a X photon whose energy allows to determine the chemical element having emitted it (sourced from https://commons.wikimedia.org/wiki/File:CharacteristicRadiation.svg).*

2. *Instrumentation*

X-ray fluorescence imaging of thin sections was carried out on two slabs of ca. 1 cm thickness (one from sample 00AU39 and one from sample 00AU40) and detached thin sections using the DiffAbs beamline (Gueriau et al., 2020) at Synchrotron SOLEIL in order to identify and map the distribution and concentration of major and traces elements. The microbeam setup consists of two cylindrical, vertically-focusing mirrors allowing to focus the beam vertically, a fixed-exit double crystal monochromator made of two Si(111) crystals (whose first crystal makes the beam monochromatic and the second restores parallelism and ensures the horizontal focusing of the monochromatic beam), and two mirrors in Kirkpatrick-Baez (KB) geometry allowing focusing of the beam down to approximatively 10 µm × 10 µm. All measurements were performed using an incident beam energy of 13 keV, permitting the detection of elements from the K line of Ar at 2.4 keV (from ambient air) to the L line of Ge at 11 keV. The spatial resolution was 10 to 40 µm and the spectral resolution was 120–150 eV, with an integration time of 80–120 ms. XRF spectra were recorded with a four-element silicon drift detector (SDD, Vortex). Large centimeter scale images were used to map the distribution of elements. Smaller images and spot measurements were acquired on specific ROIs.

3. *Data treatment*

I used the *PyMca* software to process the elemental maps and spectra obtained during the XRF analyses of samples. Large-scale and small-scale images and point spectra were acquired during the analyses. For each image obtained, a global spectrum is associated. I first calibrated each energy spectrum by identifying two peaks, including a low energy peak (e.g., the Kα line of Ti at 4.51 keV) and a high energy peak (e.g., the Kα line of Ge at 9.87 keV). Then I modeled the measured spectrum by defining the limits of the fitting region (here, between 200 and 1200 channels, i.e., between 2 and 12 keV) and selecting the chemical elements to include in the model with their appropriate transition

groups (e.g., the group of transitions K, including the transitions Kα and Kβ). Finally, on each spectrum, I selected peaks of interest for each element in order to extract elemental maps. I processed the elemental maps obtained on the *ImageJ* software in order to modify the color scale, resize the images and adjust the brightness and the contrast, for example.

H. Proton-Induced X-ray Emission (PIXE)

1. Principle

Proton-induced X-ray emission (PIXE) is a micro-destructive technique whose principle is similar to XRF spectroscopy. However, instead of using an X-ray beam to determine the elemental composition of a sample, the material is exposed to a beam of accelerated protons at several MeV (therefore more energetic than in XRF). The photons emitted by the sample as a result of interatomic interactions (**Fig. II.11**) have a wavelength which is in the X-ray range and which is specific to the chemical element of the atom where the X photon was generated.

2. Instrumentation

PIXE maps and spectra were acquired on carbon-coated, detached thin sections using µPIXE (microscale Proton-Induced X-ray Emission spectrometry; Barberet et al., 2021) combined with Rutherford Backscattering Spectrometry (RBS) at the AIFIRA facility, CENBG, Gradignan, France (**Fig. II.12**), to study the distribution of trace elements, in particular transition metals in the carbonaceous matter at a scale of 10–100 µm. Three Si-detectors (one RBS and two PIXE) collected the data: the RBS was used for charge monitoring, whereas the two PIXE detectors were used for elemental quantification and mapping. The first PIXE detector is equipped with an aluminum “Funny Filter” (thickness 100 µm, hole size 2 mm) and a Kapton filter (thickness 50 µm). Kapton is used to filter out lower atomic weight elements, and is therefore essential for determining the true concentrations of heavier trace elements such as titanium. The second PIXE detector is equipped with only an aluminum “Funny Filter” (thickness 100 µm) and was used for complete characterization of the sample. We used a microbeam of 3 MeV proton (1 µm diameter) with a current intensity of 200 pA; a scan speed of 500 µs/pixel; and a total acquisition time of ca. 10 hours per analysis. For the last analyses, we optimized these parameters using a beam of 2.5 µm with a current intensity of 900 pA, which allowed more accurate mapping and quantification, with a total acquisition time of ca. 5 hours. For some analyses, we only used one PIXE detector equipped with an aluminum “Funny Filter” (thickness 100 µm, hole size 3.64 mm) and a Kapton filter (thickness 50 µm). Two standards were used for the first setup, NIST 1411 (soft borosilicate glass) and Inox (iron, chromium, zinc and nickel metallic elements), and one for the second setup, NIST 610 (borosilicate glass). These standards cover the energy range from 1 to 20 keV in which trace elements from Si to Mo could be detected.

µPIXE analyses were performed in addition to the SEM-EDX and XRF spectroscopy analyses due to a better spatial resolution (0.5–0.8 µm for µPIXE versus 1 and 10 µm for SEM-EDX and XRF, respectively), which allows to locate more precisely the spatial distribution of the elements. Moreover, the emission energy used in µPIXE (3 MeV protons for µPIXE versus 5–20 keV X photons for SEM-EDX and XRF) allows detection of a wider range of elements (from Al to Mo), whereas the SEM-EDX is more adapted to detect lighter elements (C, O, Na, Mg…) but is less suitable for trace elements.

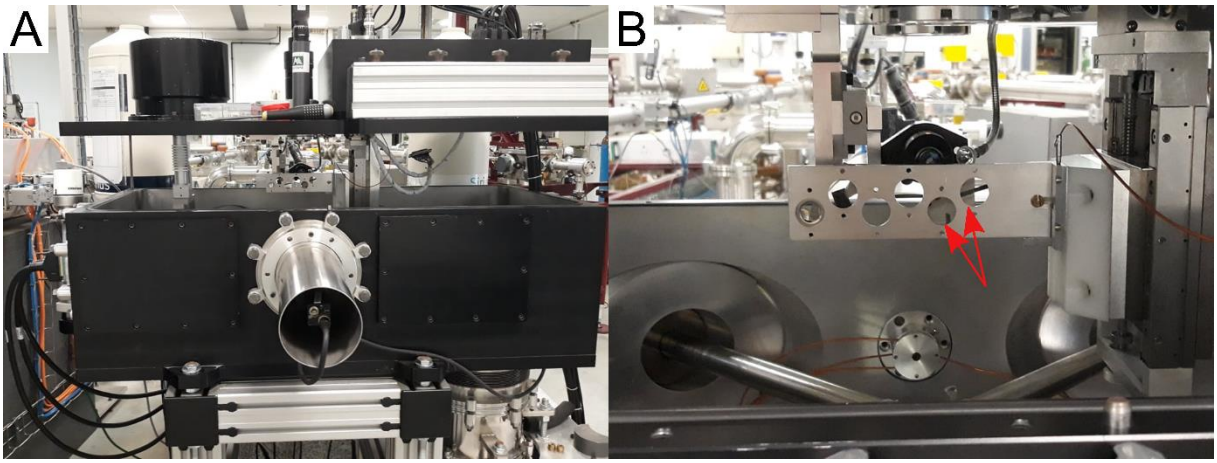

Figure II.12: *Pictures of the microbeam line chamber for PIXE analyses at AIFIRA facility where the sample fixed on its metal sample holder with carbon tape is visible from behind (red arrows).*

3. Data treatment

PIXE data processing is performed using a set of three software: *ConvertMPA3ListFile*, *SupaVisio* and *Gupix*. I first used the *ConvertMPA3ListFile* software which reads the time, position and number of counts data for the three detectors (RBS and PIXE) for each data set, and allows conversion of the spectra in a format readable and usable on the second software (.rbs for the spectra recorded by the RBS detector and .pixe for the spectra recorded by both PIXE detectors). The spectrum corresponding to the RBS detector shows backscattered ions, while the spectra corresponding to the PIXE detectors show different, non-overlapping spectra corresponding to the specific X-ray filtering.

The second software, *SupaVisio*, permits the creation of elemental maps and the transformation of the .pixe files into .gup so that they can be read by the *Gupix* program. I used it initially to convert files. Then, after having identified the characteristic peaks of certain elements on *Gupix*, I used it again to generate elemental maps of major and traces elements by selecting peaks of interest on each spectrum. In order to compare the variation in elemental concentrations of different structures, I also extracted ROIs on each global map whose spectra are extracted from the spectrum of the entire region of analysis.

Finally, I used the third software, *Gupix*, to process the spectra in order to obtain the elemental compositions of the analyzed zones. The software quantitatively determines the elemental composition by comparing the experimental spectrum with a theoretical spectrum adjusted by iterations (the reader can refer to Maxwell et al., 1995 for more information about the algorithm used by *Gupix*). The latter is obtained by considering the characteristics of the experimental device in particular. For this, a first step consists in indicating the experimental conditions, such as the different parameters related to the beam (e.g., beam angle, beam energy in keV, ion source, charge in µC) and the detector parameters (e.g., detectors used, filters applied). A second step consists in indicating the characteristics and the composition of the sample by defining the thickness of the sample and by choosing the chemical elements to add, as well as the alpha- and beta-ray (K) of each element (the use of L and M rays were not relevant for the elements in question) for the quantification. A last step consists in defining the various parameters used for the simulation such as the region of the spectrum to be simulated (values of the channel of departure and values of the channel of end of simulation),

the maximum of iterations which will be made by the program, the calibration parameters (energy calibration according to the detector used).

After performing all of these steps, I started the simulation, the results of which are presented in the form of two windows, one of which shows the superposition of the theoretical spectrum with the experimental spectrum and the other the residual, i.e., the difference between the experimental spectrum and the theoretical spectrum. The theoretical spectrum corresponds to the sum of all the individual spectra for each chemical element. Indeed, the spectrum of a chemical element is made up of all of its emission rays K, L and M. The spectra are represented in counts (number of X photons arriving at the detector) as a function of the energy expressed in keV. In the results of the simulation, there is also access to a table which summarizes the various information concerning the results of the simulation, the main ones concerning the mass concentration of elements (in part per million or ppm), the fit error (%Fit Error) on the spectrum adjustment, the statistical error (%Stat. Error) on the number of counts, and the limit of detection (LOD), which is defined as the smallest amount of material detectable in a matrix relative to the amount of material analyzed (McNaught and Wilkinson, 1997) and is determined for each of the elements sought in the particular case of the spectrum processed (the reader can refer to Teesdale et al., 1988 and Kump, 1997 for the mathematic definition of LOD). The last three parameters, which relate to the estimation of errors, allow the software to automatically indicate a judgment on the ability to dose an element: “Y”, “N”, or “?”. Generally, when the mass concentration for an element is below its LOD, the software lets the user judge whether this element is actually present or not. However, some elements below LOD may actually be present on elemental maps since the latter depend on the number of counts at a specific point, while the quantification (ppm) of an element depends on the detector-specific quantification of this element according to the *Gupix* algorithm (Halden et al., 1995; Campbell et al., 1995; Maxwell et al., 1995). I finally used twenty-five elements of interest for the quantification after several simulations: Al, Si, P, S, Cl, K, Ca, Ti, V, Cr, Fe, Co, Ni, Cu, Zn, Ga, Ge, As, Kr, Rb, Sr, Y, Zr, Nb and Mo. The PIXE quantification is reported in **Tables A1–3** of **Appendix A**.

I. Inductively Coupled Plasma Mass (ICP-MS) and Optical Emission (ICP-OES) Spectrometry

1. Principle

Inductively coupled plasma mass spectrometry (ICP-MS) is a destructive analytical technique that allows the detection and identification of metals and non-metals at very low concentrations (i.e., trace elements) by measuring their mass. The mass spectrometer comprises a source of ions, which vaporize the sample using a plasma torch, the ions of which are then separated according to their mass/charge ratio by an analyzer and then transformed into an electrical signal by a detector. The concentration of a sample is determined by calibration using certified reference materials.

Inductively coupled plasma optical emission spectrometry (ICP-OES) or ICP atomic emission spectrometry (ICP-AES) is an invasive technique that uses the light emitted from a plasma at a particular wavelength to determine the amount of an element in a sample (in particular major elements). The principle is similar to mass spectrometry, but in the case of optical emission spectrometry, we are interested in electromagnetic radiation emitted by the plasma at wavelengths characteristic of a particular element.

2. *Instrumentation*

Bulk geochemistry was measured on powders of the three samples, 00AU37b, 00AU39 and 00AU40, using ICP-OES and ICP-MS at CRPG, Nancy, France. Bulk major and trace elements were measured using iCap6500 ICP-OES and iCapQ ICP-MS instruments, respectively, in order to reconstruct characteristics of the regional paleoenvironment. Additional chemical analyses also measure the concentration of total CO_2, FeO, total S and organic C by fire loss ignition in powders of samples 00AU37b and 00AU39. The fire loss ignition is determined by gravimetric analysis (combustion analysis) whereby organic matter is combusted to ash and carbon dioxide at a temperature of 1020°C. The weight loss during the reaction is measured by weighing the samples before and after heating.

3. *Data treatment*

The results of the geochemical analyses were directly provided by the CRPG. The concentration of an element X is sometimes given as a mass percentage of the corresponding oxide $\mathrm{X_nO_m}$. The mass concentration in X, $\mathrm{C_M(X)}$, is then given from the mass concentration in $\mathrm{X_nO_m}$, $\mathrm{C_M(X_nO_m)}$, using the following equation, where n and m are the number of atoms of X and oxygen, respectively, and $\mathrm{M(X)}$ and $\mathrm{M(O)}$ are the molar mass of X and oxygen, respectively:

$$\mathrm{C_M(X)} = \frac{\mathrm{n \times M(X)}}{\mathrm{n \times M(X) + m \times M(O)}} \times \mathrm{C_M(X_nO_m)} \quad (5)$$

An example of calculation of the mass concentration of silicium from the oxide SiO_2 using equation (5) is shown below:

$$\mathrm{C_M(Si)} = \frac{\mathrm{n \times M(Si)}}{\mathrm{n \times M(Si) + m \times M(O)}} \times \mathrm{C_M(SiO_2)} \quad (5a)$$

$$\mathrm{C_M(Si)} = \frac{1 \times 28.09}{1 \times 28.09 + 2 \times 16} \times 91.79 = 42.91\% \quad (5b)$$

Then, the ICP results can be compared to the elemental abundances of the Earth's crust, before to be compared to the PIXE results, by normalizing the mass concentrations of each element relative to silicon. The enrichment factor (EF) of an element X can be calculated as follow, in which $\mathrm{EF(X)} > 1$ means an enrichment of X relative to the Earth's crust and $\mathrm{EF(X)} < 1$ means a depletion of X relative to the Earth's crust:

$$\mathrm{EF(X)} = \frac{\mathrm{C_M(X)_{sample} / C_M(Si)_{sample}}}{\mathrm{C_M(X)_{crust} / C_M(Si)_{crust}}} \quad (6)$$

An example of calculation of the factor enrichment of potassium in sample 00AU40 using equation (6) is shown below:

$$\mathrm{EF(K)} = \frac{\mathrm{C_M(K)_{sample\ 00AU40} / C_M(Si)_{sample\ 00AU40}}}{\mathrm{C_M(K)_{crust} / C_M(Si)_{crust}}} \quad (6a)$$

$$\mathrm{EF(K)} = \frac{0.162/42.91}{0.660/27.00} = 0.154 \quad (6b)$$

The ICP-MS and ICP-OES data provided in mass percentage of oxides (oxide wt.%) for major elements and in mass concentration of trace elements (in ppm) are reported in **Table A4** of **Appendix A**, and the

ICP-MS and ICP-OES results expressed in mass concentration of elements (in %), compared with the elemental abundances of the Earth's crust, are reported in **Table A5** of **Appendix A**. The results of additional chemical analyses (by fire loss ignition) are given in **Table A6** of **Appendix A**.

J. Laser Ablation Inductively Coupled Plasma Mass Spectrometry (LA-ICP-MS)

1. Principle

Laser ablation inductively coupled plasma mass spectrometry (LA-ICP-MS) is a destructive technique to detect and identify major and trace elements by using a principle similar to ICP-MS, but with a different sampling process. Indeed, this technique uses laser ablation to extract material from the surface of a sample. The interaction between the laser and the sample surface causes heating, vaporization and ionization of the sample. The material is thus converted into a plume of particles and ions, which are transported to an ICP-MS, from which the ions are separated and then analyzed by the same process as described above.

2. Instrumentation

LA-ICP-MS analyses were performed on three slabs of ca. 1–2 cm thickness (two slabs from sample 00AU39 and one from sample 00AU40) using an Element XR ICP-MS (Thermo Fischer Scientific) coupled to a 193 nm Excimer (ArF) laser ablation system RESOlution M50E (Resonetics) equipped with an S155 Laurin cell at IRAMAT, CNRS, Orléans, France. Standard Reference Materials NIST 610 and NIST 612 were used for calibration and mass spectrometer tuning. Multiple transects of laser ablation line analyses were taken through various areas of interest in order to reconstruct paleoenvironmental variations at a local scale (**Figs. II.13, 14**). Eleven lines were acquired in different laminations in sample 00AU40 (**Fig. II.13**) and fifteen lines were acquired in major different structures in sample 00AU39 (**Figs. II.14**). using a laser with an energy of 5 mJ, a frequency of 20 Hz and a spot size of 100 µm. The acquisition time was 30 seconds per spectrum after 10 seconds of uptake time to eliminate transient signal. Calibration was performed using standards reference glass NIST 610 and NIST 612 which run periodically (every 20 samples) to correct for drift. NIST 610 and 612 were used to calculate the response coefficient (k) of each element (Gratuze, 1999, 2016) and the measured values of each element were normalized against ^{28}Si, the internal standard, to produce a final percentage. Quantitative data for each structures of interest were obtained for the following isotopes: ^{23}Na, ^{24}Mg, ^{27}Al, ^{28}Si, ^{31}P, ^{39}K, ^{44}Ca, ^{47}Ti, ^{51}V, ^{52}Cr, ^{55}Mn, ^{57}Fe, ^{59}Co, ^{60}Ni, ^{65}Cu, ^{64}Zn, ^{71}Ga, ^{74}Ge, ^{75}As, ^{85}Rb, ^{88}Sr, ^{89}Y, ^{90}Zr, ^{93}Nb, ^{95}Mo, ^{121}Sb, ^{133}Cs, ^{137}Ba, ^{139}La, ^{140}Ce, ^{141}Pr, ^{146}Nd, ^{147}Sm, ^{153}Eu, ^{157}Gd, ^{159}Tb, ^{163}Dy, ^{165}Ho, ^{166}Er, ^{169}Tm, ^{172}Yb, ^{175}Lu, ^{178}Hf, ^{181}Ta, ^{208}Pb, ^{232}Th, and ^{238}U.

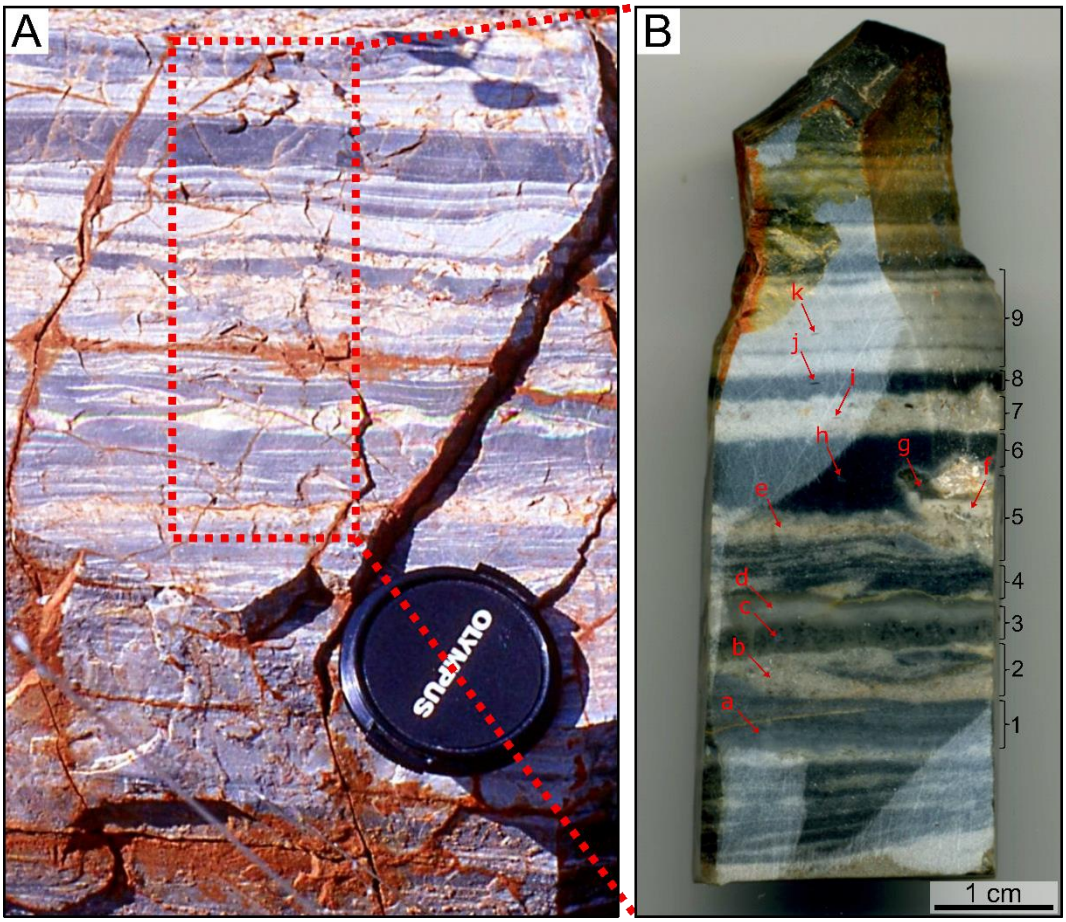

Figure II.13: *Photographs of sample 00AU40 and slab 00AU40-1. (**A**) Field photograph of sample 00AU40 with red dotted box indicating the location from which the slab 00AU40-1 was obtained. Lens cap for scale, 3.5 cm diameter. Photograph taken by Frances Westall in August 2000. (**B**) Photograph of slab 00AU40-1 with red arrows indicating location of the areas of interest and black numbers next to the slab corresponding to different layers (the reader is directed to Westall et al., 2006a for a complete sedimentological and mineralogical description of the layers). The areas of interest were selected in different laminations (a, b, c, d, e, h, i, j and k), including a pumice fragment (f and g).*

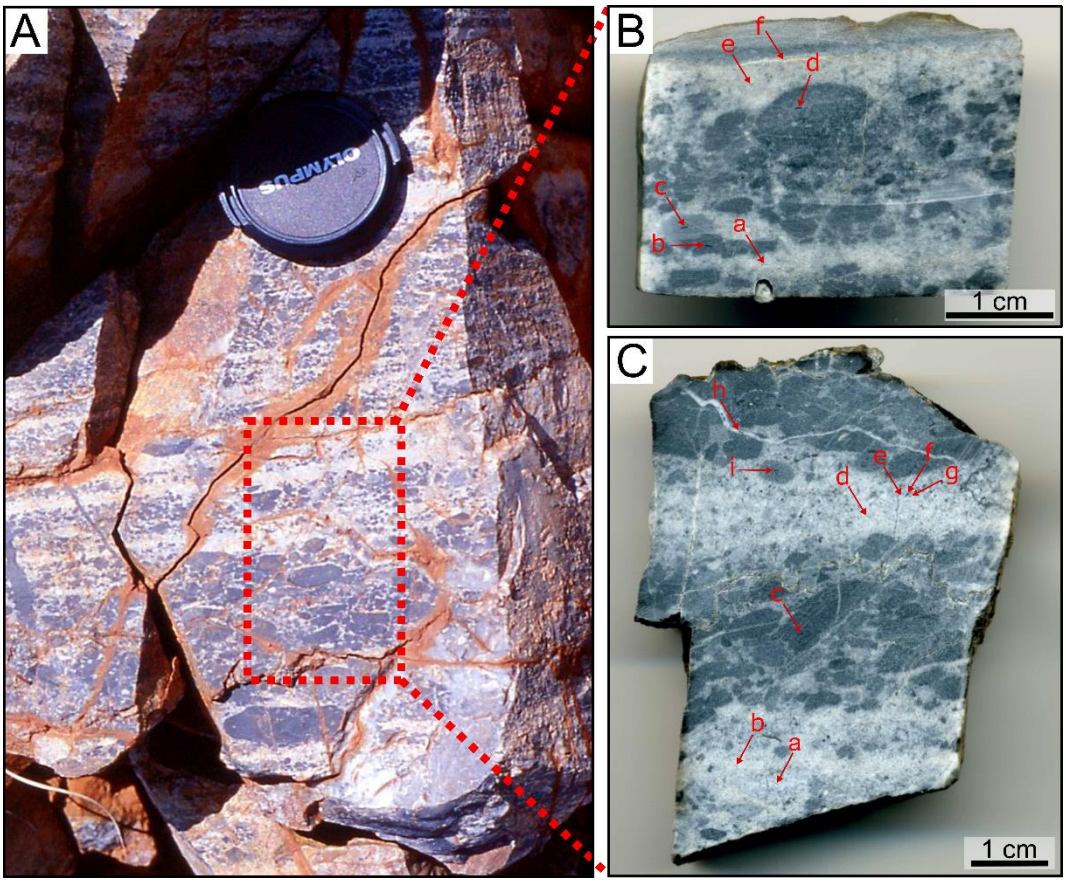

Figure II.14: *Photographs of sample 00AU39 and slabs 00AU39-1 and 00AU39-2. (**A**) Field photograph of sample 00AU39 with red dotted box indicating the location from which the slabs 00AU39-1 and 00AU39-2 were obtained. Lens cap for scale, 3.5 cm diameter. Photograph taken by Frances Westall in August 2000. Photographs of slabs (**B**) 00AU39-1 and (**C**) 00AU39-2 with red arrows indicating location of the areas of interest. In sample 00AU39-1, the areas of interest were selected in the silica matrix (a, e), in the silica-dust gel matrix (b, c, d) and in a yellow silica vein at the top (f). In sample 00AU39-2, the areas of interest were taken in the silica matrix (a, b, d, g), in the silica-dust gel matrix (c, i), in a dark grain (f), at the interface between the dark grain and the silica matrix (e) and in a white silica vein (h).*

3. *Data treatment*

The LA-ICP-MS data was processed by Bernard Gratuze (CNRS-IRAMAT, Orléans) who provided the results of the geochemical analyses in the form of tables where the major and trace elements are expressed in mass percentage of oxides (oxides wt.%), and converted into mass concentration of elements (in % and in ppm). The LA-ICP-MS data provided in mass percentage of oxides for major elements and in mass concentration of trace elements (in ppm) are reported in **Tables A7–8** of **Appendix A**.

Trace and rare-earth elements plus yttrium (REE + Y) compositions (14 lanthanides except Pm, and yttrium) of the bulk samples and areas of interest obtained by ICP-MS and LA-ICP-MS were normalized using Mud from Queensland (MuQ; Kamber et al., 2005) to remove the natural variations in REE + Y and to facilitate the comparison of measurements with the compositional characteristics of upper crustal reservoirs. MuQ represents a bimodal felsic and mafic input, i.e., the terrigenous input expected from greenstone belts in the Archean oceans. Most Precambrian sedimentary deposits are

characterized by a seawater REE + Y pattern modulated by hydrothermal and other influences (Bau and Dulski, 1996; Allwood et al., 2010; Gourcerol et al., 2015; Hickman-Lewis et al., 2020a), showing:

- an enrichment in heavy REE (HREE) compared to light REE (LREE), and a low $(Pr/Yb)_{MuQ}$ ratio, signifying a marine influence;
- super-chondritic Y/Ho ratios (≥ 27), reflecting a marine input;
- negative Ce anomalies resulting from Ce(III) oxidation in the water column;
- positive Eu anomalies linked to a hydrothermal influence;
- positive La, Y, and Gd anomalies related to a marine input;
- flattening of normalized patterns via enrichment in LREE resulting from terrigenous fluvial (continental runoff) input that is rapidly altered to typical seawater patterns during interactions with marine waters;
- an enrichment in middle REE (MREE), and particularly in HREE (Sm, Tm, Yb and Lu), resulting from the adsorption of REE onto bacterial cell walls.

Elemental anomalies relative to neighboring and near-neighboring elements in ICP-MS and LA-ICP-MS plots were calculated following the methods proposed by Lawrence et al. (2006), where X_{MuQ} is the MuQ-normalized of an element concentration and $X_{MuQ}{}^{*}$ is the predicted normalized concentration:

$$(Ce/Ce^{*})_{MuQ} = Ce_{MuQ}/(Pr_{MuQ}(Pr_{MuQ}/Nd_{MuQ})) \quad (7)$$

$$(Eu/Eu^{*})_{MuQ} = Eu_{MuQ}/(Sm^{2}{}_{MuQ} \times Tb_{MuQ})^{1/3} \quad (8)$$

$$(La/La^{*})_{MuQ} = La_{MuQ}/(Pr_{MuQ}(Pr_{MuQ}/Nd_{MuQ})^{2}) \quad (9)$$

$$(Y/Y^{*})_{MuQ} = Y_{MuQ}/(0.5Er_{MuQ} + 0.5Ho_{MuQ}) \quad (10)$$

$$(Gd/Gd^{*})_{MuQ} = Gd_{MuQ}/(Tb^{2}{}_{MuQ} \times Sm_{MuQ})^{1/3} \quad (11)$$

In particular, Ce anomaly is significant if $(Ce/Ce^{*})_{MuQ}$ is greater than 1.05 or less than 0.95 (Bau and Dulski, 1996), Eu anomaly is significant if $(Eu/Eu^{*})_{MuQ}$ is greater than 1.2 (Kerrich et al., 2013), and La anomaly is significant if $(La/La^{*})_{MuQ}$ is different from 1 (Bau and Dulski, 1996).

The different methods used for the analyses of samples during this thesis project are summarized in **Table II.1**. These methods are complementary in order to fully characterize the purported fossilized traces of life of the Kitty's Gap Chert, from macroscopic to nanoscopic scale, and demonstrate their biogenicity and syngenicity.

Table II.1: *Summary of the methods used for the analyses of samples, with location, information provided, analysis parameters, and type of sample for each method.*

	Optical microscopy	Scanning electron microscopy	Transmission electron microscopy	EDX (coupled with SEM and TEM)	Raman spectroscopy	DUV fluorescence spectroscopy	Fourier transform infrared spectroscopy	X-ray fluorescence spectroscopy	Proton-induced X-ray emission	ICP-MS/OES	LA-ICP-MS
Location (accessibility during the thesis)	CBM (unlimited for BX51 and 5 days for Ti)	ISTO & MACLE, Orléans/NHM, London (several days/year)	MACLE & ICMN, Orléans (3 days)	ISTO, MACLE & ICMN, Orléans/NHM, London (several days)	CBM (unlimited)	Synchrotron SOLEIL (2 sessions)	NHM, London (1 session)	Synchrotron SOLEIL (1 session)	AIFIRA, Bordeaux (1–2 session(s) of 3 days/year)	CRPG, Nancy (service on request)	IRAMAT, Orléans (1 half day)
Information provided	Petrology, mineralogy and identification of carbonaceous matter	Morphology of carbonaceous structures (cells, EPS, biofilm…)	Nanostructure and crystallography	Identification of minerals and composition of carbonaceous matter	Mineralogy, identification and distribution of carbonaceous matter	Identification and distribution of aromatics compounds, metallic oxides and minerals	Identification and distribution of functional groups in carbonaceous matter	Distribution and concentration of major and trace elements	Distribution and concentration of transition metals	Composition in major and trace elements in bulk rock	Composition in major and trace elements in specific locations
Analysis type	Mineralogy, morphology, texture, structure	Morphology, texture, structure	Morphology, crystallography	Elemental	Mineralogy, molecular	Fluorescence, molecular	Molecular	Fluorescence, elemental	Fluorescence, elemental	Geochemistry	Geochemistry
Analysis mode	Transmission/ Reflection	Reflection	Transmission	Reflection/ Transmission	Reflection	Reflection	Transmission	Reflection	Reflection	Ionization	Ionization
Emission energy	Visible photons (400–700 nm)	Primary electrons (5–20 keV)	Electrons (200 keV)	X photons (5–20 keV for SEM and 200 keV for TEM)	Green photons (532 nm)	UV photons (275 nm)	IR photons (675–4000 cm^{-1})	X photons (13 keV)	Protons (3 MeV)	UV–IR photons	UV photons (193 nm)
Analysis spectral range	Visible photons (400–700 nm)	Secondary (50 eV) and backscattered (<30 keV) electrons	Scattered electrons (≤200 keV)	X photons (0–20 keV)	Visible photons (0–4000 cm^{-1})	UV-visible photons (285–550 nm)	IR photons (675–4000 cm^{-1})	X photons (2.5–18 keV)	X photons (1–18 keV)	X photons (1–40 keV)	X photons (1–40 keV)
Chemical elements detected	N/A	N/A	N/A	C, O, Na, Mg, Al, Si, P, S, Cl, K, Ca, Ti, V, Fe, Zr (Cu, Ga, Pt, Au)	Covalent chemical bonds	N/A	Covalent chemical bonds	From Ar to As (+ W, Ce, Nd)	From Al to Mo	10 major oxides (+ $CO_{2\ total}$, FeO, S_{tot}, C_{org}) + 44 trace elements	47 major oxides and trace elements
Spatial resolution	<1 µm	A few tenths of nm–1 nm (SE), 1 nm–a few nm (BSE)	up to 0.1 nm	ca. 1 µm at 20 keV and <150 nm at 5 keV for SEM and 0.1 nm for TEM	1 µm	7.2 µm	30 µm	10 µm	0.5–0.8 µm	10–100 µm	100 µm
Spectral resolution	N/A	N/A	N/A	129 eV (Kα of Mn)	3 cm^{-1}	0.5 nm	4 cm^{-1}	120–150 eV	<100 eV	N/A	N/A
Analysis depth	Depending on material	>10 nm	Depending on material	Depending on material	Depending on material	≥10 µm	1–10 µm	Depending on material and energy of incident and emitted photons	Depending on material and energy of incident protons and emitted photons	N/A	Depending on material
Sample type	Standard (30 µm) or thick (70 µm) thin section	Coated thin section (70 µm)	FIB section (6 × 10 × 0.1 $µm^3$)	Coated thin section (70 µm) and FIB section (6 × 10 × 0.1 $µm^3$)	Standard (30 µm) or thick (70 µm) thin section	Detached thin section (70 µm)	Detached thin section (70 µm)	Slab (≈1 cm thick) and detached thin section (70 µm)	Detached thin section (30 µm or 70 µm)	Powder (<80 µm)	Slab (≈1 cm thick)

IV. Résumé en français

Ce second chapitre décrit le contexte géologique du chert de Kitty's Gap dont les échantillons étudiés dans ce projet de thèse ont été extraits. Le chert de Kitty's Gap est une unité stratigraphique sédimentaire bien préservée qui fait partie de la ceinture de roches vertes de Coppin Gap, localisée dans l'un des terrains les plus anciens datant de l'Archéen, le craton de Pilbara, en Australie (**Figure II.1**). Cet horizon sédimentaire d'environ 40 mètres d'épaisseur fait partie du complexe volcano-sédimentaire de Kitty's Gap qui comprend un ensemble de roches volcaniques felsiques, de basaltes et de roches sédimentaires volcanoclastiques (i.e., formées de débris de roches volcaniques et d'un peu de sable et de boue terrigènes) qui se sont déposés en milieu subaqueux au cours de l'extension de la ceinture de roches vertes (**Figure II.1C**). Le complexe de Kitty's Gap affleure actuellement sur une longueur totale de 5 kilomètres environ.

Le chert de Kitty's Gap est composé de sédiments volcaniques silicifiés datés à 3.446 Ga qui proviennent de l'érosion de terres continentales émergées composées de roches volcaniques felsiques et de coulées de lave basaltique et de cendres volcaniques. Ces sédiments ont été transportés puis déposés par des rivières jusqu'à une plage située dans un lagon où l'eau était peu profonde avant d'être silicifiés par l'eau de mer Archéenne sursaturée en silice (**Figure II.2**). La silicification a également été favorisée par l'hydrothermalisme, ainsi que par la saturation en silice des eaux interstitielles suite à la dévitrification des verres volcaniques au cours de la diagenèse. Après la diagenèse, les roches ont subi un métamorphisme régional (faciès schiste vert).

Les sédiments silicifiés affleurent désormais sous la forme d'une crête orientée est-ouest, bien visible dans le paysage, dans laquelle les couches volcano-sédimentaires sont inclinées verticalement ou légèrement renversées et sont séparées par des laves mafiques (**Figure II.3**).

Les échantillons étudiés ont été collectés sur le terrain en 2000 par Frances Westall et proviennent de la lentille de chert 1 localisée dans la partie inférieure de la succession sédimentaire du chert de Kitty's Gap. La lentille de chert est constituée de dépôts sédimentaires gris foncé à gris clair avec une texture granulaire et des structures sédimentaires bien préservées (stratifications entrecroisées, stratifications ondulées… ; **Figure II.4**). L'échantillon 00AU37b a été prélevé dans des sédiments bréchifiés par une veine hydrothermale à la base de la lentille de chert. L'échantillon 00AU39 a été extrait à quelques centimètres de la veine hydrothermale, à la base de la lentille de chert, tandis que l'échantillon 00AU40 a été prélevé à environ 15 mètres à l'est de la veine hydrothermale, en haut de la lentille de chert.

L'échantillon 00AU37b a été analysé par ICP-MS/OES afin d'obtenir des informations sur la géochimie de la source hydrothermale. Les deux autres échantillons de roches, 00AU39 et 00AU40, ont été analysés en utilisant des méthodes d'analyses complémentaires à différentes échelles et sous différents formats (**Figure II.5**). Des morceaux de roches bruts et polis de quelques centimètres d'épaisseur ont été utilisés pour décrire la minéralogie, la texture et la structure de la roche à l'œil nu, ainsi que pour des analyses géochimiques ponctuelles (LA-ICP-MS), afin de reconstituer les variations paléoenvironnementales à l'échelle locale, et des analyses élémentaires (spectroscopie de fluorescence à rayons X), pour déterminer la distribution globale des éléments chimiques. Des échantillons de roches en poudre ont été préparés au laboratoire du CRPG (Nancy, France) pour des analyses géochimiques de la roche globale (ICP-MS/OES). Des lames minces polies (30 µm et 70 µm d'épaisseur) ont été préparées à l'ISTO-CNRS (Orléans, France) et par l'entreprise Thin Section Lab (Toul, France) pour observer et identifier la minéralogie, la morphologie des dépôts carbonés, la texture et la structure de la roche (microscopie optique, microscope électronique à balayage,

spectroscopie Raman), ainsi que pour analyser et cartographier la composition élémentaire des minéraux et de la matière carbonée (spectromètre à rayons X à dispersion d'énergie, spectroscopie de fluorescence à rayons X, PIXE) et la composition moléculaire de la matière carbonée (spectroscopie Raman, spectroscopie de fluorescence UV, spectroscopie infrarouge à transformée de Fourier). Des coupes FIB (faisceau d'ions focalisé) de 100 nanomètres d'épaisseur environ ont été préparées à l'IEMN-CNRS (Lille, France) à l'aide d'un microscope ZEISS Crossbeam afin d'observer la morphologie et la cristallographie des minéraux et de la matière carbonée par microscopie électronique en transmission, et d'identifier et cartographier la composition élémentaire des minéraux et de la matière carbonée par spectrométrie à rayons X à dispersion d'énergie.

Le **Tableau II.1** présenté à la fin de ce chapitre résume les différentes méthodes utilisées pour analyser les échantillons du Kitty's Gap Chert au cours de ce projet de thèse. Ces méthodes sont complémentaires pour caractériser les potentielles traces de vie fossilisées du chert de Kitty's Gap, de l'échelle macroscopique jusqu'à l'échelle nanoscopique, et démontrer leur biogénicité et syngénicité.

Chapter III: Results

I. Introduction

The first part of this chapter describes the reconstruction of the paleodepositional environment of the silicified volcanic sediments of the Kitty's Gap Chert through sedimentological, petrological, mineralogical and geochemical characterization of the samples – within the framework of the already established field sedimentology study (de Vries, 2004; de Vries et al., 2010). The second part is dedicated to the analysis of carbonaceous matter in the samples through in situ physical and geochemical (elemental and molecular) characterization, as well as its distribution at multiple scales (from microscopic to nanoscopic scales).

II. Investigating the paleoenvironmental context

A. Sedimentological characterization

Sample 00AU37b is part of a conglomerate (00AU37) exhibiting millimeter- to centimeter-size, light-colored clasts in a black chert matrix, obtained from a hydrothermal vein (**Fig. III.1B**). Sample 00AU39 is a conglomerate composed of fine dark pebbles surrounded by coarsely laminated, millimeter to centimeter thick deposits (**Fig. III.1C**). Sample 00AU40 is a heterolithic chert alternating between coarse light gray and fine dark gray laminations characterized by diverse sedimentary structures, such as current micro-ripples, flaser-linsen bedding and undulating lamination that are typical of sediments deposition in a shallow-water, channel environment influenced by tides (**Fig. III.1D**; Westall et al., 2006a; de Vries et al., 2010). Flaser-linsen bedding is a sedimentary bedding pattern created when a sediment is deposited in a tidal environment exposed to different energy levels, resulting in opposite current directions, the rippled sand layers being formed during high tidal currents, while the mud is deposited during slack tides periods (Martin, 2000). In addition, the direction of the paleocurrents appears to be bimodal in the chert lens 1 as indicated by the imbrication of the pebbles in the basal conglomerate oriented towards the now east-northeast current direction (**Fig. III.1C**) and the ripples of the laminated chert towards the now west current direction (**Fig. III.1D**).

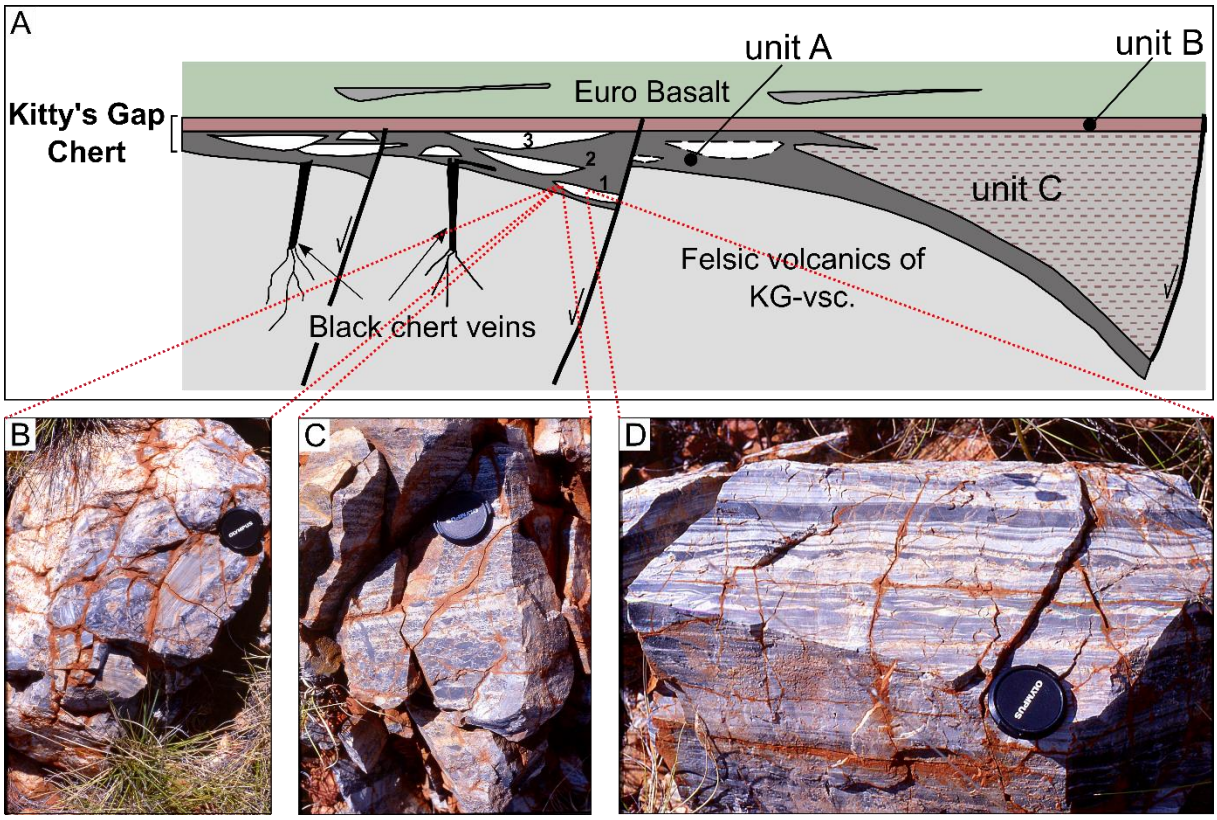

Figure III.1: *Cross-section and field photographs of samples of the Kitty's Gap Chert. (**A**) Schematic drawing (not to scale, width of geological cross-section approximately 1.5 km) of silicified sediments of Kitty's Gap and chert lenses, including chert lenses numbered 1–3 from unit A (modified after de Vries, 2004). Field photographs of (**B**) sample 00AU37 showing a conglomerate composed of white and gray clasts in a black chert vein (sample 00AU37b) extracted from a hydrothermal vein crossing the chert lens 1, (**C**) sample 00AU39 showing a conglomerate formed of dark pebbles embedded in a sandy material at the base of chert lens 1, and (**D**) sample 00AU40 showing dark and light laminations with micro-ripples, flaser-linsen bedding and undulating lamination at the top of chert lens 1. Lens cap for scale, 5.4 cm diameter. Photographs taken by Frances Westall in August 2000.*

B. Petrological characterization

Hand sample and optical microscopy observations of a rock sample and a thin section from sample 00AU37b (silica vein) show a smooth, glassy texture where light veins, a few millimeters wide and composed of microcrystalline quartz, cross a homogenous black chert matrix (**Fig. III.2**). The color of the black chert matrix is due to the submicroscopic quartz crystals (<1 µm) that constitute it.

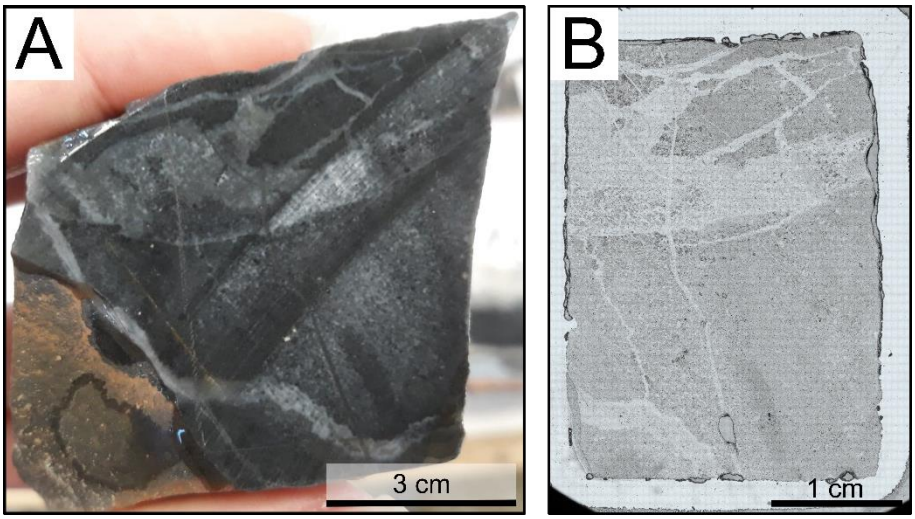

Figure III.2: *Slab and thin section of sample 00AU37b. (**A**) Photograph of the slab from which thin section 00AU37b was prepared. (**B**) Image mosaic of thin section 00AU37b (Nikon Eclipse Ti microscope).*

Rock samples and thin sections from samples 00AU39 and 00AU40 (**Figs. III.3, 4**) exhibit a microlithic texture, which is typical of volcanic rocks, with phenocrystals embedded in a matrix composed of finer minerals – microliths – that are only visible under the microscope, and volcanic glass. The volcanic protoliths (e.g., volcanic glass, K-feldspar, biotite and amphibole) have been diagenetically replaced by hydromuscovite (phyllosilicate enriched in SiO_2, Al_2O_3 and K_2O which contains variable amounts of trace elements, such as Fe_2O_3, MgO and Na_2O) and are outlined by nanometer-sized Ti-oxide spherules (Orberger et al., 2006; Westall et al., 2006a). Silica veins also appear in these samples, ranging in width from <100 µm up to a few millimeters. In sample 00AU39 located from near the hydrothermal vein, the silica veins consist of coarse-grained quartz (<300 µm in diameter) visible in analyzed polarized light and outlined with flakes of sericite (**Fig. III.5**).

Sample 00AU39 is mostly composed of rounded to angular, dark pebble-like structures surrounded by a light material composed of coarse particles (**Fig. III.3A, B**). The light layers are enriched in poorly sorted volcanic protoliths diagenetically replaced by silica and hydromuscovite (**Fig. III.3C**), with particle sizes varying between 50 and 500 µm. The dark pebbles are more homogenous and comprise fine-grained volcanic dust particles in a silica gel-like matrix with a homogenous grain size, which is less than 20 µm (well sorted), intermixed with silica and rare, larger volcanic protoliths (<100 µm; **Fig. III.3C**). Sub-horizontal stylolites are also visible throughout the rock and correspond to saw-tooth surfaces along which mineral matrix has been removed by pressure dissolution (**Fig. III.3B, C**).

Sample 00AU40 (KG1 of Orberger et al., 2006; sample studied by Westall et al., 2006a, 2011a) is characterized by several horizontal laminations alternating between light gray and dark gray (**Fig. III.4A, B**). The light gray laminations are composed of coarser material, such as volcanic protoliths replaced diagenetically by silica and hydromuscovite (**Fig. III.4C**), with particle sizes varying between 50 and 500 µm (poorly sorted). The regular and homogenous dark gray laminations are primary volcanic material formed of volcanic ash deposits (<20 µm; well sorted) mixed with silica, and with rare volcanic protoliths (<100 µm; **Fig. III.4C**). A deposit of pumice is intercalated between a coarse-grained layer and a fine-grained layer, and is composed of rounded pumice fragments ≥1 cm in size, enriched in silica. The base of the pumice is sometimes enriched in black deposits composed of crystals of anatase (**Fig. III.4B**).

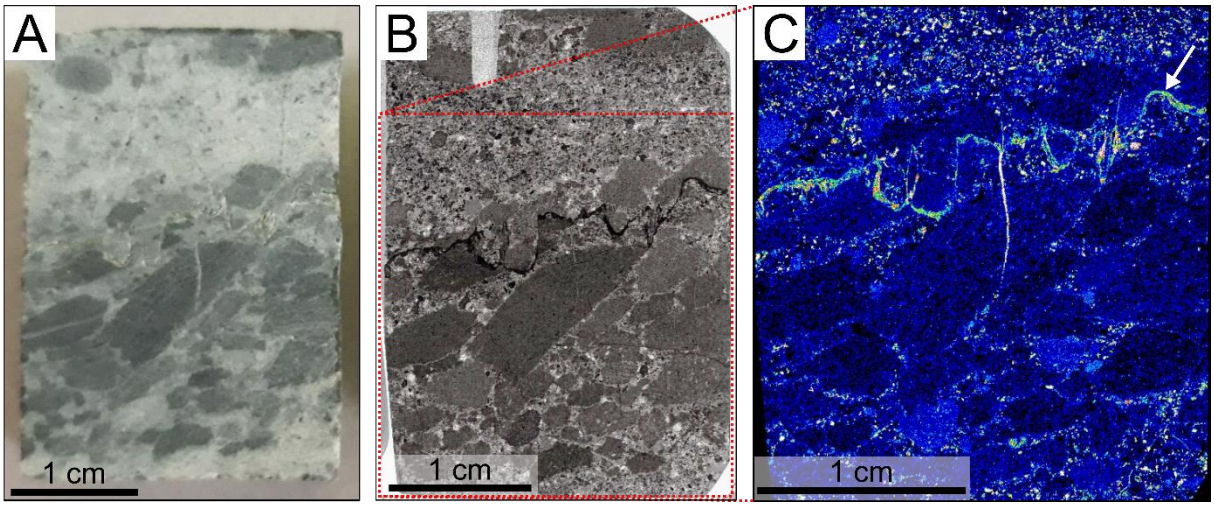

Figure III.3: *Slab and thin section of sample 00AU39. (**A**) Photograph of the slab from which thin section 00AU39c was prepared. (**B**) Image mosaic of thin section 00AU39c with red dotted box corresponding to image shown in (**C**) (Nikon Eclipse Ti microscope). (**C**) X-ray fluorescence spectroscopy map of potassium showing the distribution of this element related to the potassic composition in alteration phases of the volcanic protoliths and grain distribution throughout the sample. The concentration of K varies between low [dark blue] in areas enriched in coarse and/or slightly altered volcanic grains and high [white] in areas enriched in fine and/or very altered volcanic grains. The white arrow indicates a potassium-enriched stylolite.*

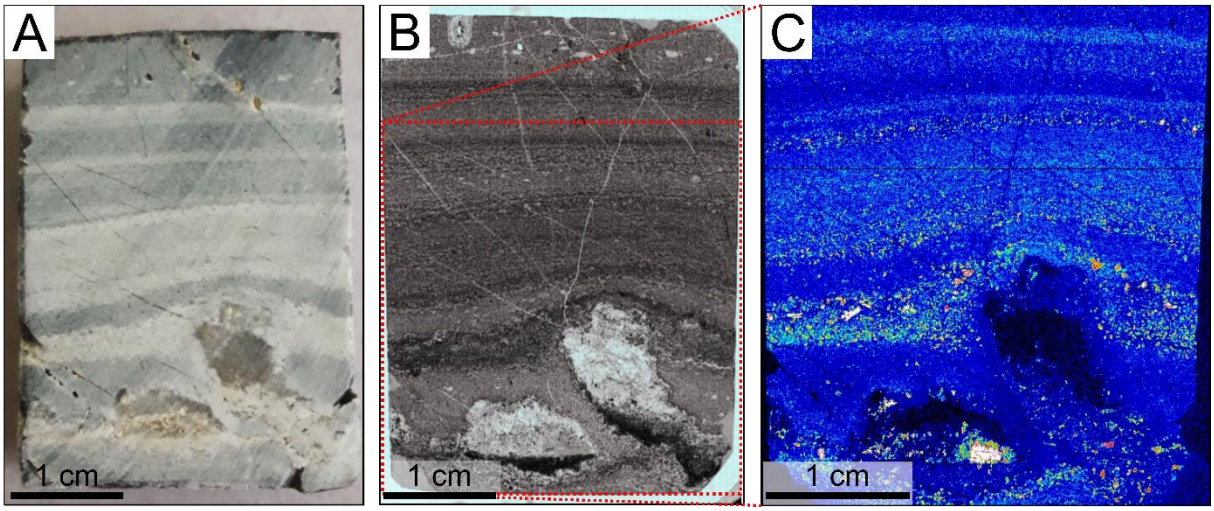

Figure III.4: *Slab and thin section of sample 00AU40. (**A**) Photograph of the slab from which thin section 00AU40b was prepared. (**B**) Image mosaic of thin section 00AU40b with red dotted box corresponding to image shown in (**C**) (Nikon Eclipse Ti microscope). Note that light gray layers observed with the naked eye appear darker under the optical microscope whereas dark gray layers appear brighter. (**C**) X-ray fluorescence spectroscopy map of potassium showing the distribution of this element related to the potassic-altered volcanic protoliths and the varying grain sizes of the protoliths in different layers. The concentration of K varies between low [dark blue] in layers enriched in coarse and/or slightly altered volcanic grains and high [white] in layers enriched in fine and/or very altered volcanic grains.*

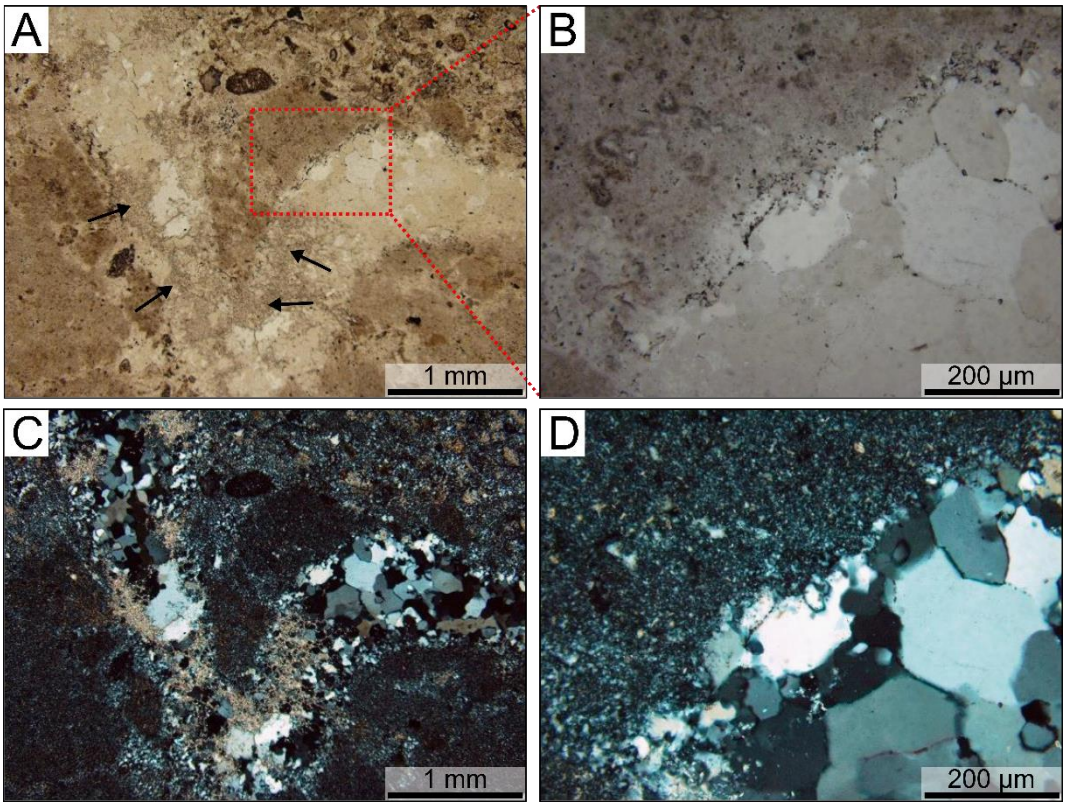

Figure III.5: *Silica vein in sample 00AU39. (**A**) Transmitted light optical image of a large silica vein a few millimeters wide composed of microcrystalline quartz (<200 µm in diameter) and outlined with flakes of sericite (black arrows). The red dotted box indicates the area corresponding to the image displayed in (**B**). (**B**) Enlarged view of the silica vein showing large crystals of quartz with a hexagonal shape. The silica vein is also surrounded by dark nanocrystals of anatase (small black dots). (**C, D**) Polarized light optical images of the same areas highlighting the different polarization shades of quartz depending on the orientation of the crystals (from white to black), and sericite flakes (in beige). The darker areas around the silica vein are fine-grained volcanic dust particles mixed with silica.*

C. Mineralogical characterization

Different types of volcanic grains were observed and described by optical microscopy and Raman spectroscopy in samples 00AU39 and 00AU40 (**Fig. III.6; Table III.1**). All volcanic grains are embedded in a mineral matrix mostly composed of silica and volcanic dust, and have been altered and replaced by secondary alteration minerals before being almost completely silicified. Two types of alteration may affect volcanic grains. The first is morphological alteration due to corrosion and mechanical processes, causing the edges of the volcanic particles to become either embayed or more rounded, respectively. The second is mineralogical alteration, in particular pseudomorphosis, i.e., mineral replacement by chemical substitution with preservation of the primary structure (appearance and dimensions). In the Kitty's Gap Chert, most volcanic clasts were diagenetically altered to clays (e.g., smectite or illite; Wilson, 2004; Fulignati, 2020) before being replaced by hydromuscovite, a metamorphic phase, and outlined by Ti-oxides (anatase and rutile). The volcanic grains can be divided into six categories defined by their size, their morphology, their color, and their protolithic origin.

Category 1 corresponds to optically light-colored, almost transparent volcanic glass protoliths generally 100–200 µm in size, with a rectangular-shape and often angular edges (less commonly with

rounded edges). The volcanic glass protoliths have been replaced by quartz (sometimes by hydromuscovite), and are outlined by anatase (more rarely by rutile; **Fig. III.6A–D**).

Category 2 comprises pumice protoliths that differ in appearance between the samples. In sample 00AU39 close to the hydrothermal source, pumice fragments are about a hundred micrometers in size, with a curved-shape and rounded edges, dark brown in color with light inclusions composed of microcrystalline quartz (some hydromuscovite), and always coated with anatase. Further from the hydrothermal source in sample 00AU40, they are of millimeter to centimeter size, with a curved-shape and rounded edges, white in color, and always coated with deposits of anatase which sometimes underline the bottom of the pumice by forming a large very dark deposit (**Figs. III.4B and III.6E, F**).

Category 3 corresponds to tabular or elongated feldspar protoliths 50–200 µm in width and >200 µm in length, with angular edges (sometimes rounded if mechanically corroded), and light-colored (pink, white or yellow). The feldspar protoliths have been replaced by hydromuscovite and/or quartz, and their edges are composed of anatase (more rarely of rutile). They may also be associated in pairs (**Fig. III.6G, H**). In sample 00AU40, far from the hydrothermal source, these grains are mostly found in dark gray laminations enriched in anatase.

Category 4 is made of amphibole or pyroxene protoliths 25–100 µm in size, of irregular shape with often angular edges, brown-green, light brown, dark brown or bluish in color, with a strong relief, and with an identical aspect in analyzed polarized light. The amphibole/pyroxene protoliths have been replaced by quartz and/or hydromuscovite, and are outlined by anatase (more rarely by rutile). Their surfaces can be completely coated with anatase (**Fig. III.6I–L**).

Category 5 are multiphase volcanic rock fragments that constitute the majority of the volcanic grains found in the samples. They probably represent volcanic rock (basaltic or rhyolitic) fragments. The multiphase volcanic rock fragments are variable in size, often of unrecognizable or curved-shape with rounded structure (more rarely angular to rounded), and light to dark-colored. They have been replaced by quartz and/or hydromuscovite, their edges are composed of anatase (more rarely of rutile), and their surfaces are sometimes completely coated with anatase (**Fig. III.6M–P**).

Category 6: In addition to the volcanic grains described above, a mixture of microcrystalline quartz (originally silica gel) and fine-grained volcanic dust forming a silica-dust gel composite occurs frequently in the samples. It appears dark to the naked eye and light to dark brown under the microscope. In sample 00AU39, the silica-dust gel forms pebble-like structures (<1 cm) that are clearly distinct from the silica matrix and the volcanic clasts (**Figs. III.5A, C and III.6Q, R**). In sample 00AU40, the silica-dust gel forms dark colored laminations a few millimeters thick that are distinct from light colored laminations, and have numerous siliceous spherules of volcanic origin (**Fig. III.6S, T**). In both samples, areas of volcanic dust are generally enriched in hydromuscovite (I therefore use potassium as a proxy; see **Figs. III.3, 4**), despite some variation due to grain size and degree of mineral alteration of volcanic protoliths.

All the categories of grains described above are present in both samples, in particular in the light grey zones, except pebbles that are only found in sample 00AU39, near the main hydrothermal vein. Other minerals were also identified, but only one specimen of each has been found in either sample and are therefore not representative of most of the grains found in the samples. A single barite crystal was identified in sample 00AU39: it has a cubic structure with a size of approximatively 50 µm², slightly colored yellow, with a strong relief, two families of 90° cleavage, and a tunnel on one side, and is

coated with small red and yellow pyrite grains. A tourmaline crystal was also identified in sample 00AU40, adjacent to a feldspar grain, with a size of 85 µm x 125 µm, blue-green colored and mostly altered to hydromuscovite (**Fig. III.6G, H**).

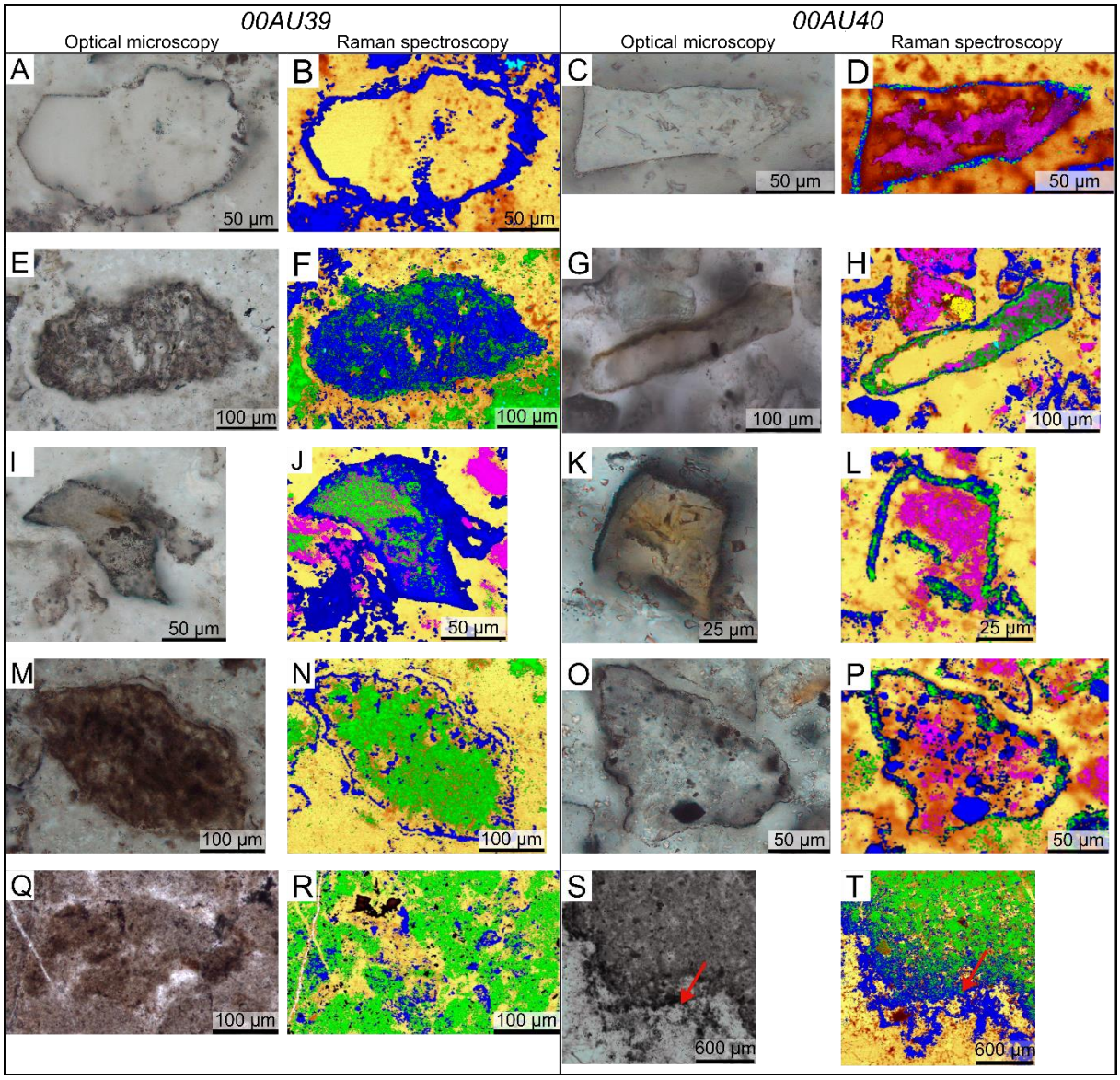

Figure III.6: *Optical images showing different grain types in transmitted light (left) and in Raman maps (right) for samples 00AU39 (left column) and 00AU40 (right column). In Raman maps, yellow/orange = quartz; dark blue = anatase; light blue = rutile, fuchsia = hydromuscovite; pale yellow = tourmaline; green = carbonaceous matter (kerogen). (**A, B**) Light-colored volcanic glass, with angular to subrounded edges composed of anatase, and replaced by quartz. (**C, D**) Light-colored volcanic glass, with angular to subangular edges composed of anatase and a small amount of carbonaceous matter, and replaced by quartz and hydromuscovite. (**E, F**) Pumice fragment, brown in color, curved-shape and rounded edges, replaced by anatase, composed of light inclusions of quartz, and carbonaceous matter located around the edges and inside the inclusions. (**G, H**) Feldspar, yellow to orange in color, elongated rod-like habit, angular to rounded edges, surrounded by anatase and rutile, replaced by quartz and hydromuscovite, and coated with carbonaceous matter. (**I, J**) Amphibole/pyroxene, brown-green in color, high relief, angular to subrounded edges composed of anatase, replaced by hydromuscovite, and coated with anatase and carbonaceous matter. (**K, L**) Amphibole/pyroxene, light brown-orange in*

*color, high relief, angular to subrounded edges composed of anatase and carbonaceous matter, and replaced by quartz and hydromuscovite. (**M**, **N**) Multiphase volcanic rock fragment coated with a dark brownish deposit and a curved-shape (corresponding to carbonaceous matter on the Raman map), and rounded edges composed of anatase. (**O**, **P**) Light-colored multiphase volcanic rock fragment, with rounded edges composed of anatase and carbonaceous matter, replaced by quartz and hydromuscovite, and coated with anatase. (**Q**, **R**) Silica-dust gel of light to dark brown in color, crossed by veins of silica, and mostly composed of quartz, anatase and carbonaceous matter. (**S**, **T**) Silica-dust gel of dark brown in color, underlined by anatase, and mostly composed of quartz and carbonaceous matter (a silica spherule is indicated by a red arrow).*

Table III.1: *Summary of the characteristics of the different structures found in the samples using optical microscopy and Raman spectroscopy.*

Category of volcanic grains	Size	Morphology	Color	Pseudomorphs	Protolith	Other specificities
Category 1 (Fig. III.6A–D)	100–200 µm	Rectangular, angular (± rounded) edges	Light-colored (almost transparent)	Quartz ± hydromuscovite + anatase ± rutile	Volcanic glass	/
Category 2 (Figs. III.4B and III.6E, F)	100–200 µm (close[1]) Several mm (far[1])	Curved, rounded edges	Dark brown (close) White (far)	Microcrystalline quartz ± hydromuscovite + anatase	Pumice	Light inclusions (close)
Category 3 (Fig. III.6G, H)	50–200 µm (width) x several µm (length)	Tabular/elongated, angular (± rounded) edges	Pink, white or yellow	Hydromuscovite and/or quartz + anatase ± rutile	Feldspars	May be found in pairs
Category 4 (Fig. III.6I–L)	25–100 µm	Irregular, angular (± rounded) edges	Brown-green, light brown, dark brown or bluish	Quartz and/or hydromuscovite + anatase ± rutile	Amphiboles or pyroxenes	Strong relief
Category 5 (Fig. III.6M–P)	Variable	Irregular or curved, rounded (rarely angular) edges	Light to dark-colored	Quartz and/or hydromuscovite + anatase ± rutile	Multiphase volcanic rock fragments	/
Category 6 (Figs. III.5A, C and III.6Q–T)	<1 cm (close) Few mm (far)	Pebbles-like (close) Laminations (far)	Light to dark brown	Microcrystalline quartz	Silica-dust gel	Silica spherules (far)

[1]close/far = sometimes I observed some differences between the sample close to the hydrothermal source and the sample far from it that are specified with a mention (close or far) in brackets.

D. Geochemical characterization

1. General distribution of major and trace elements with XRF spectroscopy

XRF spectroscopy analyses of slabs and thin sections from samples 00AU39 and 00AU40 (**Figs. III.7, 8**) were used to map the distribution of major and trace elements at large scales, thus providing an overview of the bulk samples.

General analysis of sample 00AU39 shows that light layers are enriched in volcanic protoliths replaced by hydromuscovite (K) and titanium oxides (Ti), and are associated with other transition metals (such as V, Cr, Fe, Zn, As; **Fig. III.7A**). Average elemental concentrations in a large-scale area of sample 00AU39 follow the trend: Fe > Ti > K > Cu > Zn > Ge > Ga > Ca, V > Ni, Cr > Mn, Co, As > Nd (**Fig. III.7B**).

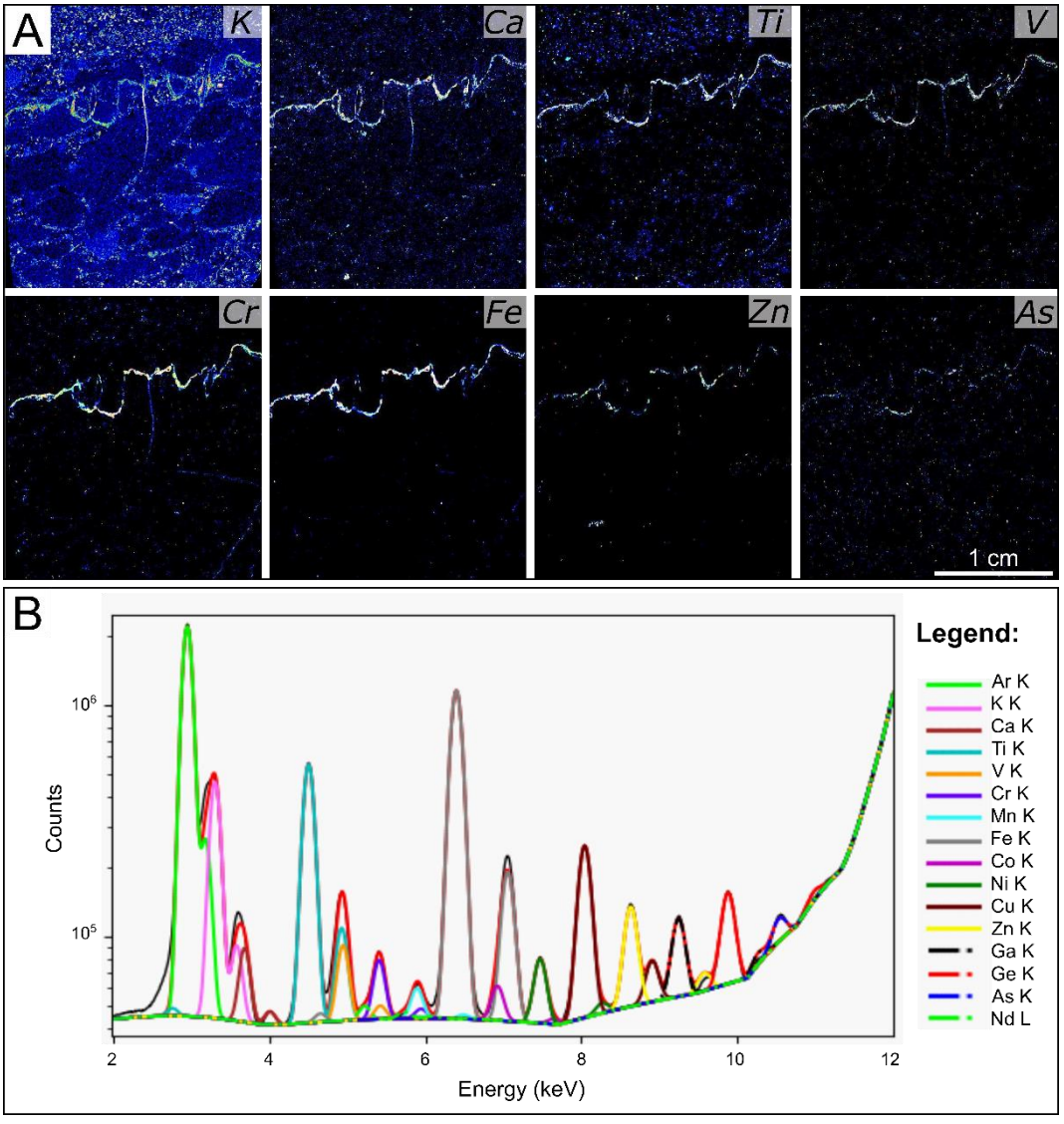

Figure III.7: *X-ray fluorescence (XRF) spectroscopy maps and spectrum of a large-scale area in thin section 00AU39c. (**A**) Elemental maps of several elements showing their spatial distribution in the sample. Scan size: 2.5 cm × 2.5 cm. Concentrations vary between low [dark blue] and high [white]. (**B**) Spectrum corresponding to the area analyzed in (**A**).*

General analysis of sample 00AU40 shows that light layers are enriched in volcanic protoliths replaced by hydromuscovite (K) and titanium oxides (Ti; **Fig. III.8A**). Other transition metals are also associated to these layers (such as Cr, Mn, Fe, Zn and W; **Fig. III.8A**). Average elemental concentrations in a large-scale area of sample 00AU40 follow the trend: Ti, Fe > K > Cu > V > Zn > Ga > Ca > Ni, Ge > Cr, Mn > Co > Nd > W, As (**Fig. III.8B**).

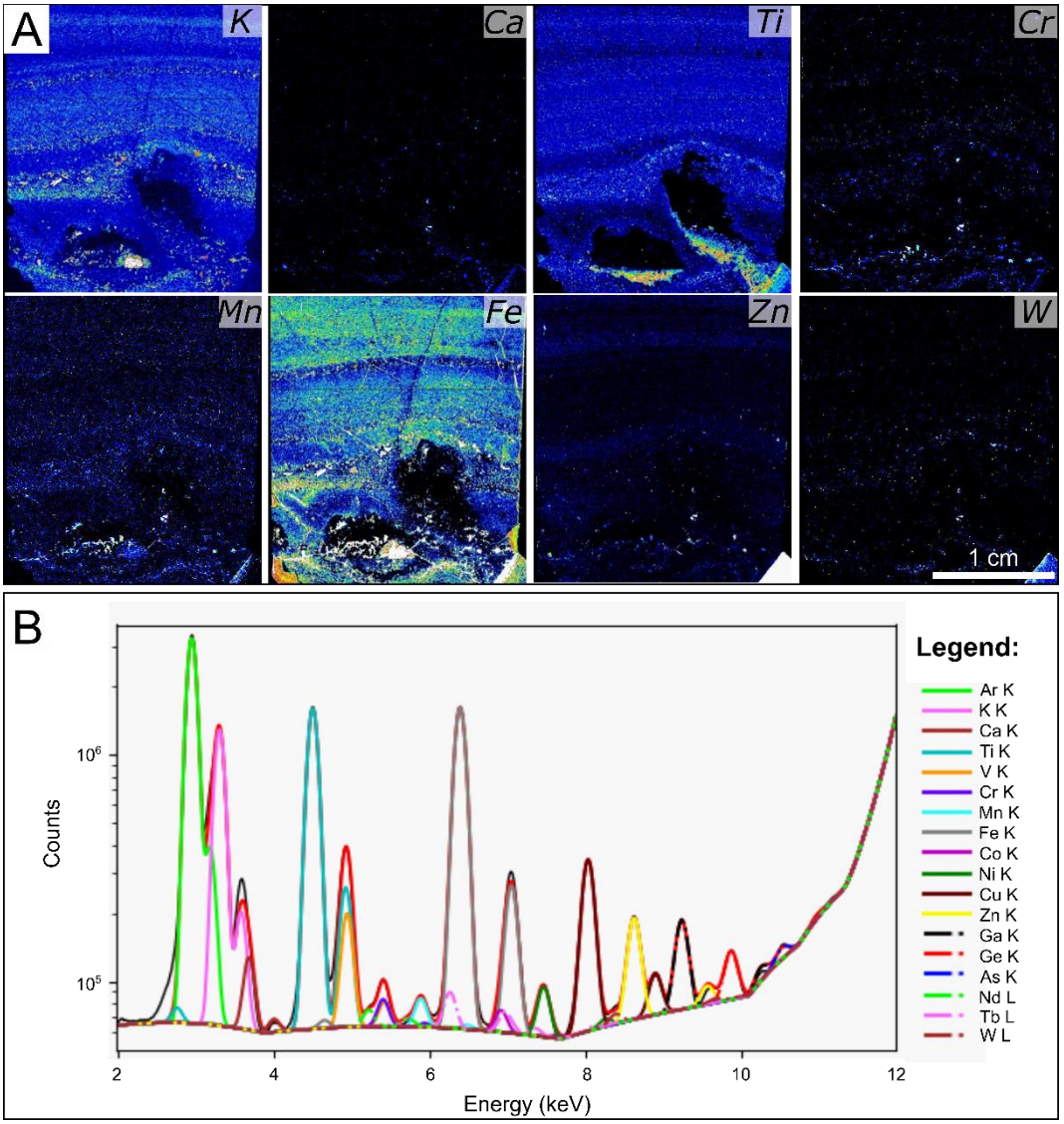

Figure III.8: *X-ray fluorescence (XRF) spectroscopy maps and spectrum of a large-scale area in thin section 00AU40b. (**A**) Elemental maps of several elements showing their spatial distribution in the sample. Scan size: 2.5 cm × 2.5 cm. Concentrations vary between low [dark blue] and high [white]. (**B**) Spectrum corresponding to the area analyzed in (**A**).*

2. Global composition in major and trace elements with ICP-OES and ICP-MS

Bulk ICP-OES and ICP-MS analyses of powdered rock samples were used to estimate the bulk geochemistry of the rocks with the objective of reconstructing characteristics of the regional paleoenvironment (**Fig. III.9; Table III.2; Appendix A, Table A4**).

The sample extracted directly from the hydrothermal vein (00AU37b) is almost pure SiO_2 (>99%), with relatively low contents of Al_2O_3 (0.26%) and Fe_2O_3 (0.05%; **Fig. III.9A**). The other two samples (00AU39 and 00AU40) are also enriched in SiO_2 (90–95%), but have relatively higher contents of Al_2O_3 (3.6–4.8%) and K_2O (0.9–1.3%), reflecting a higher volcanogenic input, a higher degree of metasomatism (diagenetic or metamorphic process during which minerals are replaced by others following the circulation of fluids in the rock), and/or the increase in clay content, and relatively low contents in Fe_2O_3 (<0.5%), TiO_2 (<0.3%) and Na_2O (<0.1%; **Fig. III.9A**).

The extended ICP-MS major and trace element compositions of samples indicate that the silica vein is relatively poor in all elements compared to the other samples, except for Sb and Ba, and some transition metals such as Cr, Fe, Co, Ni and Cu that may have been supplied by hydrothermal fluids or by the degradation of basaltic rocks (**Fig. III.9B**). The sample near the hydrothermal vein (00AU39) shows the following trend (>10 ppm): Ti > Fe > Zr > Ba > Cr > Rb, V > Sr, while the sample further from the source (00AU40) has (>10 ppm): Fe > Ti > Cr > Ba > Mn > V > Zr > Cu > Rb > Mo, Zn > Ni > Sr. Sample 00AU40 is particularly enriched in several transition metals, including V, Cr, Mn, Fe, Co, Ni, Cu, Zn, Mo, and W, and other metals (Sn, Ba) relative to sample 00AU39 (**Fig. III.9B**).

Comparison of major and trace element concentrations in the samples with those of the Earth's crust (**Appendix A, Table A5**) indicates a significant enrichment of Ba (>500%) and Sb (>400%) in the samples compared to the Earth's crust. Other elements may also be enriched, such as Rb in samples 00AU39 (>150%) and 00AU40 (>200%), as well as transition metals, including W (>450%), Cr, (>150%) and Ni (~110%), in sample 00AU40. In general, major elements are depleted to very depleted, in particular Fe (<3.5%), Na (<2%), Mn (<1.5%) and Mg (<1%), in all samples compared to those of the Earth's crust. Other trace elements are also depleted, such as V, Nb, Ta, Sc, Zn, Be, Sr and Cs in samples 00AU37b (0.4–43%), 00AU39 (0.1–48%) and 00AU40 (0.1–57%) compared to those of the Earth's crust.

Plots of Cr/V against Y/Ni from bulk ICP-MS results were used to determine the chemistry of the protoliths from which the samples were derived; these indicate that sample 00AU40 is derived from the erosion of ultramafic protoliths, whereas sample 00AU39 is sourced from mixed mafic and felsic rocks (**Fig. III.9C**).

The bulk sample MuQ-normalized REE + Y characteristics are slightly enriched in HREE (with a low $(Pr/Yb)_{MuQ}$ ratio), indicating moderately strong seawater influence for all samples (**Fig. III.9D; Table III.2**). However, sample 00AU39 has a slightly elevated LREE concentration resulting in a flatter signature indicating a more significant terrigenous input. Y/Ho ratios are sub-chondritic (Y/Ho <27) in all samples, ranging between 25.0 and 25.8. Ce anomalies are slightly negative (0.81–0.92) in samples 00AU37b and 00AU39 and negligible (0.98) in sample 00AU40. Eu anomalies are weakly positive (1.27–1.34) in all samples. La/La^*_{MuQ}, Y/Y^*_{MuQ} and Gd/Gd^*_{MuQ} are negligible (0.98–1.12, 0.99–1.00 and 0.92–0.95, respectively), except for the slightly negative Gd anomaly in sample 00AU37b (0.83).

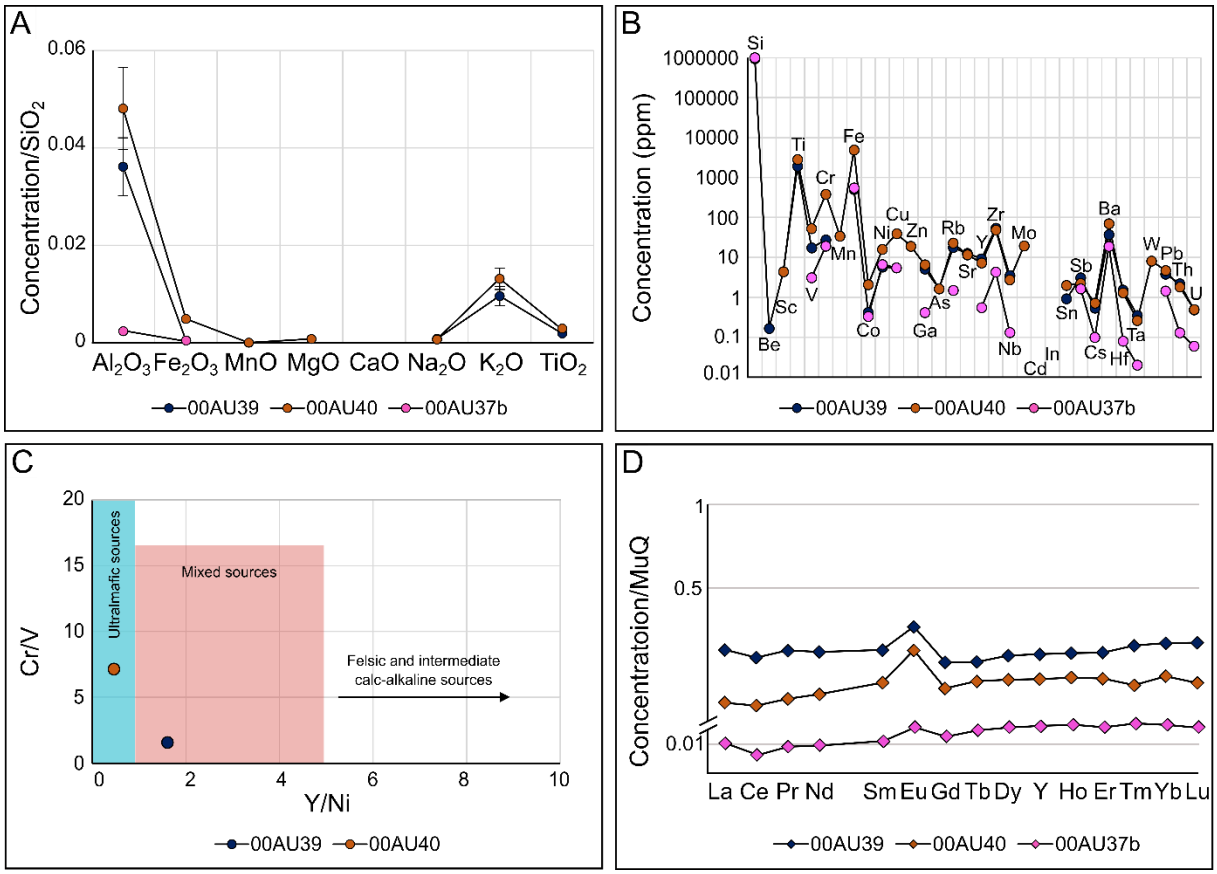

Figure III.9: *ICP-OES and ICP-MS results. (**A**) ICP-OES analyses of major element concentrations normalized to SiO_2 in bulk samples 00AU39 (blue), 00AU40 (orange) and 00AU37b (pink). The error bars indicate uncertainties calculated for oxides whose concentration relative to that of SiO_2 is >0.01 (uncertainties for other oxides are too small to be represented). (**B**) Extended ICP-MS major and trace element concentrations (ppm) in the samples (modified after Hickman-Lewis et al., 2020a). (**C**) Bulk ICP-MS results of Cr/V versus Y/Ni for samples 00AU39 and 00AU40 (modified after Hickman-Lewis et al., 2020a). (**D**) MuQ-normalized bulk ICP-MS measurements of REE + Y in the samples.*

Table III.2: *Elemental anomalies calculated from bulk ICP-MS analyses.*

Bulk	00AU39	00AU40	00AU37b
$(Pr/Yb)_{MuQ}$	0.93	0.80	0.54
Y/Ho	25.84	25.72	25.00
$(Ce/Ce^*)_{MuQ}$	0.92	0.98	0.81
$(Eu/Eu^*)_{MuQ}$	1.28	1.34	1.27
$(La/La^*)_{MuQ}$	0.98	1.05	1.12
$(Y/Y^*)_{MuQ}$	0.99	0.99	1.00
$(Gd/Gd^*)_{MuQ}$	0.95	0.92	0.83

3. Variations in local composition in major and trace elements with LA-ICP-MS

In situ LA-ICP-MS analyses of rock slabs were used to estimate the local geochemistry of the rocks in order to reconstruct the paleoenvironment conditions at local scales (**Fig. III.10; Table III.3; Appendix A, Tables A7–8**).

Analyses performed on samples 00AU39-1, 00AU39-2 and 00AU40-1 (see **Figs. II.13, 14**) indicate major element composition similar to the bulk analyses: SiO_2 > Al_2O_3 > K_2O. However, it appears that most of the areas of interest relatively enriched in SiO_2 (84–99%) are generally depleted in Al_2O_3 (<12%) and K_2O (<4%), whereas areas relatively poor in SiO_2 (52–77%) are enriched in Al_2O_3 (17–37%) and K_2O (4.5–10%); thus, the silica content is inversely proportional to the aluminum and potassium contents.

MuQ-normalized REE + Y characteristics of samples 00AU39-1 (**Fig. III.10A; Table III.3A**) and 00AU39-2 (**Fig. III.10B; Table III.3B**) vary between a high enrichment in LREE compared to HREE with high $(Pr/Yb)_{MuQ}$, indicating a significant terrigenous input, and a typical seawater pattern of HREE > LREE with low $(Pr/Yb)_{MuQ}$. Y/Ho ratios are sub-chondritic (22.3–26.7) to super-chondritic (27.0–30.1), with the exception of a very low ratio (7.30) in the silica vein (h) in 00AU39-2. Most areas of interest have a slight positive anomaly in Ce (1.07–1.14), while some (dark grain, f and silica vein, h in 00AU39-2) have a strong negative Ce anomaly (0.16–0.43). All areas of interest show a positive anomaly in Eu, ranging between 1.17 and 2.19, with a strong positive anomaly (7.38) in the yellow silica vein (f) in 00AU39-1. La/La^*_{MuQ}, Y/Y^*_{MuQ} and Gd/Gd^*_{MuQ} range from negative to positive (0.25–1.31, 0.87–1.11 and 0.70–1.33, respectively), except the silica vein (h) in 00AU39-2 with strongly La, Y and Gd anomalies (0.03, 0.36 and 0.30, respectively).

MuQ-normalized REE + Y measurements of sample 00AU40-1 (**Fig. III.10C; Table III.3C**) show two types of pattern, i.e., a relative enrichment in LREE relative to HREE with high $(Pr/Yb)_{MuQ}$ (continental pattern) and a relative enrichment in HREE relative to LREE with low $(Pr/Yb)_{MuQ}$ (seawater pattern). The Y/Ho ratios are sub-chondritic (18.1–25.4) to super-chondritic (27.9–39.0). Almost all areas of interest have a slight positive anomaly in Ce (1.02–1.43), but only the pumice fragment (g) has a strong negative anomaly (0.28). All areas of interest show a positive anomaly in Eu, ranging between 1.23–1.64, except the chalcedony layer (d) with a negative anomaly (0.85). La/La^*_{MuQ} and Y/Y^*_{MuQ} range from negative to positive (0.70–1.52 and 0.76–1.25, respectively), but Gd/Gd^*_{MuQ} is mostly slightly negative (0.33–1.09), including the chalcedony layer (d) and the pumice fragment (g), which features no Gd anomaly.

Mixing line diagrams show that samples were slightly influenced by hydrothermal fluids (**Fig. III.10D**) and relatively strongly by continental inputs (**Fig. III.10E**). Sm/Yb versus Eu/Sm indicates a very low hydrothermal influence (≤2.5%) for all areas of interest, except the yellow silica vein (f) of sample 00AU39-1 with a higher hydrothermal influence (30%). $(Pr/Nd)_{MuQ}$ versus Y/Ho suggests that the influence of seawater was greater in sample 00AU40-1, especially for areas (b), (j), (h) and (d) (5–52% seawater influence). Only the dark grain (f) in sample 00AU39-2 exhibits a greater influence of seawater (15%).

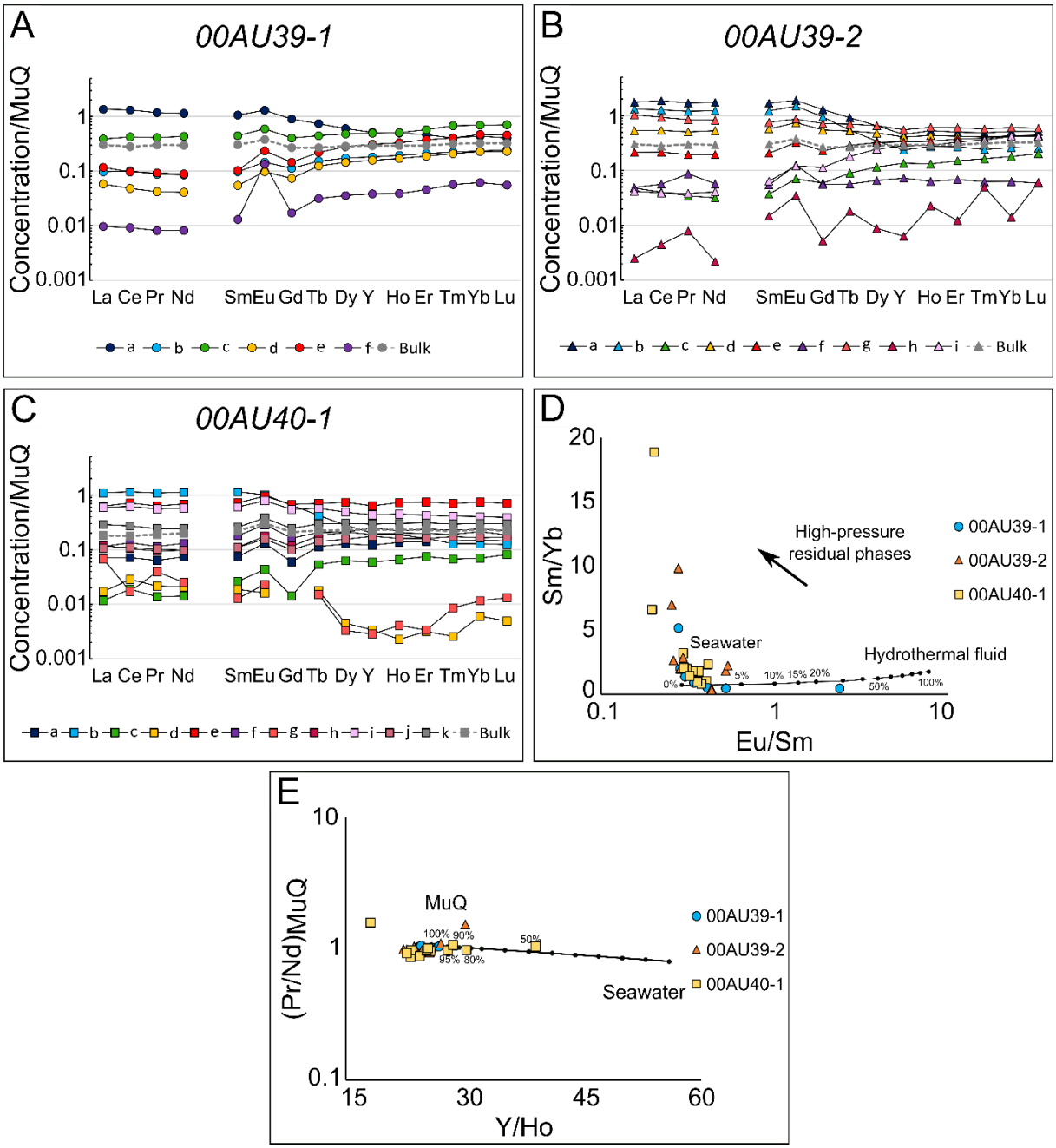

Figure III.10: *In situ LA-ICP-MS results. (**A, B, C**) In situ LA-ICP-MS results (solid lines) compared with bulk ICP-MS (dashed lines), showing MuQ-normalized REE + Y composition in samples 00AU39-1, 00AU39-2 and 00AU40-1. (**D, E**) In situ LA-ICP-MS and bulk ICP-MS data plotted against the hydrothermal fluid–seawater and MuQ–seawater mixing lines. (**D, E**) are plotted after methods described in Gourcerol et al. (2016); modified after Hickman-Lewis et al. (2020a).*

Table III.3: *Elemental anomalies calculated from LA-ICP-MS analyses.*

a) 00AU39-1	a	b	c	d	e	f
$(Pr/Yb)_{MuQ}$	2.69	0.37	0.59	0.18	0.20	0.13
Y/Ho	26.73	24.36	25.59	24.30	24.53	25.63
$(Ce/Ce^*)_{MuQ}$	1.09	1.14	1.09	1.12	1.00	1.14
$(Eu/Eu^*)_{MuQ}$	1.38	1.27	1.33	1.33	1.74	7.38
$(La/La^*)_{MuQ}$	1.09	1.06	1.07	1.31	1.16	1.20
$(Y/Y^*)_{MuQ}$	1.06	0.90	0.92	0.88	0.88	0.90
$(Gd/Gd^*)_{MuQ}$	1.07	0.85	0.90	0.76	0.83	0.70
Hydrothermal influence	0.1%	0.2%	0.15%	0.6%	2%	30%
Continental influence	98%	100%	100%	100%	100%	100%

b) 00AU39-2	a	b	c	d	e	f	g	h	i
$(Pr/Yb)_{MuQ}$	3.33	4.56	0.19	1.19	0.46	1.38	1.39	0.56	0.09
Y/Ho	22.28	22.71	27.01	24.57	25.43	30.11	23.64	7.30	25.60
$(Ce/Ce^*)_{MuQ}$	1.11	1.09	1.08	1.12	1.12	0.43	1.07	0.16	1.10
$(Eu/Eu^*)_{MuQ}$	1.38	1.60	1.37	1.33	1.38	2.19	1.17	2.11	1.31
$(La/La^*)_{MuQ}$	1.07	1.16	1.18	1.15	1.11	0.25	1.16	0.03	1.26
$(Y/Y^*)_{MuQ}$	0.88	0.87	0.96	0.96	0.93	1.11	0.91	0.36	0.91
$(Gd/Gd^*)_{MuQ}$	1.15	1.33	0.85	1.01	0.89	0.97	0.99	0.30	0.87
Hydrothermal influence	0%	0%	0.75%	0.15%	0.3%	2%	0%	2.5%	0.75%
Continental influence	100%	100%	98%	100%	100%	85%	100%	100%	100%

c) 00AU40-1	a	b	c	d	e	f	g	h	i	j	k
$(Pr/Yb)_{MuQ}$	0.42	8.49	0.20	3.57	0.84	0.53	3.40	0.40	1.38	0.62	0.81
Y/Ho	23.17	27.90	23.29	39.01	22.69	24.35	18.13	30.25	25.20	28.55	25.40
$(Ce/Ce^*)_{MuQ}$	1.31	1.10	1.43	1.29	1.24	1.34	0.28	1.14	1.16	1.02	1.12
$(Eu/Eu^*)_{MuQ}$	1.49	1.23	1.26	0.85	1.33	1.50	1.64	1.32	1.33	1.28	1.39
$(La/La^*)_{MuQ}$	1.52	1.09	0.91	0.74	1.18	1.32	0.70	1.32	1.16	0.93	1.19
$(Y/Y^*)_{MuQ}$	0.87	1.15	0.84	1.25	0.86	0.94	0.76	1.11	0.99	1.10	0.96
$(Gd/Gd^*)_{MuQ}$	0.59	1.09	0.33	0.00	0.94	0.81	0.00	0.75	0.94	0.74	0.85
Hydrothermal influence	0.55%	0%	0.4%	0%	0.15%	0.3%	0.7%	0.3%	0.15%	0.15%	0.25%
Continental influence	100%	95%	100%	48%	100%	100%	100%	82%	100%	92.5%	100%

In summary, the geochemistry of the areas of interest in the rock samples are representative of very local geochemical conditions that may differ from those of the bulk sample:

- areas of interest in samples 00AU39-1, 00AU39-2 and 00AU40-1 are either enriched in LREE compared to HREE, reflecting terrigenous inputs, or enriched in HREE compared to LREE, attributed to seawater inputs;

- Y/Ho ratios vary from sub-chondritic (<27) to super-chondritic (>27) in all samples, most of which are closer to the sub-chondritic values of bulk samples;
- Ce anomalies are slightly positive in most areas of all samples, with some areas having very strong negative Ce anomalies;
- Eu anomalies are positive in all samples;
- La and Y anomalies range from negative to positive for most of the areas in all samples, except the silica vein in 00AU39-2 with strongly negative La and Y anomalies;
- Gd anomalies are variable between the samples, ranging from negative to positive in samples 00AU39-1 and 00AU39-2 (except the silica vein in 00AU39-2 with strong Gd negative anomaly), and slightly negative in sample 00AU40-1 (including two structures without Gd anomaly).

III. Investigating the carbonaceous matter

A. Physical characterization and distribution at the microscopic scale

1. Structure and distribution of the carbonaceous matter with Raman spectroscopy

Despite the small amount of organic carbon (<0.05 wt.%) in the volcaniclastic sediments of the Kitty's Gap Chert, carbonaceous matter could be detected using Raman microspectroscopy, especially at the surface of volcanic particles and in the silica-dust gel matrix in samples 00AU39 and 00AU40 (**Figs. III.6 and III.11A–D**). The Raman spectrum of the carbonaceous matter typically shows two bands at ca. 1350 cm^{-1} and ca. 1600 cm^{-1} corresponding to the D1 (disordered) and G+D2 (graphite and disordered) bands, respectively. These characteristics are consistent with mature kerogen (**Fig. III.11E**; Beyssac et al., 2002a, 2002b). Based on Kouketsu et al. (2014), it is possible to estimate the maximal temperature undergone by the carbonaceous matter to about 300–400°C.

Nevertheless, I observed notable variations in the distribution of the carbonaceous matter, depending on the sample, the nature of the volcanic clasts, and the degree of mineralogical and/or morphological alteration. Generally, carbonaceous matter is located on volcanic clasts with rounded edges (morphological alteration) and/or replaced by mineral phases, such as hydromuscovite and anatase (mineralogical alteration). In samples 00AU39 and 00AU40, the most altered volcanic glass, pumice, feldspars, amphiboles/pyroxenes and multiphase volcanic rock fragments are richer in carbonaceous matter, which is frequently associated with hydromuscovite and anatase on the surfaces and edges of volcanic clasts, and sometimes completely replaces the volcanic protoliths (e.g., **Fig. III.6J, L, N**). In sample 00AU40, I also observed a small amount of carbonaceous matter intermixed with hydromuscovite at the surface of volcanic clasts and with anatase at the edges of the less altered volcanic glass, amphiboles/pyroxenes and multiphase volcanic rock fragments (e.g., **Fig. III.6D**). Carbonaceous matter is also a ubiquitous component of the silica-dust gel matrix, where it may co-occur with crystals of anatase, rutile and hydromuscovite (**Fig. III.6Q–T**).

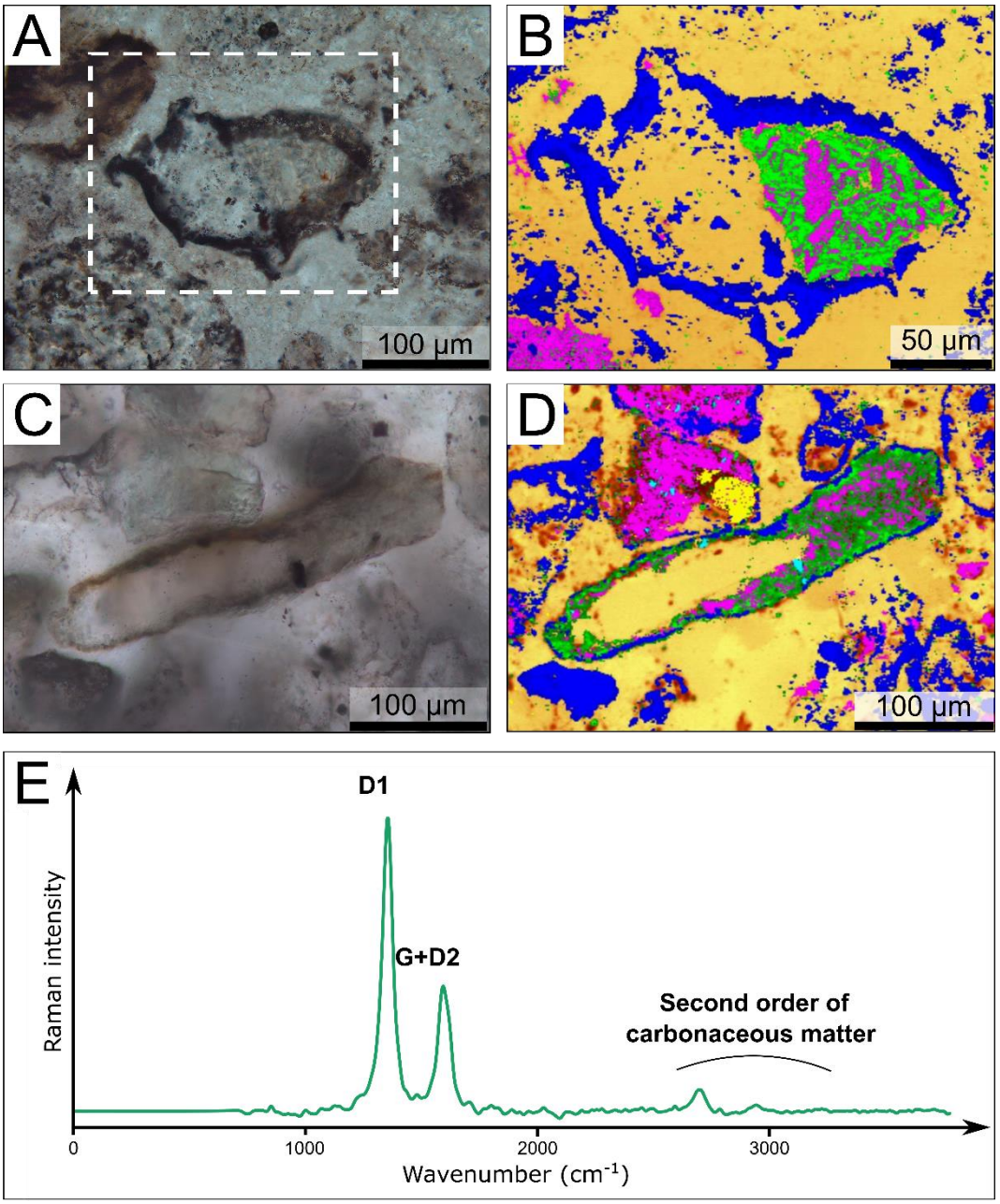

Figure III.11: *Raman maps of two volcanic grains in samples 00AU39 and 00AU40, and average Raman spectrum of the carbonaceous matter. (**A**) Transmitted light optical image of a volcanic grain in sample 00AU39. White dashed box indicates the region for which the Raman map in (**B**) is given. (**B**) Raman compositional map of the same grain with quartz in yellow/orange, anatase in dark blue, hydromuscovite in fuchsia and carbonaceous matter in green. Scan size: 240 µm × 180 µm. (**C**) Transmitted light optical image of a feldspar in sample 00AU40. (**D**) Raman compositional map of the same grain with quartz in yellow/orange, anatase in dark blue, rutile in light blue, hydromuscovite in fuchsia, tourmaline in pale yellow and carbonaceous matter in green. Scan size: 350 µm × 250 µm. (**E**) Representative average Raman spectrum of the carbonaceous matter showing the two main bands at ca. 1350 cm^{-1} (D1 band) and ca. 1600 cm^{-1} (G+D2 band). The second-order Raman signal of carbonaceous matter is also visible between 2500 cm^{-1} and 3500 cm^{-1}.*

2. Structure and distribution of the carbonaceous matter with SEM

The volcaniclastic sediments of the Kitty's Gap Chert were also observed in high-resolution using SEM to identify carbonaceous structures (**Fig. III.12**). In samples 00AU39 and 00AU40, I observed different structures of the carbonaceous matter that appear as:

1) Finely disseminated intermixed with sheet-like or rough-textured hydromuscovite (**Fig. III.12A, B, G**);
2) Filmy with a lumpy texture associated with rough-textured hydromuscovite (**Fig. III.12C**);
3) Rounded to irregular with a smooth texture associated with sheet-like or rough-textured hydromuscovite (**Fig. III.12D**);
4) Coccoidal associated with microcrystals of anatase (**Fig. III.12E, F**);
5) Fibrous with a wrinkled texture (**Fig. III.12G, H**).

The distribution of the carbonaceous matter varies with the protolith and alteration of the volcanic grains, but it is frequently associated with hydromuscovite, which presents a sheet-like (**Fig. III.12A, E**) or an irregular rough-textured (**Fig. III.12B–D, G**) structure, or more rarely associated with microcrystals of anatase at the edges of volcanic grains (**Fig. III.12E, F**).

In sample 00AU39, carbonaceous matter was not observed in the well-preserved, weakly altered (to hydromuscovite) volcanic glass. The volcanic glass protoliths are surrounded by edges composed of a heavy element appearing light-colored (anatase) and they exhibit smooth surfaces. The pumice protoliths have many light-colored inclusions of anatase at their surface, as well as some cavities containing sheet-like or rough-textured hydromuscovite mixed with disseminated carbonaceous matter (**Fig. III.12A, B**). The amphibole/pyroxene protoliths are surrounded by edges composed of anatase. They are very altered in fine sheet-like hydromuscovite mixed with smooth-textured carbonaceous matter, and show some coccoidal structures associated to microcrystal of anatase at their edges (**Fig. III.12E, F**). The multiphase volcanic rock fragment protoliths are surrounded and covered with anatase, sometimes with light-colored rod crystals (rutile), and are very altered in fine sheet-like hydromuscovite mixed with disseminated carbonaceous matter. These grains also contain many cavities composed of rough-textured hydromuscovite mixed with disseminated or filmy carbonaceous structures (**Fig. III.12C**). Elongated smooth-textured carbonaceous structures can also be visible around the edges of these grains. The silica matrix is generally very smooth compared to the volcanic grains and exhibit some light-colored inclusions of anatase. Some cavities are visible in the silica matrix but are probably due to small altered volcanic grains. They contain rough-textured hydromuscovite mixed with rounded to irregular smooth-textured carbonaceous structures (**Fig. III.12D**).

In sample 00AU40, carbonaceous matter was not observed in the well-preserved, weakly altered volcanic glass, but it was identified in volcanic glass altered in hydromuscovite where it appears as finely disseminated particles intermixed with rough-textured hydromuscovite. The volcanic glass protoliths are surrounded by edges composed of light-colored anatase. The feldspar protoliths are altered in fine sheet-like hydromuscovite mixed with disseminated carbonaceous matter (**Fig. III.12G**), and a medium-toned grain with a wrinkled texture was identified in a cavity composed of rough-textured hydromuscovite and smooth silica particles (**Fig. III.12H**). The multiphase volcanic rock fragment protoliths can be covered with anatase and are very altered, to completely altered, in fine sheet-like hydromuscovite mixed with disseminated carbonaceous matter. These grains also contain many cavities composed of rough-textured hydromuscovite mixed with disseminated carbonaceous matter. Very light areas and very dark areas have also been identified in these grains and correspond,

respectively, to a metallic element (iron) and a very light element whose composition has not been determined. The silica-dust gel matrix contains clusters of light-colored inclusions of anatase and some cavities composed of rough-textured hydromuscovite mixed with disseminated or irregular smooth structures of carbonaceous matter. As for sample 00AU39, the silica matrix is generally very smooth with some inclusions of anatase and small volcanic grains altered in hydromuscovite and enriched in carbonaceous matter.

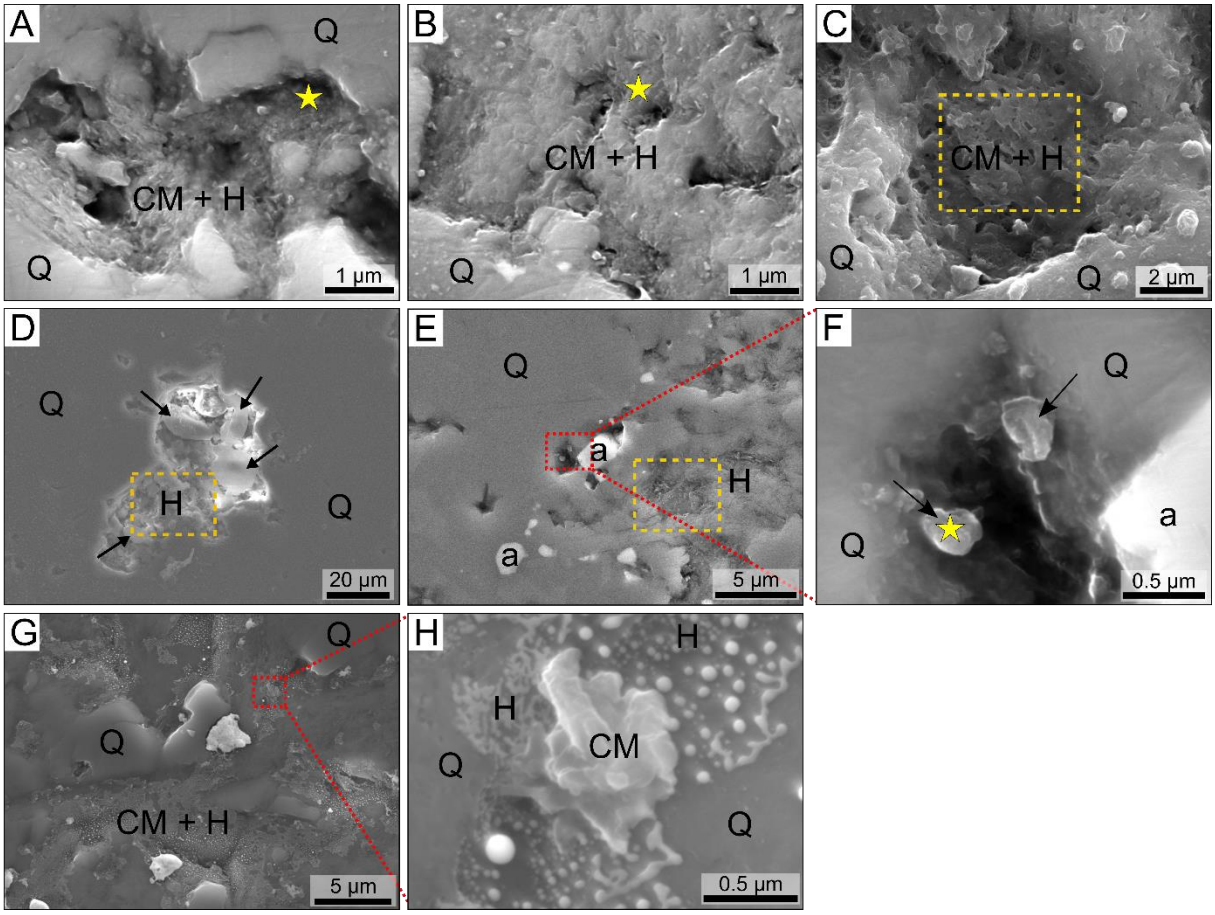

Figure III.12: *High-resolution scanning electron microscopy (SEM) images of coated thin sections from samples 00AU39 and 00AU40. (**A, B**) Finely disseminated particles of carbonaceous matter (CM) intermixed with sheet-like and rough-textured hydromuscovite (H), respectively, in a pumice fragment of sample 00AU39. The yellow stars correspond to the locations where EDX measurements were performed. The sheet-like hydromuscovite is composed of Si, O, Al, K, C ± Na, Mg, and the rough-textured hydromuscovite of Si, Al, O, K, C ± Na, Mg. (**C**) Filmy carbonaceous matter with a lumpy texture (CM) associated with rough-textured hydromuscovite (H) in a multiphase volcanic rock fragment of sample 00AU39. The yellow dashed box corresponds to the location where EDX measurement was performed. The rough-textured hydromuscovite is composed of Si, Al, O, K, C ± Na, Mg, S, Fe. The white spherules visible in the lower right of the image are artifacts after samples immersion in glycerin for DUV fluorescence analyses. (**D**) Rounded to irregular carbonaceous structures with a smooth texture (black arrows showing the most visible) associated with rough-textured hydromuscovite (H) in the silica matrix of sample 00AU39. The rough-textured hydromuscovite is composed of Si, O, C, Al ± K, Ca, Na, Fe, Mg, S. (**E**) Surface and edges of amphibole/pyroxene from sample 00AU39 altered into sheet-like hydromuscovite (H) and anatase (a), respectively, with red dotted box indicating the area corresponding to the image displayed in (**F**). The sheet-like hydromuscovite is composed of Si, O, Al, K,*

*C ± Na, Mg, Ti, Fe. (**F**) Coccoidal structures of carbonaceous matter (black arrows) associated with microcrystals of anatase (a). The coccoidal structure is composed of Si, C, O, Al ± K, Ti (yellow star). (**G**) Finely disseminated particles of carbonaceous matter (CM) intermixed with rough-textured hydromuscovite (H) in a feldspar of sample 00AU40, with red dotted box indicating the area corresponding to the image displayed in (**H**). The area was analyzed by EDX and shows a global composition in Si, O, Al, K, C ± Na, Mg, Ti, Fe, Au. (**H**) Fibrous carbonaceous matter with a wrinkled texture (CM). The area was analyzed by EDX and shows a global composition in Si, Al, O, K, C ± Na, Mg, Ti, Fe, Au. The white particles visible on the images (**G**) and (**H**) are gold particles resulting from the coating process of the thin section. In all images, the volcanic grains are embedded in a microcrystalline quartz (Q). Color-coded composition images and the spectra corresponding to the mentioned EDX analyses are displayed in **Figures B1–6** of **Appendix B**.*

B. Physical characterization and distribution at the nanoscopic scale

The nanostructure and crystallography of the carbonaceous matter were studied using STEM and HR-TEM analysis of 100 nm-thick FIB sections (**Figs. III.13; 14**). In samples 00AU39 and 00AU40, I observed different types of structure of carbonaceous matter, including:

1) Coatings around volcanic clasts (**Fig. III.13A, C**);
2) Spherical to elliptical particles (**Fig. III.13A, B, D**);
3) Elongated structures (**Fig. III.13E, F**);
4) Lenticular structures (**Fig. III.13G**);
5) Diffuse clouds (**Fig. III.13H**).

Two degrees of crystallinity of carbonaceous matter can also be distinguished in the samples: amorphous (e.g., **Fig. III.13F**) and crystallized (graphitized) carbonaceous matter, the latter presenting an onion-shaped structure (**Fig. III.14**).

The distribution of the carbonaceous matter varies with the protolith and alteration of the volcanic grains, but it is frequently associated with hydromuscovite (presenting a sheet-like structure with interplanar distances of ca. 10 Å and ca. 20 Å, corresponding to the *b* and *c* axes of hydromuscovite, respectively; e.g., **Fig. III.13D**) in microcrystals of feldspars of a few micrometers in length or located at the edge of microcrystalline quartz polygons of 2–3 µm in diameter (e.g., **Fig. III.13G**), more rarely associated with microcrystals of anatase of <1 µm in diameter at the edges of volcanic grains.

In sample 00AU39, carbonaceous matter was not observed in the well-preserved, weakly altered (to hydromuscovite) volcanic glass. Nevertheless, it was observed associated with other structures in the sample, for example, in a pumice fragment, as coatings around microcrystals of feldspars or as a diffuse cloud mixed with hydromuscovite and nanocrystals of a heavy element (possibly a transition metal element, such as zirconium; **Fig. III.13H**). It was also observed in amphibole/pyroxene, where it forms elongated structures (**Fig. III.13E**), and in a more diffuse manner where it completely replaces the grain (the carbon distribution is homogenous on the EDX map), but mostly at the edges of grains, where it appears as coatings around anatase or as inclusions in microcrystals of feldspars. The carbonaceous matter is ubiquitous in the silica-dust gel matrix, sometimes located at the edge of quartz polygons (**Fig. III.14A, B**), and also occurs in the silica matrix surrounding volcanic protoliths as isolated particles, often coated with a thick silica crust (**Fig. III.13A, B**) or as coatings around microcrystals of feldspars (**Fig. III.13A**).

In sample 00AU40, carbonaceous matter rarely occurs in association with volcanic glass, at the edges of quartz polygons (**Fig. III.13D**), or intermixed with anatase at the edges of volcanic glass. Instead, the carbonaceous matter is more frequently observed with other structures in the sample, for example, in feldspar, as coatings around microcrystals of feldspars or as inclusions in microcrystals of feldspars, sometimes at the edge of quartz polygons, and in the silica-dust gel matrix, where it is mostly located at the edge of quartz polygons, as inclusions in microcrystals of feldspars (**Fig. III.13F**), or as coatings around microcrystals of feldspars, and even as isolated particles (**Fig. III.14C, D**). The silica matrix surrounding volcanic protoliths also displays some carbonaceous matter at the edge of quartz polygons, including one lenticular structure mixed hydromuscovite and iron minerals (**Fig. III.13G**), or as coatings around microcrystals of feldspars (**Fig. III.13C**).

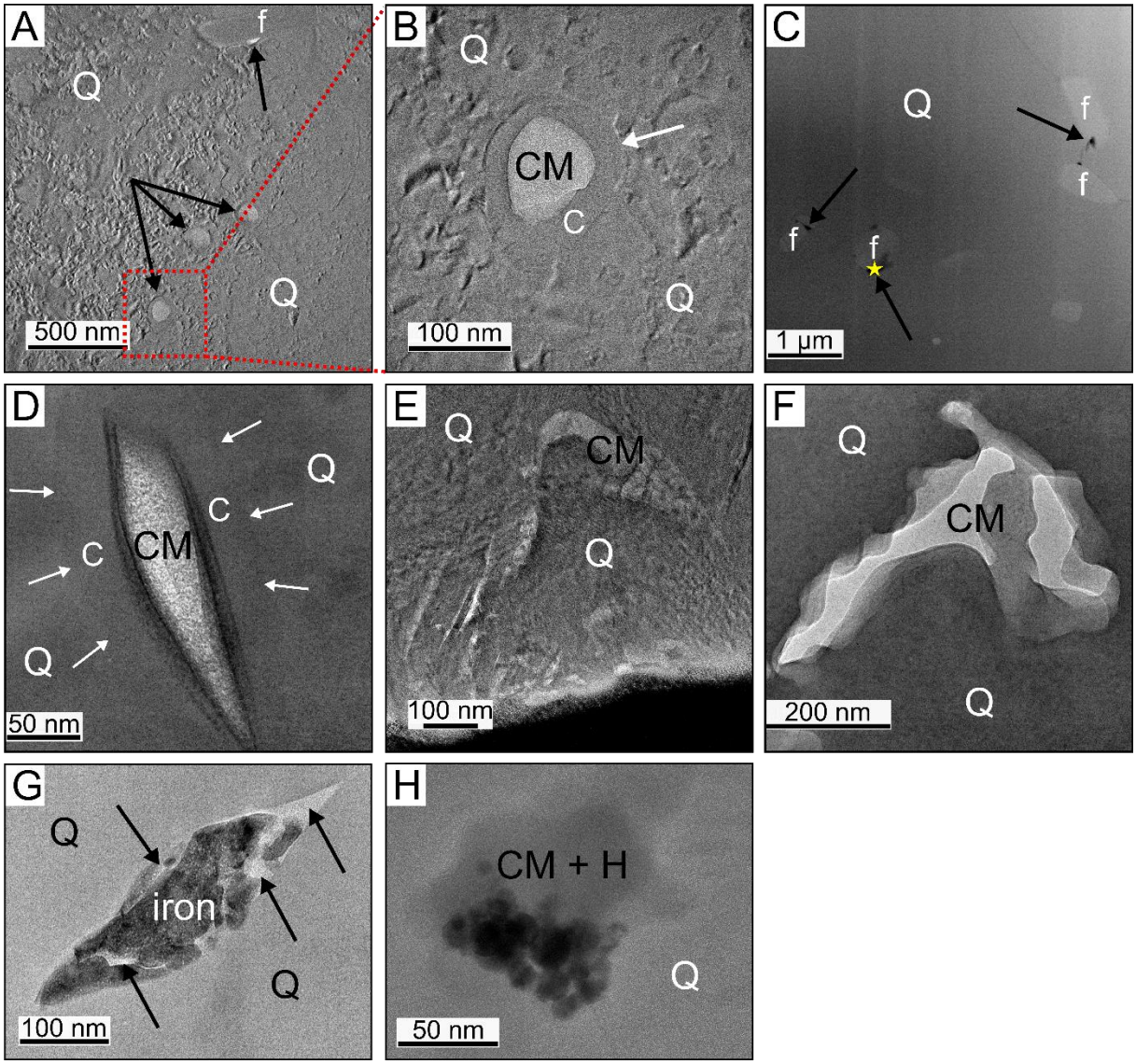

Figure III.13: *High-resolution transmission electron microscopy (HR-TEM) and annular dark field (ADF) scanning transmission electron microscopy (STEM) images of FIB sections from samples 00AU39 and 00AU40. (**A**) HR-TEM image of isolated spherical particles of carbonaceous matter (the three bottom black arrows) and coating of carbonaceous matter (top black arrow) around a microcrystal of feldspar (f) in the silica matrix of sample 00AU39, with red dotted box indicating the area corresponding to the image displayed in (**B**). (**B**) HR-TEM image of an isolated spherical particle of carbonaceous matter (CM) surrounded by a thick silica crust (c), with white arrow showing the crust. (**C**) STEM image of coatings*

*of carbonaceous matter (black arrows) around microcrystals of feldspar (f) in the silica matrix of sample 00AU40. The yellow star corresponds to the location where the EDX measurement was performed and indicates a composition in Si, C, Al, K ± Mg. (**D**) HR-TEM image of an elliptical particle of carbonaceous matter (CM) mixed with hydromuscovite (interplanar distance of ca. 20 Å corresponding to c axis of hydromuscovite) and surrounded by a thick silica crust (c) at the edge of quartz polygons in a volcanic glass particle of sample 00AU40, with white arrows showing the crust. (**E**, **F**) HR-TEM images of elongated structures of carbonaceous matter (CM) in amphibole/pyroxene of sample 00AU39 and in a microcrystal of feldspar in the silica-dust gel matrix of sample 00AU40, respectively. EDX measurements of the area displayed in (**E**) and the structure displayed in (**F**) indicates, respectively, a global composition in Si, Al, K, C and a composition in Si, Al, K, C ± Mg. (**G**) HR-TEM image of a lenticular structure of carbonaceous matter (black arrows) enriched in iron minerals and mixed with hydromuscovite (interplanar distances of ca. 10 Å and ca. 20 Å corresponding to b and c axis of hydromuscovite, respectively) at the edge of quartz polygons in the silica matrix of sample 00AU40. EDX measurement of the area indicates a global composition in Si, Fe, C ± Al. (**H**) HR-TEM image of a diffuse cloud of carbonaceous matter (CM) mixed with hydromuscovite (H) and associated with dark spherical grains of a heavy element in a pumice fragment of sample 00AU39. EDX measurement of the area indicates a global composition in Si, Zr, C, Al. In all images, the volcanic grains are embedded in a microcrystalline quartz (Q). Color-coded composition images and the spectra corresponding to the mentioned EDX analyses are displayed in **Figures B7–11** of **Appendix B**.*

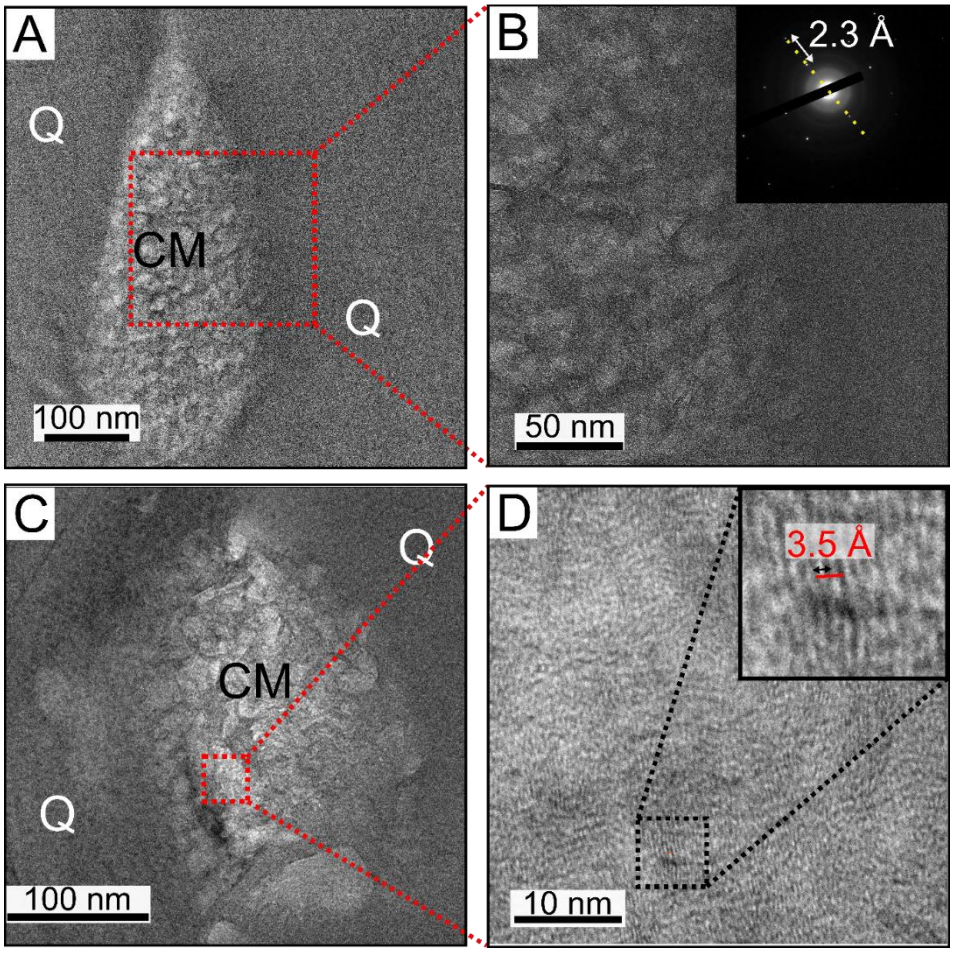

***Figure III.14:** High-resolution transmission electron microscopy (HR-TEM) images of two types of nanostructure in FIB sections from samples 00AU39 and 00AU40. (**A**) Elliptical particle of graphitized*

*carbonaceous matter (CM) with an onion-shape structure at the edge of quartz polygons in the silica dust-gel matrix of sample 00AU39, with red dotted box indicating the area corresponding to the image displayed in (**B**). (**B**) Close-up view of the onion structure characteristic of graphitized carbonaceous matter, whose interplanar distance represented on the diffraction pattern is of ca. 2.3 Å. (**C**) Isolated elliptical particle of graphitized carbonaceous matter (CM) with an onion-shape structure in the silica-dust gel matrix of sample 00AU40, with red dotted box indicating the area corresponding to the image displayed in (**D**). (**D**) Close-up view of the onion structure characteristic of graphitized carbonaceous matter, whose interplanar distance measured on the enlarged area (black dotted box) is of ca. 3.5 Å.*

The main observations on the physical characteristics and distribution of carbonaceous matter using Raman spectroscopy, SEM and (S)TEM are summarized in **Table III.4**.

Table III.4: *Summary of the physical characterization and distribution of the carbonaceous matter at microscopic and nanoscopic scales in samples 00AU39 and 00AU40.*

	00AU39	Volcanic glass		Pumice	Feldspars	Amphiboles/pyroxenes		Multiphase volcanic rock fragments		Silica-dust gel matrix	Silica matrix
		Less altered	More altered			Less altered	More altered	Less altered	More altered		
Raman spectroscopy	Raman map	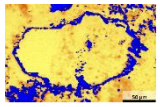	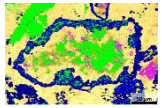	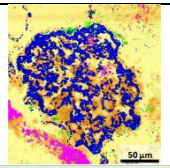	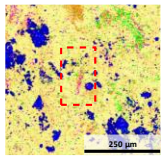	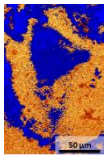	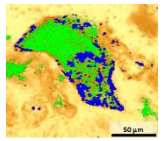	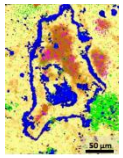	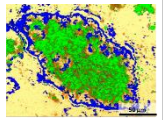	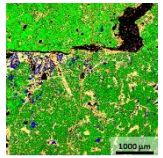	/
	Microscale distribution	Not detected	A lot of mixed with hydromuscovite ± with anatase at the edges	In inclusion and around the pumices, coating anatase	Around the feldspar?	Not detected	Almost completely replacing the grains	Mixed with hydromuscovite ± with anatase on the surfaces and edges	Completely replacing the grains	Composed mostly dusts, mixed with anatase	Mostly microcrystalline quartz
SEM	**Microscale structure**	Not detected	/	Finely disseminated	/	/	Irregular with smooth texture, coccoidal	Finely disseminated	Finely disseminated, filmy with lumpy texture, elongated with smooth texture	/	Rounded to irregular with smooth texture
	Microscale distribution	Not detected	/	Mixed with sheet-like or rough-textured hydromuscovite in the interior of the protolith	/	/	Mixed with sheet-like hydromuscovite in the interior of the protolith, or associated to anatase at the edges	Mixed with sheet-like hydromuscovite in the interior of the protolith	Mixed with sheet-like or rough-textured hydromuscovite in the interior of the protolith, or around the edges	/	Mixed with rough-textured hydromuscovite
(S)TEM	**Nanoscale structure**	Not detected	/	Coatings <25 nm width, diffuse cloud ≈150 µm² surface area	/	/	Elongated structures <0.3 µm length, diffuse, coatings <0.1 µm width, spherical particles <0.1 µm	/	/	Spherical <0.5 µm to elliptical <0.5 µm² particles, often with an onion-shape structure	Spherical particles <0.2 µm surrounded by a thick crust, including two glued spherules ≈70 nm, coatings <15 nm
	Crystallography	Not detected	/	Mainly amorphous	/	/	Mainly amorphous	/	/	Mainly graphitized (ca. 2.3 Å)	Mainly amorphous
	Nanoscale distribution	Not detected	/	Mostly in the interior of the protolith, as coatings around feldspars or as a diffuse cloud mixed with hydromuscovite and a heavy element	/	/	Mostly at the edges of the protolith, as coatings around anatase or as inclusions in feldspars, more diffuse in the protolith or forming elongated structures	/	/	Ubiquitous in the silica-dust gel matrix, sometimes located at the edges of quartz polygons	Around volcanic protoliths, as isolated particles or as coatings around feldspars

	00AU40	Volcanic glass		Pumice	Feldspars		Amphiboles/pyroxenes		Multiphase volcanic rock fragments		Silica-dust gel matrix	Silica matrix
		Less altered	More altered		Less altered	More altered	Less altered	More altered	Less altered	More altered		
Raman spectroscopy	Raman map	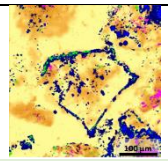	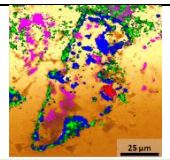	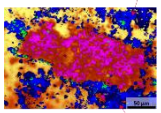	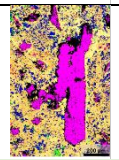	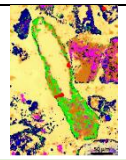	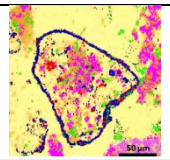	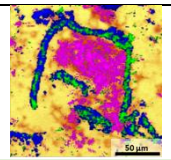	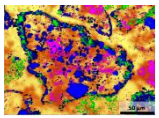	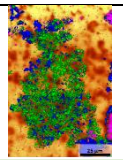	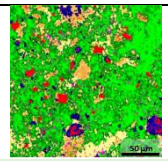	/
	Microscale distribution	Some mixed with anatase at the edges	A lot of mixed with anatase at the edges	Mixed with deposits of anatase	Not detected	Almost completely replacing the grains	Some mixed with hydromuscovite and/or with anatase at the edges	A lot mixed with anatase on the surfaces and edges	Mixed with anatase and rutile ± with hydromuscovite on the surfaces and edges	Completely replacing the grains	Composed mostly dusts, mixed with anatase, rutile and muscovite	Mostly microcrystalline quartz
SEM	**Microscale structure**	Not detected	Finely disseminated	/	/	Finely disseminated, fibrous with wrinkled texture	/	/	Finely disseminated	Finely disseminated	Finely disseminated, irregular with smooth texture	Not observed
	Microscale distribution	Not detected	Mixed with rough-textured hydromuscovite in the interior of the protolith	/	/	Mixed with sheet-like or rough-textured hydromuscovite in the interior of the protolith	/	/	Mixed with sheet-like hydromuscovite in the interior of the protolith	Mixed with sheet-like or rough-textured hydromuscovite in the interior of the protolith	Mixed with rough-textured hydromuscovite	Mixed with hydromuscovite
(S)TEM	**Nanoscale structure**	/	Elliptical particles <150 x 50 nm², sometimes coated with a thick crust, coatings <0.1 µm	/	/	Not observed	/	/	/	/	Spherical <0.3 µm to elliptical <0.5 x 0.2 µm² particles, sometimes with an onion-shaped structure, elongated structures <1 µm, coatings <0.1 µm	Rare elliptical particles ≤0.4 x 0.1 µm², including one lenticular structure, coatings <10 nm width
	Crystallography	/	Mainly amorphous	/	/	Not observed	/	/	/	/	Amorphous and graphitized (ca. 3.5 Å)	Mainly amorphous
	Nanoscale distribution	/	A few located at the edges of quartz polygons in the protolith, or associated with anatase and/or hydromuscovite at the edges	/	/	Mostly located in the feldspars as coatings or in inclusions, sometimes at the edges of quartz polygons in the protolith	/	/	/	/	Mostly located at the edges of quartz polygons, or in inclusions in feldspars or as coatings around feldspars	Around volcanic protoliths with a few located at the edges of quartz polygons, including one lenticular structure mixed with hydromuscovite and iron minerals, or as coatings around feldspars

C. Elemental composition of the carbonaceous matter

1. Elemental composition of the carbonaceous matter with XRF spectroscopy

XRF spectroscopy analyses of samples 00AU39 and 00AU40 allowed identification and mapping of the distribution of major and trace elements in several ROIs that contain the grains of interest associated with the carbonaceous matter previously documented by optical microscopy and Raman spectroscopy (**Figs. III.15–18**).

Local analysis of samples (**Figs. III.15, 16**) generally show an enrichment in the elements characteristic of phyllosilicates (K) and titanium oxides (Ti). Many transition metals are also detected, in particular Ti, V, Cr, Mn, Fe, Co, Ni, Cu and Zn. W is rare in sample 00AU39, whereas it is well detected in sample 00AU40. Some REEs, such as Nd and more rarely Ce, are detected. There is a positive correlation in the distribution of potassium and iron, and also titanium and vanadium. Interestingly, we can note that some locations enriched in iron are also enriched in transition metals, such as Cr, Co, Ni, Cu, Zn or As. In sample 00AU40, neodymium is well detected, sometimes co-occurring with iron and other metals (**Fig. III.16D**). Similarly, tungsten is sometimes correlated with titanium and vanadium.

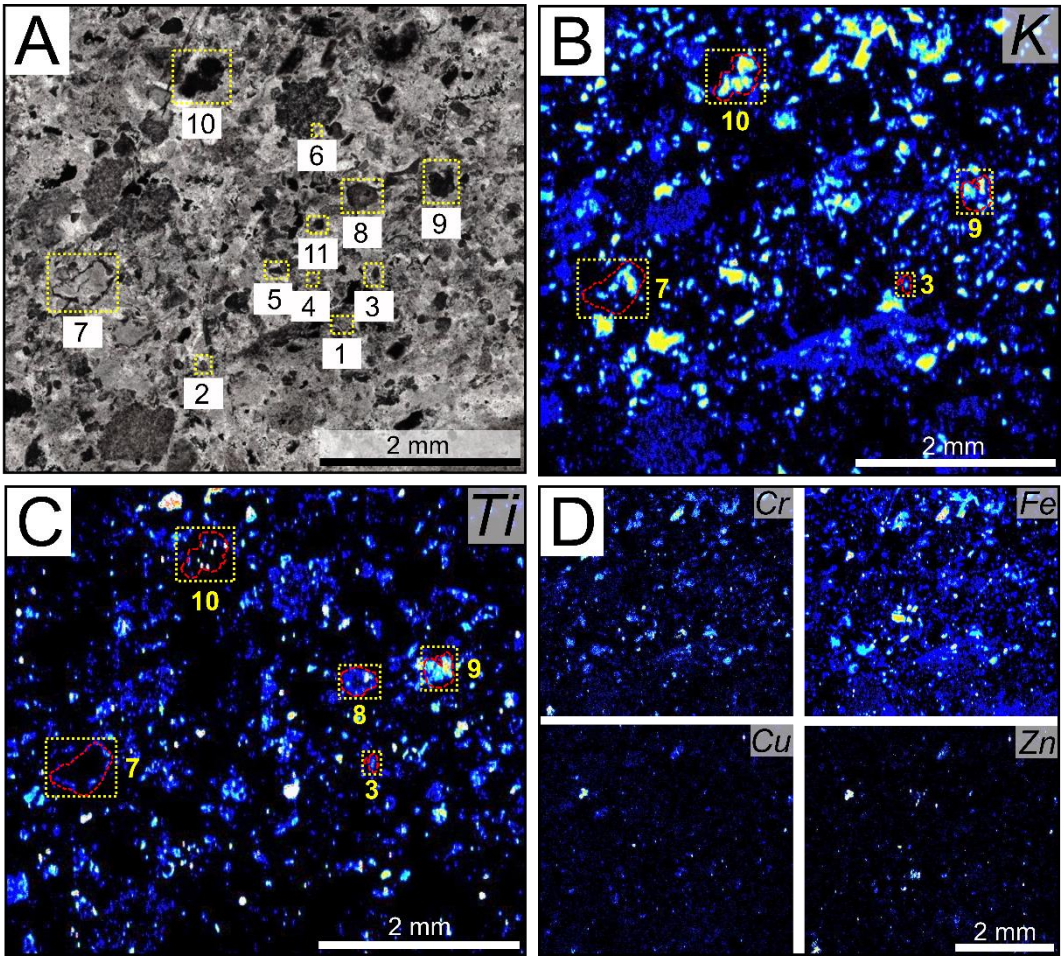

Figure III.15: *Optical image and XRF maps of specific regions of interest in sample 00AU39. (**A**) Optical image of ROI 2 containing 11 volcanic grains of interest, numbered and surrounded by yellow dotted boxes, that have been previously analyzed with optical microscopy and Raman spectroscopy. (**B, C**) Elemental maps of potassium and titanium, respectively, where the volcanic grains enriched in*

*potassium and/or titanium are surrounded by yellow dotted boxes and underlined in red. (**D**) Elemental maps of chromium, iron, copper, and zinc. Scan size: 5.5 mm × 5 mm. Concentrations vary between low [dark blue] and high [white]. The average elemental concentration of this area follows the trend: K, Ti > Fe > Cu > Ga, Ge > V > Ca, Cr, Zn > Nd, Mn, Co, Ni > As.*

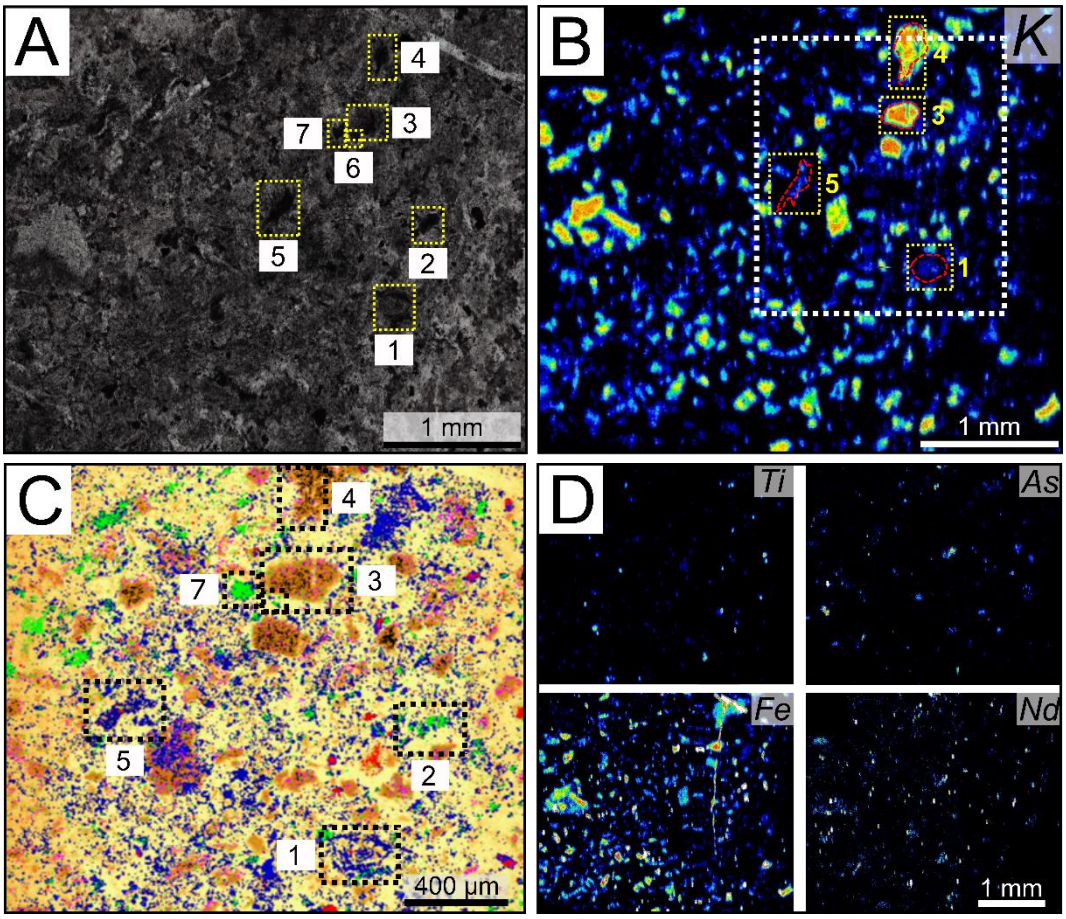

Figure III.16: *Optical image, Raman map and XRF maps of specific regions of interest in sample 00AU40. (**A**) Optical image of ROI 8 containing 7 volcanic grains of interest, numbered and surrounded by yellow dotted boxes, that have been previously analyzed with optical microscopy and Raman spectroscopy. (**B**) Elemental map of potassium where the volcanic grains enriched in this element are surrounded by yellow dotted boxes and underlined in red, with white dotted box indicating the area corresponding to the Raman map shown in (**C**). (**C**) Raman compositional map with quartz in yellow/orange, anatase in blue, rutile in red, hydromuscovite in fuchsia and carbonaceous matter in green, with black dotted boxes surrounding the volcanic grains. Scan size of the Raman map: 2 mm × 2 mm. (**D**) Elemental maps of titanium, arsenic, iron and neodymium. Scan size of the area analyzed with XRF: 4 mm × 3.5 mm. Concentrations vary between low [dark blue] and high [white]. The average elemental concentration of this area follows the trend: Ti > K > Fe > Cu > V > Ga > Ca > Zn > Ge > Co, Ni > Mn, W > Cr, Nd, As.*

Spot measurements (**Fig. III.17, 18**) were made in order to obtain spectra of the chemical composition of specific structures of interest, i.e., the silica matrix, volcanic glass fragments, pumice fragments, feldspars, multiphase volcanic rock fragments, edges of the grains, silica veins and the silica-dust gel matrix. The silica matrix and volcanic glass fragments (not coated with carbonaceous matter) are generally depleted in all elements compared to other structures, except for Cu (**Figs. III.17C–E and III.18C**). Feldspars and multiphase volcanic rock fragments coated with carbonaceous matter are highly

enriched in all the elements with respect to the silica matrix, especially in K, Ca, Cr, Mn, Fe, Zn, Ga, Ge ± W (+ Ti, Ni, Cu, As ± Ce and Nd for multiphase volcanic rock fragments; **Figs. III.17D and III.18C, E**). Carbon-coated pumice fragments are enriched in Ti, K, Fe, Ca, Ga and Cr with respect to the silica matrix in sample 00AU39 (**Fig. III.17E**), whereas pumice fragments without a carbon coating are depleted in almost all elements, except for Cu and Ge, in sample 00AU40, and their dark edges are highly enriched in Ti and W relative to their interior and the silica matrix (**Fig. III.18D**). The carbon-coated edges of the volcanic glass fragments are enriched in many elements (i.e., Ti, Mn, Fe, Ni, Cu, Zn, Ge and As) compared to their interior and the silica matrix (**Fig. III.17C**), whereas those of multiphase volcanic rock fragments have only noticeable concentrations of Ti, although the concentrations of the other elements remain relatively high (**Figs. III.17D and III.18C**). The silica veins analyzed in sample 00AU40 are notably enriched in Fe, K, Ti, Cu, V and Zn (**Fig. III.18F**). In sample 00AU39, the silica-dust gel matrix has a clay-like composition (K) and is enriched in several transition metals, such as Fe, Cu, Ti, Zn, V, Cr and Ni (**Fig. III.17F**). In sample 00AU40, the light silica-dust gel laminations have a more clay-like composition (Fe, K, Ca, Cr…) compared to the dark silica-dust gel laminations which are richer in titanium oxides (Ti; **Fig. III.8**).

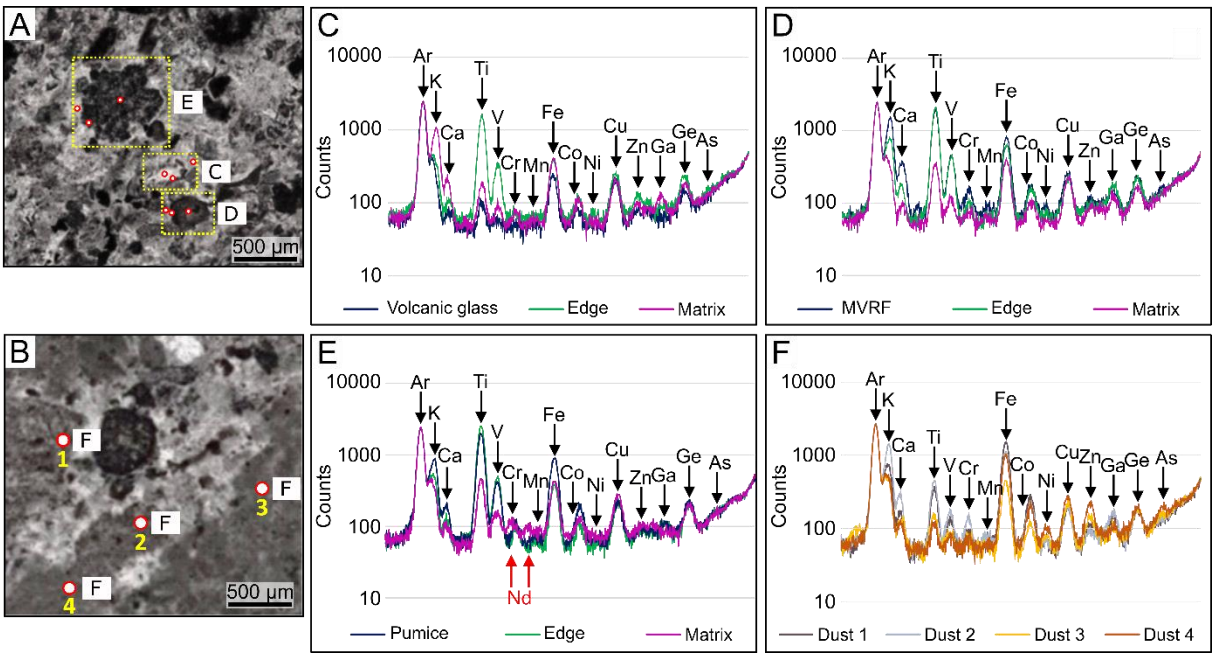

Figure III.17: *Optical images and XRF spectra of specific grains in sample 00AU39. (**A**) Optical image of 3 grains of interest located in ROI 2 (see **Fig. III.15**), surrounded by yellow dotted boxes and red dots indicating the location of spot measurements, and whose spectra are shown in (**C**), (**D**) and (**E**). (**B**) Optical image of silica-dust gel deposits located in ROI 8 and whose spectra are shown in (**F**). (**C**) Spectrum of a volcanic glass fragment compared to its edges and the adjacent silica matrix. (**D**) Spectrum of a multiphase volcanic rock fragment (MVRF) compared to its edges and the adjacent silica matrix. (**E**) Spectrum of a pumice fragment compared to its edges and the adjacent silica matrix. Note the enrichment in neodymium in the silica matrix. (**F**) Spectra of silica-dust gel deposits. The spectra corresponding to the volcanic grains are colored in dark blue, the spectra of the edges are in green, the spectra of the silica matrix are in purple, and the spectra of the silica-dust gel deposits are in dark gray (dust 1), light gray (dust 2), yellow (dust 3) and orange (dust 4).*

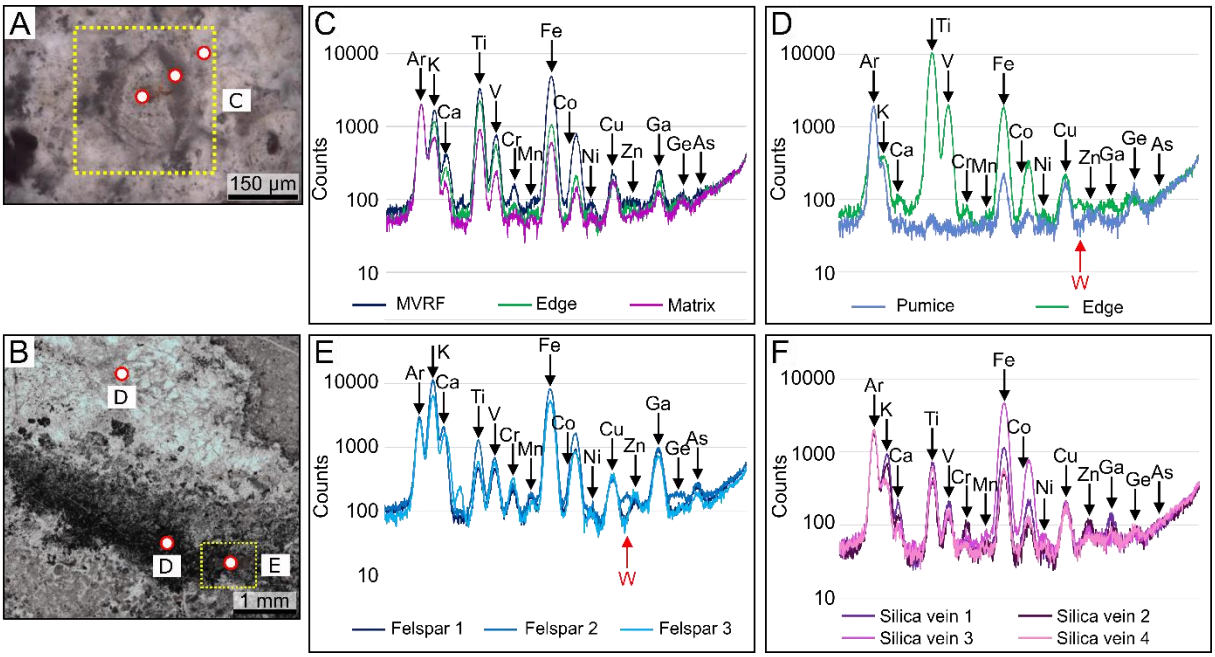

Figure III.18: *Optical images and XRF spectra of specific grains in sample 00AU40. (**A**) Optical image of a multiphase volcanic rock fragment located in ROI 8 (see **Fig. III.16**), surrounded by yellow dotted box and red dots indicating the location of spot measurements, and whose spectra are shown in (**C**). (**B**) Optical image of a pumice fragment (the large pumice on the right in **Fig. III.4B**) and a feldspar grain embedded in the edge of the pumice located in ROI 6, with yellow dotted box surrounding the feldspar and red dots indicating the location of spot measurements, and whose spectra are shown in (**D**) and (**E**). (**C**) Spectrum of a multiphase volcanic rock fragment (MVRF) compared to its edges and the adjacent silica matrix. (**D**) Spectrum of a pumice fragment compared to its dark edge. Note the enrichment in tungsten in the edge of the pumice fragment. (**E**) Spectra of feldspar grains, including the feldspar grain (feldspar 3) shown in (**B**). Note the enrichment in tungsten in feldspar 2. (**F**) Spectra of silica veins. The spectra corresponding to the volcanic grains are colored in different shades of blue, the spectra of the edges are in green, the spectrum of the silica matrix is in purple, and the spectra of the silica vein are in different shades of pink.*

2. Elemental composition of the carbonaceous matter with PIXE

µPIXE was used to map the distribution of trace elements, in particular transition metals, associated with carbonaceous matter in several ROIs in samples 00AU39 and 00AU40 (**Figs. III.19–22**). The measurements performed in ROIs were first compared with ICP-OES and ICP-MS measurements of bulk rocks to study specific local enrichments (see **Appendix A, Tables A1, 5**).

Analysis in the ROIs containing the grains of interest (**Appendix A, Table A1**) generally show an enrichment in elements characteristic of quartz (ca. 86–95% of Si), hydromuscovite (ca. 2–8% of Al and ca. 1–6% of K) and titanium oxides (ca. 0.2–2% of Ti), comparable to bulk analyses of samples 00AU49 and 00AU40 (**Appendix A, Table A5**). Analysis in ROIs of silica-dust gel deposits in sample 00AU39 also show an enrichment in Si (ca. 95–97%), K (ca. 1–2.5%), Al (ca. 1–1.5%) and Ti (ca. 0.2–0.4%), comparable to bulk analyses of sample 00AU39. The ROI of the silica vein in sample 00AU39 is mainly enriched in Si (>99%) with very low contents of Ti (0.22%) and K (0.08%), comparable to bulk analyses of sample 00AU37b (hydrothermal vein). Many transition metals are also detected, in particular V, Cr, Fe, Co, Ni, Cu, Zn, Y, Zr, Nb and Mo. Cl is not detected in sample 00AU40, whereas it is clearly detected

in sample 00AU39. Many elements co-occur with K, such as P, Ca, Fe, Cl, Cr, Rb and Sr. Other elements co-occur with Ti, such as Zr, Y and Nb.

In sample 00AU39, all ROIs are enriched (>800%) in Co relative to the bulk rock. ROIs containing volcanic grains of interest are also enriched (>150%) in Nb, Ti and K relative to the bulk rock, and some ROIs are enriched (>150%) in other elements, such as Cr, Zr and Y. ROIs of silica-dust gel deposits are enriched (>150%) in As relative to the bulk rock, but are depleted (<50%) in Al. The ROI of silica vein is enriched (>200%) in Co and Ge relative to bulk rock 00AU37b, but is depleted (<50%) in Ni, Fe and Cu. P, S, Cl, Ca, Zn, Kr and Mo were not detected in the bulk rock of sample 00AU39. In addition, I observed differences in elemental concentrations between the different types of ROIs analyzed. In particular, ROIs containing volcanic grains of interest are enriched in elements associated to phyllosilicates (Al, K, Ca, Cr, Fe, Rb and Sr) and titanium oxides (Ti, Y, Zr and Nb). On the contrary, ROIs of silica-dust gel deposits seem to be enriched in transition metals (Ni, Cu, Zn and As) and elements associated to the carbonaceous matter (P, S and Cl). Average elemental concentrations in ROIs of sample 00AU39 follow the trend: Si > K > Al > Ti > P > Ca > Fe > Zr > Cr > Cl > S > Rb > Y > Sr > Co > Nb > Cu > Ga > Ge > *Zn* > *Mo* > *As*, *Ni* > *Kr*. Elements listed in italics were mapped and are present but at concentrations below 10 ppm, precluding their direct quantification.

In sample 00AU40, all ROIs are enriched (>250%) in Co relative to the bulk rock, and some ROIs are also enriched (>150%) in other elements, such as Nb, Ti, As and Ge. However, I observed a large depletion (<50%) in Cu, Fe, Zn, Cr, Ni and Mo in ROIs relative to the bulk rock. P, S, Cl, Ca and Kr were not detected in the bulk rock of sample 00AU40. All ROIs analyzed in this sample contain only volcanic grains of interest. Almost all ROIs show a phyllosilicate (Al, K, Ca, Fe, Rb and Sr) and titanium oxides composition (Ti, Y, Zr and Nb), except ROI 7 that have a richer composition in silica (Si). Average elemental concentrations in ROIs of sample 00AU40 follow the trend: Si > Al > K > Ti > P > Fe > Ca > Zr > Rb > S > V, Sr > Cr > Co > Cu, Ga > Y > Nb > *Zn* > *As* > *Kr*, *Mo* > *Ge* > *Ni*.

I then analyzed the edges and interiors of different categories of volcanic clasts coated with carbonaceous matter (e.g., volcanic glass, pumice, multiphase volcanic rock fragments) to provide average elemental concentrations for each category of volcanic clasts, which were then compared within clasts and with the average elemental concentrations of the silica matrix adjacent to the clasts (see **Appendix A, Tables A2, 3**).

In sample 00AU39, volcanic glass (**Fig. III.19A**) shows significant enrichments (>150%) with respect to the adjacent silica matrix (**Fig. III.19B**) in 7 biofunctional elements: Cl, Ca, V, Cr, Zn, As and Sr. In addition, Fe is moderately enriched (100–150%) relative to the matrix. On the other hand, P, S, Co, Ni and Cu are depleted (<100%) relative to the matrix. Average elemental concentrations in volcanic glass follow the trend: P > Ca > Fe > Cl > Cr > V > S > Sr > Co > *Cu* > *As* > *Zn*. The edges of volcanic glass (**Fig. III.19C**) exhibit significant enrichment (>150%) with respect to their interior in 7 biofunctional elements: P, S, Ni, Cu, Zn, As and Mo. Ca, Fe, Co and Sr are moderately enriched (100–150%), whereas Cl, V and Cr are depleted (<100%) relative to their interior. Average elemental concentrations in the edges of volcanic glass follow the trend: P > Ca > Fe > S > Cl > Cr > Mo > Sr > Co > Cu > *As* > *Ni* > *Zn*.

Pumice fragments (**Figs. III.19A and III.20**) are enriched (>150%) with respect to the matrix (**Fig. III.19B**) in 7 biofunctional elements: Ca, Cr, Fe, Co, Ni, As and Sr, whereas P is moderately enriched (100–150%), and S, Cl, V, Cu, Zn and Mo are depleted (<100%). Average elemental concentrations in the pumice follow the trend: P > Ca > Fe > Cr > Cl > Co > Sr > As > *Ni* > *Mo*. The edges of the pumice (**Fig. III.19C**) are enriched (>150%) in P, S and Cu, and moderately enriched (100–150%) in Ca, but are depleted

(<100%) in Cl, Cr, Fe, Co, Ni, As, Sr and Mo with respect to their interior. Average elemental concentrations in the edges of the pumice follow the trend: P > Ca > Fe > S > Cr > Co > Sr > *As* > *Cu*.

Multiphase volcanic rock fragments poorly coated with carbonaceous matter (**Fig. III.19A**) exhibit significant enrichment (>150%) with respect to the matrix (**Fig. III.19B**) in 12 biofunctional elements: P, S, Cl, Ca, V, Cr, Fe, Co, Zn, As, Sr and Mo, whereas Ni and Cu are depleted (<100%). Average elemental concentrations in these volcanic clasts follow the trend: P > Ca > Fe > S > Cr > V > Cl > Sr > Co > Zn > *Mo* > *As*, *Cu*. The edges of these volcanic clasts (**Fig. III.19C**) are enriched (>150%) in Cl, Ni and Mo, and moderately enriched (100–150%) in Cr, Fe and Cu, but are depleted (<100%) in P, S, Ca, V, Co, Zn, As and Sr with respect to their interior. Average elemental concentrations in the edges of these volcanic clasts follow the trend: P > Fe > Ca > Cr > Cl > S > Co > Mo > Sr > *Ni*, *Cu* > *As* > *Zn*.

Multiphase volcanic rock fragments well coated with carbonaceous matter (**Fig. III.19A**) are significantly enriched (>150%) with respect to the matrix (**Fig. III.19B**) in 7 biofunctional elements: S, V, Cr, Fe, As, Sr and Mo. In addition, P and Co are moderately enriched (100–150%), whereas Ca, Cu and Zn are depleted (<100%). Average elemental concentrations in these volcanic clasts follow the trend: Fe > P > Ca > S > V > Cr > Mo > Sr > Zn > Co > As. The edges of these volcanic clasts (**Fig. III.19C**) are enriched (>150%) in P, Cr, Co and Cu, and moderately enriched (100–150%) in Mo, but are depleted (<100%) in S, Ca, V, Fe, Zn, As and Sr with respect to their interior. Average elemental concentrations in the edges of these volcanic clasts follow the trend: P > Fe > Ca > S > Cr > Mo > Co > As > *Zn* > *Cu*.

The silica-dust gel matrix was also analyzed and shows significant enrichment (>150%) with respect to the average elemental concentrations in the matrix in 8 biofunctional elements: S, Cl, Ca, Cr, Ni, Cu, Zn and As, whereas P, Fe and Co are moderately enriched (100–150%), and V, Sr and Mo are depleted (<100%). Average elemental concentrations in the silica-dust gel matrix follow the trend: P > Ca > Fe > S > Cl > Cr > Cu > Zn > Co > Ni > Sr > *As* > *Mo*.

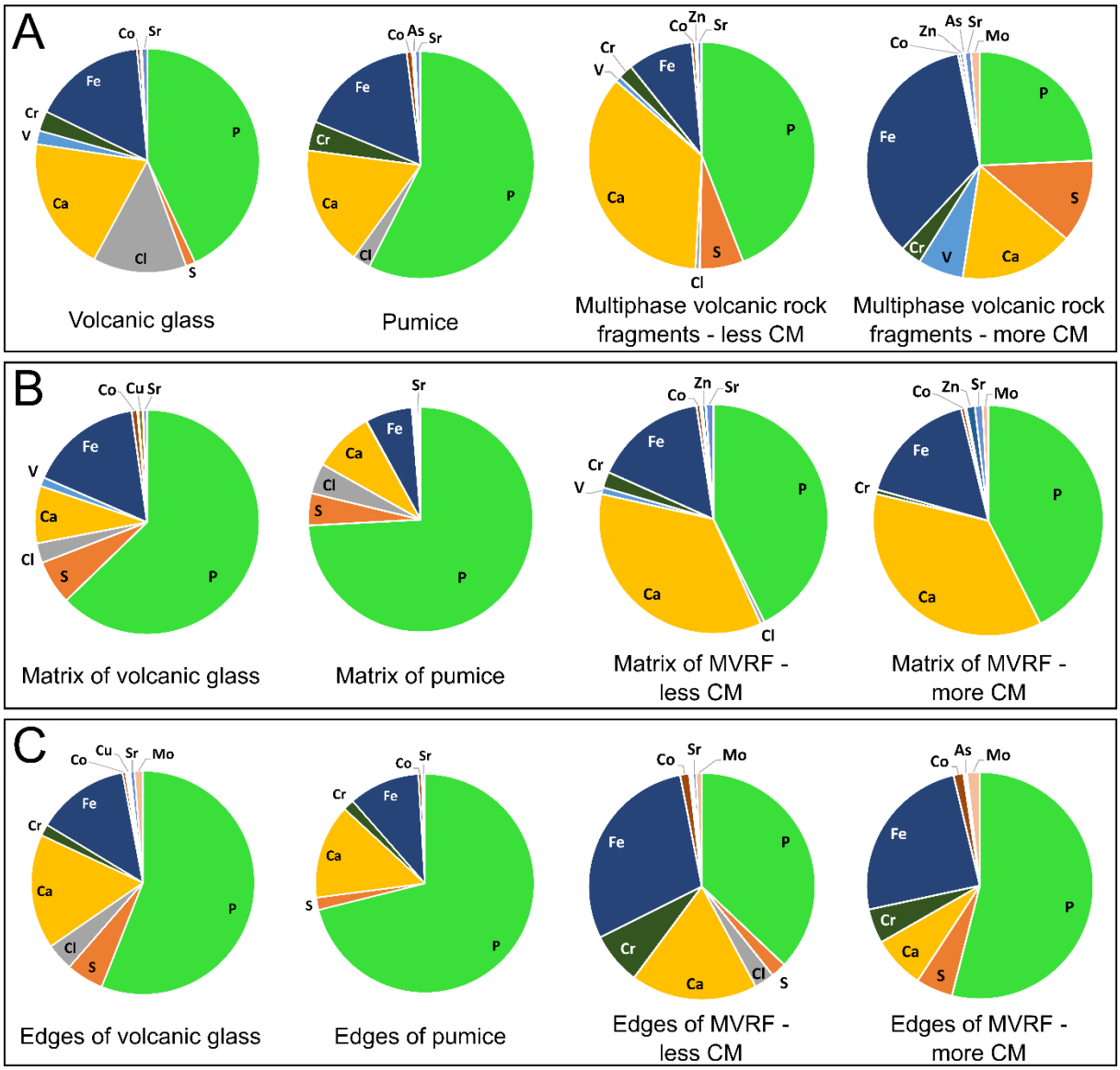

Figure III.19: *Comparison of biofunctional elements in specific structures of interest in sample 00AU39. (**A**) Relative contributions of biofunctional elements in volcanic clasts. The multiphase volcanic rock fragments (MVRF) show greater elemental diversity than volcanic glass and pumice, and the MVRF coating with more carbonaceous matter (CM) exhibits proportionally more significant enrichments in some elements (e.g., Fe, S, V…). (**B**) Relative contributions of biofunctional elements in the silica matrix adjacent to volcanic clasts. (**C**) Relative contributions of biofunctional elements in edges of volcanic clasts. Elements with concentrations below 10 ppm are not shown.*

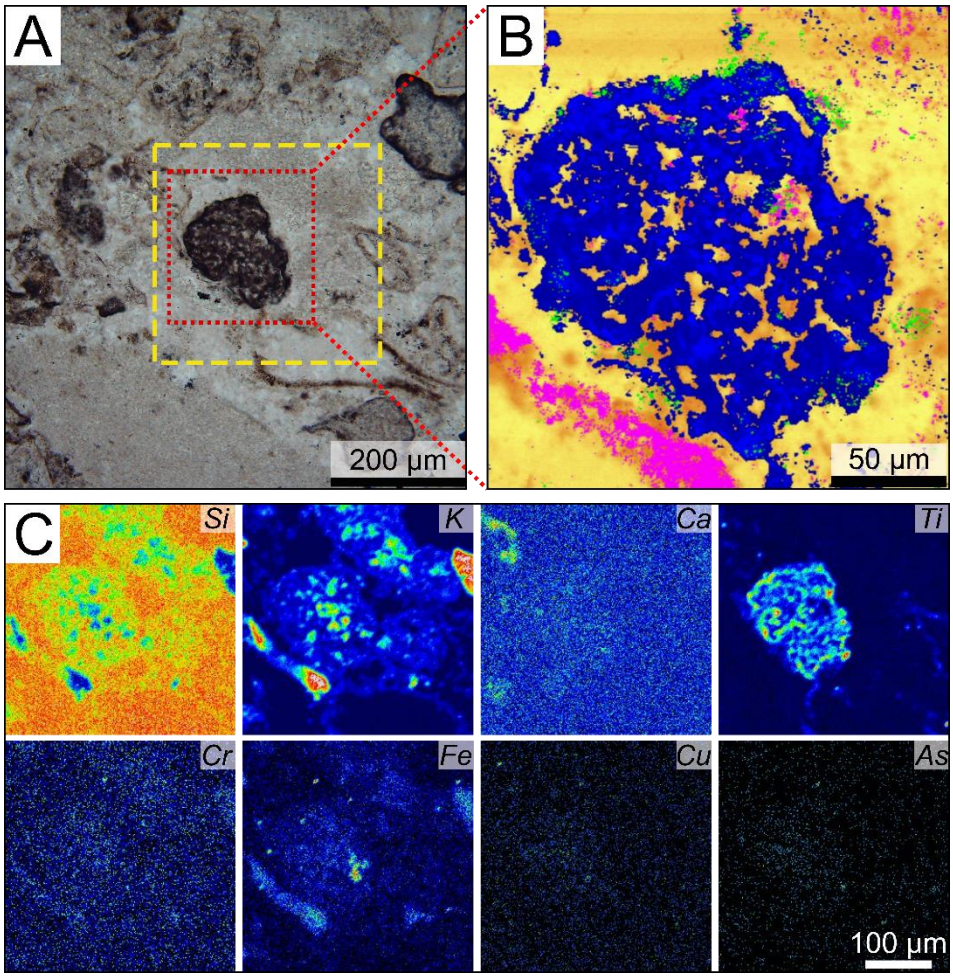

Figure III.20: *Correlated optical microscopy, Raman and µPIXE characterization of a pumice fragment in sample 00AU39. (**A**) Transmitted light optical image of a pumice fragment. Red dotted box and yellow dashed box indicate the regions for which the Raman map in (**B**) and elemental maps in (**C**) are given, respectively. (**B**) Raman compositional map of the same grain with quartz in yellow/orange, anatase in dark blue, hydromuscovite in fuchsia and carbonaceous matter in green. Scan size of the Raman map: 200 µm × 210 µm. (**C**) Elemental maps corresponding to elemental enrichments in the pumice and additional adjacent volcanic clasts. Scan size of the area analyzed with PIXE: 350 µm × 350 µm. Concentrations vary between low [dark blue] and high [white].*

In sample 00AU40, volcanic glass (**Fig. III.21A**) shows significant enrichment (>150%) with respect to the adjacent silica matrix (**Fig. III.21B**) in 8 biofunctional elements: S, Ca, V, Cr, Fe, Co, As and Sr. In addition, Cu and Zn are moderately enriched (100–150%) relative to the matrix. On the other hand, P and Ni are depleted (<100%) relative to the matrix. Average elemental concentrations in volcanic glass follow the trend: Fe > Ca > S > V > Cr > Sr > Co > *Zn*, *Cu* > *As*. The edges of volcanic glass (**Fig. III.21C**) exhibit significant enrichment (>150%) with respect to their interior in only 2 biofunctional elements: Cu and Zn. Co and As are moderately enriched (100–150%), whereas S, Ca, V, Cr, Fe and Sr are depleted (<100%) relative to their interior. Average elemental concentrations in the edges of volcanic glass follow the trend: Fe > Ca > Cr > Sr > Co > Cu > Zn > *As*.

Multiphase volcanic rock fragments poorly coated with carbonaceous matter (**Figs. III.21A and III.22**) exhibit significant enrichments (>150%) with respect to the matrix (**Fig. III.21B**) in 7 biofunctional elements: Ca, V, Cr, Fe, Zn, Sr and Mo. In addition, S is moderately enriched (100–150%), whereas P,

Co, Ni, Cu and As are depleted (<100%). Average elemental concentrations in these volcanic clasts follow the trend: Fe > Ca > V > S > Sr > Cr > Mo > Zn > Co > *Cu* > *Ni*. The edges of these volcanic clasts (**Fig. III.21C**) are enriched (>150%) in P and Ni, and moderately enriched (100–150%) in Cu, whereas S, Ca, V, Cr, Fe, Co, Zn and Sr are depleted (<100%) with respect to their interior. Average elemental concentrations in the edges of these volcanic clasts follow the trend: P > Fe > Ca > V > Cr > Sr > Ni > *Co*, *Cu* > *Zn*.

Multiphase volcanic rock fragments well coated with carbonaceous matter (**Fig. III.21A**) are significantly enriched (>150%) with respect to the matrix (**Fig. III.21B**) in 6 biofunctional elements: P, Ca, V, Fe, Cu and Zn. In addition, Co and As are moderately enriched (100–150%), whereas Sr is depleted (<100%). Average elemental concentrations in these volcanic clasts follow the trend: P > Fe > Ca > V > Cu > Co > Zn > *As*.

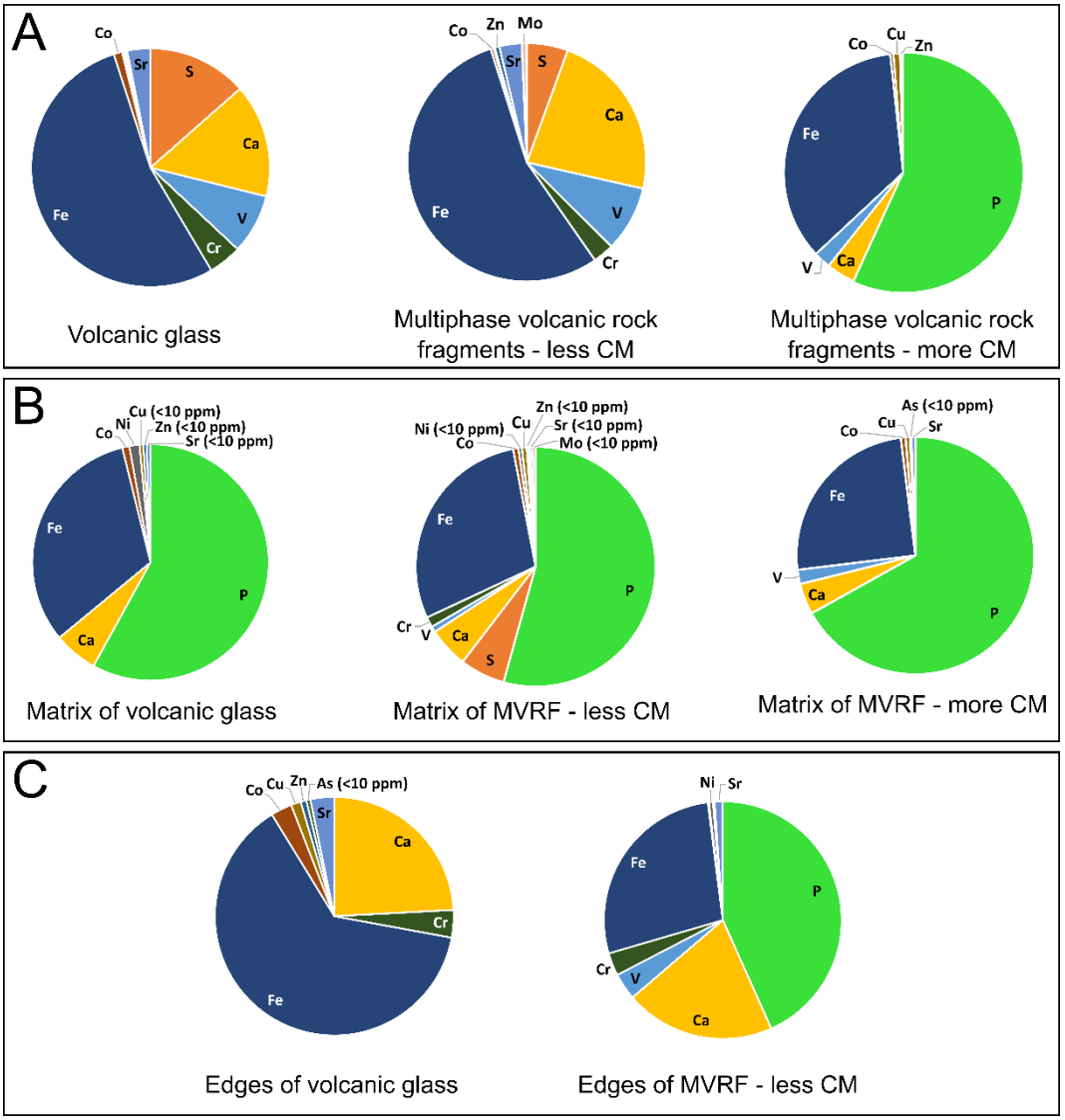

Figure III.21: *Comparison of biofunctional elements in specific structures of interest in sample 00AU40. (**A**) Relative contributions of biofunctional elements in volcanic clasts. Volcanic glass and multiphase volcanic rock fragments (MVRF) coating with less carbonaceous matter (CM) show similar contributions of biofunctional elements and a greater diversity than the MVRF coating with more carbonaceous matter, which are notably more enriched in P. (**B**) Relative contributions of biofunctional elements in*

*the silica matrix adjacent to volcanic clasts. (**C**) Relative contributions of biofunctional elements in edges of volcanic clasts. Elements having concentrations below 10 ppm are not shown (unless specified).*

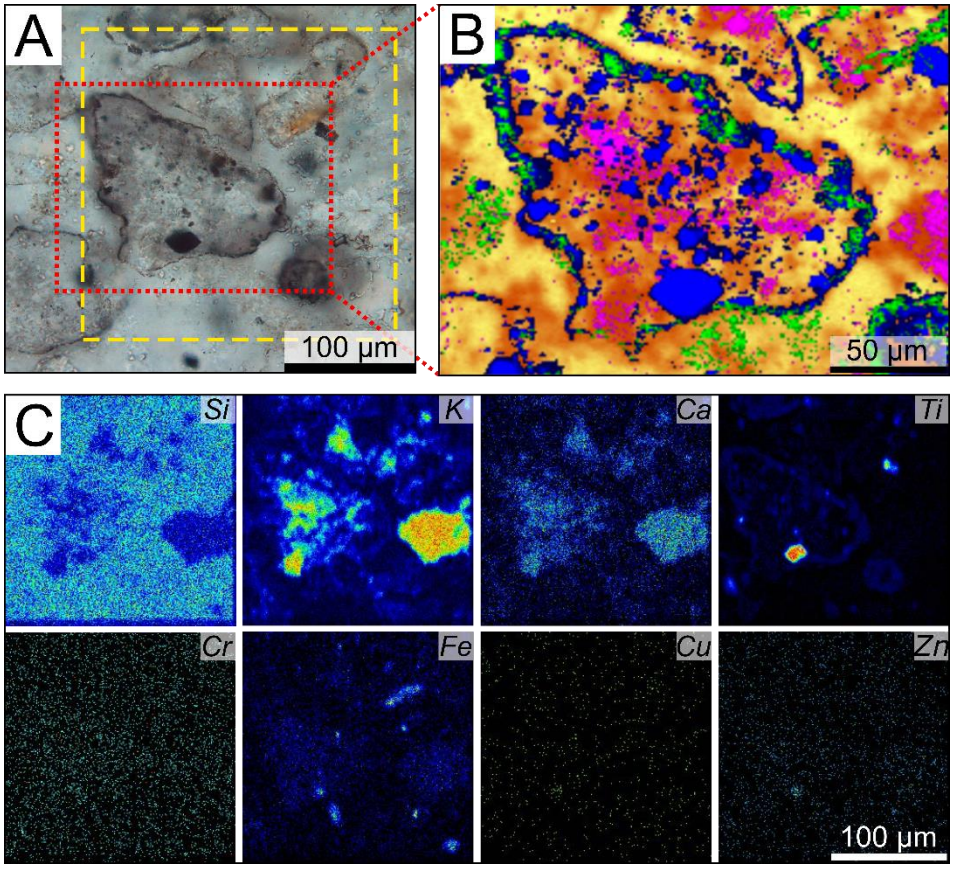

***Figure III.22:** Correlated optical microscopy, Raman and µPIXE characterization of a multiphase volcanic rock fragment in sample 00AU40. (**A**) Transmitted light optical image of a multiphase volcanic rock fragment. Red dotted box and yellow dashed box indicate the regions for which the Raman map in (**B**) and elemental maps in (**C**) are given, respectively. (**B**) Raman compositional map of the same grain with quartz in yellow/orange, anatase in dark blue, hydromuscovite in fuchsia and carbonaceous matter in green. Scan size of the Raman map: 220 µm × 160 µm. (**C**) Elemental maps corresponding to elemental enrichments in the multiphase volcanic rock fragment and additional adjacent volcanic clasts. Scan size of the area analyzed with PIXE: 200 µm × 200 µm. Concentrations vary between low [dark blue] and high [white].*

D. Molecular composition of the carbonaceous matter

1. Molecular composition of the carbonaceous matter with DUV

DUV fluorescence microimaging (Telemos) and microspectroscopy (Polypheme) were used to identify and map aromatic compounds and minerals in ROIs containing the grains of interest in samples 00AU39 and 00AU40 (**Figs. III.23–25**). In particular, aromatic compounds were analyzed in the samples to identify their structure (number of rings) and to evaluate possible differences between the samples in terms of abundance (by comparing band intensities) and diversity (number and position of the bands).

Microimaging of sample 00AU39 (**Fig. III.23A, B**) documents heterogeneity in aromatic compounds (spectral range from 329 to 351 nm), aromatic compounds mixed with hydromuscovite (352–388 nm), and anatase (420–480 nm); specifically, aromatic compounds are often spatially correlated with hydromuscovite. Spectral images (**Fig. III.24**) confirmed the presence of aromatic compounds with main fluorescent emissions at 310 and 340 nm (**Fig. III.24C**; Ménez et al., 2018). In particular, the volcanic dust-rich matrix is slightly (<300 counts, cts) to highly (>3000 cts) enriched in aromatics exhibiting two bands at 310 and 340 nm or 340 and 360 nm (the band at 340 nm is generally more prevalent). For the other structures of interest in the sample, I observed variations in the relative concentrations of aromatics and the positions of their main bands: volcanic glass is relatively enriched (>600 cts) in aromatics with two bands at 310 and 340 nm (e.g., **Fig. III.24C**); amphibole/pyroxene is slightly enriched (<400 cts) with only one band at 345 nm; some multiphase volcanic rock fragments show a high enrichment (>1000 cts) with two bands at 310 and 340 nm, whereas other multiphase volcanic rock fragments are not particularly enriched in aromatics. Other fluorescent signals have also been detected in the sample, including a major band at 415–420 nm with shoulders at 430–435 nm and 460–465 nm (**Fig. III.24C, D**); these features correspond to mineral phases, in particular hydromuscovite and anatase (Gaft et al., 2015).

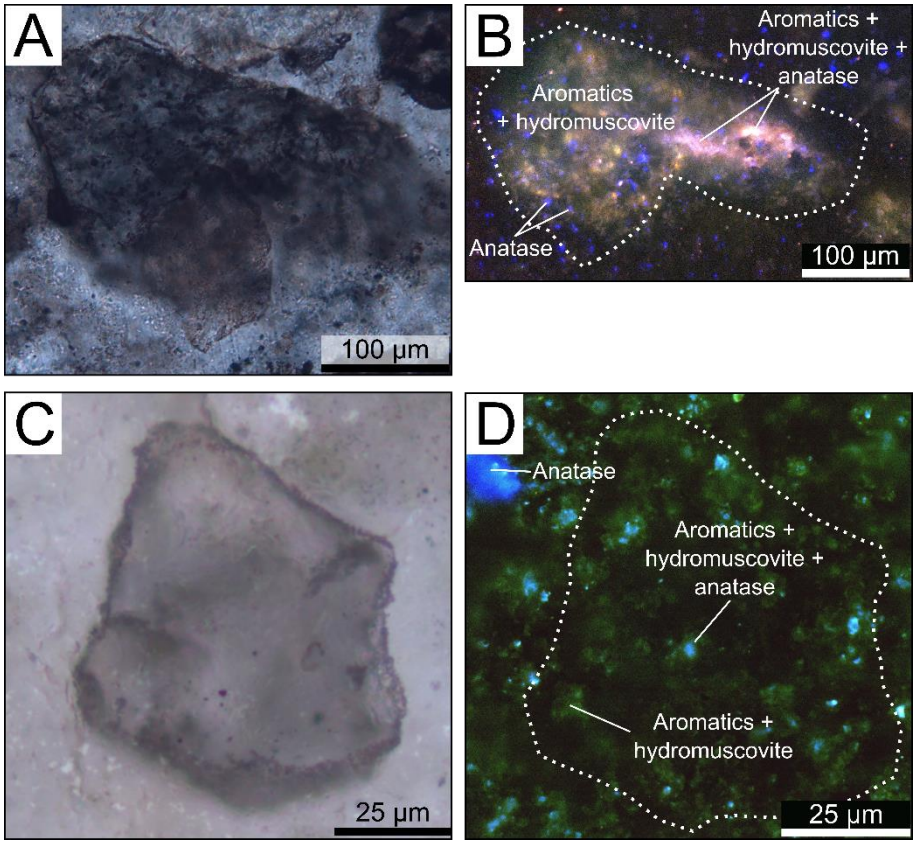

Figure III.23: *DUV fluorescence maps within multiphase volcanic rock fragments from samples 00AU39 and 00AU40. (**A, C**) Optical images in transmitted light of multiphase volcanic rock fragments altered to anatase at the edges and hydromuscovite in the interior in samples 00AU39 and 00AU40, respectively. (**B**) RGB composite of a multiphase volcanic rock fragment in sample 00AU39 showing an enrichment in aromatic molecules intermixed with hydromuscovite (green/yellow) in the interior of the volcanic grain, with an area particularly enriched in aromatic molecules intermixed with hydromuscovite and anatase (magenta), and small particles of anatase (blue). Scan size: 550 µm × 320*

*µm. (**D**) RGB composite of a multiphase volcanic rock fragment in sample 00AU40 showing several isolated spots enriched in aromatic molecules intermixed with hydromuscovite (green) in the interior of the volcanic grain, and also sometimes with anatase (cyan). Scan size: 90 µm × 90 µm. Green/yellow = aromatic molecules and hydromuscovite, blue = anatase, cyan/magenta = mix of aromatic molecules, hydromuscovite and anatase.*

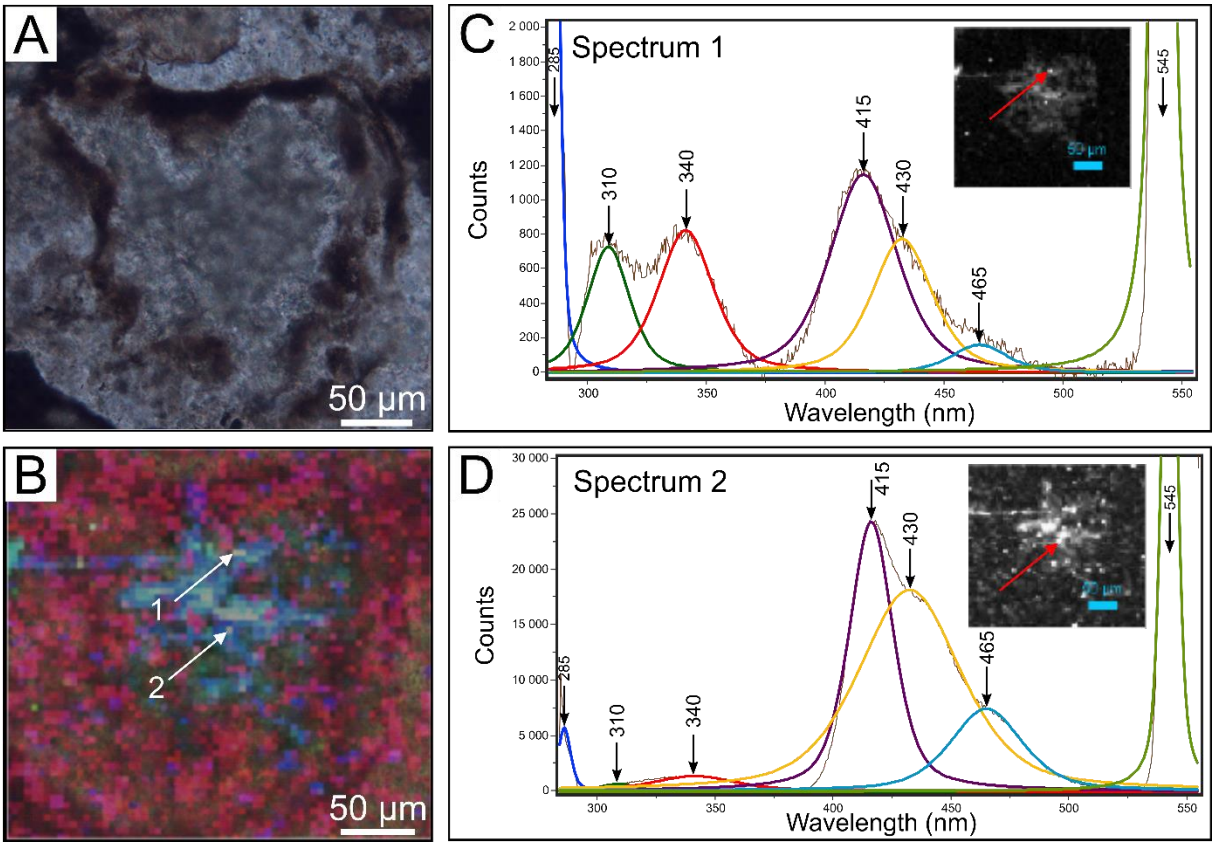

Figure III.24: *DUV fluorescence map and spectra within a volcanic glass fragment in sample 00AU39. (**A**) Transmitted light optical image of volcanic glass altered to anatase at the edges (brown color) and hydromuscovite in the interior (grey color). (**B**) RGB composite (red = 300–320 nm, green = 325–370, blue = 375–450 nm). White arrows indicate the location from which the spectra shown in (**C**) and (**D**) have been extracted. Scan size: 290 µm × 265 µm. (**C**) Spectrum of aromatic compounds (main bands at 310 and 340 nm) mixed with mineral phases (main bands at 415, 430 and 465 nm); inset shows a map corresponding to the fluorescent emission at 340 nm. (**D**) Spectrum of mineral phases (main bands at 415, 430 and 465 nm); inset shows a map corresponding to the fluorescent emission at 415 nm.*

Microimaging of sample 00AU40 (**Fig. III.23C, D**) shows a wider variety in aromatic compounds (spectral ranges from 329 to 351 nm), aromatic compounds mixed with hydromuscovite (352–388 nm), aromatic compounds with hydromuscovite and anatase (412–438 nm and 420–480 nm), and anatase mixed with other metallic oxides (499–529 nm); again, aromatic compounds are often correlated with hydromuscovite. Spectral images (**Fig. III.25**) clearly indicate the presence of aromatic compounds with one main fluorescent emission at 340–345 nm (**Fig. III.25C**; Ménez et al., 2018). In particular, disseminated volcanic particles in the silica matrix are slightly (ca. 500 cts) to highly (>3000 cts) enriched in aromatics with a band at 340–345 nm (or sometimes two bands at 310 and 340 nm). Some variation in the relative concentrations of aromatics and the positions of their main bands is observed in the other structures: some multiphase volcanic rock fragments are moderately (up to >500 cts) to

strongly (>1000 cts) enriched in aromatics with a band at 340 nm (e.g., **Fig. III.25C**), whereas the silica-dust gel matrix often shows a high enrichment (up to >2000 cts) in aromatics with either one band at 340–345 nm with a shoulder at 325 nm or two bands at 310 and 340–345 nm (the band at 340–345 nm is generally more intense). Other fluorescent signals have also been detected in the sample, including a main band at 410–415 nm (**Fig. III.25C**), with rare shoulders at 390 nm and 430 nm, corresponding to mineral phases, in particular hydromuscovite and anatase (Gaft et al., 2015).

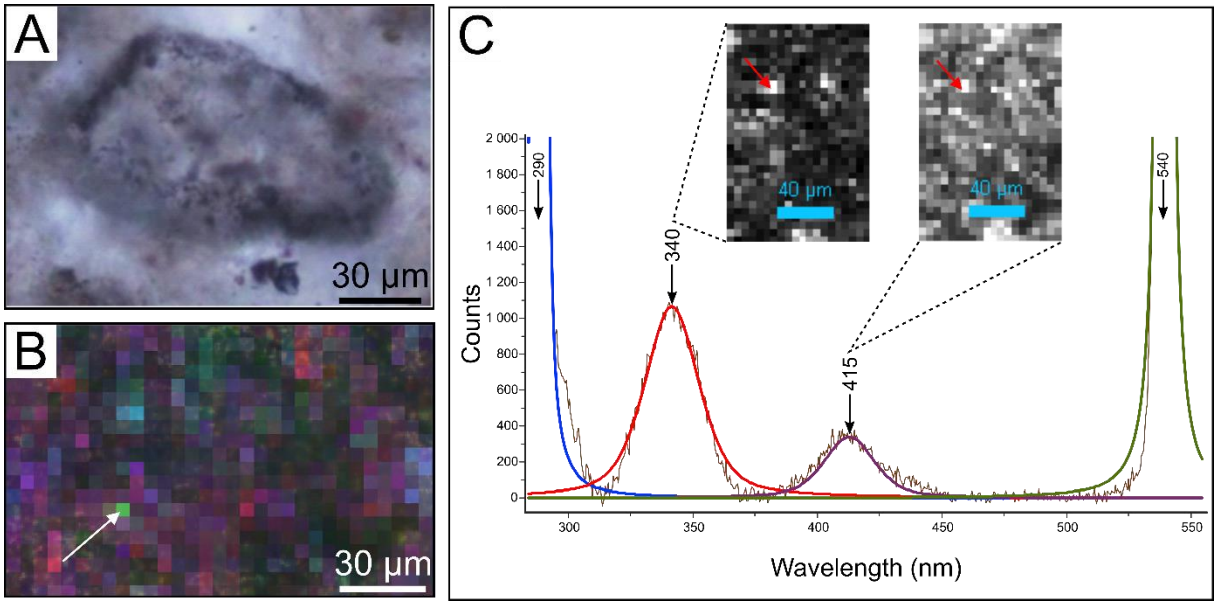

Figure III.25: *DUV fluorescence map and spectrum within a multiphase volcanic rock fragment in sample 00AU40. (**A**) Transmitted light optical image of a multiphase volcanic rock fragment altered to anatase at the edges (dark color). (**B**) RGB composite (red = 300–320 nm, green = 325–370, blue = 375–450 nm). White arrow indicates the pixel from which the spectrum shown in (**C**) has been extracted. Scan size: 150 µm × 95 µm. (**C**) Spectrum of aromatic compounds (main band at 340 nm) and mineral phases (main band at 415 nm); insets show maps corresponding to the fluorescent emissions at 340 and 415 nm, respectively.*

2. Molecular composition of the carbonaceous matter with FTIR spectroscopy

Transmission FTIR mapping and spectra were used to further characterize the molecular composition of the carbonaceous matter in samples 00AU39 and 00AU40, focusing on the aliphatic C–H stretching compounds within the wavenumber range 2800–3040 cm^{-1}, and the aromatic/alkenic compounds within the wavenumber range 1300–1800 cm^{-1} (**Figs. III.26–30**).

In the aliphatic C–H stretching region (**Fig. III.26**), i.e., between 2800 and 3040 cm^{-1}, both samples exhibit bands at 2855 and 2870 cm^{-1} corresponding to the symmetrical stretching vibrations of CH_2 and CH_3 in an aliphatic hydrocarbon, as well as bands at 2925 and 2960 cm^{-1} attributed to the asymmetrical stretching vibrations of CH_2 and CH_3 in an aliphatic hydrocarbon (Lin and Ritz, 1993). Generally, the methylene group (CH_2) bands (symmetric and asymmetric) are predominant related to the methyl group (CH_3) bands (the symmetric feature at 2870 cm^{-1} is relatively weak) in both samples. In addition, sample 00AU40 shows more intense absorbance (two to five orders of magnitude) in the aliphatic C–H stretching region with respect to 00AU39.

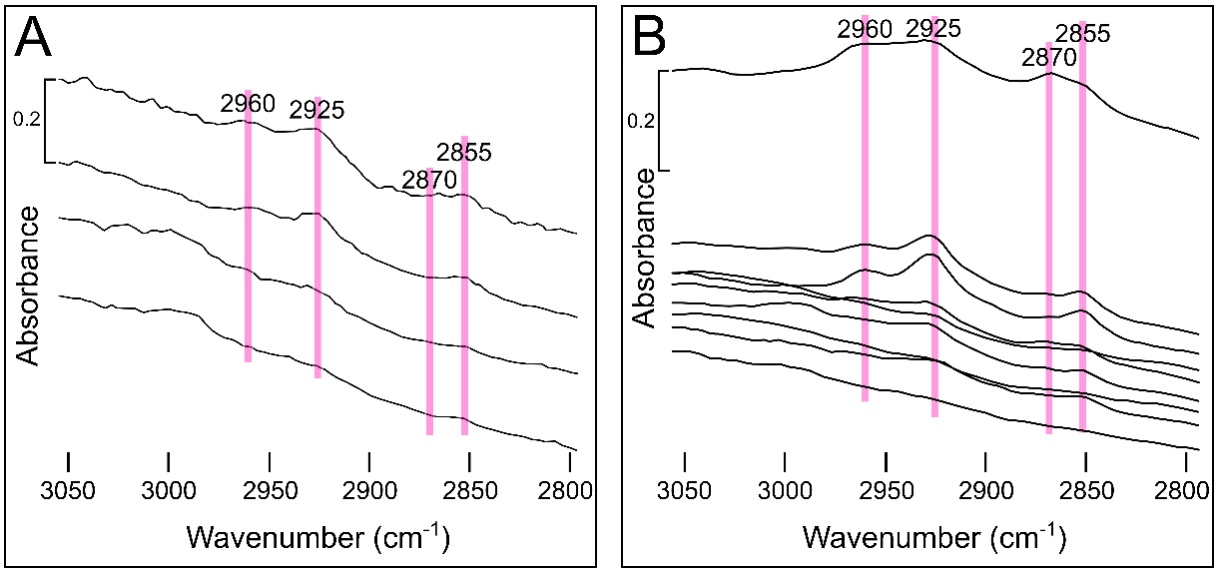

Figure III.26: *Transmission Fourier transform infrared (FTIR) absorbance spectra in the range 2800–3050 cm^{-1}. (**A**) Transmission FTIR absorbance spectra of four volcanic grains coated with carbonaceous matter in sample 00AU39. (**B**) Transmission FTIR absorbance spectra of five volcanic grains coated with carbonaceous matter (including two spectra extracted from the same two grains) and of the silica-dust gel matrix (the lowermost spectrum, characterized by the weakest absorbance and an absence of spectral features) in sample 00AU40.*

In the aromatic/alkenic region (**Figs. III.27, 28**), i.e., between 1300 and 1800 cm^{-1}, both samples exhibit a weak band at 1360 cm^{-1} (CH_3); weak bands at 1440 cm^{-1} and 1470 cm^{-1} (C–H stretching with a contribution from aromatic ring stretching); a weak band at 1545 cm^{-1} (potential C–N and N–H in amide II); weak bands at 1650 cm^{-1} (highly conjugated C=O), 1705 cm^{-1} (C=O and COOH), 1720 cm^{-1} (C=O and COOH; >C=O ester stretch) and 1735 cm^{-1} (>C=O ester stretch) attributed to carbonyl and carboxyl groups; and intense bands at 1495, 1525, 1610, 1680, 1795 and 1875 cm^{-1} interpreted as Si–O. The intensity and diversity of bands in the aromatic/alkenic region is higher in sample 00AU39 with respect to sample 00AU40.

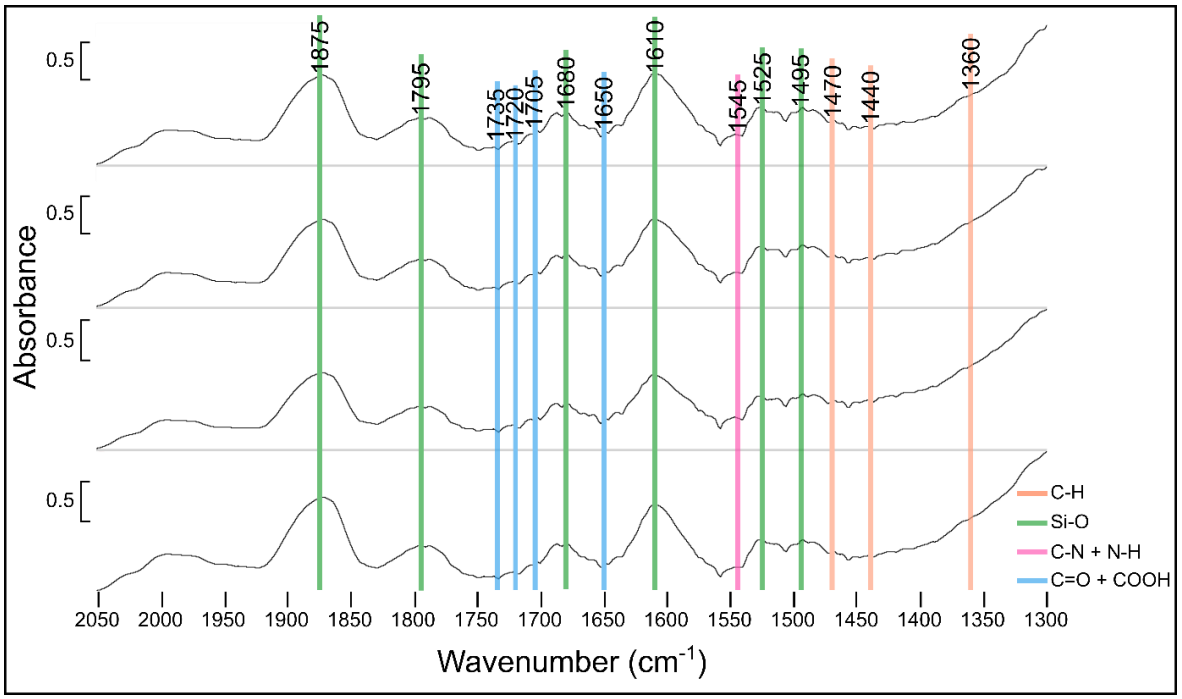

Figure III.27: *Representative transmission Fourier transform infrared (FTIR) absorbance spectra in the range 1300–2050 cm^{-1} for sample 00AU39.*

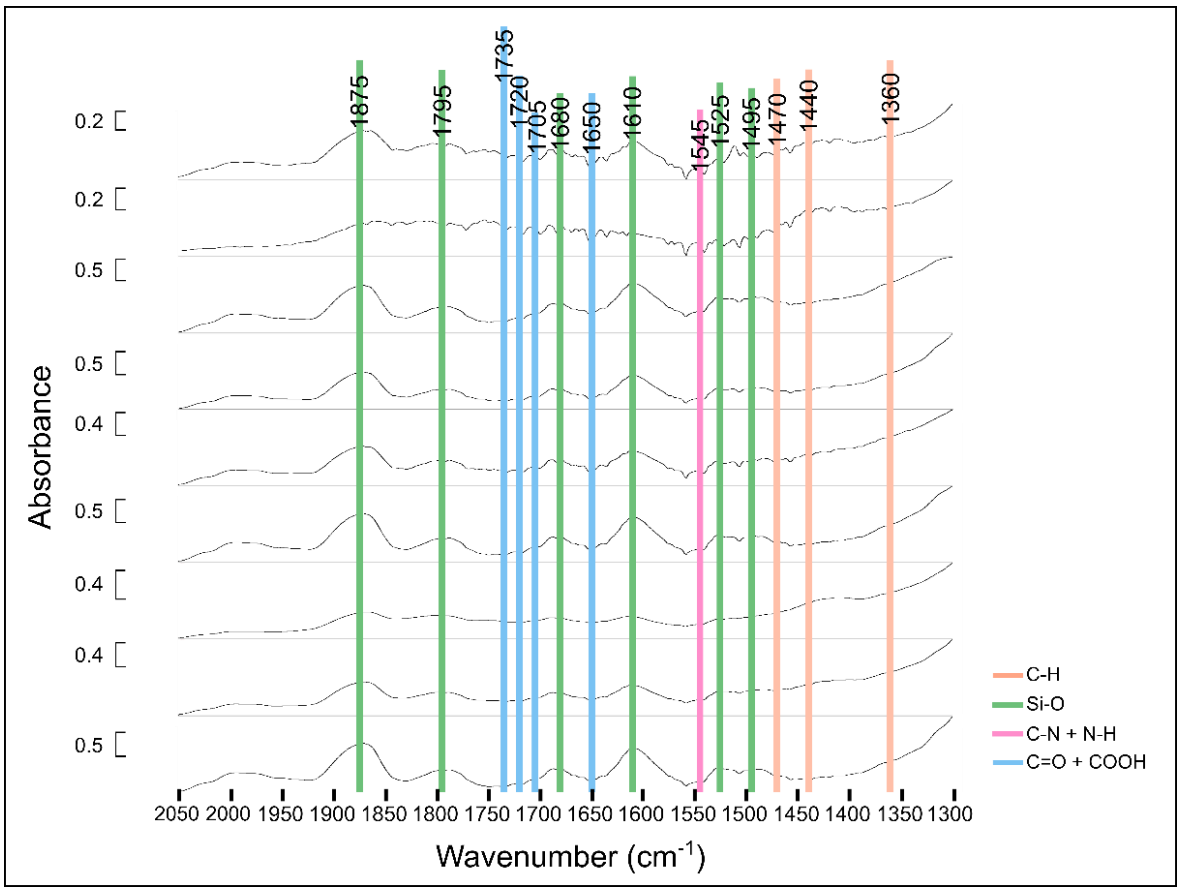

Figure III.28: *Representative transmission Fourier transform infrared (FTIR) absorbance spectra in the range 1300–2050 cm^{-1} for sample 00AU40.*

FTIR maps illustrating the distribution of organics and minerals in both samples are shown in **Figures III.29 and III.30**. In sample 00AU39, volcanic glass is rich in hydromuscovite (–OH), with some aromatics (C–H) located in the heart of the grain. Multiphase volcanic rock fragments (**Fig. III.29**) show slight spatial and spectral variations: generally, they contain high concentrations in aromatics (C–H; **Fig. III.29C, D**), and variable concentrations in aliphatics (CH_2 and CH_3; **Fig. III.29J, K**) and other functional groups (C=O, COOH…; **Fig. III.29G–I**), which are mainly concentrated in the heart of the grains. Most of the grains are silicified (Si–O; **Fig. III.29E, F**), and show evidence of alteration to hydromuscovite (represented by –OH as a proxy for phyllosilicates; **Fig. III.29L**).

In sample 00AU40, volcanic glass is very rich in –OH, rich in C–H, with some aliphatics, but shows a lesser concentration of certain functional groups (especially the >C=O ester stretch), which are instead relatively concentrated in the adjacent matrix. Multiphase volcanic rock fragments (**Fig. III.30**) present more variations according to their nature and/or their degree of alteration: some grains are particularly rich in aromatics, particularly at their edges, whereas others have interiors richer in aromatics (or more sporadically throughout the grains; **Fig. III.30C, D**). Some grains are relatively rich in aliphatics (**Fig. III.30J, K**), and other functional groups (**Fig. III.30G–I**), which are either mostly concentrated in the interior of the grains or more sporadically distributed throughout. Some grains are highly silicified (**Fig. III.30E, F**), whereas others are silica-poor; and their –OH concentration is variable (**Fig. III.30L**). The silica-dust gel matrix is enriched in –OH and Si–O, with some areas exhibiting increased concentrations of aromatics, aliphatics and/or other functional groups.

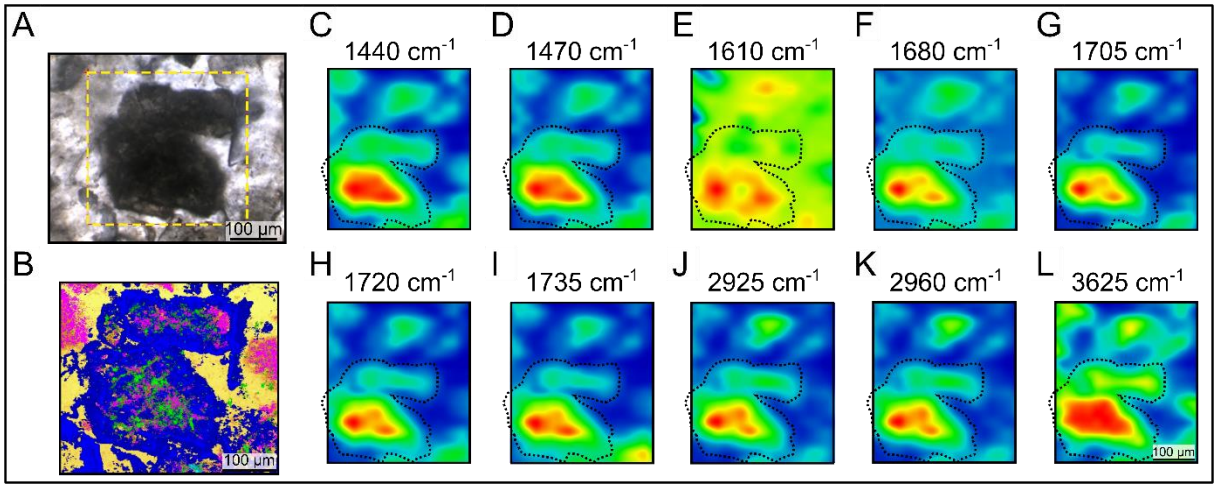

Figure III.29: *FTIR microspectroscopy of diverse compounds extracted from specific bands in spectra from sample 00AU39. (**A**) Transmitted light photomicrograph and (**B**) Raman compositional map of a multiphase volcanic rock fragment in sample 00AU39, with quartz in yellow, anatase in dark blue, rutile in light blue, hydromuscovite in fuchsia and carbonaceous matter in green. Yellow dashed box indicates the region for which the FTIR maps are given. Scan size of Raman map: 400 µm × 350 µm. FTIR maps of (**C, D**) C–H stretching with a contribution from aromatic ring stretching with main bands at 1440 and 1470 cm^{-1}; (**E, F**) Si–O with main bands at 1610 and 1680 cm^{-1}; (**G, H, I**) carbonyl and carboxyl groups with main bands at 1705 (C=O, COOH), 1720 (C=O, COOH; >C=O ester stretch) and 1735 cm^{-1} (>C=O ester stretch); (**J, K**) aliphatic C–H stretching with main bands at 2925 (asymmetrical methylene CH_2 stretching) and 2960 cm^{-1} (asymmetrical end-methyl CH_3 stretching); (**L**) –OH with a main peak at 3625 cm^{-1}. Scan size of the area analyzed with FTIR: 360 µm × 340 µm. Concentrations vary between low [dark blue] and high [red].*

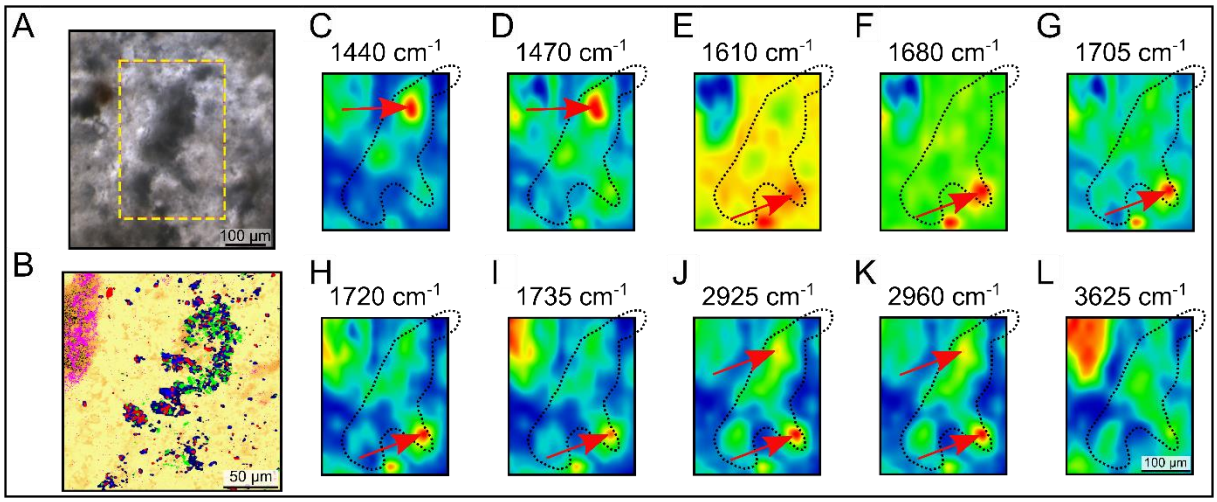

Figure III.30: *FTIR microspectroscopy of diverse compounds extracted from specific bands in spectra from sample 00AU40. (**A**) Transmitted light photomicrograph and (**B**) Raman compositional map of a multiphase volcanic rock fragment in sample 00AU40, with quartz in yellow, anatase in dark blue, rutile in red, hydromuscovite in fuchsia and carbonaceous matter in green. Yellow dashed box indicates the region for which the FTIR maps are given. Scan size of Raman map: 200 µm × 200 µm. FTIR maps of (**C, D**) C–H stretching with a contribution from aromatic ring stretching with main bands at 1440 and 1470 cm^{-1}; (**E, F**) Si–O with main bands at 1610 and 1680 cm^{-1}; (**G, H, I**) carbonyl and carboxyl groups with main bands at 1705 (C=O, COOH), 1720 (C=O, COOH; >C=O ester stretch) and 1735 cm^{-1} (>C=O ester stretch); (**J, K**) aliphatic C–H stretching with main bands at 2925 (asymmetrical methylene CH_2 stretching) and 2960 cm^{-1} (asymmetrical end-methyl CH_3 stretching); (**L**) –OH with a main peak at 3625 cm^{-1}. Scan size of the area analyzed with FTIR: 270 µm × 300 µm. Concentrations vary between low [dark blue] and high [red].*

Below is a summary of the chemical analyses carried out on volcanic grains and other structures of interest (i.e., silica matrix, silica veins and silica-dust gel matrix) in samples 00AU39 and 00AU40, which also highlights differences in the organic compositions between them:

- Based on XRF results, the silica matrix and volcanic glass fragments not coated with carbonaceous matter are depleted in all elements (except Cu) relative to feldspars and multiphase volcanic rock fragments coated with carbonaceous matter that are highly enriched in many elements (K, Ca, Cr, Mn, Fe, Zn…).
- The carbon-coated pumice fragments in sample 00AU39 are enriched in Ti, K, Fe, Ca, Ga and Cr relative to the silica matrix, while the pumice fragments without carbon coating in sample 00AU40 are depleted in almost all elements (except Cu and Ge) relative to the silica matrix and their dark edges are highly enriched in Ti and W relative to their interior and the silica matrix.
- The carbon-coated edges of the volcanic glass fragments are enriched in many elements (Ti, Fe, Mn, Ni, Cu, Zn…) relative to their interior and the silica matrix, while the carbon-coated edges of the multiphase phase volcanic rock fragments are only enriched in Ti.
- The silica veins in sample 00AU40 are mostly enriched in Fe, K, Ti, Cu, V and Zn.
- The silica-dust gel matrix, including the light silica-dust gel laminations in sample 00AU40, has a clay-like composition associated to many transition metals (Fe, Cu, Ti, Zn, V, Cr…), while the dark silica-dust gel laminations in sample 00AU40 are richer in Ti.
- Based on PIXE results, average absolute concentrations of biofunctional elements in volcanic clasts coated with carbonaceous matter follow the trend: P > Fe > Ca > Cr > S > V > Cl > Sr > Co > Mo > *As* > *Zn* > *Ni* > *Cu* in sample 00AU39, including 9 biofunctional elements (Cr, As, Mo, V, Fe, Sr, Zn, Co and Ca) that are mostly enriched relative to the adjacent silica matrix, while average absolute concentrations of biofunctional elements in volcanic clasts coated with carbonaceous matter in sample 00AU40 follow the trend: Fe > P > Ca > V > S > Cr > Sr > Co > Mo > Cu > Zn > *As* > *Ni*, including 8 biofunctional elements (V, Cr, Zn, As, S, Mo, Ca and Fe) that are mostly enriched relative to the adjacent silica matrix.
- Average absolute concentrations of biofunctional elements in carbon-coated edges of the volcanic clasts in sample 00AU39 follow the trend: P > Fe > Ca > S > Cr > Cl > Mo > Co > Sr > *As* > *Cu* > *Ni* > *Zn*, including 6 biofunctional elements (Ni, Cu, Mo, Cr, S and Co) that are mostly enriched relative to their interior; in contrast, average absolute concentrations of biofunctional elements in carbon-coated edges of the volcanic clasts in sample 00AU40 follow the trend: P > Fe > Ca > Cr > V > Sr > Co > *Ni* > *Cu* > *Zn* > *As*, including only 3 biofunctional elements (P, Cu and Co) that are mostly enriched relative to their interior.
- Average absolute concentrations of biofunctional elements in the silica-dust gel matrix in sample 00AU39 follow the trend: P > Ca > Fe > S > Cl > Cr > Cu > Zn > Co > Ni > Sr > *As* > *Mo*, including 11 biofunctional elements (Ni, As, Zn, Cl, Cr, Cu, S, Ca, P, Fe and Co) that are enriched relative to the average silica matrix.
- The carbonaceous matter in the samples comprises both aromatic and aliphatic functional groups:
  - In Raman spectroscopy, the signal of carbonaceous matter displays a large disorder band at 1350 cm^{-1};
  - In DUV fluorescence, aromatic compounds were detected based on signals at 310 and 340 nm in sample 00AU39, but only at 340–345 nm in sample 00AU40;
  - In FTIR, absorbance features consistent with aromatic compounds at 1360 cm^{-1} (CH_3); 1440 and 1470 cm^{-1} (C–H stretching); 1545 cm^{-1} (C–N and N–H in amide II); 1650, 1705, 1720 and 1735 cm^{-1} (carbonyl and carboxyl groups) were identified in both samples, but the intensity and diversity of the bands are higher in sample 00AU39;

- In FTIR, aliphatics were identified at 2855 cm^{-1} (symmetrical CH_2), 2870 cm^{-1} (symmetrical CH_3; very weak intensity), 2925 cm^{-1} (asymmetrical CH_2) and 2960 cm^{-1} (asymmetrical CH_2) in both samples, but the intensity of the bands is higher in sample 00AU40 (two to five orders of magnitude more intense);
- FTIR analysis of volcanic glass in sample 00AU39 contains –OH associated with some aromatics, whereas volcanic glass in sample 00AU40 is more enriched in –OH associated with more aromatics (C–H) and some aliphatics, but little enriched in certain functional groups (in particular, the >C=O ester stretch);
- FTIR analysis of multiphase volcanic rock fragments in sample 00AU39 contain high concentrations of aromatics and variable concentrations of aliphatics and other functional groups (e.g., C=O, COOH) that are mainly located in the interior of particles, whereas volcanic rock fragments in sample 00AU40 contain variable concentrations of aromatics, aliphatics and other functional groups that are either located at the edges or in the interior of particles;
- FTIR analysis of the silica-dust gel matrix in sample 00AU40 shows that is particularly rich in –OH and Si–O with some heterogeneously distributed aromatics, aliphatics and other functional groups.

- In DUV, signals attributed to mineral phases (in particular, hydromuscovite and anatase) were also detected at 415–420 nm with shoulders at 430–435 nm and 460–465 nm in sample 00AU39, whereas they are detected at 410–415 nm with rare shoulders at 390 nm and 430 nm in sample 00AU40.

IV. Résumé en français

Ce troisième chapitre présente les résultats de ce projet de thèse. Il se divise en deux parties. La première partie retrace le contexte paléoenvironnemental des sédiments volcaniques silicifiés du chert de Kitty's Gap à travers l'analyse sédimentologique, pétrologique, minéralogique et géochimique des échantillons étudiés. La seconde partie est consacrée à l'analyse de la matière carbonée contenue dans les sédiments volcaniques. L'objectif est d'identifier des signatures morphologiques, élémentaires et moléculaires de la matière carbonée et d'observer sa distribution à différentes échelles afin d'évaluer sa syngénicité et sa biogénicité.

L'analyse sédimentologique de l'échantillon 00AU37b indique que celui-ci provient directement d'une veine hydrothermale et qu'il fait partie d'un conglomérat (00AU37) comportant des clastes volcaniques clairs millimétriques à centimétriques englobés dans une matrice de chert noire (**Figure III.1B**). L'échantillon 00AU39 est un conglomérat composé de galets foncés entourés par des couches claires d'épaisseur millimétrique à centimétrique (**Figure III.1C**). L'échantillon 00AU40 est un chert hétérolithique composé de couches claires alternant avec des couches foncées et présentant des structures sédimentaires (micro-ondulations, flaser-linsen et stratifications ondulées) caractéristiques du dépôt des sédiments dans un chenal peu profond influencé par les marées (**Figure III.1D**).

L'analyse pétrologique de l'échantillon 00AU37b montre une texture vitreuse et lisse dans laquelle des veines millimétriques composées de quartz microcristallin s'étendent à travers une matrice de chert foncée (**Figure III.2**). Les échantillons 00AU39 et 00AU40 comportent des protolithes volcaniques qui ont été remplacés par de l'hydromuscovite et des oxydes de titane et sont entourés d'une matrice de quartz microlithique. Des veines de silice micrométriques à millimétriques recoupent également ces échantillons (**Figure III.5**). En particulier, l'échantillon 00AU39 est constitué de galets foncés composés de particules de poussières volcanique fines entourées par des couches claires plus grossières comportant les protolithes volcaniques (**Figure III.3**). L'échantillon 00AU40 est constitué de lamines claires composées de particules volcaniques grossières alternant avec des lamines foncées composées de poussières volcaniques fines, entre lesquelles est intercalé un dépôt subaérien de pierres ponces centimétriques (**Figure III.4**).

L'analyse minéralogique des échantillons 00AU39 et 00AU40 a permis d'identifier les protolithes comme étant des verres volcaniques, des pierres ponces, des feldspaths, des amphiboles (ou pyroxènes) et des fragments de roches volcaniques de natures diverses (**Figure III.6, Tableau III.1**). Ces protolithes ont subi une altération morphologique par laquelle des processus mécaniques et de corrosion ont altéré les bordures des grains volcaniques et/ou une altération minéralogique par laquelle les minéraux primaires ont été remplacés chimiquement par des minéraux secondaires. Un mélange de poussières volcaniques fines et de quartz microcristallin a également été identifié dans les échantillons de roches, qui apparaissent sous forme de galets foncés dans l'échantillon 00AU39 et de lamines foncées dans l'échantillon 00AU40 (**Figure III.6, Tableau III.1**).

L'analyse géochimique en XRF des échantillons 00AU39 et 00AU40 ont confirmé que les protolithes volcaniques ont été remplacés par de l'hydromuscovite et des oxydes de titane comme l'indique une composition riche en potassium et en titane, respectivement, auxquels sont associés des métaux de transition (V, Cr, Mn, Fe, Zn… ; **Figures III.7 et III.8**). Les analyses ICP-OES des poudres de roches vont dans le même sens et confirment la nature argileuse des grains volcaniques qui sont constituées de moins de 5 % d'aluminium et de moins de 2 % de potassium pour une teneur en silice estimée à 90–95 % (silicification des grains ; **Figure III.9A**), tandis que les analyses de la poudre de l'échantillon

00AU37b révèle une composition presque pure en silice (> 99 %). D'après les analyses ICP-MS, les sédiments volcaniques de l'échantillon 00AU40 sont plus riches en métaux de transition et proviennent d'une source ultramafique, tandis que les sédiments volcaniques de l'échantillon 00AU39 sont issus d'une source mixte (**Figure III.9B, C**). La comparaison des concentrations en éléments majeurs et traces dans les échantillons avec celles de la croûte terrestre révèle que la plupart des éléments sont généralement appauvris dans les échantillons, sauf Ba et Sb (**Annexe A, Tableau A5**). L'analyse des terres rares à l'échelle globale (ICP-MS) montre des profils REE + Y légèrement enrichis en HREE (légère influence marine), des ratios Y/Ho sub-chondritiques, des anomalies en Ce légèrement négatives à négligeables, des anomalies en Eu positives et des anomalies en La, Y et Gd négligeables (**Figure III.9D, Tableau III.2**). L'analyse des terres rares à l'échelle locale (LA-ICP-MS) montre des variations des conditions géochimiques locales, c'est-à-dire des profils REE + Y indiquant une influence de l'eau de mer ou des rivières, des ratios Y/Ho sub-chondritiques à super-chondritiques, des anomalies en Ce majoritairement positives, des anomalies en Eu positives et des anomalies en La, Y et Gd variables (**Figure III.10, Tableau III.3**).

L'analyse morphologique de la matière carbonée à l'échelle microscopique montre que la matière carbonée se présente sous forme de films carbonés autour des clastes volcaniques, dont les spectres Raman associés montrent généralement deux bandes à 1350 et 1600 cm^{-1} qui correspondent, respectivement, au carbone amorphe et au carbone graphitique superposé avec du carbone amorphe (**Figure III.11, Tableau III.4**). Ces films carbonés sont souvent localisés autour des clastes volcaniques ayant subi une altération minéralogique et/ou morphologique, associés à l'hydromuscovite et à l'anatase, ou ayant complètement remplacés les protolithes volcaniques (e.g., **Figure III.6J, L, N**). Ils sont également omniprésents dans les poussières volcaniques (**Figure III.6Q–T**).

À une échelle plus fine (MEB), la matière carbonée prend la forme :
1) De particules finement disséminées ;
2) De films avec une texture grumeleuse ;
3) De particules arrondies ou irrégulières avec une texture lisse ;
4) De coccoïdes ;
5) De particules fibreuses avec une texture plissée.

Elle est souvent associée à de l'hydromuscovite en feuillets ou à texture rugueuse, plus rarement à des microcristaux d'anatase (**Figure III.12, Tableau III.4**).

L'analyse morphologique de la matière carbonée à l'échelle nanoscopique (MET) indique que la matière carbonée se présente sous forme :
1) De films ;
2) De particules sphériques à elliptiques ;
3) De structures allongées ;
4) De structures lenticulaires ;
5) De nuages diffus.

Elle est souvent associée à de l'hydromuscovite, en inclusions ou autour des microcristaux de feldspaths, ou bien localisée à la limite des polygones de quartz, plus rarement associée à des microcristaux d'anatase sur les bordures des grains volcaniques (**Figure III.13, Tableau III.4**). La matière carbonée montre également une structure amorphe (e.g., **Figure III.13B, F**) ou une structure graphitisée (ou structure en oignon), dont l'espace interréticulaire (2,3 å et 3,5 å) est typique du carbone graphite (**Figure III.14**).

L'analyse élémentaire des régions d'intérêt (XRF) a permis de montrer une colocalisation du potassium avec le fer et d'autres métaux de transition (Cr, Co, Ni, Cu…) qui sont associés à l'hydromuscovite et à la matière carbonée à l'intérieur des grains volcaniques (**Figures III.15 et III.16**). De la même façon, le titane, le vanadium et le tungstène sont colocalisés et associés à l'anatase et à de l'éventuelle matière carbonée à l'intérieur et/ou aux bordures des grains volcaniques (**Figures III.15 et III.16**). La matrice et les verres volcaniques (sans matière carbonée) sont généralement appauvris en tous les éléments (sauf en Cu), tandis que les feldspaths et les fragments de roches volcaniques de natures diverses recouverts de matière carbonée sont enrichis en plusieurs éléments (K, Ca, Cr, Mn…) par rapport à la matrice adjacente (**Figures III.17C–E et III.18C, E**). Dans l'échantillon 00AU39, les pierres ponces recouvertes de matière carbonée sont enrichies en Ti, K, Fe, Ca, Ga et Cr par rapport à la matrice adjacente, tandis que dans l'échantillons 00AU40, les pierres ponces sans matière carbonée sont appauvries en presque tous les éléments (sauf en Cu et Ge) et leurs bordures sombres sont très enrichies en Ti et W (**Figures III.17E et III.18D**). Les bordures des verres volcaniques recouvertes de matière carbonée sont enrichies en de nombreux éléments par rapport à l'intérieur des verres et à la matrice adjacente, tandis que les bordures des fragments de roches volcaniques de natures diverses sont seulement enrichies en Ti (**Figures III.17C, D et III.18C**). Les zones de poussières, dont les zones de poussières claires dans l'échantillon 00AU40, sont généralement de composition argileuse et riches en métaux de transitions (Fe, Cu, Ti, Zn…), tandis que les zones de poussières sombres dans l'échantillon 00AU40 sont principalement enrichies en Ti (**Figures III.8 et III.17F**).

La comparaison des régions d'intérêt analysées au PIXE (**Annexe A, Tableau A1**) et de la roche globale analysée en ICP-OES/MS (**Annexe A, Tableau A5**) indique que les régions d'intérêt contenant les grains volcaniques sont comparables aux analyses globales et sont généralement enrichies en quartz (ca. 86–95 % de Si), hydromuscovite (ca. 2–8 % d'Al et ca. 1–6 % de K) et oxydes de titane (ca. 0,2–2 % de Ti), auxquels sont associés plusieurs métaux de transition (V, Cr, Fe, Co…). Les régions d'intérêt associées aux dépôts de poussières volcaniques dans l'échantillon 00AU39 montrent également un enrichissement en Si (ca. 95–97 %), K (ca. 1–2.5 %), Al (ca. 1–1.5 %) et Ti (ca. 0.2–0.4 %), tandis que la région d'intérêt comportant la veine de silice est principalement composée de Si (> 99 %). Dans l'échantillon 00AU39, les régions d'intérêt sont largement enrichies en Co par rapport à la roche globale. De plus, les régions d'intérêt comportant les grains volcaniques sont également enrichies en Nb, Ti, K et parfois d'autres éléments (Cr, Zr et Y) et celles comportant des poussières volcaniques sont enrichies en As, mais appauvries en Al. La région d'intérêt comportant la veine de silice est enrichie en Co et Ge, mais appauvrie en Ni, Fe et Cu par rapport à la roche globale 00AU37b (veine hydrothermale). Dans l'échantillon 00AU40, les régions d'intérêt montrent des concentrations en Co plus élevées que dans la roche globale, mais sont très appauvries en métaux de transition (Cu, Fe, Zn, Cr, Ni et Mo). Certaines régions d'intérêt sont également enrichies en Nb, Ti, As et Ge.

L'analyse élémentaire de la matière carbonée (PIXE) a permis d'identifier des enrichissements associés à la matière carbonée dans les clastes volcaniques. Dans l'échantillon 00AU39, la plupart des clastes volcaniques analysés sont enrichis en 9 éléments biofonctionnels (Cr, As, Mo, V, Fe… ; **Figures III.19 et III.20**) par rapport à la matrice adjacente, tandis que dans l'échantillon 00AU40, la plupart des clastes volcaniques sont enrichis en 8 éléments biofonctionnels (V, Cr, Zn, As, S… ; **Figures III.21 et III.22**). Dans l'échantillon 00AU39, la plupart des bordures des clastes volcaniques sont enrichis en seulement 6 éléments biofonctionnels (Ni, Cu, Mo, Cr…) par rapport à l'intérieur des clastes volcaniques (**Figures III.19 et III.20**), sauf la bordure des verres volcaniques qui est enrichie en 11 éléments biofonctionnels (Ni, Zn, Mo, Sr, Cu… ; **Figure III.19**), tandis que dans l'échantillon 00AU40, la plupart des bordures des clastes volcaniques sont enrichis en seulement 3 éléments biofonctionnels (P, Cu et Co ; **Figures III.21**

et III.22). De plus, les poussières volcaniques de l'échantillon 00AU39 sont enrichies en 11 éléments biofonctionnels (Ni, As, Zn, Cl, Cr…) par rapport à la moyenne des matrices.

L'analyse moléculaire de la matière carbonée a permis de démontrer sa composition en groupes fonctionnels aromatiques et aliphatiques. D'une part, les analyses DUV ont détecté des composés aromatiques qui sont souvent mélangés avec des phases minérales (**Figure III.23**). Les composés aromatiques ont été identifiés à 310 et 340 nm dans l'échantillon 00AU39, et à 340–345 nm dans l'échantillon 00AU40 (**Figures III.24 et III.25**). Des phases minérales (en particulier, l'hydromuscovite et l'anatase) ont également été identifiées à 415–420 nm avec des épaulements à 430–435 nm et 460–465 nm dans l'échantillon 00AU39, et à 410–415 nm avec de rares épaulements à 390 et 430 nm dans l'échantillon 00AU40 (**Figures III.24 et III.25**). D'autre part, les analyses FTIR ont détecté des composés aliphatiques à 2855, 2870, 2925 et 2960 cm^{-1} correspondants à des molécules comportant des CH_2 et des CH_3 (**Figure III.26**). D'autres composés ont également été identifiés dans la région des aromatiques (entre 1300 et 1800 cm^{-1}) comme des molécules CH_3, C–H, C–N, N–H, C=O ou COOH (**Figures III.27 et III.28**). L'échantillon 00AU40 montre généralement des bandes plus intenses dans la région des aliphatiques (entre 2800 et 3400 cm^{-1}) que l'échantillon 00AU39 qui montre en revanche des bandes plus intenses et plus diversifiées dans la région des aromatiques. Les verres volcaniques de l'échantillon 00AU39 sont riches en –OH avec un peu d'aromatiques (C–H), tandis que les verres volcaniques de l'échantillon 00AU40 sont plus riches en –OH associés à des concentrations plus importantes en aromatiques (C–H) avec un peu d'aliphatiques, mais sont peu enrichis en certains groupes fonctionnels (en particulier, ester >C=O). Les fragments de roches volcaniques de natures diverses de l'échantillon 00AU39 contiennent des concentrations élevées en aromatiques et des concentrations variables en aliphatiques et autres groupes fonctionnels (e.g., C=O, COOH) qui sont principalement localisés à l'intérieur des grains volcaniques (**Figure III.29**), tandis que les fragments de roches volcaniques de natures diverses de l'échantillon 00AU40 contiennent des concentrations variables en aromatiques, aliphatiques et autres groupes fonctionnels qui sont surtout localisés dans les bordures ou à l'intérieur des grains volcaniques (**Figure III.30**). Enfin, les poussières volcaniques de l'échantillon 00AU40 montrent un enrichissement spécifique en –OH et Si–O avec quelques hétérogénéités attribuées à des aromatiques, aliphatiques et autres groupes fonctionnels.

Chapter IV: Discussion

I. Paleoenvironmental reconstruction

Documentation of the paleodepositional environment of the silicified volcanic sediments of the Kitty's Gap Chert through sedimentology, petrology, mineralogy and geochemistry is of crucial importance in demonstrating habitability for microbial life. Contextualizing the regional and local paleoenvironment of potential biosignatures is a key first step to establishing their syngenicity and biogenicity, and may be used to evaluate the eventual influence of early diagenesis on biosignature preservation potential (e.g., Brasier et al., 2002).

Field observations, microscopic and spectroscopic analyses, and bulk and in situ geochemical data indicate that the environment of deposition was a volcano-sedimentary basin (de Vries, 2004; Westall et al., 2006a, 2011a; de Vries et al., 2010) dominated by the influence of seawater and, to a lesser extent, by hydrothermalism (Orberger et al., 2006). The samples were extracted from a sedimentary lens characteristic of well-developed channel-filling features and lateral accretionary bedding indicative of regular flooding and sand deposition (**Figs. II.4 and III.1**; de Vries, 2004; de Vries et al., 2010). Primary sedimentary structures observed throughout the sedimentary lens, in particular, micro-ripples, flaser-linsen bedding and undulating lamination occurring at the top (of which the chert sample 00AU40 is part), reflect the deposition of sediments under shallow water conditions, in a channel environment influenced by tides (**Fig. III.1D**; de Vries, 2004; Westall et al., 2006a; de Vries et al., 2010). The orientation of pebbles and current ripples observed in samples 00AU39 and 00AU40 indicates varying and bimodal current directions, which provide additional evidence of a tidal environment (Orberger et al., 2006; de Vries et al., 2010). The preservation of these diverse sedimentary structures (channels, flaser-linsen bedding and bimodal current directions) suggests that silicification occurred during rock formation, at the water-sediment interface (Orberger et al., 2006).

The Kitty's Gap Chert was influenced by hydrothermal activity, as indicated by micro- to macro-scale veining, brecciation and hydrothermal minerals (**Figs. III.2–5**). Brecciation is the process of transforming pre-existing rocks into breccia (see Jébrak, 1997 for a review of the main brecciation mechanisms in hydrothermal deposits). The observation of breccias in the sample 00AU37 (**Fig. III.1B**) is probably explained by an increase in pressure of hydrothermal fluids in the rock which contributed to the fracturing of the sediments into coarse breccias (e.g., Cas et al., 2011). The hydrothermal vein extracted from this conglomerate (sample 00AU37b) exhibits a smooth, glassy texture where millimeter light veins are composed of microcrystalline quartz and traverse a homogenous black chert matrix (**Fig. III.2**). Silica veins in sample 00AU39 are composed of coarse-grained quartz and are lined with flakes of sericite, a very fine-grained variety of muscovite that is a secondary alteration mineral formed under slightly acidic conditions (**Fig. III.5**; Orberger et al., 2006). A barite crystal was found in this sample, suggesting that it could be a primary barite crystal formed through hydrothermal activity or a replacement product of gypsum, as proposed by de Vries et al. (2010). The notable enrichment of Ba in bulk samples compared to the Earth's crust further indicates that Ba-rich minerals (such as barite, witherite…), provided by hydrothermal fluids, could be widespread in the rock samples. A tourmaline crystal was identified in sample 00AU40 (**Fig. 6G, H**), a common mineral in hydrothermal settings (e.g., Slack et al., 1996), and containing hydromuscovite that may have replaced primary minerals, such as plagioclase and K-feldspar (Orberger et al., 2006; Yang et al., 2015).

Despite their similar microlithic textures, samples 00AU39 and 00AU40 exhibit different sedimentary structures. Sample 00AU39, from close to the hydrothermal vein, comprises homogenous dark pebbles of fine volcanic dust (<20 μm) mixed with silica, surrounded by a coarse-grained material consisting of poorly sorted volcanic particles (50–500 μm; **Fig. III.3**). The pebbles were probably eroded from a chemical deposit of lightly consolidated silica gel and volcanic dust by more energetic conditions (waves, tides, or the injection of hydrothermal fluids and gases connected to the active volcanic system) during the deposition of the lower layers of the sediments (de Vries et al., 2010). Sample 00AU40, taken from an overlying sedimentary layer further away from the hydrothermal system, exhibits a lower part characterized by cross- and flaser-linsen bedding indicating wave and tidal reworking. This is separated by an intraformational erosional horizon, containing embedded centimeter-size pumice fragments reflecting explosive volcanism, from overlying parallel laminations of sandy ash fall, alternating with layers of fine volcanic dust mixed with silica gel that formed in a dynamically quiet environment (**Fig. III.4**; Westall et al., 2006a, 2011a).

The composition of the protoliths (volcanic glass, pumice, feldspars, amphiboles, etc.; **Fig. III.6**), is interpreted as a result of the erosion of the underlying and surrounding volcanic rocks and ashfall, with subsequent rapid alteration to hydromuscovite and anatase during diagenesis, as well as intense silicification during both deposition and the initial stages of diagenesis (**Figs. III.7, 8; Table III.1**; Orberger et al., 2006; Westall et al., 2006a, 2011a). However, the composition of the volcanic protoliths of the sediments differs between the samples. In sample 00AU40, obtained from sediments slightly stratigraphically higher than 00AU39, the volcanic sediments predominantly result from the weathering of mafic (basaltic) volcanogenic substrates. In contrast, the sediments in sample 00AU39 originate from a mix of mafic and felsic materials, as evidenced by Cr/V vs. Y/Ni plots (**Fig. III.9C**). Weathering of the underlying rhyolitic lavas would have contributed to the lower layers of the sedimentary pile. The mafic to ultramafic origin of the sediments in 00AU40 is further supported by their enrichment in transition metals, including V, Cr, Mn, Fe, Co, Ni, Cu, Zn, Mo and W, relative to 00AU39 (**Fig. III.9B**).

Rare-earth elements plus yttrium (REE + Y) plots normalized to MuQ are appropriate methods by which the relative contributions of different chemical fluid reservoirs to Archean sediments may be distinguished (Bau and Dulski, 1996; Kamber et al., 2005; Gourcerol et al., 2015). Bulk analyses of the Kitty's Gap Chert (**Fig. III.9D; Table III.2**) show an overall continental signature as demonstrated by the sub-chondritic Y/Ho ratios of the three samples and the relatively elevated LREE concentration of sample 00AU39, although slight enrichment in HREE over LREE indicates that there were also marine inputs. However, the anomalies in La, Y and Gd, diagnostic for derivation from open marine waters are often negligible, which is consistent with deposition in semi-restricted conditions where inputs from continental weathering with high REE + Y concentrations dilute anomaly magnitudes (Bau, 1999; Kato and Nakamura, 2003; Bolhar et al., 2015; Gourcerol et al., 2016). Slightly negative Ce anomalies in samples 00AU37b and 00AU39 imply very mildly oxidizing conditions. Eu positive anomalies in all samples record the global hydrothermal influence that is typical for the Paleoarchean.

In situ analyses carried out in samples 00AU39-1, 00AU39-2 and 00AU40-1 (**Fig. III.10; Table III.3**) are generally similar to those of the bulk analyses, although small-scale variations depending on the areas of interest analyzed were also identified. In particular:

- The silica matrix of samples 00AU39-1 and 00AU39-2 (and dark grain of sample 00AU39-2) are enriched in LREE over HREE, reflecting a terrigenous input, whereas the silica-dust gel matrix and silica veins show a typical seawater pattern (HREE > LREE);

- Different laminations in sample 00AU40-1 show variations between dominantly continental (LREE > HREE) and marine (HREE > LREE) deposition;
- Y/Ho ratios vary from sub-chondritic to super-chondritic in all samples, most of which are closer to the sub-chondritic values of bulk samples that are indicative of non-marine input, i.e., these may have been sourced from either the hydrothermal vein or continental input from riverine flux into the tidal channel;
- Ce anomalies are slightly positive in most analyses, implying anoxic water that is consistent with the anoxic seawater during the Archean (Kasting, 1991), while only a few have very strong negative Ce anomalies (in particular the dark grain and silica vein of sample 00AU39-2, and the pumice fragment of sample 00AU40-1), that is characteristic of oxidizing conditions (alkaline pH) that may arise from the radiolysis of H_2O in the very shallow environment, as well as phase separation of hydrothermal fluids under high pressure exiting in the shallow environment (Nakamura and Takai, 2014);
- La and Y anomalies range from negative to positive in most analyses, except the silica vein in sample 00AU39-2 with strongly negative La and Y anomalies;
- Gd anomalies are variable between the samples, ranging from negative to positive in samples 00AU39-1 and 00AU39-2 (except the silica vein in 00AU39-2 with strong Gd negative anomaly), and slightly negative in sample 00AU40-1 (including two structures without Gd anomaly).
- Despite the overall global hydrothermal Eu signal, Sm/Yb vs. Eu/Sm suggest weak hydrothermal influence for all analyses (bulk and local), except the silica vein of sample 00AU39-1 with a higher hydrothermal influence;
- $(Pr/Nd)_{MuQ}$ vs. Y/Ho suggests a relatively strong continental influence for most analyses (bulk and local), although the sample 00AU40-1 shows a greater influence by seawater.

It is possible to compare the Kitty's Gap Chert to those formed elsewhere in the Pilbara or Barberton Greenstone Belts. For example, the volcaniclastic and siliciclastic sediments of the member 4 cherts from the 3.45 Ga Strelley Pool Formation (Pilbara, Australia) have slightly different geochemical characteristics in that they do not show enrichment in LREE or HREE, but exhibit instead a strong positive Eu anomaly and a weak negative Y anomaly, suggesting that the chert likely precipitated from fluids of mixed marine-hydrothermal influence (Allwood et al., 2010).

Cherts from the Paleoarchean Barberton Greenstone Belt (South Africa) analyzed by Hickman-Lewis et al. (2020a) generally show an enrichment in HREE relative to LREE (their Fig. 6), except for the Footbridge chert which shows a strong enrichment in LREE relative to HREE (including one sample with a strong enrichment in MREE, suggesting a volcanogenic influence). The chondritic Y/Ho values, positive Eu anomalies and weak La and Y anomalies in the Middle Marker, Hooggenoeg and Footbridge cherts denote precipitation influenced by non-marine inputs, where the Eu anomaly indicates a hydrothermal origin of the fluids (their Fig. 7). Although the Josefsdal chert shows super-chondritic Y/Ho ratios (marine contribution), the high LREE concentrations also indicate a strong terrigenous contribution. In these samples, anomalies in Ce are often negligible. In situ analyses were also carried out in the same cherts, specifically within microbial mat horizons, to assess fine-scales changes in REE + Y composition during periods of microbial colonization. The main findings include the following: Y/Ho ratios increase from chondritic (~15–30) below the mat-bearing horizons to superchondritic values within (~25–50), before decreasing to chondritic values above the microbial mats; La and Y anomalies tend to be more positive in microbial mat horizons, suggesting increased marine influence; Ce anomalies typically increase in microbial mat horizons, implying the prevalence of anoxic conditions; Eu anomalies are often negative throughout microbial mat horizons, in contrast to bulk analyses (their Fig. 8).

These comparisons indicate that the sediments formed in different locations at slightly different times during the Paleoarchean recorded different environmental characteristics.

Figure IV.1 illustrates a diagram of a paragenetic sequence that outlines the main stages of deposition and subsequent alterations of the volcanic sediments of the Kitty's Gap Chert. These processes involve interactions with seawater, hydrothermal fluids, organic matter, diagenesis, and regional metamorphism.

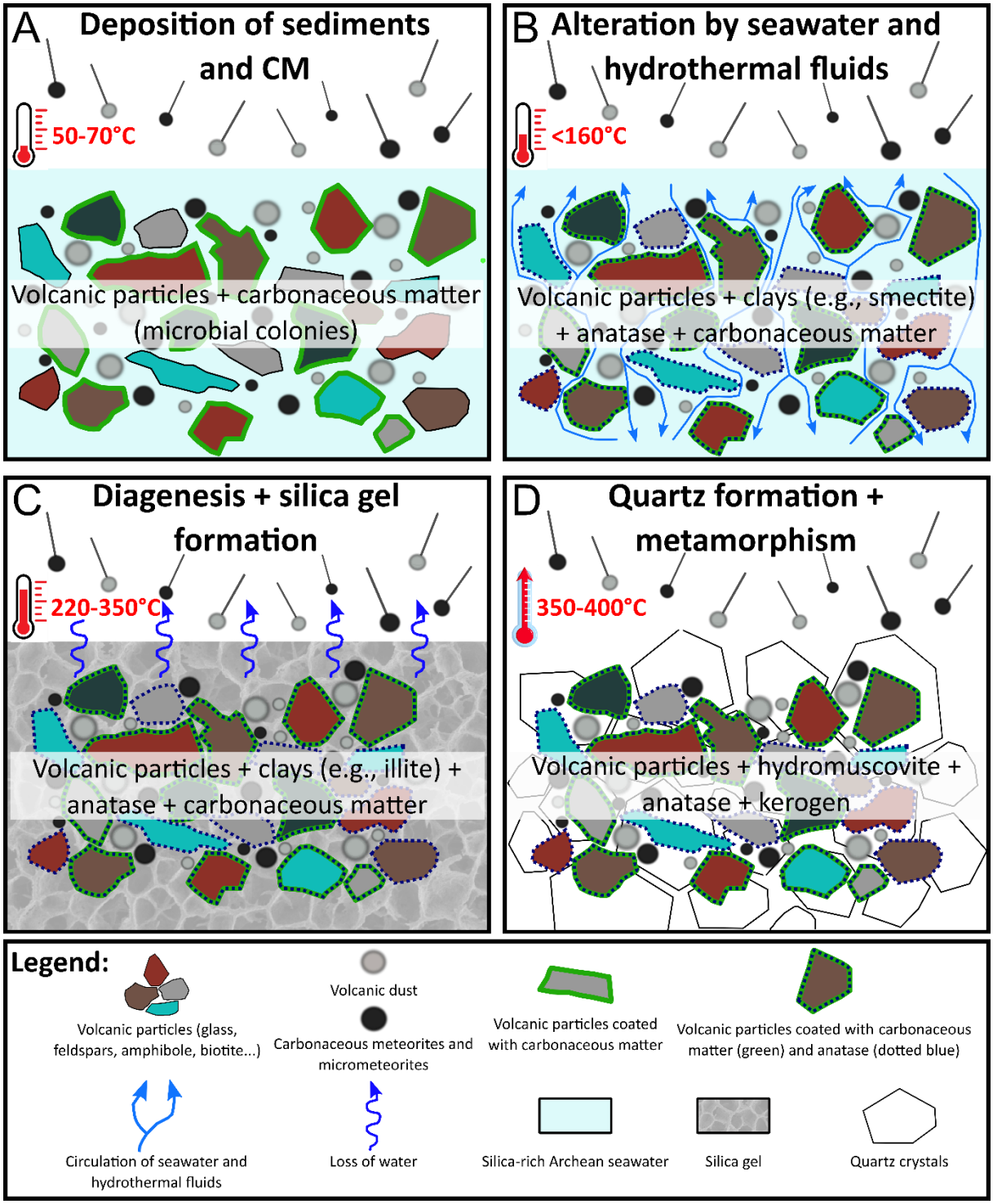

Figure IV.1: *Diagram illustrating the paragenetic sequence in the volcanic sediments of the Kitty's Gap Chert. (**A**) Volcanic particles and fine volcanic dust were deposited by rivers and volcanic eruptions, respectively, onto a beach regularly flooded by seawater. In addition, carbonaceous matter (CM) was incorporated into the volcanic sediments mainly through colonization by microorganisms (although other sources of abiotic carbon, such as carbonaceous meteorites and micrometeorites, or the mantle, were also possible). Microbial colonies coated the volcanic particles and intermixed with the volcanic dust (not shown here), the whole being increasingly silicified through impregnation by the silica-rich seawater. (**B**) The volcanic sediments were then altered by seawater and hydrothermal fluids, which seep into the pore spaces between the volcanic particles. Volcanic particles were altered to clays (smectite; Wilson, 2004; Fulignati, 2020) and titanium oxides (anatase) formed around the volcanic particles, the Ti being released form precursor minerals, such as biotite or feldspars (Orberger et al., 2006; Westall et al., 2006a; Sirantoine et al., 2021). Microorganisms probably played a role in the alteration of these particles during early diagenesis. (**C**) During diagenesis, the sediments were compacted, causing the loss of water. The volcanic particles experienced mineralogical alterations, especially the transformation of smectite to illite that occurs at temperatures of ca. 220–350°C (Fulignati, 2020). Additionally, the silica from the supersatured Paleoarchean seawater precipitated, leading to the formation of a silica gel (cement) between volcanic particles (e.g., Ledevin et al., 2019). (**D**) The polymerization of the silica gel formed a microcrystalline quartz matrix surrounding the volcanic particles. Illite was transformed into hydromuscovite (Orberger et al., 2006; Westall et al., 2006a). Later (around 3.2 Ga), the sediments underwent regional greenschist metamorphism (Wijbrans and McDougall, 1987) which contributed to the transformation of organic molecules into aromatic, refractory molecules (kerogen). The phyllosilicates (smectite, illite and hydromuscovite) are not shown in this illustration. However, they are typically intermixed with the volcanic particles and dust, forming thin sheet layers. The silica gel image displayed in (**C**) is a cryoSEM image of silica hydrogel prepared by Dass et al. (2018) from a mixture of sodium silicate and acetic acid solutions; the pore size is around 2 µm.*

The results of sedimentological, petrological, mineralogical and geochemical analyzes to characterize the depositional paleoenvironment of the silicified volcanic sediments of the Kitty's Gap Chert are summarized in **Table IV.1**.

Table IV.1: *Summary of the characteristics of the depositional paleoenvironment of the silicified volcanic sediments of the Kitty's Gap Chert.*

	00AU39 (close to hydrothermal vein, lowermost sedimentary layer)	00AU40 (further from hydrothermal vein, overlying sedimentary layer)
Sedimentology (Hand sample description)	• Silicified volcaniclastic sediments located in a lenticular structure • Conglomerate composed of fine dark pebbles in a sandy matrix • Orientation of pebbles toward the east-northeast	• Heterolithic chert composed of finer dark and coarser light laminations • Sedimentary structures such as micro-ripples and flaser-linsen bedding typical of a shallow water, channel environment influenced by tides • Orientation of current ripples towards the west
Petrology (Hand sample description, optical and XRF)	• Volcanic protoliths embedded in a microlithic matrix • Homogeneous dark pebbles composed of fine dust particles <20 µm in size mixed with silica and rare protoliths, surrounded by light-colored sandy material composed of volcanic protoliths of 50–500 µm in size replaced by silica and hydromuscovite • Silica veins from <100 µm up to a few millimeters crossing the sample, and consisting of coarse-grained quartz and flakes of sericite lining the veins	• Cross-bedded, sandy volcanic sediments overlain by parallel-bedded ashfall comprising coarse, light-colored laminations of 50–500 µm volcanic protoliths replaced by silica and hydromuscovite, alternating with darker, fine-grained volcanic dust-silica gel-rich layers • These layers are separated by a subaerial deposit composed of rounded pumice fragments of >1 cm • Silica veins from <100 µm up to a few millimeters crossing the chert sample
Mineralogy (Optical and Raman)	• Identified volcanic protoliths include volcanic glass, pumice, feldspars, amphiboles (or pyroxenes), and multiphase volcanic rock fragments • In addition to the volcanic grains, silica-dust gel composed of microcrystalline quartz and fine-grained volcanic dust occurs as dark pebbles • A barite crystal associated with pyrite was also observed	• In addition to the volcanic grains, silica-dust gel composed of microcrystalline quartz and fine-grained volcanic dust occurs as dark laminations, including silica spherules • A tourmaline crystal was also observed
Geochemistry (XRF)	• Light layers are enriched in volcanic protoliths replaced diagenetically by hydromuscovite (K) and titanium oxides (Ti), and are associated with diverse transition metals (V, Cr, Fe, Zn…)	• Light layers are enriched in volcanic protoliths replaced diagenetically by hydromuscovite (K) and titanium oxides (Ti), and are associated with diverse transition metals (Cr, Mn, Fe, Zn…)
Geochemistry (ICP-OES/MS and LA-ICP-MS)	• The samples are mostly composed of SiO_2 (90–95%), Al_2O_3 (<5%) and K_2O (<2%) • Sample 00AU39 is less enriched in transition metals than sample 00AU40 • Cr/V vs. Y/Ni indicates mixed sources (mafic and felsic) for the origin of volcanic sediments • Identification of a moderately strong seawater pattern with a slight enrichment in HREE over LREE (+ slight enrichment in LREE), sub-chondritic Y/Ho ratio, slight negative Ce anomaly, positive Eu anomaly, and negligible La, Y and Gd anomalies in bulk sample • In situ analyses indicate typical seawater and continental patterns, sub-chondritic to super-chondritic ratios, mostly slight positive Ce anomalies (rare strong negative Ce anomalies in a few analyses), positive Eu anomalies, and negative to positive La, Y and Gd anomalies	• Sample 00AU40 is more enriched in transition metals (V, Cr, Mn, Fe, Co, Ni, Cu, Zn…) compared to sample 00AU39 • Cr/V vs. Y/Ni indicates an ultramafic source for the origin of volcanic sediments • Identification of a moderately strong seawater pattern with a slight enrichment in HREE over LREE, sub-chondritic Y/Ho ratio, negligible Ce anomaly, positive Eu anomaly, and negligible La, Y and Gd anomalies in bulk sample • In situ analyses indicate typical seawater and continental patterns, sub-chondritic to super-chondritic ratios, mostly slight positive Ce anomalies (strong negative Ce anomaly in the pumice), positive Eu anomalies, and negative to positive La, Y and Gd anomalies

II. Demonstration of syngenicity and biogenicity of the carbonaceous matter

Westall et al., (2006a) documented different modes of occurrence of carbonaceous matter in the Kitty's Gap Chert. In addition to those associated with the purported microfossils, they identified detrital carbonaceous fragments comprising: 1) amorphous oval to subrounded grains up to 10 µm in size that, at times, incorporated small, submicrometric-scale, mineral particles (Westall et al., 2006a, their Fig. 4A); and 2) fragments of fibrous organic matter with attached, ribbed filaments (Westall et al., 2006a, their Fig. 4D), similar to other unattached ribbed filaments occurring in the same sample (Westall et al., 2006a, their Fig. 7). The latter were interpreted as detrital fragments of phototrophic microbial mats formed in the vicinity of the infilling tidal channel and broken up by mechanical processes during tides and/or storms. Raman analyses show that the bulk carbonaceous matter (kerogen) has a mature signature consistent with the metamorphic grade of the rock and is therefore syngenetic with sediment formation. Stepped combustion documented $\delta^{13}C$ values of –25.9 to –27.8 ‰ consistent with microbial fractionation.

In addition to this morphological and organo-geochemical evidence for potential microbial life forms (Westall et al., 2006a, 2011a), the characterization of the carbonaceous matter in silicified volcanic sediments of the Kitty's Gap Chert through in situ physical and geochemical analyses, as well as its distribution at multiple scales, is essential for identifying biosignatures and evaluating its syngenicity and biogenicity.

A. Demonstration of the syngenicity of the carbonaceous matter

The Kitty's Gap Chert was rapidly silicified, thereby preserving the morphological and geochemical characteristics of the carbonaceous matter with high fidelity (Westall et al., 2006a, 2011a, 2015b). Westall et al. (2006a) observed carbonaceous coccoidal structures interpreted as the microbial remains of chemolithotrophs in these horizons. Chemolithotrophic microorganisms use energy from redox reactions at the surface of rocks and minerals for their metabolism, and are therefore obliged to form epilithic (i.e., surface-attached) colonies over the surface of lithic particles (Nakamura and Takai, 2014), which degrade during diagenesis and metamorphism, rendering the organic matter kerogenous (Beyssac et al., 2002a, 2002b; Foucher et al., 2015). Raman spectra of carbonaceous matter in the studied samples show that it has undergone some graphitization, but is mostly amorphous, as indicated by the more intense D1 (disordered carbon) relative to the G+D2 (graphite and disordered carbon) band, despite some specific locations showing a more intense G+D2 band (**Fig. III.11E**; Foucher et al., 2015). The thermal maturity (300–400°C) of the carbonaceous matter is similar to that of the host rock (Kisch and Nijman, 2004), strongly supporting its syngenicity (Westall et al., 2006a, 2011a; Foucher et al., 2015). Raman maps documented the distribution of the carbonaceous matter, which is localized on the surface of the volcanic grains and in the silica-dust gel matrix (**Figs. III.6 and III.11A–D; Table III.4**). More precisely, I found that carbonaceous matter is preferentially associated with volcanic grains that have undergone the greatest degree of alteration, either mechanical alteration (grains with increasingly rounded edges), and/or mineralogical alteration (grains replaced by hydromuscovite and anatase), as well as in smaller quantities on some of the less altered volcanic grains. The direct association of the carbonaceous matter with both the particles, their surfaces, and the silica-dust gel matrix, as well as its mature Raman signature, demonstrates that it formed at the same time as the original sediments and is, therefore, syngenetic. Furthermore, no evidence for secondary mobilization of carbonaceous materials, either through fractures and along planes of weakness in the rock (Rasmussen et al., 2021), or through pyrobitumen formation processes (Rasmussen and Buick, 2000), has been identified in any studied samples.

The carbonaceous matter around volcanic grains may represent either a macromolecular conditioning film made up of organic macromolecules of biological origin (e.g., proteins or exopolymers) that were adsorbed onto the surface of volcanic grains after a few minutes of immersion (Jain and Bhosle, 2009), or epilithic microbial biofilms composed of silicified coccoidal microorganisms embedded in an exopolymeric monolayer on the surface of volcanic minerals (Westall et al., 2006a, 2011a, 2015b). The colonization of volcanic substrates (rocks and dust) by microbes provides them with advantageous protection against challenging external conditions (UV, abrasion by water, wind, etc.) by creating micro-environments favorable to the survival and development of certain microbial communities (Westall et al., 2011a, 2015b; Dong et al., 2022). Minerals are also crucial sources of nutrients, including bioessential elements (Fe, P, S, Mg, Ca…) and trace metals (Mo, Ni, Cu…) needed for microbial growth and metabolism, while also acting as sources of energy by serving as electron acceptor/donors and electrical conductors to facilitate extracellular electron transfer for chemolithotrophic microorganisms (Westall et al., 2011a, 2015b; Dong et al., 2022). Volcanic dust (<20 µm), notably, presents a greater surface area than coarser volcanic grains (>50 µm), making energy and nutrients more readily accessible to microorganisms. Small colonies of interpreted fossil microbes and EPS are common in the silica-dust gel, which is also an environment favorable for the preservation of microbial matter (Westall et al., 2015a; McMahon et al., 2018), thus explaining the ubiquity of the carbonaceous matter.

B. Demonstration of the biogenicity of the carbonaceous matter

1. Correlation of observations of the carbonaceous matter using SEM/TEM with optical microscopy

- *Morphology of the carbonaceous matter:*

The carbonaceous matter presents various morphologies at the submicroscopic and nanoscopic scales in SEM and TEM, respectively (**Table III.4**).

Several structures of carbonaceous matter have been observed in SEM in the form of: 1) finely disseminated; 2) filmy with a lumpy texture; 3) rounded to irregular with a smooth texture; 4) coccoidal; and 5) fibrous with a wrinkled texture. Based on the previous SEM observations by Westall et al. (2006a, 2011a) and other datasets presented here (**Fig. IV.2**), I was able to interpret the potential origins of some of these structures. Finely disseminated structures (**Fig. III.12A, B, E, G**) are commonly found intermixed with hydromuscovite and probably represent the adsorption of small organic molecules onto the surface and between the interlayer regions of hydromuscovite, which can form weak bonds with the surface of hydromuscovite (Summons et al., 2011; Keil and Mayer, 2014). The filmy structures with a lumpy texture lining cavities (**Fig. III.12C**) may represent degraded microbial matter including EPS, which consist mainly of polysaccharides in which colonies of microbes can be embedded (**Fig. IV.2B–E**), and are similar to those observed by Westall et al. (2006a, 2011a). These polymers are able to be preserved because of their open structure which allows fluids saturated with dissolved minerals ions to attach to the functional groups of the molecules (Westall et al., 2000). EPS are therefore generally more often fossilized than microbial cells (as demonstrated by Orange et al., 2009), explaining why the fossilized EPS are more frequently observed than fossil microbial cells in this study and in the fossil record in general. The rounded to irregular carbonaceous structures with a smooth texture (**Fig. III.12D**) could correspond to detrital carbonaceous particles of abiogenic origin (**Fig. IV.2A**), including those having an angular shape indicating that they come from a local source (Westall et al., 2006a). The coccoidal structures (**Fig. III.12E, F**) could represent possible coccoidal microfossils similar to those observed by Westall et al. (2006a, 2011a), with the size (0.35–0.4 µm in

diameter) and shape that are consistent with microbial cells (**Fig. IV.2B–E**). In addition, they are distributed around the edges of the volcanic clasts. However, they could also be abiotic biomorphs formed in aqueous solutions where interactions between minerals and organic molecules produce organic spheres similar to those obtained by Criouet et al. (2021; **Fig. I.9G**), although the experimental conditions of their study (200°C, ca. 15 bars) are different from the paleoenvironmental conditions of the Kitty's Gap sediments. The fibrous structures with a wrinkled texture (**Fig. III.12G, H**) are similar to the detrital fibrous, carbonaceous particles observed by Westall et al. (2006a, 2011a) and were interpreted as torn-up mat fragments.

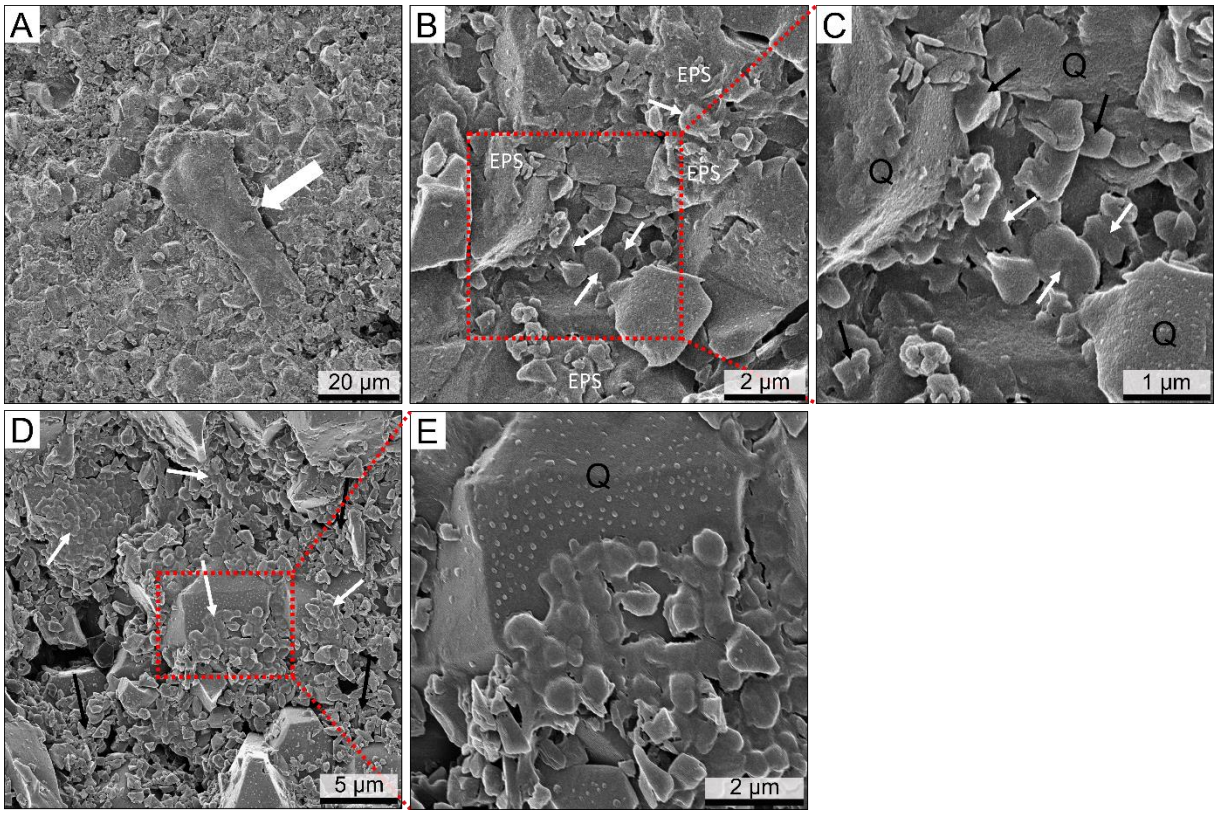

Figure IV.2: *Helium ion microscopy (HIM) micrographs of carbonaceous structures in the sediments of the Kitty's Gap Chert. (**A**) Large (>50 µm long) detrital particle of solid, angular carbonaceous matter embedded in the volcaniclastic sediments (white arrow). (**B**) Small associations (on the order of micrometers) of dispersed, dividing cells (white arrows) and associated EPS, interpreted as chemolithotrophic microorganisms, with red dotted box indicating the area corresponding to the image displayed in (**C**). (**C**) Slightly degraded cells (white arrows) and their associated EPS (see Westall et al., 2015b for further details of degraded cells in the Kitty's Gap sediments). For comparison, minute, angular volcanic dust particles trapped in the EPS matrix are highlighted with black arrows. (**D**) One of the rare areas in which a larger association (colony) of coccoids has been preserved, with white arrows showing locations of the coccoidal microfossils and black arrows the fine-grained volcanic dust-silica gel matrix comprising small, angular particles having the same dimensions (but not the same morphology) as the coccoidal cells. Red dotted box indicates the area corresponding to the image displayed in (**E**). (**E**) Slightly degraded cells embedded in EPS exhibiting cracks probably due to syneresis (i.e., expulsion of fluids from sediments or forms of soft material; e.g., EPS in this case, following the contraction of the silica gel under the effect of diagenesis). The nm sized blobs on the quartz crystal (Q) surface are gold particles from the coating process (the sample was first prepared in 2000 and it was necessary to renew the Au coating for the analyses presented herein). The HIM images were acquired*

on an etched rock slab in 2019 (data not published, courtesy of Frances Westall), using a Zeiss ORION NanoFab HIM in Faculty of Science, Agriculture & Engineering, Newcastle University, United Kingdom. The sample was observed in secondary electrons (iSE) mode, with a 25 keV energy beam, a 10 mm working distance, and a spatial resolution of <0.5 nm.

Other structures of carbonaceous matter have also been observed in TEM in the form of: 1) coatings around volcanic grains; 2) spherical to elliptical particles; 3) elongated structures; 4) lenticular structures; and 5) diffuse clouds. The coatings (**Fig. III.13A, C**) probably represent the carbonaceous films observed at a larger scale around volcanic clasts (see the section II.A. *Demonstration of the syngenicity of the carbonaceous matter*). However, abiotic carbonaceous films could theoretically also develop on aqueously submerged surfaces (e.g., in seawater, conditioning films of hydrocarbons are formed on surfaces within a few minutes of immersion). The elongated structures (**Fig. III.13E, F**) are probably the degraded remnants of EPS-rich microbial biofilms (**Fig. IV.2B–E**), similar to those observed by Westall et al. (2006a, 2011a). The lenticular structures (**Fig. III.13G**) are composed of iron minerals mixed with hydromuscovite, and are carbonaceous matter probably trapped between the quartz grains. The diffuse clouds (**Fig. III.13H**) exhibiting a brown color and irregular shape in optical microscopy (e.g., **Fig. III.6M**) probably represent highly degraded volcanic protoliths that were coated with microbial biomass. The spherical to elliptical particles (**Fig. III.13A, B, D**) are more intriguing. They could be "free-floating" detrital carbonaceous particles representing chemotrophic microbial biomass supplied with nutrients (such as Cr, Co, Ni and Cu) by the hydrothermal fluids, as identified by Westall et al. (2015b) in the Kitty's Gap and Josefsdal Cherts, or particles of insoluble carbonaceous matter similar to those found in interplanetary dust particles and meteorites (Westall et al., 2015b).

- *Crystallography of the carbonaceous matter:*

The carbonaceous matter in the Kitty's Chert presents two types of nanostructure: 1) amorphous carbon; and 2) crystallized (graphitized) carbon. Amorphous carbonaceous matter (e.g., **Fig. III.13F**) was identified in numerous different structures (coatings, spherical to elliptical particles, elongated, EPS-like matter and lenticular structures), whereas graphitized carbonaceous matter (**Fig. III.14**) was identified only in elliptical particles within the silica-dust gel matrix, where it presents an onion-shaped nanostructure. On the one hand, I hypothesize that the amorphous carbonaceous matter corresponds to the degraded remains of microorganisms in sediments. However, finely disseminated microbial remains may also be mixed with an abiotic carbonaceous matter derived from different sources (hydrothermal, meteoritic, atmospheric, etc.; Sephton, 2002; Lindsay et al., 2005; Ceburnis et al., 2011; Gourier et al., 2019). Given that there is a generally invisible background influx of extraterrestrial carbonaceous matter arriving continually on both Earth (Maurette et al., 2000; Maurette, 2006), and Mars (Eigenbrode et al., 2018), and that this influx is modelled to have been higher during the Hadean and Paleoarchean (Maurette, 2006), it is likely that a similar invisible extraterrestrial component is present in most terrestrial sediments. Mixing of this extraterrestrial component with sediments prior to silicification and metamorphism (300–400°C) would dilute the extraterrestrial signal, rendering it impossible to distinguish except in exceptional circumstances (e.g., Gourier et al., 2019).

On the other hand, the graphitized carbonaceous matter could have a different origin. Westall et al. (2006a; 2015b) noted carbonaceous fragments in the Kitty's Gap Chert that were clearly detrital in origin. Some of them have a filamentous aspect, with attached "floating" striated filaments that the authors interpreted as fragments of phototrophic microbial mats (their Fig. 4D). Others have a solid, subrounded appearance and were more resistant to erosion, suggesting a different origin (their Fig. 4A). It is possible that these solid, eroded, detrital particles are those observed here in TEM with an

onion-like nanostructure presenting a more graphitized texture, as evidenced by the measured interplanar distances of ca. 2.3 Å (**Fig. III.14B**) and 3.5 Å (**Fig. III.14D**) in carbonaceous matter, corresponding to graphitized carbon (Derenne et al., 2008). I hypothesize that these fragments might originate from the mantle, having experienced high temperatures (<1000°C; Mathez, 1987; Steele et al., 2012) and eroded from volcanic rocks, distinguishing them from surface-formed carbonaceous matter by other processes (e.g., biogenic). Alternatively, this hypothetical organic matter could be of biological origin, originating from older rocks subjected to higher thermal maturity before erosion. Subsequently, hydrothermal fluids could have mobilized and altered the organic matter before depositing it in the studied sediments, thus explaining its graphitized structure (van Zuilen et al., 2007). In such a scenario, differentiating between indigenous and exogenous organic matter could involve carbon or nitrogen isotopic measurements, with the latter exhibiting higher values due to the preferential loss of lighter isotopes during the thermal devolatilization of the rock (Thomazo et al., 2009).

- *Distribution of the carbonaceous matter:*

The submicroscopic carbonaceous matter is often associated with sheet-like or rough-textured hydromuscovite in altered volcanic protoliths (**Fig. III.12A–E, G**), or more rarely found associated with microcrystals of anatase at the edges of volcanic grains (**Fig. III.12F**). Similarly, the nanoscopic carbonaceous matter is mainly distributed as inclusions and coatings around microcrystals of feldspar (**Fig. III.13A, C, F**), intimately mixed with hydromuscovite sheets (ca. 10 Å and 20 Å interplanar distances between crystal planes), localized at the edges of microcrystalline quartz polygons (**Figs. III.13D, G and III.14A**), or more rarely found at the edges of volcanic grains associated with microcrystals of anatase. The association of carbonaceous matter and hydromuscovite is not surprising because phyllosilicates are known to play a role in preventing the degradation of organic matter due to intercalation within the interlayer spaces of phyllosilicates (Summons et al., 2011; Keil and Mayer, 2014). The presence of carbonaceous matter at the edges of the quartz polygons could be explained by the displacement of pre-existing organic matter (microbial biomass, for example) due to Ostwald ripening of the microcrystalline quartz during lithification of the silica cement (Hickman-Lewis et al., 2018, 2020c). Indeed, the quartz microcrystals present in the sediments of the Kitty's Gap Chert originated from silica resulting mainly from Paleoarchean seawater saturated with silica intermixed with pore water silica produced by devitrification of the volcanic detrital grains. The enriched porewater silica then polymerized to form a silica gel matrix cement around the volcanic grains before recrystallizing into quartz after diagenesis and then metamorphism (**Fig. IV.1**; Westall et al., 2023a). The ubiquitous presence of microcrystalline silica in the samples confirms the rapid and pervasive lithification of sediments as a mechanism for the preservation of organics.

- *Determination of the biogenicity of the observed structures:*

One outstanding issue is the fact that I was not able to identify the individual fossilized cells reported by Westall et al. (2006a, 2011a) by electronic microscopy. This may be due to a number of reasons. In particular, the SEM observations document a preponderance of generic EPS embedding the fine-grained volcanic dust-silica gel matrix (**Fig. IV.2B**) rather than actual cells (**Fig. IV.2C–E**). When present, the cells generally occur in very small groups of only a few individuals (**Fig. IV.2C**) covering an area of only a few square micrometers. Rarely, larger groups of cells up to ten or more square micrometers in areal extent are preserved (**Fig. IV.2D, E**). These associations are interpreted as mono-layers of cells, generally already slightly degraded (and flattened) when fossilized, resulting in thicknesses of a few 100 nm. Their sporadic distribution and subtle traces, often slightly displaced by the growth of

microcrystalline quartz, result in very thin layers of organic matter between quartz crystals, possibly similar to the structure shown in **Figure III.13D**. Furthermore, their diffuse distribution precludes detailed observations of carbonaceous structures in optical microscopy. Therefore, it is difficult to be certain that the accumulations of carbonaceous matter chosen for FIB preparation represents microbial biomass. These reflections underline the difficulties in determining the biogenicity of small and sporadically distributed microorganisms, such as these interpreted chemolithotrophs, and further investigations may be required to confirm the biogenicity of the carbonaceous matter.

2. Metallomics

Trace metal element enrichment in cells may reflect a combination of various processes, such as the selection of chemical elements for specific cellular needs (Fraústo Da Silva and Williams, 2001; Williams and Fraústo Da Silva, 2003), recovery and storage of elements in extracellular polymers as a response to toxicity (Czajka et al., 1997; Hickman-Lewis et al., 2019), or chelation of chemical elements to degraded organic components after the death of microbes (Gibson, 1984; Schultze-Lam et al., 1996; Orange et al., 2011). Metals are bio-essential to all life in various concentrations and fulfil diverse biological functions. Indeed, they operate as structural elements and catalytic centers in metalloproteins and metalloenzymes involved in virtually all cellular functions, including DNA and RNA synthesis, respiration and photosynthesis, electron transport and detoxification (e.g., Fraústo Da Silva and Williams, 2001; Williams and Fraústo Da Silva, 2003; Zerkle, 2005; Rickaby, 2015; Robbins et al., 2016; Moore et al., 2017). Under exceptional preservation conditions, such enrichments can be conserved in the preserved carbonaceous remains of cells and may be termed the paleo-metallome; the presence and relative concentrations of specific elements – both in isolation and in association – may be used to infer aspects of the metabolic landscape of the microbial biome (Hickman-Lewis et al., 2020c).

The detection of trace elements and mapping of their distribution using XRF and PIXE documented the presence of transition metals (V, Cr, Mn, Fe, Co, Ni…) and other elements (P, S, Cl, Ca…) of biological importance, associated with the carbonaceous matter in sedimentary rocks of the Kitty's Gap Chert.

- *Distribution and concentration of major and trace elements:*

XRF mapping of major and trace elements documented co-located distribution of some elements in local regions that contain the grains of interest enriched in carbonaceous matter (**Figs. III.15, 16**). In particular, potassium is commonly correlated with iron and other transition metals, such as Cr, Co, Ni, Cu, Zn and As in the interior of volcanic grains, associated with hydromuscovite and carbonaceous matter in both samples. Similarly, titanium is correlated with vanadium and tungsten in the interior and/or at the edges of volcanic grains, associated with anatase and possible carbonaceous matter. Generally, the silica matrix and volcanic glass fragments where carbonaceous matter was not detected with Raman spectroscopy are depleted in all elements (except for Cu) in both samples, while feldspars and multiphase volcanic rock fragments where carbonaceous matter was detected are highly enriched in many elements, in particular transition metals (Cr, Mn, Fe, Cu, Ni, Zn…) relative to the adjacent silica matrix (**Figs. III.17C–E and III.18C, E**). However, the carbon-coated edges of the volcanic glass fragments are enriched in many elements, in particular transition metals (Ti, Fe, Mn, Ni, Cu, Zn…) relative to their interior and the adjacent silica matrix, while those of the multiphase volcanic rock fragments are mainly enriched in Ti (**Figs. III.17C, D and III.18C**). The carbon-coated pumice fragments coated are enriched in Ti, K, Fe, Ca, Ga and Cr relative to the adjacent silica matrix in sample 00AU39, while the pumice fragments without carbon-coating are depleted in almost all elements (except for Cu

and Ge) in sample 00AU40 (**Figs. III.17E and III.18D**). These observations highlight an enrichment in transition metals associated to the carbon-coated interiors and edges of volcanic grains. In addition, the silica-dust gel matrix is enriched in several transition metals, such as Fe, Cu, Ti, Zn, V and Cr in both samples (**Fig. III.17F**), indicating possible enrichments in transition metals associated to carbonaceous matter that is ubiquitous in the fine-grained volcanic dust-silica gel matrix as demonstrated by Raman spectroscopy (e.g., **Fig. III.6T**).

- *Distribution and concentration of biofunctional elements:*

µPIXE quantification of biofunctional elements within specific structures of interest (volcanic clasts and their edges), as well as in the matrix surrounding the volcanic grain protoliths reveal specific local enrichments associated to the carbonaceous matter. Generally, most of the volcanic clasts where carbonaceous matter was detected with Raman spectroscopy are enriched in biofunctional elements with respect to the adjacent silica matrix (**Figs. III.19–22**). In particular, the volcanic clasts are enriched in P > Fe > Ca > Cr > S > V > Cl > Sr > Co > Mo > *As* > *Zn* > *Ni* > *Cu* in sample 00AU39, including 9 biofunctional elements (Cr, As, Mo, V, Fe, Sr, Zn, Co and Ca) that are more concentrated relative to the adjacent silica matrix, while they are enriched in Fe > P > Ca > V > S > Cr > Sr > Co > Mo > Cu > Zn > *As* > *Ni* in sample 00AU40, including 8 biofunctional elements (V, Cr, Zn, As, S, Mo, Ca and Fe) that are more concentrated relative to the adjacent silica matrix. However, I observed some variations depending on the degree of alteration of the volcanic clasts. The more altered and carbon-coated, multiphase volcanic rock fragments show more enrichment in many transition metals and other biofunctional elements than the less altered volcanic glass fragments in both samples, for instance. The edges of the volcanic clasts are more concentrated in only 6 biofunctional elements (Ni, Cu, Mo, Cr, S and Co) in sample 00AU39 and 3 biofunctional elements (P, Cu and Mo) in sample 00AU40 with respect to their interior. But, when the carbonaceous matter is localized preferentially at the edges of the volcanic clasts (none or little in their interior), the edges show enrichment in several biofunctional elements relative to their interior. For example, the carbon-coated edges of the volcanic glass fragments in sample 00AU39 are enriched in P, S, Ca, Fe, Co, Ni, Cu, Zn, As, Sr and Mo relative to their interior. When compared against the matrix, the carbonaceous matter-enriched silica-dust gel matrix shows enrichment in almost all the biofunctional elements (except V, Sr and Mo) in sample 00AU39. In general, trace elements such as Cr, V, As or Co are particularly enriched in the carbonaceous matter in both samples (**Figs. III.19 and III.21**), and their co-occurrence reinforces a potential biological origin (Hickman-Lewis et al., 2020c), while other trace elements such as P, Cl, Ca or Fe are probably mostly associated with hydromuscovite (Orberger et al., 2006). I note that phyllosilicates, featuring finely laminated structures and negatively charged surfaces, tend to attract and improve the preservation of organic matter (Summons et al., 2011); similar relationships between organic matter and phyllosilicates in the Kitty's Gap Chert (Westall et al., 2015b) can likely explain the association of phosphorus with phyllosilicates observed by Orberger et al. (2006).

- *Implication of biofunctional elements in metabolic processes of microorganisms:*

The Archean carbonaceous matter studied here recurrently concentrates a specific range of trace elements relevant to prokaryotic metallomes (Zerkle, 2005; Liermann et al., 2007; Dupont et al., 2010; Cameron et al., 2012; Rickaby, 2015), including V, Mn, Fe, Co, Ni, Cu, Zn, Mo and W, in both samples. This concurs with my hypothesis that elements required for the flourishing of prokaryotic life were present within the elemental budget of the local environment and suggests that elemental enrichments associated with the carbonaceous matter reflects the preserved metallomes of microbial cells that produced the carbonaceous matter in the Kitty's Gap samples.

Study of the biofunctional elements that constitute metallomes could potentially provide information on the possible metabolisms of microorganisms during the Paleoarchean. The range of $\delta^{13}C$ values (ca. between –26 and –28 ‰) obtained in the Kitty's Gap Chert by Westall et al. (2006a) is consistent with multiple metabolic processes, including co-existing sulfur and sulfate reduction, methanogenesis and anoxygenic photosynthesis. The essential transition metals used by prokaryotes generally follow: Fe >> Zn > Mn >> Co, Cu, Mo >> Ni > W, V (Zerkle, 2005). Iron is almost universally required by life, in particular for the transport of oxygen, the catalysis of electron transfer reactions, nitrogen fixation or DNA synthesis, and is involved in all of the metabolisms mentioned above (Zerkle, 2005; Jelen et al., 2016; Moore et al., 2017). The other transition metals (Zn, Co, Cu, Mo, Ni and V) are also essential for microbial life, in particular for metalloenzymes, and are required for the growth of some methanogens (in particular, Ni and Mo; Williams and Fraústo Da Silva, 2003; Zerkle, 2005; Jelen et al., 2016; Robbins et al., 2016; Moore et al., 2017). Despite their low bioavailability due to their insolubility in the reducing ocean (e.g., Zerkle, 2005; Dupont et al., 2010), copper, zinc and molybdenum could have been used by microorganisms in very low concentrations during the Archean, corroborating the measured concentrations with µPIXE. Specifically, molybdenum plays a crucial role in various essential enzymes, such as nitrogenase for nitrogen fixation (e.g., Robbins et al., 2016). Recent calculations suggest the presence of at least a few nanomoles per liter (nM) of dissolved molybdenum in Archean seawater (Johnson et al., 2021), potentially mobilized from hydrothermal sources (Evans et al., 2023). The incorporation of copper into the metallome seems to have begun during the Mesoarchean (3.2–2.8 Ga; Dupont et al., 2006; Rickaby, 2015) and its enrichment in carbonaceous matter likely results from non-specific binding by biomolecules as a response to its toxicity, a phenomenon observed in polysaccharides associated with contemporary microbes (Hickman-Lewis et al., 2019). Manganese and tungsten were not detected in the samples using µPIXE, but were well detected using XRF. Manganese serves as a catalyst in various redox reactions, including hydratation-dehydratation and phosphorylation-dephosphorylation (Zerkle, 2005; Moore et al., 2017). Its essential role in dioxygen production during photosynthesis indicates that its utilization likely begun around 3.0–2.45 Ma ago with the evolution of oxygenic photosynthesis (Zerkle, 2005; Moore et al., 2017). Tungsten is used as an electron source in methanogenesis and is interchangeable with molybdenum in key enzymes depending on their availability (Zerkle, 2005; Moore et al., 2017).

The other biofunctional elements are phosphorus and sulfur, which are part of the essential elements for all living organisms (CHNOPS), chlorine and calcium that are part of the essential cations for most living organisms, and chromium, arsenic and strontium, which are trace elements that can be used by some species (metabolisms based on Cr or As; Rickaby, 2015; Jelen et al., 2016; Robbins et al., 2016; Sforna et al., 2022). The localized presence of vanadium in association with other bio-functional elements may suggest the presence of nitrogen- or methane-cycling organisms, as proposed for similarly ancient carbonaceous materials in sediments from the Barberton Greenstone Belt (Hickman-Lewis et al., 2020c). However, I am aware of the ability of EPS with its plethora of functional groups to trap metals and cannot exclude the possibility of metal enrichment being due to this process, particularly seeing as chemolithotrophs are known to produce vast amounts of EPS (Orell et al., 2017; van Wolferen et al., 2018).

3. Molecular composition

The detection of organic molecules and mapping of their distribution using DUV fluorescence and FTIR documented the presence of aromatic and aliphatic organic compounds in sedimentary rocks of the Kitty’s Gap Chert. The stability of the lipid fraction of organic matter, attributed to its insolubility in

water, allows it to remain stable during diagenesis (Peters et al., 2005). Consequently, low-maturity organic materials have the potential to preserve DUV/IR spectral characteristics diagnostic of their precursor material (Igisu et al., 2009; Guido et al., 2012; Olcott Marshall and Marshall, 2015) even through low-grade metamorphism (Igisu et al., 2018).

- *Identification and distribution of aromatic organic molecules:*

In DUV fluorescence datasets, the presence of one- or two-ring aromatic organic compounds is suggested by the identification of fluorescent bands at 310 nm and 340–345 nm (**Figs. III.24C and III.25C**; Razzell Hollis et al., 2023; Sharma et al., 2023). I also identified other bands in the region ca. 400–500 nm that correspond to mineral phases (especially, hydromuscovite and anatase; **Figs. III.24C, D and III.25C**). The different fluorescence signals observed between the two samples in the regions of aromatic compounds and minerals could be attributed to different organic compound contents and a different mineralogy (Mlewski et al., 2018), respectively, the cause of which can be explained by different degrees of degradation undergone by the rocks, having affected the preservation of the structure of organic compounds and minerals. In addition, aromatic organic compounds were often found intermixed with hydromuscovite and anatase (**Figs. III.23, III.24A, B and III.25A, B**), corroborating observations made with Raman spectroscopy, SEM and TEM. This correlation might be explained by the microbial colonization of the most altered volcanic grains (Dong et al., 2022), where the alteration of volcanic grains was likely intensified by microbial activity (Samuels et al., 2020). Alternatively, it could be a result of the binding of carbonaceous matter (by biofilms containing microbial EPS) to mineral phases following the death of microorganisms (Gibson, 1984; Schultze-Lam et al., 1996; Orange et al., 2011), occurring before the silicification and lithification of sediments (Westall et al., 2011a, 2015b). I note, however, that the association of mantle carbon with phyllosilicates has been documented in martian meteorites (Steele et al., 2012, 2016, 2018). Nevertheless, there are consistent and multiple indications that, in the case of the Kitty's Gap sediments, microbial life was active and that the organic matter interleaved with the phyllosilicate layers is likely to be of biogenic origin.

- *Identification and distribution of diverse functional groups:*

In FTIR, the aliphatic C–H stretching region (ca. 2800–3040 cm^{-1}; **Fig. III.26**) and the aromatic/alkenic region (ca. 1300–1800 cm^{-1}; **Fig. III.27, 28**) contain information relevant to biological compounds, in particular spectral features of specific functional groups related to the cell that enable characterization of fossilized biopolymers (Benning et al., 2004; Igisu et al., 2009, 2018). In my samples, the aliphatic/aromatic ratios generally remain uniformly low, reflecting the degree of aromaticity of the carbonaceous matter which usually increases with metamorphic grade (Rouzaud and Oberlin, 1989; Bustin et al., 1995). With increasing metamorphic alteration, the structure of organic matter undergoes gradual graphitization, accompanied by the progressive loss of aliphatic chains, the lateral extension of polyaromatic units and their reorganization into stacked layers, resulting in changes in peak intensities (Guido et al., 2013; Igisu et al., 2018). Based on the Raman spectra, it was determined that the Kitty's Gap samples experienced moderate grade metamorphism (about 300–400°C), thus explaining the mainly aromatic nature of the carbonaceous matter. However, while the position of the bands is similar for the two samples, their intensity varies. Indeed, I observed more intense aliphatic bands for sample 00AU40, and more intense and diverse aromatic bands for sample 00AU39. More intense bands in the aliphatic C–H stretching region in sample 00AU40 indicate a better preservation of these organic compounds whereas more intense bands in the aromatic/alkenic region along with less intense bands in the aliphatic C–H stretching region in sample 00AU39 are consistent with the

degradation of aliphatic molecules. This degradation was likely influenced by a combination of many factors, including proximity to the hydrothermal source, diagenetic processes and/or mechanical processes after the formation of sediments, leading to changes or degradation of carbonaceous matter. In addition, similarly to the DUV observations, aromatic and aliphatic compounds were found co-located with hydromuscovite and anatase, as previously determined with Raman spectroscopy (**Fig. III.29, 30**). In particular, the aromatics (C–H), aliphatics (CH_2 and CH_3) and other functional groups (C=O, COOH, >C=O ester, etc.) are particularly concentrated in the heart of the volcanic clasts, in co-location with hydromuscovite (–OH) in sample 00AU39, whereas they show various types of distribution in the volcanic clasts of sample 00AU40 according to their nature and/or degree of alteration, with variable concentration of –OH. The silica-dust gel matrix is notably enriched in –OH with some heterogeneously distributed aromatics, aliphatics and other functional groups in sample 00AU40.

- *Composition of the fossilized biopolymers:*

The combined elemental and molecular compositions of the organic matter associated with altered volcanic particles and the silica-dust gel matrix strongly support the biogenic origin of the organic matter in the samples investigated. In order to evaluate the composition of the fossilized biopolymers, I calculated the methylene to end-methyl CH_2/CH_3 and end-methyl to methylene CH_3/CH_2 ($R_{3/2}$) ratios for different structures of interest in both samples (**Fig. IV.3; Table IV.2**).

The CH_2/CH_3 ratios provides an estimate of the chain length of the aliphatic hydrocarbon moiety connecting the aromatic structures, as well as its degree of branching (Lin and Ritz, 1993). For example, lower CH_2/CH_3 ratios correspond to shorter aliphatic chains and/or more branching. CH_2/CH_3 ratios range from ca. 1.1 to 2.0 in sample 00AU39 and from ca. 0.9 to 1.7 in sample 00AU40 (**Fig. IV.3A**), indicating aliphatic biopolymers of relatively short and/or highly branched membrane lipids composed of 5–6 to 7–8 alkanes (saturated hydrocarbons consisting of C and H linked with single bonds). These characteristics are tentatively interpreted as isoprenoid chains forming archaeal membranes (Lin and Ritz, 1993; Igisu et al., 2006, 2009, 2012, 2018; Hickman-Lewis et al., 2020b).

The CH_3/CH_2 ratios reflect the chemical composition of the precursor lipids which constitute cell membranes and can be used as an indicator of the biological domain to which the organisms whose organic remains have been analyzed belong (Igisu et al., 2009, 2012). For example, archaeal lipids are mainly composed of highly branched isoprenoid chains with higher CH_3/CH_2 ratios, whereas bacterial lipids are made-up of longer, straighter, fatty acid-like hydrocarbons with lower aliphatic CH_3/CH_2 ratios (Atlas, 1989; Igisu et al., 2009). All CH_3/CH_2 ratios in samples fall within the range of those of extant prokaryotes, and vary between ca. 0.5 and 0.9 in sample 00AU39 and between ca. 0.6 and 1.1 in sample 00AU40 (**Fig. IV.3B**). These values are consistent with both bacterial and archaeal origins (Igisu et al., 2009, 2018). Nevertheless, values higher than 0.8 suggest a potentially stronger input from archaeal membrane lipids, indicating an Archaea-dominated community (Igisu et al., 2012).

A similar study was made of comparably-aged (3.47–3.33 Ga) microbial mats from volcanic sediments from the Middle Marker horizon from the Barberton Greenstone Belt (Hickman-Lewis et al., 2020b). The results from the Kitty's Gap Chert very much resemble those of the Middle Marker horizon, in particular for the aliphatic molecules. The Middle Marker Chert has CH_2/CH_3 ratios varying between ca. 0.8 and 1.3 (**Fig. IV.3A**), indicating short and/or highly branched chains of 5–6 alkanes, and CH_3/CH_2 ratios between ca. 0.8 and 1.2 (**Fig. IV.3B**), all indicating a strong and likely dominant contribution from archaeal cell material.

CH_2/CH_3 ratios have been measured in diverse astronomical objects rich in organic matter. Notably, the Tagish Lake meteorite exhibits a broad range of CH_2/CH_3 ratios, varying from 1.8 to 2.7, indicating mixture of aliphatic hydrocarbons that includes both shorter/highly branched aliphatics and longer/less branched aliphatics (Yesiltas and Kebukawa, 2016). Other measurements of CH_2/CH_3 ratios were conducted on interstellar medium objects (1.1–1.2; Sandford et al., 1991; Pendleton et al., 1994), interplanetary dust particles (2.3–2.5; Flynn et al., 2003), comet 81P/Wild 2 particles (2.5; Keller, 2006), as well as grains from various carbonaceous chondrites such as Sutter's Mill, Murchison, Orgueil and Bells, respectively (2.5–4.0, 1.0, 1.4, 1.4; Kebukawa et al., 2010; Yesiltas et al., 2014). By comparison, the CH_2/CH_3 ratios measured in the Kitty's Gap Chert samples vary over a rather wide range with relatively low values (0.9–2.0), while the astronomical objects show either restricted ranges of values, relatively high values, or both (**Fig. IV.3A**).

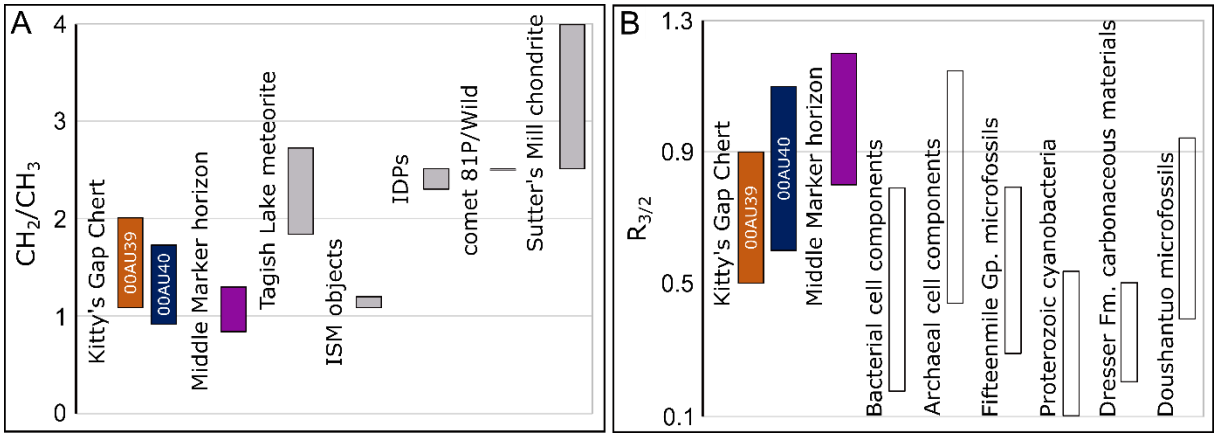

Figure IV.3: *Box plots illustrating the distributions of spectral features specific to aliphatic compounds. (**A**) Aliphatic CH_2/CH_3 ratios measured from carbonaceous matter in the Kitty's Gap Chert samples, compared with measured values from microbial mats in the Middle Marker horizon, Tagish Lake meteorite, interstellar medium (ISM) objects, interplanetary dust particles (IDPs) and Sutters' Mill chondrite. (**B**) Aliphatic $R_{3/2}$ ratios measured from carbonaceous matter in the Kitty's Gap Chert samples, compared with measured values from microbial mats in the Middle Marker horizon, extant biology (bacterial and archaeal cell components), microfossils from Proterozoic horizons and organic materials from the 3.48 Ga Dresser Formation (modified after Hickman-Lewis et al., 2020b).*

Table IV.2: *Summary of measured parameters from FTIR spectra in samples 00AU39 and 00AU40, with inferences made regarding the fossilized biopolymer composition and dominant microbial community, reflecting the community composition of microbial colonies at the time of fossilization.*

Sample	Zone	Structure of interest	Aliphatics (band intensity)	CH_2/CH_3 ratio	Length of aliphatic chains	$R_{3/2}$	Dominant biological community	Aromatics (band intensity)	Molecular diversity (1300–2050 cm^{-1})
00AU39	2	Multiphase volcanic rock fragment 3	++	2.02	7–8	0.49	Bacteria/Archaea	+++	+++
		Multiphase volcanic rock fragment 10	+++	1.57	6–7	0.63	Bacteria/Archaea	+++	+++
	3	Multiphase volcanic rock fragment 1	+	1.08	5–6	0.92	Archaea	++	+++
		Volcanic glass 5	++	1.21	5–6	0.82	Archaea	++	+++
00AU40	1	Multiphase volcanic rock fragment 1_1	+	1.32	6–7	0.76	Bacteria/Archaea	+	+++
		Multiphase volcanic rock fragment 1_2	++	1.62	6–7	0.62	Bacteria/Archaea	+	-
		Multiphase volcanic rock fragment 5	++	1.74	6–7	0.57	Bacteria/Archaea	++	+++
	5	Silica-dust gel matrix	-	-	-	-	-	++	+++
	8	Volcanic glass 1	+	1.1	5–6	0.91	Archaea	+	+
		Silica matrix 4_1	+	1.7	6–7	0.59	Bacteria/Archaea	++	+++
		Multiphase volcanic rock fragment 4_2	+++	1.23	5–6	0.81	Archaea	+	++
		Silica matrix 5	+	1.47	6–7	0.68	Bacteria/Archaea	+	+++
		Multiphase volcanic rock fragment 7	+	0.91	5–6	1.1	Archaea	+	+++

The characteristics of the carbonaceous matter in the sedimentary rocks of the Kitty's Gap Chert are summarized in **Table IV.3.**

Table IV.3: Summary of the characteristics of the carbonaceous matter in the Kitty's Gap Chert.

	00AU39 (close to hydrothermal vein, lowermost sedimentary layer)	00AU40 (further from hydrothermal vein, overlying sedimentary layer)
Microstructure (Optical and Raman)	• Carbonaceous films around volcanic clasts • The Raman spectrum of carbonaceous matter has two bands at ca. 1350 cm^{-1} (disordered) and ca. 1600 cm^{-1} (graphite + disordered) typical of a mature kerogen	• Carbonaceous films around volcanic clasts • The Raman spectrum of carbonaceous matter has two bands at ca. 1350 cm^{-1} (disordered) and ca. 1600 cm^{-1} (graphite + disordered) typical of a mature kerogen
Microscale distribution (Optical and Raman)	• Often located in volcanic clasts having experienced morphological and/or mineralogical alteration, and ubiquitous in the silica-dust gel matrix • Often mixed with hydromuscovite and anatase (more rarely with rutile), or completely replaces the volcanic protoliths	• Often located in volcanic clasts having experienced morphological and/or mineralogical alteration, and ubiquitous in the silica-dust gel matrix • Often mixed with hydromuscovite and anatase (more rarely with rutile), or completely replaces the volcanic protoliths • In sample 00AU40, the carbonaceous matter is also found in small quantity in volcanic clasts with less alteration
Microstructure (SEM)	• Finely disseminated, filmy with a lumpy texture, rounded to irregular with a smooth texture, coccoidal, fibrous with a wrinkled texture	• Finely disseminated, filmy with a lumpy texture, rounded to irregular with a smooth texture, coccoidal, fibrous with a wrinkled texture
Microscale distribution (SEM)	• Often associated with sheet-like or rough hydromuscovite (more rarely found in association with microcrystals of anatase)	• Often associated with sheet-like or rough hydromuscovite (more rarely found in association with microcrystals of anatase)
Nanostructure (TEM/STEM)	• Coatings, spherical to elliptical particles, elongated structures, lenticular structures, diffuse clouds	• Coatings, spherical to elliptical particles, elongated structures, lenticular structures, diffuse clouds
Crystallography (TEM/STEM)	• Amorphous and graphitized (onion-shaped structure) carbonaceous matter	• Amorphous and graphitized (onion-shaped structure) carbonaceous matter
Nanoscale distribution (TEM/STEM)	• Often in inclusions and around microcrystals of feldspars, or located at the edge of microcrystalline quartz polygons (more rarely found in association with microcrystals of anatase)	• Often in inclusions and around microcrystals of feldspars, or located at the edge of microcrystalline quartz polygons (more rarely found in association with microcrystals of anatase)
Elemental composition (XRF)	• Co-location of **K**, **Fe** and other transition metals (i.e., **Cr**, **Co**, **Ni**, **Cu**, **Zn** and **As**) associated with hydromuscovite and carbonaceous matter in the interior of volcanic grains • Co-location of **Ti**, **V** and **W** associated with anatase and possible carbonaceous matter in the interior and/or at the edges of volcanic grains • The feldspars and multiphase volcanic rock fragments coated with carbonaceous matter are highly enriched in many elements (**K**, **Ca**, **Cr**, **Mn**, **Fe**, **Zn**…) relative to the silica matrix • The carbon-coated edges of the volcanic glass fragments are enriched in many elements (**Ti**, **Fe**, **Mn**, **Ni**, **Cu**, **Zn**…) relative to their interior and the adjacent silica matrix, while those of the multiphase volcanic rock fragments are mainly enriched in **Ti** • In sample 00AU39, the carbon-coated pumice fragments are enriched in **Ti**, **K**, **Fe**, **Ca**, **Ga** and **Cr** relative to the adjacent silica matrix • In sample 00AU39, the silica-dust gel matrix has a clay-like composition and is enriched in many transition metals (**Fe**, **Cu**, **Ti**, **Zn**, **V**, **Cr**…)	• Co-location of **K**, **Fe** and other transition metals (i.e., **Cr**, **Co**, **Ni**, **Cu**, **Zn** and **As**) associated with hydromuscovite and carbonaceous matter in the interior of volcanic grains • Co-location of **Ti**, **V** and **W** associated with anatase and possible carbonaceous matter in the interior and/or at the edges of volcanic grains • The feldspars and multiphase volcanic rock fragments coated with carbonaceous matter are highly enriched in many elements (**K**, **Ca**, **Cr**, **Mn**, **Fe**, **Zn**…) relative to the adjacent silica matrix • The carbon-coated edges of the volcanic glass fragments are enriched in many elements (**Ti**, **Fe**, **Mn**, **Ni**, **Cu**, **Zn**…) relative to their interior and the adjacent silica matrix, while those of the multiphase volcanic rock fragments are mainly enriched in **Ti** • In sample 00AU40, the light silica-dust gel laminations have a more clay-like composition compared to the dark silica-dust gel deposits which are richer in titanium oxides

Elemental composition (PIXE)	• Average absolute concentrations of biofunctional elements in volcanic clasts coated with carbonaceous matter follow the trend: P > Fe > Ca > Cr > S > V > Cl > Sr > Co > Mo > *As* > *Zn* > *Ni* > *Cu* • Most volcanic clasts are enriched in 9 biofunctional elements (**Cr**, **As**, **Mo**, **V**, **Fe**, **Sr**, **Zn**, **Co** and **Ca**) relative to the adjacent silica matrix • Average absolute concentrations of biofunctional elements in carbon-coated edges of the volcanic clasts follow the trend: P > Fe > Ca > S > Cr > Cl > Mo > Co > Sr > *As* > *Cu* > *Ni* > *Zn* • Most of the edges of the volcanic clasts are enriched in only 6 biofunctional elements (**Ni**, **Cu**, **Mo**, **Cr**, **S** and **Co**) relative to their interior, excepted the carbon-coated edges of volcanic glass that are enriched in 11 biofunctional elements (**Ni**, **Mo**, **S**, **Cu**, **As**, **Zn**, **P**, **Co**, **Ca**, **Fe**, **Sr**) • Average absolute concentrations of biofunctional elements in the silica-dust gel matrix follow the trend: P > Ca > Fe > S > Cl > Cr > Cu > Zn > Co > Ni > Sr > *As* > *Mo* • The silica-dust gel matrix is enriched in 11 biofunctional elements (**Ni**, **As**, **Zn**, **Cl**, **Cr**, **Cu**, **S**, **Ca**, **P**, **Fe**, **Co**) relative to the average matrix	• Average absolute concentrations of biofunctional elements in volcanic clasts coated with carbonaceous matter follow the trend: Fe > P > Ca > V > S > Cr > Sr > Co > Mo > Cu > Zn > *As* > *Ni* • Most volcanic clasts are enriched in 8 biofunctional elements (**V**, **Cr**, **Zn**, **As**, **S**, **Mo**, **Ca** and **Fe**) relative to the adjacent silica matrix • Average absolute concentrations of biofunctional elements in carbon-coated edges of the volcanic clasts follow the trend: P > Fe > Ca > Cr > V > Sr > Co > *Ni* > *Cu* > *Zn* > *As* • Most of the edges of the volcanic clasts are enriched in only 3 biofunctional elements (**P**, **Cu** and **Mo**) relative to their interior
Molecular composition (DUV)	• The aromatic compounds show two main fluorescent bands at 310 and 340 nm, and the minerals one main fluorescent band at 415–420 nm and shoulders at 430–435 nm and 460–465 nm • The aromatic compounds are often mixed with mineral phases (hydromuscovite and anatase)	• The aromatic compounds show one main fluorescent band at 340–345 nm, and the minerals one main fluorescent band at 410–415 nm with rare shoulders at 390 nm and 430 nm • The aromatic compounds are often mixed with mineral phases (hydromuscovite and anatase)
Molecular composition (FTIR)	• Identification of bands at 2855 cm^{-1} (symmetrical CH_2 stretching), 2870 cm^{-1} (symmetrical CH_3 stretching), 2925 cm^{-1} (asymmetrical methylene CH_2 stretching) and 2960 cm^{-1} (asymmetrical end-methyl CH_3 stretching) in the aliphatic C–H stretching region (2800–3040 cm^{-1}) • Identification of a weak band at 1360 cm^{-1} (CH_3); weak bands at 1440 and 1470 cm^{-1} (C–H stretching); a weak band at 1545 cm^{-1} (C–H and N–H in amide II); and weak bands at 1650, 1705, 1720 and 1735 cm^{-1} (carbonyl and carboxyl groups) in the aromatic/alkenic region (1300–1800 cm^{-1}) • Sample 00AU39 shows more intense and diverse bands in the aromatic/alkenic region with respect to sample 00AU40 • Volcanic glass is rich in –OH with some aromatics, whereas multiphase volcanic rock fragments contain high concentrations of aromatics and variable concentrations of aliphatics and other functional groups	• Identification of bands at 2855 cm^{-1} (symmetrical CH_2 stretching), 2870 cm^{-1} (symmetrical CH_3 stretching), 2925 cm^{-1} (asymmetrical methylene CH_2 stretching) and 2960 cm^{-1} (asymmetrical end-methyl CH_3 stretching) in the aliphatic C–H stretching region (2800–3040 cm^{-1}) • Sample 00AU40 shows more intense bands (two to five orders of magnitude) in the aliphatic C–H stretching region (2800–3040 cm^{-1}) with respect to sample 00AU39 • Identification of a weak band at 1360 cm^{-1} (CH_3); weak bands at 1440 and 1470 cm^{-1} (C–H stretching); a weak band at 1545 cm^{-1} (C–H and N–H in amide II); and weak bands at 1650, 1705, 1720 and 1735 cm^{-1} (carbonyl and carboxyl groups) in the aromatic/alkenic region (1300–1800 cm^{-1}) • Volcanic glass is very rich in –OH, rich in aromatics with some aliphatics, but is depleted in certain functional groups, whereas multiphase volcanic rock fragments contain variable concentrations of aromatics, aliphatics and other functional groups; the silica-dust gel matrix is particularly enriched in –OH and Si–O with some heterogeneously distributed aromatics, aliphatics and other functional groups

III. Résumé en français

Ce quatrième chapitre s'articule autour de deux parties : 1) la reconstruction du paléoenvironnement de dépôt des sédiments du chert de Kitty's Gap, et 2) la démonstration de la syngénicité et de la biogénicité de la matière carbonée qu'ils contiennent, dans lesquelles les résultats sont discutés et confrontés aux données de la littérature.

L'étude de la sédimentologie, de la pétrologie, de la minéralogie et de la géochimie des échantillons a permis de reconstruire le paléoenvironnement de dépôt des sédiments volcaniques silicifiés du chert de Kitty's Gap. La caractérisation du contexte paléoenvironnemental est nécessaire pour déterminer l'habitabilité des sédiments volcaniques pour la vie microbienne et constitue une étape clé pour établir la syngénicité et la biogénicité de potentielles biosignatures, ainsi que pour évaluer l'influence éventuelle de la diagenèse précoce sur le potentiel de préservation des biosignatures.

Le couplage des différentes méthodes d'analyse indique que l'environnement de dépôt des sédiments volcaniques était un bassin volcano-sédimentaire influencé par l'eau de mer et l'hydrothermalisme. L'influence marine est démontrée par la lentille de chert d'où proviennent les échantillons étudiés et qui s'est formée par l'accumulation de sable volcanique dans un chenal soumis à des inondations régulières par l'eau de mer (**Figures II.4 et III.1**). L'observation de structures sédimentaires telles que des lits flaser-linsen s'expliquent par le dépôt des sédiments exposé à une alternance de conditions énergétiques (flaser) et de conditions plus calmes (linsen) dans un environnement tidal (**Figure III.1D**). L'orientation des galets et des rides de courant indiquant des directions de courant bimodales fournit une preuve complémentaire d'un environnement marin. L'influence hydrothermale est démontrée par la silicification des sédiments, les veines de silice qui recoupent les échantillons et la présence de minéraux d'origine hydrothermale (**Figures III.2–5**).

Les sédiments volcaniques localisés proches de la source hydrothermale (échantillon 00AU39) présentent une structure bréchifiée reflétant des conditions plus énergétiques (vagues, marées ou injection de fluides et de gaz hydrothermaux ; **Figure III.3**), contrairement aux sédiments volcaniques situées à plusieurs mètres de la source (échantillon 00AU40) qui présentent des dépôts horizontaux parallèles déposés en conditions relativement calmes (**Figure III.4**).

La composition des protolithes volcaniques identifiés dans les deux échantillons de roches (verres volcaniques, pierres ponces, feldspaths, amphiboles, etc. ; **Figure III.6**) reflètent des processus similaires, c'est-à-dire l'érosion des roches et cendres volcaniques environnantes, leur altération rapide en hydromuscovite et anatase et leur silicification intense au cours du dépôt et/ou de la diagenèse (**Figures III.7, 8 ; Tableau III.1**). Néanmoins, les sédiments volcaniques de l'échantillon 00AU40 proviennent d'une couche sédimentaire légèrement plus élevée stratigraphiquement que l'échantillon 00AU39 et sont principalement issus d'une source mafique, tandis que ceux de l'échantillon 00AU39 sont issus d'une source mixte, avec une possible contribution de l'altération des laves rhyolitiques sous-jacentes à la formation des couches inférieures de la succession sédimentaire (**Figure III.9B, C**).

L'analyse des terres rares à l'échelle globale (**Figure III.9D ; Tableau III.2**) montre une signature globalement continentale comme le démontre les ratios Y/Ho sub-chondritiques et le profil REE + Y de l'échantillon 00AU39 légèrement enrichi en LREE, bien qu'un léger enrichissement en HREE indique également un apport marin. De légère anomalies négatives en Ce dans les échantillons 00AU37b et 00AU39 impliquent également des conditions légèrement oxydantes et des anomalies positives en Eu

suggèrent une influence hydrothermale. L'analyse des terres rares à l'échelle locale montre des variations des conditions géochimiques locales, c'est-à-dire des apports de sources multiples (**Figure III.10 ; Tableau III.3**). L'influence de l'eau de mer est démontrée par des ratios Y/Ho super-chondritiques, des enrichissements en HREE et des anomalies positives en La, Y et Gd, tandis que des ratios Y/Ho sub-chondritiques, des enrichissements en LREE et des anomalies négatives en La, Y et Gd indiquent des apports non marins. De plus, des anomalies majoritairement positives en Ce impliquent des conditions anoxiques, compatibles avec l'eau de mer Archéenne anoxique et des anomalies positives en Eu suggèrent une influence hydrothermale. Cependant, la plupart des analyses (globales et locales) présentent des rapports Sm/Yb versus Eu/Sm qui reflètent une faible influence hydrothermale et des rapports $(Pr/Nd)_{MuQ}$ versus Y/Ho qui indiquent une forte influence continentale, bien que l'échantillon 00AU40 montre une plus grande influence marine.

En comparaison avec des matériaux de composition similaire, les sédiments du chert de Kitty's Gap présentent des caractéristiques géochimiques légèrement différentes par rapport aux sédiments de Strelley Pool Formation (Pilbara, Australie) et ceux issus de cherts de Barberton (Afrique du Sud). En particulier, les analyses globales indiquent que les sédiments de Strelley Pool Formation se sont déposés dans un environnement influencé par des apports marins et hydrothermaux, tandis que les sédiments de Barberton se sont déposés dans un environnement influencé par des sources terrigènes et hydrothermales avec une influence marine variable. Les analyses in situ dans les sédiments de Barberton montrent de fines variations dans la composition en REE + Y, soulignant une influence marine et des conditions anoxiques prévalentes dans les tapis microbiens. Cela suggère que les sédiments formés à des endroits distincts et à des moments légèrement différents au cours du Paléoarchéen ont enregistré des caractéristiques environnementales variées.

La **Figure IV.1** illustre un diagramme d'une séquence paragénétique décrivant les principales étapes de dépôt et d'altérations des sédiments volcaniques du chert de Kitty's Gap. Les caractéristiques du paléoenvironnement de dépôt des sédiments volcaniques silicifiés du chert de Kitty's Gap sont résumées dans le **Tableau IV.1**.

L'analyse de la structure physique et de la composition élémentaire et moléculaire de la matière carbonée, ainsi que sa distribution à plusieurs échelles, a permis d'évaluer la syngénicité et la biogénicité de potentiels restes microbiens fossiles contenus dans les sédiments du chert de Kitty's Gap.

La silicification rapide du chert de Kitty's Gap a favorisé la préservation des caractéristiques morphologiques et géochimiques de la matière carbonée. En particulier, Westall et al. (2006a) ont observé des structures coccoïdales carbonées interprétées comme des restes microbiens d'organismes chimiolithotrophes formant des films carbonés autour des clastes volcaniques. Les spectres Raman associés indiquent que la matière carbonée a subi une graphitisation plus ou moins intense, bien qu'elle soit principalement amorphe (**Figure III.11E**). De plus, la maturité thermique (environ 300–400°C) de la matière carbonée est compatible avec le degré de métamorphisme subi par la roche, tendant à démontrer sa syngénicité. Généralement, la matière carbonée est localisée à la surface des grains volcaniques ayant subi une altération mécanique et/ou minéralogique, associée à l'hydromuscovite et à l'anatase, ainsi que dans les poussières volcaniques où elle est omniprésente (**Figures III.6 et III.11A–D ; Tableau III.4**). La matière carbonée localisée autour des grains volcaniques peut représenter un film macromoléculaire constitué de macromolécules d'origine biologique ayant été adsorbées à la surface des grains volcaniques, ou bien des biofilms microbiens épilithiques composés de micro-organismes coccoïdales silicifiées incorporés dans une monocouche

exopolymérique à la surface des minéraux volcaniques. En effet, les surfaces volcaniques offrent une protection contre les conditions extérieures difficiles, ainsi qu'une source de nutriments et d'énergie pour les microorganismes chimiolithotrophes. Cependant, les poussières volcaniques présentent une aire de surface plus grande que les grains volcaniques, rendant l'énergie et les nutriments plus facilement accessibles aux microorganismes. De plus, les poussières volcaniques constituent également un environnement favorable à la matière microbienne, expliquant ainsi l'omniprésence de la matière carbonée.

À des échelles plus fines, la matière carbonée présente différentes morphologies (**Tableau III.4**) dont l'origine est expliquée grâce aux observations MEB effectuées précédemment par Westall et al. (2006a, 2011a) et à d'autres résultats présentés dans la **Figure IV.2**.

Au MEB, la matière carbonée prend la forme :

1) De particules finement disséminées (**Figure III.12A, B, E, G**) qui représentent probablement l'adsorption de molécules organiques à la surface et entre les feuillets d'hydromuscovite ;

2) De films avec une texture granuleuse (**Figure III.12C**), comparables à des restes microbiens dégradés incluant des EPS dans lesquels des colonies de microbes peuvent être incorporées (**Figure IV.2B–E**) et qui sont plus facilement fossilisés que les cellules microbiennes en raison de leurs nombreux groupes fonctionnels ;

3) De particules arrondies à irrégulières avec une texture lisse (**Figure III.12D**) qui pourraient correspondre à des particules carbonées détritiques d'origine abiotique (**Figure IV.2A**) ;

4) De structures coccoïdales (**Figure III.12E, F**) qui pourraient représenter de possibles microfossiles coccoïdaux similaires en taille et forme aux cellules microbiennes (**Figure IV.2B–E**) ;

5) De particules fibreuses avec une texture plissée (**Figure III.12G, H**) qui sont similaires aux particules détritiques carbonées fibreuses observées par Westall et al. (2006a, 2011a) et ayant été interprétées comme des fragments de tapis microbiens déchirés.

Au MET, d'autres structure de la matière carbonée ont été observées sous forme :

1) De films (**Figure III.13A, C**) similaires aux films de matière carbonée observée à une plus grande échelle autour des clastes volcaniques ;

2) De particules sphériques à elliptiques (**Figure III.13A, B, D**) qui pourraient représenter des microorganismes chimiolithotrophes « flottants » dans la matrice, alimentés par des fluides hydrothermaux, ou bien des particules de matière carbonée insoluble similaires à ceux trouvés dans les particules de poussières interplanétaires et les météorites ;

3) De structures allongées (**Figure III.13E, F**) correspondant à des restes dégradés de biofilms microbiens riches en EPS (**Figure IV.2B–E**) ;

4) De structures lenticulaires (**Figure III.13G**) composées de minéraux riches en fer mélangés avec de l'hydromuscovite et qui sont probablement piégées entre les grains de quartz ;

5) De nuages diffus (**Figure III.13H**) de couleur marron avec une forme irrégulière en microscopie optique (e.g., **Figure III.6M**) correspondant à des protolithes volcaniques très altérés, recouverts par de la biomasse microbienne.

L'étude de la cristallographie de la matière carbonée a révélé deux types de nanostructure :

1) Une structure amorphe (e.g., **Figure III.13F**) identifiée dans la plupart des structures observées (films, particules sphériques à elliptiques, structures allongées et structures lenticulaires) et interprétée comme des restes dégradés de microorganismes ayant pu être mélangés avec de la matière carbonée abiotique provenant de différentes sources possibles (hydrothermale, météoritique, atmosphérique, etc.) ;

2) Une structure graphitisée (**Figure III.14**) identifiée uniquement dans les particules sphériques à elliptiques présentes dans les poussières volcaniques et interprétées comme des particules détritiques d'origine mantellique et dont la structure en oignon montre des distances interplanaires de ca. 2.3 Å (**Figure III.14B**) et 3.5 Å (**Figure III.14D**) caractéristiques du carbone graphite. Une hypothèse alternative est que cette matière carbonée serait d'origine biologique, provenant de roches plus anciennes ayant subi une maturité thermique plus élevée avant d'être érodées. La matière organique qu'elle contient aurait ensuite été mobilisée et altérée par des fluides hydrothermaux avant d'être déposée dans les sédiments étudiés, expliquant sa structure graphitisée.

La matière carbonée submicroscopique est souvent associée à de l'hydromuscovite en feuillets ou à texture rugueuse dans les protolithes volcaniques altérés (**Figure III.12A–E, G**), plus rarement à des microcristaux d'anatase sur les bordures des grains volcaniques (**Figure III.12F**). De façon similaire, la matière carbonée nanoscopique est principalement associée à de l'hydromuscovite, en inclusions ou autour des microcristaux de feldspaths (**Figure III.13A, C, F**), ou bien localisée à la limite des polygones de quartz (**Figures III.13D, G et III.14A**), plus rarement à des microcristaux d'anatase sur les bordures des grains volcaniques. L'association de la matière carbonée et de l'hydromuscovite est expliquée par le rôle que jouent les phyllosilicates dans la préservation de la matière organique qui peut s'intercaler entre les feuillets de l'hydromuscovite. La présence de la matière carbonée au niveau des limites des polygones de quartz provient du déplacement possible de la matière organique préexistante au cours de la lithification du ciment de silice, processus connu sous le nom de « Ostwald ripening » (ou mûrissement d'Ostwald). Les microcristaux de quartz présents dans les sédiments du chert de Kitty's Gap proviennent de l'eau de mer Archéenne sursaturée en silice dont la polymérisation a conduit à la formation d'un ciment de gel de silice autour des grains volcaniques, puis qui a recristallisé en quartz suite à la diagenèse et au métamorphisme (**Figure IV.1**). L'omniprésence de la silice microcristalline dans les échantillons confirme la lithification rapide des sédiments, ayant contribué à la préservation la matière organique.

Cependant, les observations réalisées au cours de ce projet de thèse n'ont pas permis de visualiser directement les cellules fossilisées individuelles signalées par Westall et al., (2006a, 2011a) en microscopie électronique. Cela peut s'expliquer notamment par la prépondérance d'EPS générique dans les poussières volcaniques (**Figure IV.2B**) plutôt que de véritables cellules (**Figure IV.2C–E**). Quand les cellules sont présentes, elles forment généralement des petits groupes de quelques individus seulement (**Figure IV.2C**) recouvrant quelques micromètres carrés, bien que des groupes plus nombreux atteignant une dizaine de micromètres carrés ou plus soient parfois préservés (**Figure IV.2D, E**). De plus, elles forment des monocouches de quelques centaines de nanomètres d'épaisseur. Ces associations de cellules microbiennes dispersées montrant des traces subtiles et souvent déplacées par la croissance de quartz microcristallin (e.g., **Figure III.13D**), forment ainsi de très fines couches de matière organique entre les cristaux de quartz, empêchant des observations détaillées des structures carbonées en microscopie optique. D'autres analyses sont donc nécessaires pour déterminer la biogénicité de la matière carbonée.

L'étude du paléométallome des restes cellulaires, c'est-à-dire l'enrichissement en éléments métalliques traces dans les cellules anciennes, peut être utilisée pour caractériser le métabolisme passé des microorganismes fossilisés. En effet, un enrichissement en métaux traces associé à la matière carbonée peut refléter une combinaison de plusieurs processus, comme la sélection d'éléments chimiques pour des besoins cellulaires spécifiques, la récupération et le stockage d'éléments dans les polymères extracellulaires comme réponse à la toxicité, ou la chélation des éléments chimiques aux composants organiques dégradées après la mort des microbes.

La détection et la cartographie des métaux traces en XRF et PIXE ont documenté la présence de métaux de transition (V, Cr, Mn, Fe, Co, Ni…) et d'autres éléments (P, S, Cl, Ca…) bioessentiels associés à la matière carbonée dans les roches sédimentaires du chert de Kitty's Gap. En effet, les métaux sont essentiels à tous les organismes vivants sur Terre, en concentrations variées, et remplissent des fonctions biologiques diverses.

Les cartographies obtenues en XRF ont permis de montrer une colocalisation de certains éléments dans les régions contenant les grains volcaniques d'intérêt enrichis en matière carbonée (**Figures III.15, 16**) comme le potassium, le fer et d'autres métaux de transition (Cr, Co, Ni, Cu…) qui sont associés à l'hydromuscovite et à la matière carbonée à l'intérieur des grains, ou le titane, le vanadium et le tungstène qui sont associés à l'anatase et à de l'éventuelle matière carbonée à l'intérieur et/ou aux bordures des grains volcaniques. Généralement, la matrice et les verres volcaniques dépourvus de matière carbonée sont appauvris en presque tous les éléments (sauf en Cu), tandis que les autres grains volcaniques où de la matière carbonée a été détectée sont enrichis en plusieurs éléments, y compris en métaux de transition (Cr, Mn, Fe, Cu, Ni, Zn…) par rapport à la matrice adjacente (**Figures III.17C–E et III.18C, E**). Cependant, les bordures des verres volcaniques recouvertes de matière carbonée sont enrichies en de nombreux éléments, en particulier en métaux de transition (Ti, Fe, Mn, Ni, Cu, Zn…) par rapport à leur intérieur et à la matrice adjacente, tandis que celles des autres grains volcaniques sont seulement enrichies en Ti (**Figures III.17C, D et III.18C**). Les pierres ponces recouvertes de matière carbonée sont enrichies en certains éléments (Ti, K, Fe, Ca, Ga et Cr) par rapport à la matrice adjacente dans l'échantillon 00AU39, tandis que les pierres ponces dépourvues du matière carbonée sont appauvries en presque tous les éléments (sauf en Cu et Ge) dans l'échantillon 00AU40 (**Figures III.17E et III.18D**). Ces observations soulignent un enrichissement en métaux de transition associés aux intérieurs et bordures des grains volcaniques recouverts de matière carbonée. Les zones de poussières volcaniques sont également enrichies en plusieurs métaux de transition (Fe, Cu, Ti, Zn, V, Cr…), indiquant des enrichissements possibles liés à la matière carbonée omniprésente dans la matrice riche en poussières volcaniques (**Figure III.17F**).

La quantification au µPIXE des éléments biofonctionnels dans les structures d'intérêt (clastes volcaniques et leurs bordures), ainsi que dans la matrice, révèle des enrichissements locaux spécifiques associés à la matière carbonée. Généralement, la plupart des clastes volcaniques recouverts de matière carbonée sont enrichis en éléments biofonctionnels par rapport à la matrice adjacente (**Figures III.19–22**). Dans l'échantillon 00AU39, la plupart des clastes volcaniques analysés sont enrichis en P > Fe > Ca > Cr > S > V > Cl > Sr > Co > Mo > *As* > *Zn* > *Ni* > *Cu*, dont 9 éléments biofonctionnels (Cr, As, Mo, V, Fe, Sr, Zn, Co et Ca) sont plus concentrés que dans la matrice adjacente, tandis que dans l'échantillon 00AU40, ils sont enrichis en Fe > P > Ca > V > S > Cr > Sr > Co > Mo > Cu > Zn > *As* > *Ni*, dont 8 éléments biofonctionnels (V, Cr, Zn, As, S, Mo, Ca et Fe) sont plus concentrés que dans la matrice adjacente. Mais des variations sont observées selon le degré d'altération des clastes volcaniques. En particulier, les fragments de roches volcaniques de natures diverses les plus altérés et recouverts de matière carbonée sont plus enrichis en divers métaux de transition et autres éléments biofonctionnels que les verres volcaniques les moins altérés. Les bordures des clastes volcaniques dans les deux échantillons sont enrichies en seulement quelques éléments biofonctionnels (Ni, P, Cu, Mo…) par rapport à leur intérieur, sauf quand la matière carbonée est préférentiellement localisée aux bordures des grains qui sont alors plus enrichies en de nombreux éléments biofonctionnels (P, S, Ca, Fe, Co, Ni…). De plus, la matrice riche en poussières volcaniques de l'échantillon 00AU39 montre également un enrichissement en presque tous les éléments biofonctionnels par rapport à la moyenne des matrices. En général, les éléments traces comme Cr, V, As et Co sont particulièrement enrichis dans la

matière carbonée et leur co-occurrence renforce une origine biologique potentielle, tandis que d'autres éléments traces comme P, Cl, Ca ou Fe sont probablement associés à l'hydromuscovite dont les surfaces négativement chargées permettent d'attirer et de préserver la matière organique (**Figures III.19 et III.21**).

La matière carbonée étudiée concentre ainsi une gamme spécifique d'éléments traces pertinents pour les métallomes procaryotes, incluant V, Mn, Fe, Co, Ni, Cu, Zn, Mo et W, qui reflètent les métallomes préservés des cellules microbiennes ayant produit la matière carbonée dans les échantillons de Kitty's Gap. L'étude des éléments biofonctionnels qui constituent les métallomes pourrait potentiellement fournir des informations sur les métabolismes possibles des microorganismes pendant le Paléoarchéen. En particulier, les valeurs de $\delta^{13}C$ (entre –26 et –28 ‰ environ) obtenues par Westall et al. (2006a) sont cohérentes avec de nombreux processus métaboliques (réduction des sulfures et des sulfates, méthanogenèse et photosynthèse anoxygénique). Les métaux de transition essentiels utilisés par les procaryotes suivent généralement la tendance suivante : Fe >> Zn > Mn >> Co, Cu, Mo >> Ni > W, V. Le fer est utilisé universellement par la vie et est impliqué dans tous les métabolismes mentionnés précédemment. Les autres métaux de transition (Zn, Co, Cu, Mo, Ni et V) sont essentiels pour la vie microbienne et notamment pour la croissance de certains méthanogènes (en particulier, Ni et Mo). Malgré leur faible biodisponibilité dans l'océan réducteur, le cuivre, le zinc et le molybdène pourraient avoir été utilisés par des microorganismes à des concentrations très faibles pendant l'Archéen, comme le suggèrent les concentrations mesurées par µPIXE. Le manganèse catalyse plusieurs réactions, tandis que le tungstène est utilisé comme source d'électron dans la méthanogenèse. Les autres éléments biofonctionnels sont des éléments essentiels pour le vivant (P, S), des cations essentiels pour la plupart des espèces (Cl, Ca) ou bien des éléments traces utilisés seulement par certaines espèces (Cr, As, Sr). Cependant, les nombreux groupes fonctionnels des EPS peuvent piéger des métaux et il n'est donc pas exclu que les enrichissements observés soient dus à ce processus.

La détection et la cartographie des molécules organiques en fluorescence DUV et FTIR ont documenté la présence de composés organiques aromatiques et aliphatiques dans les roches sédimentaires du chert de Kitty's Gap. Les matériaux organiques ont pu préserver les caractéristiques spectrales DUV/IR de leur matériau d'origine grâce à la stabilité des lipides lors de la diagenèse et du métamorphisme.

Les analyses en fluorescence DUV ont détecté la présence de composés organiques aromatiques à un ou deux cycles à 310 et 340–345 nm (**Figures III.24C et III.25C**), ainsi que des phases minérales (en particulier, l'hydromuscovite et l'anatase) dans la région ca. 400–500 nm (**Figures III.24C, D et III.25C**). Les différences de signaux fluorescents observés entre les deux échantillons sont attribuables à des concentrations en organiques différentes et à une minéralogie différente, respectivement, dont l'origine peut être expliquée par des degrés d'altération différents subis par les roches, ayant affecté la préservation de la structure des composés organiques et des minéraux. De plus, les composés organiques aromatiques sont souvent mélangés avec l'hydromuscovite et l'anatase (**Figures III.23, III.24A, B et III.25A, B**), ce qui rejoint les observations effectuées précédemment. Cette association peut être expliquée par la colonisation microbienne des grains volcaniques les plus altérés (dont la colonisation microbienne a probablement renforcé leur altération) ou la liaison de la matière carbonée avec des phases minérales par des biofilms suite à la mort des microbes. Une origine mantellique est peu probable en raison des preuves multiples qui indiquent que la vie microbienne était active dans les sédiments de Kitty's Gap.

Les analyses en FTIR ont détecté des groupes fonctionnels spécifiques dans les régions des aliphatiques à ca. 2800–3040 cm^{-1} et des aromatiques à ca. 1300–1800 cm^{-1} (**Figures III.26–28**), permettant de caractériser les biopolymères fossilisés associés aux restes cellulaires dégradés. Dans les deux échantillons, les ratios aliphatiques/aromatiques sont uniformément bas, reflétant le degré d'aromaticité de la matière carbonée qui augmente généralement avec le degré de métamorphisme (ici, environ 300–400°C). Cependant, l'échantillon 00AU40 montre régulièrement des bandes aliphatiques plus intenses, tandis que l'échantillon 00AU39 présente des bandes aromatiques plus intenses et plus diversifiées. Ces différences peuvent s'expliquer par une dégradation des composés aliphatiques dans l'échantillon 00AU39, due à la combinaison possible de plusieurs facteurs, comme la proximité de la source hydrothermale, des processus diagénétique et/ou des processus mécaniques conduisant aux modifications ou à la dégradation de la matière carbonée. De plus, de façon similaire aux observations en DUV, les composés aromatiques et aliphatiques sont colocalisés avec l'hydromuscovite et l'anatase (**Figures III.29, 30**). Les cartographies montrent que les aromatiques (C–H), les aliphatiques (CH_2 and CH_3) et autres groupes fonctionnels (C=O, COOH, >C=O ester…) sont particulièrement concentrés au cœur des clastes volcaniques, associés avec l'hydromuscovite (–OH) dans l'échantillon 00AU39, tandis qu'ils présentent différents types de distribution dans les clastes volcaniques de l'échantillon 00AU40 selon leur nature et/ou leur degré d'altération, avec des concentrations variables en –OH. De plus, la matrice riche en poussières volcaniques de l'échantillon 00AU40 est particulièrement enrichie en –OH avec quelques hétérogénéités attribuées à des aromatiques, aliphatiques et autres groupes fonctionnels.

La combinaison des compositions élémentaires et moléculaires de la matière organique associées aux particules volcaniques altérées et à la matrice riche en poussières volcaniques soutient fortement l'origine biogénique de la matière organique dans les échantillons étudiés. Les ratios CH_2/CH_3 (méthylène/méthyle) et CH_3/CH_2 ou $R_{3/2}$ (méthyle/méthylène) permettent de retracer la composition des biopolymères fossilisés (**Figure IV.3 ; Tableau IV.2**). En particulier, les ratios CH_2/CH_3 permettent d'estimer la longueur des chaînes aliphatiques ainsi que leur degré de ramification et les ratios CH_3/CH_2 reflètent la composition chimique des lipides précurseurs qui constituent les membres cellulaires et peuvent être utilisés comme indicateur du domaine biologique auquel appartiennent les organismes dont les restes organiques ont été analysés. Les ratios CH_2/CH_3 varient entre ca. 1,1 et 2 dans l'échantillon 00AU39 et entre ca. 0,9 et 1,7 dans l'échantillon 00AU40, indiquant des chaînes aliphatiques relativement courtes et/ou ramifiées de 5–6 à 7–8 alcanes qui sont probablement issues de lipides membranaires des archées (**Figure IV.3A**). Tous les ratios CH_3/CH_2 se situent dans la gamme des procaryotes et varient entre ca. 0,5 et 0,9 dans l'échantillon 00AU39 et entre ca. 0,6 and 1,1 dans l'échantillon 00AU40 (**Figure IV.3B**). Ces valeurs sont cohérentes avec des origines bactériennes et archéennes, bien que les valeurs supérieures à 0,8 suggèrent une forte contribution des lipides membranaires archéennes, impliquant une communauté majoritairement dominée par des Archées. Ces résultats sont comparables à ceux des sédiments volcaniques de l'horizon de Middle Marker (Afrique du Sud) qui montrent des ratios CH_2/CH_3 variant entre ca. 0,8 et 1,3 et des ratios CH_3/CH_2 variant entre ca. 0,8 et 1,2, indiquant des chaînes aliphatiques courtes et/ou ramifiées de 5–6 alcanes et une contribution dominante du matériel cellulaire archéen, respectivement (**Figure IV.3A, B**). Ces résultats diffèrent cependant des ratios CH_2/CH_3 mesurés dans les objets astronomiques riches en matière organique qui présentent soit une gamme de valeurs restreintes, soit des valeurs relativement élevées, ou les deux (**Figure IV.3A**).

Les caractéristiques de la matière carbonée dans les roches sédimentaires du chert de Kitty's Gap sont résumées dans le **Tableau IV.3**.

Chapter V: Application to Martian rocks

I. The Kitty's Gap sediments as functional analogues for returned Martian sediments

The Kitty's Gap Chert is proposed as an analogue of Martian materials from the period of time during which conditions at the surface of Mars are considered to have been habitable (Noachian–Late Noachian; McKay and Stoker, 1989), and from which we could potentially find fossilized traces of life similar to those observed in Archean sediments (**Table V.1**). The Kitty's Gap Chert is more precisely considered as a "functional analogue" because it shows general characteristics more or less similar to those observed or expected in Martian rocks, but it has specific analogue properties (i.e., petrological, sedimentological, mineralogical, mechanical, chemical and/or biological) that are highly or perfectly relevant for a given use (Foucher et al., 2021a). Indeed, the volcanic sediments have a similar origin (mainly mafic sediments). The sediments were deposited in a shallow water environment under wave/wind agitation or in static water, influenced to varying degrees by hydrothermal activity. Sediments in Gale and Jezero craters on Mars were also partially formed under standing bodies of water and in shallow water depths (lakes). Recently, evidence for ripples has been found in Gale crater sediments, similar to the wave ripples exhibited by the Kitty's Gap Chert (https://www.nasa.gov/feature/jpl/nasa-s-curiosity-finds-surprise-clues-to-mars-watery-past, Feb. 8, 2023). Likely evidence for hydrothermal activity was detected by the Spirit rover at Home Plate in Gusev crater (Ruff and Farmer, 2016). Although no traces of hydrothermal activity have yet been detected in either Jezero or Gale crater, the very volcanic nature of their basement rocks and the magmatic origin of certain formations within makes it highly plausible that hydrothermal activity was associated with their eruption. Perseverance has documented the aqueous alteration of Jezero basalts (Farley et al., 2022; Scheller et al., 2022), and aqueous alteration of fine-grained volcanic sediments in Gale crater has also been documented (Mangold et al., 2019). Thus, the similarities between the early terrestrial volcanic sediments and their Martian counterparts are very strong.

The main difference between the Kitty's Gap Chert and similar volcanic sedimentary rocks on Mars is that the former was pervasively and very rapidly silicified. A similar diagenetic process apparently took place at Home Plate (Ruff and Farmer, 2016) but has not yet been identified elsewhere on Mars. Nevertheless, this is a minor point in the sense that it is the nature of the sediments, their environment of deposition, and the nature of their microbial inhabitants that is important for use as an astrobiological analogue (cf. Foucher et al., 2021a; Hickman-Lewis et al., 2022). On Mars, whereas cells may have been entombed by cementing materials in the matrix (clays, salts), it is more likely that the organic remains of microbes would have been preserved as generic heterogeneous biomass or EPS, which could have been equally entombed by the matrix cement, in particular, between clay sheets (although this has not yet been demonstrated) or possibly within hydrated silica (Tarnas et al., 2019). In addition, despite the great age of the locations investigated in situ on Mars (>3.6 Ga), primary organic matter would not have undergone the degree of metamorphism to which similar-aged sediments on Earth have been subjected through plate tectonics, although impact metamorphism is probable in many localities on Mars. It would therefore be possible to find both well-preserved or very graphitized organic matter. Despite these differences in preservation and degradation, the carbonaceous composition of the fossilized remains of microbes, associated with specific morphological, metabolic, elemental and molecular characteristics in the Kitty's Gap Chert, can be considered as good analogue biosignatures for astrobiological investigations in situ on Mars and in returned samples.

Table V.1: *Comparison of the Kitty's Gap Chert and associated biosignatures compared to Martian rocks in Jezero crater of similar age (ca. 3.5 Ga-old) and the potential traces of life they could contain (modified after Westall et al., 2015b).*

	Kitty's Gap Chert	Martian rocks in Jezero crater (Simon et al., 2023)
Rock age	• Paleoarchean (3.45 Ga)	• Noachian period (>3.6 Ga)
Depositional environment	• Shallow water, tidal basin	• Lacustrine to fluvial
Sediment composition	• Mainly basaltic sediments (mafic to ultramafic), some more evolved volcanics (rhyolitic)	• Mainly basaltic sediments, some more evolved volcanics (andesite)
Matrix	• Silica	• Secondary minerals such as phyllosilicates, salts and sulfates (with a potential amorphous or nanocrystalline silica phase)
Primary minerals	• Volcanic glass, pumice, feldspar, amphibole, pyroxene…	• Pyroxene, olivine, feldspar
Diagenetic alteration minerals	• Volcanic grains altered to phyllosilicates and anatase, secondary hydrothermal minerals (microcrystalline quartz, barite, pyrite…)	• Volcanic grains altered to phyllosilicates (Fe-Mg smectite), salts, carbonates, sulfates, phosphates, iron oxides…
Source of fluids	• Mix of seawater, hydrothermal and continental (riverine) inputs	• Lacustrine input, potential hydrothermal inputs related to volcanic activity
Habitable environment	• pH acidic-neutral (partly alkaline); anaerobic with micro amounts of abiotic O_2; moderate-high temperatures (ca. 50–70°C); metal-rich (V, Cr, Mn, Fe, Co, Ni…)	• pH neutral (possibly partly acidic and partly alkaline); anaerobic (possibly micro amount of abiotic O_2); generally low temperatures (possibly higher in the vicinity of hydrothermalism); metal-rich (Cr, Mn, Fe…)
Origin of organics	• Biological, hydrothermal, mantle, atmospheric (aerosols from volcanic ashes or sea spray), extraterrestrial	• Certainly extraterrestrial, mantle and atmospheric (aerosols from volcanic ashes), possibly biological and hydrothermal
Preservation of organics	• Rapid silicification	• Entombment by cementing phyllosilicates, salts and/or sulfates
Type of microorganisms	• Anaerobic chemolithotrophs, chemoorganotrophs, phototrophs	• Environment consistent with physicochemical requirements of anaerobic chemolithotrophs, chemoorganotrophs (in the vicinity of hydrothermal activity) and phototrophs
Energy source for microbes	• Redox reactions of inorganic (mineral) or organic (dead biological) materials; photons	• Redox reactions of inorganic (mineral) or organic (dead biological) materials if there was life; photons
Distribution of microbes	• At the surface of volcanic clasts (chemolithotrophs), most strongly associated with hydromuscovite and anatase; ubiquitous in the silica-dust gel matrix; in subaerial deposits where pumice is embedded (phototrophs)	• At the surface of volcanic clasts (if chemolithotrophs and chemoorganotrophs existed); in the phyllosilicate/salt/sulfate (amorphous silica?) matrix; on the surface of bedding planes (if phototrophs existed)
Raman spectral signature	• Raman spectra of the carbonaceous matter characterized by two bands at ca. 1350 and 1600 cm^{-1}, typical of a kerogen	• Low abundances of organics, only a possible G band (ca. 1600 cm^{-1}) were detected
Morphological biosignatures	• Coccoidal cells, lenticular cells, colonies, EPS forming carbonaceous films around volcanic clasts (coatings), degraded remnants of EPS-rich microbial biofilms (elongated structures), carbonaceous clots (spherical	• Cells, colonies, EPS forming carbonaceous films, degraded remnants of EPS-rich microbial biofilms, carbonaceous clots, degraded volcanic clasts coated with microbial biomass, if cementation was rapid; microbially induced sedimentary structures (MISS; Noffke, 2009, 2015)

	to elliptical particles), degraded volcanic clasts coated with microbial biomass (diffuse clouds)	
Metabolic biosignatures	• Carbon isotopic composition ranging from –26‰ to –30‰	• Restrictive negative carbon isotopic composition
Elemental biosignatures	• Carbonaceous matter coating the volcanic clasts concentrates the following trace elements: Fe > P > Ca > V > S > Cr > Sr > Cl > Co > Mo > *Zn* > *Cu* > *As* > *Ni*; carbonaceous matter located at the edges of the volcanic clasts concentrates the following trace elements: P > Fe > Ca > Cr > S > Cl > V > Mo > Sr > Co > *Cu*, *Ni* > *As* > *Zn*; the silica-dust gel matrix is enriched in P > Ca > Fe > S > Cl > Cr > Cu > Zn > Co > Ni > Sr > *As* > *Mo*	• Concentration of trace transition metals used by prokaryotes in volcanic minerals, such as Fe, Zn, Mn, Co, Cu, Mo, Ni, and other bioessential elements (CHNOPS…)
Molecular biosignatures	• Aliphatic/aromatic ratios relatively low • Aromatic compounds at ca. 310 and 340–345 nm in DUV • Aliphatic compounds at ca. 2855, 2870, 2925 and 2960 cm^{-1} in FTIR • CH_2/CH_3 ratios ranging from ca. 0.9 to 2 (relatively short/highly branched aliphatic biopolymers) • CH_3/CH_2 ratios ranging from ca. 0.5 to 1.1 (mixed to Archaea-dominated community)	• Aliphatic/aromatic ratios could be variable • Better detection of aromatic compounds if the biological remains have undergone impact metamorphism/better preservation and detection of aliphatic compounds if the biological remains have not been subjected to impact metamorphism • Detection of one- and two or more-ring aromatic molecules (Razzell Hollis et al., 2023)

II. Space instrumentation

Many analysis techniques used in this study were miniaturized for the exploration and characterization of habitable paleoenvironments, as well as the search for traces of life potentially preserved in the rocks in situ on Mars, such as:

- MAHLI (MSL), WATSON (Mars 2020) and CLUPI (ExoMars): optical microscopes;
- SuperCam & SHERLOC (Mars 2020) and RLS (ExoMars): Raman spectrometers;
- SHERLOC (Mars 2020): DUV spectrometer;
- SuperCam (Mars 2020), ISEM, Ma_MISS & MicrOmega (ExoMars): FTIR spectrometers;
- APXS, CheMin & ChemCam (MSL), SuperCam & PIXL (Mars 2020): XRF spectrometers and PIXE;
- SAM (MSL) and MOMA (ExoMars): mass spectrometers.

A. Space optical "microscopes"

MAHLI (MSL), WATSON (Mars 2020) and CLUPI (ExoMars) are cameras on board rovers used to obtain color images of rocks and regolith in order to identify minerals, textures and structures from microscopic to kilometer (outcrops) scales. These cameras are not microscopes and, in the absence of thin sections on Mars, the observations made with these systems are hardly comparable with those made using standard laboratory microscope (Foucher et al., 2021b). Moreover, if their spatial resolution can reach ca. 14 µm/pixel (Edgett et al., 2012), ca. 13 µm/pixel (Bhartia et al., 2021) and ca. 7 µm/pixel (Josset et al., 2017), respectively, it remains lower than the spatial resolution of the optical microscopes used in this study (ca. 1 µm). Consequently, only coarse to very coarse silt grains can be resolved by the space instruments at their finest resolution against fine clay particles for the laboratory instruments and putative microfossils would be impossible to observe.

B. Space Raman spectrometers

1. SuperCam (Mars 2020)

SuperCam is an instrument mounted on the "head" of the Perseverance rover mast used to identify minerals and organics by combining three main analysis techniques: laser induced breakdown spectroscopy (LIBS), Raman and infrared spectroscopy techniques. In particular, the Raman spectrometer uses a 532 nm green laser beam which covers the 150–4000 cm^{-1} region, with a spectral resolution of 12 cm^{-1}, that allows to determine the molecular composition of the materials (Wiens et al., 2021; Maurice et al., 2021). The spectral range covers by the space instrument is similar to the spectral range of the laboratory instrument used in this study (0–4000 cm^{-1}). However, the Raman spectrometer of SuperCam has a lower spectral resolution than its laboratory counterpart (3 cm^{-1}). SuperCam is a remote Raman spectrometer which performs long distances Raman measurements (between 2 and 7 meters) with a large laser spot size at the surface of rocks (i.e., several mm in diameter; Maurice et al., 2021). The collected data are therefore difficult to compare with those obtained in the laboratory on polished thin sections using a micro-Raman system capable of making composition maps with a sub-micrometric resolution.

2. SHERLOC (Mars 2020)

SHERLOC (Scanning Habitable Environments with Raman and Luminescence for Organics and Chemicals) is a deep-UV (DUV) resonance Raman and fluorescence spectrometer mounted on the

robotic arm of the Perseverance rover used to detect minerals, organic molecules and potential biosignatures at fine-scale. The spectrometer uses a 248.6 nm DUV laser (<100 µm diameter spot size) that interacts with the targeted surface material, allowing to simultaneously acquiring fluorescence emissions from organic materials and Raman scattered photons from organic materials and minerals in the 250–370 nm spectral range (Bhartia et al., 2021). SHERLOC is able to investigate rocks and regolith in order to provide chemical maps of organic and mineral signatures combined with micro-to-millimeter scale images obtained by its two high-resolution cameras, WATSON (13.1 to >100 µm/pixel) and ACI (10.1 µm/pixels). Chemical maps can cover areas up to 7 × 7 mm² with an acquisition time of <10 minutes. Large mosaics can also be acquired by moving the robotic arm (Bhartia et al., 2021). The deep UV resonance Raman enables detection and classification of aromatic and aliphatic organics with sensitivities below 1 ppm at <100 µm spatial scales, as well as minerals relevant to aqueous chemistry with grain sizes below 50 µm. In addition, the Raman scattering occurs in the 254–274 nm (ca. 800–4000 cm^{-1}) spectral range, with a spectral resolution of ca. 40 cm^{-1} (Razzell Hollis et al., 2021). Despite a lower spatial resolution, SHERLOC is able to produce chemical maps that are comparable to the compositional map obtained with the Raman spectroscopy used in this study as they can be used for the detection and characterization of organic molecules and minerals.

3. *RLS (ExoMars)*

The RLS (Raman Laser Spectrometer) is a Raman spectrometer located in the analytical laboratory of the Rosalind Franklin rover that will provide precise identification of the mineral phases and the possibility to detect a variety of organic functional groups in Martian samples (Rull et al., 2017). In particular, the RLS will analyse powdered drill cores collected on the surface and subsurface of Mars. The spectrometer uses a 532 nm green laser beam with a 50 µm spot size diameter, and covers the 150–3800 cm^{-1} region with a spectral resolution of ca. 6 cm^{-1} (Rull et al., 2017). Although the spatial and spectral resolutions are lower than those of the laboratory instruments, the RLS uses a classical laser wavelength and covers a similar spectral range, allowing to characterize the microbial-scale geological context and to search for possible traces of life (Foucher et al., 2013, 2019).

C. Space DUV spectrometer

1. *SHERLOC (Mars 2020)*

The fluorescence spectrometer of SHERLOC uses native fluorescence as a complementary mode of detection to Raman and resonance Raman, that allows to identify trace amounts of organics and to detect regions of interest which are then analysed by DUV resonance Raman (Bhartia et al., 2021). In particular, the fluorescence spectrometer uses a spectral range (275–354 nm) similar to the spectral range covered by its laboratory counterpart (285–370 nm), with a spectral resolution of 0.269 nm. The DUV native fluorescence can be used to detect and differentiate astrobiological relevant organics, such as aromatic amino acids and PAHs (polycyclic aromatic hydrocarbons) from mineral backgrounds (Bhartia et al., 2021).

D. Space FTIR spectrometers

1. *SuperCam (Mars 2020)*

The visible and infrared spectrometer (VISIR) of SuperCam uses the Sun as a light source and covers a band of wavelengths from visible (0.4–0.85 µm) to infrared (1.3–2.6 µm), with a spectral resolution of

5 nm at 1.3 µm to 20 nm at 2.6 µm and a spatial resolution of 1.3–7 mm, that allows to identify various functional groups (Wiens et al., 2021; Maurice et al., 2021). In particular, the VISIR wavelength range allows to identify minerals of interest for the search of traces of life such as clays, sulfates and carbonates, complex organic compounds (CH_2 and CH_3 asymmetric and symmetric stretch, C=C, C–H), as well as biologically-relevant compounds, such as N–H (ammonium), N–O (nitrates), B–O (borates) and P–O (phosphates). The spectral range of the IR spectrometer is different from the spectral range covered by the FTIR spectrometer used in this study (2.5–15 µm). As a consequence, the short-wave infrared range used by VISIR is more relevant to detect phyllosilicates and other minerals (in particular O–OH, H_2O, Si–OH, C–O molecules), whereas the mid-wave infrared range used by FTIR spectroscopy in this study is more dedicated to detect organic molecules.

2. *ISEM (ExoMars)*

ISEM (Infrared Spectrometer for ExoMars) is a pencil-beam IR spectrometer that was mounted (it was removed but will be replaced by another IR instrument whose characteristics are still being defined) on the Rosalind Franklin rover mast to record IR spectra of solar light reflected off surface targets, such as rocks and regolith, to determine their bulk mineralogical composition in order to aid in the selection of potential targets for close-up investigations and drilling sites (Korablev et al., 2017). In particular, ISEM would have performed IR investigations in the 1.1–3.3 µm spectral range, with a spectral resolution of 3.3 nm/pixel at 1.1 µm to 28 nm/pixel at 3.3 µm and a spatial resolution of 3–10 cm (Korablev et al., 2017). The spectral range of ISEM covers a part of the spectral range of the FTIR spectrometer used in this study, allowing identification of phyllosilicates and other hydrated minerals with absorption features at ca. 1.4, 1.9 and 2.2–2.3 µm, as well as carbonates and sulfates. With increasing spatial resolution, individual minerals may become more apparent, with deeper characteristic absorption features.

3. *Ma_MISS (ExoMars)*

Ma_MISS (Mars Multispectral Imager for Subsurface Studies) is a miniaturized visible and near-infrared (VNIR) spectrometer integrated in the drill tool of the Rosalind Franklin rover that will conduct mineralogical studies of the excavated borehole walls as the drill is operated in order to study the Martian subsurface environment (De Sanctis et al., 2017). In particular, Ma_MISS will perform IR spectral reflectance investigations in the 0.4–2.2 µm range, with a spectral resolution of 20 nm and a spatial resolution of 120 µm/pixel over the target (De Sanctis et al., 2017). Ma_MISS covers a lower spectral range than the FTIR spectroscope used in this study, and is therefore more adapted to detect and identify minerals as well as H_2O and volatiles with a relatively high spatial resolution.

4. *MicrOmega (ExoMars)*

MicrOmega (Micro Observatoire pour la minéralogie, l'eau, les glaces et l'activité) is a very-near IR hyperspectral microscope located in the analytical laboratory of the Rosalind Franklin rover that will characterize the texture and composition of crushed samples in order to identify particularly interesting minerals and assign them as objectives for Raman and MOMA-laser desorption mass spectrometry (Bibring et al., 2017). In particular, MicrOmega will perform IR investigation in the 0.5–3.6 µm spectral range, with a spectral resolution of 5 nm at 0.5 µm to 25 nm at 3.6 µm and a spatial resolution 20 µm/pixel (Bibring et al., 2017). The spectral range covered by MicrOmega combined with its high spatial resolution will permit to identify major and minor mineral phases, such as silicates,

oxides, hydrated minerals and ices, including potential organic compounds (carbonyl C=O, aromatic C–H stretch, aliphatic CH_2 and CH_3 stretch, etc.).

E. Space XRF spectrometers/PIXE

1. APXS (MSL)

APXS (Alpha-Particle X-ray Spectrometer) is an instrument located on the turret at the end of Curiosity rover's robotic arm that can determine the abundance of different elements in rocks and regolith in order to characterize the geological context (Campbell et al., 2012). APXS works by emitting two types of radiation, alpha particles (helium nuclei) and X-rays (radioactive source of Curium 244) which allow the measurement of major, minor and trace elements contained in an analysis zone of 1.7 cm in diameter for a depth varying between 5 µm for light elements and 50 µm for heavy elements (Campbell et al., 2012). Compared to the duration of analyzes carried out in the laboratory (5–10 hours/scan), the analyzes carried out by APXS vary between only 15 minutes for the detection of major and minor elements (>0.5 %) to 3 hours for trace elements (≤100 ppm). This instrument is an improved version of the APXS on board the Sojourner (Mars Pathfinder) and the Spirit and Opportunity rovers (MER mission) which required acquisition times of about 10 hours. In addition, the sensitivity of the Curiosity spectrometer has also been increased 3 to 6 times compared to the other space spectrometers and the analysed spectrum goes up to 25 keV instead of 15 keV for a spectral resolution of 175–190 eV, thanks to the distance between the detector and the sample which has been reduced to 19 mm. However, the sensitivity of APXS is lower than the sensitivity of its laboratory counterparts (a few ppm), increasing the percentage uncertainty to the measured concentration of some element (Campbell et al., 2012). In addition, APXS is not able to produce chemical maps to visualize the distribution of elements unlike the laboratory instruments.

2. CheMin (MSL)

CheMin (Chemistry & Mineralogy) is an instrument housed in the analytical laboratory of the Curiosity rover that performs analysis of powdered rock samples to identify the mineralogy and chemical composition of rocks and regolith in order to characterize the past habitable environments on Mars (Blake et al., 2012). CheMin uses two techniques, X-ray diffraction and X-ray fluorescence, that allows to identify the crystalline structure of minerals and the elemental composition and mass concentration of the different elements, respectively. In particular, the X-ray fluorescence uses a collimated ca. 50 µm diameter beam to analyse an 8 mm diameter, 175 µm thick sample cell in the ca. 1.5–18 keV spectral range, with a spectral resolution of 250 eV and a spatial resolution of ca. 40 µm/pixels, for an analysis duration of ca. 10 hours (Blake et al., 2012). The spectral range of CheMin is similar to the spectral range covers by the XRF spectrometer and PIXE (1–18 keV) used in this study, allowing the detection of elements from aluminum to molybdenum ($13 < Z < 42$), but the spatial resolution is too low to identify fine microscopic structures.

3. PIXL (Mars 2020)

PIXL (Planetary Instrument for X-ray Lithochemistry) is a X-ray spectrometer mounted on the robotic arm of the Perseverance rover used to identify chemical elements at a tiny scale (Allwood et al., 2020). PIXL is a legacy of the APXS spectrometers on board the Sojourner, Curiosity, Opportunity and Spirit rovers, the role of which is to determine the elemental chemical composition of rocks and regolith. But unlike them, PIXL can also produce elemental maps superimposed on super close-up pictures

showing the texture and microstructure of the materials studied. In particular, the spectrometer uses a 28 keV beam with a 100 µm spot size, emitted towards a target surface located 25 mm away, that allows to detect more than 20 major, minor and trace elements with a great sensitivity (10's ppm level) and in less than 10 seconds (Allwood et al., 2020). PIXL is able to create chemical maps of a few square centimeters with a sub-millimeter resolution (ca. 100 µm) for each element. Despite a lower spatial resolution, PIXL is able to produce chemical maps that are comparable to those obtained with its laboratory counterparts as they can be used to obtain the chemical composition of very fine structures, such as mineral grains and individuals crystals, alteration rings around crystals, laminations, veinlets, concretions, cements and interstitial deposits, allowing petrographic analysis of rocks.

4. *ChemCam (MSL) & SuperCam (Mars 2020)*

ChemCam and SuperCam are instruments that work with a different principle than that in XRF spectroscopy and PIXE but give complementary results and are more sensitive to light elements. ChemCam (Chemistry & Camera) is an instrument aboard the Curiosity rover which fires a laser to analyse the elemental composition of vaporized materials (Wiens et al., 2012). ChemCam works according to the principle of LIBS which allows a 1067 nm laser beam (infrared) to be sent towards a rock or regolith sample at a distance between 2 and 7 meters (Wiens et al., 2012). At the point of impact, the laser heats the material to a temperature of 10,000°C for a few billionths of a second, which instantly vaporizes it and forms a plasma cloud. Several spectrometers collect photons from this plasma in the ultraviolet, blue and visible-near infrared in order to determine the elemental composition of the targeted sample, such as major (O, Si, Al, K, Fe…), minor and trace (H, C, N, F, S, Cl, Cr, Mn, Cu, Zn…) elements. In particular, the ChemCam spectrometer which collects photons in the UV has a spectral analysis range located between ca. 240 and 342 nm and a spectral resolution of 0.15 nm (Wiens et al., 2012). The analysis spot diameter varies from 350 µm at 2 meters to 550 µm at 7 meters distance. The LIBS of SuperCam is an improved version of ChemCam using a 1064 nm laser beam (infrared) and is able of achieving the same or slightly better performance than its predecessor, with the same distance capability (Wiens et al., 2021).

F. Space mass spectrometers

1. *SAM (MSL)*

SAM (Sample Analysis at Mars) is an instrument housed in the analytical laboratory of the Curiosity rover dedicated to the study of organic molecules of powdered and air samples in order to assess the potential habitability of Mars (Mahaffy et al., 2012). In particular, SAM is composed of three different instruments, a gas chromatograph (GC), a mass spectrometer (MS) and a tunable laser spectrometer (TLS). The gas chromatograph comprises two ovens that can heat samples up to 1000°C in order to dissociate the molecules to obtain a gas mixture whose constituents are separated according to their mass then the volatile organic molecules are identified by the mass spectrometer (Mahaffy et al., 2012). The tunable laser spectrometer is able to measure the abundance of different gases, such as methane, water vapor, carbon dioxide at subparts per billion in the Martian atmosphere by studying the absorption of these compounds in a certain wavelength range, as well as isotopic compositions of carbon, oxygen, hydrogen and nitrogen at a few per mil, using two laser sources, a near-infrared laser at 2.78 µm for carbon dioxide and water and a mid-infrared laser at 3.27 µm for methane (Mahaffy et al., 2012). These analyses are complementary of the quantitative chemical composition analyses performed with CheMin and are supplemented by hand-lens resolution investigation of sample spots

with MAHLI. The SAM mass spectrometer operates according to the same principle as its analogue in terrestrial laboratories, such as ICP-MS and LA-ICP-MS, but the sampling processes are different.

2. MOMA (ExoMars)

MOMA (Mars Organic Molecule Analyzer) is an instrument dedicated to the analysis of a broad range of organic molecules in powdered samples collected by the drill of the Rosalind Franklin rover, even if present at very low concentrations, in order to identify molecular biosignatures in Martian surface and subsurface sediments (Goesmann et al., 2017). In particular, MOMA comprises a mass spectrometer coupled to a laser desorption (MOMA-LDMS) and a gas chromatograph (MOMA-GCMS). The high-power (≤135 µJ), pulsed (50 pulses at a 100 Hz repetition rate) UV laser (λ = 266 nm), with a spot size of 400 × 600 µm², is able to study large macromolecules and inorganic minerals, whereas the gas chromatograph, composed of 32 single-use ovens that can heat samples up to 850°C, is able to study volatile organic molecules (Goesmann et al., 2017). The MOMA mass spectrometer operates according to the same principle as its analogue in terrestrial laboratories, such as ICP-MS and LA-ICP-MS. The first analysis mode (laser desorption/ionization) used by MOMA is therefore similar to the analysis mode used in LA-ICP-MS, although the energy, frequency and size of the laser spot are different from those used by the laboratory instrument (5 mJ, 20 Hz and 100 µm, respectively), but whose sensitivity allows the detection of organic molecules lower than pmol/mm². The second analysis mode (GC-MS) is not equivalent to the analysis modes used in this study, but its sensitivity allows the detection of organic molecules lower than nmol.

Although all these space instruments on board rovers use analysis principles similar to those of the laboratory instruments on Earth, spatial and spectral resolution are generally not sufficient to observe microstructures in detail and to make fine measurements of the molecular and elemental composition of carbonaceous matter. The return of samples on Earth for verification of potentially biogenic signatures is therefore necessary.

Some characteristics of the laboratory instruments used in this study are compared with the characteristics of space instruments aboard rovers in **Table V.2**.

Table V.2: *Comparison of some characteristics of the laboratory instruments used in this study with the characteristics of space instruments.*

	Optical microscopy	Raman spectroscopy	DUV fluorescence spectroscopy	Fourier transform infrared spectroscopy	X-ray fluorescence spectroscopy	Proton-induced X-ray emission	ICP-MS/LA-ICP-MS
Laboratory instruments	*- Nikon Eclipse Ti - Olympus BX51*	*- WITec Alpha 500RA*	*- Synchrotron-based DUV spectrometer*	*- Thermo Nicolet iN40 Infrared Imaging Microscope*	*- Synchrotron-based XRF spectrometer*	*- PIXE*	*- iCapQ ICP-MS - Resonetics M50E 193 nm (ArF) UV Excimer laser system*
Analysis type	Mineralogy, morphology, texture, structure	Mineralogy, molecular	Fluorescence, molecular	Molecular	Fluorescence, elemental	Fluorescence, elemental	Geochemistry
Sample type	Thin section (30 or 70 µm)	Thin section (30 or 70 µm)	Detached thin section (70 µm)	Detached thin section (70 µm)	Slab or detached thin section (70 µm)	Detached thin section (30 or 70 µm)	Powder (<80 µm)
Emission energy	Visible photons (400–700 nm)	Green photons (532 nm)	UV photons (275 nm)	IR photons (2.5–15 µm)	X photons (13 keV)	X photons (3 MeV)	UV–IR photons; 193 nm
Analysis spectral range	Visible photons (400–700 nm)	Visible photons (0–4000 cm^{-1})	UV-visible photons (285–550 nm)	IR photons (2.5–15 µm)	X photons (2.5–18 keV)	X photons (1–18 keV)	X photons (1–40 keV)
Spatial resolution	<1 µm	1 µm	7.2 µm	30 µm	10 µm	0.5–0.8 µm	10–100 µm
Spectral resolution	N/A	3 cm^{-1}	0.5 nm	4 cm^{-1}	120–150 eV	<100 eV	N/A
Space instruments	*- MAHLI (MSL) - WATSON (Mars 2020) - CLUPI (ExoMars)*	*- SHERLOC & SuperCam (Mars 2020) - RLS (ExoMars)*	*- SHERLOC (Mars 2020)*	*- SuperCam (Mars 2020) - ISEM, Ma_MISS & MicrOmega (ExoMars)*	*- APXS, CheMin & ChemCam (MSL) - SuperCam & PIXL (Mars 2020)*		*- SAM (MSL) - MOMA (ExoMars)*
Analysis type	Mineralogy, texture, structure	Mineralogy, molecular	Fluorescence, molecular	Mineralogy, molecular	Fluorescence or LIBS, elemental		Geochemistry
Sample type	Rock and regolith (natural, abraded, cored or broken by wheels)	Rock and regolith (+ powders for RLS)	Rock and regolith	Rock and regolith (+ powders for MicrOmega)	Rock and regolith (+ powders for CheMin and vaporized material for ChemCam)		Powders (+ air for SAM)
Emission energy	400–700 nm (+ 365 nm for MAHLI)	532 nm (+ 248.6 nm for SHERLOC)	UV (248.6 nm)	Sunlight (SuperCam & ISEM); visible light (Ma_MISS & MicrOmega)	X photons (APX, CheMin & PIXL); IR (1064 nm and 1067 nm) (ChemCam & SuperCam)		Ionization (GC-MS); IR (2.78 and 3.27 µm) (TLS); UV (266 nm) (LDMS)
Analysis spectral range	400–700 nm	800–4000 cm^{-1} (SHERLOC); 150–4000 cm^{-1} (SuperCam); 150–3800 cm^{-1} (RLS)	275–354 nm	0.4–2.6 µm (SuperCam); 1.1–3.3 µm (ISEM); 0.4–2.2 µm (Ma_MISS); 0.5–3.6 µm (MicrOmega)	1–25 keV (APXS); 1.5–18 keV (CheMin); 1–28 keV (PIXL); 240–342 nm (ChemCam & SuperCam)		Depending on organics
Spatial resolution	ca. 7–14 µm	50 µm (SHERLOC); order of mm (SuperCam); ±2 µm (RLS)	50 µm	1.3–7 mm (SuperCam); 3–10 cm (ISEM); 120 µm (Ma_MISS); 20 µm (MicrOmega)	13.9 µm (APXS); ca. 15 µm (CheMin); ca. 100 µm (PIXL); ca. 10 µm (ChemCam & SuperCam)		ca. 400 × 200 µm (LMDS)
Spectral resolution	N/A	40 cm^{-1} (SHERLOC); 12 cm^{-1} (SuperCam); 6 cm^{-1} (RLS)	0.269 nm	<30 nm	175–190 eV (APXS); 250 eV (CheMin); ≤160 eV (PIXL); 0.15 nm (ChemCam & SuperCam)		0.0005 cm^{-1} (TLS)

III. Analyses of Martian rock samples

The Mars 2020 mission is performing in situ analyses with the Perseverance rover, and collecting samples, including potentially interesting samples for the search for traces of life, to be returned to Earth in order to perform more in-depth analyses in laboratories (Farley et al., 2020). Such samples are being chosen on the basis of their sedimentological characteristics, as well as the presence of organic matter detected in situ in direct association with its mineralogical context using the SHERLOC (Beegle et al., 2020) and PIXL (Allwood et al., 2021) instruments. The former uses UV resonance Raman and native deep UV fluorescence spectroscopy to document and map the distribution of carbonaceous matter, whereas the second is an X-ray fluorescence spectrometer that acquires high spatial resolution observations of rock and regolith chemistry (see the section *II. Space instrumentation*). The study of the Kitty's Gap Chert has demonstrated how arduous the determination of the biogenicity of organic matter in volcanic sediment samples can be, even in well-equipped terrestrial laboratories. In situ analysis on Mars can produce tantalizing and highly promising information but, for definitive demonstrations of biogenicity, the samples will need to be analyzed in terrestrial laboratories using state of the art instrumentation as shown herein. In particular, terrestrial environments analogous to Jezero crater sedimentary sequences have been studied using rover-like instrumentation (e.g., Azua-Bustos, 2023), showing that it is very difficult to identify organic materials and biosignatures within. This again outlines the importance of Mars Sample Return.

The selection of Martian samples for return to Earth will also need to consider the spatio-temporal stresses between the moment of the selection and analysis (approximately a decade), as well as the launch from Mars and the landing on Earth that can induce, for example, disarticulation and breaking apart of poorly consolidated samples within the sample tube. Analysis of the samples in terrestrial laboratories must also take into consideration planetary protection concerns, for example, the sterilization of the samples. As explained by Velbel et al. (2022), "*targeted investigations using analogs of MSR Campaign-relevant returned-sample types should be undertaken to fill knowledge gaps about sterilization effects on important scientific measurements*". As such, it would be informative to follow the proposed sterilization processes in Velbel et al. (2022) on terrestrial Mars analogues, including dry heating under two temperature regimes: 180°C for 3 hours and 250°C for 30 min. However, it is important to note that such heat treatments would probably not affect the Kitty's Gap Chert samples since they were naturally exposed to higher temperatures consistent with their degree of metamorphism, but this is not the case for potential martian organic matter. Additionally, the inherently limited quantity of samples available must be considered in the development of any analytical protocol. Analyses carried out in the laboratory will, however, enable the use of techniques impossible to employ in situ on Mars but must be as non-invasive and non-destructive as possible in order to extract a maximum of qualitative and quantitative data from a minimum volume of sample (Hickman-Lewis et al., 2022).

Considering the above caveat, I here propose a list of analyses to be performed in order to maximize the detection of microfossils in Martian samples where a limited amount of material samples is available, organizing these analyses according to their potential alteration effect on the samples (the first techniques being essential to decide whether one continues to analyze the samples with more invasive/destructive techniques):

- Optical microscopy: non-destructive technique to study the mineralogy of rocks and the alteration of minerals, identify potential morphological biosignatures, and contextualize and select regions of interest for subsequent analyses;

- Raman spectroscopy: mostly non-destructive technique to identify and localize carbonaceous matter related to possible remains of microfossils and provide the mineralogical context of potential biosignatures;
- Laboratory and synchrotron-based techniques such as FTIR and DUV-luminescence spectroscopies: non-destructive techniques to identify the molecular composition of the carbonaceous matter;
- SEM/TEM-EDX: micro-destructive technique to observe individual microstructures and textures and map major elements possibly associated with carbonaceous matter and (bio)minerals;
- µPIXE: micro-destructive technique (high analysis energy) to map the distribution of trace metals in the carbonaceous matter.

Most methods listed here are non-destructive during the analyses of samples, but they may require the preparation of samples (for example, preparation of thin sections or polished sections for optical microscopy or Raman spectroscopy; acid attack or metallic coating for SEM; extraction of FIB sections for TEM), which irreversibly leads to the destruction of samples and possibly the loss of information (e.g., textural and structural information).

Furthermore, I recommend that each of the methodologies proposed for MSR analyses as listed above should be evaluated in light of whether the proposed sterilization protocol (cf. Velbel et al., 2022) will have negative effects on sample integrity or the preservation of putative organic and inorganic biosignatures within, in order to determine which suite of techniques will yield important information for life detection.

IV. Résumé en français

Ce cinquième chapitre discute de l'application possible de l'étude des microfossiles du chert de Kitty's Gap à la sélection de techniques d'analyse pour l'étude des échantillons de retour de Mars. D'abord, le chert de Kitty's Gap est comparé avec des roches martiennes du cratère Jezero. Puis, les instruments spatiaux utilisés pour l'étude de roches martiennes sont comparés avec les instruments de laboratoire utilisés dans cette étude. Enfin, des techniques d'analyse pour étudier les échantillons de retour de Mars sont proposées à la fin de ce chapitre.

Les sédiments du chert de Kitty's Gap sont proposés comme analogues des sédiments martiens déposés à la surface de Mars lorsque ses conditions étaient encore habitables (<3,5 milliards d'années) et dans lesquels on pourrait trouver de potentielles traces de vie fossiles similaires à celles observées dans les sédiments Archéens (**Tableau V.1**). Les sédiments volcaniques de Kitty's Gap sont considérés comme « analogues fonctionnels » en raison de leurs caractéristiques générales qui sont plus ou moins similaires à celles observées ou attendues dans les roches martiennes, mais ayant des propriétés analogues spécifiques (pétrologiques, sédimentologiques, minéralogiques, mécaniques, chimiques et/biologiques) qui sont très pertinentes pour une utilisation donnée. En effet, les sédiments volcaniques de Kitty's Gap ont une origine (mafique) et un environnement de dépôt (eau peu profonde) similaires aux sédiments des roches martiennes présentes dans les cratères Gale et Jezero. Une activité hydrothermale a aussi probablement influencé les sédiments martiens comme l'indiquent les observations du rover Spirit dans le cratère Gusev, bien qu'aucun autre indice n'ait été retrouvé ailleurs sur Mars.

Cependant, le chert de Kitty's Gap a été largement et rapidement silicifié contrairement aux roches sédimentaires volcaniques sur Mars qui ne semblent pas avoir subi un tel processus. Malgré cette différence, ce sont la nature des sédiments, leur environnement de dépôt et la nature de leur habitants microbiens qui sont pertinents dans l'utilisation du chert de Kitty's Gap comme analogue astrobiologique. Sur Mars, les cellules microbiennes ont pu être ensevelies par des ciments minéraux comme les argiles ou les sels, tandis que les restes organiques des microbes ont pu être préservés sous forme de biomasse hétérogène générique (ou EPS) ensevelie par le ciment matriciel, en particulier entre les feuillets d'argile ou par la silice hydratée. De plus, malgré l'âge des sites étudiés in situ sur Mars (>3,6 milliards d'années), la matière organique n'aurait pas subi le degré de métamorphisme auquel les sédiments terrestres d'âge similaire ont été soumis, bien que le métamorphisme d'impact soit probable sur Mars. Il serait donc possible de trouver de la matière organique bien préservée ou très graphitisée. En dépit de ces différentes de préservation et de dégradation, la composition carbonée des restes fossilisés de microbes, associés à des caractéristiques morphologiques, métaboliques, élémentaires et moléculaires dans le chert de Kitty's Gap peuvent être considérées comme des biosignatures analogues pour les recherches astrobiologiques in situ sur Mars et dans les échantillons de retour.

Plusieurs techniques d'analyse utilisées dans l'étude du chert de Kitty's Gap ont été miniaturisées pour l'exploration et la caractérisation des paléoenvironnements habitables et la recherche de traces de vie potentiellement préservées dans les roches in situ sur Mars (**Tableau V.2**), tels que :

- MAHLI (MSL), WATSON (Mars 2020) et CLUPI (ExoMars) qui sont des caméras utilisées pour obtenir des images en couleur des roches et du régolithe, afin d'identifier des minéraux, des textures et des structures depuis l'échelle microscopique jusqu'à l'échelle des affleurements. Cependant, leur résolution spatiale est inférieure (14, 13 et 7 µm/pixels, respectivement) à

celle des microscopes optiques utilisés dans cette étude (ca. 1 µm), ce qui leur permet d'observer des grains de la taille de silts grossiers à très grossiers, mais ne permet pas d'observer de potentiels microfossiles.

- SuperCam (Mars 2020), SHERLOC (Mars 2020) et RLS (ExoMars) qui utilisent la spectroscopie Raman pour détecter et identifier des minéraux et des molécules organiques dans les roches et le régolithe, afin d'identifier des biosignatures minéralogiques et moléculaires. La gamme spectrale d'analyse de ces instruments (150–4000 cm^{-1}) couvre une gamme spectrale similaire au spectromètre Raman utilisé dans cette étude (0–4000 cm^{-1}), permettant de détecter divers minéraux et groupes fonctionnels, bien que leurs résolutions spatiale (2–50 µm) et spectrale (6–40 cm^{-1}) soient inférieures aux résolutions spatiale (1 µm) et spectrale (3 cm^{-1}) de l'instrument de laboratoire. Malgré une résolution spatiale limitée, SHERLOC permet également de réaliser des cartographies des phases minérales et organiques jusqu'à 7 × 7 mm^2 avec un temps d'acquisition inférieur à 10 minutes.

- SHERLOC (Mars 2020) qui utilise également la fluorescence native DUV en complément de la spectroscopie Raman pour détecter et identifier la composition moléculaire des matériaux organiques dans les roches et le régolithe, afin d'identifier des biosignatures moléculaires. SHERLOC utilise une source de photons UV (248.6 nm) qui permet de couvrir une gamme spectrale d'analyse (275–354 nm) similaire à la gamme spectrale des aromatiques détectés avec le spectromètre DUV basé sur le rayonnement synchrotron (285–370 nm). De plus, SHERLOC utilise une meilleure résolution spectrale (0,27 nm) que celle de l'instrument de laboratoire (0,5 nm), bien que la résolution spatiale (50 µm) soit inférieure à celle de ce dernier (7,2 µm).

- SuperCam (Mars 2020), ISEM, Ma_MISS & MicrOmega (ExoMars) qui utilisent la spectroscopie IR pour détecter et identifier différents groupes fonctionnels associés à des minéraux et à des matériaux organiques dans les roches et le régolithe, afin de sélectionner des cibles d'intérêt pour des analyses complémentaires et d'identifier des biosignatures minéralogiques et moléculaires. Les instruments spatiaux utilisent la lumière du Soleil ou la lumière visible afin d'étudier la région spectrale située entre le visible et le début de l'infrarouge moyen (0,4–3,6 µm), contrairement au microscope d'imagerie infrarouge utilisé dans cette étude qui envoie et reçoit des photons IR principalement dans l'infrarouge moyen (2,5–15 µm). Par conséquent, la plupart de ces instruments spatiaux sont surtout adaptés à la caractérisation des phases minérales, incluant des minéraux hydratés (e.g., phyllosilicates), et de certains composés organiques (étirement aromatique C–H, étirement aliphatique CH_2 et CH_3 notamment).

- APXS & CheMin (MSL) et PIXL (Mars 2020) qui utilisent la fluorescence à rayons X pour déterminer la composition élémentaire des roches et du régolithe, afin de caractériser l'environnement géologique des échantillons étudiés. Les instruments spatiaux utilisent une source de photons X pour mesurer les éléments majeurs, mineurs et traces dans une gamme spectrale d'analyse (1–28 keV) couvrant une partie de celles des spectromètre XRF basé sur le rayonnement synchrotron (2,5–18 keV) et PIXE (1–18 keV), mais dont les résolutions spatiale (14 µm–100 µm) et spectrale (160–250 eV) sont inférieures aux résolutions spatiale (10 µm et 0,5–0,8 µm) et spectrale (120–150 eV et < 100 eV) des instruments de laboratoire. Bien que la résolution de PIXL soit limitée, cet instrument permet également de cartographier les éléments chimiques, dont les cartographies de quelques centimètres carré sont utiles pour obtenir la composition chimique de différentes structures d'intérêt (e.g., cristaux, laminations,

dépôts interstitiels), afin de réaliser une étude pétrographique des roches analysées. Par ailleurs, les instruments ChemCam (MSL) et SuperCam (Mars 2020) permettent d'obtenir des résultats complémentaires à ceux des autres instruments cités précédemment, mais en utilisant un principe différent, la technique du LIBS. En effet, ces instruments peuvent vaporiser les échantillons à analyser à une température de 10 000°C par un laser infrarouge, afin de déterminer la composition élémentaire des échantillons avec une résolution spatiale de 10 µm et une résolution spectrale de 0,15 nm.

- SAM (MSL) et MOMA (ExoMars) qui utilisent la spectrométrie de masse pour déterminer la composition géochimique des poudres de roche et de l'atmosphère, afin de caractériser l'habitabilité potentielle de Mars et d'identifier des biosignatures moléculaires. La chromatographie en phase gazeuse couplée à la spectrométrie de masse (GC-MS) est une technique d'analyse présente sur les deux instruments qui permet de chauffer les échantillons afin d'identifier les molécules organiques volatiles en fonction de leur rapport masse sur charge. Le spectromètre laser de l'instrument SAM (TLS) permet de mesurer l'abondance de différents gaz (e.g., vapeur d'eau, méthane, dioxyde de carbone) et la composition isotopique de certains éléments (e.g., carbone, oxygène, hydrogène) en utilisant des sources IR proche et moyen. L'instrument MOMA comporte un spectromètre de masse couplé à un laser de désorption (LDMS) qui permet d'étudier des grosses molécules organiques et des minéraux inorganiques en utilisant une source de photons UV (266 nm), dont le mode d'analyse (désorption laser/ionisation) est similaire à celui du LA-ICP-MS utilisé dans cette étude.

Bien que le fonctionnement des instruments spatiaux soit similaire à ceux des instruments de laboratoire utilisés sur Terre, les résolutions spatiale et spectrale ne sont généralement pas suffisantes pour observer les microstructures de manière détaillée, ni pour mesurer la composition élémentaire et moléculaire de la matière carbonée plus précisément. Le retour d'échantillons sur Terre est donc nécessaire afin de vérifier la présence de signatures potentiellement biogéniques.

La rover Perseverance de la mission Mars 2020 réalise actuellement des analyses in situ et récupère des échantillons potentiellement intéressants pour la recherche de traces vie qui seront ramenés sur Terre afin d'effectuer des analyses plus approfondies en laboratoire. Ces échantillons sont notamment choisis en fonction de leur caractéristiques sédimentologique, ainsi que de la présence de matière organique détectée en association directe avec des minéraux, grâce aux instruments SHERLOC et PIXL. L'étude des sédiments du chert de Kitty's Gap a démontré à quel point la détermination de la biogénicité de la matière organique peut être compliquée, même en disposant d'équipements de pointe. L'analyse in situ de sédiments martiens peut donc s'avérer particulièrement délicate, malgré des informations prometteuses et nécessite donc des analyses plus poussées en laboratoire pour démontrer la biogénicité de microfossiles martiens supposés. En particulier, des environnements terrestres analogues aux séquences sédimentaires du cratère Jezero ont été étudiés en utilisation une instrumentation similaire à celle embarquée par les rovers, soulignant la difficulté à identifier des matériaux organiques et des biosignatures et confirmant l'importance d'une mission de retour d'échantillons.

La sélection d'échantillons martiens destinés à être renvoyés sur Terre devra également prendre en compte les contraintes spatio-temporelles entre le moment de la sélection et de l'analyse, ainsi que le lancement depuis Mars et l'atterrissage sur Terre qui peuvent induire, par exemple, la fragmentation d'échantillons mal consolidés dans leur tube. L'analyse des échantillons dans les laboratoires terrestres doit également prendre en compte la protection planétaire, par exemple (e.g., la stérilité des

échantillons), ainsi que la quantité limitée d'échantillons disponibles. Cependant, les analyses effectuées en laboratoire permettront d'utiliser des techniques impossibles à mettre en œuvre in situ sur Mars, mais elles devront être les moins invasives et non-destructives possibles afin d'extraire un maximum de données qualitatives et quantitatives à partir d'un volume minimum d'échantillon.

Je propose ici une liste d'analyses pouvant être utilisées pour maximiser la détection de microfossiles dans les échantillons martiens, dont l'ordre dépend de l'effet d'altération possible sur les échantillons (les premières techniques étant essentielles pour décider de continuer à analyser les échantillons avec des techniques plus invasives/destructives) :

- Microscopie optique : technique non destructive pour étudier la minéralogie des roches et l'altération des minéraux, identifier de possibles biosignatures morphologiques, contextualiser et sélectionner les régions d'intérêt pour les analyses suivantes ;
- Spectroscopie Raman : technique majoritairement non destructive pour identifier et localiser la matière carbonée associée à d'éventuels restes de microfossiles et fournir le contexte minéralogique de biosignatures potentielles ;
- Techniques de laboratoire ou basées sur le rayonnement synchrotron telles que les spectroscopies FTIR et luminescence DUV : techniques non destructives pour identifier la composition moléculaire de la matière carbonée ;
- MEB/MET-EDX: technique micro-destructive pour observer des microstructures individuelles et des textures et cartographier les éléments majeurs pouvant être associés à la matière carbonée et aux (bio)minéraux ;
- µPIXE : technique micro-destructive (haute énergie d'analyse) pour cartographier la distribution des métaux traces dans la matière carbonée.

Chapter VI: Conclusions

I. Main findings and perspectives

The objectives of this thesis were the use of complementary, multi-scale analyses techniques in order to study some of the earliest purported traces of life on Earth, and the application of these results into the search for life on Mars. Three samples were collected from the sedimentary horizon of the 3.446 Ga-old Kitty's Gap Chert in Coppin Gap Greenstone Belt, Pilbara Craton, Australia, including one sample from a hydrothermal vein, one sample from a conglomerate located a few centimeters from the hydrothermal vein and one sample from a laminated chert located about 15 meters from the vein. The first sample was studied to obtain geochemical information about the hydrothermal source. The other two samples were characterised in terms of sedimentology, petrology, mineralogy, geochemistry, morphology, and elemental and molecular composition in order to estimate the habitability of the paleoenvironment for microbial life, as well as to evaluate the syngenicity and biogenicity of the purported fossilized traces of life.

My approach, based on the combination of physico-chemical data, provided multiple lines of evidence making possible the interpretation of the co-evolution of microbial life and the paleoenvironment in early Archean sediments. However, demonstrating the biogenicity of early Archean fossil remains of microorganisms remains ambiguous and highly controversial without resorting to high-resolution microscopy combined with biogeochemistry. This study highlights the degree of analytical rigor that will be necessary in the search for potential traces of life in Martian rocks. Although the study of samples in their geological context at regional and local scales is possible, it appears that the identification of carbonaceous structures at the microbiome scale in situ on Mars is particularly delicate due to the low spatial resolution of the instruments on board the rovers. Mars Sample Return mission will probably be the only way to establish the biogenicity of putative Martian microfossils.

The main findings of this study are:

- The documentation of the paleoenvironment of the Kitty's Gap Chert through sedimentological, petrological, mineralogical and geochemical characterization revealed that the volcaniclastic sediments were deposited in a shallow-water, semi-enclosed tidal basin influenced by the erosion of landmasses of volcanic origin and hydrothermal fluids. However, the inputs from terrigenous (riverine) sources were greater as shown by relatively elevated LREE concentrations and low Y/Ho ratios, which correlate with trace element patterns and concentrations indicating mixed mafic and felsic contributions. The paleoenvironment of the Kitty's Gap Chert was therefore metal-rich, thermophilic, slightly acidic (although, at times, partly alkaline) and supplied with chemical fluids derived from different reservoirs. The studied samples indicate that **the sedimentary environment of the Kitty's Gap Chert was therefore habitable for microbial life during the Paleoarchean**.

- The syngenicity and biogenicity of the carbonaceous matter associated with putative degraded remains of fossilized microorganisms were determined using morphological, elemental and molecular analyses, as well as by its distribution at multiple scales.

- The carbonaceous matter was detected in direct association with the surface of volcanic particles, preferentially with morphologically and/or mineralogically altered volcanic clasts,

where it forms coatings and is ubiquitous in the silica-dust gel matrix, supporting the previous interpretation of chemolithotrophic microorganisms. In addition, the thermal maturity (300–400°C) of the carbonaceous matter is consistent with the degree of metamorphism experienced by the host rock, **confirming its syngenicity**.

- Comparison of the microfossil-like carbonaceous structures revealed previously by SEM with those investigated herein using petrological thin sections and FIB sections allowed to verify the presence of EPS forming carbonaceous films around volcanic clasts, possible coccoidal and lenticular cells, degraded remnants of microbial biofilms and completely degraded volcanic clasts coated with microbial biomass. In addition, graphitized detrital particles of probable mantle and/or biological origin have been identified in the samples. All the structures observed by SEM and TEM were often found associated with hydromuscovite sheets, more rarely with anatase, or sometimes located between quartz polygons. Nevertheless, incontrovertible identification in the TEM preparations of the microorganisms observed by SEM proved to be more difficult, likely as a result of their extremely delicate and probably subtle appearance in thin section. This underlines the challenges that will be faced if returned Martian samples contain similar traces of chemotroph-like microorganisms. Further work will be needed to address this aspect.

- The analysis of the chemical elements co-located with the carbonaceous matter indicated excess concentrations of biologically useful transition metals, such as Cr, V, As, Mo, Zn and Fe relative to other parts of the volcanic clasts and the matrix, both being poor in carbonaceous matter. This trace metal budget could be an indication of the possible microbial metabolisms present during the deposition of the sediments of the Kitty's Gap Chert, such as sulfur and possibly sulfate reduction (although there was little sulfate in the Paleoarchean oceans), or methanogenesis. Alternatively, it may represent metal chelation to abundant microbial EPS characteristic of chemolithotrophic microorganisms. Most likely the signature is a mixture of these two phenomena.

- The molecular composition of the carbonaceous matter shows variations in aromatic and aliphatic compounds, reflecting significant preservation of biomolecular diversity in the Kitty's Gap Chert despite its great age. The aromatics, aliphatics and other functional groups were often observed mixed with mineral phases, such as hydromuscovite and anatase, confirming the previous observations made by the other techniques. The CH_2/CH_3 and CH_3/CH_2 ratios suggest a mixed community composed of Bacteria and Archaea, with potential dominance by the latter.

- The microstructure, nanostructure, as well as elemental and molecular composition of the carbonaceous matter were therefore used as complementary biosignatures, **confirming its biological origin**.

The very simple nature of the fossilized life forms occurring in the sediments of the Kitty's Gap Chert and the shallow, volcanic and hydrothermal, aqueous environment in which they formed, make such sediments excellent functional analogues for Martian sediments. Such sediments could be used in the elaboration of procedural protocols for searching for traces of fossilized life in samples returned from Mars. An example of such a protocol for the analysis of sedimentary samples is given below:

- Macroscopic observations and imaging of structures (bedding, laminations, fractures, veining, stylolites, orientation of the clasts, brecciation, deformation, redox fronts, concretions, secondary mineral precipitation, etc.) and textures (grain size, grain roundness, sorting, etc.) in sub-samples extracted from the core samples collected by the Perseverance rover. These details will contribute to the evaluation of habitability already assessed at the sampling sites on Mars and will provide additional information related to the preservation of potential biosignatures (also note that half of each sample will be set aside for future analysis with more advanced technology, some of which may not yet have been invented).

- For each subsample taken for analysis the following information will be needed:
  - Mineralogical identification and analysis of alteration features (diagenetic, post-diagenetic, shock, etc.). This information can be obtained using optical microscopy coupled with Raman and/or IR spectroscopy, for example;
  - Documentation of the distribution of carbonaceous matter, and verification of its association with mineral grains or vein features using spectral techniques, such as Raman and IR;
  - Documentation of any (microscopically) visible microstructures and textures of potentially biogenic origin (microfossils, biofilms, filaments, EPS, etc.) using high-resolution microscopic observations, such as SEM or TEM;
  - Mapping of major and trace elements associated with the carbonaceous matter and identification of (bio)minerals using elemental spectroscopy (techniques such as µPIXE, EDX, and fluorescence spectroscopy);
  - Identification of the molecular composition of the carbonaceous matter using methods such as synchrotron-based FTIR and DUV-luminescence spectroscopy.

Combining a range of techniques yielding complementary datasets at different spatial scales will represent the most appropriate means of characterizing putative biosignatures in returned Martian samples while carefully addressing the potential non-biological processes by which such features could have formed. Finally, it will also be necessary to consider the effects of sterilization processes that will be applied to returned Martian samples to comprehensively understand their effects on putative biosignatures within rock samples.

II. Résumé en français

Les objectifs de cette thèse étaient l'utilisation de techniques d'analyses complémentaires à plusieurs échelles afin d'étudier parmi les plus anciennes traces de vie possibles sur Terre, et l'application de ces résultats à la recherche de vie sur Mars. Trois échantillons du chert de Kitty's Gap âgé de 3,446 milliards d'années ont été collectés puis analysés en laboratoire, incluant un échantillon extrait d'une veine hydrothermale et deux échantillons issus, respectivement, de quelques centimètres et 15 mètres de la veine. Le premier échantillon a permis d'obtenir des informations concernant la source hydrothermale. Les deux derniers échantillons ont été caractérisés en termes de sédimentologie, pétrologie, minéralogie, géochimie, morphologie et composition élémentaire et moléculaire, afin d'estimer l'habitabilité du paléoenvironnement pour la vie microbienne, ainsi que pour évaluer la syngénicité et la biogénicité des traces de vie fossiles supposées.

Mon approche, basée sur une combinaison de données physico-chimiques, a fourni de nombreuses preuves rendant possible l'interprétation de la coévolution de la vie microbienne et du paléoenvironnement dans les sédiments archéens primitifs. Cependant, la biogénicité de restes fossiles de microorganismes datant de l'Archéen reste ambiguë et très controversée sans avoir recours à la microscopie à haute résolution combinée avec la biogéochimie. Cette étude souligne le degré de rigueur analytique qui sera nécessaire dans la recherche de potentielles traces de vie dans les roches martiennes. Bien que l'étude d'échantillons dans leur contexte géologique aux échelles régionale et locale soit possible, l'identification de structures carbonées à l'échelle du microbiome in situ sur Mars est particulièrement délicate en raison de la faible résolution spatiale des instruments embarqués. La mission de retour d'échantillons de Mars sera probablement la seule façon de déterminer la biogénicité de microfossiles martiens supposés.

Les principaux résultats de cette étude sont :

- La documentation du paléoenvironnement du chert de Kitty's Gap à travers sa caractérisation sédimentologique, pétrologique, minéralogique et géochimique a révélé que les sédiments volcanoclastiques se sont déposés dans un bassin de marée semi-fermé de faible profondeur, influencé par l'érosion de terres émergées volcaniques et des fluides hydrothermaux. Cependant, les apports des rivières étaient plus importants comme le montrent les concentrations relativement élevées en LREE et les faibles ratios Y/Ho qui sont corrélés avec les profils et les concentrations des éléments traces indiquant des contributions mafiques et felsiques. Le paléoenvironnement était donc riche en métaux, thermophile, légèrement acide (bien que parfois alcalin) et alimenté en fluides chimiques issus de différents réservoirs. Les échantillons étudiés montrent **un environnement habitable pour la vie microbienne pendant le Paléoarchéen.**

- La syngénicité et la biogénicité de la matière carbonée associées aux restes dégradés supposés de microorganismes fossilisés ont été étudiées par des analyses morphologiques, élémentaires et moléculaires, ainsi que par sa distribution à plusieurs échelles.

- La matière carbonée a été détectée en association directe avec la surface des particules volcaniques, préférentiellement avec les clastes volcaniques morphologiquement et/ou minéralogiquement altérés, où elle forme des films et est omniprésente dans les poussières volcaniques, confortant l'interprétation précédente de microorganismes chimiolithotrophes.

De plus, la maturité thermique (300–400°C) de la matière carbonée est cohérente avec le degré de métamorphisme subie par la roche encaissante, **confirmant sa syngénicité**.

- La comparaison de structures carbonées de type microfossile révélées précédemment par MEB avec celles étudiées ici à l'aide de lames minces et de coupes FIB a permis de vérifier la présence d'EPS formant des films carbonés autour des clastes volcaniques, d'éventuelles cellules coccoïdales et lenticulaires, des restes dégradés de biofilms microbiens et des clastes volcaniques complètement dégradées recouverts par de la biomasse microbienne. De plus, des particules détritiques graphitisées d'origine probable du manteau et/ou biologique ont été identifiées dans les échantillons. Toutes les structures observées au MEB et au MET ont souvent été retrouvées associées avec des feuillets d'hydromuscovite, plus rarement à de l'anatase, ou parfois localisées entre les polygones de quartz. Néanmoins, l'identification incontestable dans les préparations MET des microorganismes observés au MEB s'est avérée plus difficile, probablement en raison de leur aspect extrêmement délicat et probablement subtil en lames minces. Cela souligne les défis qui seront rencontrés sur les échantillons de retour de Mars pour y détecter des traces similaires de microorganismes de type chimiotrophe.

- L'analyse des éléments chimiques colocalisés avec la matière carbonée a indiqué des concentrations excessives de métaux de transition, incluant Cr, V, As, Mo, Zn et Fe, par rapport à d'autres parties des clastes volcaniques et de la matrice, toutes deux appauvries en matière carbonée. Cet équilibre de métaux traces pourrait indiquer d'éventuels métabolismes microbiens présents lors du dépôt des sédiments, comme la réduction du soufre et éventuellement du sulfate (bien qu'il y ait peu de sulfate dans les océans Paléoarchéens), ou la méthanogenèse. Alternativement, cela peut représenter une chélation des métaux aux EPS microbiens abondants caractéristiques des microorganismes chimiolithotrophes. Il est fort probable que cette signature soit un mélange de ces deux phénomènes.

- La composition moléculaire de la matière carbonée montre des variations en composés aromatiques et aliphatiques, reflétant une préservation significative de la diversité biomoléculaire dans le chert de Kitty's Gap malgré ses 3,446 milliards d'années. Les aromatiques, aliphatiques et autres groupes fonctionnels ont souvent été observés mélangés à des phases minérales, telles que l'hydromuscovite et l'anatase, confirmant les observations précédentes. Les ratios CH_2/CH_3 et CH_3/CH_2 suggèrent une communauté mixte composée de bactéries et d'archées, avec une dominance potentielle de ces dernières.

- La microstructure, la nanostructure ainsi que la composition élémentaire et moléculaire de la matière carbonée ont donc été utilisées comme biosignatures complémentaires, **confirmant son origine biologique**.

La nature très simple des formes de vie fossilisées présentes dans les sédiments du chert de Kitty's Gap et l'environnement aqueux peu profond, volcanique et hydrothermal dans lequel elles se sont formées, font de ces sédiments d'excellents analogues fonctionnels des sédiments martiens. De tels sédiments pourraient être utilisés dans l'élaboration de protocoles pour la recherche de traces de vie fossiles dans des échantillons rapportés de Mars. Un exemple d'un tel protocole pour l'analyse d'échantillons sédimentaire est donné ci-dessous :

- Observations macroscopiques et imagerie des structures (stratification, laminations, fractures, veines, orientation des clastes…) et des textures (granulométrie, sphéricité des grains, tri…) dans des sous-échantillons extraits des carottes collectées par le rover Perseverance. Ces détails contribueront à l'évaluation de l'habitabilité déjà évaluée sur les sites d'échantillonnage sur Mars et fourniront des informations supplémentaires liées à la préservation de biosignatures potentielles (à noter également que la moitié de chaque échantillon sera mise de côté pour de futures analyses avec une technologie plus avancée, dont certaines n'ont peut-être pas encore été inventées).

- Pour chaque sous-échantillon prélevé pour analyse, les informations suivantes seront nécessaires :
  - Identification minéralogique et analyse des caractéristiques d'altération par microscopie optique couplée à la spectroscopie Raman et/ou infrarouge, par exemple ;
  - Documentation de la distribution de la matière carbonée et vérification de son association avec les minéraux ou des veines à l'aide de techniques spectrales comme la Raman et l'infrarouge ;
  - Documentation de toutes les microstructures et textures visibles (microscopiquement) d'origine potentiellement biogénique (microfossiles, biofilms, EPS…) à l'aide d'observations à haute résolution par MEB ou MET ;
  - Cartographie des éléments majeurs et traces associés à la matière carbonée et identification de (bio)minéraux par spectroscopie élémentaire (techniques telles que µPIXE, EDX et spectroscopie de fluorescence) ;
  - Identification de la composition moléculaire de la matière carbonée à l'aide de méthodes telles que les spectroscopie FTIR et luminescence DUV par synchrotron.

La combinaison de plusieurs techniques produisant des données complémentaires à différentes échelles spatiales représentera le moyen le plus approprié de caractériser les biosignatures supposées dans les échantillons de retour de Mars tout en abordant soigneusement les processus non biologiques potentiels par lesquels de telles caractéristiques auraient pu se former. Enfin, il sera également nécessaire de considérer les effets des processus de stérilisation appliqués aux échantillons de retour de Mars pour comprendre de manière globale leurs effets sur les biosignatures potentielles au sein des échantillons de roches.

References

Adam, Z.R., Hongo, Y., Cleaves, H.J., Yi, R., Fahrenbach, A.C., Yoda, I., Aono, M., 2018. Estimating the capacity for production of formamide by radioactive minerals on the prebiotic Earth. Sci. Rep. 8, 265. https://doi.org/10.1038/s41598-017-18483-8

Addadi, L., Raz, S., Weiner, S., 2003. Taking advantage of disorder: amorphous calcium carbonate and its roles in biomineralization. Adv. Mater. 15, 959–970. https://doi.org/10.1002/adma.200300381

Alleon, J., Summons, R.E., 2019. Organic geochemical approaches to understanding early life. Free Radic. Biol. Med. 140, 103–112. https://doi.org/10.1016/j.freeradbiomed.2019.03.005

Allwood, A.C., Walter, M.R., Kamber, B.S., Marshall, C.P., Burch, I.W., 2006. Stromatolite reef from the Early Archaean era of Australia. Nature 441, 714–718. https://doi.org/10.1038/nature04764

Allwood, A.C., Walter, M.R., Burch, I.W., Kamber, B.S., 2007. 3.43 billion-year-old stromatolite reef from the Pilbara Craton of Western Australia: ecosystem-scale insights to early life on Earth. Precambrian Res. 158, 198–227. https://doi.org/10.1016/j.precamres.2007.04.013

Allwood, A.C., Kamber, B.S., Walter, M.R., Burch, I.W., Kanik, I., 2010. Trace elements record depositional history of an Early Archean stromatolitic carbonate platform. Chem. Geol. 270, 148–163. https://doi.org/10.1016/j.chemgeo.2009.11.013

Allwood, A.C., Rosing, M.T., Flannery, D.T., Hurowitz, J.A., Heirwegh, C.M., 2018. Reassessing evidence of life in 3,700-million-year-old rocks of Greenland. Nature 563, 241–244. https://doi.org/10.1038/s41586-018-0610-4

Allwood, A.C., Wade, L.A., Foote, M.C., Elam, W.T., Hurowitz, J.A., Battel, S., Dawson, D.E., Denise, R.W., Ek, E.M., Gilbert, M.S., 2020. PIXL: Planetary instrument for X-ray lithochemistry. Space Sci. Rev. 216, 1–132. https://doi.org/10.1007/s11214-020-00767-7

Allwood, A.C., Hurowitz, J.A., Clark, B.C., Cinquini, L., Davidoff, S., Denise, R.W., Elam, W.T., Foote, M.C., Flannery, D.T., Gerhard, J.H., 2021. The PIXL instrument on the mars 2020 perseverance rover. Presented at the 52nd Lunar and Planetary Science Conference, LPI Contributions [Abstract]. URL https://www.hou.usra.edu/meetings/lpsc2021/pdf/1591.pdf [accessed: 06.12.23].

Amelinckx, S., Van Dyck, D., Van Landuyt, J., van Tendeloo, G., 2008. Electron microscopy: principles and fundamentals. John Wiley & Sons, New York.

Arndt, N.T., Nisbet, E.G., 2012. Processes on the Young Earth and the Habitats of Early Life. Annu. Rev. Earth Planet. Sci. 40, 521–549. https://doi.org/10.1146/annurev-earth-042711-105316

Arndt, S., LaRowe, D.E., 2018. Organic matter degradation and preservation, in: White, W. (Eds.), Encyclopedia of Geochemistry, Encyclopedia of Earth Sciences Series. Springer, Cham, pp. 1–6.

Atlas, R.M., 1989. Microbiology: Fundamentals and Applications, 2nd Edition. Maxwell Macmillan, New York.

Azua-Bustos, A., 2023. Dark microbiome and extremely low organics in Atacama fossil delta unveil Mars life detection limits. Nat. Commun. 14, 808. https://doi.org/10.1038/s41467-023-36172-1

Bahcall, J.N., Pinsonneault, M.H., Basu, S., 2001. Solar models: Current epoch and time dependences, neutrinos, and helioseismological properties. Astrophys. J. 555, 990. https://doi.org/10.48550/arXiv.astro-ph/0010346

Bak, F., Pfennig, N., 1987. Chemolithotrophic growth of Desulfovibrio sulfodismutans sp. nov. by disproportionation of inorganic sulfur compounds. Arch. Microbiol. 147, 184–189. https://doi.org/10.1007/BF00415282

Balci, N., Bullen, T.D., Witte-Lien, K., Shanks, W.C., Motelica, M., Mandernack, K.W., 2006. Iron isotope fractionation during microbially stimulated Fe (II) oxidation and Fe (III) precipitation. Geochim. Cosmochim. Acta 70, 622–639. https://doi.org/10.1016/j.gca.2005.09.025

Barberet, P., Jouve, J., Sorieul, S., Alfaurt, P., Mathieu, L., 2021. AIFIRA: a light ion beam facility for ion beam analysis and irradiation. Eur. Phys. J. Plus 136, 67. https://doi.org/10.1140/epjp/s13360-020-01045-9

Barboni, M., Boehnke, P., Keller, B., Kohl, I.E., Schoene, B., Young, E.D., McKeegan, K.D., 2017. Early formation of the Moon 4.51 billion years ago. Sci. Adv. 3, e1602365. https://doi.org/10.1126/sciadv.1602365

Barge, L.M., Cardoso, S.S., Cartwright, J.H., Cooper, G.J., Cronin, L., De Wit, A., Doloboff, I.J., Escribano, B., Goldstein, R.E., Haudin, F., 2015. From chemical gardens to chemobrionics. Chem. Rev. 115, 8652–8703. https://doi.org/10.1021/acs.chemrev.5b00014

Bau, M., Dulski, P., 1996. Distribution of yttrium and rare-earth elements in the Penge and Kuruman iron-formations, Transvaal Supergroup, South Africa. Precambrian Res. 79, 37–55. https://doi.org/10.1016/0301-9268(95)00087-9

Bau, M., 1999. Scavenging of dissolved yttrium and rare earths by precipitating iron oxyhydroxide: experimental evidence for Ce oxidation, Y-Ho fractionation, and lanthanide tetrad effect. Geochim. Cosmochim. Acta 63, 67–77. https://doi.org/10.1016/S0016-7037(99)00014-9

Beard, B.L., Johnson, C.M., Cox, L., Sun, H., Nealson, K.H., Aguilar, C., 1999. Iron isotope biosignatures. Science 285, 1889–1892. https://doi.org/10.1126/science.285.5435.1889

Beegle, L.W., Bhartia, R., DeFlores, L., Abbey, W., Miller, E., Bailey, Z., Razzell Hollis, J., Pollack, R., Asher, S., Burton, A., 2020. The SHERLOC Investigation on the Mars 2020 Rover. Presented at the 51st Lunar and Planetary Science Conference, LPI Contributions, The Woodlands, Texas [Abstract]. URL https://www.hou.usra.edu/meetings/lpsc2020/pdf/2081.pdf [accessed: 06.12.23].

Bell, E.A., Boehnke, P., Harrison, T.M., Mao, W.L., 2015. Potentially biogenic carbon preserved in a 4.1 billion-year-old zircon. Proc. Natl. Acad. Sci. 112, 14518–14521. https://doi.org/10.1073/pnas.1517557112

Benison, K.C., Bosak, T., Clark, B.C., Czaja, A.D., Fornaro, T., Gill, K.K., Gómez, F., Herd, C.D.K., Martinez-Frias, J., Núñez, J.I., Randazzo, N., Siljeström, S., 2023. Biosignature potential and possible environmental indicators of sulfate-rich rocks from Hogwallow Flats and Yori Pass, Jezero crater delta front, Mars. Presented at the 54th Lunar and Planetary Science Conference, LPI Contributions, The Woodlands, Texas [Abstract]. URL https://www.hou.usra.edu/meetings/lpsc2023/pdf/2570.pdf (accessed: 05.31.23).

Benning, L.G., Phoenix, V.R., Yee, N., Tobin, M.J., 2004. Molecular characterization of cyanobacterial silicification using synchrotron infrared micro-spectroscopy. Geochim. Cosmochim. Acta 68, 729–741. https://doi.org/10.1016/S0016-7037(03)00489-7

Berner, R.A., 1989. Biogeochemical cycles of carbon and sulfur and their effect on atmospheric oxygen over Phanerozoic time. Glob. Planet. Change 1, 97–122. https://doi.org/10.1016/0031-0182(89)90186-7

Beyssac, O., Rouzaud, J.-N., Goffé, B., Brunet, F., Chopin, C., 2002a. Graphitization in a high-pressure, low-temperature metamorphic gradient: a Raman microspectroscopy and HRTEM study. Contrib. Mineral. Petrol. 143, 19–31. https://doi.org/10.1007/s00410-001-0324-7

Beyssac, O., Goffé, B., Chopin, C., Rouzaud, J.N., 2002b. Raman spectra of carbonaceous material in metasediments: a new geothermometer. J. Metamorph. Geol. 20, 859–871. https://doi.org/10.1046/j.1525-1314.2002.00408.x

Bhartia, R., Beegle, L.W., DeFlores, L., Abbey, W., Razzell Hollis, J., Uckert, K., Monacelli, B., Edgett, K.S., Kennedy, M.R., Sylvia, M., Aldrich, D., Anderson, M., Asher, S.A., Bailey, Z., Boyd, K., Burton, A.S., Caffrey, M., Calaway, M.J., Calvet, R., Cameron, B., Caplinger, M.A., Carrier, B.L., Chen, N., Chen, A., Clark, M.J., Clegg, S., Conrad, P.G., Cooper, M., Davis, K.N., Ehlmann, B., Facto, L., Fries, M.D., Garrison, D.H., Gasway, D., Ghaemi, F.T., Graff, T.G., Hand, K.P., Harris, C., Hein, J.D., Heinz, N., Herzog, H., Hochberg, E., Houck, A., Hug, W.F., Jensen, E.H., Kah, L.C., Kennedy, J., Krylo, R., Lam, J., Lindeman, M., McGlown, J., Michel, J., Miller, E., Mills, Z., Minitti, M.E., Mok, F., Moore, J., Nealson, K.H., Nelson, A., Newell, R., Nixon, B.E., Nordman, D.A., Nuding, D., Orellana, S., Pauken, M., Peterson, G., Pollock, R., Quinn, H., Quinto, C., Ravine, M.A., Reid, R.D., Riendeau, J., Ross, A.J., Sackos, J., Schaffner, J.A., Schwochert, M., O Shelton, M., Simon,

R., Smith, C.L., Sobron, P., Steadman, K., Steele, A., Thiessen, D., Tran, V.D., Tsai, T., Tuite, M., Tung, E., Wehbe, R., Weinberg, R., Weiner, R.H., Wiens, R.C., Williford, K., Wollonciej, C., Wu, Y.-H., Yingst, R.A., Zan, J., 2021. Perseverance's Scanning Habitable Environments with Raman and Luminescence for Organics and Chemicals (SHERLOC) Investigation. Space Sci. Rev. 217, 58. https://doi.org/10.1007/s11214-021-00812-z

Bibring, J.-P., Langevin, Y., Mustard, J.F., Poulet, F., Arvidson, R., Gendrin, A., Gondet, B., Mangold, N., Pinet, P., Forget, F., 2006. Global mineralogical and aqueous Mars history derived from OMEGA/Mars Express data. science 312, 400–404. https://doi.org/10.1126/science.1122659

Bibring, J.-P., Hamm, V., Pilorget, C., Vago, J.L., 2017. The micrOmega investigation onboard ExoMars. Astrobiology 17, 621–626. https://doi.org/10.1089/ast.2016.1642

Blake, D., Vaniman, D., Achilles, C., Anderson, R., Bish, D., Bristow, T., Chen, C., Chipera, S., Crisp, J., Des Marais, D., 2012. Characterization and calibration of the CheMin mineralogical instrument on Mars Science Laboratory. Space Sci. Rev. 170, 341–399. https://doi.org/10.1007/s11214-012-9905-1

Blake, R.E., Chang, S.J., Lepland, A., 2010. Phosphate oxygen isotopic evidence for a temperate and biologically active Archaean ocean. Nature 464, 1029–1032. https://doi.org/10.1038/nature08952

Boak, J.L., Dymek, R.F., 1982. Metamorphism of the ca. 3800 Ma supracrustal rocks at Isua, West Greenland: implications for early Archaean crustal evolution. Earth Planet. Sci. Lett. 59, 155–176. https://doi.org/10.1016/0012-821X(82)90123-6

Bolhar, R., Hofmann, A., Siahi, M., Feng, Y., Delvigne, C., 2015. A trace element and Pb isotopic investigation into the provenance and deposition of stromatolitic carbonates, ironstones and associated shales of the∼ 3.0 Ga Pongola Supergroup, Kaapvaal Craton. Geochim. Cosmochim. Acta 158, 57–78. https://doi.org/10.1016/j.gca.2015.02.026

Bontognali, T.R., Sessions, A.L., Allwood, A.C., Fischer, W.W., Grotzinger, J.P., Summons, R.E., Eiler, J.M., 2012. Sulfur isotopes of organic matter preserved in 3.45-billion-year-old stromatolites reveal microbial metabolism. Proc. Natl. Acad. Sci. 109, 15146–15151. https://doi.org/10.1073/pnas.1207491109

Bosak, T., Moore, K.R., Gong, J., Grotzinger, J.P., 2021. Searching for biosignatures in sedimentary rocks from early Earth and Mars. Nat. Rev. Earth Environ. 2, 490–506. https://doi.org/10.1038/s43017-021-00169-5

Bost, N., 2012. Geochemical and mineralogical analysis of Mars analogue materials and the creation of the International Space Analogue Rock Store (ISAR) [Thesis]. Orléans, France.

Bost, N., Westall, F., Ramboz, C., Foucher, F., Pullan, D., Meunier, A., Petit, S., Fleischer, I., Klingelhöfer, G., Vago, J.L., 2013. Missions to Mars: Characterisation of Mars analogue rocks for the International Space Analogue Rockstore (ISAR). Planet. Space Sci. 82–83, 113–127. https://doi.org/10.1016/j.pss.2013.04.006

Bost, N., Ramboz, C., LeBreton, N., Foucher, F., Lopez-Reyes, G., De Angelis, S., Josset, M., Venegas, G., Sanz-Arranz, A., Rull, F., Medina, J., Josset, J.-L., Souchon, A., Ammannito, E., De Sanctis, M.C., Di Iorio, T., Carli, C., Vago, J.L., Westall, F., 2015. Testing the ability of the ExoMars 2018 payload to document geological context and potential habitability on Mars. Planet. Space Sci. 108, 87–97. https://doi.org/10.1016/j.pss.2015.01.006

Boston, P.J., Alexander, C., 2016. Preservation of microbial-mineral biosignatures in caves. Presented at the Biosignature Preservation and Detection in Mars Analog Environments, LPI Contributions, Lake Tahoe, Nevada [Abstract]. URL https://www.hou.usra.edu/meetings/biosignature2016/pdf/2074.pdf (accessed: 08.08.23).

Botta, O., Bada, J.L., 2002. Extraterrestrial organic compounds in meteorites. Surv. Geophys. 23, 411–467. https://doi.org/10.1023/A:1020139302770

Bowring, S.A., Williams, I.S., 1999. Priscoan (4.00–4.03 Ga) orthogneisses from northwestern Canada. Contrib. Mineral. Petrol. 134, 3–16. https://doi.org/10.1007/s004100050465

Brack, A., 1993. Liquid water and the origin of life. Orig. Life Evol. Biosph. 23, 3–10. https://doi.org/10.1007/BF01581985

Brain, D.A., Jakosky, B.M., 1998. Atmospheric loss since the onset of the Martian geologic record: Combined role of impact erosion and sputtering. J. Geophys. Res. Planets 103, 22689–22694. https://doi.org/10.1029/98JE02074

Brantley, S.L., Liermann, L., Bullen, T.D., 2001. Fractionation of Fe isotopes by soil microbes and organic acids. Geol. Soc. Am. 6, 535–538. https://doi.org/10.1130/0091-7613(2001)029<0535:FOFIBS>2.0.CO;2

Brantley, S.L., Liermann, L.J., Guynn, R.L., Anbar, A., Icopini, G.A., Barling, J., 2004. Fe isotopic fractionation during mineral dissolution with and without bacteria. Geochim. Cosmochim. Acta 68, 3189–3204. https://doi.org/10.1016/j.gca.2004.01.023

Brasier, M.D., Green, O.R., Jephcoat, A.P., Kleppe, A.K., Van Kranendonk, M.J., Lindsay, J.F., Steele, A., Grassineau, N.V., 2002. Questioning the evidence for Earth's oldest fossils. Nature 416, 76–81. https://doi.org/10.1038/416076a

Brasier, M.D., Green, O.R., Lindsay, J.F., McLoughlin, N., Steele, A., Stoakes, C., 2005. Critical testing of Earth's oldest putative fossil assemblage from the∼ 3.5 Ga Apex chert, Chinaman Creek, Western Australia. Precambrian Res. 140, 55–102. https://doi.org/10.1016/j.precamres.2005.06.008

Brasier, M.D., Matthewman, R., McMahon, S., Kilburn, M.R., Wacey, D., 2013. Pumice from the∼ 3460 Ma Apex Basalt, Western Australia: A natural laboratory for the early biosphere. Precambrian Res. 224, 1–10. https://doi.org/10.1016/j.precamres.2012.09.008

Brasier, M.D., Antcliffe, J., Saunders, M., Wacey, D., 2015. Changing the picture of Earth's earliest fossils (3.5–1.9 Ga) with new approaches and new discoveries. Proc. Natl. Acad. Sci. 112, 4859–4864. https://doi.org/10.1073/pnas.1405338111

Brasier, A.T., Culwick, T., Battison, L., Callow, R.H.T., Brasier, M.D., 2017. Evaluating evidence from the Torridonian Supergroup (Scotland, UK) for eukaryotic life on land in the Proterozoic, in: Brasier, A.T., McIlroy, D., McLoughlin, N. (Eds), Earth System Evolution and Early Life: A Celebration of the Work of Martin Brasier. Geological Society of London, pp. 121–144.

Brasier, A.T., Dennis, P.F., Still, J., Parnell, J., Culwick, T., Brasier, M.D., Wacey, D., Bowden, S.A., Crook, S., Boyce, A.J., 2019. Detecting ancient life: Investigating the nature and origin of possible stromatolites and associated calcite from a one billion year old lake. Precambrian Res. 328, 309–320. https://doi.org/10.1016/j.precamres.2019.04.025

Brooke, S., Fox, S.W., 1977. Compartmentalization in proteinoid microspheres. BioSystems 9, 1–22. https://doi.org/10.1016/0303-2647(77)90028-4

Brown, A.J., Viviano, C.E., Goudge, T.A., 2020. Ancient Australian Rocks and the Search for Life on Mars. ArXiv Prepr. ArXiv200706656. https://arxiv.org/abs/2007.06656

Broz, A.P., 2020. Organic matter preservation in ancient soils of Earth and Mars. Life 10, 113. https://doi.org/10.3390/life10070113

Bruylants, G., Bartik, K., Reisse, J., 2011. Prebiotic chemistry: a fuzzy field. Comptes Rendus Chim. 14, 388–391. https://doi.org/10.1016/j.crci.2010.04.002

Buick, R., Dunlop, J.S.R., Groves, D.I., 1981. Stromatolite recognition in ancient rocks: an appraisal of irregularly laminated structures in an Early Archaean chert-barite unit from North Pole, Western Australia. Alcheringa 5, 161–181. https://doi.org/10.1080/03115518108566999

Buick, R., 1990. Microfossil recognition in Archean rocks: an appraisal of spheroids and filaments from a 3500 my old chert-barite unit at North Pole, Western Australia. Palaios 5, 441–459. https://doi.org/10.2307/3514837

Burne, R.V., Moore, L.S., 1987. Microbialites: organosedimentary deposits of benthic microbial communities. Palaios 2, 241–254. https://doi.org/10.2307/3514674

Burt, D.M., Knauth, L.P., 2003. Electrically conducting, Ca-rich brines, rather than water, expected in the Martian subsurface. J. Geophys. Res. Planets 108, 8026. https://doi.org/10.1029/2002JE001862

Bustin, R.M., Ross, J.V., Rouzaud, J.-N., 1995. Mechanisms of graphite formation from kerogen: experimental evidence. Int. J. Coal Geol. 28, 1–36. https://doi.org/10.1016/0166-5162(95)00002-U

Cady, S.L., Farmer, J.D., Grotzinger, J.P., Schopf, J.W., Steele, A., 2003. Morphological biosignatures and the search for life on Mars. Astrobiology 3, 351–368. https://doi.org/10.1089/153110703769016442

Cady, S.L., Farmer, J.D., 2007. Fossilization Processes in Siliceous Thermal Springs: Trends in Preservation Along Thermal Gradients, in: Bock, G.R., Goode, J.A. (Eds.), Ciba Foundation Symposium 202 - Evolution of Hydrothermal Ecosystems on Earth (And Mars?). John Wiley & Sons, Ltd, pp. 150–173.

Cameron, V., House, C.H., Brantley, S.L., 2012. A First Analysis of Metallome Biosignatures of Hyperthermophilic Archaea. Archaea 2012, 1–12. https://doi.org/10.1155/2012/789278

Campbell, J.L., Teesdale, W.J., Halden, N.M., 1995. Theory, practice and application of micro-PIXE analysis and element-distribution maps. Can. Mineral. 33, 279–292. https://pubs.geoscienceworld.org/canmin/article-abstract/33/2/279/12644/Theory-practice-and-application-of-micro-PIXE

Campbell, J.L., Perrett, G.M., Gellert, R., Andrushenko, S.M., Boyd, N.I., Maxwell, J.A., King, P.L., Schofield, C.D., 2012. Calibration of the Mars Science Laboratory alpha particle X-ray spectrometer. Space Sci. Rev. 170, 319–340. https://doi.org/10.1007/s11214-012-9873-5

Canfield, D.E., 2001. Biogeochemistry of sulfur isotopes. Rev. Mineral. Geochem. 43, 607–636. https://doi.org/10.2138/gsrmg.43.1.607

Carr, M.H., Head III, J.W., 2010. Geologic history of Mars. Earth Planet. Sci. Lett. 294, 185–203. https://doi.org/10.1016/j.epsl.2009.06.042

Carter, J., Quantin, C., Thollot, P., Loizeau, D., Ody, A., Lozach, L., 2016. Oxia Planum: A Clay-Laden Landing Site Proposed for the ExoMars Rover Mission: Aqueous Mineralogy and Alteration Scenarios. Presented at the 47th Lunar and Planetary Science Conference, LPI Contributions, The Woodlands, Texas [Abstract]. URL https://ui.adsabs.harvard.edu/abs/2016LPI....47.2064C/abstract (accessed: 05.26.21).

Cas, R., Giordano, G., Balsamo, F., Esposito, A., Mastro, S.L., 2011. Hydrothermal breccia textures and processes: Lisca bianca islet, Panarea volcano, Aeolian Islands, Italy. Econ. Geol. 106, 437–450. https://doi.org/10.2113/econgeo.106.3.437

Cates, N.L., Mojzsis, S.J., 2007. Pre-3750 Ma supracrustal rocks from the Nuvvuagittuq supracrustal belt, northern Québec. Earth Planet. Sci. Lett. 255, 9–21. https://doi.org/10.1016/j.epsl.2006.11.034

Catling, D.C., Kasting, J.F., 2007. Planetary atmospheres and life, in: Sullivan III, W.T., Baross, J.A. (Eds.), Planets and Life: The Emerging Science of Astrobiology. Cambridge University Press, pp. 91–116.

Catling, D.C., Zahnle, K.J., 2020. The archean atmosphere. Sci. Adv. 6, eaax1420. https://doi.org/10.1126/sciadv.aax1420

Cavalazzi, B., Westall, F., Cady, S.L., Barbieri, R., Foucher, F., 2011. Potential Fossil Endoliths in Vesicular Pillow Basalt, Coral Patch Seamount, Eastern North Atlantic Ocean. Astrobiology 11, 619–632. https://doi.org/10.1089/ast.2011.0657

Cavalazzi, B., Lemelle, L., Simionovici, A., Cady, S.L., Russell, M.J., Bailo, E., Canteri, R., Enrico, E., Manceau, A., Maris, A., 2021. Cellular remains in a~ 3.42-billion-year-old subseafloor hydrothermal environment. Sci. Adv. 7, eabf3963. https://doi.org/10.1126/sciadv.abf3963

Cavosie, A.J., Valley, J.W., Wilde, S.A., 2005. Magmatic δ18O in 4400–3900 Ma detrital zircons: A record of the alteration and recycling of crust in the Early Archean. Earth Planet. Sci. Lett. 235, 663–681. https://doi.org/10.1016/j.epsl.2005.04.028

Ceburnis, D., Garbaras, A., Szidat, S., Rinaldi, M., Fahrni, S., Perron, N., Wacker, L., Leinert, S., Remeikis, V., Facchini, M.C., 2011. Quantification of the carbonaceous matter origin in submicron marine aerosol by 13 C and 14 C isotope analysis. Atmospheric Chem. Phys. 11, 8593–8606. https://doi.org/10.5194/acp-11-8593-2011

Chan, M.A., Hinman, N.W., Potter-McIntyre, S.L., Schubert, K.E., Gillams, R.J., Awramik, S.M., Boston, P.J., Bower, D.M., Marais, D.J.D., Farmer, J.D., Jia, T.Z., King, P.L., Hazen, R.M., Léveillé, R.J., Papineau, D., Rempfert, K.R., Sánchez-Román, M., Spear, J.R., Southam, G., Stern, J.C., Cleaves,

H.J., 2019. Deciphering Biosignatures in Planetary Contexts. Astrobiology 19, 1075–1185. https://doi.org/10.1089/ast.2018.1903

Chan, Q.H.S., Stroud, R., Martins, Z., Yabuta, H., 2020. Concerns of Organic Contamination for Sample Return Space Missions. Space Sci. Rev. 216, 1–40. https://doi.org/10.1007/s11214-020-00678-7

Clarke, A., 2014. The thermal limits to life on Earth. Int. J. Astrobiol. 13, 141–154. https://doi.org/10.1017/S1473550413000438

Cleaves, H.J., Miller, S.L., 1998. Oceanic protection of prebiotic organic compounds from UV radiation. Proc. Natl. Acad. Sci. 95, 7260–7263. https://doi.org/10.1073/pnas.95.13.7260

Clifford, S.M., 1993. A model for the hydrologic and climatic behavior of water on Mars. J. Geophys. Res. Planets 98, 10973–11016. https://doi.org/10.1029/93JE00225

Clifford, S.M., Parker, T.J., 2001. The evolution of the Martian hydrosphere: Implications for the fate of a primordial ocean and the current state of the northern plains. Icarus 154, 40–79. https://doi.org/10.1006/icar.2001.6671

Clifford, S.M., Lasue, J., Heggy, E., Boisson, J., McGovern, P., Max, M.D., 2010. Depth of the Martian cryosphere: Revised estimates and implications for the existence and detection of subpermafrost groundwater. J. Geophys. Res. Planets 115, E07001. https://doi.org/10.1029/2009JE003462

Cloud, P., 1976. Beginnings of biospheric evolution and their biogeochemical consequences. Paleobiology 2, 351–387. https://doi.org/10.1017/S009483730000498X

Cockell, C.S., Balme, M., Bridges, J.C., Davila, A., Schwenzer, S.P., 2012. Uninhabited habitats on Mars. Icarus 217, 184–193. https://doi.org/10.1016/j.icarus.2011.10.025

Cockell, C.S., Bush, T., Bryce, C., Direito, S., Fox-Powell, M., Harrison, J.P., Lammer, H., Landenmark, H., Martin-Torres, J., Nicholson, N., 2016. Habitability: a review. Astrobiology 16, 89–117. https://doi.org/10.1089/ast.2015.1295

Colella, A., Prior, D.B., 1990. Coarse-Grained Deltas. International Association of Sedimentologists, Special Publication 10. Blackwell Scientific Publications, Oxford.

Cosmidis, J., Templeton, A.S., 2016. Self-assembly of biomorphic carbon/sulfur microstructures in sulfidic environments. Nat. Commun. 7, 12812. https://doi.org/10.1038/ncomms12812

Cosmidis, J., Nims, C.W., Diercks, D., Templeton, A.S., 2019. Formation and stabilization of elemental sulfur through organomineralization. Geochim. Cosmochim. Acta 247, 59–82. https://doi.org/10.1016/j.gca.2018.12.025

Criouet, I., Viennet, J.-C., Jacquemot, P., Jaber, M., Bernard, S., 2021. Abiotic formation of organic biomorphs under diagenetic conditions. Geochem. Perspect. Lett. 16, 40–46. https://doi.org/10.7185/geochemlet.2102

Crosby, H.A., Roden, E.E., Johnson, C.M., Beard, B.L., 2007. The mechanisms of iron isotope fractionation produced during dissimilatory Fe (III) reduction by Shewanella putrefaciens and Geobacter sulfurreducens. Geobiology 5, 169–189. https://doi.org/10.1111/j.1472-4669.2007.00103.x

Czajka, D.R., Lion, L.W., Shuler, M.L., Ghiorse, W.C., 1997. Evaluation of the utility of bacterial extracellular polymers for treatment of metal-contaminated soils: Polymer persistence, mobility, and the influence of lead. Water Res. 31, 2827–2839. https://doi.org/10.1016/S0043-1354(97)00129-2

Damer, B., Deamer, D., 2020. The hot spring hypothesis for an origin of life. Astrobiology 20, 429–452. https://doi.org/10.1089/ast.2019.2045

Dass, A.V., Jaber, M., Brack, A., Foucher, F., Kee, T.P., Georgelin, T., Westall, F., 2018. Potential role of inorganic confined environments in prebiotic phosphorylation. Life 8, 7. https://doi.org/10.3390/life8010007

Davis, J.M., Balme, M.R., Fawdon, P., Grindrod, P.M., Favaro, E.A., Banham, S.G., Thomas, N., 2023. Ancient alluvial plains at Oxia Planum, mars. Earth Planet. Sci. Lett. 601, 117904. https://doi.org/10.1016/j.epsl.2022.117904

De Sanctis, M.C., Altieri, F., Ammannito, E., Biondi, D., De Angelis, S., Meini, M., Mondello, G., Novi, S., Paolinetti, R., Soldani, M., 2017. Ma_MISS on ExoMars: mineralogical characterization of the martian subsurface. Astrobiology 17, 612–620. https://doi.org/10.1089/ast.2016.1541

de Vries, S.T., 2004. Early Archaean sedimentary basins: depositional environment and hydrothermal systems [Thesis]. Utrecht, The Netherlands.

de Vries, S.T., Nijman, W., Wijbrans, J.R., Nelson, D.R., 2006. Stratigraphic continuity and early deformation of the central part of the Coppin Gap Greenstone Belt, Pilbara, Western Australia. Precambrian Res. 147, 1–27. https://doi.org/10.1016/j.precamres.2006.01.004

de Vries, S.T., Nijman, W., de Boer, P.L., 2010. Sedimentary geology of the Palaeoarchaean Buck Ridge (South Africa) and Kittys Gap (Western Australia) volcano-sedimentary complexes. Precambrian Res. 183, 749–769. https://doi.org/10.1016/j.precamres.2010.09.005

De Yoreo, J.J., Gilbert, P.U., Sommerdijk, N.A., Penn, R.L., Whitelam, S., Joester, D., Zhang, H., Rimer, J.D., Navrotsky, A., Banfield, J.F., 2015. Crystallization by particle attachment in synthetic, biogenic, and geologic environments. Science 349, aaa6760. https://doi.org/10.1126/science.aaa6760

Deamer, D., 2017. The role of lipid membranes in life's origin. Life 7, 5. https://doi.org/10.3390/life7010005

Derenne, S., Robert, F., Skrzypczak-Bonduelle, A., Gourier, D., Binet, L., Rouzaud, J.-N., 2008. Molecular evidence for life in the 3.5 billion year old Warrawoona chert. Earth Planet. Sci. Lett. 272, 476–480. https://doi.org/10.1016/j.epsl.2008.05.014

Des Marais, D.J., 2010. Exploring Mars for Evidence of Habitable Environments and Life. Proc. Am. Philos. Soc. 154, 402–421. http://www.jstor.org/stable/23056860

Djokic, T., Van Kranendonk, M.J., Campbell, K.A., Walter, M.R., Ward, C.R., 2017. Earliest signs of life on land preserved in ca. 3.5 Ga hot spring deposits. Nat. Commun. 8, 15263. https://doi.org/10.1038/ncomms15263

Dobrică, E., Engrand, C., Duprat, J., Gounelle, M., Leroux, H., Quirico, E., Rouzaud, J.-N., 2009. Connection between micrometeorites and Wild 2 particles: From Antarctic snow to cometary ices. Meteorit. Planet. Sci. 44, 1643–1661. https://doi.org/10.1111/j.1945-5100.2009.tb01196.x

Dodd, M.S., Papineau, D., Grenne, T., Slack, J.F., Rittner, M., Pirajno, F., O'Neil, J., Little, C.T., 2017. Evidence for early life in Earth's oldest hydrothermal vent precipitates. Nature 543, 60–64. https://doi.org/10.1038/nature21377

Dong, H., Huang, L., Zhao, L., Zeng, Q., Liu, X., Sheng, Y., Shi, L., Wu, G., Jiang, H., Li, F., Zhang, L., Guo, D., Li, G., Hou, W., Chen, H., 2022. A critical review of mineral–microbe interaction and co-evolution: mechanisms and applications. Natl. Sci. Rev. 9, nwac128. https://doi.org/10.1093/nsr/nwac128

Dupont, C.L., Yang, S., Palenik, B., Bourne, P.E., 2006. Modern proteomes contain putative imprints of ancient shifts in trace metal geochemistry. Proc. Natl. Acad. Sci. 103, 17822–17827. https://doi.org/10.1073/pnas.0605798103

Dupont, C.L., Butcher, A., Valas, R.E., Bourne, P.E., Caetano-Anolles, G., 2010. History of biological metal utilization inferred through phylogenomic analysis of protein structures. Proc. Natl. Acad. Sci. 107, 10567–10572. https://doi.org/10.1073/pnas.0912491107

Durand, B., 1980. Kerogen: Insoluble organic matter from sedimentary rocks. Editions technip.

Edgett, K.S., Yingst, R.A., Ravine, M.A., Caplinger, M.A., Maki, J.N., Ghaemi, F.T., Schaffner, J.A., Bell, J.F., Edwards, L.J., Herkenhoff, K.E., 2012. Curiosity's Mars hand lens imager (MAHLI) investigation. Space Sci. Rev. 170, 259–317. https://doi.org/10.1007/s11214-012-9910-4

Ehlmann, B.L., Mustard, J.F., Murchie, S.L., Bibring, J.-P., Meunier, A., Fraeman, A.A., Langevin, Y., 2011. Subsurface water and clay mineral formation during the early history of Mars. Nature 479, 53–60. https://doi.org/10.1038/nature10582

Eigenbrode, J.L., Summons, R.E., Steele, A., Freissinet, C., Millan, M., Navarro-González, R., Sutter, B., McAdam, A.C., Franz, H.B., Glavin, D.P., Archer, P.D., Mahaffy, P.R., Conrad, P.G., Hurowitz, J.A., Grotzinger, J.P., Gupta, S., Ming, D.W., Sumner, D.Y., Szopa, C., Malespin, C., Buch, A., Coll,

P., 2018. Organic matter preserved in 3-billion-year-old mudstones at Gale crater, Mars. Science 360, 1096–1101. https://doi.org/10.1126/science.aas9185

Engel, C.G., Sharp, R.P., 1958. Chemical data on desert varnish. Geol. Soc. Am. Bull. 69, 487–518. https://doi.org/10.1130/0016-7606(1958)69[487:CDODV]2.0.CO;2

Etiope, G., Schoell, M., Hosgörmez, H., 2011. Abiotic methane flux from the Chimaera seep and Tekirova ophiolites (Turkey): understanding gas exhalation from low temperature serpentinization and implications for Mars. Earth Planet. Sci. Lett. 310, 96–104. https://doi.org/10.1016/j.epsl.2011.08.001

Evans, G.N., Coogan, L.A., Kaçar, B., Seyfried, W.E., 2023. Molybdenum in Basalt-Hosted Seafloor Hydrothermal Systems: Experimental, Theoretical, and Field Sampling Approaches. Geochim. Cosmochim. Acta. 353, 28–44. https://doi.org/10.1016/j.gca.2023.05.018

Falini, G., Albeck, S., Weiner, S., Addadi, L., 1996. Control of aragonite or calcite polymorphism by mollusk shell macromolecules. Science 271, 67–69. https://doi.org/10.1126/science.271.5245.6

Fanale, F.P., 1976. Martian volatiles: Their degassing history and geochemical fate. Icarus 28, 179–202. https://doi.org/10.1016/0019-1035(76)90032-4

Farley, K.A., Williford, K.H., Stack, K.M., Bhartia, R., Chen, A., de la Torre, M., Hand, K., Goreva, Y., Herd, C.D.K., Hueso, R., Liu, Y., Maki, J.N., Martinez, G., Moeller, R.C., Nelessen, A., Newman, C.E., Nunes, D., Ponce, A., Spanovich, N., Willis, P.A., Beegle, L.W., Bell, J.F., Brown, A.J., Hamran, S.-E., Hurowitz, J.A., Maurice, S., Paige, D.A., Rodriguez-Manfredi, J.A., Schulte, M., Wiens, R.C., 2020. Mars 2020 Mission Overview. Space Sci. Rev. 216, 142. https://doi.org/10.1007/s11214-020-00762-y

Farley, K.A., Stack, K.M., Shuster, D.L., Horgan, B.H.N., Hurowitz, J.A., Tarnas, J.D., Simon, J.I., Sun, V.Z., Scheller, E.L., Moore, K.R., McLennan, S.M., Vasconcelos, P.M., Wiens, R.C., Treiman, A.H., Mayhew, L.E., Beyssac, O., Kizovski, T.V., Tosca, N.J., Williford, K.H., Crumpler, L.S., Beegle, L.W., Bell, J.F., Ehlmann, B.L., Liu, Y., Maki, J.N., Schmidt, M.E., Allwood, A.C., Amundsen, H.E.F., Bhartia, R., Bosak, T., Brown, A.J., Clark, B.C., Cousin, A., Forni, O., Gabriel, T.S.J., Goreva, Y., Gupta, S., Hamran, S.-E., Herd, C.D.K., Hickman-Lewis, K., Johnson, J.R., Kah, L.C., Kelemen, P.B., Kinch, K.B., Mandon, L., Mangold, N., Quantin-Nataf, C., Rice, M.S., Russell, P.S., Sharma, S., Siljeström, S., Steele, A., Sullivan, R., Wadhwa, M., Weiss, B.P., Williams, A.J., Wogsland, B.V., Willis, P.A., Acosta-Maeda, T.A., Beck, P., Benzerara, K., Bernard, S., Burton, A.S., Cardarelli, E.L., Chide, B., Clavé, E., Cloutis, E.A., Cohen, B.A., Czaja, A.D., Debaille, V., Dehouck, E., Fairén, A.G., Flannery, D.T., Fleron, S.Z., Fouchet, T., Frydenvang, J., Garczynski, B.J., Gibbons, E.F., Hausrath, E.M., Hayes, A.G., Henneke, J., Jørgensen, J.L., Kelly, E.M., Lasue, J., Le Mouélic, S., Madariaga, J.M., Maurice, S., Merusi, M., Meslin, P.-Y., Milkovich, S.M., Million, C.C., Moeller, R.C., Núñez, J.I., Ollila, A.M., Paar, G., Paige, D.A., Pedersen, D.A.K., Pilleri, P., Pilorget, C., Pinet, P.C., Rice, J.W., Royer, C., Sautter, V., Schulte, M., Sephton, M.A., Sharma, S.K., Sholes, S.F., Spanovich, N., St. Clair, M., Tate, C.D., Uckert, K., VanBommel, S.J., Yanchilina, A.G., Zorzano, M.-P., 2022. Aqueously altered igneous rocks sampled on the floor of Jezero crater, Mars. Science 377, eabo2196. https://doi.org/10.1126/science.abo2196

Farmer, J.D., 1999. Taphonomic modes in microbial fossilization, in: Size Limits of Very Small Microorganisms: Proceedings of a Workshop, Space Studies Board, National Research Council, National Academies Press, Washington, DC. National Academies Press, Washington, DC, pp. 94–102.

Farquhar, J., Savarino, J., Airieau, S., Thiemens, M.H., 2001. Observation of wavelength-sensitive mass-independent sulfur isotope effects during SO2 photolysis: Implications for the early atmosphere. J. Geophys. Res. Planets 106, 32829–32839. https://doi.org/10.1029/2000JE001437

Ferris, F.G., Fyfe, W.S., Beveridge, T.J., 1987. Bacteria as nucleation sites for authigenic minerals in a metal-contaminated lake sediment. Chem. Geol. 63, 225–232. https://doi.org/10.1016/0009-2541(87)90165-3

Ferris, F.G., Fyfe, W.S., Beveridge, T.J., 1988. Metallic ion binding by Bacillus subtilis: implications for the fossilization of microorganisms. Geology 16, 149–152. https://doi.org/10.1130/0091-7613(1988)016<0149:MIBBBS>2.3.CO;2

Ferus, M., Rimmer, P., Cassone, G., Knížek, A., Civiš, S., Šponer, J.E., Ivanek, O., Šponer, J., Saeidfirozeh, H., Kubelík, P., 2020. One-pot hydrogen cyanide-based prebiotic synthesis of canonical nucleobases and glycine initiated by high-velocity impacts on early Earth. Astrobiology 20, 1476–1488. https://doi.org/10.1089/ast.2020.2231

Flynn, G.J., Keller, L.P., Feser, M., Wirick, S., Jacobsen, C., 2003. The origin of organic matter in the solar system: Evidence from the interplanetary dust particles. Geochim. Cosmochim. Acta 67, 4791–4806. https://doi.org/10.1016/j.gca.2003.09.001

Foucher, F., Westall, F., Brandstätter, F., Demets, R., Parnell, J., Cockell, C.S., Edwards, H.G.M., Bény, J.-M., Brack, A., 2010. Testing the survival of microfossils in artificial martian sedimentary meteorites during entry into Earth's atmosphere: The STONE 6 experiment. Icarus 207, 616–630. https://doi.org/10.1016/j.icarus.2009.12.014

Foucher, F., Lopez-Reyes, G., Bost, N., Rull-Perez, F., Rüßmann, P., Westall, F., 2013. Effect of grain size distribution on Raman analyses and the consequences for in situ planetary missions. J. Raman Spectrosc. 44, 916–925. https://doi.org/10.1002/jrs.4307

Foucher, F., Ammar, M.-R., Westall, F., 2015. Revealing the biotic origin of silicified Precambrian carbonaceous microstructures using Raman spectroscopic mapping, a potential method for the detection of microfossils on Mars: Revealing the biotic origin of silicified carbonaceous microstructures. J. Raman Spectrosc. 46, 873–879. https://doi.org/10.1002/jrs.4687

Foucher, F., Guimbretière, G., Bost, N., Westall, F., 2017. Petrographical and Mineralogical Applications of Raman Mapping, in: Maaz, K. (Ed.), Raman Spectroscopy and Applications. InTech, Rijeka, Croatia, pp. 163–180.

Foucher, F., 2019. Detection of biosignatures using Raman spectroscopy, in: Cavalazzi, B., Westall, F. (Eds.), Biosignatures for Astrobiology. Springer, Cham, pp. 267–282.

Foucher, F., Guimbretière, G., Bost, N., Hickman-Lewis, K., Courtois, A., Luengo, L., Marceau, E., Bergounioux, M., Westall, F., 2019. The CaliPhoto Method. Inventions 4, 67. https://doi.org/10.3390/inventions4040067

Foucher, F., Hickman-Lewis, K., Hutzler, A., Joy, K.H., Folco, L., Bridges, J.C., Wozniakiewicz, P., Martínez-Frías, J., Debaille, V., Zolensky, M., Yano, H., Bost, N., Ferrière, L., Lee, M., Michalski, J., Schroeven-Deceuninck, H., Kminek, G., Viso, M., Russell, S., Smith, C., Zipfel, J., Westall, F., 2021a. Definition and use of functional analogues in planetary exploration. Planet. Space Sci. 197, 105162. https://doi.org/10.1016/j.pss.2021.105162

Foucher, F., Bost, N., Janiec, S., Fonte, A., Le Breton, N., Perron, P., Bouquin, M., Lebas, F., Viso, M., Chazalnoël, P., 2021b. LithoSpace: An Idea for an Automated System for in situ Petrographic Thin Section Preparation on Mars and Other Extraterrestrial Rocky Bodies. Front. Astron. Space Sci. 8, 749494. https://doi.org/10.3389/fspas.2021.749494

Fox, S.W., Yuyama, S., 1963. Abiotic production of primitive protein and formed microparticles. Ann. N. Y. Acad. Sci. 108, 487–494. https://doi.org/10.1111/j.1749-6632.1963.tb13404.x

Frank, K.L., Rogers, D.R., Olins, H.C., Vidoudez, C., Girguis, P.R., 2013. Characterizing the distribution and rates of microbial sulfate reduction at Middle Valley hydrothermal vents. ISME J. 7, 1391–1401. https://doi.org/10.1038/ismej.2013.17

Fraústo Da Silva, J.J.R., Williams, R.J.P., 2001. The biological chemistry of the elements: the inorganic chemistry of life. Oxford University Press.

Freissinet, C., Glavin, D.P., Mahaffy, P.R., Miller, K.E., Eigenbrode, J.L., Summons, R.E., Brunner, A.E., Buch, A., Szopa, C., Archer, P.D., Franz, H.B., Atreya, S.K., Brinckerhoff, W.B., Cabane, M., Coll, P., Conrad, P.G., Des Marais, D.J., Dworkin, J.P., Fairén, A.G., François, P., Grotzinger, J.P., Kashyap, S., ten Kate, I.L., Leshin, L.A., Malespin, C.A., Martin, M.G., Martin-Torres, F.J., McAdam, A.C., Ming, D.W., Navarro-González, R., Pavlov, A.A., Prats, B.D., Squyres, S.W., Steele, A., Stern, J.C., Sumner, D.Y., Sutter, B., Zorzano, M.-P., the MSL Science Team, 2015. Organic molecules in the Sheepbed Mudstone, Gale Crater, Mars: Detection of organics in

martian sample. J. Geophys. Res. Planets 120, 495–514. https://doi.org/10.1002/2014JE004737

Fulignati, P., 2020. Clay minerals in hydrothermal systems. Minerals 10, 919. https://doi.org/10.3390/min10100919

Furnes, H., Banerjee, N.R., Muehlenbachs, K., Staudigel, H., de Wit, M., 2004. Early Life Recorded in Archean Pillow Lavas. Science 304, 578. https://doi.org/10.1126/science.1095858

Furnes, H., Banerjee, N.R., Staudigel, H., Muehlenbachs, K., McLoughlin, N., de Wit, M., Van Kranendonk, M., 2007. Comparing petrographic signatures of bioalteration in recent to Mesoarchean pillow lavas: Tracing subsurface life in oceanic igneous rocks. Precambrian Res. 158, 156–176. https://doi.org/10.1016/j.precamres.2007.04.012

Furukawa, Y., Chikaraishi, Y., Ohkouchi, N., Ogawa, N.O., Glavin, D.P., Dworkin, J.P., Abe, C., Nakamura, T., 2019. Extraterrestrial ribose and other sugars in primitive meteorites. Proc. Natl. Acad. Sci. 116, 24440–24445. https://doi.org/10.1073/pnas.1907169116

Gaboyer, F., Le Milbeau, C., Bohmeier, M., Schwendner, P., Vannier, P., Beblo-Vranesevic, K., Rabbow, E., Foucher, F., Gautret, P., Guégan, R., Richard, A., Sauldubois, A., Richmann, P., Perras, A.K., Moissl-Eichinger, C., Cockell, C.S., Rettberg, P., Marteinsson, Monaghan, E., Ehrenfreund, P., Garcia-Descalzo, L., Gomez, F., Malki, M., Amils, R., Cabezas, P., Walter, N., Westall, F., 2017. Mineralization and Preservation of an extremotolerant Bacterium Isolated from an Early Mars Analog Environment. Sci. Rep. 7, 8775. https://doi.org/10.1038/s41598-017-08929-4

Gaft, M., Reisfeld, R., Panczer, G., 2015. Modern luminescence spectroscopy of minerals and materials. Springer, Berlin, Heidelberg.

García-Ruiz, J.M., Hyde, S.T., Carnerup, A.M., Christy, A.G., Van Kranendonk, M.J., Welham, N.J., 2003. Self-assembled silica-carbonate structures and detection of ancient microfossils. Science 302, 1194–1197. https://doi.org/10.1126/science.1090163

García-Ruiz, J.M., Melero-García, E., Hyde, S.T., 2009. Morphogenesis of self-assembled nanocrystalline materials of barium carbonate and silica. Science 323, 362–365. https://doi.org/10.1126/science.1165349

García-Ruiz, J.M., Van Zuilen, M.A., Bach, W., 2020. Mineral self-organization on a lifeless planet. Phys. Life Rev. 34, 62–82. https://doi.org/10.1016/j.plrev.2020.01.001

Gargaud, M., Amils, R., 2011. Encyclopedia of astrobiology. Springer Science & Business Media.

Gendrin, A., Mangold, N., Bibring, J.-P., Langevin, Y., Gondet, B., Poulet, F., Bonello, G., Quantin, C., Mustard, J., Arvidson, R., 2005. Sulfates in Martian layered terrains: the OMEGA/Mars Express view. Science 307, 1587–1591. https://doi.org/10.1126/science.1109087

Ghassal, B.I., El Atfy, H., 2022. Sedimentary Organic Matter: Origin, Productivity, Preservation, and Role in Source Rock Development, in: El Atfy, H., Ghassal, B.I. (Eds.), Advances in Petroleum Source Rock Characterizations: Integrated Methods and Case Studies: A Multidisciplinary Source Rock Approach. Springer, pp. 3–22.

Gibson, D.T., 1984. Microbial degradation of organic compounds. Marcel Dekker Inc., New York.

Giggenbach, W.F., 1997. The origin and evolution of fluids in magmatic-hydrothermal systems, in: Barnes, H.L. (Eds.), Geochemistry of Hydrothermal Ore Deposits. John Wiley & Sons, Inc., New York, pp. 699–736.

Glikson, M., Duck, L.J., Golding, S.D., Hofmann, A., Bolhar, R., Webb, R., Baiano, J.C., Sly, L.I., 2008. Microbial remains in some earliest Earth rocks: comparison with a potential modern analogue. Precambrian Res. 164, 187–200. https://doi.org/10.1016/j.precamres.2008.05.002

Goesmann, F., Brinckerhoff, W.B., Raulin, F., Goetz, W., Danell, R.M., Getty, S.A., Siljeström, S., Mißbach, H., Steininger, H., Arevalo Jr, R.D., 2017. The Mars Organic Molecule Analyzer (MOMA) instrument: characterization of organic material in martian sediments. Astrobiology 17, 655–685. https://doi.org/10.1089/ast.2016.1551

Goldstein, J.I., Newbury, D.E., Michael, J.R., Ritchie, N.W., Scott, J.H.J., Joy, D.C., 2017. Scanning electron microscopy and X-ray microanalysis. Springer.

Goudge, T.A., Mustard, J.F., Head, J.W., Fassett, C.I., Wiseman, S.M., 2015. Assessing the mineralogy of the watershed and fan deposits of the Jezero crater paleolake system, Mars. J. Geophys. Res. Planets 120, 775–808. https://doi.org/10.1002/2014JE004782

Goudge, T.A., Milliken, R.E., Head, J.W., Mustard, J.F., Fassett, C.I., 2017. Sedimentological evidence for a deltaic origin of the western fan deposit in Jezero crater, Mars and implications for future exploration. Earth Planet. Sci. Lett. 458, 357–365. https://doi.org/10.1016/j.epsl.2016.10.056

Gourcerol, B., Thurston, P.C., Kontak, D.J., Côté-Mantha, O., 2015. Interpretations and implications of LA ICP-MS analysis of chert for the origin of geochemical signatures in banded iron formations (BIFs) from the Meadowbank gold deposit, Western Churchill Province, Nunavut. Chem. Geol. 410, 89–107. https://doi.org/10.1016/j.chemgeo.2015.06.008

Gourcerol, B., Thurston, P.C., Kontak, D.J., Côté-Mantha, O., Biczok, J., 2016. Depositional setting of Algoma-type banded iron formation. Precambrian Res. 281, 47–79. https://doi.org/10.1016/j.precamres.2016.04.019

Gourier, D., Binet, L., Calligaro, T., Cappelli, S., Vezin, H., Bréhéret, J., Hickman-Lewis, K., Gautret, P., Foucher, F., Campbell, K., Westall, F., 2019. Extraterrestrial organic matter preserved in 3.33 Ga sediments from Barberton, South Africa. Geochim. Cosmochim. Acta 258, 207–225. https://doi.org/10.1016/j.gca.2019.05.009

Gratuze, B., 1999. Obsidian Characterization by Laser Ablation ICP-MS and its Application to Prehistoric Trade in the Mediterranean and the Near East: Sources and Distribution of Obsidian within the Aegean and Anatolia. J. Archaeol. Sci. 26, 869–881. https://doi.org/10.1006/jasc.1999.0459

Gratuze, B., 2016. Glass Characterization Using Laser Ablation-Inductively Coupled Plasma-Mass Spectrometry Methods, in: Dussubieux, L., Golitko, M., Gratuze, B. (Eds.), Recent Advances in Laser Ablation ICP-MS for Archaeology. Springer Berlin Heidelberg, Berlin, Heidelberg, pp. 179–196.

Greer, J., Caro, G., Cates, N.L., Tropper, P., Bleeker, W., Kelly, N.M., Mojzsis, S.J., 2020. Widespread poly-metamorphosed Archean granitoid gneisses and supracrustal enclaves of the southern Inukjuak Domain, Québec (Canada). Lithos 364, 105520. https://doi.org/10.1016/j.lithos.2020.105520

Grotzinger, J.P., Crisp, J., Vasavada, A.R., Anderson, R.C., Baker, C.J., Barry, R., Blake, D.F., Conrad, P., Edgett, K.S., Ferdowski, B., Gellert, R., Gilbert, J.B., Golombek, M., Gómez-Elvira, J., Hassler, D.M., Jandura, L., Litvak, M., Mahaffy, P., Maki, J., Meyer, M., Malin, M.C., Mitrofanov, I., Simmonds, J.J., Vaniman, D., Welch, R.V., Wiens, R.C., 2012. Mars Science Laboratory Mission and Science Investigation. Space Sci. Rev. 170, 5–56. https://doi.org/10.1007/s11214-012-9892-2

Grotzinger, J.P., Gupta, S., Malin, M.C., Rubin, D.M., Schieber, J., Siebach, K., Sumner, D.Y., Stack, K.M., Vasavada, A.R., Arvidson, R.E., Calef, F., Edgar, L., Fischer, W.F., Grant, J.A., Griffes, J., Kah, L.C., Lamb, M.P., Lewis, K.W., Mangold, N., Minitti, M.E., Palucis, M., Rice, M., Williams, R.M.E., Yingst, R.A., Blake, D., Blaney, D., Conrad, P., Crisp, J., Dietrich, W.E., Dromart, G., Edgett, K.S., Ewing, R.C., Gellert, R., Hurowitz, J.A., Kocurek, G., Mahaffy, P., McBride, M.J., McLennan, S.M., Mischna, M., Ming, D., Milliken, R., Newsom, H., Oehler, D., Parker, T.J., Vaniman, D., Wiens, R.C., Wilson, S.A., 2015. Deposition, exhumation, and paleoclimate of an ancient lake deposit, Gale crater, Mars. Science 350, aac7575. https://doi.org/10.1126/science.aac7575

Gueriau, P., Réguer, S., Leclercq, N., Cupello, C., Brito, P.M., Jauvion, C., Morel, S., Charbonnier, S., Thiaudière, D., Mocuta, C., 2020. Visualizing mineralization processes and fossil anatomy using synchronous synchrotron X-ray fluorescence and X-ray diffraction mapping. J. R. Soc. Interface 17, 20200216. https://doi.org/10.1098/rsif.2020.0216

Guido, A., Mastandrea, A., Tosti, F., Demasi, F., Blanco, A., D'Elia, M., Orofino, V., Fonti, S., Russo, F., 2012. Characterization of fossil organic matter with Fourier-Transform Infrared (FTIR) Spectroscopy: an attempt to record extraterrestrial life. Mem. Della Soc. Astron. Ital. Suppl. 20, 64.

Guido, A., Mastandrea, A., Russo, F., 2013. Biotic vs abiotic carbonates: characterisation of the fossil organic matter with Fourier-Transform Infrared (FT-IR) Spectroscopy. Boll. Della Soc. Paleontol. Ital. 52, 63–70. https://doi.org/10.4435/BSPI.2013.11

Halden, N.M., Campbell, J.L., Teesdale, W.J., 1995. PIXE analysis in mineralogy and geochemistry. Can. Mineral. 33, 293–302.

Halevy, I., Bachan, A., 2017. The geologic history of seawater pH. Science 355, 1069–1071. https://doi.org/10.1126/science.aal4151

Harrison, A.G., Thode, H.G., 1958. Mechanism of the bacterial reduction of sulphate from isotope fractionation studies. Trans. Faraday Soc. 54, 84–92. https://doi.org/10.1039/TF9585400084

Hassenkam, T., Andersson, M.P., Dalby, K.N., Mackenzie, D.M.A., Rosing, M.T., 2017. Elements of Eoarchean life trapped in mineral inclusions. Nature 548, 78–81. https://doi.org/10.1038/nature23261

Hays, L.E., Graham, H.V., Des Marais, D.J., Hausrath, E.M., Horgan, B., McCollom, T.M., Parenteau, M.N., Potter-McIntyre, S.L., Williams, A.J., Lynch, K.L., 2017. Biosignature Preservation and Detection in Mars Analog Environments. Astrobiology 17, 363–400. https://doi.org/10.1089/ast.2016.1627

Hazen, R.M., Sverjensky, D.A., 2010. Mineral surfaces, geochemical complexities, and the origins of life. Cold Spring Harb. Perspect. Biol. 2, a002162. https://doi.org/10.1101/cshperspect.a002162

Hickman, A.H., Van Kranendonk, M.J., 2012. Early Earth evolution: evidence from the 3.5–1.8 Ga geological history of the Pilbara region of Western Australia. Episodes J. Int. Geosci. 35, 283–297. https://doi.org/10.18814/epiiugs/2012/v35i1/028

Hickman-Lewis, K., Cavalazzi, B., Foucher, F., Westall, F., 2018. Most ancient evidence for life in the Barberton greenstone belt: Microbial mats and biofabrics of the ~3.47 Ga Middle Marker horizon. Precambrian Res. 312, 45–67. https://doi.org/10.1016/j.precamres.2018.04.007

Hickman-Lewis, K., Gautret, P., Arbaret, L., Sorieul, S., De Wit, R., Foucher, F., Cavalazzi, B., Westall, F., 2019. Mechanistic Morphogenesis of Organo-Sedimentary Structures Growing Under Geochemically Stressed Conditions: Keystone to Proving the Biogenicity of Some Archaean Stromatolites? Geosciences 9, 359. https://doi.org/10.3390/geosciences9080359

Hickman-Lewis, K., Gourcerol, B., Westall, F., Manzini, D., Cavalazzi, B., 2020a. Reconstructing Palaeoarchaean microbial biomes flourishing in the presence of emergent landmasses using trace and rare earth element systematics. Precambrian Res. 342, 105689. https://doi.org/10.1016/j.precamres.2020.105689

Hickman-Lewis, K., Westall, F., Cavalazzi, B., 2020b. Diverse communities of Bacteria and Archaea flourished in Palaeoarchaean (3.5–3.3 Ga) microbial mats. Palaeontology 63, 1007–1033. https://doi.org/10.1111/pala.12504

Hickman-Lewis, K., Cavalazzi, B., Sorieul, S., Gautret, P., Foucher, F., Whitehouse, M.J., Jeon, H., Georgelin, T., Cockell, C.S., Westall, F., 2020c. Metallomics in deep time and the influence of ocean chemistry on the metabolic landscapes of Earth's earliest ecosystems. Sci. Rep. 10, 4965. https://doi.org/10.1038/s41598-020-61774-w

Hickman-Lewis, K., Westall, F., 2021. A southern African perspective on the co-evolution of early life and environments. South Afr. J. Geol. 2021 124, 225–252. https://doi.org/10.25131/sajg.124.0016

Hickman-Lewis, K., Moore, K.R., Hollis, J.J.R., Tuite, M.L., Beegle, L.W., Bhartia, R., Grotzinger, J.P., Brown, A.J., Shkolyar, S., Cavalazzi, B., Smith, C.L., 2022. In Situ Identification of Paleoarchean Biosignatures Using Colocated Perseverance Rover Analyses: Perspectives for In Situ Mars Science and Sample Return. Astrobiology 22, 1143–1163. https://doi.org/10.1089/ast.2022.0018

Hoehler, T.M., 2017. Biosignatures in the Context of Low Energy Flux. Presented at the Astrobiology Science Conference 2017 (AbSciCon 2017), Lunar and Planetary Inst., NASA Ames Research Center, Mesa, AZ, United States [Abstract]. URL https://ntrs.nasa.gov/citations/20170009809 [accessed: 01.16.24].

Hofmann, H.J., Grey, K., Hickman, A.H., Thorpe, R.I., 1999. Origin of 3.45 Ga coniform stromatolites in Warrawoona group, Western Australia. Geol. Soc. Am. Bull. 111, 1256–1262. https://doi.org/10.1130/0016-7606(1999)111<1256:OOGCSI>2.3.CO;2

Holm, N.G., Andersson, E., 2005. Hydrothermal simulation experiments as a tool for studies of the origin of life on earth and other terrestrial planets: a review. Astrobiology 5, 444–460. https://doi.org/10.1089/ast.2005.5.444

Homann, M., Heubeck, C., Airo, A., Tice, M.M., 2015. Morphological adaptations of 3.22 Ga-old tufted microbial mats to Archean coastal habitats (Moodies Group, Barberton Greenstone Belt, South Africa). Precambrian Res. 266, 47–64. https://doi.org/10.1016/j.precamres.2015.04.018

Homann, M., Heubeck, C., Bontognali, T.R., Bouvier, A.-S., Baumgartner, L.P., Airo, A., 2016. Evidence for cavity-dwelling microbial life in 3.22 Ga tidal deposits. Geology 44, 51–54. https://doi.org/10.1130/G37272.1

Horita, J., 2005. Some perspectives on isotope biosignatures for early life. Chem. Geol. 218, 171–186. https://doi.org/10.1016/j.chemgeo.2005.01.017

Hren, M.T., Tice, M.M., Chamberlain, C.P., 2009. Oxygen and hydrogen isotope evidence for a temperate climate 3.42 billion years ago. Nature 462, 205–208. https://doi.org/10.1038/nature08518

Hurst, R.W., Bridgwater, D., Collerson, K.D., Wetherill, G.W., 1975. 3600-my RbSr ages from very early Archaean gneisses from Saglek Bay, Labrador. Earth Planet. Sci. Lett. 27, 393–403. https://doi.org/10.1016/0012-821X(75)90058-8

Hynek, B.M., Beach, M., Hoke, M.R., 2010. Updated global map of Martian valley networks and implications for climate and hydrologic processes. J. Geophys. Res. Planets 115. https://doi.org/10.1029/2009JE003548

Hyslop, E.V., Valley, J.W., Johnson, C.M., Beard, B.L., 2008. The effects of metamorphism on O and Fe isotope compositions in the Biwabik Iron Formation, northern Minnesota. Contrib. Mineral. Petrol. 155, 313–328. https://doi.org/10.1007/s00410-007-0244-2

Igisu, M., Nakashima, S., Ueno, Y., Awramik, S.M., Maruyama, S., 2006. In situ infrared microspectroscopy of∼ 850 million-year-old prokaryotic fossils. Appl. Spectrosc. 60, 1111–1120. https://doi.org/10.1366/000370206778664707

Igisu, M., Ueno, Y., Shimojima, M., Nakashima, S., Awramik, S.M., Ohta, H., Maruyama, S., 2009. Micro-FTIR spectroscopic signatures of Bacterial lipids in Proterozoic microfossils. Precambrian Res. 173, 19–26. https://doi.org/10.1016/j.precamres.2009.03.006

Igisu, M., Takai, K., Ueno, Y., Nishizawa, M., Nunoura, T., Hirai, M., Kaneko, M., Naraoka, H., Shimojima, M., Hori, K., 2012. Domain-level identification and quantification of relative prokaryotic cell abundance in microbial communities by Micro-FTIR spectroscopy. Environ. Microbiol. Rep. 4, 42–49. https://doi.org/10.1111/j.1758-2229.2011.00277.x

Igisu, M., Ueno, Y., Takai, K., 2018. FTIR microspectroscopy of carbonaceous matter in ~ 3.5 Ga seafloor hydrothermal deposits in the North Pole area, Western Australia. Prog. Earth Planet. Sci. 5, 85. https://doi.org/10.1186/s40645-018-0242-1

Iizuka, T., Komiya, T., Johnson, S.P., Kon, Y., Maruyama, S., Hirata, T., 2009. Reworking of Hadean crust in the Acasta gneisses, northwestern Canada: evidence from in-situ Lu–Hf isotope analysis of zircon. Chem. Geol. 259, 230–239. https://doi.org/10.1016/j.chemgeo.2008.11.007

Jain, A., Bhosle, N.B., 2009. Biochemical composition of the marine conditioning film: implications for bacterial adhesion. Biofouling 25, 13–19. https://doi.org/10.1080/08927010802411969

Jakosky, B.M., Phillips, R.J., 2001. Mars' volatile and climate history. Nature 412, 237–244. https://doi.org/10.1038/35084184

Jakosky, B.M., 2021. Atmospheric loss to space and the history of water on Mars. Annu. Rev. Earth Planet. Sci. 49, 71–93. https://doi.org/10.1146/annurev-earth-062420-052845

Javaux, E.J., Marshall, C.P., Bekker, A., 2010. Organic-walled microfossils in 3.2-billion-year-old shallow-marine siliciclastic deposits. Nature 463, 934–938. https://doi.org/10.1038/nature08793

Jébrak, M., 1997. Hydrothermal breccias in vein-type ore deposits: a review of mechanisms, morphology and size distribution. Ore Geol. Rev. 12, 111–134. https://doi.org/10.1016/S0169-1368(97)00009-7

Jelen, B.I., Giovannelli, D., Falkowski, P.G., 2016. The Role of Microbial Electron Transfer in the Coevolution of the Biosphere and Geosphere. Annu. Rev. Microbiol. 70, 45–62. https://doi.org/10.1146/annurev-micro-102215-095521

Jenkins, R., 1999. X-Ray Fluorescence Spectrometry, Volume 152. Wiley Online Library.

Johannessen, K.C., McLoughlin, N., Vullum, P.E., Thorseth, I.H., 2020. On the biogenicity of Fe-oxyhydroxide filaments in silicified low-temperature hydrothermal deposits: Implications for the identification of Fe-oxidizing bacteria in the rock record. Geobiology 18, 31–53. https://doi.org/10.1111/gbi.12363

Johnson, A.C., Ostrander, C.M., Romaniello, S.J., Reinhard, C.T., Greaney, A.T., Lyons, T.W., Anbar, A.D., 2021. Reconciling evidence of oxidative weathering and atmospheric anoxia on Archean Earth. Sci. Adv. 7, eabj0108. https://doi.org/10.1126/sciadv.abj0108

Johnson, S.S., Anslyn, E.V., Graham, H.V., Mahaffy, P.R., Ellington, A.D., 2018. Fingerprinting non-terran biosignatures. Astrobiology 18, 915–922. https://doi.org/10.1089/ast.2017.1712

Josset, J.-L., Westall, F., Hofmann, B.A., Spray, J., Cockell, C., Kempe, S., Griffiths, A.D., De Sanctis, M.C., Colangeli, L., Koschny, D., 2017. The Close-Up Imager onboard the ESA ExoMars Rover: objectives, description, operations, and science validation activities. Astrobiology 17, 595–611. https://doi.org/10.1089/ast.2016.1546

Kamber, B.S., Greig, A., Collerson, K.D., 2005. A new estimate for the composition of weathered young upper continental crust from alluvial sediments, Queensland, Australia. Geochim. Cosmochim. Acta 69, 1041–1058. https://doi.org/10.1016/j.gca.2004.08.020

Kasting, J.F., 1991. Box models for the evolution of atmospheric oxygen: an update. Glob. Planet. Change 5, 125–131. https://doi.org/10.1016/0921-8181(91)90133-H

Kato, Y., Nakamura, K., 2003. Origin and global tectonic significance of Early Archean cherts from the Marble Bar greenstone belt, Pilbara Craton, Western Australia. Precambrian Res. 125, 191–243. https://doi.org/10.1016/S0301-9268(03)00043-3

Kebukawa, Y., Nakashima, S., Ishikawa, M., Aizawa, K., Inoue, T., NAKAMURA-MESSENGER, K., Zolensky, M.E., 2010. Spatial distribution of organic matter in the Bells CM2 chondrite using near-field infrared microspectroscopy. Meteorit. Planet. Sci. 45, 394–405. https://doi.org/10.1111/j.1945-5100.2010.01030.x

Keil, R.G., Mayer, L.M., 2014. Mineral Matrices and Organic Matter, in: Turekian, K.K., Holland, H.D. (Eds.), Treatise on Geochemistry, 2nd ed. Elsevier, Amsterdam, Netherlands, pp. 337–359.

Keller, L.P., 2006. Infrared Spectroscopy of Comet 81P/Wild 2 Samples Returned by Stardust. Science 314, 1728–1731. https://doi.org/10.1126/science.1135796

Kellermeier, M., Cölfen, H., García-Ruiz, J.M., 2012. Silica biomorphs: Complex biomimetic hybrid materials from “sand and chalk.” Eur. J. Inorg. Chem. 2012, 5123–5144. https://doi.org/10.1002/ejic.201201029

Kempe, S., Degens, E.T., 1985. An early soda ocean? Chem. Geol. 53, 95–108. https://doi.org/10.1016/0009-2541(85)90023-3

Kempes, C.P., Krakauer, D.C., 2021. The multiple paths to multiple life. J. Mol. Evol. 89, 415–426. https://doi.org/10.1007/s00239-021-10016-2

Kerrich, R., Said, N., Manikyamba, C., Wyman, D., 2013. Sampling oxygenated Archean hydrosphere: Implications from fractionations of Th/U and Ce/Ce* in hydrothermally altered volcanic sequences. Gondwana Res. 23, 506–525. https://doi.org/10.1016/j.gr.2012.02.007

Kisch, H.J., Nijman, W., 2004. Metamorphic grade from K-micas in the metasediments of the Pilbara and Barberton Greenstone Belts, in: Reimold W.U., Hofmann A. (Eds.), Field Forum on Processes on the Early Earth, Kaapvaal Craton, South Africa. Johannesburg, University of Witwatersrand, pp. 47–48.

Kleber, M., Mikutta, R., Torn, M.S., Jahn, R., 2005. Poorly crystalline mineral phases protect organic matter in acid subsoil horizons. Eur. J. Soil Sci. 56, 717–725. https://doi.org/10.1111/j.1365-2389.2005.00706.x

Klein, C., Beukes, N.J., 1989. Geochemistry and sedimentology of a facies transition from limestone to iron-formation deposition in the early Proterozoic Transvaal Supergroup, South Africa. Econ. Geol. 84, 1733–1774. https://doi.org/10.2113/gsecongeo.84.7.1733

Klein, H.P., Lederberg, J., Rich, A., Horowitz, N.H., Oyama, V.I., Levin, G.V., 1976. The Viking Mission search for life on Mars. Nature 262, 24–27. https://doi.org/10.1038/262024a0

Klein, H.P., 1979. The Viking mission and the search for life on Mars. Rev. Geophys. 17, 1655–1662. https://doi.org/10.1029/RG017i007p01655

Kleine, T., Münker, C., Mezger, K., Palme, H., 2002. Rapid accretion and early core formation on asteroids and the terrestrial planets from Hf–W chronometry. Nature 418, 952–955. https://doi.org/10.1038/nature00982

Klingelhofer, G., Morris, R.V., Bernhardt, B., Schroder, C., Rodionov, D.S., de Souza Jr, P.A., Yen, A., Gellert, R., Evlanov, E.N., Zubkov, B., 2004. Jarosite and hematite at Meridiani Planum from Opportunity's Mossbauer spectrometer. Science 306, 1740–1745. https://doi.org/10.1126/science.110465

Kminek, G., Benardini, J.N., Brenker, F.E., Brooks, T., Burton, A.S., Dhaniyala, S., Dworkin, J.P., Fortman, J.L., Glamoclija, M., Grady, M.M., 2022. COSPAR Sample Safety Assessment Framework (SSAF). Astrobiology 22, S186–S216. https://doi.org/10.1089/ast.2022.0017

Knauth, L.P., 1998. Salinity history of the Earth's early ocean. Nature 395, 554–555. https://doi.org/10.1038/26879

Knoll, A.H., Barghoorn, E.S., 1977. Archean microfossils showing cell division from the Swaziland System of South Africa. Science 198, 396–398. https://doi.org/10.1126/science.198.4315.396

Koga, S., Williams, D.S., Perriman, A.W., Mann, S., 2011. Peptide–nucleotide microdroplets as a step towards a membrane-free protocell model. Nat. Chem. 3, 720–724. https://doi.org/10.1038/nchem.1110

Korablev, O.I., Dobrolensky, Y., Evdokimova, N., Fedorova, A.A., Kuzmin, R.O., Mantsevich, S.N., Cloutis, E.A., Carter, J., Poulet, F., Flahaut, J., 2017. Infrared spectrometer for ExoMars: a mast-mounted instrument for the rover. Astrobiology 17, 542–564. https://doi.org/10.1089/ast.2016.1543

Kotopoulou, E., Lopez-Haro, M., Calvino Gamez, J.J., García-Ruiz, J.M., 2021. Nanoscale anatomy of iron-silica self-organized membranes: implications for prebiotic chemistry. Angew. Chem. Int. Ed. 60, 1396–1402. https://doi.org/10.1002/anie.202012059

Kouketsu, Y., Mizukami, T., Mori, H., Endo, S., Aoya, M., Hara, H., Nakamura, D., Wallis, S., 2014. A new approach to develop the Raman carbonaceous material geothermometer for low-grade metamorphism using peak width. Isl. Arc 23, 33–50. https://doi.org/10.1111/iar.12057

Krissansen-Totton, J., Arney, G.N., Catling, D.C., 2018. Constraining the climate and ocean pH of the early Earth with a geological carbon cycle model. Proc. Natl. Acad. Sci. 115, 4105–4110. https://doi.org/10.1073/pnas.1721296115

Kump, P., 1997. Some considerations on the definition of the limit of detection in X-ray fluorescence spectrometry. Spectrochim. Acta Part B At. Spectrosc. 52, 405–408. https://doi.org/10.1016/S0584-8547(96)01590-X

Kung, C.-C., Hayatsu, R., Studier, M.H., Clayton, R.N., 1979. Nitrogen isotope fractionations in the Fischer-Tropsch synthesis and in the Miller-Urey reaction. Earth Planet. Sci. Lett. 46, 141–146. https://doi.org/10.1016/0012-821X(79)90072-4

Lagaly, G., 1984. Clay-organic interactions. Philos. Trans. R. Soc. Lond. Ser. Math. Phys. Sci. 311, 315–332. https://doi.org/10.1098/rsta.1984.0031

Lambert, J.-F., 2008. Adsorption and polymerization of amino acids on mineral surfaces: a review. Orig. Life Evol. Biospheres 38, 211–242. https://doi.org/10.1007/s11084-008-9128-3

Lammer, H., Chassefière, E., Karatekin, Ö., Morschhauser, A., Niles, P.B., Mousis, O., Odert, P., Möstl, U.V., Breuer, D., Dehant, V., 2013. Outgassing history and escape of the Martian atmosphere

and water inventory. Space Sci. Rev. 174, 113–154. https://doi.org/10.1007/s11214-012-9943-8

Lan, Z., Kamo, S.L., Roberts, N.M., Sano, Y., Li, X.-H., 2022. A Neoarchean (ca. 2500 Ma) age for jaspilite-carbonate BIF hosting purported micro-fossils from the Eoarchean (≥ 3750 Ma) Nuvvuagittuq supracrustal belt (Québec, Canada). Precambrian Res. 377, 106728. https://doi.org/10.1016/j.precamres.2022.106728

LaRowe, D.E., Van Cappellen, P., 2011. Degradation of natural organic matter: a thermodynamic analysis. Geochim. Cosmochim. Acta 75, 2030–2042. https://doi.org/10.1016/j.gca.2011.01.020

Laurent, O., Martin, H., Moyen, J.-F., Doucelance, R., 2014. The diversity and evolution of late-Archean granitoids: Evidence for the onset of "modern-style" plate tectonics between 3.0 and 2.5 Ga. Lithos 205, 208–235. https://doi.org/10.1016/j.lithos.2014.06.012

Lawrence, M.G., Greig, A., Collerson, K.D., Kamber, B.S., 2006. Rare earth element and yttrium variability in South East Queensland waterways. Aquat. Geochem. 12, 39–72. https://doi.org/10.1007/s10498-005-4471-8

Lawrence, M.G., Kamber, B.S., 2006. The behaviour of the rare earth elements during estuarine mixing—revisited. Mar. Chem. 100, 147–161. https://doi.org/10.1016/j.marchem.2005.11.007

Lederberg, J., 1960. Exobiology: approaches to life beyond the Earth. Science 132, 393–400. https://doi.org/10.1126/science.132.3424.393

Ledevin, M., Arndt, N., Chauvel, C., Jaillard, E., Simionovici, A., 2019. The sedimentary origin of black and white banded cherts of the Buck Reef, Barberton, South Africa. Geosciences 9, 424. https://doi.org/10.3390/geosciences9100424

Lepot, K., Philippot, P., Benzerara, K., Wang, G.-Y., 2009. Garnet-filled trails associated with carbonaceous matter mimicking microbial filaments in Archean basalt. Geobiology 7, 393–402. https://doi.org/10.1111/j.1472-4669.2009.00208.x

Lepot, K., Benzerara, K., Philippot, P., 2011. Biogenic versus metamorphic origins of diverse microtubes in 2.7Gyr old volcanic ashes: Multi-scale investigations. Earth Planet. Sci. Lett. 312, 37–47. https://doi.org/10.1016/j.epsl.2011.10.016

Lepot, K., Williford, K.H., Ushikubo, T., Sugitani, K., Mimura, K., Spicuzza, M.J., Valley, J.W., 2013. Texture-specific isotopic compositions in 3.4 Gyr old organic matter support selective preservation in cell-like structures. Geochim. Cosmochim. Acta 112, 66–86. https://doi.org/10.1016/j.gca.2013.03.004

Lewis, I.R., Edwards, H., 2001. Handbook of Raman spectroscopy: from the research laboratory to the process line. CRC press.

Li, J., Benzerara, K., Bernard, S., Beyssac, O., 2013. The link between biomineralization and fossilization of bacteria: insights from field and experimental studies. Chem. Geol. 359, 49–69. https://doi.org/10.1016/j.chemgeo.2013.09.013

Liermann, L.J., Hausrath, E.M., Anbar, A.D., Brantley, S.L., 2007. Assimilatory and dissimilatory processes of microorganisms affecting metals in the environment. J. Anal. At. Spectrom. 22, 867. https://doi.org/10.1039/b705383e

Lin, R., Ritz, G.P., 1993. Studying individual macerals using ir microspectrometry, and implications on oil versus gas/condensate proneness and "low-rank" generation. Org. Geochem. 20, 695–706. https://doi.org/10.1016/0146-6380(93)90055-G

Lindsay, J.F., Brasier, M.D., McLoughlin, N., Green, O.R., Fogel, M., Steele, A., Mertzman, S.A., 2005. The problem of deep carbon—an Archean paradox. Precambrian Res. 143, 1–22. https://doi.org/10.1016/j.precamres.2005.09.003

Liu, Y., Whitman, W.B., 2008. Metabolic, Phylogenetic, and Ecological Diversity of the Methanogenic Archaea. Ann. N. Y. Acad. Sci. 1125, 171–189. https://doi.org/10.1196/annals.1419.019

Lollar, B.S., McCollom, T.M., 2006. Biosignatures and abiotic constraints on early life. Nature 444, E18–E18. https://doi.org/10.1038/nature05499

Lotfi-Kalahroodi, E., Pierson-Wickmann, A.-C., Rouxel, O., Marsac, R., Bouhnik-Le Coz, M., Hanna, K., Davranche, M., 2021. More than redox, biological organic ligands control iron isotope fractionation in the riparian wetland. Sci. Rep. 11, 1933. https://doi.org/10.1038/s41598-021-81494-z

Lowe, D.R., 1994. Abiological origin of described stromatolites older than 3.2 Ga. Geology 22, 387–390. https://doi.org/10.1130/0091-7613(1994)022<0387:AOODSO>2.3.CO;2

Lowe, D.R., Byerly, G.R., 1999. Geologic evolution of the Barberton greenstone belt, South Africa. Geological Society of America. https://doi.org/10.1130/SPE329

Lowe, D.R., Byerly, G.R., 2020. The non-glacial and non-cratonic origin of an early Archean felsic volcaniclastic unit, Barberton Greenstone Belt, South Africa. Precambrian Res. 341, 105647. https://doi.org/10.1016/j.precamres.2020.105647

Luisi, P.L., Ferri, F., Stano, P., 2006. Approaches to semi-synthetic minimal cells: a review. Naturwissenschaften 93, 1–13. https://doi.org/10.1007/s00114-005-0056-z

MacRae, C.M., Wilson, N.C., 2008. Luminescence database I—minerals and materials. Microsc. Microanal. 14, 184–204. https://doi.org/doi:10.1017/S143192760808029X

Mahaffy, P.R., Webster, C.R., Cabane, M., Conrad, P.G., Coll, P., Atreya, S.K., Arvey, R., Barciniak, M., Benna, M., Bleacher, L., 2012. The sample analysis at Mars investigation and instrument suite. Space Sci. Rev. 170, 401–478. https://doi.org/10.1007/s11214-012-9879-z

Mangold, N., Dehouck, E., Fedo, C., Forni, O., Achilles, C., Bristow, T., Downs, R.T., Frydenvang, J., Gasnault, O., L'Haridon, J., 2019. Chemical alteration of fine-grained sedimentary rocks at Gale crater. Icarus 321, 619–631. https://doi.org/10.1016/j.icarus.2018.11.004

Mann, S., 2001. Biomineralization: principles and concepts in bioinorganic materials chemistry. Oxford University Press on Demand.

Marin-Carbonne, J., Chaussidon, M., Robert, F., 2012. Micrometer-scale chemical and isotopic criteria (O and Si) on the origin and history of Precambrian cherts: implications for paleo-temperature reconstructions. Geochim. Cosmochim. Acta 92, 129–147. https://doi.org/10.1016/j.gca.2012.05.040

Marshall, S.M., Mathis, C., Carrick, E., Keenan, G., Cooper, G.J., Graham, H., Craven, M., Gromski, P.S., Moore, D.G., Walker, S.I., 2021. Identifying molecules as biosignatures with assembly theory and mass spectrometry. Nat. Commun. 12, 3033. https://doi.org/10.1038/s41467-021-23258-x

Martin, A.J., 2000. Flaser and wavy bedding in ephemeral streams: a modern and an ancient example. Sediment. Geol. 136, 1–5. https://doi.org/10.1016/S0037-0738(00)00085-3

Martin, H., Moyen, J.-F., 2002. Secular changes in tonalite-trondhjemite-granodiorite composition as markers of the progressive cooling of Earth. Geology 30, 319–322. https://doi.org/10.1130/0091-7613(2002)030<0319:SCITTG>2.0.CO;2

Martin, W.F., 2011. Early evolution without a tree of life. Biol. Direct 6, 1–25. https://doi.org/10.1186/1745-6150-6-36

Marty, B., Avice, G., Bekaert, D.V., Broadley, M.W., 2018. Salinity of the Archaean oceans from analysis of fluid inclusions in quartz. Comptes Rendus Geosci. 350, 154–163. https://doi.org/10.1016/j.crte.2017.12.002

Mathez, E.A., 1987. Carbonaceous matter in mantle xenoliths: Composition and relevance to the isotopes. Geochim. Cosmochim. Acta 51, 2339–2347. https://doi.org/10.1016/0016-7037(87)90288-2

Matrajt, G., Pizzarello, S., Taylor, S., Brownlee, D., 2004. Concentration and variability of the AIB amino acid in polar micrometeorites: Implications for the exogenous delivery of amino acids to the primitive Earth. Meteorit. Planet. Sci. 39, 1849–1858. https://doi.org/10.1111/j.1945-5100.2004.tb00080.x

Maurette, M., Duprat, J., Engrand, C., Gounelle, M., Kurat, G., Matrajt, G., Toppani, A., 2000. Accretion of neon, organics, CO2, nitrogen and water from large interplanetary dust particles on the early Earth. Planet. Space Sci. 48, 1117–1137. https://doi.org/10.1016/S0032-0633(00)00086-6

Maurette, M., 2006. Micrometeorites and the mysteries of our origins. Springer, Berlin, Heidelberg.

Maurice, S., Wiens, R.C., Bernardi, P., Caïs, P., Robinson, S., Nelson, T., Gasnault, O., Reess, J.-M., Deleuze, M., Rull, F., 2021. The SuperCam instrument suite on the Mars 2020 rover: science objectives and mast-unit description. Space Sci. Rev. 217, 1–108. https://doi.org/10.1007/s11214-021-00807-w

Maxwell, J.A., Teesdale, W.J., Campbell, J.L., 1995. The Guelph PIXE software package II. Nucl. Instrum. Methods Phys. Res. Sect. B Beam Interact. Mater. At. 95, 407–421. https://doi.org/10.1016/0168-583X(94)00540-0

Mayer, L.M., 1994. Surface area control of organic carbon accumulation in continental shelf sediments. Geochim. Cosmochim. Acta 58, 1271–1284. https://doi.org/10.1016/0016-7037(94)90381-6

McCarthy, K., Rojas, K., Niemann, M., Palmowski, D., Peters, K., Stankiewicz, A., 2011. Basic petroleum geochemistry for source rock evaluation. Oilfield Rev. 23, 32–43.

McCollom, T.M., Hynek, B.M., Rogers, K.L., 2016. Potential for Preservation of Biosignatures from Endolithic Photosynthetic Communities in a Mars Analog Fumarole Environment. Presented at the Biosignature Preservation and Detection in Mars Analog Environments, LPI Contributions, Lake Tahoe, Nevada [Abstract]. URL https://ui.adsabs.harvard.edu/abs/2016LPICo1912.2006M/abstract (accessed: 08.08.23).

McKay, C.P., Stoker, C.R., 1989. The early environment and its evolution on Mars: Implication for life. Rev. Geophys. 27, 189. https://doi.org/10.1029/RG027i002p00189

McKay, D.S., Gibson, E.K., Thomas-Keprta, K.L., Vali, H., Romanek, C.S., Clemett, S.J., Chillier, X.D., Maechling, C.R., Zare, R.N., 1996. Search for past life on Mars: Possible relic biogenic activity in Martian meteorite ALH84001. Science 273, 924–930. https://doi.org/10.1126/science.273.5277.924

McLennan, S.M., Bell Iii, J.F., Calvin, W.M., Christensen, P.R., Clark, B. d, De Souza, P.A., Farmer, J., Farrand, W.H., Fike, D.A., Gellert, R., 2005. Provenance and diagenesis of the evaporite-bearing Burns formation, Meridiani Planum, Mars. Earth Planet. Sci. Lett. 240, 95–121. https://doi.org/10.1016/j.epsl.2005.09.041

McLoughlin, N., Brasier, M.D., Wacey, D., Green, O.R., Perry, R.S., 2007. On biogenicity criteria for endolithic microborings on early Earth and beyond. Astrobiology 7, 10–26. https://doi.org/10.1089/ast.2006.0122

McLoughlin, N., Wilson, L.A., Brasier, M.D., 2008. Growth of synthetic stromatolites and wrinkle structures in the absence of microbes–implications for the early fossil record. Geobiology 6, 95–105. https://doi.org/10.1111/j.1472-4669.2007.00141.x

McLoughlin, N., Staudigel, H., Furnes, H., Eickmann, B., Ivarsson, M., 2010. Mechanisms of microtunneling in rock substrates: distinguishing endolithic biosignatures from abiotic microtunnels: Mechanisms of microtunneling in rock substrates. Geobiology 8, 245–255. https://doi.org/10.1111/j.1472-4669.2010.00243.x

McLoughlin, N., 2014. Biogenicity, in: Amils, R., Gargaud, M., Cernicharo Quintanilla, J., Cleaves, H.J., Irvine, W.M., Pinti, D., Viso, M. (Eds.), Encyclopedia of Astrobiology. Springer Berlin Heidelberg, Berlin, Heidelberg, pp. 1–3.

McLoughlin, N., Grosch, E.G., 2015. A hierarchical system for evaluating the biogenicity of metavolcanic-and ultramafic-hosted microalteration textures in the search for extraterrestrial life. Astrobiology 15, 901–921. https://doi.org/10.1089/ast.2014.1259

McMahon, S., Bosak, T., Grotzinger, J.P., Milliken, R.E., Summons, R.E., Daye, M., Newman, S.A., Fraeman, A., Williford, K.H., Briggs, D.E.G., 2018. A Field Guide to Finding Fossils on Mars. J. Geophys. Res. Planets 123, 1012–1040. https://doi.org/10.1029/2017JE005478

McMahon, S., 2019. Earth's earliest and deepest purported fossils may be iron-mineralized chemical gardens. Proc. R. Soc. B 286, 20192410. https://doi.org/10.1098/rspb.2019.2410

McMahon, S., Cosmidis, J., 2022. False biosignatures on Mars: anticipating ambiguity. J. Geol. Soc. 179, jgs2021-050. https://doi.org/10.1144/jgs2021-050

McNaught, A.D., Wilkinson, A., 1997. Compendium of chemical terminology. Blackwell Science Oxford.

Meadows, V., Graham, H., Abrahamsson, V., Adam, Z., Amador-French, E., Arney, G., Barge, L., Barlow, E., Berea, A., Bose, M., 2022. Community Report from the Biosignatures Standards of Evidence Workshop. ArXiv Prepr. ArXiv221014293. https://doi.org/10.48550/arXiv.2210.14293

Ménez, B., Pisapia, C., Andreani, M., Jamme, F., Vanbellingen, Q.P., Brunelle, A., Richard, L., Dumas, P., Réfrégiers, M., 2018. Abiotic synthesis of amino acids in the recesses of the oceanic lithosphere. Nature 564, 59–63. https://doi.org/10.1038/s41586-018-0684-z

Michalski, J.R., Cuadros, J., Niles, P.B., Parnell, J., Deanne Rogers, A., Wright, S.P., 2013. Groundwater activity on Mars and implications for a deep biosphere. Nat. Geosci. 6, 133–138. https://doi.org/10.1038/ngeo1706

Miller, S.L., 1955. Production of some organic compounds under possible primitive earth conditions. J Am Chem Soc 77, 2351–2361. https://doi.org/10.1021/ja01614a001

Milojevic, T., Kölbl, D., Ferrière, L., Albu, M., Kish, A., Flemming, R.L., Koeberl, C., Blazevic, A., Zebec, Z., Rittmann, S.K.-M.R., Schleper, C., Pignitter, M., Somoza, V., Schimak, M.P., Rupert, A.N., 2019. Exploring the microbial biotransformation of extraterrestrial material on nanometer scale. Sci. Rep. 9, 18028. https://doi.org/10.1038/s41598-019-54482-7

Milojevic, T., Albu, M., Kölbl, D., Kothleitner, G., Bruner, R., Morgan, M.L., 2021. Chemolithotrophy on the Noachian Martian breccia NWA 7034 via experimental microbial biotransformation. Commun. Earth Environ. 2, 39. https://doi.org/10.1038/s43247-021-00105-x

Ming, D.W., Mittlefehldt, D.W., Morris, R.V., Golden, D.C., Gellert, R., Yen, A., Clark, B.C., Squyres, S.W., Farrand, W.H., Ruff, S.W., 2006. Geochemical and mineralogical indicators for aqueous processes in the Columbia Hills of Gusev crater, Mars. J. Geophys. Res. Planets 111. https://doi.org/10.1029/2005JE002560

Mlewski, E.C., Pisapia, C., Gomez, F., Lecourt, L., Soto Rueda, E., Benzerara, K., Ménez, B., Borensztajn, S., Jamme, F., Réfrégiers, M., Gérard, E., 2018. Characterization of Pustular Mats and Related Rivularia-Rich Laminations in Oncoids From the Laguna Negra Lake (Argentina). Front. Microbiol. 9, 996. https://doi.org/10.3389/fmicb.2018.00996

Mojzsis, S.J., Harrison, T.M., Pidgeon, R.T., 2001. Oxygen-isotope evidence from ancient zircons for liquid water at the Earth's surface 4,300 Myr ago. Nature 409, 178–181. https://doi.org/10.1038/35051557

Moorbath, S., Allaart, J.H., Bridgwater, D., McGregor, V.R., 1977. Rb–Sr ages of early Archaean supracrustal rocks and Amîtsoq gneisses at Isua. Nature 270, 43–45. https://doi.org/10.1038/270043a0

Moore, E.K., Jelen, B.I., Giovannelli, D., Raanan, H., Falkowski, P.G., 2017. Metal availability and the expanding network of microbial metabolisms in the Archaean eon. Nat. Geosci. 10, 629–636. https://doi.org/10.1038/ngeo3006

Moore, J.M., Howard, A.D., 2005. Large alluvial fans on Mars. J. Geophys. Res. Planets 110, E04005. https://doi.org/10.1029/2004JE002352

Morag, N., Williford, K.H., Kitajima, K., Philippot, P., Van Kranendonk, M.J., Lepot, K., Thomazo, C., Valley, J.W., 2016. Microstructure-specific carbon isotopic signatures of organic matter from∼ 3.5 Ga cherts of the Pilbara Craton support a biologic origin. Precambrian Res. 275, 429–449. https://doi.org/10.1016/j.precamres.2016.01.014

Morbidelli, A., Chambers, J., Lunine, J.I., Petit, J.-M., Robert, F., Valsecchi, G.B., Cyr, K.E., 2000. Source regions and timescales for the delivery of water to the Earth. Meteorit. Planet. Sci. 35, 1309–1320. https://doi.org/10.1111/j.1945-5100.2000.tb01518.x

Morris, R.C., 1993. Genetic modelling for banded iron-formation of the Hamersley Group, Pilbara Craton, Western Australia. Precambrian Res. 60, 243–286. https://doi.org/10.1016/0301-9268(93)90051-3

Morris, R.V., Klingelhoefer, G., Schröder, C., Rodionov, D.S., Yen, A., Ming, D.W., de Souza Jr, P.A., Fleischer, I., Wdowiak, T., Gellert, R., 2006. Mössbauer mineralogy of rock, soil, and dust at Gusev crater, Mars: Spirit's journey through weakly altered olivine basalt on the plains and pervasively altered basalt in the Columbia Hills. J. Geophys. Res. Planets 111, E02S13. https://doi.org/10.1029/2005JE002584

Morse, J.W., Mackenzie, F.T., 1998. Hadean ocean carbonate geochemistry. Aquat. Geochem. 4, 301–319. https://doi.org/10.1023/A:1009632230875

Moyen, J.-F., Martin, H., 2012. Forty years of TTG research. Lithos 148, 312–336. https://doi.org/10.1016/j.lithos.2012.06.010

Moyen, J.-F., Laurent, O., 2018. Archaean tectonic systems: A view from igneous rocks. Lithos 302, 99–125. https://doi.org/10.1016/j.lithos.2017.11.038

Muirhead, B.K., Nicholas, A.K., Umland, J., Sutherland, O., Vijendran, S., 2020. Mars Sample Return Campaign Concept Status. Acta Astronaut. 176, 131–138. https://doi.org/10.1016/j.actaastro.2020.06.026

Müller, P.J., Suess, E., 1979. Productivity, sedimentation rate, and sedimentary organic matter in the oceans—I. Organic carbon preservation. Deep Sea Res. Part Oceanogr. Res. Pap. 26, 1347–1362. https://doi.org/10.1016/0198-0149(79)90003-7

Munir, N., Hanif, M., Dias, D.A., Abideen, Z., 2021. The role of halophytic nanoparticles towards the remediation of degraded and saline agricultural lands. Environ. Sci. Pollut. Res. 28, 60383–60405. https://doi.org/10.1007/s11356-021-16139-9

Muscente, A.D., Czaja, A.D., Tuggle, J., Winkler, C., Xiao, S., 2018. Manganese oxides resembling microbial fabrics and their implications for recognizing inorganically preserved microfossils. Astrobiology 18, 249–258. https://doi.org/10.1089/ast.2017.1699

Mustard, J.F., Adler, M., Allwood, A., Bass, D.S., Beaty, D.W., Bell, J.F., Brinckerhoff, W., Carr, M., Des Marais, D.J., Brake, B., 2013. Report of the Mars 2020 science definition team. Mars Explor Progr Anal Gr 150, 155–205. https://www.researchgate.net/profile/Kenneth-Edgett/publication/316741129_Report_of_the_Mars_2020_Science_Definition_Team/links/592d97530f7e9beee72c6212/Report-of-the-Mars-2020-Science-Definition-Team.pdf

Mustard, J.F., 2019. Sequestration of volatiles in the Martian crust through hydrated minerals: A significant planetary reservoir of water, in: Filiberto, J., Schwenzer S.P. (Eds.), Volatiles in the Martian Crust. Elsevier, pp. 247–263.

Muyzer, G., Stams, A.J.M., 2008. The ecology and biotechnology of sulphate-reducing bacteria. Nat. Rev. Microbiol. 6, 441–454. https://doi.org/10.1038/nrmicro1892

Nakamura, K., Takai, K., 2014. Theoretical constraints of physical and chemical properties of hydrothermal fluids on variations in chemolithotrophic microbial communities in seafloor hydrothermal systems. Prog. Earth Planet. Sci. 1, 5. https://doi.org/10.1186/2197-4284-1-5

Naraoka, H., 2014. Insoluble Organic Matter, in: Amils, R., Gargaud, M., Cernicharo Quintanilla, J., Cleaves, H.J., Irvine, W.M., Pinti, D., Viso, M. (Eds.), Encyclopedia of Astrobiology. Springer Berlin Heidelberg, Berlin, Heidelberg, pp. 1–2.

Nelson, D.R., Trendall, A.F., Altermann, W., 1999. Chronological correlations between the Pilbara and Kaapvaal cratons. Precambrian Res. 97, 165–189. https://doi.org/10.1016/S0301-9268(99)00031-5

Neveu, M., Hays, L.E., Voytek, M.A., New, M.H., Schulte, M.D., 2018. The Ladder of Life Detection. Astrobiology 18, 1375–1402. https://doi.org/10.1089/ast.2017.1773

Nier, A.O., Gulbransen, E.A., 1939. Variations in the relative abundance of the carbon isotopes. J. Am. Chem. Soc. 61, 697–698. https://doi.org/10.1021/ja01872a047

Nijman, W., Willigers, B.J., Krikke, A., 1998. Tensile and compressive growth structures: relationships between sedimentation, deformation and granite intrusion in the Archaean Coppin Gap greenstone belt, Eastern Pilbara, Western Australia. Precambrian Res. 88, 83–108. https://doi.org/10.1016/S0301-9268(97)00065-X

Nisbet, E.G., Arndt, N.T., Bickle, M.J., Cameron, W.E., Chauvel, C., Cheadle, M., Hegner, E., Kyser, T.K., Martin, A., Renner, R., 1987. Uniquely fresh 2.7 Ga komatiites from the Belingwe greenstone belt, Zimbabwe. Geology 15, 1147–1150. https://doi.org/10.1130/0091-7613(1987)15<1147:UFGKFT>2.0.CO;2

Nisbet, E.G., Sleep, N.H., 2001. The habitat and nature of early life. Nature 409, 1083–1091. https://doi.org/10.1038/35059210

Noffke, N., 2009. The criteria for the biogeneicity of microbially induced sedimentary structures (MISS) in Archean and younger, sandy deposits. Earth-Sci. Rev. 96, 173–180. https://doi.org/10.1016/j.earscirev.2008.08.002

Noffke, N., Awramik, S.M., 2013. Stromatolites and MISS—differences between relatives. GSA Today 23, 4–9. https://doi.org/10.1130/GSATG187A.1

Noffke, N., Christian, D., Wacey, D., Hazen, R.M., 2013. Microbially induced sedimentary structures recording an ancient ecosystem in the ca. 3.48 billion-year-old Dresser Formation, Pilbara, Western Australia. Astrobiology 13, 1103–1124. https://doi.org/10.1089/ast.2013.1030

Noffke, N., 2015. Ancient sedimentary structures in the< 3.7 Ga Gillespie Lake Member, Mars, that resemble macroscopic morphology, spatial associations, and temporal succession in terrestrial microbialites. Astrobiology 15, 169–192. https://doi.org/10.1089/ast.2014.1218

Nutman, A.P., Mojzsis, S.J., Friend, C.R., 1997. Recognition of ≥3850 Ma water-lain sediments in West Greenland and their significance for the early Archaean Earth. Geochim. Cosmochim. Acta 61, 2475–2484. https://doi.org/10.1016/S0016-7037(97)00097-5

Nutman, A.P., Bennett, V.C., Friend, C.R., Van Kranendonk, M.J., Chivas, A.R., 2016. Rapid emergence of life shown by discovery of 3,700-million-year-old microbial structures. Nature 537, 535–538. https://doi.org/10.1038/nature19355

Nutman, A.P., Bennett, V.C., Friend, C.R., Van Kranendonk, M.J., Rothacker, L., Chivas, A.R., 2019. Cross-examining Earth's oldest stromatolites: Seeing through the effects of heterogeneous deformation, metamorphism and metasomatism affecting Isua (Greenland)∼ 3700 Ma sedimentary rocks. Precambrian Res. 331, 105347. https://doi.org/10.1016/j.precamres.2019.105347

Oaki, Y., Kotachi, A., Miura, T., Imai, H., 2006. Bridged nanocrystals in biominerals and their biomimetics: Classical yet modern crystal growth on the nanoscale. Adv. Funct. Mater. 16, 1633–1639. https://doi.org/10.1002/adfm.200600262

Oehler, D.Z., Cady, S.L., 2014. Biogenicity and syngeneity of organic matter in ancient sedimentary rocks: recent advances in the search for evidence of past life. Challenges 5, 260–283. https://doi.org/10.3390/challe5020260

Oehler, D.Z., Walsh, M.M., Sugitani, K., Liu, M.-C., House, C.H., 2017. Large and robust lenticular microorganisms on the young Earth. Precambrian Res. 296, 112–119. https://doi.org/10.1016/j.precamres.2017.04.031

Olariu, C., Bhattacharya, J.P., 2006. Terminal distributary channels and delta front architecture of river-dominated delta systems. J. Sediment. Res. 76, 212–233. https://doi.org/10.2110/jsr.2006.026

Olcott Marshall, A., Marshall, C.P., 2015. Vibrational spectroscopy of fossils. Palaeontology 58, 201–211. https://doi.org/10.1111/pala.12144

O'Neil, J., Carlson, R.W., Paquette, J.-L., Francis, D., 2012. Formation age and metamorphic history of the Nuvvuagittuq Greenstone Belt. Precambrian Res. 220, 23–44. https://doi.org/10.1016/j.precamres.2012.07.009

Onstott, T.C., Ehlmann, B.L., Sapers, H., Coleman, M., Ivarsson, M., Marlow, J.J., Neubeck, A., Niles, P., 2019. Paleo-rock-hosted life on Earth and the search on Mars: a review and strategy for exploration. Astrobiology 19, 1230–1262. https://doi.org/10.1089/ast.2018.1960

Opel, J., Kellermeier, M., Sickinger, A., Morales, J., Cölfen, H., García-Ruiz, J.-M., 2018. Structural transition of inorganic silica–carbonate composites towards curved lifelike morphologies. Minerals 8, 75. https://doi.org/10.3390/min8020075

Orange, F., Westall, F., Disnar, J.-R., Prieur, D., Bienvenu, N., Le Romancer, M., Défarge, Ch., 2009. Experimental silicification of the extremophilic Archaea Pyrococcus abyssi and Methanocaldococcus jannaschii: applications in the search for evidence of life in early Earth and extraterrestrial rocks. Geobiology 7, 403–418. https://doi.org/10.1111/j.1472-4669.2009.00212.x

Orange, F., Disnar, J.-R., Westall, F., Prieur, D., Baillif, P., 2011. Metal cation binding by the hyperthermophilic microorganism, Archaea Methanocaldococcus jannaschii, and its effects on silicification. Palaeontology 54, 953–964. https://doi.org/10.1111/j.1475-4983.2011.01066.x

Orberger, B., Rouchon, V., Westall, F., de Vries, S.T., Pinti, D.L., Wagner, C., Wirth, R., Hashizume, K., 2006. Microfacies and origin of some Archean cherts (Pilbara, Australia), in: Reimold, W.U., Gibson, R.L. (Eds.), Processes on the Early Earth. Geological Society of America, New York, pp. 133–156.

Orell, A., Schopf, S., Randau, L., Vera, M., 2017. Biofilm lifestyle of thermophile and Acidophile Archaea, in: Witzany G. (Eds.), Biocommunication of Archaea. Springer, pp. 133–146.

Osinski, G.R., Tornabene, L.L., Banerjee, N.R., Cockell, C.S., Flemming, R., Izawa, M.R., McCutcheon, J., Parnell, J., Preston, L.J., Pickersgill, A.E., 2013. Impact-generated hydrothermal systems on Earth and Mars. Icarus 224, 347–363. https://doi.org/10.1016/j.icarus.2012.08.030

Osinski, G.R., Cockell, C.S., Pontefract, A., Sapers, H.M., 2020. The role of meteorite impacts in the origin of life. Astrobiology 20, 1121–1149. https://doi.org/10.1089/ast.2019.2203

Papineau, D., 2020. Chemically oscillating reactions in the formation of botryoidal malachite. Am. Mineral. 105, 447–454. https://doi.org/10.2138/am-2020-7029

Papineau, D., She, Z., Dodd, M.S., Iacoviello, F., Slack, J.F., Hauri, E., Shearing, P., Little, C.T.S., 2022. Metabolically diverse primordial microbial communities in Earth's oldest seafloor-hydrothermal jasper. Sci. Adv. 8, eabm2296. https://doi.org/10.1126/sciadv.abm2296

Parenteau, M.N., Cady, S.L., 2010. Microbial biosignatures in iron-mineralized phototrophic mats at Chocolate Pots hot springs, Yellowstone National Park, United States. Palaios 25, 97–111. https://doi.org/10.2110/palo.2008.p08-133r

Parker, E.T., Zhou, M., Burton, A.S., Glavin, D.P., Dworkin, J.P., Krishnamurthy, R., Fernández, F.M., Bada, J.L., 2014. A plausible simultaneous synthesis of amino acids and simple peptides on the primordial Earth. Angew. Chem. Int. Ed. 126, 8270–8274. https://doi.org/10.1002/ange.201403683

Parkes, R.J., Wellsbury, P., Mather, I.D., Cobb, S.J., Cragg, B.A., Hornibrook, E.R., Horsfield, B., 2007. Temperature activation of organic matter and minerals during burial has the potential to sustain the deep biosphere over geological timescales. Org. Geochem. 38, 845–852. https://doi.org/10.1016/j.orggeochem.2006.12.011

Parnell, J., McMahon, S., 2016. Physical and chemical controls on habitats for life in the deep subsurface beneath continents and ice. Philos. Trans. R. Soc. Math. Phys. Eng. Sci. 374, 20140293. https://doi.org/10.1098/rsta.2014.0293

Pendleton, Y.J., Sandford, S.A., Allamandola, L.J., Tielens, A., Sellgren, K., 1994. Near-infrared absorption spectroscopy of interstellar hydrocarbon grains. Astrophys. J. 437, 683–696.

Perry, R.S., Mcloughlin, N., Lynne, B.Y., Sephton, M.A., Oliver, J.D., Perry, C.C., Campbell, K., Engel, M.H., Farmer, J.D., Brasier, M.D., Staley, J.T., 2007. Defining biominerals and organominerals: Direct and indirect indicators of life. Sediment. Geol. 201, 157–179. https://doi.org/10.1016/j.sedgeo.2007.05.014

Peters, K.E., Walters, C.C., Moldowan, J.M., 2005. The biomarker guide. Cambridge university press.

Pflug, H.D., 1966. Structured Organic Remains from the Fig Tree Series of the Barbeton Mountain Land. University of the Witwatersrand, Johannesburg, Economic Geology Research Unit.

Pflug, H.D., 1967. Structured organic remains from the Fig Tree Series (Precambrian) of the Barberton mountain land (South Africa). Rev. Palaeobot. Palynol. 5, 9–29. https://doi.org/10.1016/0034-6667(67)90205-9

Pflug, H.D., Meinel, W., Neumann, K.H., Meinel, M., 1969. Entwicklungstendenzen des frühen Lebens auf der Erde. Naturwissenschaften 56, 10–14. https://doi.org/10.1007/BF00599585

Pickard, A.L., 2003. SHRIMP U–Pb zircon ages for the Palaeoproterozoic Kuruman Iron Formation, northern Cape Province, South Africa: evidence for simultaneous BIF deposition on Kaapvaal and Pilbara cratons. Precambrian Res. 125, 275–315. https://doi.org/10.1016/S0301-9268(03)00113-X

Pinti, D.L., 2005. The Origin and Evolution of the Oceans, in: Gargaud, M., Barbier, B., Martin, H., Reisse, J. (Eds.), Lectures in Astrobiology, Advances in Astrobiology and Biogeophysics. Springer Berlin Heidelberg, Berlin, Heidelberg, pp. 83–112.

Pinti, D.L., Mineau, R., Clement, V., 2009. Hydrothermal alteration and microfossil artefacts of the 3,465-million-year-old Apex chert. Nat. Geosci. 2, 640–643. https://doi.org/10.1038/ngeo601

Pirajno, F., 2020. Subaerial hot springs and near-surface hydrothermal mineral systems past and present, and possible extraterrestrial analogues. Geosci. Front. 11, 1549–1569. https://doi.org/10.1016/j.gsf.2020.04.001

Pizzarello, S., Schrader, D.L., Monroe, A.A., Lauretta, D.S., 2012. Large enantiomeric excesses in primitive meteorites and the diverse effects of water in cosmochemical evolution. Proc. Natl. Acad. Sci. 109, 11949–11954. https://doi.org/10.1073/pnas.1204865109

Polat, A., Hofmann, A.W., 2003. Alteration and geochemical patterns in the 3.7–3.8 Ga Isua greenstone belt, West Greenland. Precambrian Res. 126, 197–218. https://doi.org/10.1016/S0301-9268(03)00095-0

Poulet, F., Bibring, J.-P., Mustard, J.F., Gendrin, A., Mangold, N., Langevin, Y., Arvidson, R.E., Gondet, B., Gomez, C., Berthé, M., Bibring, J.-P., Langevin, Y., Erard, S., Forni, O., Gendrin, A., Gondet, B., Manaud, N., Poulet, F., Poulleau, G., Soufflot, A., Combes, M., Drossart, P., Encrenaz, T., Fouchet, T., Melchiorri, R., Bellucci, G., Altieri, F., Formisano, V., Fonti, S., Capaccioni, F., Cerroni, P., Coradini, A., Korablev, O., Kottsov, V., Ignatiev, N., Titov, D., Zasova, L., Mangold, N., Pinet, P., Schmitt, B., Sotin, C., Hauber, E., Hoffmann, H., Jaumann, R., Keller, U., Arvidson, R., Mustard, J., Forget, F., The Omega Team, 2005. Phyllosilicates on Mars and implications for early martian climate. Nature 438, 623–627. https://doi.org/10.1038/nature04274

Quantin, C., Flahaut, J., Clenet, H., Allemand, P., Thomas, P., 2012. Composition and structures of the subsurface in the vicinity of Valles Marineris as revealed by central uplifts of impact craters. Icarus 221, 436–452. https://doi.org/10.1016/j.icarus.2012.07.031

Quantin-Nataf, C., Carter, J., Mandon, L., Thollot, P., Balme, M., Volat, M., Pan, L., Loizeau, D., Millot, C., Breton, S., Dehouck, E., Fawdon, P., Gupta, S., Davis, J., Grindrod, P.M., Pacifici, A., Bultel, B., Allemand, P., Ody, A., Lozach, L., Broyer, J., 2021. Oxia Planum: The Landing Site for the ExoMars "Rosalind Franklin" Rover Mission: Geological Context and Prelanding Interpretation. Astrobiology 21, 345–366. https://doi.org/10.1089/ast.2019.2191

Rampe, E.B., Blake, D.F., Bristow, T.F., Ming, D.W., Vaniman, D.T., Morris, R.V., Achilles, C.N., Chipera, S.J., Morrison, S.M., Tu, V.M., 2020. Mineralogy and geochemistry of sedimentary rocks and eolian sediments in Gale crater, Mars: A review after six Earth years of exploration with Curiosity. Geochemistry 80, 125605. https://doi.org/10.1016/j.chemer.2020.125605

Rasmussen, B., 2000. Filamentous microfossils in a 3,235-million-year-old volcanogenic massive sulphide deposit. Nature 405, 676–679. https://doi.org/10.1038/35015063

Rasmussen, B., Buick, R., 2000. Oily old ores: evidence for hydrothermal petroleum generation in an Archean volcanogenic massive sulfide deposit. Geology 28, 731–734. https://doi.org/10.1130/0091-7613(2000)28<731:OOOEFH>2.0.CO;2

Rasmussen, B., Fletcher, I.R., Brocks, J.J., Kilburn, M.R., 2008. Reassessing the first appearance of eukaryotes and cyanobacteria. Nature 455, 1101–1104. https://doi.org/10.1038/nature07381

Rasmussen, B., Muhling, J.R., Fischer, W.W., 2021. Ancient oil as a source of carbonaceous matter in 1.88-billion-year-old Gunflint stromatolites and microfossils. Astrobiology 21, 655–672. https://doi.org/10.1089/ast.2020.2376

Raulin, F., 2008. De l'exobiologie à l'astrobiologie: Émergence et développement d'une nouvelle science interdisciplinaire. Rev. Pour L'histoire CNRS. https://doi.org/10.4000/histoire-cnrs.8883

Raven, M.R., Sessions, A.L., Adkins, J.F., Thunell, R.C., 2016. Rapid organic matter sulfurization in sinking particles from the Cariaco Basin water column. Geochim. Cosmochim. Acta 190, 175–190. https://doi.org/10.1016/j.gca.2016.06.030

Razzell Hollis, J., Abbey, W., Beegle, L.W., Bhartia, R., Ehlmann, B.L., Miura, J., Monacelli, B., Moore, K., Nordman, A., Scheller, E., Uckert, K., Wu, Y.-H., 2021. A deep-ultraviolet Raman and Fluorescence spectral library of 62 minerals for the SHERLOC instrument onboard Mars 2020. Planet. Space Sci. 209, 105356. https://doi.org/10.1016/j.pss.2021.105356

Razzell Hollis, J., Sharma, S., Abbey, W., Bhartia, R., Beegle, L., Fries, M., Hein, J.D., Monacelli, B., Nordman, A.D., 2023. A Deep Ultraviolet Raman and Fluorescence Spectral Library of 51 Organic Compounds for the SHERLOC Instrument Onboard Mars 2020. Astrobiology 23, 1–23. https://doi.org/10.1089/ast.2022.0023

Rettberg, P., Anesio, A.M., Baker, V.R., Baross, J.A., Cady, S.L., Detsis, E., Foreman, C.M., Hauber, E., Ori, G.G., Pearce, D.A., 2016. Planetary protection and Mars special regions—a suggestion for updating the definition. Astrobiology 16, 119–125. https://doi.org/10.1089/ast.2016.1472

Rickaby, R.E.M., 2015. Goldilocks and the three inorganic equilibria: how Earth's chemistry and life coevolve to be nearly in tune. Philos. Trans. R. Soc. Math. Phys. Eng. Sci. 373, 20140188. https://doi.org/10.1098/rsta.2014.0188

Riding, R., 1991. Classification of microbial carbonates, in: Riding R. (Eds.), Calcareous Algae and Stromatolites. Springer, Berlin, Heidelberg, pp. 21–51.

Riquelme, C., Marshall Hathaway, J.J., Enes Dapkevicius, M. de L., Miller, A.Z., Kooser, A., Northup, D.E., Jurado, V., Fernandez, O., Saiz-Jimenez, C., Cheeptham, N., 2015. Actinobacterial diversity in volcanic caves and associated geomicrobiological interactions. Front. Microbiol. 6, 1342. https://doi.org/10.3389/fmicb.2015.01342

Robbins, L.J., Lalonde, S.V., Planavsky, N.J., Partin, C.A., Reinhard, C.T., Kendall, B., Scott, C., Hardisty, D.S., Gill, B.C., Alessi, D.S., Dupont, C.L., Saito, M.A., Crowe, S.A., Poulton, S.W., Bekker, A., Lyons, T.W., Konhauser, K.O., 2016. Trace elements at the intersection of marine biological and geochemical evolution. Earth-Sci. Rev. 163, 323–348. https://doi.org/10.1016/j.earscirev.2016.10.013

Robert, F., Chaussidon, M., 2006. A palaeotemperature curve for the Precambrian oceans based on silicon isotopes in cherts. Nature 443, 969–972. https://doi.org/10.1038/nature05239

Rodriguez-Navarro, C., Jimenez-Lopez, C., Rodriguez-Navarro, A., Gonzalez-Muñoz, M.T., Rodriguez-Gallego, M., 2007. Bacterially mediated mineralization of vaterite. Geochim. Cosmochim. Acta 71, 1197–1213. https://doi.org/10.1016/j.gca.2006.11.031

Rogers, A.D., 2011. Crustal compositions exposed by impact craters in the Tyrrhena Terra region of Mars: Considerations for Noachian environments. Earth Planet. Sci. Lett. 301, 353–364. https://doi.org/10.1016/j.epsl.2010.11.020

Rosing, M.T., 1999. 13C-depleted carbon microparticles in >3700-Ma sea-floor sedimentary rocks from West Greenland. Science 283, 674–676. https://doi.org/10.1126/science.283.5402.674

Rothschild, L.J., Mancinelli, R.L., 2001. Life in extreme environments. Nature 409, 1092–1101. https://doi.org/10.1038/35059215

Rouillard, J., García-Ruiz, J.-M., Gong, J., Van Zuilen, M.A., 2018. A morphogram for silica-witherite biomorphs and its application to microfossil identification in the early earth rock record. Geobiology 16, 279–296. https://doi.org/10.1111/gbi.12278

Rouzaud, J.N., Oberlin, A., 1989. Structure, microtexture, and optical properties of anthracene and saccharose-based carbons. Carbon 27, 517–529. https://doi.org/10.1016/0008-6223(89)90002-X

Ruff, S.W., Farmer, J.D., 2016. Silica deposits on Mars with features resembling hot spring biosignatures at El Tatio in Chile. Nat. Commun. 7, 13554. https://doi.org/10.1038/ncomms13554

Rull, F., Maurice, S., Hutchinson, I., Moral, A., Perez, C., Diaz, C., Colombo, M., Belenguer, T., Lopez-Reyes, G., Sansano, A., 2017. The Raman laser spectrometer for the ExoMars rover mission to Mars. Astrobiology 17, 627–654. https://doi.org/10.1089/ast.2016.1567

Rye, R., Holland, H.D., 2000. Life associated with a 2.76 Ga ephemeral pond?: Evidence from Mount Roe# 2 paleosol. Geology 28, 483–486. https://doi.org/10.1130/0091-7613(2000)28<483:LAWAGE>2.0.CO;2

Samuels, T., Bryce, C., Landenmark, H., Marie-Loudon, C., Nicholson, N., Stevens, A.H., Cockell, C., 2020. Microbial Weathering of Minerals and Rocks in Natural Environments, in: Dontsova, K., Balogh-Brunstad, Z., Le Roux, G. (Eds.), Biogeochemical Cycles: Ecological Drivers and Environmental Impact, Geophysical Monograph Series. American Geophysical Union, pp. 59–79.

Sandford, S.A., Allamandola, L.J., Tielens, A., Sellgren, K., Tapia, M., Pendleton, Y., 1991. The interstellar CH stretching band near 3.4 microns-Constraints on the composition of organic material in the diffuse interstellar medium. Astrophys. J. 371, 607–620. https://doi.org/10.1086/169925

Scheller, E.L., Razzell Hollis, J., Cardarelli, E.L., Steele, A., Beegle, L.W., Bhartia, R., Conrad, P., Uckert, K., Sharma, S., Ehlmann, B.L., 2022. Aqueous alteration processes in Jezero crater, Mars—implications for organic geochemistry. Science 378, 1105–1110. https://doi.org/10.1126/science.abo5204

Schidlowski, M., 2001. Carbon isotopes as biogeochemical recorders of life over 3.8 Ga of Earth history: evolution of a concept. Precambrian Res. 106, 117–134. https://doi.org/10.1016/S0301-9268(00)00128-5

Schopf, J.M., 1975. Modes of fossil preservation. Rev. Palaeobot. Palynol. 20, 27–53. https://doi.org/10.1016/0034-6667(75)90005-6

Schopf, J.W., Packer, B.M., 1987. Early Archean (3.3-billion to 3.5-billion-year-old) microfossils from Warrawoona Group, Australia. Science 237, 70–73. https://doi.org/10.1126/science.11539686

Schopf, J.W., Kudryavtsev, A.B., Agresti, D.G., Wdowiak, T.J., Czaja, A.D., 2002. Laser–Raman imagery of Earth's earliest fossils. Nature 416, 73–76. https://doi.org/10.1038/416073a

Schreiber, U., Locker-Grütjen, O., Mayer, C., 2012. Hypothesis: Origin of life in deep-reaching tectonic faults. Orig. Life Evol. Biospheres 42, 47–54. https://doi.org/10.1007/s11084-012-9267-4

Schrenk, M.O., Brazelton, W.J., Lang, S.Q., 2013. Serpentinization, Carbon, and Deep Life. Rev. Mineral. Geochem. 75, 575–606. https://doi.org/10.2138/rmg.2013.75.18

Schultze-Lam, S., Fortin, D., Davis, B.S., Beveridge, T.J., 1996. Mineralization of bacterial surfaces. Chem. Geol. 132, 171–181. https://doi.org/10.1016/S0009-2541(96)00053-8

Sephton, M.A., 2002. Organic compounds in carbonaceous meteorites. Nat. Prod. Rep. 19, 292–311. https://doi.org/10.1039/B103775G

Sephton, M.A., Love, G.D., Watson, J.S., Verchovsky, A.B., Wright, I.P., Snape, C.E., Gilmour, I., 2004. Hydropyrolysis of insoluble carbonaceous matter in the Murchison meteorite: new insights into its macromolecular structure. Geochim. Cosmochim. Acta 68, 1385–1393. https://doi.org/10.1016/j.gca.2003.08.019

Sephton, M.A., Hazen, R.M., 2013. On the origins of deep hydrocarbons. Rev. Mineral. Geochem. 75, 449–465. https://doi.org/10.2138/rmg.2013.75.14

Sforna, M.C., Loron, C.C., Demoulin, C.F., François, C., Cornet, Y., Lara, Y.J., Grolimund, D., Ferreira Sanchez, D., Medjoubi, K., Somogyi, A., Addad, A., Fadel, A., Compère, P., Baudet, D., Brocks, J.J., Javaux, E.J., 2022. Intracellular bound chlorophyll residues identify 1 Gyr-old fossils as eukaryotic algae. Nat. Commun. 13, 146. https://doi.org/10.1038/s41467-021-27810-7

Sharma, S., Roppel, R.D., Murphy, A.E., Beegle, L.W., Bhartia, R., 2023. Diverse organic-mineral associations in Jezero crater, Mars. Nature 619, 724–732. https://doi.org/10.1038/s41586-023-06143-z

Shaw, G.H., 2008. Earth's atmosphere–Hadean to early Proterozoic. Geochemistry 68, 235–264. https://doi.org/10.1016/j.chemer.2008.05.001

Sheldon, N.D., Tabor, N.J., 2009. Quantitative paleoenvironmental and paleoclimatic reconstruction using paleosols. Earth-Sci. Rev. 95, 1–52. https://doi.org/10.1016/j.earscirev.2009.03.004

Sim, M.S., Bosak, T., Ono, S., 2011. Large sulfur isotope fractionation does not require disproportionation. Science 333, 74–77. https://doi.org/10.1126/science.1205103

Simon, J.I., Hickman-Lewis, K., Cohen, B.A., Mayhew, L.E., Shuster, D.L., Debaille, V., Hausrath, E.M., Weiss, B.P., Bosak, T., Zorzano, M. -P., Amundsen, H.E.F., Beegle, L.W., Bell, J.F., Benison, K.C., Berger, E.L., Beyssac, O., Brown, A.J., Calef, F., Casademont, T.M., Clark, B., Clavé, E., Crumpler, L., Czaja, A.D., Fairén, A.G., Farley, K.A., Flannery, D.T., Fornaro, T., Forni, O., Gómez, F., Goreva, Y., Gorin, A., Hand, K.P., Hamran, S. -E., Henneke, J., Herd, C.D.K., Horgan, B.H.N., Johnson, J.R., Joseph, J., Kronyak, R.E., Madariaga, J.M., Maki, J.N., Mandon, L., McCubbin, F.M., McLennan, S.M., Moeller, R.C., Newman, C.E., Núñez, J.I., Pascuzzo, A.C., Pedersen, D.A., Poggiali, G., Pinet, P., Quantin-Nataf, C., Rice, M., Rice, J.W., Royer, C., Schmidt, M., Sephton, M., Sharma,

S., Siljeström, S., Stack, K.M., Steele, A., Sun, V.Z., Udry, A., VanBommel, S., Wadhwa, M., Wiens, R.C., Williams, A.J., Williford, K.H., 2023. Samples Collected From the Floor of Jezero Crater With the Mars 2020 Perseverance Rover. J. Geophys. Res. Planets 128, e2022JE007474. https://doi.org/10.1029/2022JE007474

Sirantoine, E., Wacey, D., Bischoff, K., Saunders, M., 2021. Authigenic anatase within 1 billion-year-old cells. Geobiology 19, 3–17. https://doi.org/10.1111/gbi.12417

Slack, J.F., Grew, E.S., Anovitz, L.M., 1996. Tourmaline associations with hydrothermal ore deposits. Rev. Mineral. 33, 559–644. https://doi.org/10.1515/9781501509223-013

Sleep, N.H., 2010. The hadean-archaean environment. Cold Spring Harb. Perspect. Biol. 2, a002527. https://doi.org/10.1101/cshperspect.a002527

Solomon, S.C., Head, J.W., 1990. Heterogeneities in the thickness of the elastic lithosphere of Mars: Constraints on heat flow and internal dynamics. J. Geophys. Res. Solid Earth 95, 11073–11083. https://doi.org/10.1029/JB095iB07p11073

Steele, A., McCubbin, F.M., Fries, M., Kater, L., Boctor, N.Z., Fogel, M.L., Conrad, P.G., Glamoclija, M., Spencer, M., Morrow, A.L., Hammond, M.R., Zare, R.N., Vicenzi, E.P., Siljeström, S., Bowden, R., Herd, C.D.K., Mysen, B.O., Shirey, S.B., Amundsen, H.E.F., Treiman, A.H., Bullock, E.S., Jull, A.J.T., 2012. A Reduced Organic Carbon Component in Martian Basalts. Science 337, 212. https://doi.org/10.1126/science.1220715

Steele, A., McCubbin, F.M., Fries, M.D., 2016. The provenance, formation, and implications of reduced carbon phases in Martian meteorites. Meteorit. Planet. Sci. 51, 2203–2225. https://doi.org/10.1111/maps.12670

Steele, A., Benning, L.G., Wirth, R., Siljeström, S., Fries, M.D., Hauri, E., Conrad, P.G., Rogers, K., Eigenbrode, J., Schreiber, A., 2018. Organic synthesis on Mars by electrochemical reduction of CO2. Sci. Adv. 4, eaat5118. https://doi.org/10.1126/sciadv.aat5118

Stillman, D.E., Michaels, T.I., Grimm, R.E., Hanley, J., 2016. Observations and modeling of northern mid-latitude recurring slope lineae (RSL) suggest recharge by a present-day martian briny aquifer. Icarus 265, 125–138. https://doi.org/10.1016/j.icarus.2015.10.007

Stoks, P.G., Schwartz, A.W., 1982. Basic nitrogen-heterocyclic compounds in the Murchison meteorite. Geochim. Cosmochim. Acta 46, 309–315. https://doi.org/10.1016/0016-7037(82)90222-8

Straub, K.L., Benz, M., Schink, B., Widdel, F., 1996. Anaerobic, nitrate-dependent microbial oxidation of ferrous iron. Appl. Environ. Microbiol. 62, 1458–1460. https://doi.org/10.1128/aem.62.4.1458-1460.1996

Stüeken, E.E., 2016. Nitrogen in ancient mud: a biosignature? Astrobiology 16, 730–735. https://doi.org/10.1089/ast.2016.1478

Stüeken, E.E., Som, S.M., Claire, M., Rugheimer, S., Scherf, M., Sproß, L., Tosi, N., Ueno, Y., Lammer, H., 2020. Mission to Planet Earth: The First Two Billion Years. Space Sci. Rev. 216, 31. https://doi.org/10.1007/s11214-020-00652-3

Sugitani, K., Grey, K., Allwood, A., Nagaoka, T., Mimura, K., Minami, M., Marshall, C.P., Van Kranendonk, M.J., Walter, M.R., 2007. Diverse microstructures from Archaean chert from the Mount Goldsworthy–Mount Grant area, Pilbara Craton, Western Australia: microfossils, dubiofossils, or pseudofossils? Precambrian Res. 158, 228–262. https://doi.org/10.1016/j.precamres.2007.03.006

Sugitani, K., Lepot, K., Nagaoka, T., Mimura, K., Van Kranendonk, M., Oehler, D.Z., Walter, M.R., 2010. Biogenicity of morphologically diverse carbonaceous microstructures from the ca. 3400 Ma Strelley Pool Formation, in the Pilbara Craton, Western Australia. Astrobiology 10, 899–920. https://doi.org/10.1089/ast.2010.0513

Sugitani, K., Mimura, K., Nagaoka, T., Lepot, K., Takeuchi, M., 2013. Microfossil assemblage from the 3400 Ma Strelley Pool Formation in the Pilbara Craton, Western Australia: results form a new locality. Precambrian Res. 226, 59–74. https://doi.org/10.1016/j.precamres.2012.11.005

Sugitani, K., Mimura, K., Takeuchi, M., Lepot, K., Ito, S., Javaux, E.J., 2015a. Early evolution of large micro-organisms with cytological complexity revealed by microanalyses of 3.4 Ga organic-walled microfossils. Geobiology 13, 507–521. https://doi.org/10.1111/gbi.12148

Sugitani, K., Mimura, K., Takeuchi, M., Yamaguchi, T., Suzuki, K., Senda, R., Asahara, Y., Wallis, S., Van Kranendonk, M.J., 2015b. A Paleoarchean coastal hydrothermal field inhabited by diverse microbial communities: the Strelley Pool Formation, Pilbara Craton, Western Australia. Geobiology 13, 522–545. https://doi.org/10.1111/gbi.12150

Summons, R.E., Albrecht, P., McDonald, G., Moldowan, J.M., 2008. Molecular biosignatures, in: Botta, O., Bada, J.L., Gomez-Elvira, J., Javaux, E., Selsis, F., Summons, R. (Eds.), Strategies of Life Detection, Space Sciences Series of ISSI. Springer, Boston, MA, pp. 133–159.

Summons, R.E., Amend, J.P., Bish, D., Buick, R., Cody, G.D., Des Marais, D.J., Dromart, G., Eigenbrode, J.L., Knoll, A.H., Sumner, D.Y., 2011. Preservation of Martian Organic and Environmental Records: Final Report of the Mars Biosignature Working Group. Astrobiology 11, 157–181. https://doi.org/10.1089/ast.2010.0506

Tait, K.T., McCubbin, F.M., Smith, C.L., Agee, C.B., Busemann, H., Cavalazzi, B., Debaille, V., Hutzler, A., Usui, T., Kminek, G., 2022. Preliminary planning for Mars Sample Return (MSR) curation activities in a Sample Receiving Facility (SRF). Astrobiology 22, S57–S80. https://doi.org/10.1089/ast.2021.0105

Tarnas, J.D., Mustard, J.F., Lin, H., Goudge, T.A., Amador, E.S., Bramble, M.S., Kremer, C.H., Zhang, X., Itoh, Y., Parente, M., 2019. Orbital Identification of Hydrated Silica in Jezero Crater, Mars. Geophys. Res. Lett. 46, 12771–12782. https://doi.org/10.1029/2019GL085584

Tartèse, R., Chaussidon, M., Gurenko, A., Delarue, F., Robert, F., 2016. Warm Archaean oceans reconstructed from oxygen isotope composition of early-life remnants. Geochem. Perspect. Lett. 3, 55–65. https://doi.org/10.7185/geochemlet.1706

Teesdale, W.J., Maxwell, J.A., Perujo, A., Campbell, J.L., Van Der Zwan, L., Jackman, T.E., 1988. Limits of detection and quantitation in PIXE analysis of thick targets. Nucl. Instrum. Methods Phys. Res. Sect. B Beam Interact. Mater. At. 35, 57–66. https://doi.org/10.1016/0168-583X(88)90098-5

Thomazo, C., Pinti, D.L., Busigny, V., Ader, M., Hashizume, K., Philippot, P., 2009. Biological activity and the Earth's surface evolution: Insights from carbon, sulfur, nitrogen and iron stable isotopes in the rock record. Comptes Rendus Palevol 8, 665–678. https://doi.org/10.1016/j.crpv.2009.02.003

Tice, M.M., Lowe, D.R., 2004. Photosynthetic microbial mats in the 3,416-Myr-old ocean. Nature 431, 549–552. https://doi.org/10.1038/nature02888

Tosca, N.J., McLennan, S.M., Clark, B.C., Grotzinger, J.P., Hurowitz, J.A., Knoll, A.H., Schröder, C., Squyres, S.W., 2005. Geochemical modeling of evaporation processes on Mars: Insight from the sedimentary record at Meridiani Planum. Earth Planet. Sci. Lett. 240, 122–148. https://doi.org/10.1016/j.epsl.2005.09.042

Tosca, N.J., Agee, C.B., Cockell, C.S., Glavin, D.P., Hutzler, A., Marty, B., McCubbin, F.M., Regberg, A.B., Velbel, M.A., Kminek, G., 2022. Time-sensitive aspects of Mars Sample Return (MSR) science. Astrobiology 22, S81–S111. https://doi.org/10.1089/ast.2021.0115

Uebe, R., Schüler, D., 2016. Magnetosome biogenesis in magnetotactic bacteria. Nat. Rev. Microbiol. 14, 621–637. https://doi.org/10.1038/nrmicro.2016.99

Ueno, Y., Isozaki, Y., Yurimoto, H., Maruyama, S., 2001. Carbon isotopic signatures of individual Archean microfossils (?) from Western Australia. Int. Geol. Rev. 43, 196–212. https://doi.org/10.1080/00206810109465008

Ueno, Y., Yamada, K., Yoshida, N., Maruyama, S., Isozaki, Y., 2006. Evidence from fluid inclusions for microbial methanogenesis in the early Archaean era. Nature 440, 516–519. https://doi.org/10.1038/nature04584

Ueno, Y., 2007. Stable carbon and sulfur isotope geochemistry of the ca. 3490 Ma Dresser Formation hydrothermal deposit, Pilbara Craton, Western Australia, in: Van Kranendonk, M.J., Smithies, R.H., Bennett, V.C. (Eds.), Developments in Precambrian Geology. Elsevier, pp. 879–896.

Ueno, Y., Ono, S., Rumble, D., Maruyama, S., 2008. Quadruple sulfur isotope analysis of ca. 3.5 Ga Dresser Formation: New evidence for microbial sulfate reduction in the early Archean. Geochim. Cosmochim. Acta 72, 5675–5691. https://doi.org/10.1016/j.gca.2008.08.026

Vago, J.L., Westall, F., Pasteur Instrument Teams, L.S.S.W.G., and Other Contributors, Coates, A.J., Jaumann, R., Korablev, O., Ciarletti, V., Mitrofanov, I., Josset, J.-L., De Sanctis, M.C., Bibring, J.-P., Rull, F., Goesmann, F., Steininger, H., Goetz, W., Brinckerhoff, W., Szopa, C., Raulin, F., Westall, F., Edwards, H.G.M., Whyte, L.G., Fairén, A.G., Bibring, J.-P., Bridges, J., Hauber, E., Ori, G.G., Werner, S., Loizeau, D., Kuzmin, R.O., Williams, R.M.E., Flahaut, J., Forget, F., Vago, J.L., Rodionov, D., Korablev, O., Svedhem, H., Sefton-Nash, E., Kminek, G., Lorenzoni, L., Joudrier, L., Mikhailov, V., Zashchirinskiy, A., Alexashkin, S., Calantropio, F., Merlo, A., Poulakis, P., Witasse, O., Bayle, O., Bayón, S., Meierhenrich, U., Carter, J., García-Ruiz, J.M., Baglioni, P., Haldemann, A., Ball, A.J., Debus, A., Lindner, R., Haessig, F., Monteiro, D., Trautner, R., Voland, C., Rebeyre, P., Goulty, D., Didot, F., Durrant, S., Zekri, E., Koschny, D., Toni, A., Visentin, G., Zwick, M., van Winnendael, M., Azkarate, M., Carreau, C., the ExoMars Project Team, 2017. Habitability on Early Mars and the Search for Biosignatures with the ExoMars Rover. Astrobiology 17, 471–510. https://doi.org/10.1089/ast.2016.1533

Valdez-Vazquez, I., Poggi-Varaldo, H.M., 2009. Hydrogen production by fermentative consortia. Renew. Sustain. Energy Rev. 13, 1000–1013. https://doi.org/10.1016/j.rser.2008.03.003

van den Boorn, S.H.J.M., van Bergen, M.J., Vroon, P.Z., de Vries, S.T., Nijman, W., 2010. Silicon isotope and trace element constraints on the origin of ~3.5Ga cherts: Implications for Early Archaean marine environments. Geochim. Cosmochim. Acta 74, 1077–1103. https://doi.org/10.1016/j.gca.2009.09.009

Van Kranendonk, M.J., Djokic, T., Poole, G., Tadbiri, S., Steller, L., Baumgartner, R., 2018. Depositional setting of the fossiliferous, c. 3480 Ma Dresser Formation, Pilbara Craton: A review, in: Van Kranendonk, M.J., Bennett, V., Hoffmann, E. (Eds.), Earth's Oldest Rocks. Elsevier, Amsterdam, pp. 985–1006.

Van Kranendonk, M.J., Baumgartner, R., Djokic, T., Ota, T., Steller, L., Garbe, U., Nakamura, E., 2021. Elements for the origin of life on land: a deep-time perspective from the Pilbara Craton of Western Australia. Astrobiology 21, 39–59. https://doi.org/10.1089/ast.2019.2107

van Wolferen, M., Orell, A., Albers, S.-V., 2018. Archaeal biofilm formation. Nat. Rev. Microbiol. 16, 699–713. https://doi.org/10.1038/s41579-018-0058-4

van Zuilen, M.A., Chaussidon, M., Rollion-Bard, C., Marty, B., 2007. Carbonaceous cherts of the Barberton Greenstone Belt, South Africa: Isotopic, chemical and structural characteristics of individual microstructures. Geochim. Cosmochim. Acta 71, 655–669. https://doi.org/10.1016/j.gca.2006.09.029

Velbel, M.A., Cockell, C.S., Glavin, D.P., Marty, B., Regberg, A.B., Smith, A.L., Tosca, N.J., Wadhwa, M., Kminek, G., Meyer, M.A., 2022. Planning implications related to sterilization-sensitive science investigations associated with Mars Sample Return (MSR). Astrobiology 22, S112–S164. https://doi.org/10.1089/ast.2021.0113

Villafañe-Barajas, S.A., Colín-García, M., 2021. Submarine hydrothermal vent systems: the relevance of dynamic systems in chemical evolution and prebiotic chemistry experiments. Int. J. Astrobiol. 20, 427–434. https://doi.org/doi:10.1017/S1473550421000331

Wacey, D., Kilburn, M., Stoakes, C., Aggleton, H., Brasier, M., 2008. Ambient inclusion trails: their recognition, age range and applicability to early life on Earth, in: Dilek, Y., Furnes, H., Muehlenbachs, K. (Eds.), Links Between Geological Processes, Microbial Activities&Evolution of Life: Microbes and Geology. Springer, pp. 113–134.

Wacey, D., 2009. Early life on earth: a practical guide. Springer, Dordrecht.

Wacey, D., Kilburn, M.R., Saunders, M., Cliff, J., Brasier, M.D., 2011. Microfossils of sulphur-metabolizing cells in 3.4-billion-year-old rocks of Western Australia. Nat. Geosci. 4, 698–702. https://doi.org/10.1038/ngeo1238

Wacey, D., Saunders, M., Kong, C., Brasier, A., Brasier, M., 2016. 3.46 Ga Apex chert 'microfossils' reinterpreted as mineral artefacts produced during phyllosilicate exfoliation. Gondwana Res. 36, 296–313. https://doi.org/10.1016/j.gr.2015.07.010

Wacey, D., Noffke, N., Saunders, M., Guagliardo, P., Pyle, D.M., 2018. Volcanogenic pseudo-fossils from the∼ 3.48 Ga dresser formation, Pilbara, Western Australia. Astrobiology 18, 539–555. https://doi.org/10.1089/ast.2017.1734

Walsh, M.M., Lowe, D.R., 1985. Filamentous microfossils from the 3,500-Myr-old Onverwacht Group, Barberton Mountain Land, South Africa. Nature 314, 530–532. https://doi.org/10.1038/314530a0

Walsh, M.M., 1992. Microfossils and possible microfossils from the early archean onverwacht group, Barberton mountain land, South Africa. Precambrian Res. 54, 271–293. https://doi.org/10.1016/0301-9268(92)90074-X

Walsh, M.M., Lowe, D.R., 1999. Modes of accumulation of carbonaceous matter in the early Archean: A petrographic and geochemical study of the carbonaceous cherts of the Swaziland Supergroup, in: Lowe, D.R., Byerly, G.R. (Eds.), Geologic evolution of the Barberton greenstone belt, South Africa. Geological Society of America, pp. 115–132.

Walter, M.R., Buick, R., Dunlop, J.S.R., 1980. Stromatolites 3,400–3,500 Myr old from the North pole area, Western Australia. Nature 284, 443–445. https://doi.org/10.1038/284443a0

Walter, M.R., Des Marais, D.J., 1993. Preservation of Biological Information in Thermal Spring Deposits: Developing a Strategy for the Search for Fossil Life on Mars. Icarus 101, 129–143. https://doi.org/10.1006/icar.1993.1011

Watanabe, Y., Stewart, B.W., Ohmoto, H., 2004. Organic-and carbonate-rich soil formation∼ 2.6 billion years ago at Schagen, East Transvaal district, South Africa. Geochim. Cosmochim. Acta 68, 2129–2151. https://doi.org/10.1016/j.gca.2003.10.036

Weiss, D.K., Head, J.W., 2017. Evidence for stabilization of the ice-cemented cryosphere in earlier Martian history: Implications for the current abundance of groundwater at depth on Mars. Icarus 288, 120–147. https://doi.org/10.1016/j.icarus.2017.01.018

Welch, S.A., Beard, B.L., Johnson, C.M., Braterman, P.S., 2003. Kinetic and equilibrium Fe isotope fractionation between aqueous Fe (II) and Fe (III). Geochim. Cosmochim. Acta 67, 4231–4250. https://doi.org/10.1016/S0016-7037(03)00266-7

Westall, F., Rincé, Y., 1994. Biofilms, microbial mats and microbe-particle interactions: electron microscope observations from diatomaceous sediments. Sedimentology 41, 147–162. https://doi.org/10.1111/j.1365-3091.1994.tb01396.x

Westall, F., 1997. Influence of cell wall composition on the fossilisation of bacteria and the implications for the search for early life forms. Presented at the IAU Colloq. 161: Astronomical and Biochemical Origins and the Search for Life in the Universe [Abstract]. URL https://ui.adsabs.harvard.edu/abs/1997abos.conf..491W/abstract (accessed: 05.23.21).

Westall, F., Steele, A., Toporski, J., Walsh, M., Allen, C., Guidry, S., McKay, D., Gibson, E., Chafetz, H., 2000. Polymeric substances and biofilms as biomarkers in terrestrial materials: implications for extraterrestrial samples. J. Geophys. Res. Planets 105, 24511–24527. https://doi.org/10.1029/2000JE001250

Westall, F., de Wit, M.J., Dann, J., van der Gaast, S., de Ronde, C.E.J., Gerneke, D., 2001. Early Archean fossil bacteria and biofilms in hydrothermally-influenced sediments from the Barberton greenstone belt, South Africa. Precambrian Res. 106, 93–116. https://doi.org/10.1016/S0301-9268(00)00127-3

Westall, F., 2005. Life on the early Earth: a sedimentary view. Science 308, 366–367. https://doi.org/10.1126/science.1107227

Westall, F., de Vries, S.T., Nijman, W., Rouchon, V., Orberger, B., Pearson, V., Watson, J., Verchovsky, A., Wright, I., Rouzaud, J.-N., Marchesini, D., Severine, A., 2006a. The 3.466 Ga "Kitty's Gap Chert," an early Archean microbial ecosystem, in: Reimold, W.U., Gibson, R.L. (Eds.), Processes on the Early Earth. Geological Society of America, New York, pp. 105–131.

Westall, F., de Ronde, C.E.J., Southam, G., Grassineau, N., Colas, M., Cockell, C., Lammer, H., 2006b. Implications of a 3.472–3.333 Gyr-old subaerial microbial mat from the Barberton greenstone belt, South Africa for the UV environmental conditions on the early Earth. Philos. Trans. R. Soc. B Biol. Sci., b 361, 1857–1876. https://doi.org/10.1098/rstb.2006.1896

Westall, F., 2008. Morphological Biosignatures in Early Terrestrial and Extraterrestrial Materials. Space Sci. Rev. 135, 95–114. https://doi.org/10.1007/s11214-008-9354-z

Westall, F., Cavalazzi, B., 2011. Biosignatures in rocks, in: Thiel, V., Reitner, J. (Eds.), Encyclopedia of Geobiology. Springer, Berlin, p. 482.

Westall, F., Foucher, F., Cavalazzi, B., de Vries, S.T., Nijman, W., Pearson, V., Watson, J., Verchovsky, A., Wright, I., Rouzaud, J.-N., Marchesini, D., Anne, S., 2011a. Volcaniclastic habitats for early life on Earth and Mars: A case study from ∼3.5Ga-old rocks from the Pilbara, Australia. Planet. Space Sci. 59, 1093–1106. https://doi.org/10.1016/j.pss.2010.09.006

Westall, F., Cavalazzi, B., Lemelle, L., Marrocchi, Y., Rouzaud, J.-N., Simionovici, A., Salomé, M., Mostefaoui, S., Andreazza, C., Foucher, F., Toporski, J., Jauss, A., Thiel, V., Southam, G., MacLean, L., Wirick, S., Hofmann, A., Meibom, A., Robert, F., Défarge, C., 2011b. Implications of in situ calcification for photosynthesis in a ~3.3Ga-old microbial biofilm from the Barberton greenstone belt, South Africa. Earth Planet. Sci. Lett. 310, 468–479. https://doi.org/10.1016/j.epsl.2011.08.029

Westall, F., Loizeau, D., Foucher, F., Bost, N., Betrand, M., Vago, J., Kminek, G., 2013. Habitability on Mars from a Microbial Point of View. Astrobiology 13, 887–897. https://doi.org/10.1089/ast.2013.1000

Westall, F., Campbell, K.A., Bréhéret, J.G., Foucher, F., Gautret, P., Hubert, A., Sorieul, S., Grassineau, N., Guido, D.M., 2015a. Archean (3.33 Ga) microbe-sediment systems were diverse and flourished in a hydrothermal context. Geology 43, 615–618. https://doi.org/10.1130/G36646.1

Westall, F., Foucher, F., Bost, N., Bertrand, M., Loizeau, D., Vago, J.L., Kminek, G., Gaboyer, F., Campbell, K.A., Bréhéret, J.-G., Gautret, P., Cockell, C.S., 2015b. Biosignatures on Mars: What, Where, and How? Implications for the Search for Martian Life. Astrobiology 15, 998–1029. https://doi.org/10.1089/ast.2015.1374

Westall, F., Brack, A., 2018. The importance of water for life. Space Sci. Rev. 214, 1–23. https://doi.org/10.1007/s11214-018-0476-7

Westall, F., Hickman-Lewis, K., 2018. Fossilization of Bacteria and Implications for the Search for Early Life on Earth and Astrobiology Missions to Mars, in: Kolb, V.M. (Eds.), Handbook of Astrobiology. CRC Press, pp. 609–631.

Westall, F., Hickman-Lewis, K., Hinman, N., Gautret, P., Campbell, K.A., Bréhéret, J.G., Foucher, F., Hubert, A., Sorieul, S., Dass, A.V., Kee, T.P., Georgelin, T., Brack, A., 2018. A Hydrothermal-Sedimentary Context for the Origin of Life. Astrobiology 18, 259–293. https://doi.org/10.1089/ast.2017.1680

Westall, F., Hickman-Lewis, K., Cavalazzi, B., Foucher, F., Clodoré, L., Vago, J.L., 2021. On biosignatures for Mars. Int. J. Astrobiol. 20, 377–393. https://doi.org/10.1017/S1473550421000264

Westall, F., Brack, A., Fairén, A.G., Schulte, M.D., 2023a. Setting the geological scene for the origin of life and continuing open questions about its emergence. Front. Astron. Space Sci. 9, 1095701. https://doi.org/10.3389/fspas.2022.1095701

Westall, F., Höning, D., Avice, G., Gentry, D., Gerya, T., Gillmann, C., Izenberg, N., Way, M.J., Wilson, C., 2023b. The Habitability of Venus. Space Sci. Rev. 219, 17. https://doi.org/10.1007/s11214-023-00960-4

Whitehouse, M.J., Fedo, C.M., 2007. Microscale heterogeneity of Fe isotopes in> 3.71 Ga banded iron formation from the Isua Greenstone Belt, southwest Greenland. Geology 35, 719–722. https://doi.org/10.1130/G23582A.1

Widdel, F., Hansen, T.A., 1992. The dissimilatory sulfate-and sulfur-reducing bacteria., in: Balows A., Trüper, H.G., Dworkin, M., Harder, W., Schleifer, K.-H. (Eds.), The Prokaryotes: A Handbook on the Biology of Bacteria: Ecophysiology, Isolation, Identification, Applications, Vol. I. Springer-Verlag Inc., New York, pp. 582–624.

Widdel, F., Schnell, S., Helsing, S., Ehrenreich, A., Assmus, B., Schink, B., 1993. Ferrous iron oxidation by anoxygenic phototrophic bacteria. Nature 362, 834–836. https://doi.org/10.1038/362834a0

Wiens, R.C., Maurice, S., Barraclough, B., Saccoccio, M., Barkley, W.C., Bell, J.F., Bender, S., Bernardin, J., Blaney, D., Blank, J., 2012. The ChemCam instrument suite on the Mars Science Laboratory (MSL) rover: Body unit and combined system tests. Space Sci. Rev. 170, 167–227. https://doi.org/10.1007/s11214-012-9902-4

Wiens, R.C., Maurice, S., Robinson, S.H., Nelson, A.E., Cais, P., Bernardi, P., Newell, R.T., Clegg, S., Sharma, S.K., Storms, S., 2021. The SuperCam instrument suite on the NASA Mars 2020 rover: Body unit and combined system tests. Space Sci. Rev. 217, 1–87. https://doi.org/10.1007/s11214-020-00777-5

Wijbrans, J.R., McDougall, I., 1987. On the metamorphic history of an Archaean granitoid greenstone terrane, East Pilbara, Western Australia, using the40Ar/39Ar age spectrum technique. Earth Planet. Sci. Lett. 84, 226–242. https://doi.org/10.1016/0012-821X(87)90088-4

Wilde, S.A., Valley, J.W., Peck, W.H., Graham, C.M., 2001. Evidence from detrital zircons for the existence of continental crust and oceans on the Earth 4.4 Gyr ago. Nature 409, 175–178. https://doi.org/10.1038/35051550

Williams, A.J., Alpers, C.N., Sumner, D.Y., Campbell, K.M., 2017. Filamentous hydrous ferric oxide biosignatures in a pipeline carrying acid mine drainage at Iron Mountain Mine, California. Geomicrobiol. J. 34, 193–206. https://doi.org/10.1080/01490451.2016.1155679

Williams, R.J.P., Fraústo Da Silva, J.J.R., 2003. Evolution was Chemically Constrained. J. Theor. Biol. 220, 323–343. https://doi.org/10.1006/jtbi.2003.3152

Wilson, M.J., 2004. Weathering of the primary rock-forming minerals: processes, products and rates. Clay Miner. 39, 233–266. https://doi.org/10.1180/0009855043930133

Winters, Y.D., Lowenstein, T.K., Timofeeff, M.N., 2013. Identification of carotenoids in ancient salt from Death Valley, Saline Valley, and Searles Lake, California, using laser Raman spectroscopy. Astrobiology 13, 1065–1080. https://doi.org/10.1089/ast.2012.0952

Wordsworth, R., Forget, F., Millour, E., Head, J.W., Madeleine, J.-B., Charnay, B., 2013. Global modelling of the early martian climate under a denser CO2 atmosphere: Water cycle and ice evolution. Icarus 222, 1–19. https://doi.org/10.1016/j.icarus.2012.09.036

Yang, S.-Y., Jiang, S.-Y., Palmer, M.R., 2015. Chemical and boron isotopic compositions of tourmaline from the Nyalam leucogranites, South Tibetan Himalaya: Implication for their formation from B-rich melt to hydrothermal fluids. Chem. Geol. 419, 102–113. https://doi.org/10.1016/j.chemgeo.2015.10.026

Yesiltas, M., Kebukawa, Y., Peale, R.E., Mattson, E., Hirschmugl, C.J., Jenniskens, P., 2014. Infrared imaging spectroscopy with micron resolution of Sutter's Mill meteorite grains. Meteorit. Planet. Sci. 49, 2027–2037. https://doi.org/10.1111/maps.12321

Yesiltas, M., Kebukawa, Y., 2016. Associations of organic matter with minerals in Tagish Lake meteorite via high spatial resolution synchrotron-based FTIR microspectroscopy. Meteorit. Planet. Sci. 51, 584–595. https://doi.org/doi: 10.1111/maps.12609

Zawaski, M.J., Kelly, N.M., Orlandini, O.F., Nichols, C.I., Allwood, A.C., Mojzsis, S.J., 2020. Reappraisal of purported ca. 3.7 Ga stromatolites from the Isua Supracrustal Belt (West Greenland) from detailed chemical and structural analysis. Earth Planet. Sci. Lett. 545, 116409. https://doi.org/10.1016/j.epsl.2020.116409

Zerkle, A.L., 2005. Biogeochemical signatures through time as inferred from whole microbial genomes. Am. J. Sci. 305, 467–502. https://doi.org/10.2475/ajs.305.6-8.467

Zhyrovetsky, V.M., Popovych, D.I., Savka, S.S., Serednytski, A.S., 2017. Nanopowder metal oxide for photoluminescent gas sensing. Nanoscale Res. Lett. 12, 1–5. https://doi.org/10.1186/s11671-017-1891-5

Zou, C., Zhang, G., Zhu, R., Yuan, X., Zhao, X., Hou, L., Wen, B., Wu, X., 2013. Chapter 3 - Characteristics of Volcanic Reservoirs, in: Zou, C., Zhang, G., Zhu, R., Yuan, X., Zhao, X., Hou, L., Wen, B., Wu, X. (Eds.), Volcanic Reservoirs in Petroleum Exploration. Elsevier, Boston, pp. 31–90.

Scientific production

Publications:

Are reported below two publications (including one as first author) associated with the work presented in this manuscript:

- **Clodoré, L.**, Foucher, F., Hickman-Lewis, K., Sorieul, S., Jouve, J., Réfrégiers, M., Collet, G., Petoud, S., Gratuze, B., Westall, F., 2024. Multi-technique characterization of 3.45 Ga microfossils on Earth: a key approach to detect possible traces of life in returned samples from Mars. Astrobiology 24, 190–226. https://doi.org/10.1089/ast.2023.0089

- Westall, F., Hickman-Lewis, K., Cavalazzi, B., Foucher, F., **Clodoré, L.**, Vago, J.L., 2021. On biosignatures for Mars. Int. J. Astrobiol. 20, 377–393. https://doi.org/10.1017/S1473550421000264

Oral communications:

Are reported below eleven abstracts (including six as first author) having given rise to oral presentations in congress and associated with the work presented in this manuscript:

- **Clodoré, L.**, Foucher F., Hickman-Lewis, K., Westall, F., September 2023. How to search for fossil life in returned martian samples? European Astrobiology Network Association (EANA) 2023 Conference, Madrid (Spain).

- Foucher, F., Baqué, M., de Vera, J. P. P., **Clodoré, L.**, Canizarès, A., Martellotti, R., Sauvage, T., Sigot, P., Westall, F., May 2023. Detection of biosignatures on Mars using Raman spectroscopy: expectations and limits. Biennial European Astrobiology Conference (BEACON) 2023, La Palma (Spain). https://elib.dlr.de/196867/

- **Clodoré, L.**, Foucher, F., Hickman-Lewis, K., Westall, F., November 2022. Mars Sample Return: The challenge of detecting putative ancient traces of life in Martian rocks. Forming and Exploring Habitable Worlds Meeting, Edinburgh (Scotland).

- **Clodoré, L.**, Foucher, F., Hickman-Lewis, K., Sorieul, S., Réfrégiers, M., Collet, G., Westall, F., September 2022. Identifying biosignatures in a Mars-analogue volcanic rock: The ~3.5 Ga Kitty's Gap chert. Europlanet Science Congress (EPSC) 2022, Grenada (Spain). https://doi.org/10.5194/epsc2022-15

- Westall, F., **Clodoré, L.**, Foucher, F., Milojevic, T., Kölbl, D., Guérillot, P., Hickman-Lewis, K., Cavalazzi, B., Vago, J., September 2022. The search for extraterrestrial life and the problem of primitive life forms, now you see them, now you don't. Europlanet Science Congress (EPSC) 2022. https://doi.org/10.5194/epsc2022-187

- Westall, F., **Clodoré, L.**, Foucher, F., Milojevic, T., Hickman-Lewis, K., Cavalazzi, B., July 2022. The challenges of detecting traces of life in martian sediments: the necessity of sample return. Committee on Space Research (COSPAR) 2022. https://ui.adsabs.harvard.edu/abs/2022cosp...44..440W/abstract

- **Clodoré, L.**, Foucher, F., Hickman-Lewis, K., Sorieul, S., Collet, G., Réfrégiers, M., Westall, F., May 2022. Identifying biosignatures in a Mars-analogue volcanic rock: The ~3.5 Ga Kitty's Gap chert. Astrobiology Science Conference (AbSciCon) 2022, Atlanta (USA). https://doi.org/10.1002/essoar.10511149.1

- Westall, F, Milojevic, T., **Clodoré, L.**, Foucher, F., Collet, G., Petoud, S., Hickman-Lewis, K., Purvis, G., Sheriff, J., May 2022. Early planetary organisms and their biosignatures. Astrobiology Science Conference (AbSciCon) 2022. https://agu.confex.com/agu/abscicon21/meetingapp.cgi/Paper/1030088

- **Clodoré, L.**, March 2022. The search for traces of life in martian rocks. RED'22, Société Française d'Exobiologie (SFE), Réserve Ornithologique du Teich, France.

- **Clodoré, L.**, Foucher, F., Hickman-Lewis, K., Réfrégiers, M., Westall, F., September 2021. Identifying biosignatures in a Mars-analogue volcanic rock: The Kitty's Gap chert. Astrobiology Graduate Conference (AbGradCon) 2021 virtual conference. https://www.youtube.com/watch?v=pIoQb1mo6rA&t=1s

- Westall, F., Hickman-Lewis, K., Foucher, F., Cavalazzi, B., **Clodoré, L.**, Vago, J., September 2021. Biosignatures: lessons from the martian meteorite ALH84001. European Astrobiology Network Association (EANA) 2021. https://hal.archives-ouvertes.fr/hal-03674935/

Poster:

Is reported below one poster as first author having given rise to a presentation in congress and associated with the work presented in this manuscript:

- **Clodoré, L.**, Foucher, F., Hickman-Lewis, K., Réfrégiers, M., Westall, F., October 2021. "Identifier des biosignatures dans une roche volcanique analogue de Mars : le chert de Kitty's Gap". Conférence Nationale Exobiologie, Société Française d'Exobiologie (SFE), Marseille, France.

Other:

Are reported below two dissemination activities carried out during my thesis concerning the topic of exobiology but not directly related to the work presented in this manuscript:

- Project "Leave and live on Mars" with the Collège Guillaume de Lorris and the foundation La main à la pâte & Maison pour la science, September 2021 to June 2023.

- Intervention in the journal of sciences for the radio France Culture on "The risks of extraterrestrial biological invasion", November 2021.

Appendix

I. Appendix A: Geochemical data

This appendix includes the results of the PIXE quantification (**Tables A1–3**), the ICP-MS and ICP-OES data (**Table A4**), the ICP-MS and ICP-OES results compared with the elemental abundances in the Earth's crust (**Table A5**), the results of additional chemical analyses (**Table A6**), as well as the LA-ICP-MS data (**Tables A7–8**).

Table A1: *µPIXE quantification: mass concentration (C_M) of major and trace elements (in ppm) in regions of interest (ROIs) in samples 00AU39 (close to hydrothermal vein) and 00AU40 (far from hydrothermal vein).*

	00AU39										00AU40			
Element C_M (ppm)	*ROI 1 – Grain 1*	*ROI 3 – Grain 3*	*ROI 4 – Grain 4*	*ROI 5 – Grain 5*	*ROI 6 – Grain 6*	*ROI 7 – Grain 7*	*ROI 8 – Grain 8*	*ROI 9 – Silica-dust gel 1*	*ROI 10 – Silica vein*	*ROI 11 – Silica dust-gel 2*	*ROI 1 – Grain 1*	*ROI 4 – Grain 4*	*ROI 5 – Grain 5*	*ROI 7 – Grain 7*
Al	18500	30471	21313	79114	29759	56186	17469	9769	0	14088	51459	58062	58327	34260
Si	933166	897440	930372	861035	905025	887892	935853	973742	997282	954329	925521	912591	909446	950725
P	2072	1669	2298	2844	2202	974	2867	2414	1595	2104	1021	1041	1550	1219
S	133	8	0	0	98	0	0	153	8	166	0	142	0	85
Cl	356	0	112	0	121	0	45	0	0	277	0	0	0	0
K	35895	57649	39512	46635	51420	35374	28527	10237	830	23663	17157	18322	20457	11000
Ca	1192	791	779	880	924	923	2315	1006	154	1201	378	329	357	170
Ti	8493	11114	6385	8971	10212	17803	13012	2256	37	3835	3370	8310	7302	2115
V	0	0	0	0	0	0	0	0	0	0	24	0	119	9
Cr	71	165	109	107	121	65	51	72	0	96	33	62	0	20
Fe	692	581	535	506	631	714	479	367	78	595	868	828	2083	633
Co	25	24	19	12	25	28	18	18	8	22	15	11	31	12
Ni	0	5	0	5	4	1	3	14	7	14	4	2	8	0
Cu	9	13	6	4	13	7	11	13	1	43	9	10	34	12
Zn	2	1	2	11	2	6	5	10	3	40	6	7	14	5
Ga	10	15	11	12	13	14	11	8	0	9	18	17	21	9
Ge	11	12	11	5	11	6	13	9	5	15	3	6	6	6
As	4	3	4	9	4	6	7	8	0	6	5	6	15	3
Kr	3	1	0	2	4	2	5	2	0	3	4	6	11	1

Rb	38	70	52	40	52	28	38	14	3	33	62	56	76	46
Sr	39	38	25	31	29	16	31	9	1	17	31	30	42	17
Y	19	10	55	127	16	18	46	8	0	16	9	32	17	0
Zr	154	89	424	780	136	101	278	41	0	119	95	197	125	48
Nb	28	22	14	12	23	17	36	6	0	7	9	15	16	0
Mo	4	6	2	19	6	24	3	0	0	3	2	12	7	4
Total	1000914	1000194	1002040	1001158	1000849	1000203	1001120	1000175	1000012	1000702	1000103	1000093	1000063	1000397

Table A2: *µPIXE quantification: average mass concentration (C_M) of major and trace elements (in ppm) within specific structures of interest (left) and in the matrix (right) surrounding the volcanic grain protoliths in sample 00AU39 (close to hydrothermal vein).*

	Structures of interest								Matrix			
Element C_M (ppm)	*Volcanic glass*	*Edges of volcanic glass*	*Pumice*	*Edges of pumice*	*MVRF with less kerogen*	*Edges of MVRF with less kerogen*	*MVRF with more kerogen*	*Edges of MVRF with more kerogen*	*Volcanic glass*	*Pumice*	*MVRF with less kerogen*	*MVRF with more kerogen*
Al	23276	12523	35095	10810	42030	11436	280914	19230	3384	6988	18786	8387
Si	930478	918119	879031	932665	866041	894232	589715	893804	987396	983883	944971	968465
P	1518	2772	2835	4302	3663	1024	999	2165	1865	2286	1243	863
S	48	268	0	110	517	60	487	211	189	142	0	0
Cl	477	196	126	0	51	79	0	0	85	135	17	0
K	41387	19985	51856	35892	67968	31476	115861	33044	5323	5656	30488	13706
Ca	687	821	842	846	2950	498	667	301	245	271	1028	734
Ti	1421	43879	27292	14313	12442	58631	8016	47669	904	361	2727	5038
V	69	0	0	0	66	0	266	0	38	2	28	0
Cr	102	82	204	99	173	205	123	197	0	0	65	13
Fe	575	665	829	636	772	809	1437	989	484	207	465	342
Co	16	21	38	29	40	36	14	57	24	8	15	10
Ni	0	7	9	0	0	5	0	0	4	0	1	0
Cu	4	12	0	3	4	5	0	4	19	8	8	6
Zn	2	6	0	0	19	1	15	5	1	5	13	24
Ga	13	8	11	17	23	25	39	29	3	0	12	6
Ge	8	16	7	10	5	10	1	4	12	10	12	11
As	3	9	13	6	4	3	12	11	2	1	2	0

Kr	3	10	2	0	5	3	0	4	3	0	1	0
Rb	50	15	69	31	81	28	94	21	14	12	33	4
Sr	28	31	34	20	48	12	36	0	15	10	29	22
Y	3	40	290	44	35	36	158	108	5	0	16	14
Zr	18	576	2169	398	206	409	1004	855	53	14	31	33
Nb	8	97	56	52	23	65	0	0	3	0	5	0
Mo	0	60	4	0	5	23	51	73	0	8	1	16
Total	1000192	1000218	1000810	1000285	997172	999111	999909	998779	1000071	1000006	999996	997692

Table A3: *µPIXE quantification: average mass concentration (C_M) of major and trace elements (in ppm) within specific structures of interest (left) and in the matrix (right) surrounding the volcanic grain protoliths in sample 00AU40 (far from hydrothermal vein).*

	Structures of interest					Matrix		
Element C_M (ppm)	*Volcanic glass*	*Edges of volcanic glass*	*MVRF with less kerogen*	*Edges of MVRF with less kerogen*	*MVRF with more kerogen*	*Volcanic glass*	*MVRF with less kerogen*	*MVRF with more kerogen*
Si	166382	61372	152815	55273	19278	5767	10223	10485
Al	775801	906892	793748	918140	967714	991515	984564	983856
P	0	0	0	898	2198	738	886	1315
S	382	0	135	0	0	0	99	0
Cl	0	0	0	0	0	0	0	0
K	53592	23043	46566	16007	6773	1166	2403	2801
Ca	436	341	557	423	151	76	89	83
Ti	1223	6483	3164	8101	2415	177	1174	975
V	229	0	216	76	90	0	13	38
Cr	128	53	69	64	0	0	23	0
Fe	1515	894	1328	570	1362	409	472	491
Co	33	41	10	3	17	12	11	13
Ni	0	0	2	11	0	18	8	0
Cu	7	19	3	3	34	7	10	12
Zn	7	11	15	2	11	6	5	0
Ga	56	35	43	22	10	10	6	0
Ge	0	0	9	5	11	0	2	0
As	6	8	0	0	6	0	3	4

Kr	10	0	4	0	6	0	0	0
Rb	227	164	150	53	47	0	13	24
Sr	89	45	74	23	0	7	6	10
Y	0	0	33	7	0	7	2	0
Zr	60	0	215	100	66	16	29	33
Nb	0	0	10	0	0	0	0	0
Mo	0	0	16	0	0	0	7	0
Total	1000180	999400	999182	999781	1000188	999929	1000048	1000138

Table A4: *ICP-MS and ICP-OES data: mass percentage of oxides (oxides wt.%) for major elements and mass concentration (C_M) of trace elements (in ppm) in bulk samples 00AU37b (hydrothermal vein), 00AU39 (close to hydrothermal vein) and 00AU40 (far from hydrothermal vein).*

Major elements (oxides wt.%)	00AU37b	00AU39	00AU40
SiO_2	99.61	94.54	91.79
TiO_2	<L.D.[2]	0.19	0.27
Al_2O_3	0.26	3.62	4.81
Fe_2O_3	0.05	0.05	0.49
MnO	<L.D.	<L.D.	0.0034
MgO	<L.D.	<L.D.	0.08
CaO	<L.D.	<L.D.	<L.D.
K_2O	<L.D.	0.96	1.32
Na_2O	<L.D.	0.08	0.07
P_2O_5	<L.D.	<L.D.	<L.D.
F.L.[3]	0.15	0.74	0.59
Total	100.07	100.18	99.42
Trace elements C_M (ppm)	**00AU37b**	**00AU39**	**00AU40**
As	<L.D.	1.65	1.64
Ba	19.00	36.97	69.14
Be	<L.D.	0.17	<L.D.
Bi	<L.D.	<L.D.	<L.D.

[2]L.D. = lower limit of detection.
[3]F.L. = fire loss ignition.

Cd	<L.D.	<L.D.	<L.D.
Co	0.33	0.42	2.07
Cr	18.90	27.56	379.72
Cs	0.10	0.53	0.72
Cu	5.40	5.44	39.20
Ga	0.42	5.07	6.50
Ge	1.24	5.20	1.71
Hf	0.08	1.52	1.30
In	<L.D.	<L.D.	<L.D.
Mo	<L.D.	<L.D.	19.45
Nb	0.13	3.54	2.75
Ni	6.70	5.77	15.81
Pb	1.44	3.82	4.70
Rb	1.50	17.45	22.73
Sb	1.64	3.12	2.22
Sc	<L.D.	4.40	4.34
Sn	<L.D.	0.91	1.99
Sr	<L.D.	12.62	11.60
Ta	0.02	0.35	0.26
Th	0.13	2.19	1.81
U	0.06	0.49	0.50
V	3.10	17.41	53.05
W	<L.D.	<L.D.	8.15

Y	0.55	9.25	7.28
Zn	<L.D.	<L.D.	19.28
Zr	4.29	54.57	48.72
La	0.34	9.86	5.92
Ce	0.54	19.96	12.58
Pr	0.08	2.55	1.60
Nd	0.33	9.77	6.51
Sm	0.08	2.08	1.52
Eu	0.03	0.59	0.47
Gd	0.08	1.71	1.33
Tb	0.02	0.27	0.22
Dy	0.10	1.69	1.34
Ho	0.02	0.36	0.28
Er	0.06	0.99	0.78
Tm	0.01	0.16	0.11
Yb	0.06	1.05	0.76
Lu	0.01	0.16	0.11

Table A5: *ICP-MS and ICP-OES results and comparison with elemental abundances in the Earth's crust: mass percentage of oxides (oxides wt.%) for major elements, and mass concentration (C_M) of major and trace elements (in %) in bulk samples 00AU37b (hydrothermal vein), 00AU39 (close to hydrothermal vein) and 00AU40 (far from hydrothermal vein), compared with the mass concentration (C_M) of major and trace elements (in %) in the Earth's crust.*

	00AU37b		00AU39		00AU40		Earth's crust
Element	*oxides wt.%*	*C_M (%)*	*oxides wt.%*	*C_M (%)*	*oxides wt.%*	*C_M (%)*	*C_M (%)*
Si	99.61	46.56424	94.54	44.19419	91.79	42.90866	27.00000
Al	0.26	0.13760	3.62	1.91580	4.81	2.54558	8.10000
Fe	0.05	0.03497	0.05	0.03497	0.49	0.34272	6.30000
Mn	<L.D.[4]	<L.D.	<L.D.	<L.D.	0.0034	0.00263	0.11000
Mg	<L.D.	<L.D.	<L.D.	<L.D.	0.08	0.04825	2.90000
Ca	<L.D.	<L.D.	<L.D.	<L.D.	<L.D.	<L.D.	5.00000
Na	<L.D.	<L.D.	0.08	0.05935	0.07	0.05193	2.30000
K	<L.D.	<L.D.	0.96	0.79694	1.32	1.09580	1.50000
Ti	<L.D.	<L.D.	0.19	0.11389	0.27	0.16184	0.66000
Be		<L.D.		0.00002		<L.D.	0.00019
Sc		<L.D.		0.00044		0.00043	0.00260
V		0.00031		0.00174		0.00530	0.01900
Cr		0.00189		0.00276		0.03797	0.01400
Co		0.00003		0.00004		0.00021	0.00030
Ni		0.00067		0.00058		0.00158	0.00090
Cu		0.00054		0.00054		0.00392	0.00680

[4]L.D. = lower limit of detection.

Zn		<L.D.		<L.D.		0.00193	0.00780
Ga		0.00004		0.00051		0.00065	0.00190
As		<L.D.		0.00016		0.00016	0.00021
Rb		0.00015		0.00175		0.00227	0.00060
Sr		<L.D.		0.00126		0.00116	0.03600
Y		0.00006		0.00093		0.00073	0.00290
Zr		0.00043		0.00546		0.00487	0.01300
Nb		0.00001		0.00035		0.00027	0.00170
Mo		<L.D.		<L.D.		0.00194	0.00011
Cd		<L.D.		<L.D.		<L.D.	0.00002
In		<L.D.		<L.D.		<L.D.	0.00002
Sn		<L.D.		0.00009		0.00020	0.00022
Sb		0.00016		0.00031		0.00022	0.00002
Ba		0.00190		0.00370		0.00691	0.00019
Cs		0.00001		0.00005		0.00007	0.03400
Hf		0.00001		0.00015		0.00013	0.00033
Ta		0.00000		0.00004		0.00003	0.00017
W		<L.D.		<L.D.		0.00082	0.00011
Pb		0.00014		0.00038		0.00047	0.00100
Th		0.00001		0.00022		0.00018	0.00060
U		0.00001		0.00005		0.00005	0.00018
Total	99.92	46.74319	99.44	47.13666	98.83	47.22990	54.01486

Table A6: *Results of additional chemical analyses (by fire loss ignition): mass percentage of oxides (oxides wt.%) of total CO_2, FeO, total S and organic C in bulk samples 00AU37b (hydrothermal vein) and 00AU39 (close to hydrothermal vein).*

Oxides wt.%	00AU37b	00AU39
Total CO_2	X	X
FeO	<0.5	<0.5
Total S	0.01	<0.01
Organic C	0.04	0.03

Table A7: *LA-ICP-MS data: mass percentage of oxides (oxides wt.%) for major elements and mass concentration (C_M) of trace elements (in ppm) in areas of interest in slab samples 00AU39-1 from (a) to (f) and 00AU39-2 from (a) to (h).*

	00AU39-1							00AU39-2							
Major elements (oxides wt.%)	*a*	*b*	*c*	*d*	*e*	*f*	*Major elements (oxides wt.%)*	*a*	*b*	*c*	*d*	*e*	*f*	*g*	*h*
SiO_2	83.6438	95.9659	91.0023	95.2435	87.1946	51.8177	SiO_2	96.3132	93.8094	96.2121	90.1763	77.1395	54.9431	91.2478	99.4034
TiO_2	0.6792	0.1058	0.0317	0.0578	0.7168	0.1087	TiO_2	0.0896	0.5496	0.0849	0.8787	0.4493	0.0379	0.7256	0.0023
Al_2O_3	11.6638	2.8265	6.6711	3.4226	9.0319	36.7858	Al_2O_3	2.5395	4.0899	2.6722	6.5948	17.1105	34.7982	5.8281	0.2405
Fe_2O_3	0.0513	0.0258	0.0193	0.0259	0.0338	0.2817	Fe_2O_3	0.0108	0.0231	0.0223	0.0301	0.0492	0.0544	0.0230	0.0112
MnO	0.0006	0.0004	0.0003	0.0004	0.0004	0.0030	MnO	0.0002	0.0003	0.0003	0.0004	0.0009	0.0016	0.0004	0.0003
MgO	0.0999	0.0327	0.0447	0.0387	0.0828	0.3899	MgO	0.0240	0.0374	0.0330	0.0651	0.1665	0.3354	0.0527	0.0045
CaO	0.1698	0.1391	0.1157	0.1583	0.1260	0.1261	CaO	0.1569	0.1575	0.1430	0.1784	0.1375	0.1525	0.1700	0.1176
K_2O	3.3695	0.7677	1.9187	0.9095	2.5991	9.7615	K_2O	0.7166	1.1700	0.7248	1.8670	4.5433	8.9291	1.7250	0.0786
Na_2O	0.1833	0.0852	0.1278	0.0958	0.1455	0.5432	Na_2O	0.0459	0.0703	0.0738	0.1077	0.3064	0.6269	0.1046	0.0846
P_2O_5	0.0494	0.0054	0.0121	0.0038	0.0084	0.0119	P_2O_5	0.0251	0.0276	0.0033	0.0361	0.0113	0.0030	0.0329	0.0022
Total	**99.91**	**99.95**	**99.94**	**99.96**	**99.94**	**99.83**	Total	**99.92**	**99.94**	**99.97**	**99.93**	**99.91**	**99.88**	**99.91**	**99.95**
Trace elements C_M (ppm)	*a*	*b*	*c*	*d*	*e*	*f*	*Trace elements C_M (ppm)*	*a*	*b*	*c*	*d*	*e*	*f*	*g*	*h*
V	49.61	17.21	32.00	16.02	36.70	245.60	V	9.42	17.81	14.48	27.53	93.60	195.56	27.62	1.07
Cr	41.00	19.45	24.81	17.87	33.67	319.05	Cr	11.95	21.41	18.36	27.75	112.79	235.47	32.71	4.66
Mn	4.83	2.71	2.17	3.05	2.75	22.96	Mn	1.90	2.66	2.27	2.83	7.31	12.12	3.31	2.00
Co	0.16	1.77	0.07	2.19	1.22	0.92	Co	0.30	0.45	0.80	0.23	0.44	0.59	0.60	0.46
Ni	0.55	4.47	0.23	7.00	0.34	10.34	Ni	0.52	1.36	3.71	0.68	1.76	2.93	1.34	0.85
Zn	5.82	13.22	2.24	86.55	4.34	10.60	Zn	6.53	13.06	11.78	13.66	9.04	6.71	13.61	7.28

Cu	7.88	52.17	14.15	17.35	17.36	9.38	Cu	10.76	17.03	21.59	23.70	20.37	16.56	28.64	57.84
Ga	15.21	5.05	7.06	5.58	9.00	50.52	Ga	8.46	7.52	4.18	8.42	18.16	36.92	8.74	1.90
Ge	6.05	6.42	9.62	7.00	6.23	5.45	Ge	9.04	7.11	5.32	6.19	4.50	3.15	6.99	0.81
As	3.12	5.46	2.13	8.69	2.14	0.29	As	4.71	3.83	3.68	2.08	2.15	0.52	4.49	1.02
Rb	52.34	14.88	31.61	17.59	38.45	185.25	Rb	11.88	17.83	14.20	28.13	71.28	138.21	26.46	1.84
Sr	55.14	8.59	16.95	11.54	33.46	43.44	Sr	19.15	20.43	7.78	46.01	35.18	53.59	41.26	0.97
Y	16.27	5.79	15.80	5.03	9.89	1.22	Y	14.51	7.59	4.35	13.01	10.61	2.33	17.65	0.20
Zr	100.81	39.23	102.65	36.60	123.52	11.49	Zr	72.89	58.69	31.50	95.28	79.23	12.67	131.57	4.65
Nb	16.70	2.49	1.30	1.44	18.33	1.41	Nb	2.53	12.55	1.55	20.29	8.85	0.20	17.81	0.23
Mo	0.06	0.12	0.03	0.36	0.04	0.04	Mo	0.04	0.29	0.04	0.14	0.24	0.01	0.15	0.15
Sb	5.00	4.02	2.14	5.17	5.24	1.60	Sb	4.54	4.35	4.02	4.40	4.54	1.79	9.18	6.10
Cs	1.71	0.55	0.93	0.54	1.15	5.05	Cs	0.41	0.94	0.39	0.84	1.47	2.50	0.85	0.30
Ba	89.86	59.06	66.92	72.07	54.85	360.40	Ba	34.73	41.92	55.80	59.34	86.30	129.20	79.86	15.21
La	44.14	3.15	12.61	1.89	3.81	0.31	La	57.31	42.90	1.56	17.30	7.01	1.60	33.96	0.08
Ce	93.65	7.23	29.97	3.43	6.87	0.66	Ce	132.52	90.36	2.88	38.47	15.44	4.01	66.22	0.32
Pr	9.92	0.74	3.46	0.36	0.78	0.07	Pr	14.51	10.16	0.29	4.29	1.66	0.74	7.19	0.07
Nd	37.47	2.82	14.28	1.35	2.93	0.27	Nd	57.63	40.56	1.05	17.52	6.48	1.89	27.22	0.07
Sm	7.30	0.67	3.06	0.38	0.71	0.09	Sm	11.66	8.40	0.26	3.95	1.43	0.38	5.21	0.10
Eu	2.04	0.23	0.93	0.15	0.37	0.21	Eu	2.98	2.34	0.11	1.17	0.51	0.20	1.36	0.05
Gd	5.69	0.72	2.57	0.47	0.92	0.11	Gd	8.23	6.05	0.37	3.50	1.47	0.36	4.57	0.03
Tb	0.73	0.15	0.44	0.12	0.22	0.03	Tb	0.91	0.54	0.09	0.52	0.28	0.06	0.70	0.02
Dy	3.55	1.02	2.81	0.86	1.65	0.21	Dy	3.86	2.03	0.68	2.86	1.91	0.39	3.88	0.05
Ho	0.61	0.24	0.62	0.21	0.40	0.05	Ho	0.65	0.33	0.16	0.53	0.42	0.08	0.75	0.03

Er	1.56	0.71	1.93	0.64	1.26	0.16	Er	1.69	0.92	0.51	1.42	1.27	0.23	2.03	0.04
Tm	0.21	0.11	0.34	0.11	0.21	0.03	Tm	0.25	0.12	0.08	0.21	0.20	0.03	0.29	0.03
Yb	1.42	0.76	2.25	0.74	1.52	0.20	Yb	1.67	0.86	0.59	1.39	1.40	0.21	1.98	0.05
Lu	0.20	0.12	0.35	0.11	0.22	0.03	Lu	0.25	0.13	0.10	0.21	0.21	0.03	0.29	0.03
Hf	2.28	1.44	2.90	1.37	3.12	0.86	Hf	2.18	1.54	0.94	2.80	2.42	1.47	3.39	0.11
Ta	1.19	0.21	0.21	0.10	1.29	0.09	Ta	0.41	0.96	0.13	1.74	0.74	0.02	1.63	0.04
Pb	21.89	89.45	27.09	16.46	49.57	3.56	Pb	116.53	58.00	27.54	35.33	39.94	2.13	105.91	384.95
Th	8.69	1.91	4.17	1.12	1.98	0.38	Th	11.37	5.90	0.85	7.42	3.06	0.39	10.15	0.07
U	1.08	0.58	1.50	0.52	0.68	0.16	U	2.11	0.85	0.37	1.27	0.71	0.11	1.43	0.42

Table A8: *LA-ICP-MS data: mass percentage of oxides (oxides wt.%) for major elements and mass concentration (C_M) of trace elements (in ppm) in areas of interest in slab sample 00AU40-1 from (a) to (k).*

00AU40-1

Major elements (oxides wt.%)	*a*	*b*	*c*	*d*	*e*	*f*	*g*	*h*	*i*	*j*	*k*
SiO_2	91.0274	85.7245	98.8226	99.6848	90.5204	88.3003	89.7008	92.7174	88.3948	92.3902	88.6129
TiO_2	0.2941	0.2585	0.0095	0.0039	0.7553	1.3650	0.0319	0.1763	0.4425	0.1876	0.4552
Al_2O_3	6.2867	10.1914	0.6517	0.0337	6.2836	7.5450	7.3735	5.1109	8.1381	5.3976	8.0809
Fe_2O_3	0.0435	0.0876	0.0289	0.0145	0.0870	0.0786	0.1056	0.0592	0.0482	0.0520	0.0421
MnO	0.0008	0.0013	0.0005	0.0004	0.0009	0.0012	0.0019	0.0006	0.0005	0.0004	0.0005
MgO	0.0570	0.1396	0.0127	0.0071	0.0861	0.1199	0.1666	0.0683	0.1148	0.0681	0.0773
CaO	0.1742	0.1998	0.1433	0.1521	0.1582	0.1854	0.1911	0.1357	0.1259	0.0980	0.1110
K_2O	1.9548	3.1259	0.2629	0.0436	1.8874	2.1962	2.2577	1.5722	2.5048	1.6582	2.4159
Na_2O	0.0999	0.1435	0.0286	0.0229	0.1003	0.1112	0.1070	0.0952	0.1079	0.0899	0.1166
P_2O_5	0.0154	0.0457	0.0139	0.0112	0.0352	0.0198	0.0178	0.0187	0.0337	0.0084	0.0238
Total	**99.95**	**99.92**	**99.97**	**99.97**	**99.91**	**99.92**	**99.95**	**99.95**	**99.91**	**99.95**	**99.94**
Trace elements C_M (ppm)	*a*	*b*	*c*	*d*	*e*	*f*	*g*	*h*	*i*	*j*	*k*
V	43.67	75.88	2.64	0.24	55.45	93.19	35.03	48.86	67.75	47.25	67.92
Cr	13.64	18.15	7.16	4.14	13.65	22.99	10.53	16.15	12.03	10.51	10.68
Mn	6.35	9.97	4.11	3.23	7.13	9.65	15.00	5.00	3.54	3.44	3.55
Co	<L.D.[5]	0.64	<L.D.	<L.D.	1.66	0.02	<L.D.	<L.D.	0.70	0.22	0.92
Ni	4.17	4.27	4.15	2.89	8.48	3.81	7.32	3.93	3.22	3.30	1.21

[5]L.D. = lower limit of detection.

Zn	31.61	48.76	33.21	24.87	27.43	41.20	56.09	32.87	10.79	17.80	8.40
Cu	17.70	44.74	24.29	19.40	12.68	40.15	30.59	16.46	41.24	12.30	11.31
Ga	5.76	14.42	1.72	0.20	8.91	9.85	10.26	6.32	10.45	6.67	8.21
Ge	0.51	<L.D.	<L.D.	13.53	0.41	0.78	<L.D.	<L.D.	0.52	0.11	0.47
As	0.76	1.92	0.93	2.99	1.93	2.08	0.57	1.63	2.69	2.71	2.44
Rb	29.82	52.69	4.69	0.64	33.67	41.04	43.25	27.80	36.68	30.15	39.54
Sr	11.22	18.91	2.37	1.13	16.38	15.21	11.23	9.11	22.78	7.97	13.69
Y	3.83	6.37	1.87	0.11	20.12	5.99	0.09	8.07	13.77	5.58	9.31
Zr	41.27	37.94	26.05	93.90	142.53	116.24	1.63	53.31	120.37	40.58	69.28
Nb	3.80	3.03	0.28	0.06	10.22	17.84	0.27	1.90	5.84	2.11	5.22
Mo	0.05	0.11	0.07	0.01	0.22	0.18	0.05	0.44	0.41	0.06	0.41
Sb	1.87	2.10	6.44	1.47	3.40	6.79	2.40	3.76	7.23	3.50	2.08
Cs	0.78	1.51	0.18	<L.D.	1.02	1.19	1.04	0.62	1.33	0.89	1.03
Ba	71.58	111.97	27.17	10.00	137.80	105.88	99.27	64.10	69.80	58.72	67.94
La	2.31	35.54	0.38	0.55	20.25	3.70	2.19	3.83	19.36	3.46	9.38
Ce	5.05	81.26	1.34	2.01	50.62	9.47	1.21	7.39	43.80	7.85	19.23
Pr	0.53	9.16	0.12	0.18	5.30	0.96	0.33	0.80	4.68	0.87	2.04
Nd	2.42	36.96	0.46	0.68	22.49	4.30	0.82	3.19	18.95	3.19	7.94
Sm	0.51	7.84	0.18	0.13	4.96	1.23	0.09	0.76	4.15	0.76	1.77
Eu	0.21	1.58	0.07	0.03	1.49	0.45	0.04	0.27	1.24	0.25	0.60
Gd	0.37	4.11	0.09	<L.D.	4.25	1.03	<L.D.	0.73	3.48	0.63	1.54
Tb	0.11	0.42	0.05	0.02	0.69	0.20	0.01	0.18	0.56	0.14	0.29
Dy	0.75	1.65	0.37	0.03	4.34	1.23	0.02	1.21	2.86	0.91	1.78

Ho	0.17	0.23	0.08	<L.D.	0.89	0.25	<L.D.	0.27	0.55	0.20	0.37
Er	0.48	0.54	0.25	0.01	2.50	0.66	0.01	0.80	1.43	0.54	1.04
Tm	0.07	0.07	0.03	<L.D.	0.36	0.10	<L.D.	0.12	0.21	0.09	0.15
Yb	0.49	0.41	0.22	0.02	2.41	0.69	0.04	0.77	1.30	0.53	0.97
Lu	0.07	0.06	0.04	<L.D.	0.34	0.09	0.01	0.11	0.19	0.08	0.15
Hf	1.69	0.92	0.31	2.10	3.98	2.51	0.08	1.75	2.81	1.27	2.27
Ta	0.33	0.21	0.02	<L.D.	0.81	1.23	0.03	0.19	0.48	0.17	0.40
Pb	66.68	21.32	63.37	17.61	48.18	33.66	62.80	31.72	171.32	126.84	133.64
Th	2.25	4.36	0.46	0.10	7.60	0.49	0.06	2.03	6.22	1.88	4.45
U	0.45	0.43	0.30	0.08	2.00	1.37	0.07	0.68	1.25	0.52	0.90

II. Appendix B: Compositional images and spectra from EDX data

This appendix includes the color-coded composition images and the spectra corresponding to the EDX analyses mentioned in the results for SEM (**Figs. B1–6**) and STEM (**Figs. B7–11**) analyses.

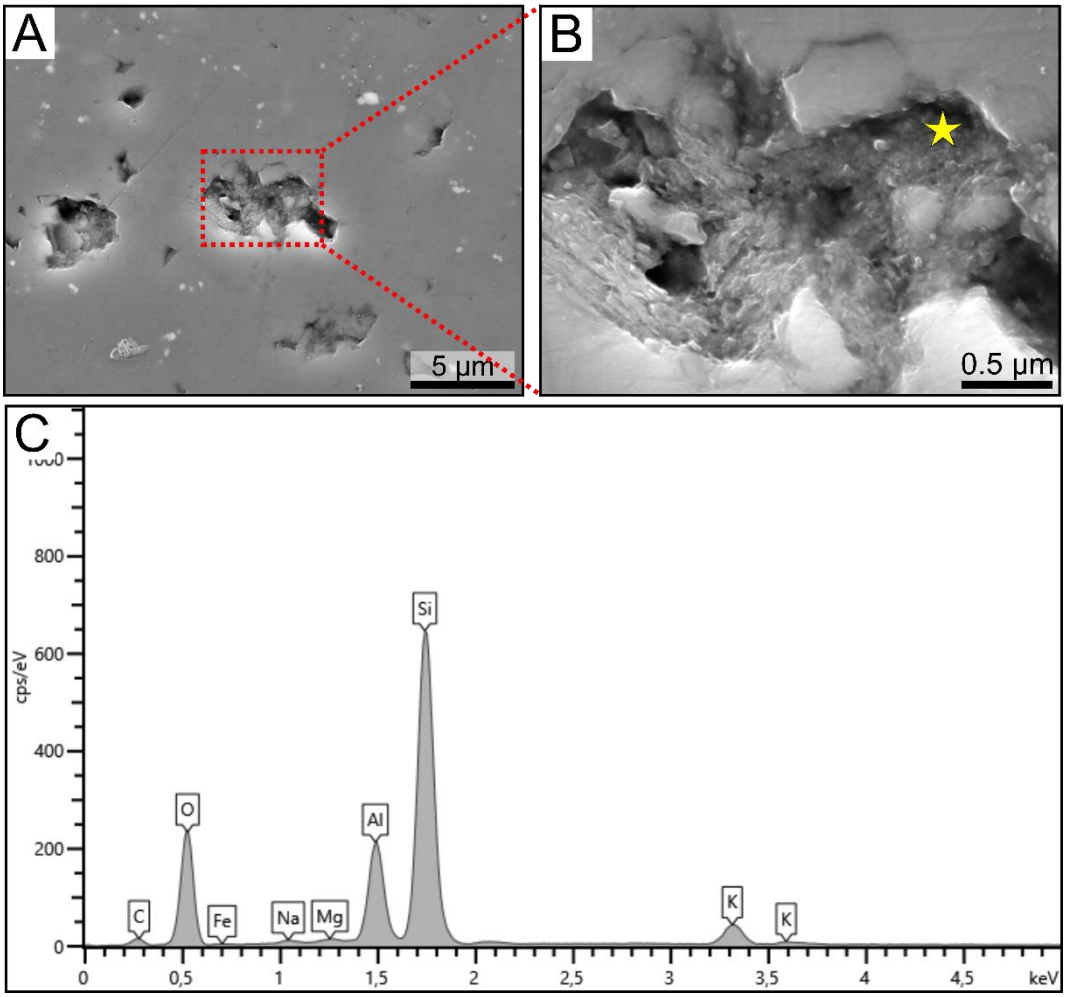

Figure B1: *EDX-SEM results of the analysis of a pumice fragment in sample 00AU39. (**A**) SEM image of a cavity containing carbonaceous matter in the pumice fragment, with red dotted box indicating the area corresponding to the image displayed in (**B**). (**B**) SEM image of finely disseminated particles of carbonaceous matter intermixed with sheet-like hydromuscovite, with the yellow star corresponding to the location where the EDX measurement was performed and whose spectrum is shown in (**C**). (**C**) EDX spectrum associated to the punctual analysis performed in (**B**).*

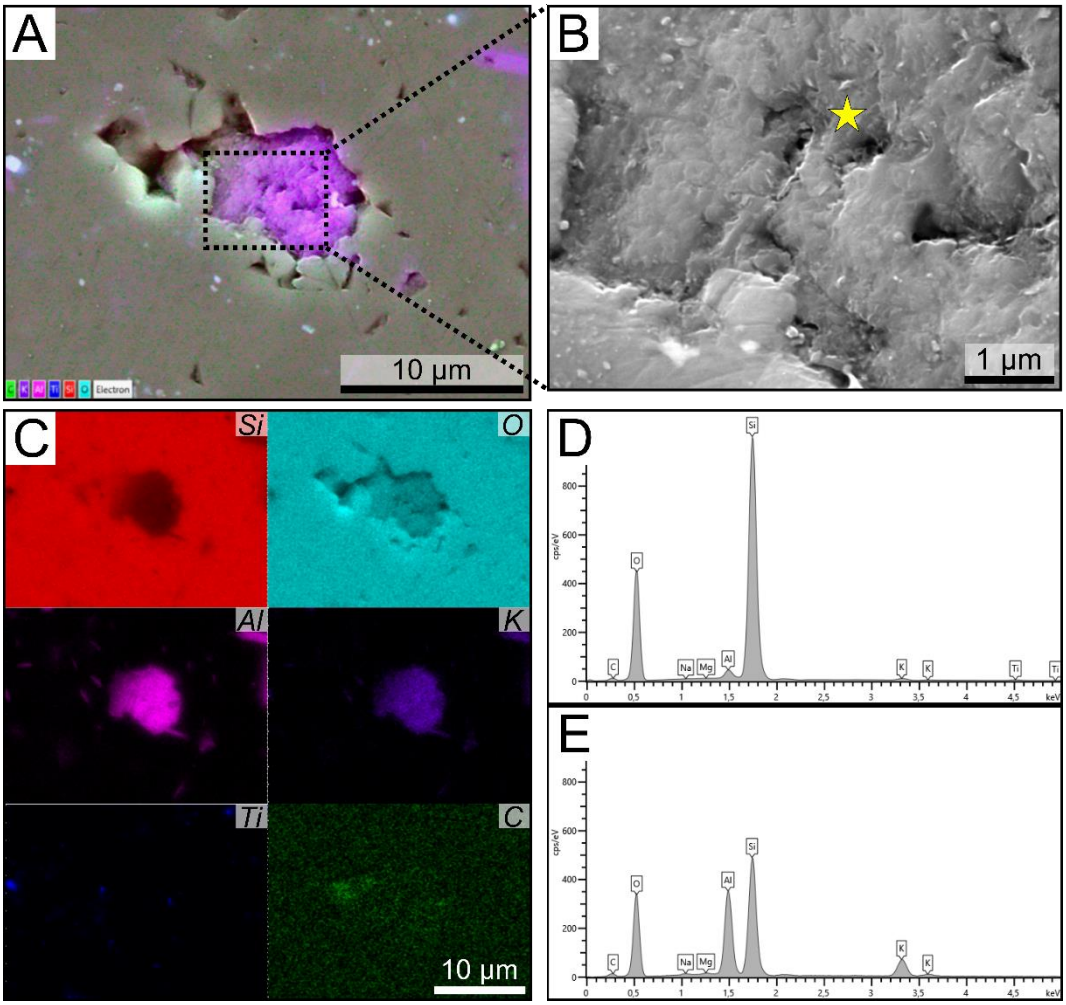

Figure B2: *EDX-SEM results of the analysis of a pumice fragment in sample 00AU39. (**A**) Color-coded composition image of a cavity containing carbonaceous matter in the pumice fragment, with black dotted box indicating the area corresponding to the image displayed in (**B**), and the global spectrum associated to this area is shown in (**D**). (**B**) SEM image of finely disseminated particles of carbonaceous matter intermixed with rough-textured hydromuscovite, with the yellow star corresponding to the location where the EDX measurement was performed and whose spectrum is shown in (**E**). (**C**) Elemental maps corresponding to elemental enrichments in the global area. (**D**) EDX global spectrum of the area analyzed in (**A**). (**E**) EDX spectrum associated to the punctual analysis performed in (**B**).*

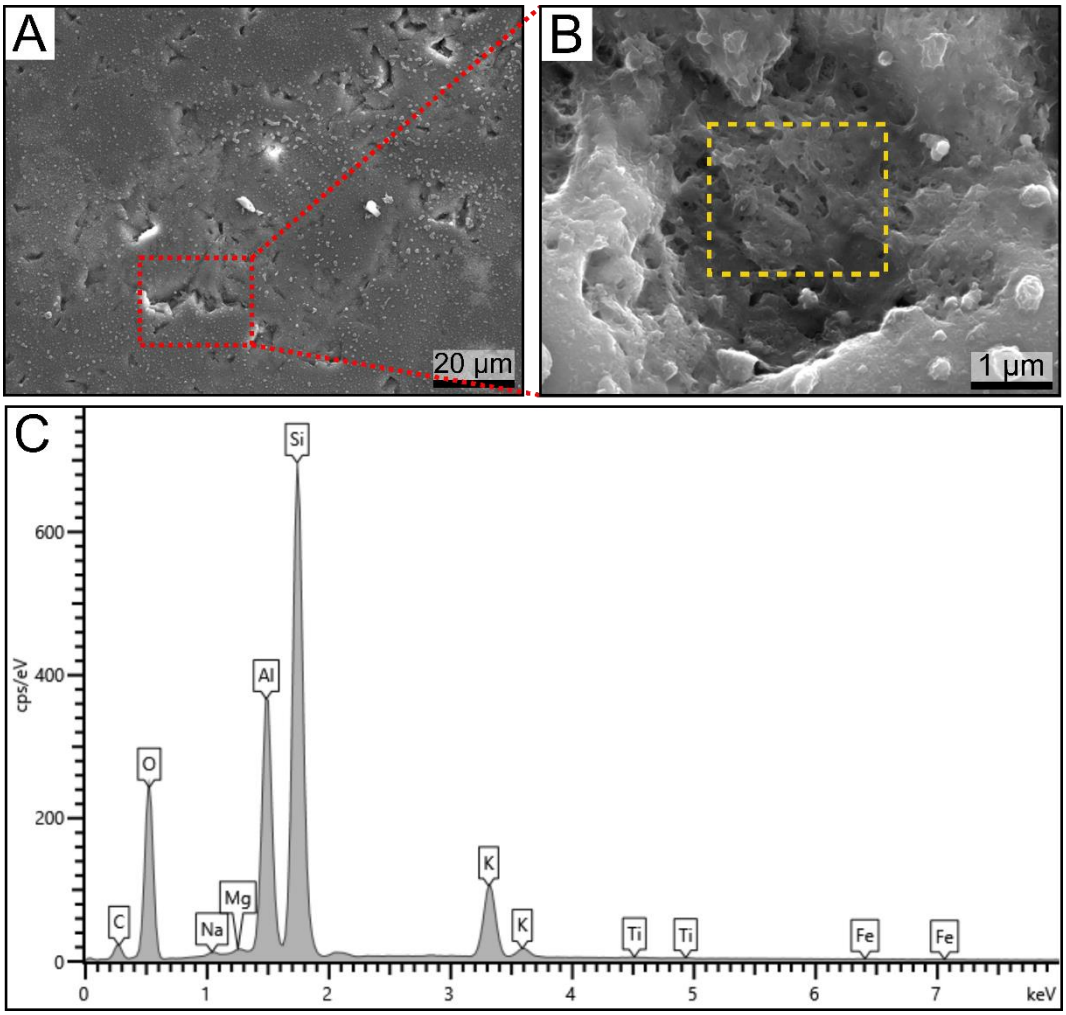

Figure B3: *EDX-SEM results of the analysis of a multiphase volcanic rock fragment in sample 00AU39. (**A**) SEM image of the surface of the multiphase volcanic rock fragment with a large crack crossing it, with red dotted box indicating the area corresponding to the image displayed in (**B**). (**B**) SEM image of Filmy carbonaceous matter with a lumpy texture associated to rough-textured hydromuscovite, with the yellow dashed box corresponding to the location where the EDX measurement was performed and whose spectrum is shown in (**C**). The white spherules visible in the lower right of the image are artifacts after samples immersion in glycerin for DUV fluorescence analyses. (**C**) EDX spectrum associated to the location analyzed in (**B**).*

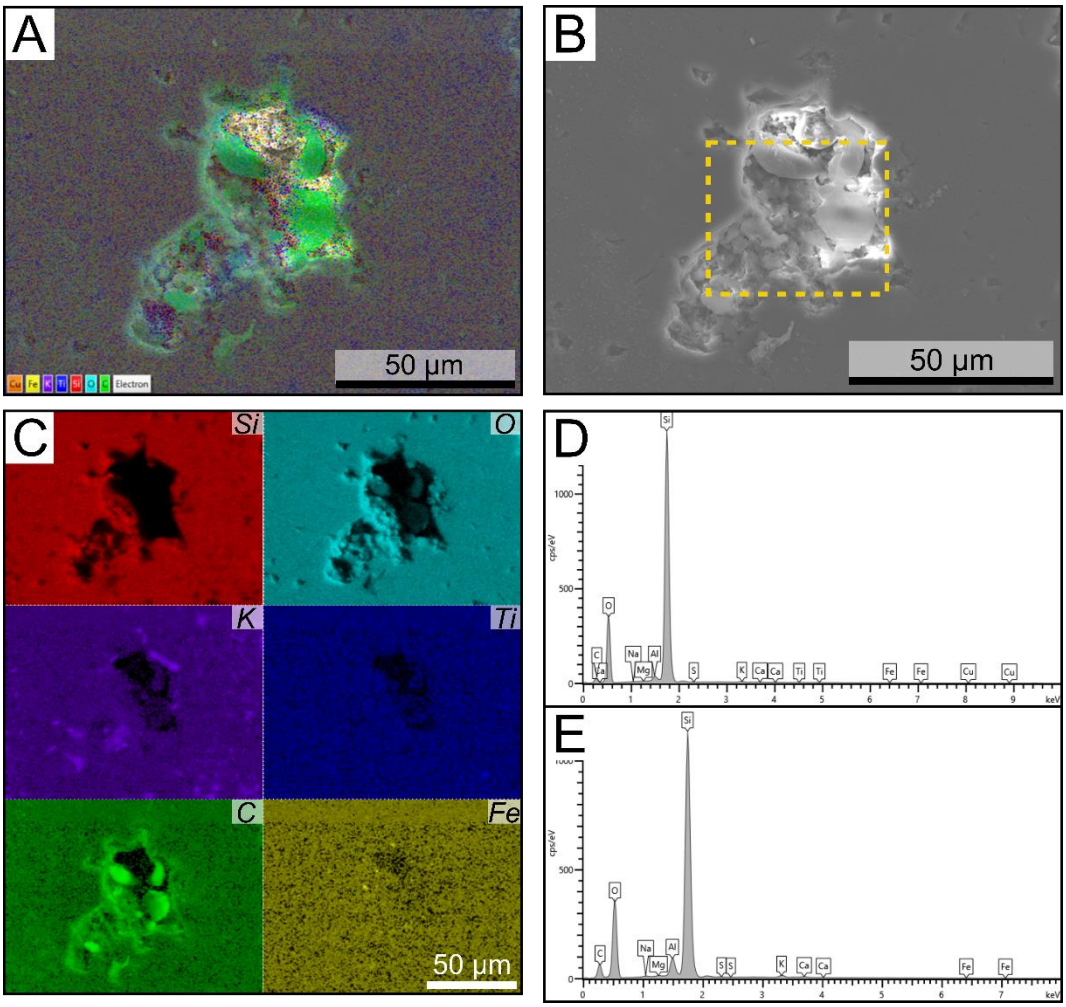

Figure B4: *EDX-SEM results of the analysis of the silica matrix in sample 00AU39. (**A**) Color-coded composition image of a cavity containing carbonaceous matter in the silica matrix, with the global spectrum associated to this area shown in (**D**). (**B**) SEM image of rounded to irregular carbonaceous structures with a smooth texture associated with rough-textured hydromuscovite, with the yellow dashed box corresponding to the location where the EDX measurement was performed and whose spectrum is shown in (**E**). (**C**) Elemental maps corresponding to elemental enrichments in the global area. (**D**) EDX global spectrum of the area analyzed in (**A**). (**E**) EDX spectrum associated to the location analyzed in (**B**).*

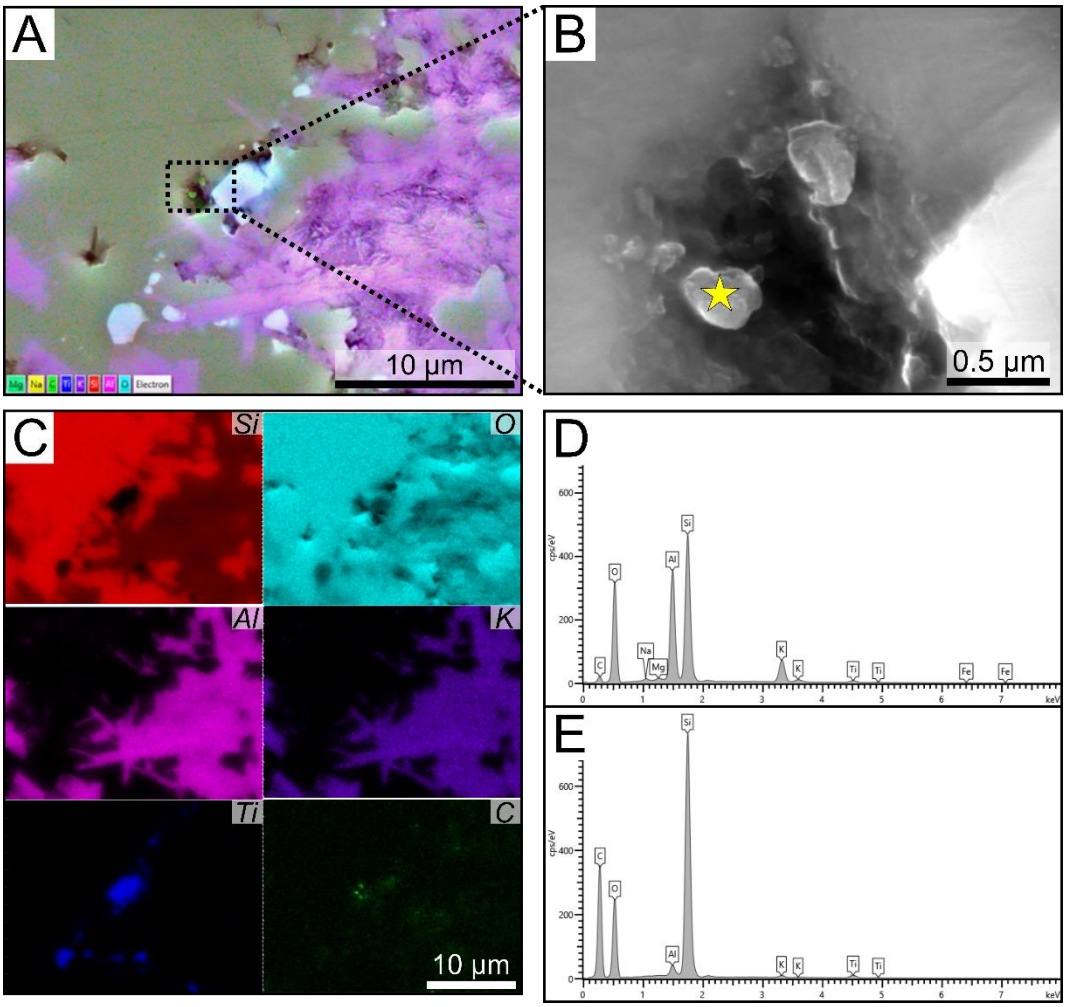

Figure B5: *EDX-SEM results of the analysis of an amphibole/pyroxene in sample 00AU39. (**A**) Color-coded composition image of the surface of the amphibole/pyroxene altered in sheet-like hydromuscovite mixed with carbonaceous matter and surrounding by edges composed of anatase, with black dotted box indicating the area corresponding to the image displayed in (**B**), and the global spectrum associated to this area is shown in (**D**). (**B**) SEM image of coccoidal structures of carbonaceous matter associated with microcrystals of anatase, with the yellow star corresponding to the location where the EDX measurement was performed and whose spectrum is shown in (**E**). (**C**) Elemental maps corresponding to elemental enrichments in the global area. (**D**) EDX global spectrum of the area analyzed in (**A**). (**E**) EDX spectrum associated to the punctual analysis performed in (**B**).*

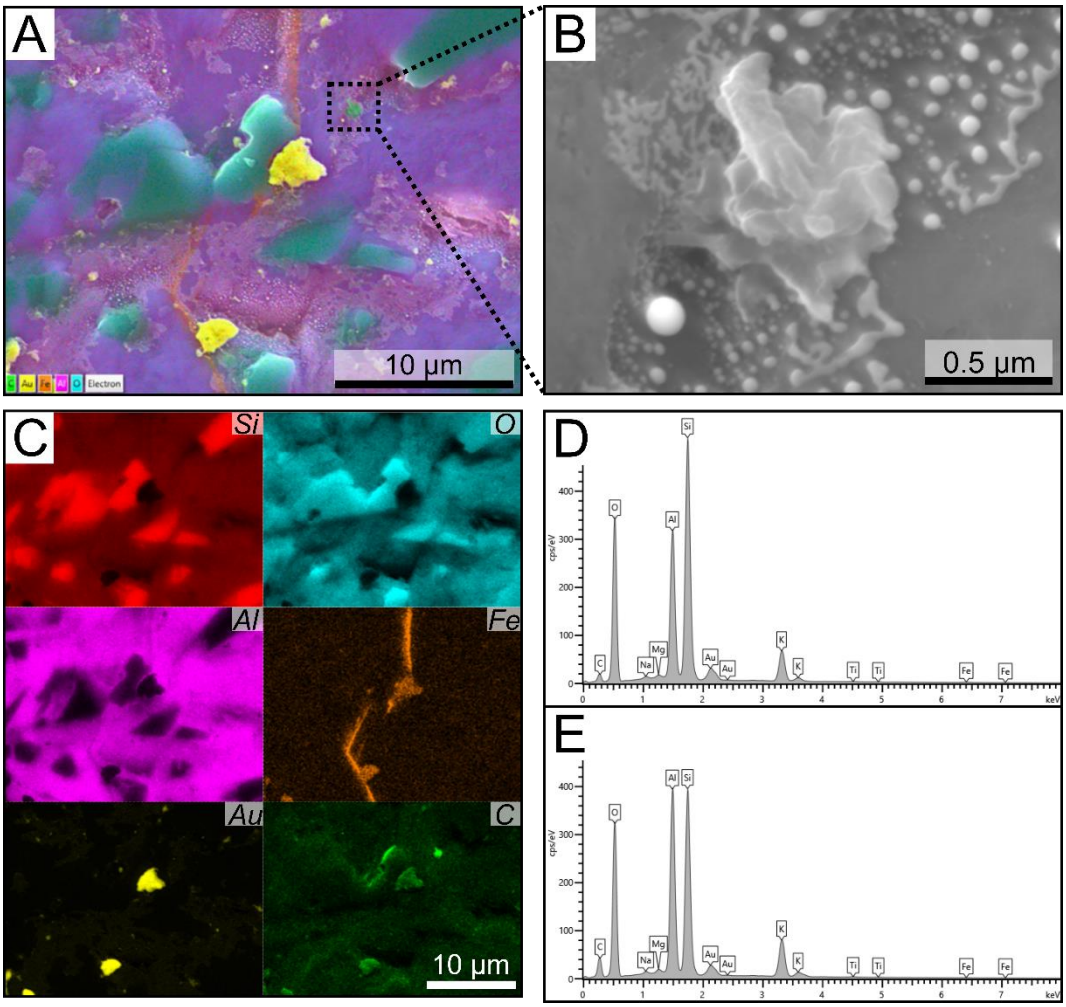

Figure B6: *EDX-SEM results of the analysis of a feldspar in sample 00AU40. (**A**) Color-coded composition image of a cavity containing carbonaceous matter in the feldspar, with black dotted box indicating the area corresponding to the image displayed in (**B**), and the global spectrum associated to this area is shown in (**D**). (**B**) SEM image of fibrous carbonaceous matter with a wrinkled texture, with the spectrum associated to this area shown in (**E**). The white particles visible on the images (**A**) and (**B**) are gold particles resulting from the coating process of the thin section. (**C**) Elemental maps corresponding to elemental enrichments in the global area. (**D**) EDX global spectrum of the area analyzed in (**A**). (**E**) EDX spectrum associated to the area analyzed in (**B**).*

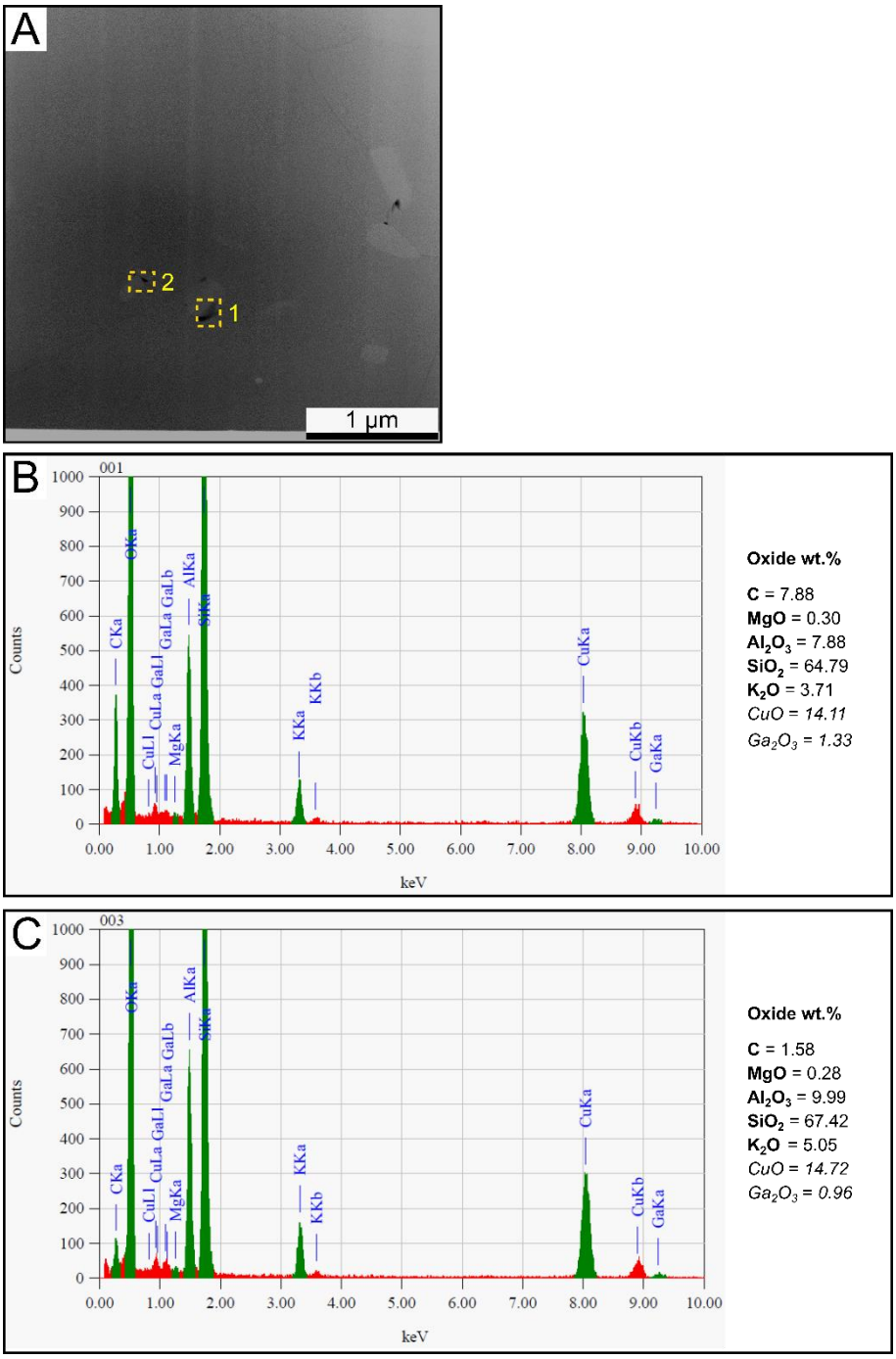

Figure B7: *EDX-STEM results of the analysis of the silica matrix in sample 00AU40. (**A**) STEM image of coatings of carbonaceous matter (dark color) around microcrystals of feldspar, with the yellow dashed boxes corresponding to the locations where the EDX measurements were performed and whose spectra are shown in (**B**) and (**C**). (**B**) EDX spectrum associated to the location 1. (**C**) EDX spectrum associated to the location 2. The mass percentage of each compound is given in oxide wt.% to the right of the spectra (the copper comes from the sample holder and the gallium from the laser beam used to make the FIB section).*

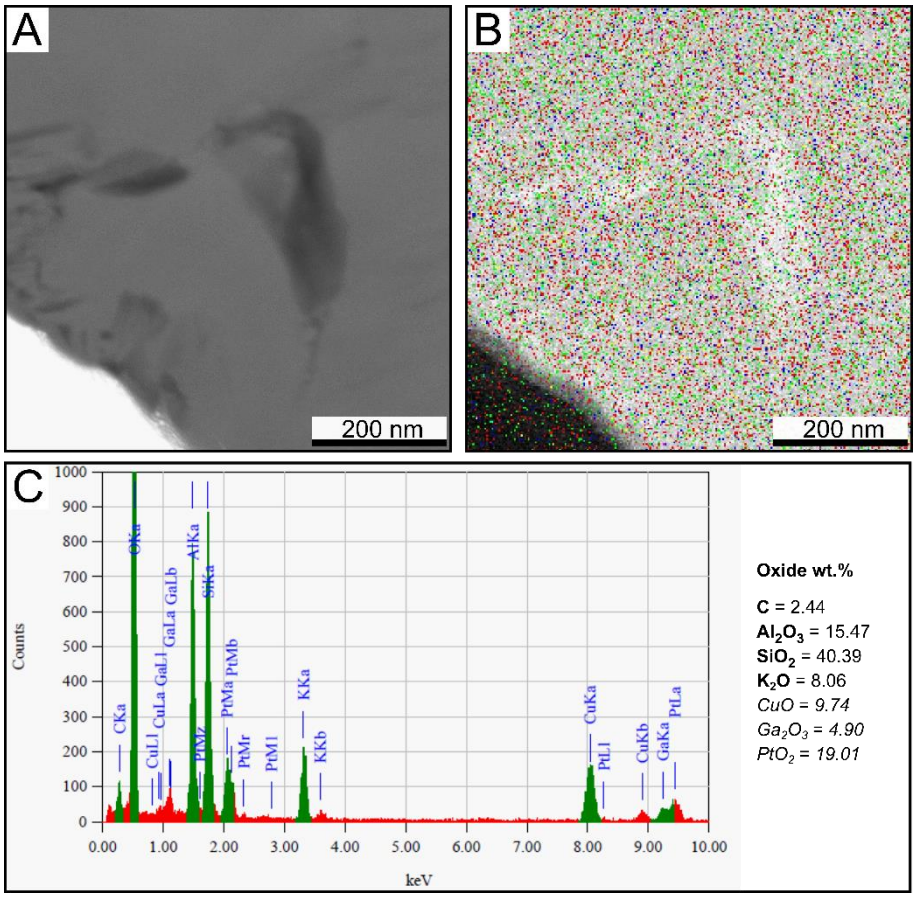

Figure B8: *EDX-STEM results of the analysis of an amphibole/pyroxene in sample 00AU39. (**A**) STEM image of an elongated structure of carbonaceous matter (dark color) in the interior of the protolith, with the global spectrum associated to this area shown in (**C**). (**B**) Color-coded composition image of the area analyzed in (**A**), with silicium in red, aluminum in green and potassium in blue (the carbonaceous matter constituting the elongated structure does not emerge on the image). (**C**) EDX global spectrum of the area analyzed in (**A**). The mass percentage of each compound is given in oxide wt.% to the right of the spectrum (the copper comes from the sample holder, the gallium from the laser beam used to make the FIB section and the platinum from the deposit used to make the FIB section).*

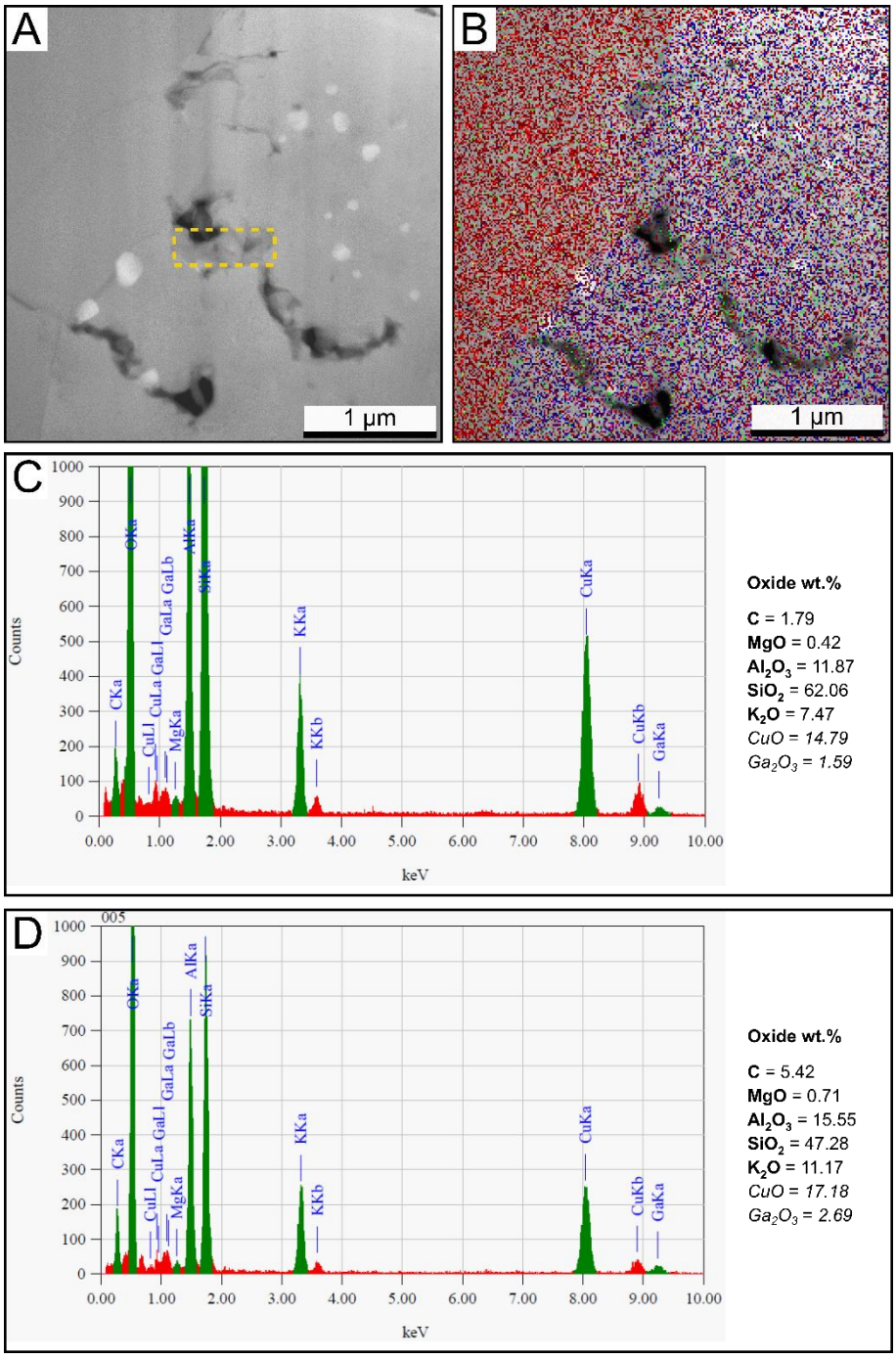

Figure B9: *EDX-STEM results of the analysis of the silica-dust gel matrix in sample 00AU40. (**A**) STEM image of elongated structures of carbonaceous matter (dark color) in a microcrystal of feldspar, with the yellow dashed box corresponding to the location where the EDX measurement was performed and whose spectra is shown in (**D**), and the global spectrum associated to this area is shown in (**C**). (**B**) Color-coded composition image of the area analyzed in (**A**), with the microcrystalline quartz enriched in silicium (red) and the microcrystal of feldspar enriched in aluminum (blue) where the elongated structures of carbonaceous matter (green) are embedded. (**C**) EDX global spectrum of the area analyzed in (**A**). (**D**) EDX spectrum associated to the location analyzed in (**A**). The mass percentage of each compound is given in oxide wt.% to the right of the spectra (the copper comes from the sample holder and the gallium from the laser beam used to make the FIB section).*

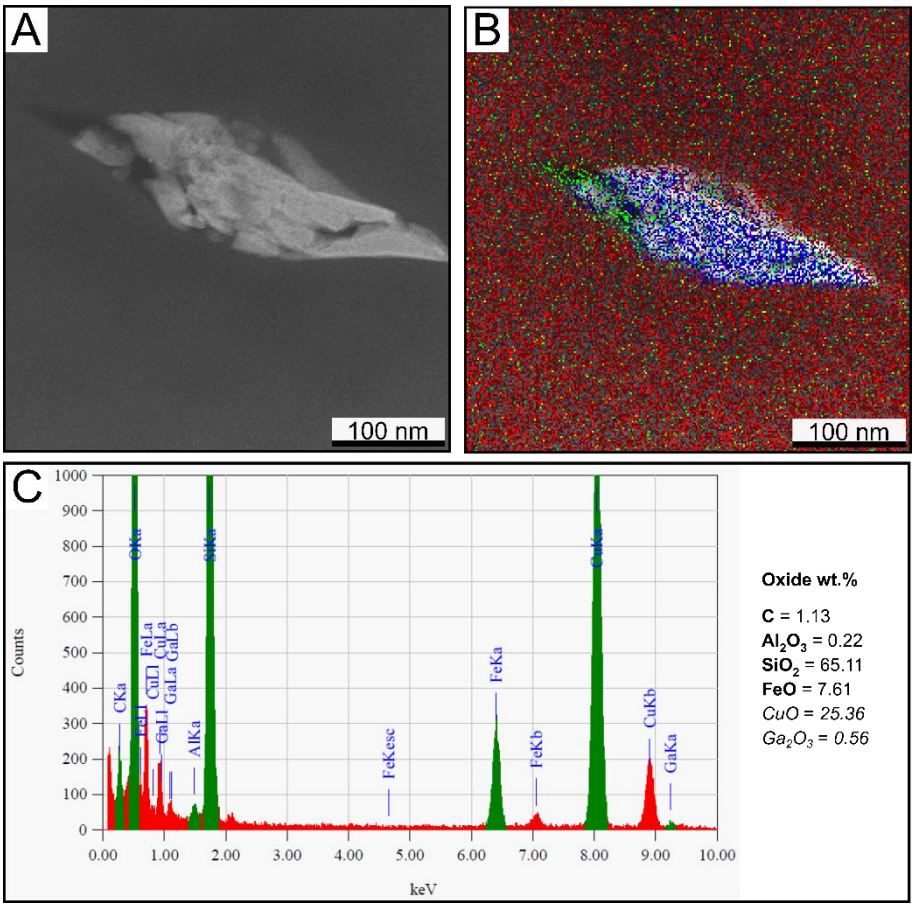

Figure B10: *EDX-STEM results of the analysis of the silica matrix in sample 00AU40. (**A**) STEM image of a lenticular structure of carbonaceous matter (dark color) mixed with heavy compounds (light color) at the edge of quartz polygons, with the global spectrum associated to this area shown in (**C**). (**B**) Color-coded composition image of the area analyzed in (**A**), with the microcrystalline quartz enriched in silicium (red) and the lenticular structure of carbonaceous matter (green) enriched in iron minerals (blue). (**C**) EDX global spectrum of the area analyzed in (**A**). The mass percentage of each compound is given in oxide wt.% to the right of the spectrum (the copper comes from the sample holder and the gallium from the laser beam used to make the FIB section).*

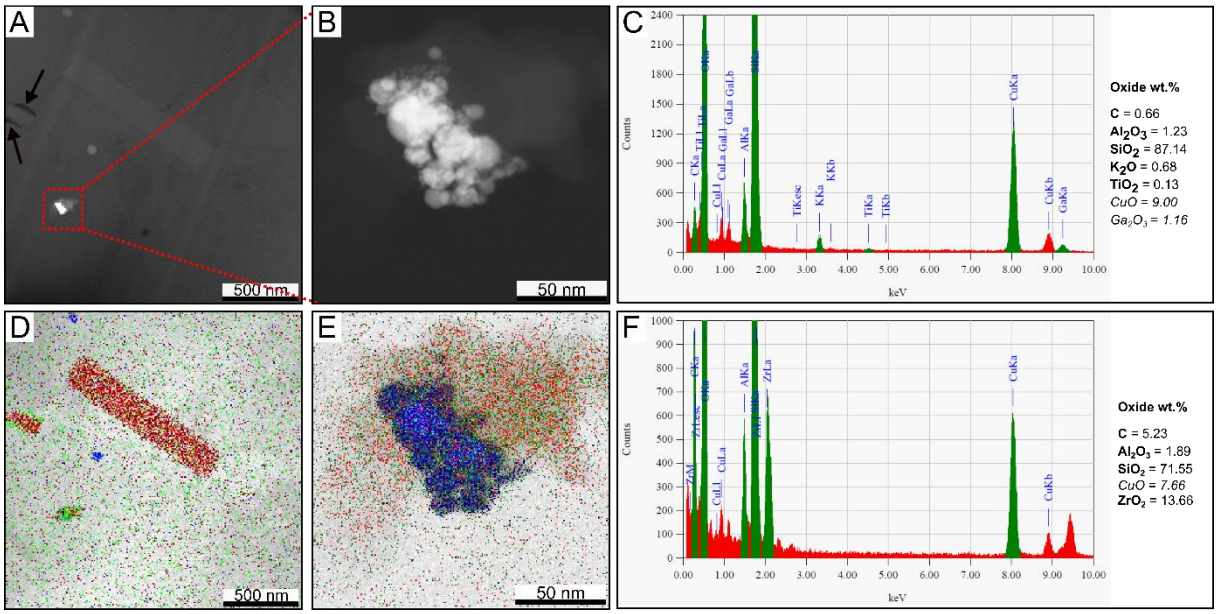

Figure B11: *EDX-STEM results of the analysis of a pumice fragment in sample 00AU40. (**A**) STEM image of heavy compounds (light color) and two rectangular microcrystals of feldspar (medium color), including one coated with carbonaceous matter (dark color) in the interior of the protolith, with red dotted box indicating the area corresponding to the image displayed in (**B**), and the global spectrum associated to this area is shown in (**E**). (**B**) STEM image of heavy spherical grains (light color) associated with a diffuse cloud (medium color). (**C**) EDX global spectrum of the area analyzed in (**A**). (**D**) Color-coded composition image of the area analyzed in (**A**), with feldspars enriched in aluminum (red), some tiny particles enriched in titanium (blue), and coating of the feldspar grain with carbonaceous matter (green). (**E**) Color-coded composition image of the area analyzed in (**B**), with nanocrystals of a heavy element (maybe zirconium, blue) associated with a diffuse cloud of carbonaceous matter (green) mixed with aluminum (red). (**F**) EDX spectrum associated to the area analyzed in (**B**). The mass percentage of each compound is given in oxide wt.% to the right of the spectra (the copper comes from the sample holder and the gallium from the laser beam used to prepare the FIB section).*

Laura CLODORÉ

À la recherche de traces de vie dans une roche analogue de Mars : le chert de Kitty's Gap

L'objectif de cette thèse est de caractériser la matière organique associée à de potentielles traces de vie fossiles dans des roches terrestres anciennes afin de maximiser la détection de microfossiles analogues à ceux que l'on pourrait trouver sur Mars et leurs biosignatures associées. Les sédiments volcaniques du chert de Kitty's Gap, âgé de 3,446 milliards d'années, contiennent des formes de vie primitive supposées considérées comme analogues de potentiels organismes primitifs martiens. Des techniques d'analyses complémentaires multi-échelles ont été utilisées pour documenter l'habitabilité du paléoenvironnement et évaluer la syngénicité et la biogénicité des traces de vie fossiles supposées. Des analyses sédimentologiques, pétrologiques, minéralogiques et géochimiques ont permis de reconstruire le paléoenvironnement de dépôt des sédiments du chert de Kitty's Gap en se basant sur des observations macroscopiques et optiques, ainsi que sur des analyses spectroscopiques (fluorescence à rayons X, Raman, ICP-MS…). Les résultats démontrent que les sédiments se sont déposés dans un bassin semi-fermé, influencé par les marées, les rivières et les fluides hydrothermaux, dont les conditions sont compatibles avec la colonisation et le développement de la vie microbienne. Des analyses morphologiques, élémentaires et moléculaires de la matière carbonée associée aux restes dégradés de microfossiles potentiels ont confirmé sa syngénicité et sa biogénicité. En particulier, la combinaison d'analyses élémentaires (fluorescence à rayons X et PIXE) et moléculaires (DUV et FTIR) ont révélé un enrichissement en métaux traces (e.g., V, Cr, Fe, Zn) et molécules aromatiques et aliphatiques associés à la matière carbonée, soutenant son origine biologique. Des observations MEB et MET ont permis d'observer des structures amorphes (e.g., films carbonés, cellules coccoïdales et lenticulaires) interprétées comme des restes dégradés de microorganismes et leurs produits (e.g., EPS). Néanmoins, une petite fraction de particules détritiques graphitisées d'origine probable du manteau (abiotique) et/ou biologique ont été identifiées. Cette étude souligne l'importance de préparer en amont l'analyse des échantillons de retour de Mars et sert d'exemple pour l'élaboration de protocoles pour la recherche de traces de vie fossiles dans les roches martiennes.

Mots clés : exobiologie, Mars, Terre primitive, matière organique, biosignatures, analogues, microfossiles, microanalyses, multi-échelle, ExoMars, Mars 2020, mission de retour d'échantillons

Searching for traces of life in a Mars analogue rock: The Kitty's Gap Chert

The objective of this thesis is to characterize the organic matter associated with potential traces of fossil life in ancient terrestrial rocks in order to maximize the detection of microfossils analogous to those that could be found on Mars and their associated biosignatures. Volcanic sediments from the 3.446 billion-year-old Kitty's Gap Chert contain putative primitive life forms considered analogues of potential primitive Martian life. I used complementary multi-scale analytical techniques to document the habitability of the paleoenvironment and assess the syngenicity and biogenicity of putative fossil traces of life. Sedimentological, petrological, mineralogical and geochemical analyses were used to reconstruct the paleoenvironment of deposition of the Kitty's Gap Chert sediments based on macroscopic and optical observations, as well as spectroscopic analyses (X-ray fluorescence, Raman, ICP-MS…). The results demonstrated that the sediments were deposited in a semi-enclosed basin, influenced by tides, rivers and hydrothermal fluids, whose conditions are compatible with the colonization and development of microbial life. Morphological, elemental and molecular analyses of the carbonaceous matter associated with the putative degraded remains of microfossils, as well as its multi-scale distribution, confirmed its syngenicity and biogenicity. In particular, the combination of elemental (X-ray fluorescence and PIXE) and molecular (DUV and FTIR) analyses revealed an enrichment in trace metal (e.g., V, Cr, Fe, Zn) and aromatic and aliphatic molecules associated with the carbonaceous matter, supporting its biological origin. SEM and TEM observations documented amorphous structures (e.g., carbonaceous films, coccoidal and lenticular cells) interpreted as the degraded remains of microbes and their products (e.g., EPS). Nevertheless, a small fraction of graphitized detrital particles of probable mantle (abiotic) and/or biological origin was identified. This study highlights the importance of prior preparations for the study of returned samples from Mars and serves as an example for the development of protocols for the search for fossil traces of life in Martian rocks.

Keywords: astrobiology, Mars, early Earth, organic matter, biosignatures, analogues, microfossils, microanalyses, multi-scale, ExoMars, Mars 2020, Mars Sample Return (MSR)

Centre de Biophysique Moléculaire
3 Avenue de la Recherche Scientifique
45071 Orléans Cedex 2